NATIONAL INSTITUTE FOR FUSION SCIENCE

Proceeding of A3 Foresight Program Seminar on Critical Physics Issues
Specific to Steady State Sustainment of High-Performance Plasmas
6-9 January, 2015, Nanning, China

Eds. L. Hu, S. Morita, Y.-k. Oh

Proceeding of A3 Foresight Program Seminar on

Critical Physics Issues Specific to Steady State Sustainment

of High-Performance Plasmas

6-9 January, 2015, Nanning, China

Edited by

Liqun HU, Shigeru MORITA and Yeong-Kook OH

Abstract

To enhance close collaborations among scientists in three Asian countries (China, Japan and Korea), A3 foresight program on Plasma Physics was launched from August 2012 under the auspice of JSPS (Japan), NRF (Korea) and NSFC (China). The main purpose of this project is to solve several key physics issues through joint experiments on three Asian advanced fully superconducting fusion devices (EAST in China, LHD in Japan and KSTAR in Korea) and other magnetic confinement devices to carry out multi-faceted and complementary physics researches. To summarize the progress and achievement in the second academic year under this A3 foresight program, the 6th workshop hosted by Institute of Plasma Physics, Chinese Academy of Sciences was held in Nanning during 6-9 January, 2015. The research collaboration carried out by young scientists was also encouraged with participation of graduated students. The three topics of steady state sustainment of magnetic configurations, edge and divertor plasma control and confinement of alpha particles are mainly discussed in addition to relevant studies in small devices.

Key words: magnetically confined devices, toroidal plasmas, high performance plasmas, steady state operation, edge plasma, divertor plasma and alpha particle.

Preface

Steady-state sustainment of high-performance plasmas is one of the crucial issues needed to be addressed for fusion reactor development. To enhance close collaborations among scientists in three Asian countries (China, Japan and Korea), A3 foresight program on Plasma Physics was started from August 2012 under the auspice of JSPS (Japan), NRF (Korea) and NSFC (China). The main purpose of this project is to solve several key physics issues through joint experiments on three Asian advanced fully superconducting fusion devices (EAST in China, LHD in Japan and KSTAR in Korea) and other magnetic confinement devices to carry out multi-faceted and complementary physics researches. The topics include steady state sustainment of magnetic configurations, edge and divertor plasma control and confinement of alpha particles.

The 1st coordinator meeting hosted by NFRI (Korea) was held in Jeju Island, Korea on 22nd August, 2012. The second meeting of A3 foresight program on Plasma Physics, i.e. the first seminar hosted by NIFS (Japan), was held in Kushiro, Japan from 22nd to 25th January, 2013. The third meeting hosted by ASIPP (China), the fourth meeting hosted by NFRI (Korea) and the fifth meeting hosted by NIFS (Japan) were held in Beijing, China, from 19th to 24th May, 2013, Gyeungju, Korea, from 3rd to 4th November, 2013 and Kagoshima, Japan from 23rd to 26th June, 2014, respectively. To summarize the progress and achievement in the past two academic years including intermediate evaluation in China on the A3 foresight program, the sixth meeting of A3 foresight program, hosted by Institute of Plasma Physics, Chinese Academy of Sciences (ASIPP), was held in Nanning during 6-9 January, 2015. The workshop was also motivated by reviews of ongoing collaborations and discussions on future collaborations to make further progress of the present A3 foresight program. The participation of young scientists to the workshop was strongly encouraged as well as the participation to the research collaboration.

In total 75 participants joined this meeting, i.e. 13 from Japan, 15 from Korea and 47 from China, and 63 scientific reports were submitted as the meeting proceeding. The achievement by young scientists reached more than half in both the oral presentations and scientific reports.

The presentation in the workshop is focused on the following topics which are the key issues in the present A3 foresight program and also the critical issues in both the tokamak and helical devices;

(i) Current drive and profile control

(ii) Transport of edge and divertor plasmas

(iii) Stability of edge plasma

(iv) Interaction between energetic particle and bulk plasma

(v) Relevant studies in small devices

A lot of productive results based on the A3 foresight program were presented in the workshop including fruitful reports from many young scientists. A remarkable progress is obtained through the A3 collaboration in the researches, in particular, the above-mentioned key physics issues. The organizing and program committees greatly appreciate all participants for their cooperation to make successful operation in the workshop and foundation in three countries of NSFC in China, JSPS in Japan and NRF in Korea for their continuous supports, with which the seminar was smoothly and successfully concluded.

Liqun HU, Shigeru MORITA and Yeong-KooK OH

Chairpersons of the Organizing Committee

Contents

Daiji KATO (NFRI)

Near UV-visible line emission from tungsten highly-charged ions in Large Helical Device

Ling ZHANG (ASIPP)

A fast-response extreme ultraviolet spectrometer for measurement of impurity line emissions in EAST tokamak

Chunfeng DONG (SWIP)

Preliminary result and initial analysis on radial profiles of impurity line emissions measured with EUV spectrometer on HL-2A

Yongcai SHEN (ASIPP)

Impurity behavior and molybdenum transport study on EAST

Liqing XU (ASIPP)

Repetitive "snakes" and their damping effect on core toroidal rotation in EAST plasmas with multiple H-L-H transitions

◆Session 6

Jinhyun JEONG (NFRI)

Upgrade activities of long pulse operation in KSTAR ECH/CD system

Sonjong WANG (NIFS)

The characteristics of RF heating in KSTAR

Haejin KIM (NFRI)

Reliable high power RF injection through the upgrade of ICRF transmission line system

Chengming QIN (ASIPP)

Current status of ICRF system on EAST

Bingjia XIAO (ASIPP)

First Quasi-snwoflake Divertor Experiment on EAST

◆Session 7

Yasushi TODO(NIFS)

Validation of comprehensive magnetohydrodynamic hybrid simulations for Alfvén eigenmode induced energetic particle transport in DIII-D plasmas

Youjun HU(ASIPP)

Simulations of energetic particles driven modes on EAST tokamak

Yi LIU (SWIP)

Development of the fusion-neutron diagnostics for the HL-2Atokamak

Guoqiang ZHONG (ASIPP)

Study of the ICRF minority heating performance by neutron signal on EAST

◆Session 8

Haishan ZHOU (ASIPP)

Effects of surface conditions on the plasma-driven permeation behavior through a ferritic steel alloy observed in VEHICLE-1 and QUEST

Jayhyun KIM (NFRI)

Exploration of extremely low q_{edge} regime in KSTAR

◆ Session 9

Mitsutaka ISOBE (NIFS)

LHD neutron diagnostics

Ichihiro YAMADA (NIFS)

Electron temperature measurement using backward and forward Thomson scatterings in the LHD Thomson scattering system

Satoshi OHDACHI (NIFS)

Heat pulse propagation experiments with the MHD event for the estimation of the magnetic field topology

Deng ZHOU(ASIPP)

The residual zonal dynamics in a toroidally rotating Tokamak

◆Session 14

Ting LAN (ASIPP)

Design of geometric phase measurement on EAST Tokamak

Jianyuan XIAO (USTC)

Numerical simulation on nonlinear effects in extraordinary to bernstein mode conversion

Yulei WANG (USTC)

Simulation of long-term dynamic behavior of runaway electrons

Wentao WU (USTC)

Stochastic simulation of backward runaway electrons

◆Session 15

Hongming ZHANG (Sokendai)

Evaluation of poloidal distribution from edge impurity emissions measured at different toroidal positions in Large Helical Device

Xianli HUANG (Sokendai)

Analysis of Z_{eff} profiles based on space-resolved measurement of extreme ultraviolet bremsstrahlung in the Large Helical Device

ZongXU (ASIPP)

Filterscope diagnostic System on EAST Tokamak

◆ Session 16

Zhengkun HAO (ASIPP)

Transmission simulation and shielding design of microwave for EAST bolometer diagnostic system

Manni JIA (Donghua Univ.)

Numerical modeling of 3D magnetic field topology under RMPs and the comparison with experimental observations on EAST

A3 Foresight Scientific Report

Name of visitor: Satoru SAKAKIBARA
Affiliation: National Institute for Fusion Science　(Japan)
Category: I
Study subject: Presentation on Foresight Program Workshop
Duration of visit: 2015 January 6 (Tue) - January 9 (Fri)
Place of visit: Nanning, China
Responsible person in visiting country: Liqun HU

1. Introduction

I joined the A3 Foresight Program Workshop held on Jan.6-9, 2015 in Nanning, China, in order to introduce recent progress of LHD experiments and discuss research results in Korea and China. Hear I introduce the present status of LHD, KSTAR, EAST and others.

2. Present status of LHD, KSTAR, EAST and others

2-1. LHD

The present status of LHD, KSTAR and EAST was introduced. I talked about "Recent progress of LHD experiments" and discuss experimental results related to extensions of high-temperature, high beta and steady state operation regimes. And also I introduced program of the deuterium experiments planned in the near future. As regards with extension of high temperature regime, ion temperature of 8.1 keV was obtained and both ion and electron temperatures reached to 6 keV in 2013FY experiments. The averaged beta value of 5 % had been obtained in previous experiments with weak magnetic field (0.425T), whereas we aimed at realization high-beta plasmas in low-collisaionality regime. The averaged beta of 3.7 % was realized in the configuration with 1 T. The plasma with 2 keV was successfully sustained for about 48 minutes by using ICRF and ECH. The plasma was terminated by contamination of heavy impurity, which has been studied from a viewpoint of PWI study.

2-2 KSTAR

Dr. Yeong-Kooh Oh talked about status of the KSTAR operation and upgrade. Main upgrades were as follows:

- ✓ The passive stabilizer for suppression of VDE was upgraded, which realized stable operation under the large number of VDE up to 1MA.
- ✓ W-marker tiles were fabricated and installed on divertor for PWI study
- ✓ 200MV/A motor generator was installed to ramp-up plasma current over 1MA
- ✓ Heating devices such as 3rd beam of NBI-1 were improved

The following discharges were successfully demonstrated:

- ✓ Long-pulse H-mode discharge up to 48 seconds at 0.5 MA
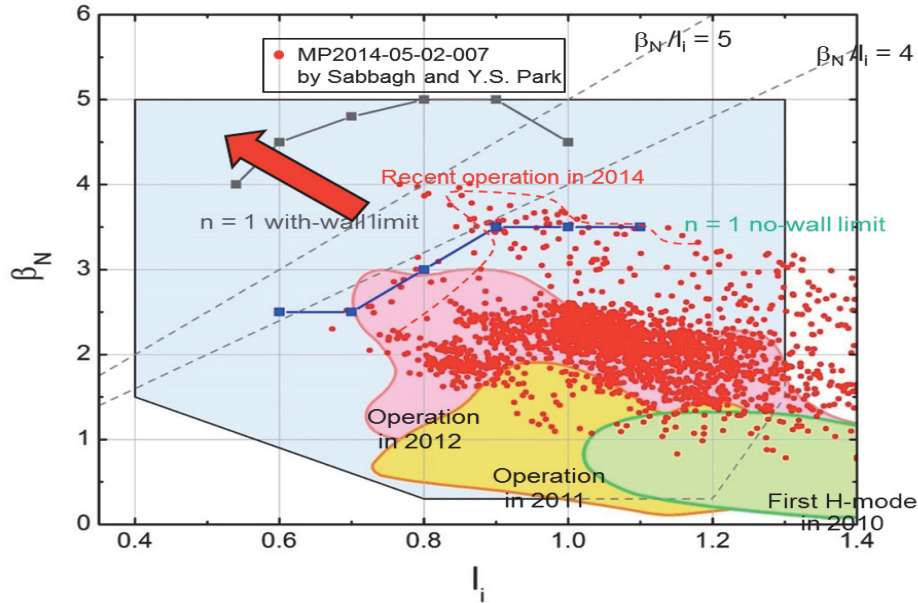
Fig.1 Achievement of high normalized beta value

✓ Large current H-mode discharge up to 1MA
✓ Higher β_N up to 4.0 (Figure 1)

In KSTAR, lowest intrinsic error field (dB/B ~ 10^{-5}) and TF ripple compared to present other tokamaks were confirmed. It is effective to avoid violent MHD instabilities such as locked mode, which was demonstrated by applying RMP in-vessel coils. Also n=2 RMP coils were applied to sustain ELM suppression for 5 seconds. The n=1 RMP coils could reduce heat flux due to ELM.

2-3 EAST

Prof. Liang Wang introduced recent progress in EAST. EAST aims at long pulse high performance operations, and heating devices and PFC have been upgraded. In 2014, the power of LHCD increased to 10MW, and ICRH and NBI were improved to 12MW and 4MW, respectively. ITER-like PFC (water-cooled, cassetted and W top divertor) was installed. New RMP systems with 16 coils were set for error field correction, RWM control, ELM control and 3D physics study. Figure 2
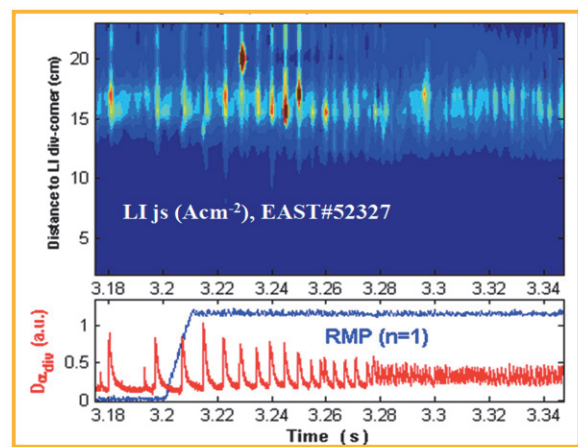
Fig.2   ELM control by n=1 RMP coils

shows the ELM control by n=1 RMP coils. Type-I ELM was successfully suppressed by n=1 RMP. The SMBI and Li aerosol injection were also useful tool for ELM mitigation, and ELM frequency and amplitude could be controlled by SMBI, and Li injection realized ELM-firee H-mode. The interesting comparison of H-mode in different heating methods was reported as shown in Figure 4. It shows that H-mode heated by LHW is quite stable compared to NBI dominated H-mode.
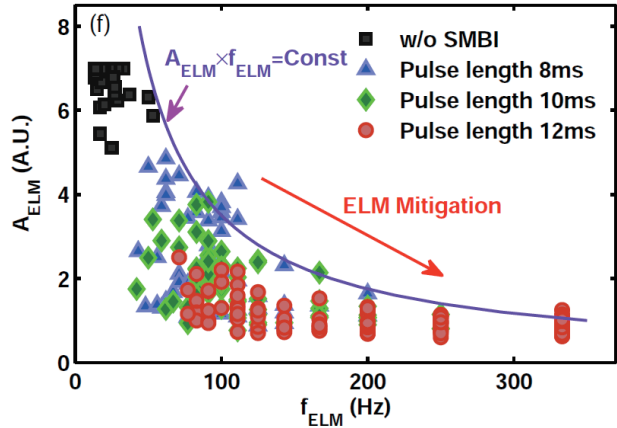
Fig. 3　change of ELM amplitude as a function of the frequency

2-4 Other devices

In J-TEXT tokamak in Huazhong Univeristy, turbulent particle and momentum transport has been studied by electrode biasing. Dr. Z.P.Chen reported that plasma edge fluctuations and turbulent particle transport are obviously suppressed under bias in different degrees with different polarities. Edge rotation can be greatly modified by electrode biasing. The experiments show that the intrinsic rotation torque exists at the edge.

The development of a space-resolved EUV spectrometer in HL-2A was reported by Dr.
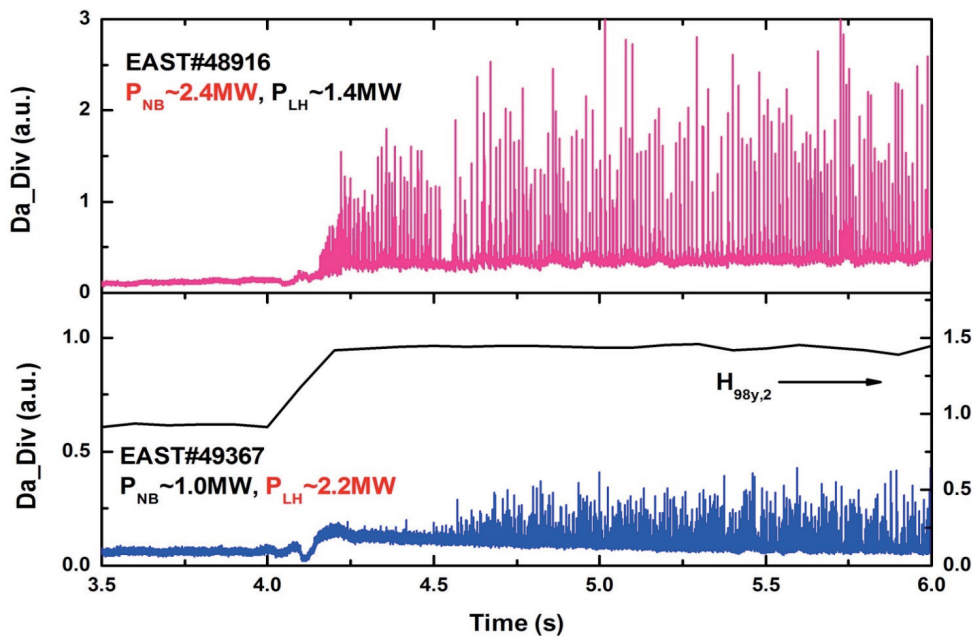
Fig. 4 (Top) NBI dominated H-mode and (Bottom) LHW H-mode

Chunfeng Dong. Dr Yi Liu presented the development of energetic particle diagnostics in HL-2A. The detection of the neutron emission rate is performed by means of a 235U fission chamber. The neutron camera was also installed, which enables us to estimation of neutron profile. The preliminary results by using these measurements were shown in this meeting.

3. Summary

There were 65 presentations in A3 Foresight program workshop, and many researchers and students discussed experimental and theoretical results of various topics. The next 7th A3 meeting will be held on May 19-22, 2015, in Gangwon, Korea.

Recent results of long pulse discharge and prospect of steady-state operation in KSTAR

Young-soon Bae[a], Y.M. Jeon[a], S.W. Yoon[a], S.H. Hahn[a], J. Kim[a], D.C. Seo[a], J.S. Kim[a], H.T. Park[a], W. Cho[a], J.H. Jeong[a], M. Joung[a], J.W. Han[a], I.H. Rhee[a], K.S. Lee[a], H.K. Kim[a], H.L. Yang[a], L. Tezoro[a], J.G. Kwak[a], Y.K. Oh[a], J.M. Park[b], D. Humphrey[c], H.S. Kim[d], C.S. Byeon[d], Y.S. Na[d], S.H. Jeong[e], T.S. Kim[e], D.H. Chang[e], K. Watanabe[f], A. Kojima[f], M. Kashiwagi[f], M. Dairaku[f], M. Hanada[f], T. Inoue[f], K. Sakamoto[f], R. Ellis[g], J. Hosea[g], H. Park[h,a], E.M. Choi[h], W. Namkung[i], M.H. Cho[i], and KSTAR team

[a]National Fusion Research Institute, Daejeon, Korea
[b]Oak Ridge National Laboratory, Oak Ridge, US
[c]General Atomics, San Diego, US
[d]Seoul National University, Seoul, Korea
[e]Korea Atomic Energy Research Institute, Daejeon, Korea
[f]Japan Atomic Energy Agency, Naka, Ibaraki 311-0193, Japan
[g]Princeton Plasma Physics Laboratory, Princeton, US
[h]Ulsan National Institute of Science and Technology, Ulsan, Korea
[i]Pohang University of Science and Technology, Pohang, Korea

Email: ysbae@nfri.re.kr

The main mission of KSTAR is to demonstrate the advanced tokamak operation mode with high performance and steady state for 300 s. Key technologies for the long pulse operation with high performance is addressed to be developed in KSTAR. KSTAR is presently focusing to develop the necessary technologies for long pulse H-mode discharge before the high performance operation phase which requires the high power auxiliary heating and current drive system including efficient off-axis current drive. Recently, we achived a 43-s long pulse H-mode discharge at the plasma current of 0.6 MA with 4.3 MW neutral beam injection. The achieved $\beta_N \sim 2$ and stored energy is about 400 kJ. Transient advanced operation mode with the fully non-inductive and $\beta_N \sim 3$ has been also demonstrated at the lower plasma current of 0.4 MA and earlier neutral beam injection. This high performance phase is not sustained with long pulse due to the lack of radial position controllability for earlier neutral beam injection. Toward the higher performance steady state operation in KSTAR, we plan to develop off-axis neutral beam injector (NBI) and new two-frequency electron cyclotron heating (ECH) system. By combination of on-axis and off-axis NBI and ECCD, the fully non-inductive operation with higher β_N is predicted using FASTRAN transport solver. The target performance of $\beta_N \sim 5$ and high bootstrap current fraction should need additional far off-axis current drive by lower hybrid current drive (LHCD) with limited off-axis NBI power.

1. Introduction

The target operation mode in KSTAR is an "advanced tokamak" (AT) operation mode which aims to demonstrate β_N ($=100\beta_t/(I_p/aB_t)$) = 5 and bootstrap current fraction, $f_{BS} > 0.5$. The β_t is defined as plasma stored energy to toroidal magnetic energy. This target is preferrable requirement in fusion reactor in terms of high fusion output power and minimized recirculating power for auxiliar heating and current drive system. This operation regime will require high power off-axis current drive by off-axis neutral beam injector (NBI), electron cyclotron current drive (ECCD), and lower hybrid current drive (LHCD) by predictive study using the time dependent integrated simulation code. The attractiveness of off-axis NBI is well demonstrated in DIII-D experiments for the steady state high performance plasma with enhanced MHD stability limit [1, 2].

The research plan in KSTAR is also emphasizing the long pulse operation issues that should be addressed in the other important mission in KSTAR. It aims to develop key technologies of long pulse operation maintaining the steady-state high performance plasma for very long pulse duration longer than wall saturation time. Since the available high power heating and current drive system is only on-axis NBI, KSTAR operation is so far aiming to achieve long pulse standard H-mode discharge since 2012. Adding the third neutral beam source and motor generator enabled the longer pulse H-mode discharge at the level of plasma current, 0.6 MA at toroidal magnetic field of 2 T. This paper presents the recent results of the long pulse H-mode discharge and predictive studies of high performance steady state operation scenario using off-axis current drive toward the final target of KSTAR operation, $\beta_N \sim 5$ and $f_{BS} > 0.5$ at the plasma current (~1 MA).

2. Recent results of long pulse H-mode discharge

The main heating and current drive sources in KSTAR is at present NBI and ECH. The long pulse discharge in recent campaign has been progressed by the upgrade in NBI power and long pulse capability in ECH. The KSTAR first neutral beam injector (NBI-1) system is recently upgraded with final third beam source [3,4]. In recent campaign, the injected power was maximum 4.5 MW, which is basically limited by insufficient conditioning of beam sources after some modifications in accelerator grid system for the enhanced transport efficiency by the partly beam focusing [5]. The third beam (no. 3) line is less tangential and expected to have higher shine-through armor loss at inboard tile compared with other two beams. The upgrade of ECH launcher with water-cooled mirrors also enabled long pulse H-mode discharge with higher toroidal magnetic field for second harmonic ECCD. The successful 50-s long pulse is obtained using JAEA 170 GHz gyrotron and water-cooled mirror made by CuCrZr alloy using e-beam welding technology. Using the feedback control in anode voltage and cathode heater voltage, the stationary RF output is achieved up to 50 s pulse duration without the cut-off of RF oscillation.

For the long pulse H-mode discharge, the gain elements for plasma current in plasma control matrix is optimized first to avoid the fast grid power (MVA) consumption by the fast current change in solenoid coils. The power capacity of the reactive power compensator (RPC) in KSTAR is one of main limitation for plasma discharges. The typical long pulse H-mode discharge attempted in KSTAR is designed to have lower single null diverted plasma with outer strike-points at the outer divertor, i.e., the intersections of the separatrix with outer divertor. But, the exhaust particles collected in the divertor during long pulse discharge caused a localized thermal load around strike-points, and it prevented the longer pulse discharge by the temperature interlock system of plasma face component (PFC). Please note that active water cooling of divertor is not presently available. Later, a sweeping of strike-points is attempted to spread on a larger region in divertors by a periodic sweeping of the radial and vertical position of lower X-point. But, the periodic control of X-point position was not well working. Therefore, X-point is moved and fixed to have outer strike-points intersecting the central divertor. Figure 1 shows the result of 43-s long pulse H-mode discharge at the plasma current level of 0.6 MA using only NBI (~ 4.3 MW) with new X-point target accompanying outer strike-points at the central divertor. The high β_N (2.1) is achieved (β_t = 1.26%) and W_{tot} is ~ 0.4 MJ. In this discharge, the use of motor generator helped to extend pulse length at the higher plasma current. Figure 2 shows the magnetic flux lines in the scrape-off-layer (SOL) region and the captured image by another tangential infrared camera whose view is focused at the lower divertor region. It shows that the strike-points are moved to the central region and the heat load spreads on the large region.
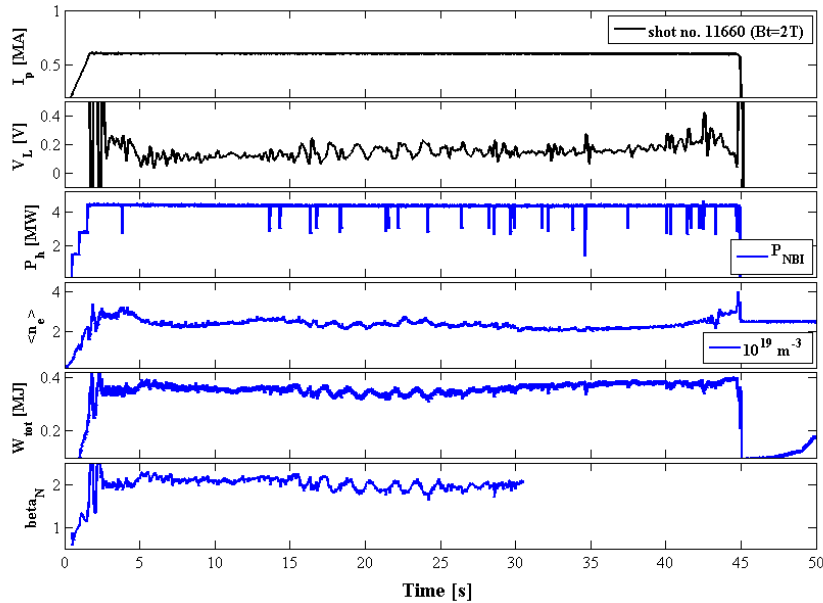
Fig. 1. The waveforms of plasma parameters of the recent 43-s long pulse discharge at the plasma current of 0.6 MA using only NBI power of 4.3 MW with lower single null shape. In this discharge, the toroidal magnetic field is 2 T, the line averaged density is about $2 \times 10^{19}/m^3$, the maximum stored energy is very close to 0.4 MJ, and the β_N obtained from EFIT (data is not stored after ~ 30 s) is 2.
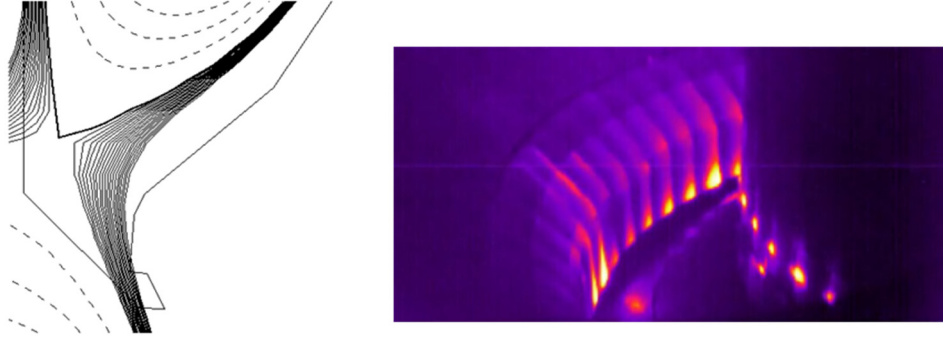
Fig. 2. Magnetic flux lines reconstructed by the real-time EFIT equilibrium solver and the captured image by tangential infrared camera at lower divertor region (11660).

In this long pulse H-mode discharge, the plasma is terminated by the limitation of grid power capacity for poloidal coil power system. It is strongly suspected that the strong plasma wall interaction in the divertor region is occurring according to D_α signal. It caused the increase of error of X-point control and the saturation of corresponding divertor coil current (PF4 coil in KSTAR), hence the fast increase of grid power consumption.

While the long pulse H-mode discharge experiments are being carried out to extend longer pulse duration under limitations of electricity of PF coil power system, the advanced plasma operation scenario is also attempted with reduced plasma current for the higher β_p and early heating with current ramp rate of 0.3 MA/s in the current ramp-up phase. Figure 3 shows a high β discharge experimental result. The on-axis ECH heating and current drive in the startup phase followed by early neutral beam injections enabled the fully non-inductive high β_p (max. 3.5) and β_N (max. 3.1) for 2 s after flat-top at the line averaged density level of ~ $2.8 \times 10^{19}/m^3$. In this experiment, the third beam is injected after the flat-top to avoid the damage of the inboard shine-through armor loss. However, the high β regime is oscillatory due to the lack of robust radial control. The present radial control only by outer superconducting poloidal field coils is not sufficiently fast to keep the plasma from immediate outward radial movement touching the outboard limiter in early NBI heating case and hence the back transition to L-mode (see fig. 3 (d) and (f)). The interpretative analysis at the high β regime shows the f_{NI} ~ 1.1 with the NB-driven current fraction, f_{NB} ~ 0.4, and high bootstrap current fraction, f_{BS} ~ 0.7.
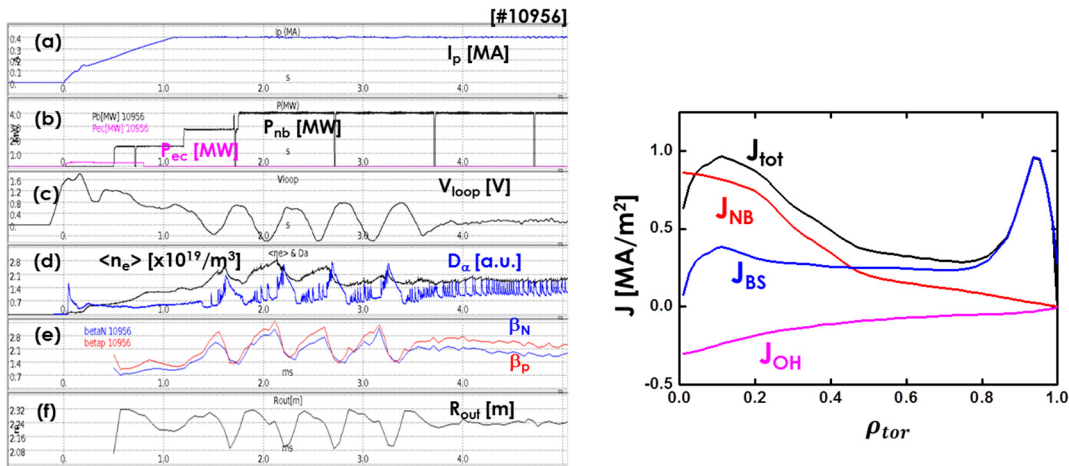
Fig. 3. The transient fully non-inductive high β discharge with reduced plasma current to 0.4 MA and early auxiliary heating and current drive. (a) is the plasma current, (b) is the auxiliary heating power, (c) is the smoothed loop voltage, (d) line-average density and D_α signal, (e) is the β_N and β_p obtained in EFIT solver, and (f) is the outer plasma boundary position. The achieved highest β_N and β_p is about 3.1 and 3.5, respectively and the confinement factor, H_{89} is about 2 by interpretative analysis.

3. High performance steady-state operation scenario in KSTAR

To access the high performance steady-state operation, the external current drive should be off-axis for the high confinement, high low-n ideal wall β_N limit, and high bootstrap current fraction. In particular, the high bootstrap current fraction plasma regime is important for steady-state tokamak operation for very long pulse because it reduces the required power for external non-inductive current drive. As high non-inductive plasma with high β_N using off-axis NBI and ECCD has been shown in DIII-D experiments toward steady state high performance operation scenario development demonstrated, the key part is the broaden current density and pressure profiles by off-axis neutral beam injection with elevated q_{min} (the minimum safety factor). The off-axis ECCD can be effective to broaden the total current density profile and improve the coupling of the plasma to the conducting vacuum vessel wall, hence the effectiveness of ideal-wall stabilization. This report is to find the fully non-inductive solutions with high β_N (> 3) and appropriate q_{95} using off-axis NBI and ECCD in KSTAR as a first step toward the final goal of β_N (~5) with high bootstrap current fraction. The goal of β_N (~ 5) requires the excellent confinement associated with the formation of an ITB at large minor radius in all channels of density, electron temperature, ion temperature, and rotation. The ITB formation is deeply associated with strong reversed magnetic shear profile with high qmin which might needs further off-axis current drive such as lower hybrid current drive (LHCD).

Figure 4 shows the preliminary design of 4 MW off-axis NBI in KSTAR. The two off-axis beams injections are designed with maximum tilt angle of 7.5 deg in vertical plane from top and bottom. This design shows very efficient current drive at mid-radius.
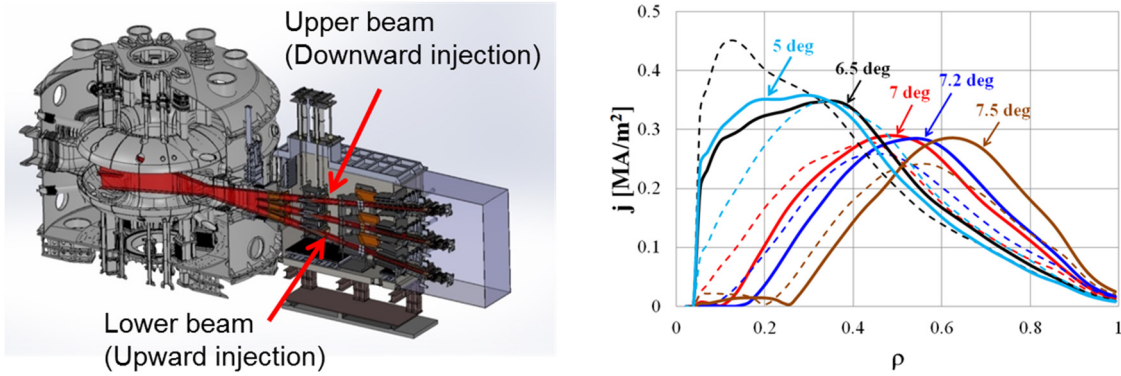
Fig. 4. The preliminary design of 4MW off-axis NBI and predicted current drive profile using NUBEAM code.

The second NBI is being considered as a tangential off-axis neutral beam injection to have the center of the two beam sources aimed at a sufficient vertical offset from the geometric center of the plasma. Ideally the system should be made such that the beam is injected in the same horizontal plane at an elevation below or above the median plane. So the off-axis plan by tilting the beam angle in vertical plane is an expedient method. In this steering angle, the beam transport ratio is calculated by 85% using the superposition of Gaussian beam profile of each beam-let with a divergence angle of 1 deg with all beam-let focusing and the beam source size same as the present beam source in existing NBI. The maximum vertical steering angle is mainly limited by the maximum acceptance of port duct and passive stabilizer.

The FASTRAN transport solver [6] is used for the predictive studies for the steady state scenario with high β_N, Figure 5 shows a predicted steady state scenario using only NBI and 105 GHz ECCD. In this calculation, the plasma current is 0.6 MA, the toroidal magnetic field is 1.8 T. The equilibrium plasma shape is lower single null with elongation factor of 1.8. The input heating mixture is 8 MW NBI (4 MW on-axis NBI and 4 MW off-axis NBI based on present design described in previous section) and 2.4 MW ECCD (3 MW source power) aimed at normalized minor radius, $\rho \sim 0.35$. Due to the low ECCD power, the EC beam is not aimed at far off-axis ($\rho \sim 0.5$) to maximize the current drive to obtain the reversed magnetic shear profile. The plasma density is determined with trade-off between the bootstrap current fraction and current drive efficiency to reach the fully non-inductive regime. The obtained non-inductive current fraction, $f_{NI} = 1.02$ with bootstrap current fraction $f_{BS} = 0.5$, and the $\beta_N = 3.45$. The safety factor profile is

reversed with minimum value of 1.54 (q_{min}) at $\rho = 0.35$ and $q_{95} = 5$.
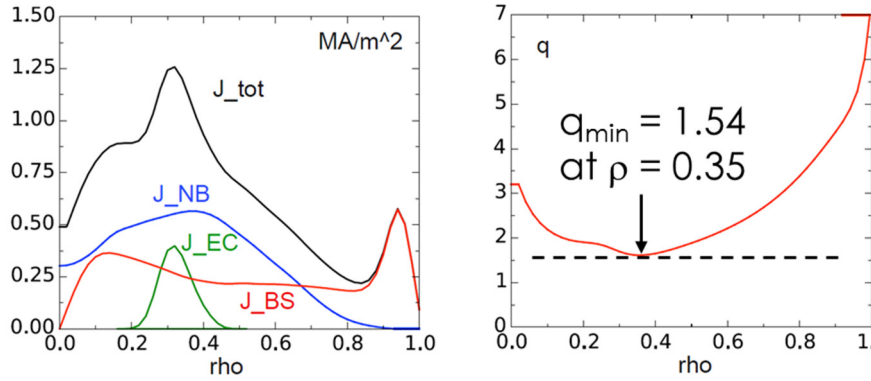
Fig. 5. The current density profile and safety factor profile calculated by FASTRAN solver.

The steady state regime with higher q_{min} at large radius, which is beneficial on the low-n MHD instability such as 2/1 NTM, would require more ECCD power aimed at far off-axis or efficient far off-axis current drive source such as LHCD at higher plasma current level (~ 1 MA) for the large ITB formation extended to $\rho \sim 0.7$. With the help of LHCD, the steady state scenario regime aiming at fully non-inductive operation and $\beta_N \sim 5$ is being searched using FASTRAN solver. The higher toroidal magnetic field will be favorable for the efficient current drive by 5 GHz LHCD in KSTAR through the strong single pass Landau damping particularly in H-mode pedestal density profile in the aspect of LH wave accessibility.

4. Summary

Recent experimental results showed the big progress in the long pulse standard H-mode discharge at the plasma current level of 0.6 MA. The plasma shape and safety factor is not designed for ITER similar shape due to various limitations such as the vertical stabilization for the higher plasma current, heat load at the divertor, limited heating power. Toward the high performance steady state operation mode, the 100% non-inductive high β_p discharge is achieved with early heating and current drive in the ramp-up phase and little reduced plasma current. The time-dependent self-consistent integrated transport simulation shows that new off-axis NBI and upgraded EC power enables to access steady state operation of $\beta_N = 3.45$ with $q_{95} = 5$ and $q_{min} = 1.54$. The steady state operation with higher β_N and high q_{min} will be investigated with LHCD or additional EC power.

References

[1] C.T. Holcomb et al., EX/1-5, IAEA FEC, San Diego, Oct. 8-13, 2012.
[2] J.R. Ferron et al., Phys. Plasmas20, 092504 (2013).
[3] Y.S. Bae et al., Fusion Eng. Design 87, 1597 (2012)
[4] D.H. Chang et al., Fusion Eng. Design 86, 244 (2011).
[5] T.S. Kim et al., Plasma Sci. Tech. 16, No.6, 620 (2014).
[6] J.M. Park, DPP/APS, Nov. 2013

Recent progress in EAST towards long-pulse high-performance operations

Liang Wang, Baonian Wan, Jiangang Li, Houyang Guo, Yunfeng Liang, Guosheng Xu, Xianzu Gong, and Andrea Garofalo for the EAST team and international collaborators*

Institute of Plasma Physics, Chinese Academy of Sciences, Hefei 230031, China

E-mail: bnwan@ipp.ac.cn, lwang@ipp.ac.cn

Abstract: Significant advance has been made in EAST on both physics and technology fronts towards the long-pulse operation of high-confinement plasma regimes since the last IAEA-FEC. The EAST capabilities have been greatly upgraded, including the significantly enhanced CW H&CD system with up to 26 MW heating power, more than 70 diagnostics, ITER-like W monoblock top divertor, two internal cryo-pumps and RMP coils, enabling EAST to investigate long-pulse H-mode operation with dominant electron heating and low input torque, and to address some of critical issues for ITER. Remarkable physics progress has been made on controlling transient ELM and stationary divertor heat fluxes, e.g., ELM mitigation/suppression/pacing with LHCD and SMBI, real-time Li aerosol injection for long pulse ELM-free H-mode, edge coherent mode for continuous pedestal particle and power removal, and the combination of LHCD and SMBI to actively modify the stationary power footprint by regulating the divertor conditions. *In the 2014 commissioning campaign, long-pulse high-performance H-mode up to 28 s has been obtained with $H_{98} \sim 1.15$, i.e., about $\sim 30\%$ higher than the record 32 s H-mode achieved in the 2012 campaign.* Other key new experimental achievements are: (1) high performance H-mode with $\beta_N \sim 2$ and plasma stored energy ~ 220 kJ, (2) high performance operation with core $T_e \sim 4.5$ keV, (3) H-mode plasma enabled by NBI alone or LHW+NBI modulation for the first time in EAST, (4) demonstration of a quasi snowflake divertor configuration, (5) new findings on L-H transition and pedestal physics.

1. Introduction

Experimental Advanced Superconducting Tokamak (EAST) [1-3] is the first fully superconducting torus of advanced divertor configuration and heating scheme similar to ITER, which started operation in 2006. The main objectives of EAST are to demonstrate long pulse divertor operation over 1000 s and high performance H-mode operation over hundreds of seconds, and to address key physics and engineering issues for the next step fusion devices such as ITER, CFETR (China Fusion Engineering Test Reactor, currently under conceptual design) and DEMO. The major and minor radii of EAST are $R = 1.7 - 1.9$ m and $a = 0.4 - 0.45$ m, respectively. The toroidal field and maximum plasma current presently achieved are $B_t = 3.5$ T and $I_p = 1$ MA, to be extended to 4 T and 1.5 MA by reducing the temperature of the superconducting magnets from 4.5 to ~ 3.8 K. The machine can be operated in lower single null (LSN), double null (DN) and upper single null (USN) divertor configurations with a flexible poloidal field control system, which can also be periodically switched between different configurations to facilitate long-pulse operation.

The first H-mode in EAST was achieved in 2010. In the 2012 campaign EAST has achieved a highly reproducible long pulse H-mode over 30 s [3] and steady-state divertor operation over 400 s with nearly fully non-inductive current drive [2]. EAST has just finished its Phase-II upgrade and the 2014 commissioning campaign is ongoing. In addition to the engineering upgrade, exciting progress has been made on H-mode physics for long pulse operations in the last two years. This overview will report the main advances in long pulse H-mode physics since the last IAEA-FEC. The technique and engineering advances towards long pulse operations will also be presented.

2. EAST upgrade capabilities

To improve the machine capabilities and power/particle exhaust toward advanced steady state high performance operations, EAST carried out a new, extensive Phase-II upgrade, started in September 2012 and completed in May 2014. Nearly every sub-system except superconducting magnets has been upgraded or modified to enable higher performance and truly steady state operation. The major upgrades are as follows:

- H&CD systems have been upgraded to 26 MW, including 4 MW, CW, 2.45GHz and 6MW, 4.6GHz LHCD systems; 12MW, CW ICRF system with a wide band frequency band of 24-70MHz; 4MW, 50-80keV NBI system. The second 4MW NBI and 2MW ECRH of 140GHz will be ready for the next campaign.
- The upper divertor has been converted into an ITER-like W monoblock configuration with up to 10 MW/m^2 heat exhaust capability.
- More than 70 different diagnostics have been modified, upgraded or newly implemented, with key profiles of plasma parameters available.
- A top internal cryopump with a 160 m^3/s pumping speed has been newly installed for improving divertor particle exhaust capability in addition to the existing bottom internal cryopump.
- 16 ITER-like RMP coils together with several other new ELM mitigation methods, such as supersonic beam molecular injection (SMBI), CW Li&D$_2$ pellet injection, real time Li aerosol injection, and gas puffing from different target plates.
- 2 ITER-like VS coils have been installed to better control plasma vertical displacements.

FIG. 1 EAST internal plasma phase component structure.

- Fast control power supply and robust plasma control system have been upgraded to facilitate the control of high plasma performance discharges.
- Other systems, such as the poloidal and toroidal field power suppliers, cryogenic and transmission line, high-temperature superconducting current leads and fueling systems have also been upgraded towards more reliable operation conditions.

Fig. 1 shows the internal view of EAST superconducting tokamak with top tungsten divertor, lower graphite divertor, molybdenum HFS & LFS plasma facing components (PFCs), main auxiliary heating systems and a number of diagnostics. The newly completed upgrade signals the start of the EAST Phase-II program.

3. Transient ELM and stationary heat flux control

New physics understanding has been obtained in controlling transient edge-localized-mode (ELM) and stationary divertor heat fluxes in EAST since the last IAEA-FEC, such as ELM mitigation/suppression/pacing with LHCD [4], effect of SMBI on the pedestal [5], ELM pacing by lithium/deuterium pellet injection, real-time Li aerosol injection for achieving long pulse ELM-free H-mode [6], edge coherent mode for continuous pedestal particle and power removal [7-8], and the synergy of LHCD and multi-pulse SMBI to actively modify the stationary power footprint pattern by regulating the divertor conditions [3,9].

3.1. LHCD

ELM mitigation has been achieved on EAST when lower hybrid waves (LHWs) are applied to H-mode plasmas sustained mainly with ICRH [4]. This has been demonstrated to be due to the LHW-induced helical current filaments (HCFs) flowing along field lines in the scrape-off layer, which changes the edge magnetic topology and leads to the splitting of strike points, similar to RMPs. In comparison to previous RMP ELM mitigation experiments, ELM mitigation with LHWs on EAST has been achieved with a wider range of q_{95} as shown in Fig. 2. In this experiment, a long ELMy H-mode phase is established mainly by ICRH with an input power of 1 MW in a relatively high-density regime (n_e/n_G ~0.9) after a fresh Li wall coating [3]. The plasma currents in the three discharges were 0.4, 0.45 and 0.5 MA, which correspond to a q_{95} of 4.7, 4.2 and 3.8, respectively. A 10 Hz modulation of LHWs with a power of 1.3 MW has a 50% duty cycle in all three discharges, thus the duration of the LHW-off phase is 50 ms, which is about half of the energy confinement time. Without LHWs, the ELM frequency is fairly regular at ~150 Hz.

FIG. 2 Effect of LHWs on ELMs by modulating LHW power in a series of target H-mode plasmas sustained by ICRH with a different edge safety factor, q_{95} of 3.8, 4.2 and 4.7. The time traces are the peak ion-flux in the outer divertor (red), and injected LHW power.

When the LHWs were switched on, both a significant increase in ELM frequency (up to ~1 kHz) and a significant reduction in ELM peak particle flux (up to a factor of 4) were observed. For the low q_{95} discharge, the influence of LHWs on ELMs can be rather quick in time, and ELMs can even be completely suppressed. However, a longer delay time before the appearance of large ELMs was observed in the high q_{95} discharge after fast switching-off of LHW, sometimes longer than 50 ms, as shown in Fig. 2 (c).

3.2. SMBI

Recently, a new technique with SMBI has been demonstrated to be effective for ELM mitigation in HL-2A, KSTAR and EAST. However, the mechanism for ELM mitigation by SMBI still remains unclear. A new analysis has shown that the intermittent small scale turbulence generated by SMBI inside the pedestal is responsible for ELM mitigation and suppression [5]. We find, for the first time, that the particle flux released by ELMs is strongly correlated with large scale low frequency turbulence, but anti-correlated with small scale high frequency turbulence, as shown in Fig. 3. It has been shown that ELM mitigation is due to the enhancement of the particle transport in the pedestal, caused by

FIG. 3 Particle flux Γ_{div}^{ELM} released by ELMs versus small (a) and large (b) scale turbulence intensity averaged over 40 ms. The turbulence inside the pedestal is measured by a 74 GHz Doppler reflectometry in X-mode.

the intermittent small scale turbulence induced by SMBI or self-generated by mitigated ELMs. ELM suppression requires that the small scale turbulence intensity exceeds a critical threshold. The influence time of SMBI for ELM mitigation is governed by this turbulence.

3.3. Real-time Li aerosol injection for long-pulse ELM-free H-mode

ELM suppression using active Li aerosol injection has been successfully demonstrated on EAST. It was found that ELMs gradually decreased during real-time Li injection, as shown in Fig. 4. With successive real time Li injection, long-pulse, teproducibleELM-free H-mode plasmas were obtained with ELM-free phase up to 18 s [6]. It is truly remarkable that Li injection appear to promote the growth of ECM (section 3.4), owing to the increase in Li concentration and hence collisionality at the edge, as predicted by GYRO simulations.

With lithium pre-coated walls, real time Li injection can further reduce recycling and suppress ELMs, while avoiding impurity accumulation in the core plasma. As shown in Fig. 4, compared with a plasma (EAST#41081) without the active Li injection, ELMs, the induced MHD activity and divertor peak heat flux in an H-mode plasma (EAST#41079) were effectively suppressed by the real-time injection of Li aerosol at a flow rate of about 50 mg/s, as highlighted by the grey shade. Li aerosol injection also enhances edge radiation near the divertor.

FIG. 4 Comparison of two similar plasmas with and without Li aerosol injection, P_{ICRF}~0.8 MW, P_{LHW}~1.4 MW, Bt~1.9 T, DN, H_{98} ~ 0.8.

This new steady-state ELM-free H-mode regime, enabled by real-time Li injection, may open a new avenue for next-step fusion development.

3.4. ECM in long pulse H-mode

An edge coherent mode (ECM) with frequency near the local electron diamagnetic frequency (20-90 kHz) in the steep-gradient pedestal region has been found to persist throughout a long-pulse H-mode regime [7,8]. The ECM has been observed with the pedestal electron collisionality, $\nu_e^* = 0.5$-5. The appearance of the ECM is independent of ICRF or LHCD heating schemes. The associated H-mode regime is either ELM-free or mixed with irregular small ELMs with target heat load < 2 MW/m^2, exhibiting a good global energy confinement quality with H_{98} = 0.8-1.The ECM usually starts to appear during pedestal buildup following an L-H transition, or a transition from the ELMy to ELM-free phase. Fig. 5 shows an ELM-free H-mode period with the ECM detected by the Langmuir probes. Detailed measurement of the newly developed gas puff imaging system in a similar discharge shows that ECM appears to be localized at the steep-gradient pedestal region, peaking at ~1 cm inside the separatrix with a radial spread of ~1 cm. The ECM exhibits a strongly tilted structure in the plane perpendicular to the local magnetic field lines and propagates in the electron diamagnetic drift direction with poloidal wavelength λ_θ ~ 8 cm, corresponding to a poloidal mode number m over 60.

Clear evidence of particle and heat exhaust by the ECM has been provided by a new diamond-coated reciprocating probe array. The plasma potential fluctuation associated with the ECM lags behind the electron pressure fluctuation by a phase angle of $\alpha \sim 10°$ and the electron density fluctuation by $\alpha \sim 20°$. The ECM-driven radial particle flux is estimated to be $\Gamma = 2\text{-}4 \times 10^{20} \text{m}^{-2}\text{s}^{-1}$, and outward heat flux $Q = 5\text{-}10$ kW/m^2. The total heat exhaust is estimated to be 0.2-0.4MW, corresponding to about 15%-30% of the loss power. Thus, ECM can provide an effective channel for continuous particle and heat exhaust across the pedestal, which is highly beneficial for ELM mitigation and long pulse H-mode sustainment.

3.5. Synergetic effect of LHCD and SMBI on stationary heat flux control

In section 3.1, we have demonstrated that LHCD induces a profound change in the magnetic topology of the edge plasma, leading to a 3D distortion of the edge magnetic topology similar to RMPs. What is truly remarkable [3] is that we have demonstrated on EAST, for the first time, that the stationary divertor heat flux footprint can be actively modified by transferring heat from the outer strike point (OSP) to the striated heat flux (SHF) region in plasmas heated by LHCD, via regulating divertor particle fluxes with multi-pulse SMBI, as shown in Fig. 6. For OSP, increasing the ion flux leads to an initial decrease and then a nearly constant value of the divertor power flux, as expected for a high recycling divertor, $q_{OSP} \sim \Gamma_i T_{div}$, where the divertor temperature T_{div} decreases as the ion flux Γ_i increases, i.e., $T_{div} \sim 1/\Gamma_i$, at constant edge power flow. On the contrary, for SHF, the divertor power flux increases with the ion flux on the field lines directly connecting the divertor to locations in the edge transport barrier. On these field lines the divertor electron temperature is expected to be similar to $T_{ped} \sim 350$ eV for typical long-pulse H-mode plasmas in EAST, so that $q_{SHF} \sim \Gamma_i T_{ped}$ increases with ion flux [10].

This potentially offers a new means for steady state heat flux control, which is a key issue for next-step fusion development. Similar results have also been observed with
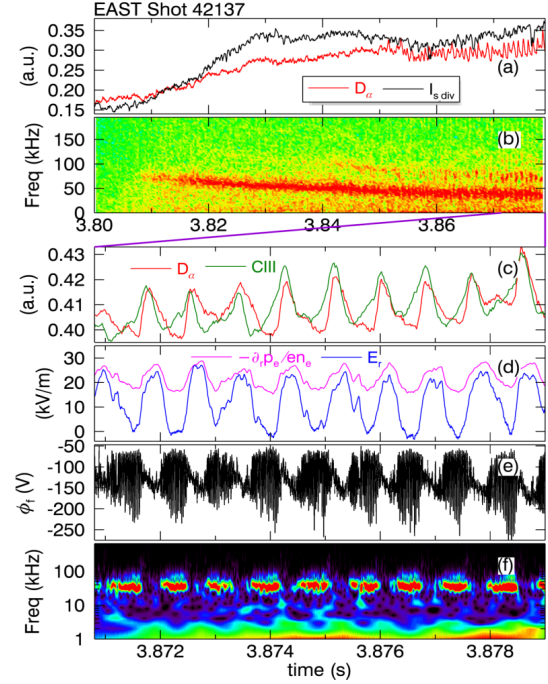
FIG. 5 Time evolution of (a) divertor D_α emission (red) and ion saturation current from a target probe (black) near the strike point, (b) power spectrum of a floating potential at ~ 8 mm inside the separatrix. The zoom-in plots show the time evolution of (c) divertor D_α (red) and CIII emission (green), (d) radial electric field (blue) and electron pressure gradient (pink), (e) floating potential at ~8 mm inside the separatrix, (f) wavelet power spectrum of the floating potential in (e) with a complex Gaussian wavelet.
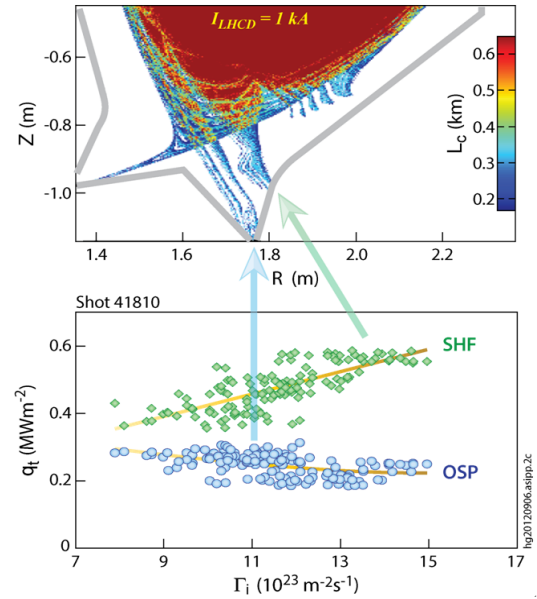
FIG. 6 Control of divertor power deposition pattern with striated heat flux (SHF) induced by LHCD via regulating edge plasma conditions using SMBI.

14

divertor argon seeding [9]. This provides an additional knob for the control of the stationary divertor power load, beyond or in addition to the achievement of highly radiating divertor conditions, which is essential for advanced long-pulse high-performance operations.

4. L-H transition and pedestal structure

Although significant progress has been made to study the L-H transition over the past two decades, the details of the physical mechanism still remain elusive. In order to quantitatively study the interaction of turbulence and sheared flows across L-I-H transition, most LCO (or named I-phase) studies are focused on the dynamics of turbulence amplitude rather than turbulence structure. Therefore, more attention should be paid to the dynamics of turbulence structure in the LCO research. A tangential CO_2 laser collective scattering system was first installed on EAST to provide the measurement of short-scale turbulent fluctuations. The wave-numbers of the measured fluctuations are: $k_1=10 cm^{-1}$, $k_2=18 cm^{-1}$, and the measured region is: $r/a \sim 0.4-0.5$, with the wavenumber resolution Δk about 2 cm^{-1} and the sampling rate of 2 MHz. Fig. 7 displays the cross-correlation time-frequency spectrum between the two core turbulence components (k_1 and k_2) across L-I-H transition, and the corresponding average cross-correlation spectrum in L-mode, LCO and H-mode regime. It can be seen that, in L-mode regime, there is always a consistent relevant structure with a quasi-coherent frequency of $f \approx 19 kHz$ between the two core wavenumber components. The quasi-coherent structure exhibits no obvious changes at the earlier-stage and mid-stage of the LCO, after the L-I transition. However, it suddenly disappears and is replaced by another relevant structure with broad-band frequency just about 9 ms before the final transition to H-mode. Clearly, the sudden disappearance of the quasi-coherent structure and the following appearance of the new relevant structure with a broad-band frequency, suggest a nonlinear change in the core fluctuation structure at the end of the LCO regime. This suggest that the nonlinear change of the turbulent fluctuation structure may play an active role in L-H transition.

An example of the pedestal (also named edge transport barrier, ETB) density profile evolution before, during and after an L-H transition is shown in Fig. 8, measured by the reflectometry system on EAST [11]. The L-H transition timing is shown by a divertor $D\alpha$ signal, fig. 8 (a), in which the vertical lines represent the times for the density profile sequences shown in fig. 8 (b). The plasma parameters for this NBI H-mode discharge
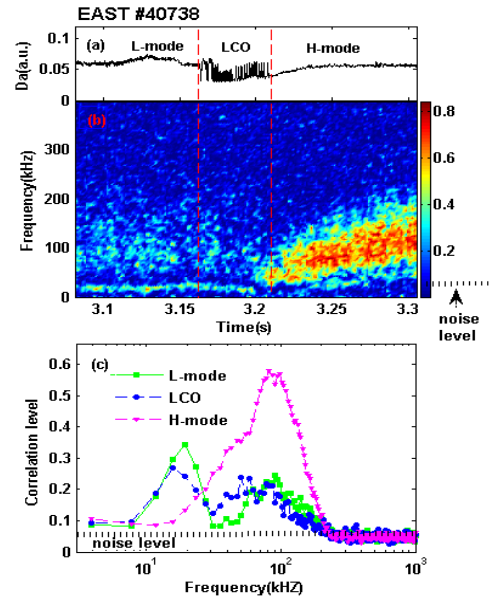
FIG. 7 The divertor D_α emission signal (a), the cross-correlation time-frequency spectrum (b) and the corresponding average cross-correlation spectrum (c) in L-mode, LCO and H-mode regime for the core wavenumber components (k_1 and k_2).
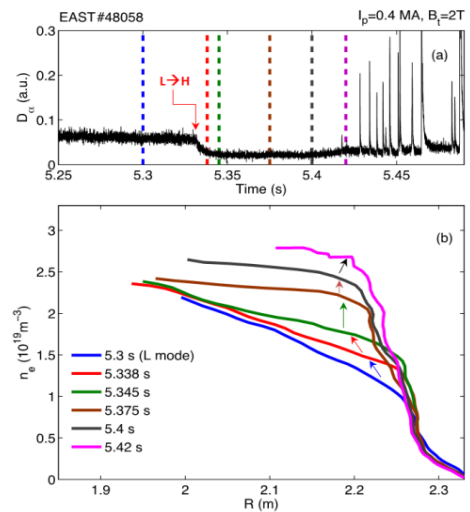
FIG. 8 Comparison of n_e pedestal structures in different phases of an NBI H-mode.

are Ip = 0.4 MA, B_T=2 T and NBI source power P_{NBI} =1.8 MW, with the plasma configuration in LSN. The density at the pedestal top $n_{e,ped}$ = 2.75×10^{19}m^{-3}, corresponding to a line-averaged plasma density n_e = 3.2 $\times 10^{19}$ m^{-3}. As clearly shown in fig. 8 (b), the density pedestal forms immediately after L-H transition (t = 5.33s) with both height and gradient increasing significantly. It is interesting to note that about 20 ms after L-H transition the pedestal gradient begins to decrease, while the pedestal height increases continuously. The decrease of the pedestal gradient may be related to some edge MHD modes that can release particles outwards much more weakly than an ELM event. Furthermore, the pedestal steeps again after t =5.4 s with the pedestal height increasing further until the first ELM occurs. Before the occurrence of the first ELM, the density pedestal height reaches ~2.75×10^{19}m^{-3}, while the density pedestal width reaches ~ 5 cm.

5. Plasma-wall interaction and disruption mitigation

The interaction between edge plasma and surrounding walls is a critical issue. The intense PWI will limit the wall life to an unacceptably low level. In addition, it has a profound influence on the core plasma performance, especially for a superconducting tokamak with long pulse operations like EAST. Disruption is a destructive transient event that must be avoided, whose power load on PFCs is even much larger than giant ELMs and will cause intolerable PWI. This section reports the PWI and disruption mitigation study in the last two years on EAST.

5.1. PMI study on MAPES

The Material and Plasma Evaluation System (MAPES) has been installed at the mid-plane of EAST and used for different plasma-material interaction (PMI) studies relevant to ITER. Fig. 9 shows a photograph of the MAPES system. It has a gate valve with nominal diameter of 500 mm, which allows the exposure of large samples. The maximum weight of a sample is 20 kg with a roller support structure. The samples can be inserted from the LFS to the SOL region and even inside the LCFS of EAST. Several PMI experiments have been successfully conducted using the MAPES, such as erosion/redeposition of ITER first wall (FW), hydrogenic retention in the gaps of castellation structure, deterioration of diagnostic mirrors
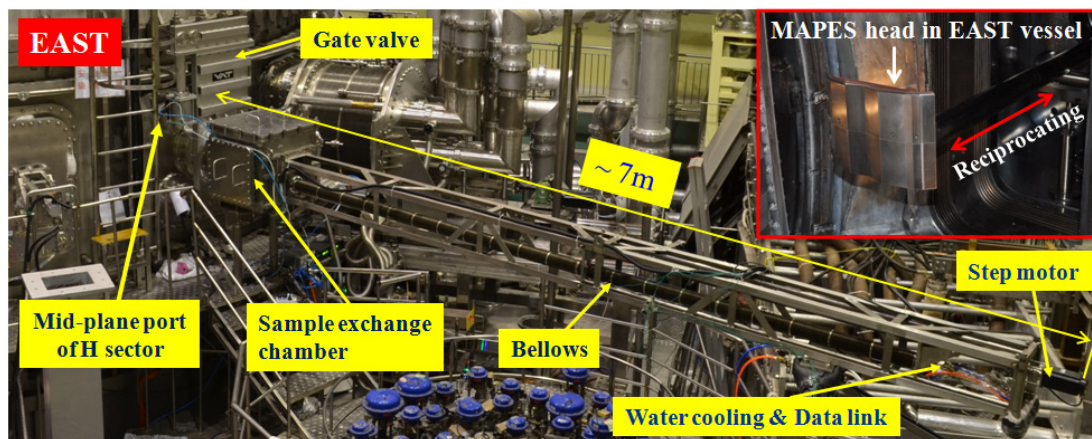
FIG. 9 MAPES system in EAST, shown inset is the reciprocating MAPES head in EAST chamber.

from impurity deposition and protective techniques and so on [12].

5.2. Disruption mitigation by MGI

Disruption mitigation by massive gas injection (MGI) provides a promising approach for ITER and has been studied in many present tokamaks. On EAST, an electromagnetic valve has been developed for the study of mitigation experiment by MGI. The valve opens in 0.5 ms

and remains open for 4 ms. With a reservoir volume of 400 ml and a maximum pressure of 5 MPa, up to 4.9×10^{23} particles can be injected. The valve is mounted at the midplane of the machine and gas is guided by a 1.7 m long tube to the plasma. Experiments of MGI into ohmic plasmas have been carried out. The typical parameters prior to MGI are $I_p = 0.4$MA, line average density $n_e = 2.2 - 2.9\times10^{19}$ m^{-3}, $\kappa = 1.76$, $q_{95} = 4.8$, and $B_t = 1.8$ T. The quantity of gas varies between 48 PaL and 136 PaL, and two types of gas, He and He/Ar (99:1) mixture, are injected.

Fig. 10 shows the sequence of a typical EAST disruption triggered by injection of 76 PaL of He gas into the ohmic plasma. The disruption mitigation valve is triggered at t = 5.983 s. After 8 ms, the gas arrives at the plasma edge, leading to a decrease in the edge temperature Te. A pre-thermal quench (pre-TQ) phase is defined as the duration of edge cooling process prior to the plasma center temperature Te collapse. During this phase, the total radiation power increases gradually with 25% of plasma thermal energy (~ 40 kJ) being lost mostly by radiation. Within 1 ms, the central Te decreases from 0.3 to 0.1 keV and then the plasma undergoes a current quench (CQ). The CQ begins with a current hump, indicating a redistribution of plasma current profile. In fact, the He gas injection extends the duration of current quench, which consists of the current redistribution and the current decay. It is found that the duration of current redistribution is almost three times longer than the nature disruption. It is determined only by the gas species, independent on the quantity of gas. Plasma vertical displacement is observed during current quench, and therefore a halo current is detected by a sensor mounted on the tile near the low divertor target. The value reaches up to 12.7 kA at t = 6.033. Although the current quench duration is extended, the halo current can still be reduced about 50% by MGI, compared to the nature disruption. This is probably because part of induced eddy current goes into the halo current sensor. Runaway electrons are rarely observed in either nature or MGI induced disruptions on EAST.
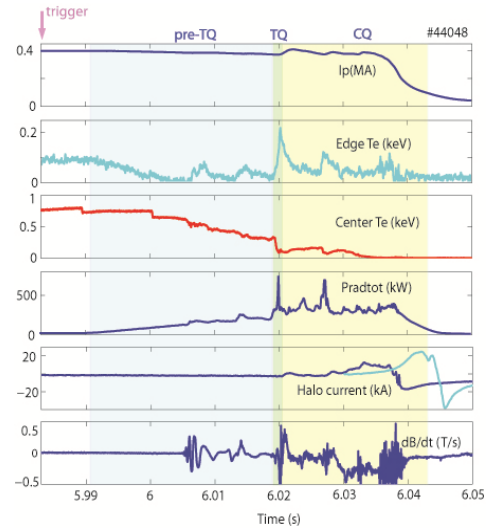
FIG. 10 Time evolution of an induced disruption after the injection of 76 PaL of He with DMV on EAST. The traces shown in local halo current (I_{halo}) panel are: during the MGI-induced disruption (blue) compared with the nature disruption (cyan).

6. High-performance long-pulse operation and advanced scenario development

6.1. Progress towards high-performance long-pulse H-mode operation on EAST

Magnetic fusion development has now entered the ITER era. Although long pulse plasma operation has been demonstrated in various fusion experiments, it is urgently required to address critical issues facing long pulse operations that entail high input power while maintaining high energy confinement. With advanced Li wall conditioning and predominant LHCD, assisted with ICRH, we achieved highly reproducible, long pulse H-modes in EAST with the pulse length over 30 s in the 2012 campaign [3], with H$_{98}$ ~ 0.9 and divertor peak heat flux largely below 2 MWm^{-2}. In the ongoing 2014 commissioning campaign, the H-mode performance has been further enhanced with the augmented heating capability. Fig. 11 shows a 28 s long pulse H-mode obtained with the newly implemented 4.6GHz-LHW in the 2014 commissioning campaign with H$_{98}$ ~ 1.15, about 30% higher than that of the record 32 s H-mode achieved in the 2012 campaign. The plasma current and the toroidal field are Ip = 350

kA and Bt = 2T, respectively. The plasma disrupted at 30.6 s, possibly resulting from the rise of in plasma density and radiation, as shown in Fig. 11. A key feature of long pulse H-mode plasmas in EAST relies on the achievement of tiny ELMs, which leads to a dramatic reduction in energy ejection per ELM event, as compared to the standard type-I ELMs [13]. The divertor peak heat flux of the 28 s high-performance H-mode was controlled largely below 3 MW/m^2, as determined by the divertor probe arrays. Another important factor for the achievement of the 28s high-performance H-mode is the high triangularity, $\delta \sim$ 0.55, and high density, $n_e/n_G \sim 0.55$.

6.2. Joint EAST/DIII-D experiments for steady state operation

In order to develop and test for steady-state advanced tokamak demonstration scenarios on

FIG. 11 High performance long pulse H-mode with $H_{98} \sim 1.15$ in EAST: (a) LHW and total radiation powers, (b) H_{98}, (c) normalized line-averaged density n_e/n_G, (d) Peak heat flux on divertor targets.

EAST, a joint experiment was designed and carried out on the DIII-D tokamak, USA. The experiment has demonstrated that fully non-inductive H-mode plasma operation is possible with plasma parameters and plasma formation schemes consistent with capabilities expected for EAST after the recent Phase II upgrade [14]. The chosen approach is based on a previously developed high β_P scenario on DIII-D, which is fully non-inductive and characterized by high β_N and an ITB with high bootstrap current fraction $f_{BS} \geq 80\%$ [15]. Such a plasma regime is desirable for steady-state tokamak operation since it reduces the demands on external current drive. The new experiments exploited new DIII-D capabilities to test such a steady-state scenario under EAST relevant conditions, including more off-axis external current drive, low NBI torque, and low Ip ramping rate. The approach for fully non-inductive operation is to remove the current drive from the transformer via clamping the OH coils. The target plasma is an upper biased double null divertor shape, with elongation $\kappa \sim 1.86$ and average triangularity $\delta \sim 0.6$, a shape that EAST can reproduce. The toroidal field is $B_T = 2.0$ T. The plasma current ramp up rate is limited to 0.25 MA/s, consistent with EAST constraints. After an approximate equilibrium is established, the current in the transformer coil is fixed so that the plasma current is forced to relax noninductively. A flat-top at approximately 0.6 MA is maintained by increasing β_N and thus the bootstrap current fraction, until a 100% noninductive condition is achieved and maintained for the rest of the discharge up to heating limitation. The discharge was achieved and maintained at $\beta_N \sim \beta_P \geq 3$ and $\beta_T \sim 1.5\%$ using a total heating and current drive power of ~11 MW including ~5 MW of off-axis NBI ($\rho \sim 0.4$), and 2.5 MW of off axis electron cyclotron current drive (ECCD) ($\rho \sim 0.5$), intended to simulate as close as possible the off-axis current drive from LHW on EAST.

FIG. 12 A H-mode plasma heated by NBI alone in EAST.

6.3. NBI H-mode and plasma rotation

The first NBI (EAST-NBI-1) system of EAST has been recently built and operational. More than 2.8 MW of NBI at 60 keV of the beam energy has been successfully demonstrated in the 2014 commissioning

campaign, and contributed to the achievement of H-mode and scenario development in EAST. Significant progress on NBI heating in EAST have been made [16]: (1) achieving H-mode with NBI alone in EAST for the first time, (2) assisting in long pulse H-mode maintenance (up to 22 s) with NBI modulation and LHW. Fig. 12 shows a typical H-mode plasma with total NBI source power about 2.3 MW, Ip = 500kA, Bt=2T and line-averaged density $n_e = 3.5\times10^{19}m^{-3}$ during the H-mode phase. It can be seen clearly that both the normalized β and plasma stored energy increase dramatically, reaching 1.8 and 200 kJ, respectively. Together with LHW, the stored energy has been further raised to ~ 220 kJ (e.g., EAST#48899-#48902, not shown here).

Fig. 13 shows the waveforms of a discharge with 4.6GHz-LHW and NBI at ~ 60 keV/1.8MW. About 2.0 MW of LHW was injected from 2.5s-7.5s, while NBI was initiated at 4.0 s and ended at 7s. When LHW was switched on, there was already a slight co-current increase in plasma rotation, which was overshadowed by a much larger rotation increment when NBI was on subsequently. When NBI power reached its steady state, a rotation change in the co-current direction of ~100 km/s was seen. In addition, the ion temperature increased substantially to the level of electron temperature for the entire NBI phase. In particular, Ti/Te changed from 0.8 (ohmic phase), to 0.4 (LHCD phase), and 0.95 (NBI phase), indicating good ion heating with tangential NBI besides rotation production [17]. The plasma rotation, Ti, and Te were measured by the X-ray crystal spectrometer.

FIG. 13 Waveforms of EAST discharge #48914: a) Ip, b) chord-averaged ne, c) LHW power, d) NBI power, e) plasma stored energy, f) Dα intensity, g) Te, h) Ti and i) core plasma rotation.
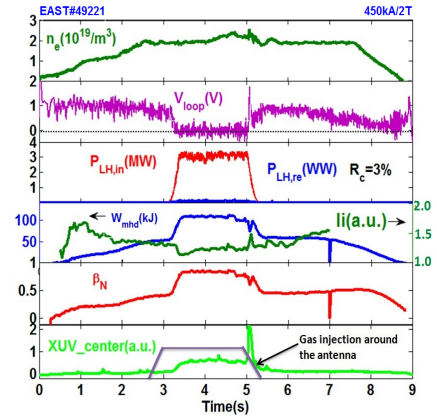
FIG. 14 A high performance plasma obtained with 4.6GHz LHCD.

6.4. High performance plasma with new LHCD system

Recent experimental results have demonstrated that LHW can be coupled to the plasma with a low reflection, driving plasma current, and heating plasma effectively with the 4.6GHz-LHCD system [18]. Good LHW-plasma coupling with reflection coefficient less than 5% has been obtained by optimizing the plasma configuration and puffing local plasma gas near the LHW antenna so as to improve local density at the LH grill. The maximum LHW power coupled to plasma is up to 3.2 MW. Full wave driven plasma has been obtained with different plasma currents, with the current drive efficiency up to $1.1\times 10^{19}Am^{-2}W^{-1}$, assuming that the absorption efficiency of LHW power is 75%. The typical waveforms of 4.6GHz-LHCD heated high-performance plasma with $N_{//}^{peak}$ =2.04 are shown in Fig. 14, in which full wave driven plasma is obtained and stored energy is

FIG. 15 Profiles of Te, measured by TS diagnostic, at different times of Fig. 14.

increased during LHCD application. Based on the internal inductance, the plasma current profile is broadened by LHCD compared to the ohmic phase. In addition, the plasma is simultaneously heated by LHW by means of slowing down of fast electrons. The core electron temperature measured by the Thomson scatting (TS) diagnostic reaches up to 4.5 keV, which is the highest core electron temperature achieved in EAST so far, as shown in Fig. 15.

7. Summary and future plans

In summary, significant progress has been made in EAST on both technology and physics fronts towards high-performance long pulse operations. The machine capabilities have been greatly enhanced during the recent EAST Phase II upgrade to address key physics and engineering issues for ITER and beyond, especially in the area of high performance and truly steady state operations. In particular, the H&CD capability has been upgraded to 26 MW and is being further augmented to ~ 40 MW in the next campaign. The upper divertor has been converted to ITER-like tungsten structure with actively water cooling. In addition, a set of 2 ×8 ITER-like RMPs coils have been installed during the upgrade, along with more than 70 new or upgrade diagnostics. More importantly, significant advances on H-mode physics for long pulse operations have been achieved in EAST, e.g., transient ELM and stationary heat flux control physics with various innovative techniques, long pulse high performance H-mode operations with dominant LHCD heating. In the ongoing 2014 commissioning campaign, the confinement of long pulse H-mode has been further improved with H_{98} ~ 1.15, i.e., about ~ 30% higher than the record 32 s H-mode achieved in 2012 campaign. H-mode plasmas with NBI heating alone or LHCD plus NBI modulation have been both demonstrated for the first time in EAST. In addition, high-performance operation with core Te up to 4.5 keV has been obtained, which is the highest Te achieved on EAST so far. High performance H-mode with β_N ~ 2 and stored energy ~ 220 kJ has also been successfully achieved. Furthermore, a quasi snowflake divertor configuration has been demonstrated on EAST in the commissioning campaign.

FIG. 16 Operation windows for EAST at Ip= 500kA. ζ_{QSS}, which has the meaning of several times (here is 10) of current diffusion time (τ_R) over the duration of current flattop (Flux/V_{surf}), indicates the long pulse feature of a plasma. $\zeta_{QSS} > 0$, $\zeta_{QSS} < 0$ and $\zeta_{QSS}=0$ are quasi SS, over-drive and SS regions, respectively. Dash lines are constant H_{98} cases. Dot lines stand for constant n_e/n_G. The color coding is the bootstrap current fraction, the pressure peaking index is 4 here.

Based on the newly upgraded H&CD system and wide operation regime (I_p= 0.2-1.0 MA, B_t =1.8-2.8 T, f_{nG}=n_e/n_{eG}<0.8, etc.), EAST has been equipped with the capability to explore advanced scenarios with designed parameters, entailing the integration of high performance operating conditions, high heat flux to PFCs and RF H&CD. Preliminary simulations (predictions) of advanced scenarios using 0-D estimation have been carried out to guide the detailed scenario development. The results of 0-D estimation indicate that due to the limitation of EAST PF coils ($\leq$ 4V-s at Ip flattop), 500kA of Ip is a good candidate for SS operation, while hybrid scenario (quasi steady state) can be tested in 800 kA. With I_p=800kA, very high energy confinement (H_{98}~1.5) or maximum total auxiliary power (~28MW) is required in order to access SS regime. However, with lower Ip (500kA),

by using more realistic half-maximum RF power instead of maximum power, EAST still has a reasonable operation window for steady state scenarios. Good energy confinement ($H_{98}>1.3$) is the necessary condition for high density ($f_{nG}\sim0.7$) operation, as shown in Fig. 16. On the basis of the 0-D results, the detailed 1.5-D time-dependent predictions for EAST future plans are being carried out. In addition, the advanced steady-state, fully non-inductive H-mode operation demonstrated on DIII-D during the joint EAST/DIII-D experiments is possible with plasma parameters and plasma formation schemes consistent with current capabilities of EAST. Exciting physics experiments will be carried out after the 2014 commissioning campaign to address critical issues facing high-power, long-pulse plasma operations.

Acknowledgements

References

[1] Y. X. Wan et al., "Overview progress and future plan of EAST Project", Proc. of 21st IAEA-FEC (Chengdu, China 2006) (Vienna: IAEA) OV/1-1

[2] B. N. Wan et al., "Progress of long pulse and H-mode experiments in EAST", Proc. of 24th IAEA-FEC (San Diego, USA 2012) (Vienna: IAEA) OV/2-5

[3] J. Li et al., Nature Physics 9, 817 (2013)

[4] Y. Liang et al., Phys. Rev. Lett. 110, 235002 (2013)

[5] X. L. Zou et al., 24th IAEA Int. Conf. on Fusion Energy San Diego 2014

[6] J. S. Hu et al., Phys. Rev. Lett. 114, 055001 (2015)

[7] G. S. Xu et al., "A Long-Pulse H-mode Regime with a New Coherent Mode Providing Continuous Transport across Pedestal in EAST" EX/9-5, 25th IAEA Int. Conf. on Fusion Energy St Petersburg 2014

[8] H. Q. Wang et al., Phys. Rev. Lett. 112, 185004 (2014)

[9] H. Y. Guo et al., Phys. Plasmas 21, 056107 (2014)

[10] L. Wang et al., "Progress in Active Control of Divertor Power Load in the EAST Superconducting Tokamak" EX/P3-10, 25th IAEA Int. Conf. on Fusion Energy St Petersburg 2014

[11] X. Gao et al., "Study of pedestal turbulence on EAST" EX/P3-9, 25th IAEA Int. Conf. on Fusion Energy St Petersburg 2014

[12] R. Ding et al., "Material migration studies on EAST-MAPES and implications for ITER" I5, 21st Int. Conf. on PSI in Controlled Fusion Devices, May 26 - 30, 2014 Japan

[13] L. Wang et al., Nucl. Fusion 53, 073028 (2013)

[14] X. Z. Gong et al., "Development of Fully Noninductive Scenario at High Bootstrap Current Fraction for Steady State Tokamak Operation on EAST and DIII-D" EX/P2-39, 25th IAEA Int. Conf. on Fusion Energy St Petersburg 2014

[15] Y. J. Xu et al., "The latest development of EAST NBI" EX/P3-12, 25th IAEA Int. Conf. on Fusion Energy St Petersburg 2014

[16] B. Lu et al., "Core plasma rotation characteristics of RF-Heated H-Mode discharges on EAST" EX/P3-5, 25th IAEA Int. Conf. on Fusion Energy St Petersburg 2014

[17] B. J. Ding et al., "Investigation of LHW-Plasma coupling and current drive related to H-Mode experiments in EAST" EX/P3-11, 25th IAEA Int. Conf. on Fusion Energy St Petersburg 2014

KSTAR LHCD SYSTEM OPERATION IN 2014

Jeehyun Kim, S. J. Wang, H. J. Kim, B. H. Park, Y. Bae, J.G. Kwak, W. Namkung, M. Cho
National Fusion Research Institute, Daejeon, Korea
Email : jeehkim@nfri.re.kr

KSTAR Lower Hybrid Current Drive (LHCD) system operated for 5 GHz 500 kW 2 sec was first installed and commissioned during 2012 campaign. Vacuum, large reflection, and arcing problems hindered the nominal operation of the system in 2012 campaign. However, those problems were fixed and thus the lower hybrid wave with the power > 100 kW for longer than 1 sec could be nominally coupled to the KSTAR tokamak in 2014 campaign.

1. Introduction

KSTAR Lower Hybrid Current Drive (LHCD) system operated for 5 GHz 500 kW 2 sec was first installed and commissioned during 2012 campaign. KSTAR LHCD system adopted 5 GHz 500 kW CW klystron. Prototype klystron was developed by TETD and POSTECH. Main transmission line (MTL) connecting the klystron to KSTAR over 80 m consists of oversized WR284 waveguide and is pressurized to 1.7 bar with SF6 gas. RF power from one klystron is delivered to tokamak hall through the MTL and divided into eight channel by power dividing network (PDN). PDN is composed of seven magic tees forming triple bifurcation and fixed phase shifters as illustrated in Fig. 2(a). After dividing into eight channels, each channel is fed into each column of launcher which consists of eight columns by four rows. The waves launched from adjacent columns have 90 degree phase shift by adjusting the waveguide length or the fixed phase shifters. KSTAR launcher is composed of eight stacks of 4-way splitters which bench-marked Alcator C-mod [1]. KSTAR initial LHCD system has fixed N// value of 1.9. Detailed design of the KSTAR LHCD system and launcher was describe in several papers [2,3].

It was difficult to operate the LHCD system at a high power for a long pulse because arcing in some waveguide components and larger reflection than prediction triggered the interlock during high power commissioning in 2012 campaign. Phase shifts between columns had measured and found out to be different from the design after the 2012 campaign. Reflected power was traveled back to klystron instead of dissipated at the dummy load in the PDN due to the wrong phase shift. The phase shifts were corrected by inserting and replacing the fixed phase shifters in the PDN in 2013. However, vacuum problem between LHCD antenna and KSTAR vacuum prohibited the high power application and thus have repaired by replacing the O-ring. For the 2014 KSTAR campaign, the waveguide components causing arcs were found out and repaired. Then, high power conditioning of the transmission line with the matched load and the preliminary LHCD coupling experiments were performed.

Next sections, it will be presented the characteristics of KSTAR LHCD antenna measured using network analyzer, high power conditioning, and preliminary coupling experiments results.

2. High power conditioning of LHCD system

The reflected power was supposed to be directed to and dissipated at the dummyload in the power dividing network by 90º phase shift. It is very important that the reflected power is directed toward dummyload at the magic tees in the PDN since the KSTAR LHCD system

does not have circulator. The reflection, however, was as large as 4-10% which is larger than prediction near at the klystron and thus triggered the interlock during high power commissioning in 2012 campaign. The phase shift in the antenna turned out to be wrong. The reflection was reduced to <1% after phase correction. In the Figure 2, the measured phase shift (a), and the reflection at each column (b), the resulting power spectrum (c), reflection at each column (d), average reflection depending on the density at the grill calculated with ALOHA before and after the corrections are compared.

In order to figure out the arcing in the main transmission line and antenna, S-band dummy load made by Spinner was connected to the end of transmission line and high power conditioning was performed. S11 of the S-band dummy load at 5 GHz was measured to be less than -20 dB using network analyzer before the connection. The power and the pulse length were increased gradually up to 500 kW 2 sec pulse at the klystron. During the conditioning the waveguide component causing arcing in the transmission line was specified and repaired. Then, PDN and antenna was connected to the end of the transmission line and their conditioning was performed as well. During the conditioning, dummy load absorbing reflection from column 5 and 6 were damaged and replaced because these two columns have the largest reflection among the 8 columns as in Figure 2(b).

During 2014 KSTAR campaign, LHCD system powered to KSTAR at various conditions of plasma to study the coupling efficiency. Figure 3 shows the reflection change by the gap control of plasma. The red line in the lower middle is the reflected power and the middle upper is the radial position of the plasma. The larger radial position, the closer to the plasma. When the gap distance is 6.2 mm in this shot, the reflection was increased by 50% comparing with the one with gap distance 3.9 mm.

Strong changes of the ECE signal were observed at most of the shots with LH power injection. Slight increase of ECE signal and stored energy were observed in the # 11145 shown in Figure 4, as well, with LH power injection. The stored energy change was not accompanied with LH power at the most shots.

References
[1] S. Shiraiwa, et al., Design, and initial experiment results of a novel LH launcher on Alcator C-Mod, Nuclear Fusion 51 (2011) 103024
[2] S. Park, et al., Progress of KSTAR 5-GHz Lower Hybrid Current Drive System, Fusion Science and Technology 63 (2013) 49-58
[3] H. Do, et al., Test Result of 5 GHz, 500 kW CW Prototype Klystron for KSTAR LHCD System, Fusion Engineering and Design 86 (2011) 992
[4] J. Hillairet, et al., ALOHA: an Advanced LOwer Hybrid Antenna coupling code ALOHA code, Nuclear Fusion 50 (2010) 125010
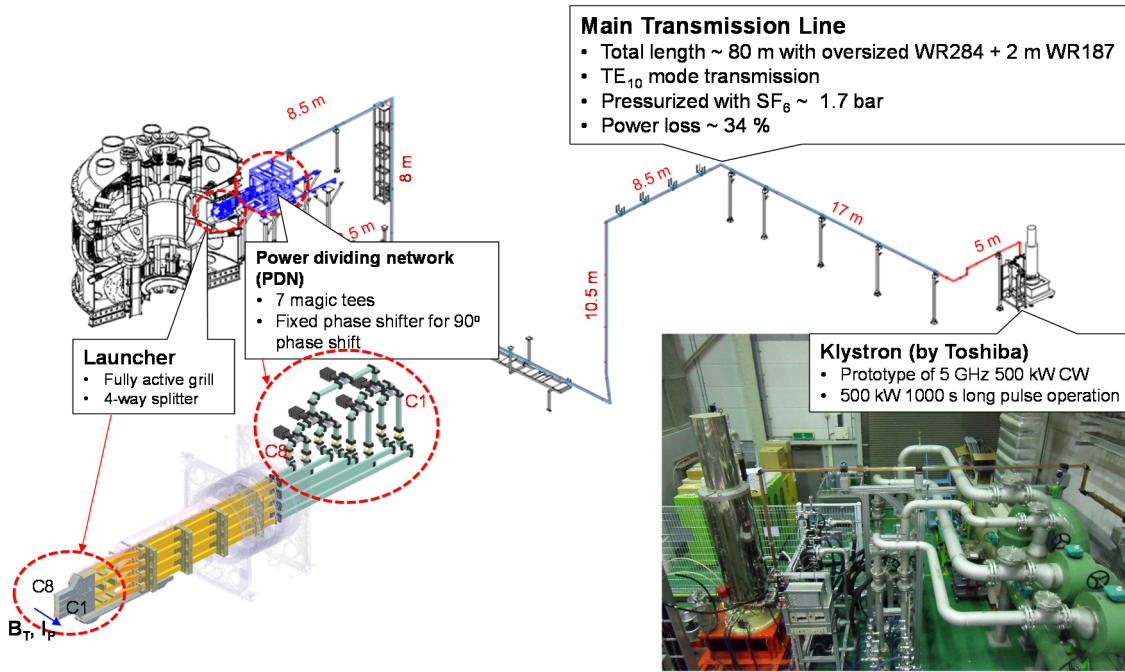
Figure 1. Birds-eye view of KSTAR LHCD system
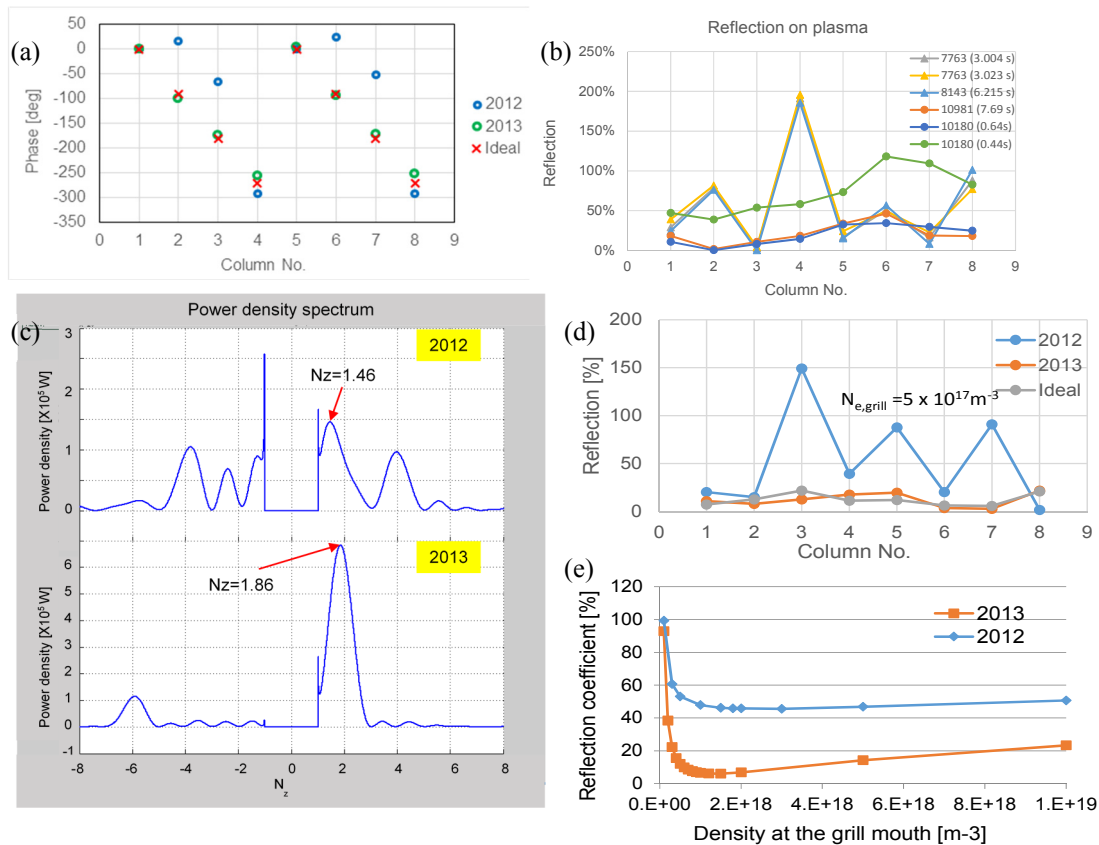
Figure 2. (a) Measured phase shift of the antenna (b) Measured reflection of each column with plasma load (c) Antenna spectrum calculate with ALOHA code with different phase shift (d) reflection calculated with ALOHA code (e) Reflection coefficient change depending on the density at the grill mouth with different phase shift
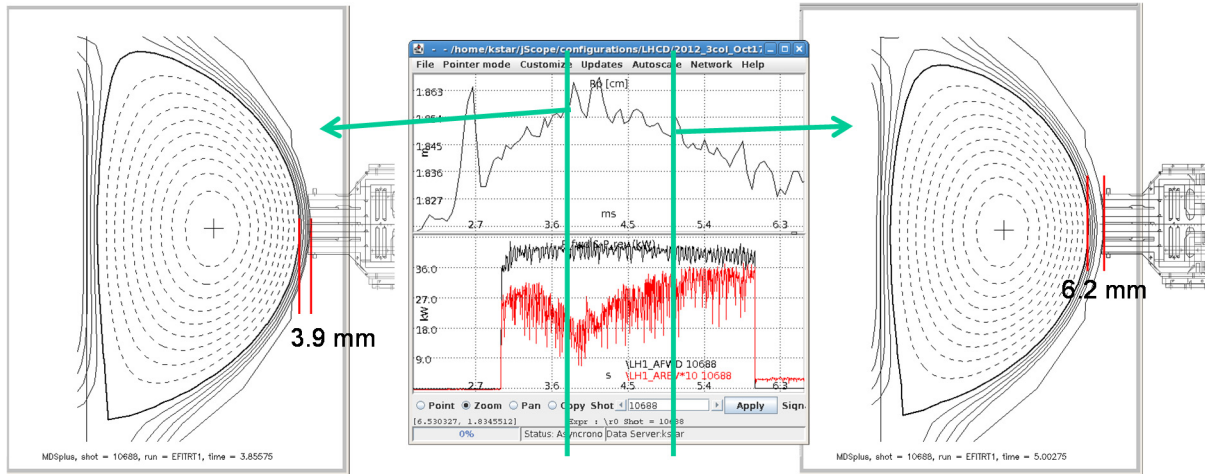
Figure 3. Change of the reflection depending on the launcher –LCFS distance. Red line in the middle is the reflected power. Upper middle is the radial position of the plasma center.
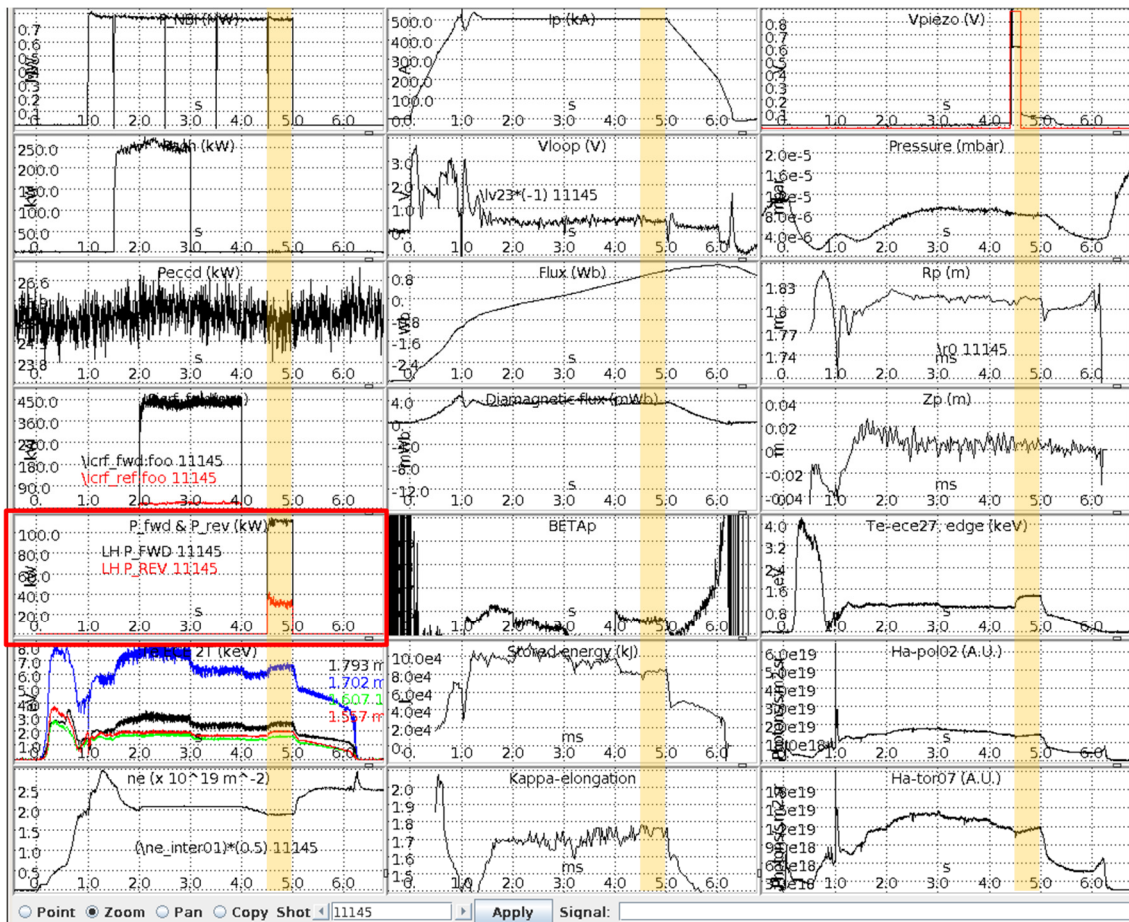
Figure 4. Change of diagnostic signal with LH power. Slight increase of ECE and stored energy were detected.

Dynamics of Pedestal Rotation and Ion Temerature Profile Evolution in KSTAR

Won-Ha Ko[a*], J.H. Lee[a], K.D. Lee[a], S. H. Ko[b], J.M. Kown[b], K. Ida[c], P. Diamond[b,d],
Y.M. Jeon[a], S.W. Yoon[a], J.G. Kwak[a], Y.K. Oh[a]
[a]National Fusion Research Institute, Daejeon, Korea
[b]WCI Center for Fusion Theory, NFRI, Daejeon, 305-806, Korea
[c]National Institute for Fusion Science, Toki, 509-5292, Japan
[d]CMTFO and CASS, University of California, San Diego, CA92093
*Email : whko@nfri.re.kr

Pedestal rotation profiles are of great importance for ITER, in the multiple contexts of confinement enhancement, the source of intrinsic torque in H-mode, and their response to ELMs and to ELM suppression techniques. We report on findings from charge exchange spectroscopy, of toroidal rotation and profile structure and evolution in KSTAR H-mode pedestal plasmas. We emphasize pedestal rotation from charge exchange spectroscopy at the L to H transitions plays an essential role in determining transport which is related in rotation shear and stability which is affected by increased rotation with the high spatial resolution from charge exchange spectroscopy. The evident disparity between the width of the toroidal rotation pedestal and that of the ion temperature pedestal is interesting, since we usually expect that parallel shear flow instability could be a candidate in which the resulting momentum transport can make toroidal velocity profile broader.

Magnetic perturbations make not only ELM disappeared but also toroidal rotation from the charge exchange spectroscopy decreased on KSTAR. Changes of the toroidal rotation profiles are observed from during ELM and ELM suppression. The pedestal top of the toroidal rotation during ELMy-H-mode is higher than that during suppression by RMPs.

1. Introduction

The recent tokamak research has been emphasizing that the plasma rotation plays an essential role in determining transport which is related in rotation shear and stability which is affected by increased rotation [1, 2].

The charge exchange spectroscopy is one of the important diagnostics on the KSTAR to get ion temperature and toroidal rotation velocity from Doppler broadening and Doppler shift of the excited carbon impurity spectral lines. The charge exchange spectroscopy systems looking at the KSTAR neutral beam which is modulated 5 Hz for special period [3, 4]. The system has a spectrometer with f/2.8 lent from NIFS [5] with pitch-controlled double slit fiber bundle with back-illuminated CCD. It focuses on improved edge spatial interval from increasing of plasma viewing channels to 5 mm and enhanced time resolution from a high throughput spectrometer with back-illuminated CCD. The system has allowed to measure pedestal ion temperature and toroidal rotation profiles in KSTAR H-mode [6].

The measurements of the ion temperature and toroidal rotation velocity profiles with the high spatial resolution have been conducted for the L- and H-mode plasma discharges in KSTAR. Ion temperature gradient increased near pedestal in H-mode while it is monotonous near edge region in L-mode. Shear increased near pedestal in H-mode while it decreased near edge in L-mode. The pedestal structures both in the ion temperature and toroidal rotation speed were observed and the major radius of the last closed flux surface is around 2.25m in H-mode while the last closed flux surface is 2.3 m in L-mode.

In Section2, a description of rotation and temperature pedestal characteristics in L- and H-mode, followed by the analysis of Gyrokinetic linear stability for parallel shear flow stability effect on pedestal. In Section 3, the effect of RMP in pedestal region for ELM suppression and other uncertainties are discussed. A summary is given in Section 4.

2. Rotation Pedestal and Gyrokinetic Linear Stability Analysis

The differences in the edge regions between the L- and H-mode plasmas have been found very clearly due to the high spatial resolution measurement. The ion temperature increases linearly in the edge region of the L-mode plasma. However, the ion temperature profile of the H-mode plasma shows that there is an abrupt increase so called, large radial gradient of the temperature in the edge region, which is representing the edge transport barrier. It seems that the large core temperature of the H-mode plasma relative to that of the L-mode plasma can be achieved by the formation of the edge transport barrier.

It is found that there is also a very sharp radial gradient of the toroidal rotation in the edge region of the H-mode plasma. It also seems that the toroidal rotation increases in the whole region of the plasma in the H-mode state compared to that of the L-mode state. However, it is uncertain whether this increase of the toroidal rotation velocity is due to the large radial gradient of the velocity even though it seems that there is also a momentum transport barrier in the edge region like an edge transport barrier. Since the carbon velocity is expected to be much different from the main ion velocity in the edge region, the main ion rotation profile is necessary for the correct momentum transport analysis. The detailed transport analysis remains for the future since the estimation of the main ion velocity and the measurement of the radial electric field have not been available yet.

These detailed ion temperature and toroidal rotation evolutions during sawtooth is very interesting. The neutral beam power was insufficient to suppress sawtooth and it can trigger an LH transition at substantially lower threshold power than what is required without sawtooth [7]. Sawteeth periods get longer to double during LH transition in KSTAR. During the L to H transition, the toroidal rotation pedestal is observed to form ahead of the ion temperature pedestal, and build inward from the separatrix. This observation is consistent with the expectation that toroidal momentum transport is effectively governed by turbulence only, while neoclassical ion thermal transport plays a significant role in ion temperature profile evolution. Thus, toroidal rotation can react more rapidly to the suppression of turbulence at the L to H transition than ion temperature does. The conventional neoclassical picture says the ion temperature pedestal should be broader than toroidal rotation pedestal but the width of the toroidal rotation pedestal (~ 4 cm) is broader than that of the ion temperature pedestal (~ 2 cm) in the H-mode. It strongly suggests that there should be instabilities regulating the toroidal rotation pedestal. The instability may be the parallel shear flow instability which is driven by a strong rotation shear and mediate anomalous momentum transport. The parallel shear flow instabilities are propagating in the ion diamagnetic direction for a strong rotation shear case while the trapped electron mode instability is weakly excited for no rotation shear case from Gyrokinetic analysis of GYRO code. This indicates that a strong rotation shear is the main driving force of these instabilities.

As we discussed, steeper ion temperature pedestal can result in stronger intrinsic torque and higher central rotation [8, 9] So, it would be very interesting to check very carefully how RMPs modifies ion temperature pedestal. Next part shows the effect of RMPs on the ion temperature and toroidal rotation.

3. Rotation pedestal during ELM suppression with RMP

The segmented in-vessel control coil system of the KSTAR device is capable of applying n=1 or 2 RMP with various parity. The application of n=1 RMP showed an apparent ELM suppression and mitigation in various parity. ELM-suppression *by n=1* RMPs was appeared at first time in KSTAR compared in other machines. ELM-suppression *by n=2* RMPs was measured in both DIII-D and KSTAR[10, 11].

The toroidal rotation from charge exchange spectroscopy decreased when n=1 and n=2 RMPs were applied and there is ELM suppression region. The whole toroidal rotation during ELM is higher than that during suppression by RMPs and rotation damping rate is similar. Toroidal rotation speed is recovered when ELM starts to appear. Torodial rotation responds faster and more strongly drop by RMP before ELM suppression in both n=1 and n=2 RMP cases while tops of rotation pedestal and ion temperature pedestal drop during ELM suppression by n=1 RMP. Toroidal rotation also responds faster and more strongly to the ELM than ion temperature does in n=2 RMP case which is similar during ELM burst. It is difficult to distinguish the change of ion temperature pedestal.

There is a little change of pedestal slope of toroidal rotation speed profiles compared to that without ELM suppression. Steeper ion temperature pedestal can result in stronger intrinsic torque and higher central rotation. If the ion temperature pedestal variation is negligible, then next suspect is ne-pedestal. The experimental observation is a linear proportionality between rotation velocity and ion temperature pedestal gradient but it is not clear relation between rotation speed and density gradient. However, some theory people expect similar linear proportionality. We should check very carefully how RMPs modify pedestal in next campaign and the detail physics study is ongoing.

The temporal evolution of ion temperature and toroidal rotation profiles were measured during an inter-ELM period. The toroidal rotation profile collapses immediately after the ELM burst but its pedestal is quickly increased and the whole profile continues to build up during the period until it collapses again at the next ELM burst. However, the reduced ion temperature pedestal remains almost the same after the ELM burst.

4. Summary

There are some relations between sawtooth crash and L to H transition from ion temperature and toroidal rotation profiles in co-NBI heated KSTAR plasmas. The toroidal rotation responds faster and more strongly than ion temperature does during the LH transition from rotation transport barrier in edge after sawtooth crash. There are small increases in electron temperature and toroidal rotation in comparison with other parameters during L to H transition with ECH.

The toroidal rotation pedestal is broader than ion temperature in H-mode and it is explained from the parallel shear flow instability from Gyrokinetic linear stability analysis which is driven by a strong rotation shear.

Magnetic perturbations make not only ELM disappeared but also toroidal rotation from the charge exchange spectroscopy decreased on KSTAR. The change of toroidal rotation and ion temperature pedestal during ELM suppression with n=2 RMP. The toroidal rotation and ion temperature pedestal globally reduced and had big drop by n=1 and toroidal rotation has always globally big drop with both n=1 and n=2 RMPs. The pedestal drops at first time and core following the pedestal on both ion temperature and toroidal rotation when RMPs applied.

The toroidal rotation behavior was shown from the effect of RMPs in KSTAR associated with the helical magnetics related to the RMP. The RMPs make not only ELM suppression but also torodial rotation decrease in KSTAR H-mode plasma. Changes of the toroidal rotation profiles show that there is the edge rotations which is related with the intrinsic torque. The physics model related RMP effect should be further studied. What interaction of RMP with pedestal intrinsic torque is in ITER from the toroidal rotation behavior related intrinsic torque by RMP. What further advancement in RMP experiments is in pedestal and further studies are still needed to resolve the mechanism of it.

Acknowledgement

References

[1] M. Yoshida, Y. Koide, et al., Nucl. Fusion **47**, 856(2007).
[2] T Tala, K Cromb´e, et al., Plasma Phys. Control. Fusion **49**, B291–B302 (2007).
[3] W. -H. Ko, S. Oh, and M. Kwon, IEEE. Trans. Plasma Sci. **38**, 996 (2010)
[4] W. -H. Ko, H. Lee, D. Seo, and M. Kwon, Rev. Sci. Instrum. **81**, 10D740 (2010)
[5] M. Yoshinuma, K. Ida, M. Yokoyama, et al., Fus. Sci. Tech. **58**, 375 (2010)
[6] S.W. Yoon, et al., Nucl. Fusion. **51**, 113009 (2011)
[7] T N Carlstrom, H Burrell and R J Groebner, Plasma Phys. Control. Fusion **40** 669 (1998)
[8] J.E. Rice, at al., Nucl. Fusion **47** 1618 (2007)
[9] K. Ida and J.E. Rice, Nucl. Fusion **47** 045001 (2014)
[10] Y.M. Jeon *et al.,* Phys. Rev. Lett. **109,** 035004 (2012)
[11] T.E. Evans *et al*, Phys. Rev. Lett. **92,** 235003 (2004)

Tungsten pellet injection in LHD

Shigeru MORITA[1,2], Tetsutarou OISHI[1,2], Xianli HUANG[2], Hongming ZHANG[2], Motoshi GOTO[1,2], Liqun HU[3], Zenwei WU[3], Ling ZHANG[3] and Fudi WANG[3]

[1] National Institute for Fusion Science, Toki 509-5292, Gifu, Japan
[2] Dept. of Fusion Sci., The Graduate University for Advanced Studies, Toki 509-5292, Gifu, Japan
[3] Institute of Plasma Physics Chinese Academy of Science, Hefei 230031, China

Two coaxial pellets with tungsten inserted into graphite carbon and polyethylene (PE) tubes are compared for tungsten spectroscopic study in the Large Helical Device (LHD). The tungsten pellet with carbon tube causes plasma collapse, while that with PE tube smoothly ablates without collapse. The deposition profile of the pellets is analyzed with a help of pellet ablation spectroscopy. It is found that the tungsten pellet with carbon tube can significantly penetrate into the core plasma and leads to the plasma collapse. A tungsten spectrum with radial profile is successfully observed when the tungsten pellet with PE tube is used.

I. Introduction

The study on tungsten (W) is an urgently important current topic in the fusion research, since the tungsten is adopted as a divertor material of the International Thermonuclear Experimental Reactor (ITER) [1]. Experiments on tungsten-seeded plasmas have been extensively carried out in many fusion devices [2-5] for studying the effect of tungsten material on the plasma performance. A comprehensive understanding of spectral structures and atomic processes in tungsten ions is then strongly required to diagnose the tungsten behavior in high-temperature plasmas [6]. However, several tungsten spectra still remain unknown and the tungsten atomic database, in particular, recombination rates, are extremely inaccurate for use in the transport study. Therefore, spectral identification of tungsten emissions and reevaluation of atomic data related to tungsten ions based on the profile measurement are necessary for the tungsten transport study in the ITER. For the purpose a bright light source of tungsten is strongly desired for accurate data analysis.

In the study of tungsten on the Large Helical Device (LHD), an active method is necessary for introducing it into plasmas, e.g. laser blow-off. However, the laser blow-off technique seems to be impossible because of the existence of edge ergodic layer [7] by which the coming ablated particles are easily screened. Therefore, a method of impurity pellet injection has been adopted until now for the impurity study using a cylindrical pellet with sizes of 0.5-1.5mm [8]. However, the discharge is easily terminated through radiative collapse, when a pure tungsten pellet with such a size is injected in the LHD plasma. Use of extremely small pellet is not easy due to several technical problems. A coaxial-structure pellet has been thus developed for the spectroscopic study of tungsten. As the first step a coaxial molybdenum pellet was tested. The LHD discharge could be excellently sustained after the injection [9]. The plasma response after the tungsten pellet is also discussed.

II. Coaxial tungsten pellets

The pellet used in the present study consists of a tungsten wire and a cylindrical tube made of polyethylene (PE) or graphite carbon (C) [10], as shown in Figs. 1 (a) and (b), respectively. The diameter of tungsten wire is 0.15mm and the dimension of PE and C tubes is 0.6^L (length) $\times$ 0.6^ϕ (outer diameter) $\times$ 0.3^ϕ (inner diameter) and $0.7^L \times 0.7^\phi \times 0.25^\phi$, respectively. The W-in-PE and W-in-C contain $7\text{-}8\times10^{17}$ tungsten atoms.
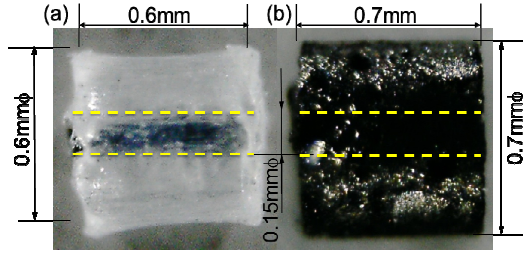
FIG. 1. Photos of (a) W-in-PE and (b) W-in-C coaxial pellets.   Yellow dashed lines denote the position of tungsten wire.

Figure 2 shows velocity of the tungsten pellet against pellet mass.   It also includes results from C tube, PE tube, Al-in-PE, Al-in-C, Fe-in-PE and Fe-in-C.   The velocity tends to decrease with the mass.   The W-in-PE velocity is then slightly higher than the W-in-C velocity.   It may be interpreted by the acceleration of α_{pellet} (=F/m_{pellet}) at which the kinetic force is basically given by the pellet size and the helium gas pressure in addition to acceleration length.
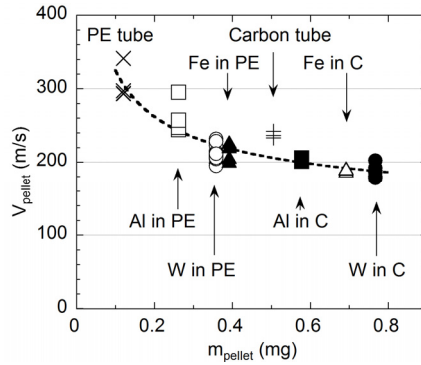
FIG. 2. Pellet velocity against pellet mass; W-in-PE (open circles), W-in-C (solid circles), Fe-in-PE (solid triangles), Fe-in-C (open triangles), Al-in-PE (open squares), Al-in-C (solid squares), PE tube (crosses) and C tube (plus signs).   Dashed line denotes a polynomial fitting.

III. Comparison of plasma response between two pellets

Typical waveforms of discharges with W-in-PE and W-in-C pellets are shown in Fig. 3.   The discharges are maintained by two counter-close-wise NBIs (#1 and #3) and a close-wise NBI (#2). The tungsten pellet is injected at t=5.5s.   After the injection the discharge with W-in-PE smoothly recovers with density increase of $1.8 \times 10^{13} cm^{-3}$, whereas the discharge with W-in-C is terminated by the collapse just after the injection (see Figs. 3(c) and (d)).   The WXXV at 32.3Å with 5g-4f transition is clearly observed after the W-in-PE injection (see Fig. 3(g)).   In the discharge with W-in-C, the WXXV and CVI lines only display a sharp peak at the injection.   The small signal after the plasma collapse is due to high-energy neutral particles from NBI [11].

Most discharges with W-in-PE can be sustained, but most discharges with W-in-C are terminated just after the injection.   Such a clear difference can be explained by pellet deposition profile.   Figure 4(a) shows time evolution of H_α, visible bremsstrahlung and CI emissions observed along the path of W-in-PE pellet with velocity of 216 m/s.   The time sequence of emissions is first converted into pellet movement distance assuming a constant velocity during the ablation.   The distance is again converted into magnetic surface coordinate as indicated at upper abscissa in Fig. 4 (a).   The H_α emission exhibits a wide ablation between $\rho = 0.75$ and 1.0 with a peak at $\rho = 0.82$, indicating the deposition range of PE tube surrounding the tungsten wire.   The radial location of tungsten deposition is revealed by the narrow H_α peak at $\rho = 0.72$, which coincides with peaks of bremsstrahlung and CI emissions.   Since the tungsten wire does not include any C atoms, the CI peak may originate in emissions of WI and/or WII in wavelength range of the CI filter.   Since numerous tungsten lines appear in the visible range during the tungsten ablation, the intensity

31

increase in three signals is caused by the tungsten visible line. The deposition layer of PE tube and tungsten wire is also verified by a time evolution of electron temperature (T_e) measured by electron cyclotron emission (ECE) diagnostic, as shown in Fig. 4(b). The ordinate indicates a relative change in T_e from the pellet trigger timing, $t_0 = 5.503$s. At two H_α peaks the T_e gradient at $\rho = 0.812$ and $\rho = 0.718$ drastically changes, suggesting the pellet deposition layer, i.e. T_e at $\rho = 0.892$ rapidly decreases before T_e at $\rho = 0.812$ starts to drop. It means the pellet already starts to ablate before the H_α meets the peak intensity. The T_e at $\rho = 0.663$ decreases with a constant decay time during the pellet ablation, suggesting no ablation occurs at $\rho = 0.663$. Therefore, the T_e evolution at four radii indicates the same result as the H_α behavior. It is thus confirmed that the PE tube is ablated first in the outer part of the plasma, $0.75 \le \rho \le 1.0$ and the tungsten wire is ablated in a narrow radial location around $\rho = 0.72$.
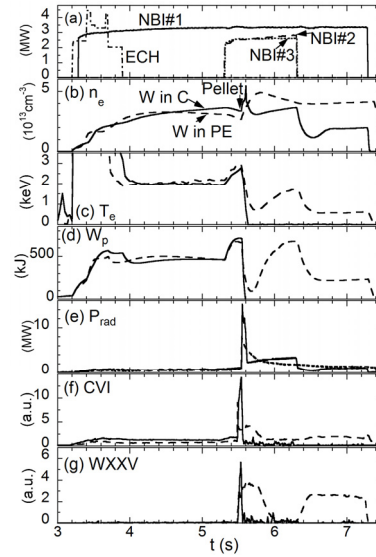
FIG. 3. Waveform of discharges with W-in-PE (dash lines) and W-in-C (solid line) pellets; (a) ECH and NBI port-through power, (b) line-averaged electron density, (c) central electron temperature, (d) plasma stored energy, (e) radiation power, (f) CVI at 33.73Å and (g) WXXV at 32.3Å.

The time evolution of ablation light from W-in-C pellet with velocity of 190 m/s is shown in Fig. 4(c). The emission is widely distributed compared to W-in-PE case. It suggests a deeper penetration while the velocity is slower. The bump in the H_α profile at $0.7 \le \rho \le 0.9$ seems to reflect the ablation of adhesive consisting of hydrocarbon, which is used to fix the wire with the tube. Though it is not easy to interpret each peak in the range $0.53 \le \rho \le 0.70$, three peaks are at least a sign of pellet ablation. The CI emission gradually increases until the pellet arrives at $\rho = 0.56$ and then sharply drops. The H_α and bremsstrahlung behave similarly to the CI emission. It is found that these time behaviors resemble closely those from C pellet without tungsten. After the C tube is fully ablated, the tungsten wire is exposed to plasmas and starts to ablate near $\rho \sim 0.53$. The ablation is completed at $\rho \sim 0.43$. As well as the analysis of T_e signals in Fig. 4(b), the time evolution of T_e shown in Fig. 4(d) also confirms the radial location of two H_α peaks indicated with dashed lines.

It is obvious that both the C and PE tubes are ablated before the tungsten wire is exposed to plasmas. Since the sublimation energy of carbon (7.5eV per atom) is much higher than that of PE (0.08eV per molecule), the C tube can survive longer in plasmas and reach deeper position. As a result, the tungsten in C can penetrate into deeper radius ($\rho = 0.43$) compared to that in PE ($\rho = 0.7$). When the tungsten is ablated in the plasma core, all the tungsten ions are confined and resultant radiation loss becomes really huge in a relatively small plasma volume in addition to the ionization loss. On the contrary, when the tungsten is ablated in the edge, the LHD plasma can decrease the plasma radius to minimize the edge cooling because helical plasmas have free boundary. The coaxial pellet with carbon tube can be probably applicable to lighter element such as Fe and Mo.

The density increase by tungsten ($\Delta n_{e,W}$) is much larger than that by PE tube ($\Delta n_{e,PE}$). The density increase is also calculated as $\Delta n_{e,W,cal.}$ and $\Delta n_{e,PE,cal}$ for tungsten and PE, respectively. The experimental value of $\Delta n_{e,W}$ is one order of magnitude larger than the calculated value of $\Delta n_{e,W,cal}$, while $\Delta n_{e,PE}$ is close to $\Delta n_{e,PE,cal}$. This strongly suggests that the reduced plasma radius due to the edge cooling deletes the edge particle screening [12] based on the presence of stochastic magnetic field layer and resultantly increases the edge particle confinement.
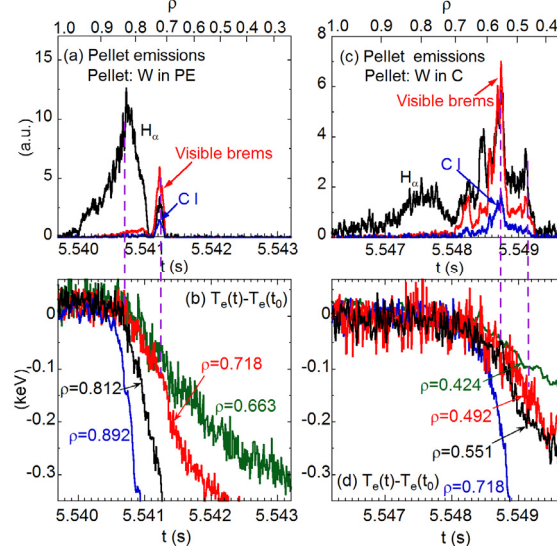
FIG. 4. Time behavior of visible emissions from (a) W-in-PE and (c) W-in-C and relative change in electron temperature of (b) W-in-PE and (d) W-in-C. Visible emissions are plotted for H_α (black solid line), CI (blue solid line) and bremsstrahlung (red solid line). Radial position at the upper abscissa in (a) and (c) is derived from velocity of W-in-C (190m/s) and W-in-PE (216m/s).

IV. Comparison of plasma response with other impurity pellet injection

The plasma response after the pellet injection has been investigated in relation to the size and density rise systematically changing the Z number (H, C, Al, Ti, Fe, Mo, Sn and W) [13]. The results are shown in Figs.5 (a) and (b). Maximum size of the pellets, S_{max}, which can maintain a discharge without plasma collapse under $P_{in} \sim 10\text{-}18MW$, is $3.4^\phi mm \times 3.4mm^L$ in cylinder for an H_2 ice pellet and $1.8^\phi mm \times 1.8mm^L$ for a carbon pellet. The 3.8mm H_2 and 2.0mm carbon pellets were tried, but the smooth operation of discharges was a little difficult. The S_{max} of course decreases with Z, i.e. ~1mm for Al and Ti and 0.2-0.3mm for Mo and W. The density rise, Δn_e, is close to $10 \times 10^{14} cm^{-3}$ for single H_2 and carbon pellet injection. However, the upper limit of Δn_e reduces down to $1 \times 10^{13} cm^{-3}$ for Al pellet. The access to high-density operation is therefore limited to both of H_2 and C pellets.
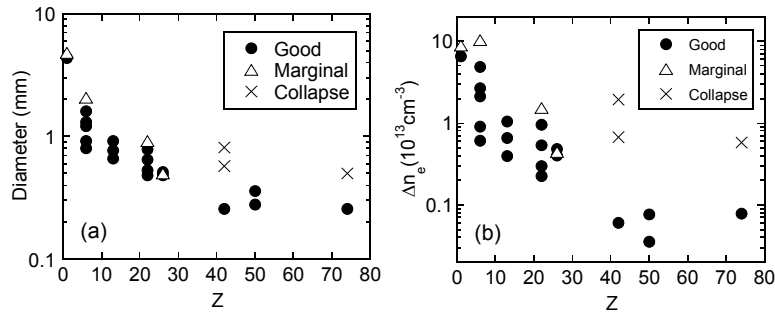
Fig.5 Plasma response after pellet injection (H,C, Al, Ti, Fe, Mo, Sn and W); Z dependence for (a) diameter and (b) density rise.

After the high-Z impurity injection the beta value measured from diamagnetic loop decreases monotonically whereas the density gradually goes up and keeps a constant density increment until the complete disappearance of the plasma energy.   The decay time of the plasma energy is approximately equal to τ_E of the discharge.   In such collapsed phases any strong MHD mode excitation has not been observed.   The m/n=2/1 mode amplitude during the plasma collapse is quite small.   It is thus concluded that the plasma collapse following after the impurity pellet injection is not induced by the MHD instability

V. Summary

Coaxial tungsten pellets, which have been newly developed for producing bright tungsten light source, are successfully injected in LHD plasmas with relatively higher densities ($\leq 5 \times 10^{13} cm^{-3}$) without plasma collapse.   The tungsten spectra from visible, VUV and EUV ranges have been observed with sufficient intensity including radial profiles.   The data are analyzed for ITER tungsten diagnostics.

Acknowledgements

References

[1] R. A. Pitts et al, Phys. Scr. **2009**, 014001 (2009).
[2] G. F. Matthews et al., Phys. Scr. **2011**, 014001 (2011).
[3] R. Neu et al., Plasma Phys. Control. Fusion **44**, 811 (2002).
[4] S. Morita et al., AIP Conf. Proc. **1545**, 143 (2013).
[5] J. Clementson et al., Rev. Sci. Instrum. **81**, 10E326 (2010).
[6] J. Clementson et al., AIP Conf. Proc. **1525**, 78(2013).
[7] S.Morita et al., Plasma Phys. Contr. Fusion **56** (2014) 094007.
[8] H. Nozato et al., Rev. Sci. Instrum. **74**, 2032 (2003).
[9] R. Katai et al., Jpn. J. Appl. Phys. **46**, 3667 (2007).
[10] X.L.Huang et al., Rev. Sci. Instrum. **81**, 11E818 (2010).
[11] C. F. Dong *et al.*, Rev. Sci. Instrum. **83**, 10D509 (2012).
[12] S. Morita, *et al.*, Nucl. Fusion **53**, 093017 (2013).
[13] S. Morita *et al.*, Plasma Sci. Technol. **13**, 290 (2011).

Particle Transport Analyses using Transient MHD Events and Proposal of a New Two-dimensional Diagnostics

Tomohiro Morisaki and LHD Experiment Group

National Institute for Fusion Science

1. introduction

In the last A3 foresight program workshop held in Kagoshima in June 2014, I presented the transport analysis results for the super dense core (SDC) mode in the Large Helical Device (LHD), using the particle pulse propagation induced by the pellet injection [1]. From the time evolution of the local electron density and its profile, i.e., gradient, the diffusion coefficient D and the convective velocity v were derived by using the one-dimensional transport equation. Comparing D in the nested flux surface region and the stochastic region, it was found that the difference of the magnetic topology affects the particle transport. It was also observed that D is further increased by applying resonant magnetic perturbations (RMPs). These results agree well to those expected in the numerical study with the HINT2 code [2]. The particle pulse induced by the pellet injection is useful for the transport analysis, because one can easily estimate the source quantity and can determine the injection timing as he/she wants. However, there exist some disadvantages. For example, its perturbation is sometimes so large that the plasma itself is disturbed by the pellet injection, i.e., diagnostics. Ablation of the pellet during the penetration into the plasma also complicates the analyzing process, since it increases the density along the path. Although another method using, e.g., gas puffing modulation has also been used in many tokamaks and stellarators, it also has similar advantages and disadvantages.

I have recently developed a new particle transport analysis technique using transient MHD phenomena like saw-tooth oscillation and/or core density collapse (CDC) which is ballooning-type instability destabilized in the SDC mode in LHD. If once CDC takes place, it evacuates certain amount of particles from the confinement region to the divertor through edge stochastic region. The CDC itself occurs quite fast, since it is an MHD phenomenon. After the collapse, however, its particle pulse propagates, depending on D and v in the region. The superior thing of this method is that the particle source is originated at the core region, which enables the measurement to be free from taking account of the source in the edge region.

2. Experimental results

Experiments were carried out at the outward shifted configuration at $R_{ax} = 3.85$ m with $B_T = 2$ T. The plasma was produced and maintained by the neutral beam injection. The density was increased by the repetitive pellet injection. The line integrated electron densities at various radial positions were measured

with a multi-channel CO_2 laser interferometer, where the plasma is vertically elongated. Time trends of main plasma parameters are shown in Fig. 1.
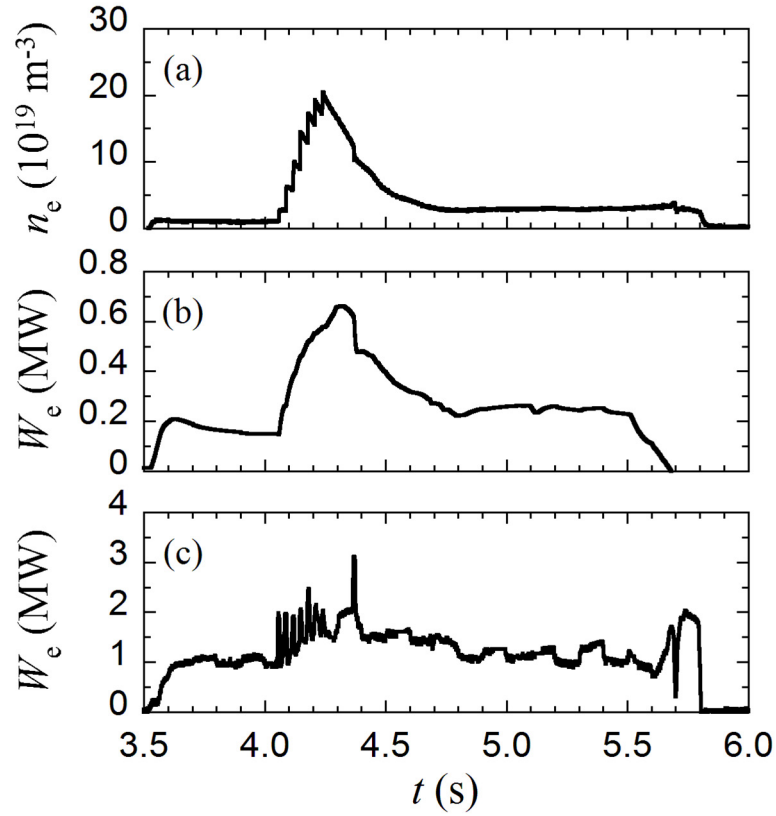
Fig. 1. Time evolution of (a) line averaged density, (b) stored energy and (c) radiated power.

In order to modify the edge stochasticity, RMPs ($m/n = 1/1$ and $2/1$) were applied with the normal conducting RMP coils installed in outside the cryostat of the LHD. The configuration of the RMP coils installed in LHD is depicted in Fig. 2.
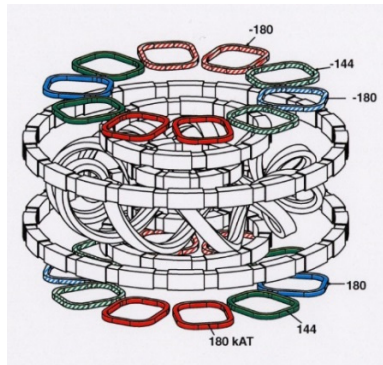
Fig. 2. RMP coils. Each colored group is driven by independent power supply.

Figure 3 shows the time evolution of (a), (c) line averaged electron density at different radial positions and (b), (d) divertor flux measured with Langmuir probes embedded in divertor plates. The left and right columns are from the discharges without and with RMPs, respectively. As seen from Fig. 3 (a) and (c), CDC takes place at $t = 4.368$ s in both discharges. After the CDC, the particle pulse propagates from the core ($r = 4.157$ m) to edge ($r = 4.228$ m) regions and finally reaches the divertor, as shown in Fig. 3. The propagation were compared between different edge stochasticities. It is found that the delay of the propagation observed in the edge region changes when the RMP is applied, as depicted with red closed circles. This result suggests that the particle transport is different in different magnetic topologies. In this experiment, the difference between two discharges was not so clear, since the CDC was too big to keep the original density profile. The CDC broke not only the core region but even the edge region. Optimization of the CDC amplitude is mandatory to see the clear pulse propagation. In addition, higher sampling frequency is required to increase the accuracy of the observation.
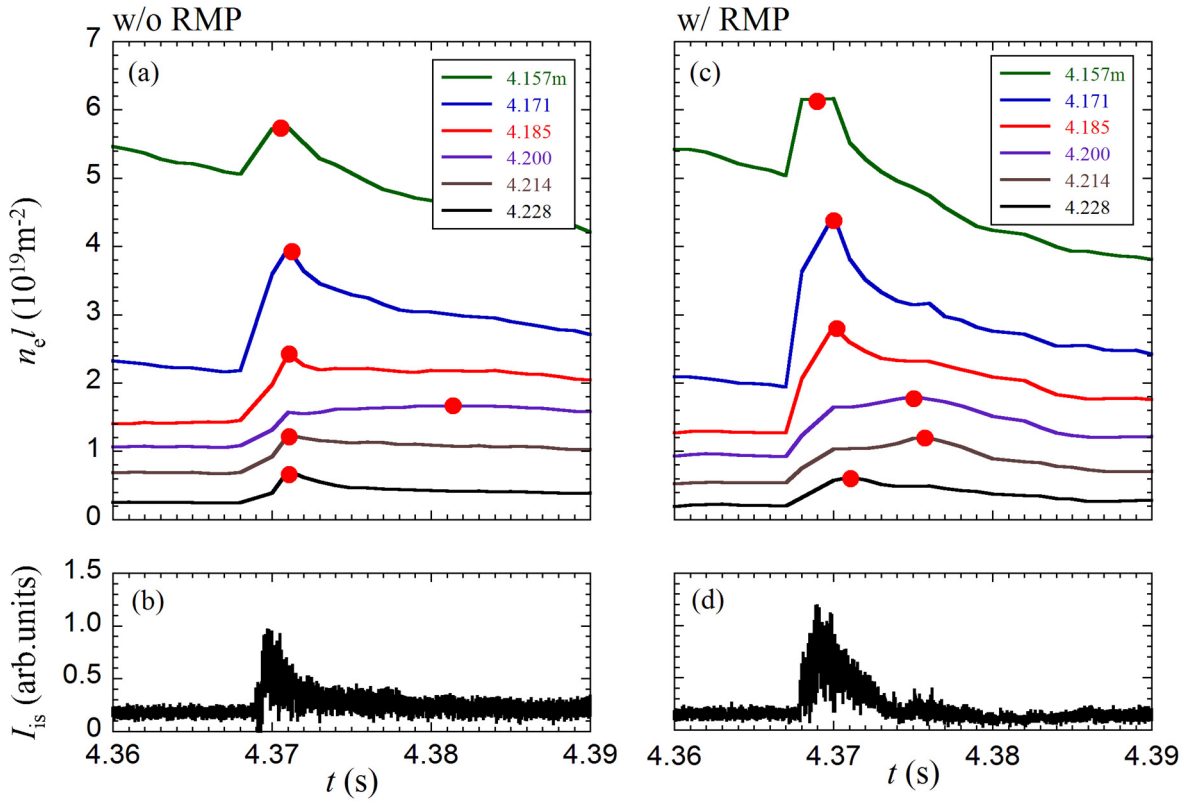
Fig. 3. Time evolution of (a), (c) line averaged electron density at different radial positions and (b), (d) divertor flux measured with Langmuir probes embedded in divertor plates. The left and right columns are from the discharges without and with RMPs, respectively. CDC occurs at t = 4.368 s in both discharges. Closed red circles indicate peak of the density pulse.

3. Proposal of helium beam probe for edge two-dimensional n_e, T_e measurements

I would like to propose a new edge diagnostics, helium beam probe (HeBP), which can measure particle pulses passing through the edge stochastic region two-dimensionally, with high time and spatial resolutions [3].

Using three (667.8, 706.5, 728.1 nm) line emissions from helium atoms in the plasma, edge electron temperature and density can be derived with the collisional-radiative model. For the beam injector, a Laval nozzle with a fast solenoid valve is recommended to produce the collimated beam. Three He I line emission images are spectroscopically detected with an image-intensifier-coupled fast camera behind three interference filters. An image-guide fiber may be necessary to keep the camera away from the high magnetic and/or radiation field region.

A schematic view of the HeBP system is shown in Fig. 4.
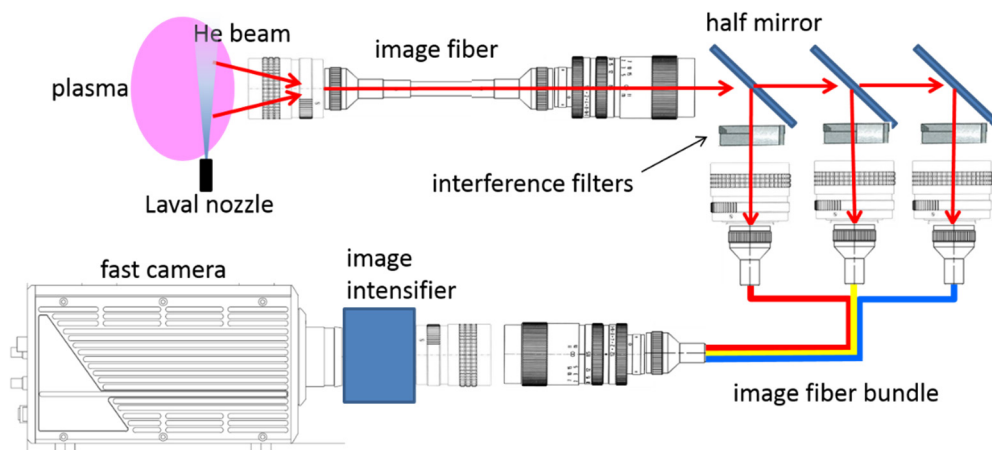
Fig. 4. Schematic of HeBP system.

Acknowledgements

References

[1] T. Morisaki, "Estimation of Heat and Particle Transport by Means of Transient Phenomena", NIFS-PROC-97 p.183 Oct.30 (2014).

[2] Y. Suzuki, K. Ida, K. Kamiya et al., "3D plasma response to magnetic field structure in the Large Helical Device", Nuclear Fusion, **53** (2013) 073045-1.

[3] T. Morisaki, et al., "Development of Helium Beam Probe for Edge Plasma Measurements" 39th EPS Conference & 16th Int. Congress on Plasma Physics.

VUV spectroscopy for WVI line spectrum in Large Helical Device

T. Oishi[1,2], S. Morita[1,2], X. L. Huang[2], H. M. Zhang[2], M. Goto[1,2] and the LHD Experiment Group

[1] National Institute for Fusion Science, 322-6, Oroshi-cho, Toki, 509-5292, Japan

[2] Department of Fusion Science, Graduate University for Advanced Studies, 322-6, Oroshi-cho, Toki, 509-5292, Japan

Abstract

Vacuum ultraviolet (VUV) spectra of emissions released from tungsten ions at lower ionization stages were measured in the Large Helical Device (LHD) using a 3 m normal incidence spectrometer with high wavelength dispersion of 0.037 Å/CCD-pixel for detailed spectral shapes in the wavelength range of 500 to 2200 Å and three 20 cm normal incidence spectrometers with low wavelength dispersion of 0.88 Å/CCD-pixel for routinely monitoring of the spectra in the wavelength range of 300-2400 Å. Among many spectral lines which were identified as lowly ionized tungsten ions WIV, WV, WVI, and WVII, especially WVI 639.683 Å and 677.722 Å 5d-6p transitions had large intensities and were isolated from other intrinsic impurity lines, which would be useful for the spectroscopic studies of tungsten ions in ITER and other tungsten-wall machines.

I. INTRODUCTION

Tungsten is regarded as a leading candidate material for the plasma facing components in ITER and future fusion reactors[1-3]. Considering transport processes of tungsten impurity in ITER, firstly neutral tungsten atoms are released from the divertor plates, then tungsten ions at lower ionization stages are transported in the edge plasmas, and finally tungsten ions at higher ionization stages are accumulated in the core plasmas. Therefore, diagnostics for tungsten impurity ions in magnetically-confined high-temperature plasmas have been intensively conducted, such as visible spectroscopy for neutral tungsten atoms in the wavelength range around 4000 Å and extreme ultraviolet (EUV) spectroscopy for highly-ionized tungsten ions in the wavelength range around 15-70 Å[4]. However, tungsten ions at lower ionization stages have not been measured except for several cases of vacuum ultraviolet (VUV) spectroscopy in basic plasma experiments even though it is necessary for accurate evaluation of tungsten influx and comprehensive understanding of the tungsten impurity transport in high temperature plasmas[5,6]. In the present study, VUV spectra of emissions released from tungsten ions are measured in the Large Helical Device (LHD) for exploration of tungsten lines at low ionization stages which will contribute spectroscopic studies of edge plasmas in ITER and other tungsten-wall machines.

II. EXPERIMENTAL SETUP

LHD has the major/minor radii of 3.6/0.64 m in the standard configuration with maximum plasma volume of 30 m^3 and toroidal magnetic field of 3 T. The coil system consists of a set of two continuous superconducting helical coils with poloidal pitch number of 2 and toroidal pitch number of 10 and three pairs of superconducting poloidal coils[7]. Tungsten ions are distributed in the LHD plasma by injecting a polyethylene pellet containing a small piece of tungsten metal. The length and diameter of tungsten wire is 0.6 mm and 0.15 mm, respectively. Owing to the advantages of steady-state current-free helical systems, the LHD plasma can be sustained even though substantial amount of tungsten atoms are injected[8]. The pellet is accelerated by pressurized He gas of 10-20 atm. The pellet injection orbit is located on the midplane of the plasma having a 12° angle from the normal to the toroidal magnetic axis[9].

A 3m normal incidence VUV spectrometer (McPherson model 2253) is installed on an outboard midplane diagnostic port which is the same as the impurity pellet injector[10,11]. The working wavelength range of the spectrometer is 300-3200 Å. The elliptical plasma of LHD can be fully observed at the horizontally-elongated plasma cross section. A back-illuminated CCD detector (Andor model DO435-BN: 1024 × 1024 pixels) is placed at the position of the exit slit of the spectrometer. Time resolutions are 50 ms for the "full-binning" measurement in which all 1024 vertical pixels are replaced by single channel and the spatial resolution is entirely eliminated and 100 ms for "space-resolved" measurement in which the wavelength-dispersed image of the VUV emission is projected on a corresponding vertical position on CCD through a space-resolved slit mounted between the entrance slit and the grating. A high wavelength dispersion of 0.037 Å/pixel enables

measurements of the Doppler broadening of the impurity lines to obtain the ion temperature[12]. The wavelength interval which can be measured in a single discharge is about 37 Å. Therefore, we conducted measurements by scanning the wavelength shot by shot between the wavelength range of 500-2200 Å in this study.

Three 20 cm normal incidence VUV spectrometers named "102R", "106R", and "109L" have been installed in LHD for routinely monitoring of impurity spectra[13]. Each spectrometer covered a wavelength range, $\Delta\lambda$, of 300-1050 Å with a wavelength dispersion, $d\lambda/dx$, of 0.85 Å/pixel (109L), $\Delta\lambda$ of 1000-1850 Å with $d\lambda/dx$ of 0.88 Å/pixel (106R), and $\Delta\lambda$ of 1550-2400 Å with $d\lambda/dx$ of 0.88 Å/pixel (102R), respectively, in a single discharge. Back-illuminated CCD detectors (Andor model DO420-BN: 1024 × 256 pixels, pixel size 26 × 26 μm^2) were placed at the positions of the exit slits of the spectrometers. A time resolution of 5 ms was applied to measure temporal evolution of the spectra. It is important that these three spectrometers are routinely operated in LHD, therefore we can obtain spectroscopic data in $\Delta\lambda$ of 300-2400 Å for all discharges.

III. WVI LINE SPECTRA MEASUREMENT

Figure 1 shows VUV spectra in the wavelength range between 600 to 705 Å measured using the 3 m normal incidence VUV spectrometer in the time frame just after the tungsten pellet injection in hydrogen discharge in LHD. The plasma was initiated by the electron cyclotron heating, and three neutral hydrogen beams based on negative ion sources with total port-through power of 8 MW were injected. Central electron density and
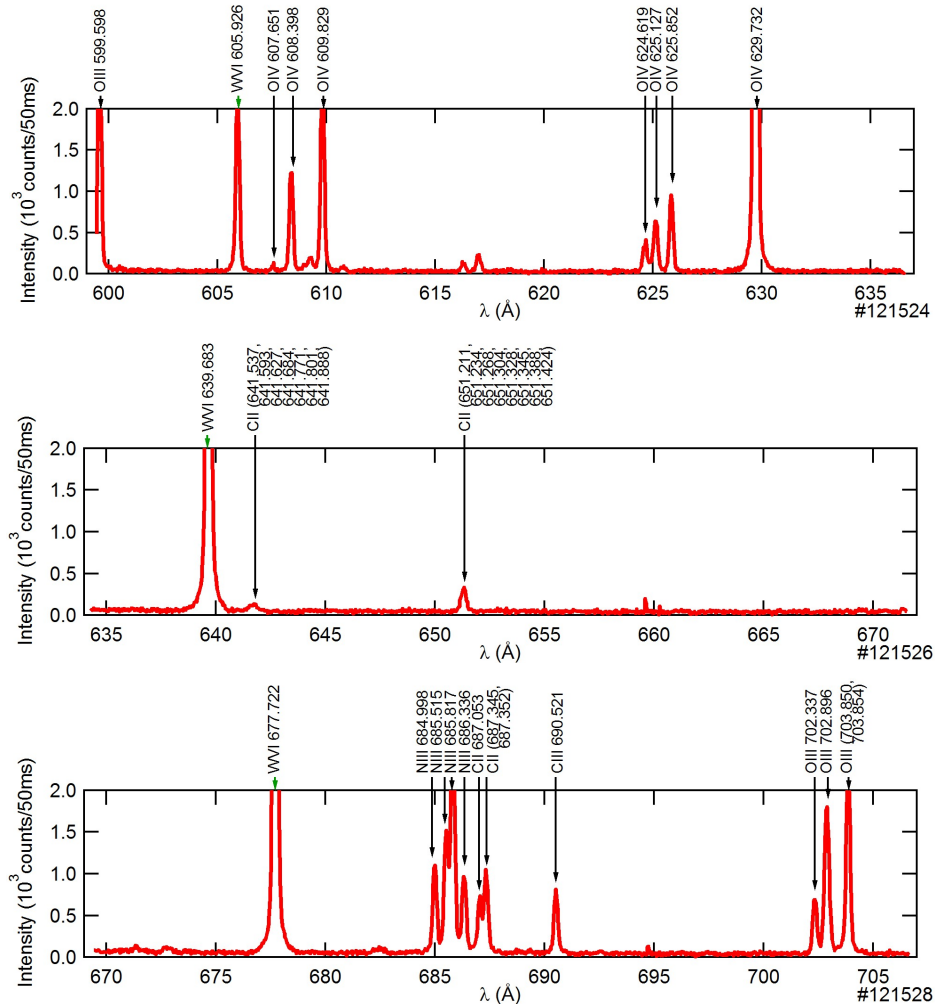
FIG. 1. VUV spectra in the wavelength range between 600 to 705 Å measured using the 3 m normal incidence VUV spectrometer in the time frame just after the tungsten pellet injection.

temperature just before the pellet injection was 2×10^{13} cm^{-3} and 3 keV, respectively. Several bright WVI lines with 5d-6p transitions located at the wavelengths of 605.926 Å, 639.683 Å, and 677.722 Å have been successfully observed. They had large intensities and were isolated from other intrinsic impurity lines. The second and third order emissions of these three lines were also observed[14].

Figure 2(a) shows the VUV spectra including tungsten emissions of WVI 605.926 Å, 639.683 Å, and 677.722 Å lines measured using a 3 m normal incidence spectrometer. Spectra of three shots measured with scanning the wavelength for shot by shot to cover a wavelength range of 600-700 Å are shown together. Figures (b-d) show spectra measured using three 20 cm normal incidence spectrometers. Wavelength ranges of 600-700 Å, 1200-1400 Å and 1800-2100 Å are enlarged to investigate above three tungsten lines and their second and third order emissions. Spectra measured before the pellet injections are also shown together. As shown in Figs, 2(b) and (c), WVI 639.683 Å and 677.722 Å lines, and their second order lines were isolated from other intrinsic impurity lines even under the observation with the wavelength resolution of a 20 cm VUV spectrometer while WVI 605.926 Å was blended with intrinsic OIV lines. Third orders of WVI lines were not found as shown in Fig. 2(d).

IV. SPACIAL PROFILE OF WVI LINE

We succeeded a measurement of the vertical profile of the emission intensity of WVI line by using the 3 m normal incident VUV spectrometer. Figure 3(a) shows a typical temporal evolution of the central electron density, $n_e(0)$, and temperature, $T_e(0)$. At the pellet injection, $n_e(0)$ increases and $T_e(0)$ decreases. Figure 3(b) shows a temporal evolution of the second order of WVI 639.683 Å line measured using a 20 cm normal incident VUV spectrometer. A large emission was observed at the same time of the pellet injection, which is an emission from the pellet ablation cloud.

Figure 3(c) shows a vertical profiles of WVI 639.683 Å line measured using a 3 m VUV spectrometer in time frame just after the pellet injection. It is regarded that the profile consists of the WVI emissions from a pellet ablation cloud located at the vertical center of the plasma and a plasma confinement region. The enlarged figure for this time frame around the signal level of the emission from plasma confinement region is shown in Fig. 3(d). The positions of the last closed flux surface (LCFS) in the vaccum magnetic field are shown together. The profile has a vertical asymmetry that the signal intensity in the lower half is larger than that in the upper half. This asymmetry having a peak close to the lower edge pf the plasma is more obvious in the time frame 100-200 ms after the pellet injection as shown in Fig. 3(e). Mechanisms forming the asymmetrical profile of WVI line and similarity with asymmetrical W profiles in tokamaks should be investigated in future studies.
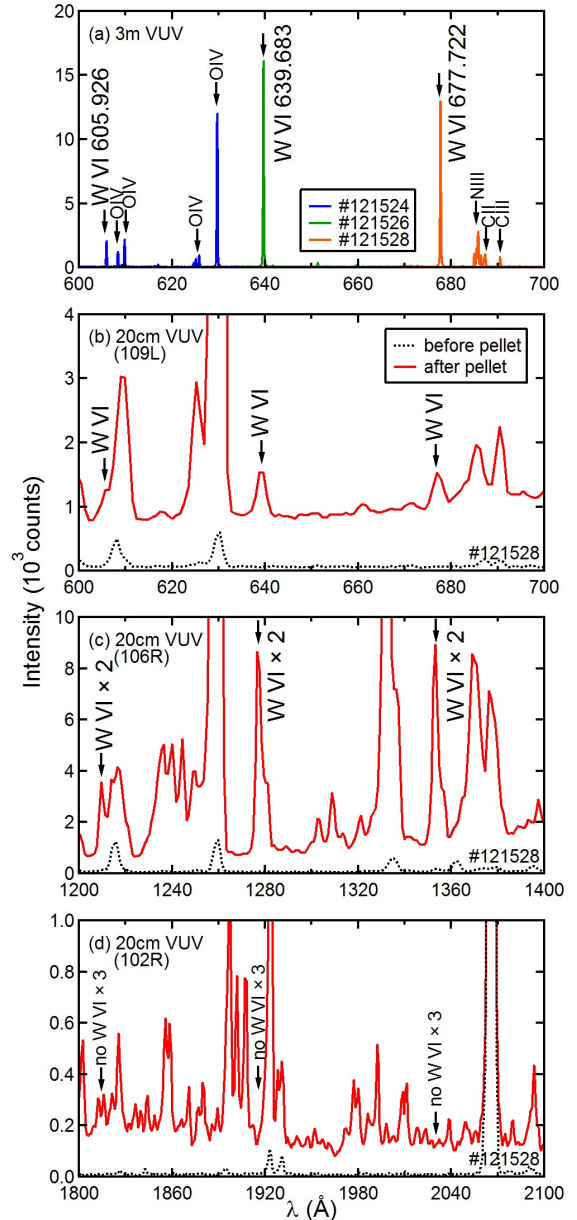
FIG. 2. VUV spectra including tungsten emissions of WVI 605.926 Å, 639.683 Å, and 677.722 Å lines. (a) Spectra measured using a 3 m normal incidence spectrometer for the wavelength range of 600-700 Å. (b-d) Spectra measured using three 20 cm normal incidence spectrometers. Wavelength ranges of 600-700 Å, 1200-1400 Å, and 1800-2100 Å are enlarged.

V. SUMMARY

For the diagnostics of tungsten ions in lower ionization stages in LHD, a 3 m normal incidence spectrometer with a high wavelength dispersion measured detailed spectral shapes and the spatial profiles in the wavelength range of 500-2200 Å and three 20 cm normal incidence spectrometers with low wavelength dispersion were utilized as survey spectrometers routinely monitoring the wavelength range of 300-2400 Å. WVI 639.683 Å and 677.722 Å 5d-6p transitions had large intensities and were isolated from other intrinsic impurity lines. They have possibility to be used for the measurement of W influx in ITER and tungsten-wall machines. Intensity profile of WVI 639.683 Å has a vertical asymmetry with a peak close to the bottom edge of the horizontally elongated plasma cross section, of which the mechanisms should be investigated in future studies.

REFERENCES

[1] ITER Physics Basis Editors *et al.*, Nucl. Fusion **39**, 2137 (1999).
[2] R. Neu *et al.*, Nucl. Fusion **45**, 209 (2005).
[3] J. Roth et al., *Plasma Phys. Control. Fusion* **50**, 103001 (2008).
[4] S. Morita *et al.*, AIP Conf. Proc. **1545**, 143 (2013); *Proceedings of ICAMDATA-2012*, Gaithersburg, 30 September–4 October 2012.
[5] R. Radtke *et al.*, *Atomic and Plasma-Material Interaction Data for Fusion* (IAEA, 2007), Vol. 13, p. 45.
[6] J. Clementson *et al.*, J. Phys. B: At. Mol. Opt. Phys. **43**, 144009 (2010).
[7] H. Yamada for the LHD Experiment Group, Nucl. Fusion **51**, 094021 (2011).
[8] X. L. Huang *et al.*, Rev. Sci. Instrum. **85**, 11E818 (2014).
[9] H. Nozato *et al.*, Rev. Sci. Instrum. **74**, 2032 (2003).
[10] T. Oishi *et al.*, Appl. Opt. **53**, 6900 (2014).
[11] T. Oishi *et al.*, Plasma Fusion Res. **8**, 2402093 (2013).
[12] T. Oishi *et al.*, J. Korean Phys. Soc. **64**, 840 (2014).
[13] T. Oishi *et al.*, *submitter to* Plasma Fusion Res.
[14] T. Oishi *et al.*, Rev. Sci. Instrum. **85**, 11E415 (2014).
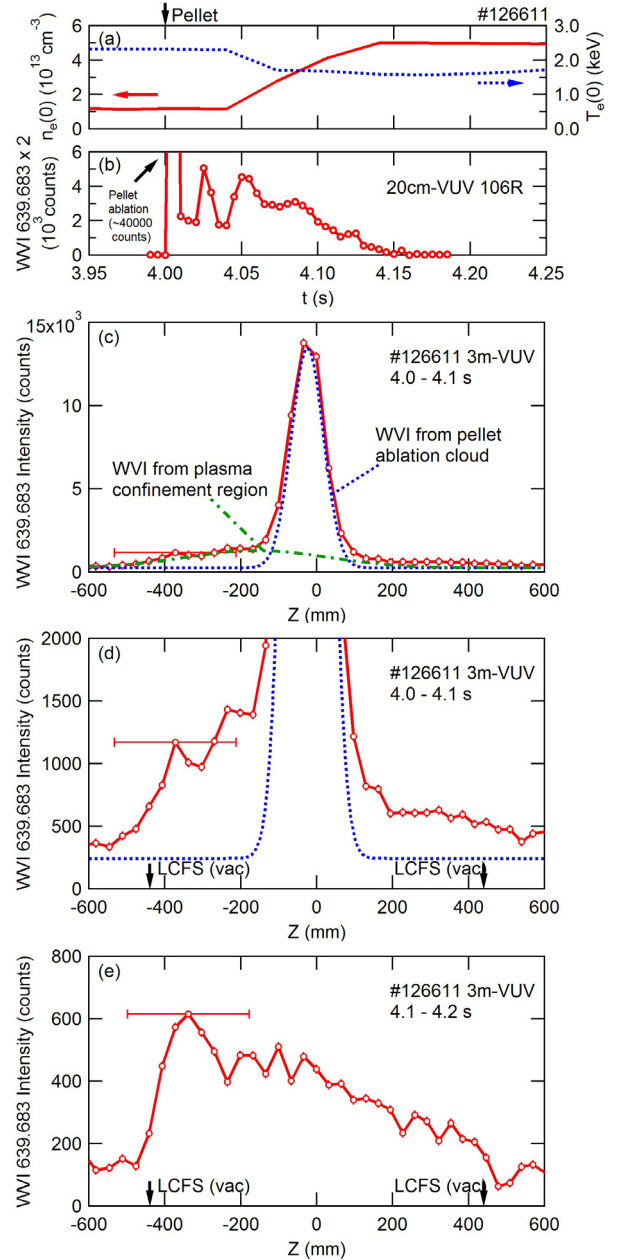
FIG. 3. Temporal evolutions of (a) central electron density and temperature with tungsten pellet injection and (b) intensity of WVI 639.683 × 2 Å line measured using a 20 cm VUV spectrometer. Vertical profiles of WVI 639.683 Å line measured using a 3 m VUV spectrometer in time frames (c) just after the pellet injection, (d) its enlarged figure around the signal level of the emission from plasma confinement region, and (e) 100-200 ms after the pellet injection.

Near UV-visible line emission from tungsten highly-charged ions in Large Helical Device

D. Kato[1,2], H. A. Sakaue[1], I. Murakami[1,2], K. Fujii[3], M. Goto[1,2], T. Oishi[1,2], S. Morita[1,2], N. Nakamura[4], F. Koike[5], A. Sasaki[6], X. -B. Ding[7], C. -Z. Dong[7]

[1]National Institute for Fusion Science, Toki, 509-5292 Japan
[2]Dept. Fusion Science, SOKENDAI (The Graduate University for Advanced Studies), Toki, Gifu 509-5292, Japan
[3]Graduate School of Engineering, Kyoto University, Kyoto 615-8540, Japan
[4]Inst. Laser Science, The Univ. Electro-Communications, Tokyo 182-8585, Japan
[5]Faculty of Sci. and Tech., Sophia University, Tokyo 102-8554, Japan
[6]Japan Atomic Energy Agency (JAEA), Kyoto 619-0215, Japan
[7]College of Phys. and Electronic Eng., Northwest Normal University, Lanzhou, 730070, P. R. China

E-mail: `kato.daiji@nifs.ac.jp`

February 2015

Abstract.
　Wavelengths of emission lines from tungsten highly-charged ions have been precisely measured in near UV-visible range ($320 - 356$ nm and $382 - 402$ nm) at Large Helical Device (LHD) by tungsten pellet injection. The tungsten emission lines were assigned based on its line-integrated intensity profiles on a poloidal cross section. The ground-term magnetic-dipole (M1) lines of $W^{26+,27+}$ and an M1 line of a metastable excited state of W^{28+}, whose wavelengths have been determined by measurements using electron-beam-ion-traps (EBITs), are identified in the LHD spectra. The present results partially compliment wavelength data of tungsten highly-charged ions in the near UV-visible range.

1. Introduction

Tungsten will be used as divertor materials in the International Thermonuclear Experimental Reactor (ITER) due to its high thermal conductivity, small thermal expansion, lower tritium retention and higher sputtering threshold. However, high-energy ions intermittently exhausted from edge plasmas of ITER, *i. e.*, the edge-localized mode, and heavy cooling gas particles (*e. g.*, Ne, Ar) seeded in peripheral plasmas to reduce a heat load to the divertor plate may increase sputtering of the tungsten divertor plate. Tungsten accumulation in core plasmas will induce drastic radiation cooling and may result in collapse of the plasmas. Tungsten transport in the plasmas is, therefore, a key issue for the stability of plasma confinements with the tungsten divertor.

Feldman *et al.* [1] in their pioneering work pointed out the potential usefulness of near UV-visible lines emitted via magnetic-dipole (M1) transitions in ground-term fine structures of highly-charged ions for high-temperature plasma diagnostics. The intrinsically narrow and isolated lines are suitable for identification of associated ion species and measurement of Doppler broadening which represents ion temperature. Doron *et al.* [2] suggested that the intensity ratios of some line pairs would also be useful for the density diagnostics of fusion plasmas. Fiber optics is available in this wavelength range to detect photon emission behind neutron shielding which is advantageous to prevent the detectors from neutron damage.

Spectral data for the near UV-visible lines of highly-charged ions, however, still limited [3]. An M1 transition of Ti-like W^{52+} $(3d^4)$ $^5D_3$ - $^5D_2$ has been investigated by a number of experimental and theoretical studies ([4] and references therein), because wavelengths of the M1 line exhibited an apparently peculiar behavior along the iso-electronic sequence, which has firstly been predicted by Feldman [1]. The wavelengths stay around an constant value in the near UV-visible range for Lanthanides and then very gently decrease upto U^{70+}. Recently, Komatsu [5] and Watanabe [6] found visible M1 lines of Cd-like W^{26+} by means of electron-beam-ion-traps (EBITs). The lines are identified as the ground-term fine-structure transitions of $(4f^2)$ $^3H_5$ - $^3H_4$, $^3H_6$ - $^3H_5$, and $^3F_3$ - $^3F_2$ [5, 7]. A Near UV M1 transition, $(4f)$ $^2F_{7/2}$ - $^2F_{5/2}$, of Ag-like W^{27+} was identified in spectra measured by using a permanent magnet EBIT at Fudan University [8]. Wavelength data of visible line emissions in $365 - 475$ nm from W^{8+} through W^{28+} are presented by a systematic measurement using a compact EBIT (CoBIT) [9]. Recently, the EBIT group at the Fudan University reported new line identification for $W^{25+,26+,28+}$ in a series of works [10].

Ab-initio calculations of fine structures of many electron ions with open-shells are challenging, because subtle electronic correlation and Breit interaction effects have remarkable influences on the results. Therefore, precise measurements of the wavelengths serve as a benchmark for atomic theories. Multi-configuration Dirac-Fock calculations for the M1 lines of $W^{26+,27+}$ have been performed by using grasp2K code [7, 8].

The first measurement of the visible M1 line emission in magnetic-confinement plasma devices was reported at the Large Helical Device (LHD) using tungsten pellet injection [11]. Precise measurements of near UV-visible forbidden lines from highly-charged ions colliding with high density hydrogen plasma particles (electron + proton), say 10^{19-20} m^{-3}, are feasible with the LHD. Therefore, the LHD enables experimental studies to identify tungsten emission lines useful for plasma diagnostics and provide new spectroscopic data complementing measurements by the EBITs operating at much lower electron densities ($\sim 10^{16}$ m^{-3}). Recently, high-resolution wide-band spectral measurements in $423 - 715$ nm have been performed at the LHD with a specially designed échelle spectrometer [12]. 13 lines in the measured spectra are assigned to tungsten highly-charged ions. Spatial distributions of the line intensity and polarization resolved measurements have also been performed [13]. In this contribution, we present
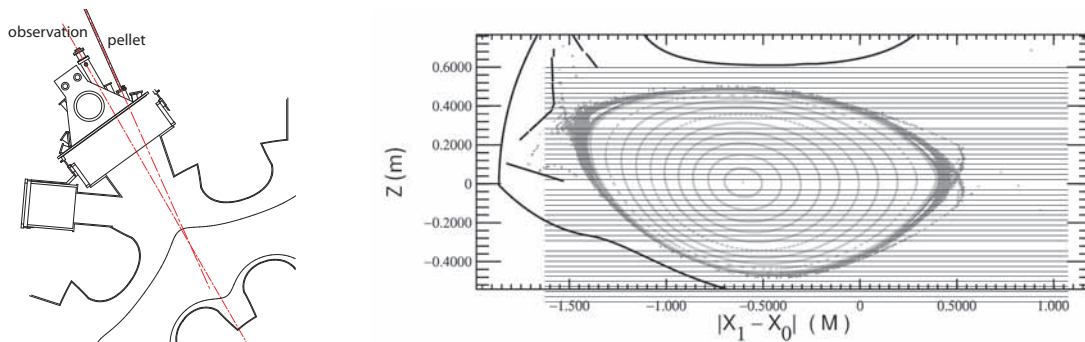
Figure 1. Left) A top view of the observation and pellet injection ports. Right) Horizontally elongated poloidal cross section and lines of sight. Viewing point is on the right-hand side.

wavelengths of emission lines in $320 - 356$ nm and $382 - 402$ nm from highly-charged tungsten ions in the LHD core plasmas.

2. Experimental setup

Tungsten was introduced into the LHD plasmas by injecting a polyethylene pellet (0.6 mm long and 0.6 mm diameter) containing a tungsten wire. Size of the tungsten wire in the polyethylene tube is 0.15 mm in diameter and 0.6 mm in length. Number of tungsten atoms in the single pellet is estimated roughly to be 6.7×10^{19}.

Time-resolved (sampling times for 38 ms at every 100 ms) measurements were conducted using a Czerny-Turner visible-UV spectrometer (1200 gr/mm, slit width of $50\ \mu$m) equipped with a CCD detector. Figure 1 shows an observation port as well as the pellet injection port. Using an optical fiber array, line-integrated photon emission was measured at 44 lines of sight divided along the vertical direction (Z) of a horizontally elongated poloidal cross section of a helical plasma, as shown in Fig. 1. The poloidal cross section is asymmetric with respect to Z=0, because the cross section is tilted a little (about 6 degrees) from the normal direction. This asymmetry manifests itself in asymmetric vertical distributions of the line-integrated intensities (along each line of sight) of emission lines in peripheral regions of the poloidal cross section.

Discharges for present measurements were started with electron cyclotron heating followed by hydrogen neutral beam injection (NBI) heating using three NBIs. In a steady state, the maximum electron temperature was 3 keV at the plasma center. After the pellet injection ($t = 4.0$ s), the peak electron temperature decreases to 2 keV in 100 ms. The present measurements for $320-356$ nm and $382-402$ nm were performed with two different discharges (shot no. 121534 and 121541), respectively, because of a limited band width of a single measurement. Electron temperature distributions for the two discharges are almost identical and kept its profile constant during the measurements ($t = 4.1 - 4.138$ s), while the temperatures decrease significantly in the core region. Judging from the temperature profiles, the plasma edge may be around $r_{\text{eff}} = 0.6$ m (see
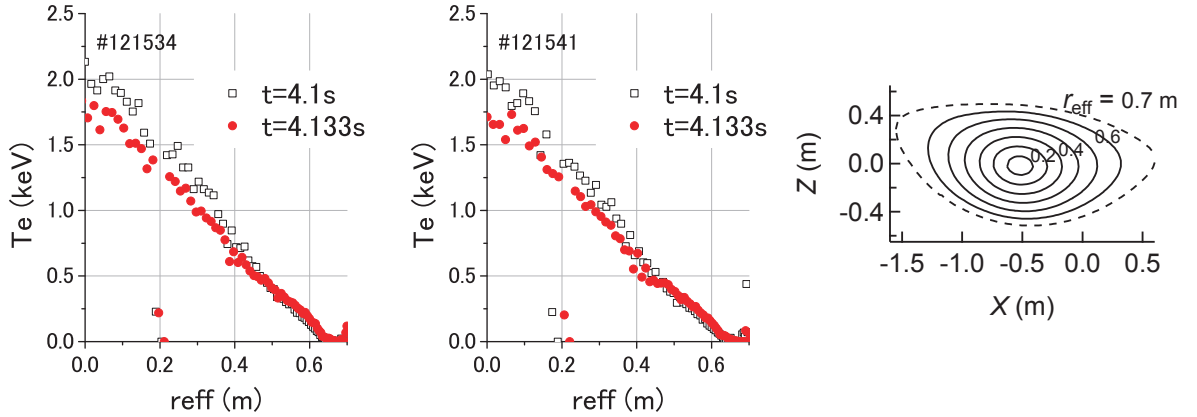
Figure 2. Electron temperature profiles for two discharges (121534 and 121541) as a function of effective minor radius ($r_{\rm eff}$) measured by Thomson scattering. The rightmost figure shows the effective minor radius on the poloidal cross section.

Fig. 2).

3. Results and discussion

Figures 3 and 4 are the measured spectra in $320-356$ nm and $382-402$ nm, respectively. Wavelength calibration was done using emission lines of hydrogen and helium in the same discharges. Uncertainties in the wavelength calibration are estimated to be about 0.02 nm. Emission lines indicated by red arrows in the figures are absent in the spectra taken before the tungsten injection (drawn by light gray color). Those lines are tentatively assigned to the emission lines of tungsten. Vertical distributions of the emission lines are shown in the upper panels of the figures. The tungsten lines have large intensities inside the vertical edge of the core plasma ($Z \sim 0.4$ m), while other lines have broader vertical distributions of the intensities. The lines at 337.7 nm in Fig. 3 and 389.4 nm in Fig. 4 are assigned to the M1 lines of W^{27+} and W^{26+}, respectively, whose wavelengths have been determined to be 337.743(26) nm and 389.41(6) by the EBIT measurements [8, 5].

In Table 1, the present measurements of wavelengths are summarized. For comparison, corresponding values by EBIT measurements and theoretical calculations are also shown in the table. In the EBIT measurements, the charge state associated to each emission line is determined from the appearance energy of each emission line. The present measurements are in good agreement with the EBIT measurements. It is noted that the line no. 15 at 344.48 nm is assigned to an M1 transition in a metastable excited state of W^{28+}. However, many unidentified lines are remained.

Radial distributions of the tungsten line intensities are deduced by Abel inversion from the vertical distribution of the line-integrated intensities. The radial distributions for the M1 lines of W^{27+} at 337.7 nm and W^{26+} at 333.7 nm are shown in Fig. 5. The deduced radial distribution shows a single maximum around $r_{\rm eff} \sim 0.3$ m, which
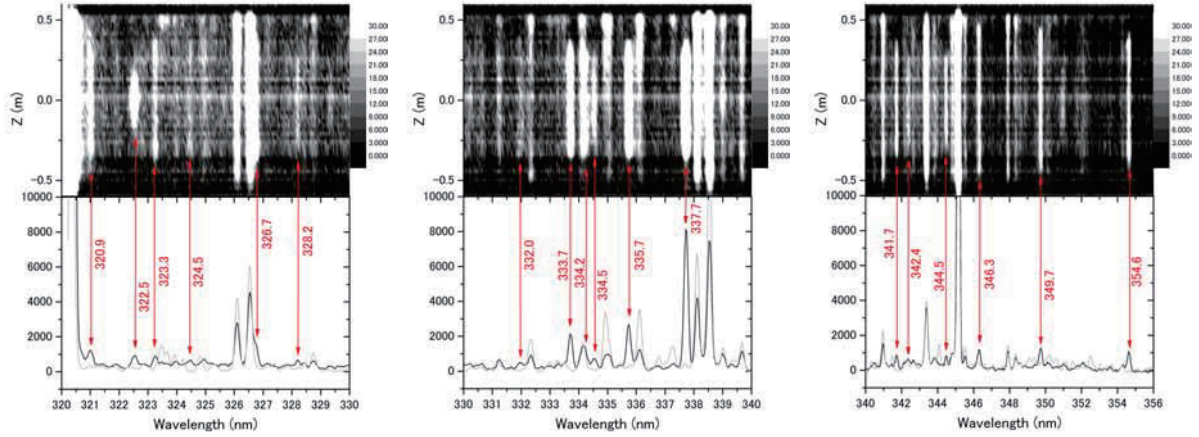
Figure 3. Line emission spectra in $320 - 356$ nm measured at the LHD (shot no. 121534). Upper panels show vertical distributions of line-integrated intensities. Solid indicates spectra measured after tungsten injection ($t = 4.1 - 4.138$ s), and light gray those before the tungsten injection. Red arrows indicate the emission lines assigned to tungsten. Numbers are the central wavelengths in nm.
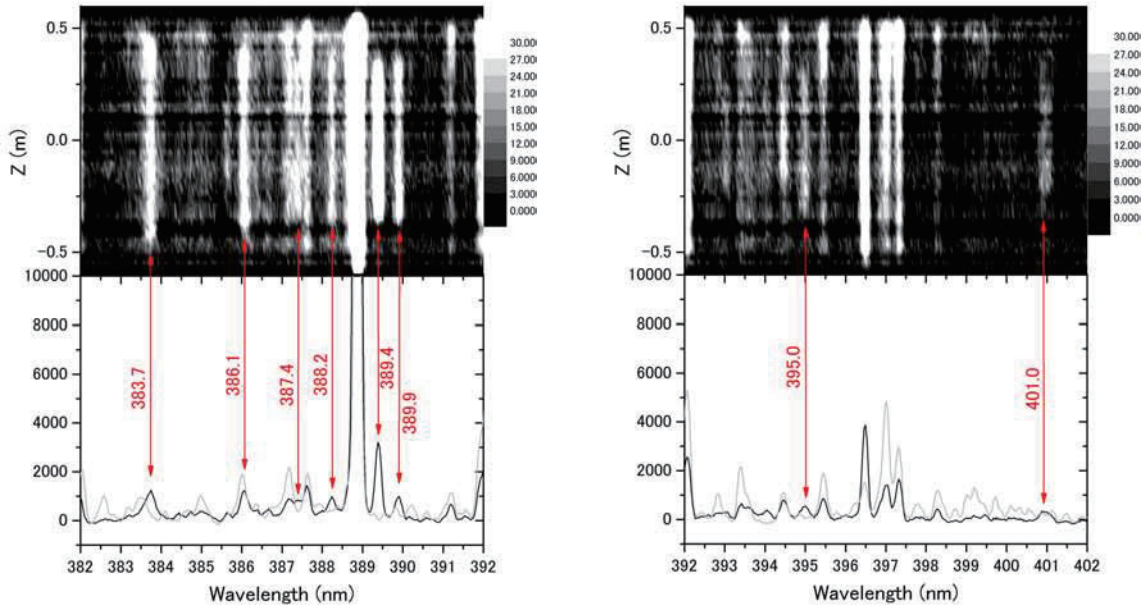
Figure 4. Line emission spectra in $382 - 402$ nm measured at the LHD (shot no. 121541). Same as Fig. 3

Table 1. Present measurements of wavelengths in air (nm) for W^{q+} ions. Numbers in parentheses are uncertainties.

Line	Wavelength	q	Other experiments	Theories	Transition
1	320.98(2)	-	-	-	-
2	322.53(2)	-	-	-	-
3	323.25(2)	-	-	-	-
4	324.45(2)	-	-	-	-
5	326.74†	-	-	-	-
6	328.19(2)	-	-	-	-
7	331.98(2)	-	-	-	-
8	333.70(2)	26	$333.748(9)^{a*}$	-	$(4f^2)\ {}^3F_4 - {}^3F_3$
9	334.16(2)	-	-	-	-
10	334.54(2)	-	-	-	-
11	335.73(2)	26	$335.758(11)^{a*}$	-	$(4f^2)\ {}^3F_4 - {}^1G_4$
12	337.72(2)	27	$337.743(26)^{b}$	338.18^b, 338.4^g	$(4f)\ {}^2F_{7/2} - {}^2F_{5/2}$
13	341.72(2)	-	-	-	-
14	342.36(2)	-	-	-	-
15	344.48(2)	28	$344.588(33)^{a*}$	345.87^a	$(4d^9 4f)\ (5/2,5/2)_3 - (5/2,7/2)_4$
16	346.30(2)	-	-	-	-
17	349.73(2)	-	-	-	-
18	354.63(2)	-	-	-	-
19	383.72†	25	383.99(6)	-	-
20	386.06†	24	$386.23(6)^{c}$	-	-
21	387.41†	25	$387.3^{c\dagger}$	-	-
22	388.24(2)	20	$388.25(6)^{c}$	-	-
		23	$388.27(6)^{c}$	-	-
23	389.39(2)	26	$389.433(12)^{a*}$, $389.41(6)^{c,d}$, $389.35(3)^{e}$	388.43^f	$(4f^2)\ {}^3H_5 - {}^3H_4$
24	389.88(2)	24	$389.89(6)^{c}$	-	-
25	394.98(2)	-	-	-	-
26	400.95†	-	-	-	-

^{a}SH-HtscEBIT [14]; ^{b}SH-PermEBIT [8]; ^{c,d}CoBIT [9, 5]; ^{e}Tokyo-EBIT [6].
^{b,f}MCDF using grasp2K [8, 7]; ^{a,g}RMBPT [14, 15].
†blend line; *converted to wavelength in vacuum.

corresponds to the local electron temperature of about 1 keV (see Fig. 2).

Acknowledgments

References

[1] Feldman U *et al* 1991 *J. Opt. Soc. Am.* **B8** 3.
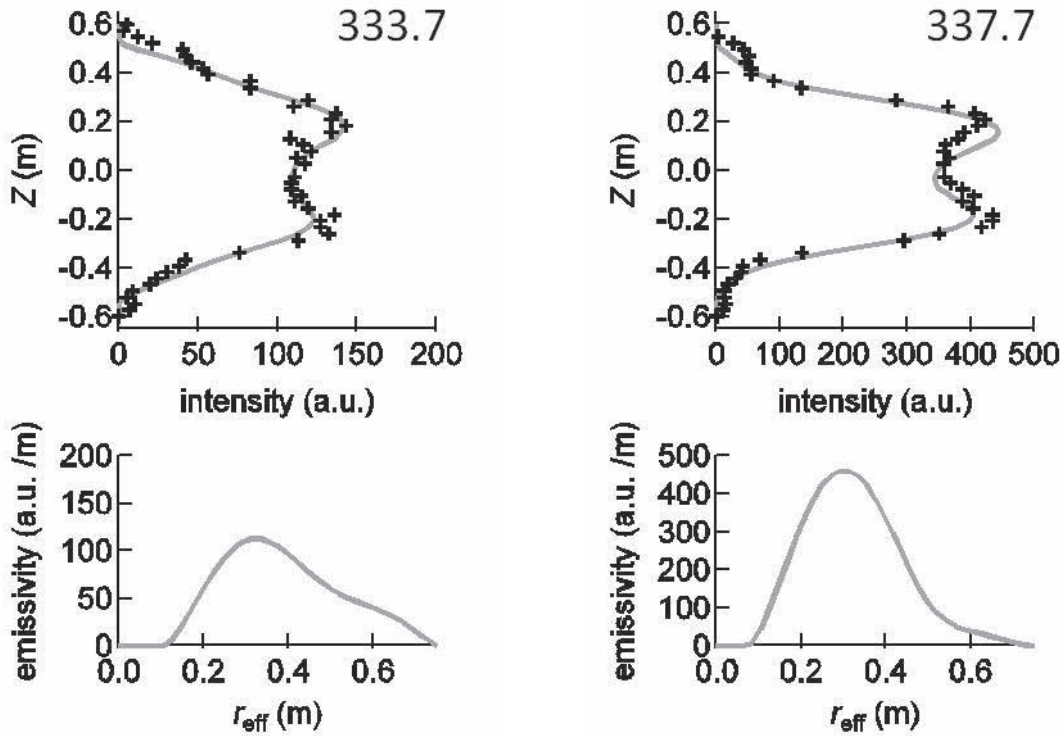
Figure 5. Radial distributions for M1 lines of W^{26+} at 333.7 nm and W^{27+} at 337.7 nm.

[2] Doron R, Feldman U 2001 *Phys. Scr.* **64** 319.
[3] Karmida A E and Shirai T 2009 *At. Data Nucl. Data Tables* **95** 305.
[4] Watanabe H *et al* 2001 *Phys. Rev. A* **63** 042513.
[5] Komatsu A *et al* 2011 *Phys. Scr.* **T144** 014012.
[6] Watanabe H *et al* 2012 *Can. J. Phys.* **90** 197.
[7] Ding X-B *et al* 2011 *J. Phys. B: At. Mol. Opt. Phys.* **44** 145004.
[8] Fei Z *et al* 2012 *Phys. Rev. A* **86** 062501.
[9] Komatsu A *et al* 2012 *Plasma and Fusion Res. : Rapid Commun.* **7** 1201158.
[10] Zhang L *et al* 2015 presentation in this A3 seminar.
[11] Kato D *et al* 2013 *Phys. Scr.* **T156** 014081.
[12] Shinohara M, Fujii K, Kato D *et al* 2015 *Phys. Scr.* submitted.
[13] Fujii K *et al* 2015 *Phys. Scr.* submitted.
[14] Qiu M *et al* 2014 *J. Phy. B: At. Mol. Opt. Phys.* **47** 175002.
[15] Safronova U I, Safronova A S *et al* 2010 *J. Phy. B: At. Mol. Opt. Phys.* **43** 074026.

A fast-response extreme ultraviolet spectrometer
for measurement of impurity line emissions in EAST tokamak

Ling Zhang[1], Shigeru Morita[2,3], Zong Xu[1], Zhenwei Wu[1], Pengfei Zhang[1], Chengrui Wu[1], Wei Gao[1], Tetsutarou Ohishi[2,3], Motoshi Goto[2,3], Junsong Shen[1], Yingjie Chen[1], Wei Gao[1], Juan Huang[1], Xiang Liu[1], Yong Liu[1], Yumin Wang[1], Chunfeng Dong[4], Hongmin Zhang[3], Xianli Huang[3], Xianzu Gong[1], Liqun Hu[1], Junlin Chen[1], Xiaodong Zhang[1], Baonian Wan[1], Jiangang Li[1]

[1]*Institute of Plasma Physics Chinese Academy of Sciences, Hefei 230026, Anhui, China*

[2] *National Institute for Fusion Science, Toki 509-5292, Gifu, Japan*

[3] *Department of Fusion Science, Graduate University for Advanced Studies, Toki 509-5292, Gifu, Japan*

[4] *Southwestern Institute of Physics, Chengdu 610041, Sichuan, China*

A flat-field extreme ultraviolet (EUV) spectrometer working in 20-500Å wavelength range with fast response has been newly developed to measure line emissions from highly ionized low, medium and high Z impurities in EAST. A flat-field focal plane for spectral image detection is made by a laminar-type varied line spacing concave holographic grating with an incidence angle of 87°. A back-illuminated charge-coupled device (CCD) with a size of 26.6×6.6 mm^2 and the channels of 1024×255 is used for measuring the focal image of spectral lines. Excellent spectral resolution $\Delta\lambda_0$ (full width at foot position of spectral line) of 3-4 channels at 60-400Å wavelength range is obtained after careful adjustment of the components. The high readout rate and the full vertical binning of the CCD can improve the temporal resolution of time-resolved spectrum, at least 5milliseconds per frame, which makes possible a variety of studies, e.g., impurity behavior during edge-localized mode (ELM) activity and ELM mitigation in long pulse discharges. The EUV spectrometer is absolutely calibrated using EUV bremsstrahlung continuum at 20-150Å initially. The tungsten spectra in this wavelength range are also presented.

I. INTRODUCTION

The passive spectroscopy in extreme ultraviolet (EUV/XUV: 10-500Å) wavelength range is conventionally used on the magnetic confinement fusion devices to study the physics of impurity transport and provide the information on impurity levels to assist the experimental operations. EUV spectrometer is the primary tool to observe the impurities line emission, which consist of three optical elements: entrance slit, diffraction grating and the detector.

Over the past 2-3 decades, significant progress has been achieved in the instrument benefiting from the development of both grating and detector technology. For spectroscopic instruments with the wavelengths below 200-300 Å, a grazing incidence mount is used to increase the reflectance of the grating surface. The typical EUV spectrometer constructed in the 1980s based on entrance slit and a spherical concave grating positioned on the same Rowland circle, and the grating diffracting and focusing the light to the micro channel plate (MCP) which was mounted tangential to the Rowland circle.[1-4] However the concave grating causes curved image and strong astigmatism perpendicular to the plane of the circle, which does not allow mounting the multichannel flat detector to do the simultaneous spatially resolved measurements of the plasma. The mechanically ruled aberration-corrected concave[5, 6] or aberration-corrected toroidal holographic gratings[7-10] were used to construct the flat focal field spectrometers in the following 10-20 years. Before 2000, the typical detector unit was very complicated. The head of the detector was composed of a flat rectangle MCP, which was coupled to a phosphor screen image intensifier. The XUV photons produce the photoelectrons at the MCP surface then photoelectrons are multiplied inside the micro channel. The exiting electrons are then accelerated and focused onto the phosphor screen which converts the electron signal to visible photons. The visible photons are optically coupled and transferred to a photodiode array (PDA) [1, 3, 4, 7-9] or a charge-coupled device (CCD) [2, 6, 10] by fiber optic bundle. Recently, the laminar-type concave holographic gratings with varied line spacing (VLS) grooves were widely used to construct the flat focal field EUV spectrometer.[11, 12-18] And at the meanwhile, the development of manufacture of high energy CCD camera makes the spectrometer system more compact and easier control, and most important to take the spectral-, time- and space- resolved measurement simultaneously. For instance, the fast-response EUV spectrometer in longer (50-500Å) [13] and shorter (10-130Å) [14] wavelength range was installed on LHD in 2007 and 2008, respectively, and the space-resolved EUV spectrometers in longer wavelength range have been developed on LHD [15, 16], HL-2A[17] and

EAST[18]successively. And a space-resolved EUV spectrometer in shorter wavelength range has been constructed in LHD last year[19].

In last EAST campaign, various materials have been used for plasma facing components in EAST, e.g., molybdenum for main vacuum chamber, W/Cu monoblocks for upper divertor and SiC-coated graphite tiles for lower divertor. And the lithium coating has been routinely applied for wall conditioning to suppress the hydrogen and deuterium recycling. Therefore, fast-response impurity diagnostics are very important to improve the plasma performance of EAST discharges. In particular, the measurement of intrinsically existing high-Z impurities of Mo and W is crucially important in addition to light impurities of Li, C, O and N, because radiation loss from such high-Z impurities is really big. For the purpose, a fast-response EUV spectrometer working in 20-500Å wavelength range has been newly developed in EAST to measure line emissions from such impurities.

This paper is organized as follows: the characteristics and performance of the EUV spectrometer is described in Sec. II. The method and result of the absolute intensity calibration is introduced in Sec. III. The observed tungsten spectra at 20-70 wavelength range are presented in the Sec. IV. The paper is summarized in Sec. V.

II. DETAILS ON FAST-RESPONSE EUV SPECTROMETER WORKING AT 20-500Å

A. Characteristic feature of the EUV spectrometer

The newly constructed fast-response EUV spectrometer here is to observe the EUV radiation in the wavelength range of 20-500 Å from EAST plasma. Fig. 1 shows the top view of the optical layout in the spectrometer. It is a glazing incidence flat field spectrometer, which consists of an entrance slit with the width of 30μm, a gold-coated concave varied line spacing (VLS) groove laminar-type holographic grating with 1200 grooves/mm at grating center, and a back-illuminated CCD (Andor DO920-BN) with effective area of 26.6×6.6mm^2 and channel number of 1024×256 pixels. The distance between grating and entrance slit is 237mm, and the distance between the focal plane perpendicular to the grating surface is 235mm. EUV radiation emitted from EAST plasma passes through the entrance slit and arrived at the grating center at the incidence angle of 87°. The diffracted emission is then focused onto the flat focal plane as a function of wavelength expressed by the following equations:

$$m\lambda = \sigma_0(\sin\alpha + \sin\beta) \quad (1)$$

where $m, \lambda, \sigma_0, \alpha$, and β stand for the diffraction order, the wavelength of the emission, the groove spacing, and the angles of incidence and diffraction, respectively. The focal length between the grating center and the focal plane slightly changes according to the wavelength.

Fig.2 shows the three-dimensional schematic drawing of the EUV spectrometer system. A laser light is focused to grating center for the alignment of the spectrometer viewing axis. A remotely controlled pulse motor is used to move the CCD along the focal plane to change the wavelength range to be measured. The spectrometer is evacuated by a compact turbo molecular pump system (Agilent Turbo-V301, TriScroll 300 as the backing pump). The pressure of the spectrometer is kept in the order of 10^{-5} Pa.

The schematic drawing of the EUV spectrometer working on EAST is illustrated in Fig. 3.The EUV spectrometer is installed at the backside of extension chamber for a bottom sub-port on port D. The elevation angle of the viewing axis is 8°. The distance from the entrance slit to plasma center is 5.665m.Under this arrangement, the vertical and horizontal image field of about30 and 5 cm in the plasma position could be observed when the CCD is placed horizontally to the horizontal dispersion. Normally, the CCD is cooled down to -20°C to suppress the thermal noise and operated in the full vertical binning(FVB) mode with pixel read out rate of 1MHz to take the measurement with the interval of 5ms.

B. Performance of the EUV spectrometer

Before routine operation, the CCD is carefully rotated in the focal plane with the result of full image spectrum measurement to make sure that it is horizontal to the dispersion direction to achieve the best spectral resolution. The experimentally obtained spectral resolution (defined as full width at foot position of spectrum) as a function of wavelength both in image mode and FVB mode are presented in Fig. 4. It could be found that the spectral resolution of $\Delta\lambda_0$ is quite good with 3-4 channels in the wide wavelength range of 60-400Å, which indicates a good alignment of the incidence angle of the grating and the exact position and inclination angle of CCD comparing with the designed position of CCD for the incident angle of 87° (Fig. 5, from ref. [13])

The reciprocal linear dispersion are experimentally determined and compared with theoretical values, as shown in Fig. 6.The theoretical values are calculated via equation (1) and the following equation:

$$L = 235 \cdot \cot \beta \quad (2)$$

where L stands for the distance along the focal plane from each focal point for the emission at different wavelength to the grating plane. It is found that the reciprocal linear dispersion varies from 3.05 to 10.78Å/mm (0.08to 0.28Å/channel) over the wavelength range of 20-500 Å. Experimental values shown with solid circles are in fairly good agreement with the calculated ones. However, there still exists unavoidable discrepancy between them at longer wavelength. For example, the discrepancy is 0.46Å/mm (0.012Å/channel) at 430Å, which doesn't influence the wavelength calibration and line identification.

C. Typical spectra from EAST plasma

The whole spectra with the wavelength range of 20-500Å could be recorded from three discharges by moving CCD detector. **Fig. 7(a)** shows the typical spectra in 20-150Å obtained from EAST Ohmic discharge. There are abundant spectrum lines in this shorter wavelength range. Separated line emission from H- and He-like C, N and O ions are shown in the wavelength range of 20-40Å all the time, sometimes 2nd and 3rd order of these lines are still very strong. Lyman series (up to n=8) from H-like Li at 100-135Åare observed in very cold plasma. Line emission from 2p-2s transitions of Cr XVI-XXI, Fe XVIII-XXIII and Cu XXI-XXVI, and 3d-2p transitions of Cu XI-XIV shown in low hybrid wave current driven plasma with frequency of 4.6GHz (with newly developed antenna). In the initial phase of last EAST campaign, the unresolved spectra array from molybdenum at around 65-90Å were observed due to the very close distance from plasma to first wall, and strong unresolved spectra array or pseudo-continuum bands from tungsten at 20-75Å were observed during H-mode phase with neutral beam injection . **Fig. 7(b)** shows the spectra at 100-290Å in Ohmic discharge. There are just a few emission lines in the longer wavelength range of 250-500Å even after Ar gas puffing, as shown in **Fig. 7(c)**.

D. Time behaviors of impurity lines during ELMy H-mode phase

Normally, the spectra are recorded by the EUV spectrometer with the interval of 5ms, which is benefit for the study of fast response from impurity to plasma sudden change such as EMLs activity. In the shot of #49030 shown in **Fig. 8**, neutral beam from left source and right source

each with power of 1.1MW is injected from 4 to 6s and 5 to 7s, respectively. L-H transition happens at 4.312s, 5.068s and 5.822s, and the ELMy H-mode phase lasts for 568, 441 and 237ms respectively. Followed by L-H transition, there is ELMy free phase last for about 90ms, and small ELMs with frequency of about 120-150Hz, then big ELMs with frequency of 10-45Hz. There are also small ELMs between two big ELMs. **Figs. 8(c)-(d)** show the time behavior of the intensity of several lines from light impurities, i.e. OVII 21.6Å, NVII 24.78 Å, CV40.73 Å, LiIII134.99 Å, and several lines or band from medium-heavy impurities, i.e. FeXVIII 93.926Å, CuXXI 78.384Å, sum of unresolved tungsten array (UTA) in 45-70 Å, sum of W^{40+} and W^{43+}. It could be found that, the intensity of all the lines is a little higher in L-mode phase with neutral beam injection (NBI) than Ohmic phase. And the intensity of all the lines is increasing during ELMy-free and small ELMs phase, but drop rapidly and dramatically with most big ELMs.

III. ABSOLUTE INTENSITY CALIBRATION

Absolute intensity calibration is necessary because the quantitative analysis is important for study of impurity content, Z_{eff} profile, radiation power loss and impurity transport. The EUV spectrometer could be calibrated using visible bremsstrahlung emissivity profile in which the intensity is already calibrated by an integrating sphere standard light source. Recently, an in-situ technique using EUV bremsstrahlung continuum profile in comparison with absolute values of visible bremsstrahlung(VB) continuum profile is more and more popular.[13, 15, 19-21]There are three steps applying this technique. Firstly, absolute value of the local emissivity of VB (ε_{brem_vis}) could be derived from the measured line-integrated brightness of VB (B_{brem_vis}) by means of Abel inversion. Secondly, the value of emissivity of bremsstrahlung in EUV wavelength range (ε_{brem_EUV}) could be calculated via equation (3):

$$\varepsilon_{brem\_EUV} = \varepsilon_{brem\_vis} \left(\frac{\lambda_{vis}}{\lambda_{EUV}}\right)^2 \frac{g_{ff\_EUV}}{g_{ff\_vis}} \times \exp\left[-\frac{12400}{T_e}\left(\frac{1}{\lambda_{EUV}} - \frac{1}{\lambda_{vis}}\right)\right] \quad (3)$$

where the subscripts of 'EUV' and 'vis' denote a wavelength range at EUV and visible bremsstrahlung emission, respectively. ε[photons s^{-1} $m^{-3}Å^{-1}Sr^{-1}$], λ[Å], g_{ff} and T_e[eV] stand for emissivity, the wavelength, free-free gaunt factor, and the electron temperature, respectively. Finally B_{brem_EUV} could be calculated by integrating ε_{brem_EUV} along the viewing chords and compared with the experimental value measured by EUV spectrometer, and then the calibration factor could be determined.

However, sometimes measurement system in EUV and visible wavelength range don't share the same viewing chords. For instance, it is very difficult to compare precise ε_{brem_EUV} profile with multi-channel VB profile in EAST. In this case, the effective ionized charge (Z_{eff}) profile need to be derived with T_e profile, electron density (n_e) profile and ε_{brem_vis} profile at the first step, B_{brem_EUV} then could be calculated via equation (4):

$$B_{brem} = \frac{9.5 \times 10^{-20} \Delta\lambda}{4\pi\lambda} \int \frac{g_{ff} n_e^2 Z_{eff}}{T_e^{1/2} \exp(12400/T_e\lambda)} \, dl \quad (\text{photons s}^{-1} \text{m}^{-2} \text{Sr}^{-1}) \quad (4).$$

During last campaign, most spectra are recorded in shorter wavelength range of 20-150Å. In this paper, the absolute intensity calibration is addressed using this method with assuming certain Z_{eff} profile in this shorter wavelength range as an initial result.

Due to a lots of line emissions appearing in EUV wavelength range at high n_e, the bremsstrahlung intensity is examined at different wavelengths and densities to reduce the uncertainty of bremsstrahlung intensity measured with EUV spectrometer. The free-free gaunt factor in this wavelength range is evaluated using a Chebyshev expansion as an analytical approximation.[22] **Fig. 9** presents the **(a)** n_e profiles measured by microwave reflectometry[23,24], **(b)** T_e profiles measured by 32-channel heterodyne radiometer[25], **(c)** assumed Z_{eff} profile. On EAST, there is a 9-channel photomultiplier tube (PMT) array for measurement of VB at center wavelength of 5230Å, which is already absolutely calibrated by an integrating sphere standard light source. The line-averaged effective ionized charge ($<Z_{eff}>$) could be obtained with this VB measurement system.[26] Before absolute calibration, the assumed Z_{eff} profile is checked by the experimentally obtained $<Z_{eff}>$. **Fig. 10(a)** shows the viewing chords of the multi-channel VB measurement system and the results of EFIT equilibrium reconstruction of shot 51015 at 2.89s. The B_{brem_vis} in mW m^{-2}Å^{-1} Sr^{-1} is calculated via equation (4) with the profiles in **Fig. 9** as a function of minimum value of normalized magnetic flux at each viewing chord and compared with measured values by multi-channel VB measurement system, as presented in **Fig. 10(b).** During the calculation, it was found that, with the same value of $<Z_{eff}>$, the shape of Z_{eff} profiles have little influence on the results. The results in **Fig. 10(b)** shows acceptable discrepancy between the calculated and experimental values of B_{brem_vis}, which means all the profiles are consistent. Experimental chord-integrated brightness of EUV bremsstrahlung as the function of wavelength at different $<n_e>$ are shown in **Fig. 11**, and the calibration factor as a function of

wavelength at this shorter wavelength range is determined and presented in **Fig. 12**. With this calibration factor, the impurity content will be attempted to calculate in the near future.

IV. UNRESOLVED TUNGSTEN ARRAYS AND ISOLATED TUNGSTEN LINES

Tungsten spectra always appear with strong intensity during H-mode with neutral beam injection. **Fig. 13** shows the typical unresolved tungsten array at 20-70 Å at center T_e of 1.7keV. It is found that three unresolved arrays are shown with center wavelength of around 30, 50 and 60Å. The tungsten spectra at 20-45Å (the spectral resolution is worse in this wavelength range) may be composed of W XX-W XXXV. Some tungsten lines at 45-70Å are identified to come from 4f-4d transition of W XXVIII-W XXX, 4f-4d, 4d-4p and 4p-4s transition of W XXXVIII-XLV. 2nd order of tungsten spectra at 45-70 Å with strong intensity has also been observed during several shots, which is very helpful for W line identification because the spectral resolution is higher and the wavelength position can be well calibrated with several spectral lines from other intrinsic impurities.

V. Summary

A fast response EUV spectrometer has been newly constructed in EAST, and several impurity spectra are successfully observed with good spectral resolution. Spectral intensity from the EUV spectrometer is absolutely calibrated in the wavelength range of 20-150Å initially. Unresolved tungsten arrays at 20-70Å from highly ionized ions of tungsten always appear with strong intensity during H-mode with neutral beam injection. Several lines of W XXVIII-XXX and W XXXVIII-XLV are identified which are useful for study of tungsten behavior in EAST discharges.

REFERENCES

[1] W. L. Hodge, B. C. Stratton, and H. W. Moos, Rev. Sci. Instrum. **55**, 16 (1984).

[2] D.Content, D.Wroblewski, M.Perry, and H.W.Moos, Rev.Sci.Instrum. 57, 2041(1986).

[3] J. L. Schwob, A. W. Wouters, S. Suckewer, and M. Finkenthal, Rev. Sci. Instrum. **58**, 1601 (1987).

[4] M. A. Graf, J. E. Rice, J. L. Terry, E. S. Marmar, J. A. Goetz, G. M. McCracken, F. Bombarda, and M. J. May, Rev. Sci. Instrum. **66**, 636(1995).

[5] T. Kita, T. Harada, N. Nakano, and H. Kuroda, Appl. Opt. 22, 512 (1983).

[6] N. Yamaguchi, J.Katoh, Y. Sato, T.Aota, A.Mase, and T.Tamano, Rev. Sci. Instrum. **65**, 3408 (1994).

[7] R.J. Fonck, A.T. Ramsey and R.V. Yelle, Appl. Opt. 21, 2115(1982).

[8] B. C. Stratton, R. J. Fonck, K. Ida, K. P. Jaehnig, and A. T. Ramsey, Rev. Sci. Instrum. **57**, 2043(1986).

[9] H. Kubo, T. Sugie, A. Sakasai, N. Nishino, H. Yokomizo, H. Takeuchi, ST-60 Team, K. Tanaka, H. Maezawa, and N. Yamaguchi, Rev. Sci. Instrum.59, 1515 (1988).

[10] W. Biel, G. Bertschinger, R. Burhenn, R. König, and E. Jourdain, Rev. Sci. Instrum. **75**, 3268 (2004).

[11] M. L. Reinke, P. Beiersdorfer, N. T. Howard, E. W. Magee, Y. Podpaly, J. E. Rice, and J. L. Terry, Rev. Sci. Instrum. 81, 10D736 (2010).

[12] P. Beiersdorfer, J. K. Lepson, M. Bitter, K. W. Hill, and L. Roquemore, Rev. Sci. Instrum. 79, 10E318 (2008).

[13] M. B. Chowdhuri, S. Morita, M. Goto, H. Nishimura, K. Nagai, and S. Fujioka, Rev. Sci. Instrum. 78, 023501 (2007).

[14] M. B. Chowdhuri, S. Morita, and M. Goto, Appl. Opt. 47, 135 (2008).

[15] C.Dong, S. Morita, M. Goto, H. Zhou, Rev. Sci. Instrum. **81**, 033107(2010).

[16] E. Wang, S. Morita, M. Goto, C. Dong, Rev. Sci. Instrum. **83**, 043503(2012).

[17] Z. Cui, H. Zhou, S. Morita, B. Fu, Y. Xu, C. Dong and Q. Yang. Plasma Sci. Technol., 15,110(2013).

[18] Y. Shen, X. Du, W. Zhang, Q. Wang, Y. Li, J. Fu, F. Wang, J. Xu, B. Lu, Y. Shi and B. Wan, Nucl. Instrum.Meth.A 700, 86 (2013).

[19] X. Huang, S. Morita, T. Oishi, M. Goto, C. Dong, Rev. Sci. Instrum. **85**, 043511(2014).

[20] Z. Cui, S. Morita, B. Fu, Y. Huang, P. Sun, Y. Gao, Y. Xu, C. Dong, P. Lu,Q. Wang,X. Ding, Q. Yang, and X. Duan, Rev. Sci. Instrum. **81**, 043503 (2010).

[21] C.Dong, S. Morita, M. Goto, and E. Wang, Rev. Sci. Instrum. **82**, 113102(2011).

[22] P. J. Storey and D. G. Hummer, Comput. Phys. Commun. 66, 129(1991).

[23]S. Zhang, X. Gao, B. Ling, Y. Wang, T. Zhang, X. Han, Z. Liu, J. Bu, J. Li, and EAST team, Plasma Sci. and Technol. 16(4),311(2014).

[24] Y. Wang, X. Gao, B. Ling, S. Zhang, T. Zhang, X. Han, S. Liu, Z. Liu, Y. Liu, A. Ti, EAST Team, Development of the W-band density profile and fluctuation reflectometer on EAST, Fusion Engineering and Design, 2013, 88: 2950-2955

[25]X. Han, X. Liu, Y. Liu, C. W. Domier, N. C. Luhmann , Jr., E. Z. Li, L. Q. Hu and X. Gao, Rev. Sci. Instrum., 85, 073506(2014).

[26]Y. Chen, Z.Wu, W. Gao, L. Zhang, Y. Jie, J. Zhang, Q. Zang, J. Huang, G. Zuo, J. Zhao, Plasma Phys. Control. Fusion 56,105006 (2014).
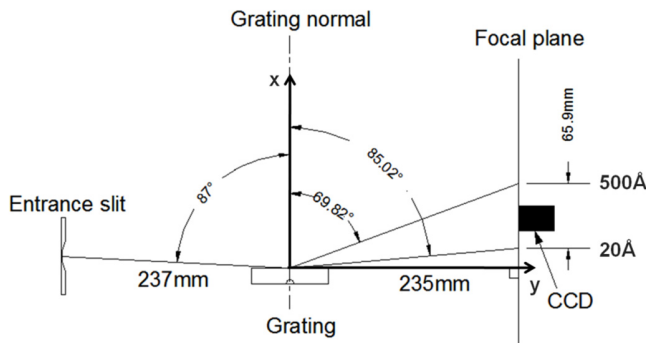
FIG. 1 Optical layout of fast-response EUV spectrometer in top view.
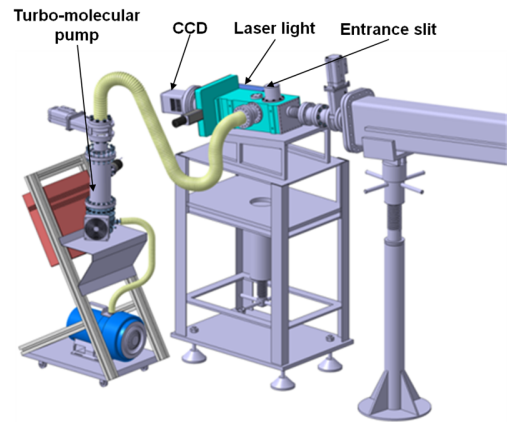
FIG. 2 Three-dimensional schematic drawing of the arrangement for EUV spectrometer system.
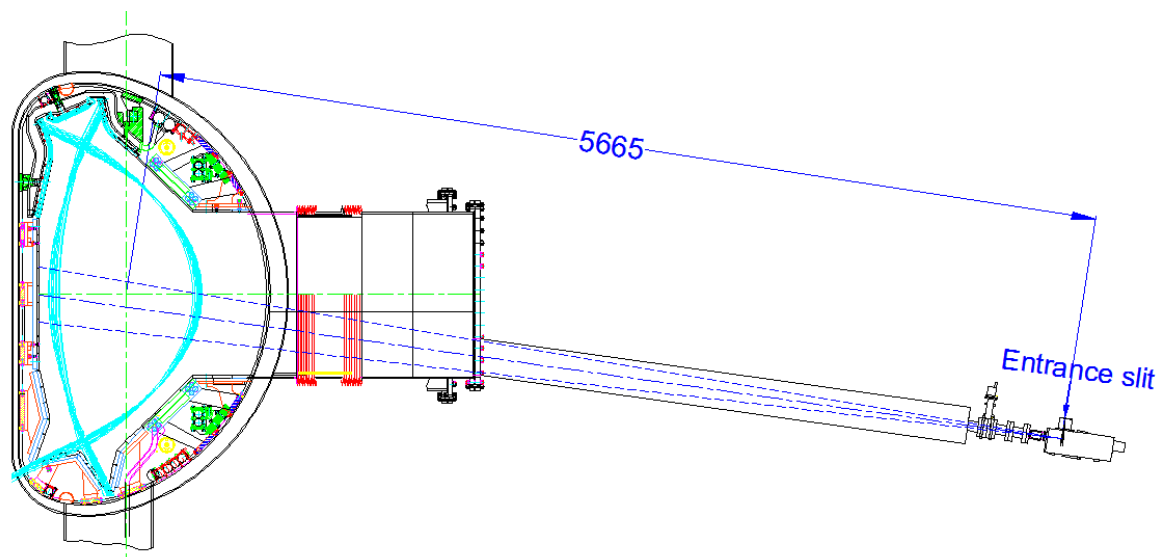
FIG. 3 Side view of fast-response EUV spectrometer working on EAST.The elevation angle of the viewing axis is 8°. Under this arrangement, the field of view of the spectrometer is about 30cm in poloidal direction and 5cm in toroidal direction, respectively.
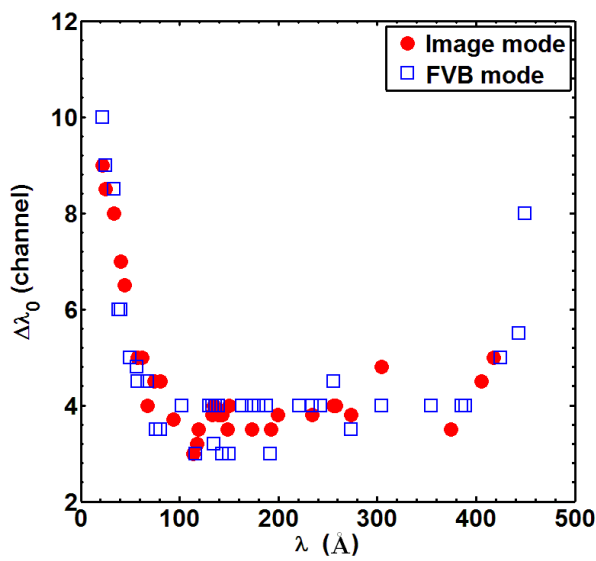
FIG. 4 Experimentally obtained spectral resolution $\Delta\lambda_0$ (full width at foot position of spectral line) as a function of wavelength in FVB mode (solid circles) and Image mode (open squares).
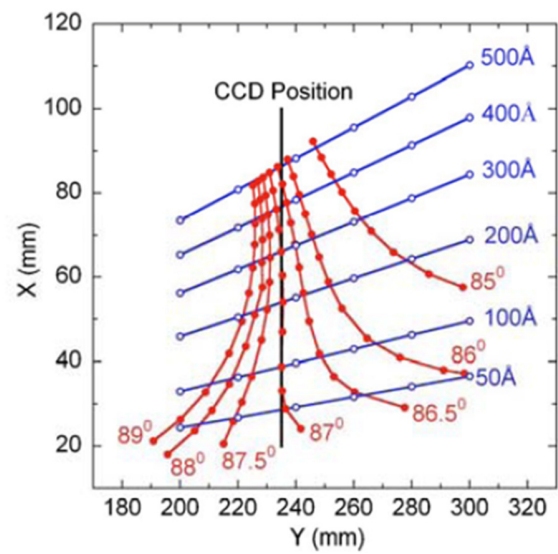
FIG. 5 Theoretical focal positions as a function of incidence angles. Positions of X and Y axes are indicated in Fig. 1. A solid vertical line denoted with CCD position means a designed position of detector for this EUV spectrometer [13]
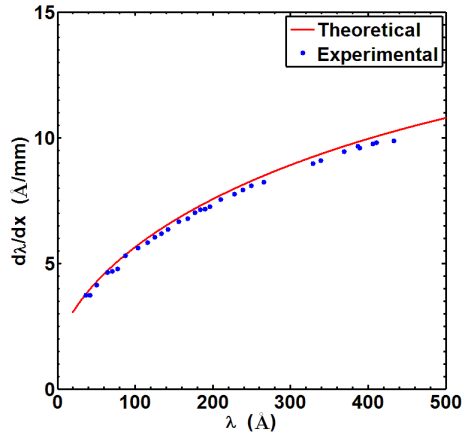
FIG. 6 Theoretical and experimental reciprocal linear dispersion as a function of wavelength.
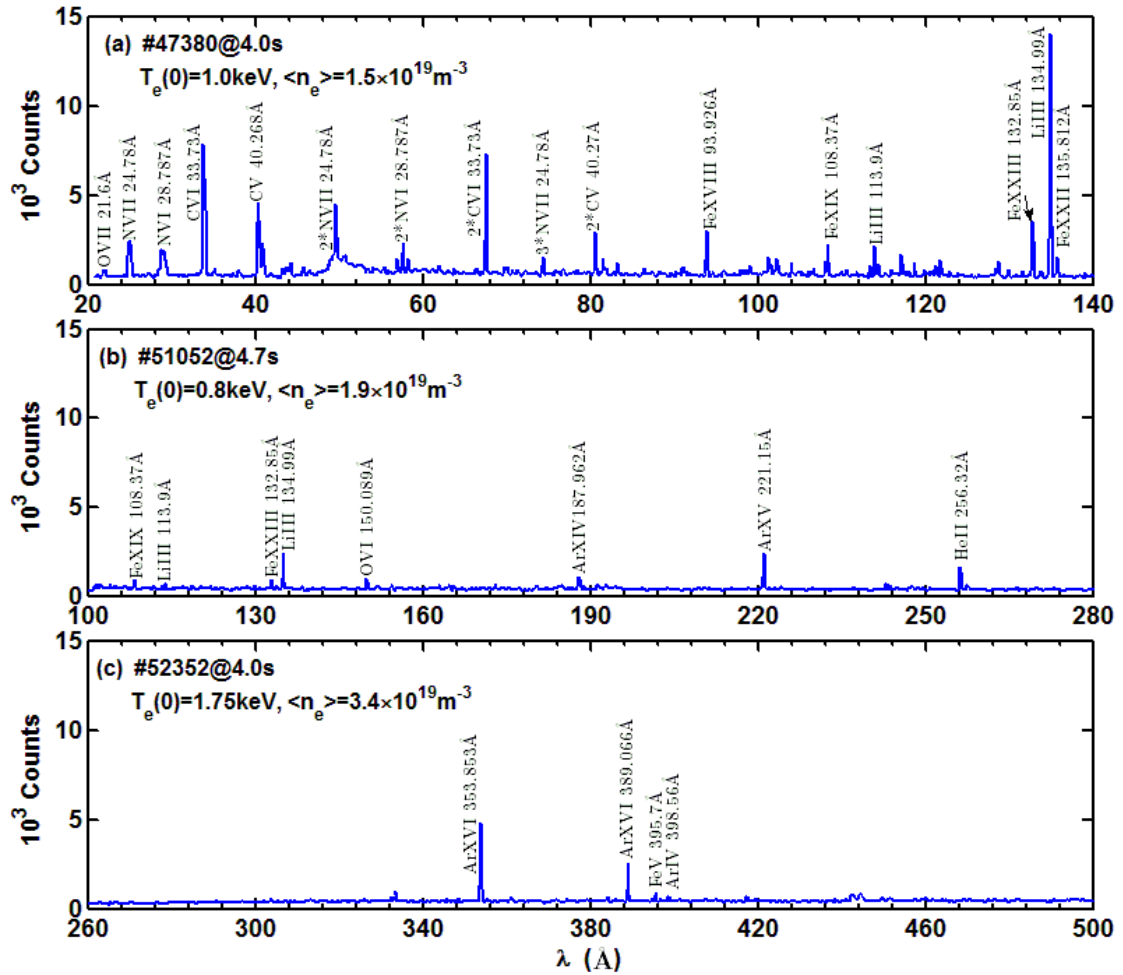
FIG. 7 Typical spectra in (a) 20-150Å, (b) 100-280Å and (c) 260-500Å from EAST plasma. Spectra in (b) and (c) are obtained after Ar gas puffing
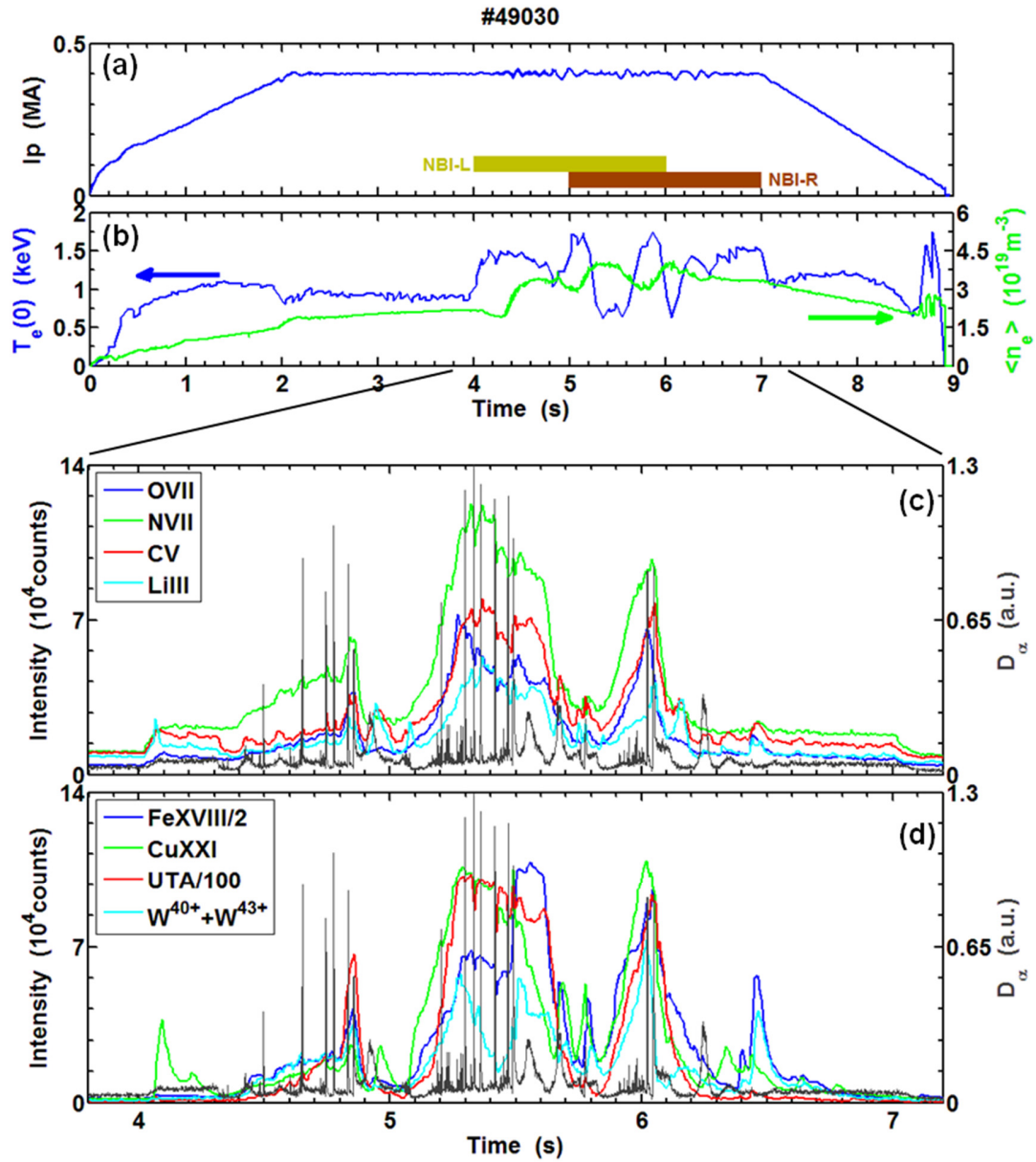
FIG. 8 Time evolution of (a) plasma current and NBI, (b) center T_e and $<n_e>$, (c) intensity of line emissions from light impurities, OVII 21.6Å, NVII 24.78 Å, CV40.73 Å, LiIII134.99 Å during ELMy H-mode phase, (d) intensity of line emissions from medium-heavy impurities, FeXVIII 93.926Å, CuXXI 78.384Å, sum of unresolved tungsten array (UTA) in 45-70 Å, sum of W^{40+} and W^{43+} during ELMy H-mode phase in shot 49030
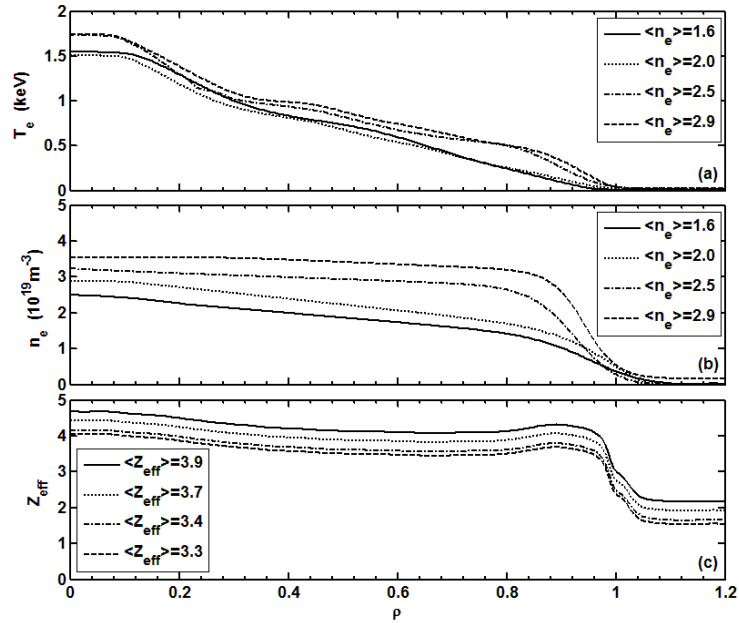
FIG. 9 (a) n_e profiles measured by microwave reflectometry, (b) T_e profiles measured by 32-channel heterodyne radiometer, (c) assumed Z_{eff} profile, checked by experimental value of $<Z_{eff}>$
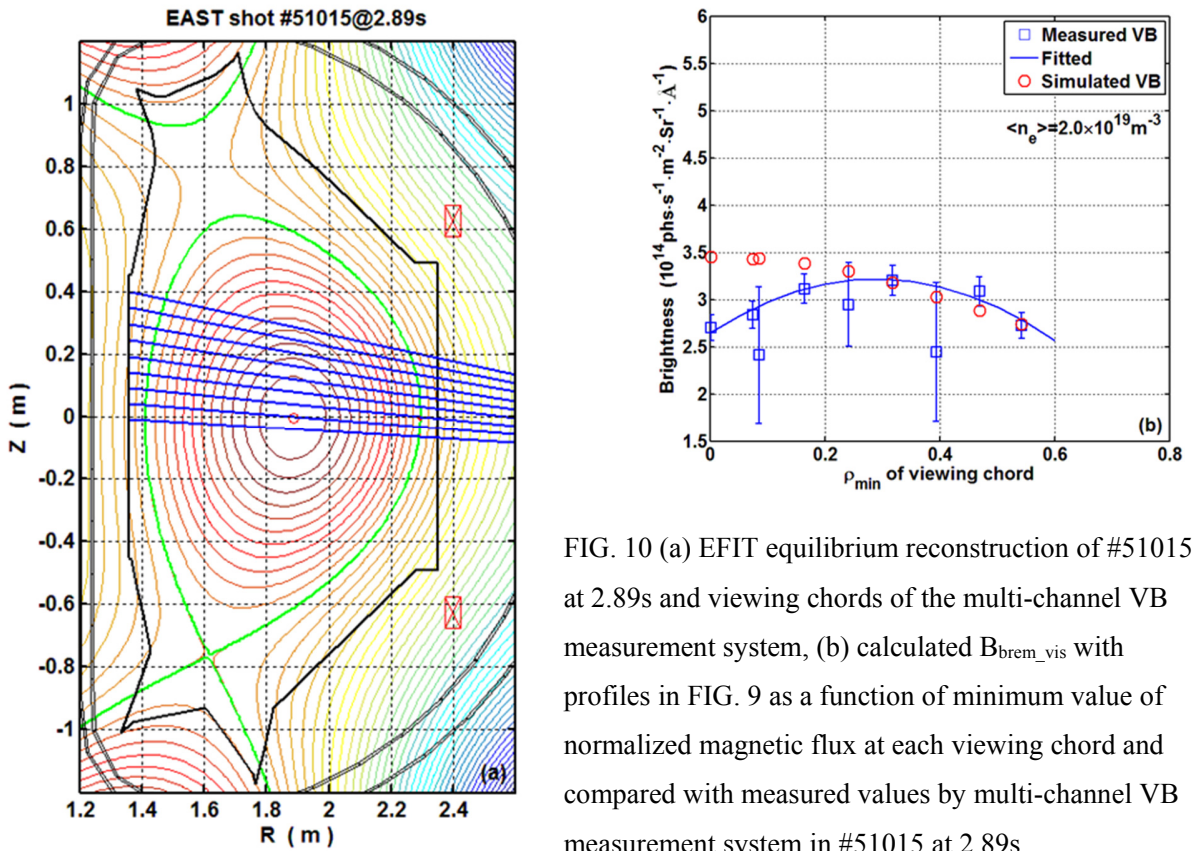
FIG. 10 (a) EFIT equilibrium reconstruction of #51015 at 2.89s and viewing chords of the multi-channel VB measurement system, (b) calculated B_{brem_vis} with profiles in FIG. 9 as a function of minimum value of normalized magnetic flux at each viewing chord and compared with measured values by multi-channel VB measurement system in #51015 at 2.89s.
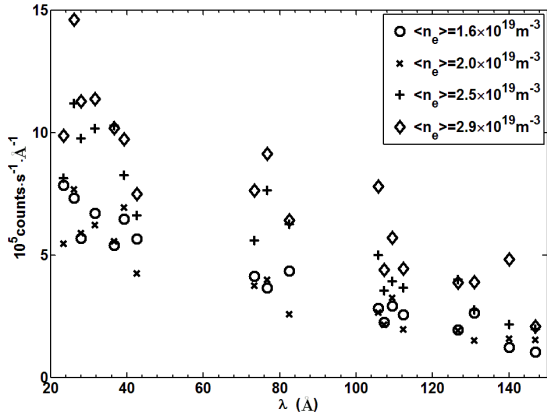
FIG. 11 Experimental chord-integrated brightness of EUV bremsstrahlung as the function of wavelength at different $\langle n_e \rangle$.
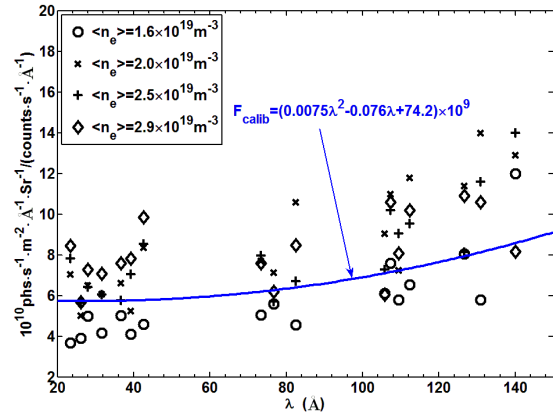
FIG. 12 Calibration factor as a function of wavelength, and fitted with polynomial expression which is denoted with solid line.

$F_{calib} = (0.0075\lambda^2 - 0.076\lambda + 74.2) \times 10^9$
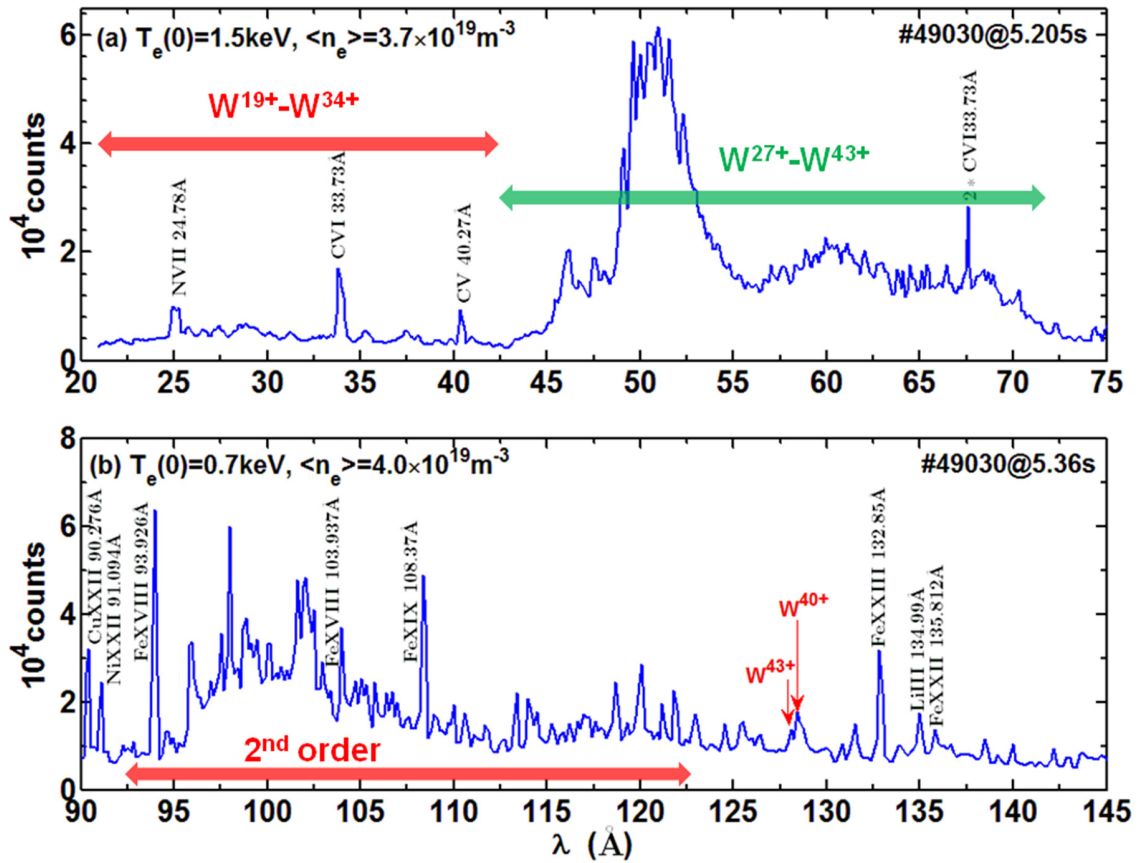
FIG. 13 Unresolved tungsten arrays at 20-70 Å at center T_e of 1.7keV.

Preliminary result and initial analysis on radial profiles of impurity line emissions measured with EUV spectrometer on HL-2A

Chunfeng Dong[1], Zhengying Cui[1], Shigeru Morita[2], Ping Sun[1], Kai Zhang[1], Bingzhong Fu[1],

Ping Lu[1], Yan Zhou[1], Yuan Huang[1], Qingwei Yang[1] and Xuru Duan[1]

[1]*Southwestern Institute of Physics, P. O. Box 432, Chengdu 610041, China*
[2]*National Institute for Fusion Science, Toki 509-5292, Japan*

Abstract：

A space-resolved extreme ultraviolet (EUV) spectrometer has been developed on HL-2A to monitor the impurity behavior and to study the impurity transport. A gold-coated varied-line-spacing (VLS) holographic grating with curvature of 5600mm is adopted as a dispersion component and a back-illuminated charge-coupled device (CCD) with size of 6.6×26.6 mm^2 (1024×256 pixels) is utilized to record the spectral image. A two-stage wavelength scanning system is designed to enable the measurement in wider wavelength range of 30-600Å. The line of sight of the spectrometer is inclined to a downward direction to measure an entire profile of the impurity line emission at lower half (0≤Z≤-40cm) of HL-2A tokamak plasmas. The vertical profile of line emissions from several impurity spices such as carbon, oxygen, iron, copper and molybdenum is successfully observed with a good spacial resolution. The vertical profile of CIV (312Å) measured from limiter and divertor discharges show a slight different radial location at the peak intensity position. The intensity of CIV significantly increases in the limiter configuration because the graphite is used as the limiter material and further increases when the auxiliary heating of ECRH and NBI is turned on. A similar result is also observed in the CVI emission. When the discharge encounters the H-mode transition, the vertical profile of CIV and CVI indicates a substantial change. A preliminary result on the vertical profile of several impurity spices observed from a variety of discharges is presented with an initial analysis.

1. Introduction

Impurity transport study is one of the essential subjects to the magnetically confined fusion plasma research. Plasma confinement capability is strongly affected by the impurity behavior through radiation loss, plasma dilution. In addition, high-Z impurity accumulation at plasma core predicated by the neoclassical theory will have a serious damage to the device, such as ITER with tungsten divertor plates[1]. On the other hand, plasma performance can benefit from the presence of impurity at plasma edge, since head load onto divertor plates could significantly reduced by seeding impurities in divertor region[2]. Therefore, it is important to study impurity transport for impurity control in present device and ITER.

Spectroscopy plays an important role in both the impurity diagnostics and the impurity transport study. A normal incidence vacuum ultraviolet (VUV) spectrometer has been developed to measure edge impurity line emissions in the wavelength range of 300-3200Å in HL-2A in 2008. The electron temperature is dramatically increased in HL-2A due to the recently improved electron cyclotron resonant heating (ECRH) system and neutral beam injection (NBI) heating system. Wavelength of impurity line emissions radiated from plasma core shifts towards extreme ultraviolet (EUV) range (≤500Å). Particularly for the high-Z material tungsten, the spectra are mainly measured below 100Å in the high temperature plasma from previous study [3-5]. On the other hand, a new method for the impurity transport study based on impurity

profile measurement [6,7] has been proposed, instead of tracing the time evolution of impurity line emission, which has been used as a conventional method for impurity transport study for years. Therefore, an EUV spectrometer with spatial resolution is desired for HL-2A tokamka.

2. Space-resolved EUV spectrometer system

HL-2A tokamak is a device with axi-symmetric X-point poloidal divertor configuration, and the major and minor radii of the tokamak are 1.65m and ~0.4m, respectively. The arrangement of space-resolved EUV spectrometer in HL-2A tokamak is shown in Fig. 1. The line of sight of the spectrometer is not perpendicular to the magnetic field line and has a angle of 76° with toroidal magnetic field direction. The distance between entrance slit and plasma center is about 7.37m along the horizontal direction. The space-resolved EUV spectrometer consists of an entrance slit, a spatial-resolution slit, a varied-line-spacing holographic grating and a CCD detector. A varied-line-spacing holographic grating with 1200 grooves/mm is equipped to this spectrometer. The detective area of CCD camera is $26.6 \times 6.6 mm^2$ corresponding to 124×255 pixels. The width of entrance slit and space-resolved slit are 100μm and 0.5mm, respectively. The angle of incidence of this spectrometer is 87°. The distance between the entrance slit and grating center is 237mm and the distance from grating center to focal plane is 235mm. Two-stage wavelength scanning system for moving CCD position along the focal plane is designed to enable the vertical profile measurement in wavelength range of 30-600Å. Electric motor is externally controlled for the wavelength scan through LAN network.
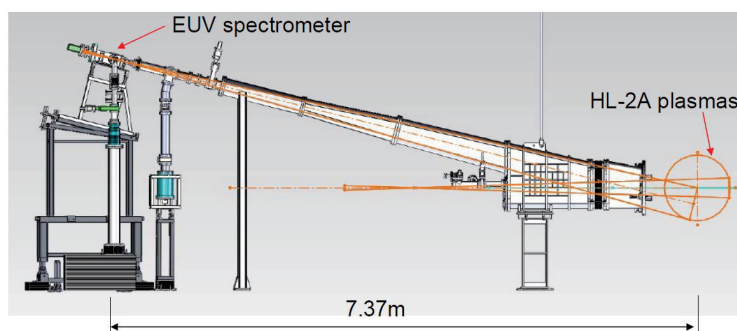
Fig. 1 The arrangement of space-resolved EUV spectrometer in HL-2A.

The impurity spectra emitted from lower half of HL-2A plasma (~40cm) is measured by the space-resolved EUV spectrometer, as shown in Fig.1. Figure 2 presents the poloidal cross section of HL-2A with lower divertor configuration, and the observable range of EUV spectrometer is denoted by the two blue lines. A metal bar with width of 3cm is installed at the diagnostic port position for the vertical position calibration of impurity profile. A sign will be produced in the impurity vertical profile as reference position. This bar could not be removed during the experiment since it is inside the machine vacuum.

Therefore, all the profile analyzed here will be with a intensity well at Z=-15~-18cm, as shown in Fig. 3.
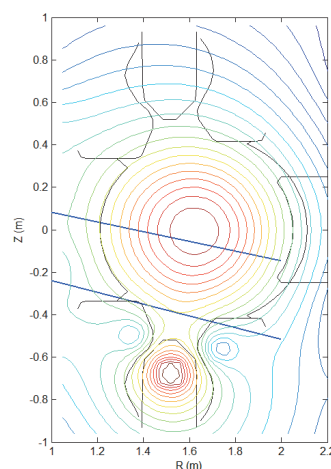
Fig. 2 Poloidal cross section of HL-2A tokamak.

3. Preliminary analysis on impurity profiles

The first wall of HL-2A tokamak is covered by graphite, and the divertor plates are made of copper with graphite baffle. The previous result shows that the impurity in HL-2A plasma is dominated by carbon in addition with oxygen and nitrogen, which are due to the air leakage. The vertical profile from carbon, oxygen and iron with different charge states are plotted in Fig. 3. The profiles of CIV (1s-2p: 33.73Å) shown in Fig. 3(a) has a clear difference with CVI ($1s^22s$-$1s^23p$: 312.4Å) due to the difference in ionization potentials of the two ions, i.e., 490eV for C^{5+} and 64.5eV for C^{3+}. In contrast, the profiles of OV (2s2p-2s3d: 192.8Å) and OVI ($1s^22s$-$1s^23p$: 150.09Å) show a similar pattern except the edge peak positions, since the ionization potentials for this two ions are close to each other, i.e., 113.9eV for O^{4+} and 138.12eV for O^{5+}. The profiles of FeXV ($3s^2$ -3s3p: 284.15Å) and FeXVI ($2p^63s$-$2p^63p$:

Fig. 3 Verical profiles of (a) CIV and CVI, (b) OV and CVI, (c) FeXV and FeXVI measured by space-resolved EUV spectrometer.

335.407Å) show a similar tendency as OV and OVI with the same reason of the similar ionization potentials for the two ions, i.e., 457eV for Fe^{14+} and 489.27eV for Fe^{15+}.

The plasma in HL-2A tokamak can be operated with two different configurations, i.e., limiter and lower null divertor and a clear difference in the two configuration has been observed in carbon profiles. The vertical profiles of CIV and CVI obtained from limiter and divertor configurations with similar plasma parameters are shown in Fig. 4, in which red line denotes limiter configuration and blue line denotes divertor configuration. Seen from Fig. 4(a), CIV profiles tends to be flat in limiter configuration and shows a sharp peak in divertor configuration. CVI vertical profiles shows similar distribution in two configurations. It has to be noted that the carbon intensity is enhanced in limiter configuration, since the limiter is

Fig. 4 Verical profiles of (a) CIV and (b) CVI obtained from divertor and limiter configurations.

covered by graphite in HL-2A.

The vertical profile of CIV with different vertical displacements from limiter configuration are plotted in Fig. 5, in which blue line denotes the small vertical displacement and red line denotes the large vertical displacement. Although the two profiles have similar pattern, a clear difference in edge of CIV vertical profile is observed. C^{3+} ion usually exists at the very edge of plasma with a narrow width due to its low ionization potential, in other word, the position of plasma boundary can be presented by the location of C^{3+} ion. When the plasma moves upwardly with the same minor radius, the position of plasma boundary is also shifted up. In contrast, the similar result is not observed in CVI profile.
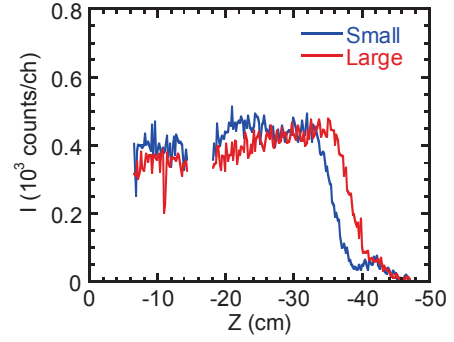
Fig. 5 Verical profiles of CIV obtained from discharges with small and large vertical displacements.

In order to increase the plasma stored energy and improve the plasma confinement, auxiliary heating is introduced in HL-2A tokamak. There are two different heating systems, i.e., electron cyclotron resonant heating (ECRH) with frequency of 65GHz and neutral beam injection (NBI) with positive ion source of 40keV. The intrinsic impurity, carbon, shows a different vertical profile for the different heating system. The vertical profiles of CIV and CVI obtained before and during ECRH heating are shown in Fig. 6. As we know, one of the advantages of ECRH heating is to avoid additional impurity introduced into plasma. However, the intensity of carbon is dramatically enhanced for both charge states of CIV and CVI during ECRH heating period as shown in Fig. 6.
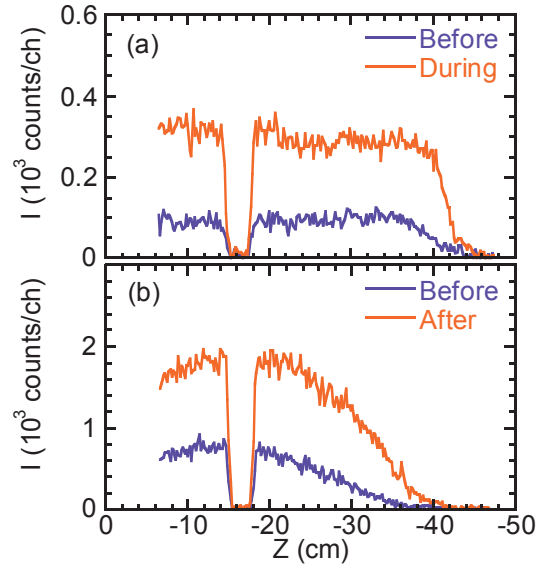
Fig. 6 Verical profiles of (a) CIV and (b) CVI obtained from plasma with ECRH heating.

In addition, the plasma size seems to be expanded as seen from CIV profile in Fig. 6(a). The plasma has a chance to touch the limiter or other parts covered with graphite inside the vacuum vessel when the plasma is expanded. Therefore, the carbon intensity is increased when ECRH is launched. On the other hand, according to the fluid model which is generally used to describe the impurity transport at plasma edge, the impurity transport is governed by the balance of friction force and thermal force. And the thermal force is proportional to the temperature gradient. The temperature profile measured by electron cyclotron emission (ECE) system shows that the temperature is significantly increased at plasma edge. Increased thermal force is also the possible reason for the increased carbon intensity. The detailed analysis will be done later.

The vertical profiles of CIV and CVI obtained before and during NBI heating are shown in Fig. 7. Time of 400ms (201-400ms) in Fig.7 denotes before NBI heating, 800ms (601-800ms) denotes during NBI heating phase, and in time interval of 600ms (401-600ms) NBI heating is just carried out in 501-600ms. The intensity of CIV in time interval of 800ms changes a lot due to

plasma performance and it has nothing to do with NBI heating. The increased carbon intensity during NBI heating period is also observed as the result in ECRH heating discharge. However, the plasma size seen from Fig. 7 is not expanded as ECRH heating case. The reason for the enhanced carbon intensity seems to be different from ECRH heating case. It is also found that the neutral beam could penetrate the plasma to hit the wall and bring the carbon into plasma.

The H-mode plasma could be achieved by the combination of NBI and ECRH heating. The increased intensity of CIV and CVI are also observed as the ECRH and NBI heating, as shown in Fig. 8. The times in Fig. 8 have the same meaning as in Fig 7. It is seen that

Fig. 7 Verical profiles of (a) CIV and (b) CVI obtained from plasma with NBI heating.

location of CIV and CVI is shifted outwardly in H-mode phase, and possibly this is due to the temperature profile is changed. On the other hand, increasement of CIV and CVI intensity is due to the confinement improvement.

4. Summary

A space-resolved EUV spectrometer is successfully developed in HL-2A for impurity profile measurement and impurity transport study. Vertical position of impurity profile is absolutely calibrated based on a metal bar. Vertical profiles emitted from various impurities are excellently measured. Carbon intensity in limiter configuration is significantly enhanced compared with divertor configuration. CIV profile at plasma edge shows a clear difference for different vertical displacement in limiter configuration. Carbon intensity is enhanced with auxiliary heating of ECRH and NBI. However, the mechanism for increasement of carbon intensity with different discharge conditions possibly is different. The carbon transport will be studied based on the EMC3-EIRENE code in the future.

Fig. 8 Verical profiles of (a) CIV and (b) CVI obtained from H-mode plasma heated by ECRH and NBI.

Reference

[1] ITER Physics Basis Editors, Nucl. Fusion **39**, 2391 (1999).

[2] ITER Physics Basis Editors, Nucl. Fusion **39**, 2137 (1999).

[3] R. Isler et al., Phys. Lett. A **63**, 295 (1977).

[4] Hinnov et al., Phys. Lett. A **66**, 109 (1978).

[5] K. Asmussen, el al., Nucl. Fusion **38**, 967 (1998).

[6] C. F. Dong, et al., Jns. J. Appl. Phys. **51**, 010205 (2012).

[7] S. Morita, et al., Nucl. Fusion **53**, 093017 (2013).

Impurity behavior and molybdenum transport study on EAST

Yongcai Shen[1, 2], Bo Lu[1*],Yuejiang Sh[3, 4], Jia Fu[1], Yingying Li[1], Xuewei Du[3], Fudi Wang[1], Qiuping Wang[3], Baonian Wan[1], Jun Chen[3]

[1.]Institute of Plasma Physics Chinese Academy of Sciences, Hefei 230031, China
[2]School of Physics and Electrical Engineering of Anqing Normal college, Anqing 246011, China
[3] University of Science and Technology of China, Hefei 230039, China
[4] WCI center for fusion theory, National fusion research Institute, 52 Eoeun-Dong, Yusung-Gu, Daejeon 305-333, Korea

Abstract

Spectroscopy in soft x-ray and extreme ultraviolet range offers a useful tool to survey core impurity radiation from high-temperature magnetic confined fusion plasma due to the abundance of emission lines from many elements in this range. Spectra in the wavelength intervals of 1-5 nm and 5-13 nm contained strong metal lines, especially molybdenum lines during H-mode phases were measured in EAST tokamak using extreme ultraviolet spectrometer (EUV) with certain temporal and spatial resolution. Detailed measurements of radial emission profiles from various impurity line emissions were also presented. The molybdenum density has been calculated after absolute calibration of the EUV spectrometer and is found to be quite low, about five orders smaller than electron density, even if the impurity accumulation occurs. The impurity transport coefficients are determined by reproducing the experimental measured emissivity profiles of Mo^{29+}、 Mo^{30+} and Mo^{31+} using a one-dimensional empirical impurity code, STRAHL.

1. Introduction

Impurity behavior plays a key role in magnetic confined fusion research as impurity radiation can affect the power balance, cool down the plasma, and degrade the performance [1-10]. To support the long-pulse and high-performance plasma research, two flat-field spectrometers (XEUV) that were designed to cover the wavelength range of 1-50 nm have been established on EAST plasma, which can provide time- and space-resolved measurements of line emissions. Line emissions from both low-Z impurities such as C and O and medium-Z impurities such as Fe and Mo have been successfully recorded by the system. For example, spectra from highly-ionized molybdenum ions in wavelength 5-13 nm were first observed on EAST plasma during the 2012 campaign.

The paper was organized as follows. In Section 2 an introduction of the experimental setup and preliminary results were presented, the spectral lines which including metal lines (such as iron and molybdenum lines) were showed. Following a description of molybdenum transport study, conclusions were given in Section 4.

2. Experiment setup and preliminary results

EAST is the first non-circular fully superconducting tokamak for studies on steady-state high performance operation scenarios. Lower hybrid current drive (LHCD) and ion cyclotron range of frequency (ICRF) systems have been equipped on

EAST since 2008.   During the 2012 campaign, lower-hybrid waves (LHWs) were injected by a 20 waveguide launcher capable of delivering up to 4 MW of power at 2.45 GHz and four 1.5 MW ICRF transmitters with frequencies ranging from 25-70 MHz were put into operation.

For impurities, there were many sources that could contribute to the impurity accumulation in the plasma on EAST.   Plasma facing surfaces (PFMs) on EAST were mainly carbon (divertors) and molybdenum (first wall).   The antenna of LHCD and ICRF were made of stainless steel with tin coating.   To measure the impurity emission, the XEUV system was installed at port C and attached to the end of the pumping duct (Fig. 1).   The upper system was the soft x-ray spectrometer and the lower one was the extreme ultraviolet spectrometer.   As could be seen from Fig .1(b), the distance between the plasma center and the entrance slit was ~8335 mm and the distance between entrance slit and the CCD is 472 mm, which resulted in a spatial coverage of 0-450 mm above the equatorial plane.   Spatial resolution was realized with pinhole imaging scheme and determined by the height of entrance slit and the CCD's pixels [11] binned for one channel.

Metal impurity emissions were normally excited with lower hybrid wave (LHW) or ion cyclotron resonance heating (ICRH) applied, especially during high-performance mode (H-mode) discharges.   Molybdenum was the most commonly seen metal impurity as the first wall was mainly made up of molybdenum. Other major metal impurities were iron, nickel, chromium and copper, which exist in the stainless-steel components, such as the antennas of LHCD and ICRF.   The presence of metal lines in EAST plasma was a useful indication of wall material erosion that might degrade the PFM and the plasma conditions.   Typical spectral lines observed on EAST in 1-5 nm were shown in Fig. 2.   It could be seen that hydrogen-like and helium-like emissions from ions like O VIII, O VII and O VI, C VI and C V were very strong and were actually used for wavelength calibration.   The abundance of O VIII at 1.897 nm ($2p_{3/2} \rightarrow 2s_{1/2}$ and $2p_{1/2} \rightarrow 2s_{1/2}$) was probably because there were plenty of oxide such as water, carbonic oxide and carbon dioxide absorbed on the PFMs **.**

Another soft X-ray spectrum from highly ionized molybdenum in the wavelength range of 5-13 nm was also shown in Fig. 3.   Mo XXX-XXXII observed in 10-13 nm were not difficult to identify when the central electron temperature was relatively high due to high ionization energy (Mo XXX: 1601 eV, Mo XXXI: 1726 eV, Mo XXXII: 1791 eV).   We also noticed there was a burst in 6.5-8.5 nm indicating there existed a complex structure, where the very precise identification was impossible and many lines are still unknown.   However, it was shown that lines in this region mainly consist of charge states of Mo XVIII and Mo XXIV-XXVIII.

The measurement of the radial profile of impurity emissions was also available for impurity transport study.   The current set up of the spectrometers was able to cover 0-450 mm above the equatorial plane of EAST.   Fig. 4   (a)-(d) shows the radial profiles of impurity line emissions and the corresponding local impurity emissivities are illustrated in Fig. 4 (e)-(h) from the measurement of the same discharge (# 39912, limiter configuration).   The impurity emissivity was obtained by Abel inversion method under the assumption of constant emissivity on the same flux surface.

Li III at 13.5 nm was located at the edge region of the main plasma due to its low ionization energy (E_i=122.45 eV).   The radial profiles and emissivities of O VIII and

Ar XV were different from each other which could be explained since their ionization energy were different, i.e., Ei = 871 eV for O VIII and Ei = 854 eV for Ar XV.   As for Mo XXXI, the profile was much more peaked since its ionization energy (Ei = 1726 eV) was much higher.

3. Molybdenum transport study

The waveform of a typical EAST H-mode discharge from shot 38300 in which LHW and ICRF are all injected is shown in Fig. 5.   The plasma current is about 400 kA.   ICRF wave is injected at t=2.1 s and the discharge enters H-mode quickly later as can be seen in the abrupt H_α signal drop.   In the meantime Mo XXXI signal builds up quickly.   Core soft x-ray signal has a very similar trend as Mo XXXI since Mo is the main contribution to the core soft x-ray radiation.   Mo XXXI intensity reaches its highest value at t =3.8 s as a result of impurity accumulation.

In order to determine the molybdenum transport coefficients, the molybdenum profile has been calculated using a 1D impurity code, STRAHL, and matched with measured results.   The STRAHL code solves the couples of radial impurity transport equations for all ions, which reads for stage Z.   For a charge stage Z, the coupled radial impurity transport equation can be expressed as

$$\frac{\partial n_Z}{\partial t} = \frac{1}{r}\frac{\partial}{\partial r}\left(D\frac{\partial n_Z}{\partial r} - vn_Z\right) + Q_Z, \tag{1}$$

where D is the diffusion coefficient and v is the velocity due to convective flows inside the tokamak plasma.   The source/sink term Q couples the transport equation of each ionization stage with the neighboring stages according to

$$Q_Z = -\left(n_e S_Z + n_e \alpha_Z + n_H C_Z\right)n_Z + n_e S_{Z-1}n_{Z-1} + \left(n_e \alpha_{Z+1} + n_H C_{Z+1}\right)n_{Z+1} \tag{2}$$

where S is the rate coefficient for ionization, α is the rate coefficient for recombination (radiative and dielectronic) and C is for charge exchange recombination [31, 32].   The main inputs to the STRAHL code are electron density and temperature profiles, impurity source rate, diffusion, convective and atomic database from ADAS for ionization and recombination.   Impurity ions densities of Mo^{29+}, Mo^{30+}, and Mo^{31+} are calculated by STRAHL code from the molybdenum ionization balance on the basis of given plasma parameters.   The diffusion coefficient is set to be 0.2 m/s^2 and the radial profiles of convective coefficient are shown in Fig. **6**.   It can be seen from **Fig. 7** that a big ELM happens at t= 3.55 s and the transient heat loads will bombard the PFMs.   A great deal of Mo impurity will be formed by physical sputtering and enter the core plasma.   Then the core radiation will go up which can be seen from the core soft x-ray signal.   For heavy impurity, the gradient of density causes an inward convective velocity and the gradient of temperature drives the opposite direction velocity towards the plasma edge which is called temperature screening.   A large density gradient after big ELMs which drives high inward convective velocity may be a main reason to the appearance of the impurity accumulation.   In order to avoid high-Z accumulation in the core plasma, big ELMs should be controlled.

4. Conclusion

In this paper, spectral lines from both highly ionized medium- and high-Z impurities in the extreme ultraviolet region in EAST plasma were presented.   Radial profiles and local emissivities were also shown.   Emission from light impurity ionization state Li III is located at edge area of the plasma, while emission from heavy

impurity ionization state Mo XXXI is located at core area. Molybdenum transport research in core plasma of EAST has been studied by using EUV spectrometer and the impurity transport code, STRAHL. The core Mo XXXI intensity increases quickly as the electron density goes up from 3 to 4.5×10^{13} cm^{-3} in H-mode discharge. Big Edge Localized Modes (ELMs) bring high energetic plasma particles to the edge and cause molybdenum accumulation in the core plasma. The diffusion coefficient of molybdenum is 0.2 m/s^2 and the radial profiles of convective coefficient are also obtained by using STRAHL code.

References

[1] Lepson J K, Beiersdorfer P, Clementson J, et al. 2010, J. Phys. B: At. Mol. Opt. Phys., 43:144018

[2] Chowdhuri M B, Morita S, Goto M, et al. 2007, Rev. Sci. Instrum., 78: 023501.

[3] Delgado-Aparicio L, Bitter M, Granetz R, et al. 2012, Rev. Sci. Instrum., 83: 10E517

[4] Zhou H Y, Morita S, Goto M, et al. 2008, Rev. Sci. Instrum., 79: 10F536

[5] Beiersdorfer P, Bitter M, Roquemore L, et al. 2006, Rev. Sci. Instrum., 77: 10F306

[6] Clementson J, Beiersdorfer P, Magee E W, et al. 2008, Rev. Sci. Instrum.,79: 10F538

[7] Stratton B C, Fonck R J, Ida K, et al. 1986, Rev. Sci. Instrum., 57: 2043

[8] Hodge W L, Stratton B C, Moos H W, et al. 1984, Rev. Sci. Instrum., 55: 16

[9] Cui Z Y, Morita S, Fu B, et al. 2010, Rev. Sci. Instrum., 81: 043503

[10] Shen Y C, Du X W, Zhang W, et al. 2013, Nucl. Instrum. Methods. Phys. Res. A.,700:86

[11] Shen Y C, Lu B, Du X W , et al. 2013, Fusion Engineering and Design., 88:3072
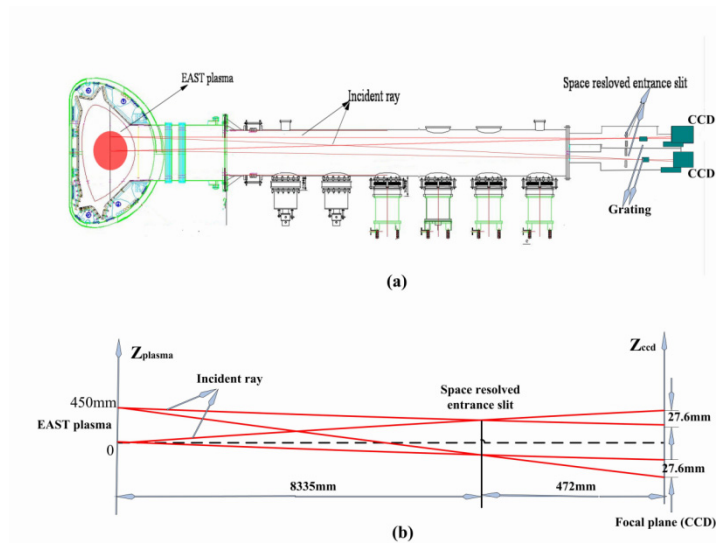
Fig.1 Schematic draws of space-resolved XEUV system's installation in EAST (a) in side view and (b) principle of spatial resolution in vertical view.
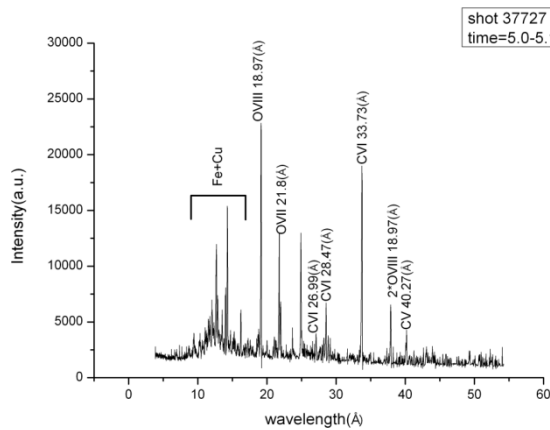
Fig.2 Spectrum of 1-5 nm taken with soft x-ray spectrometer in EAST tokamak plasmas.
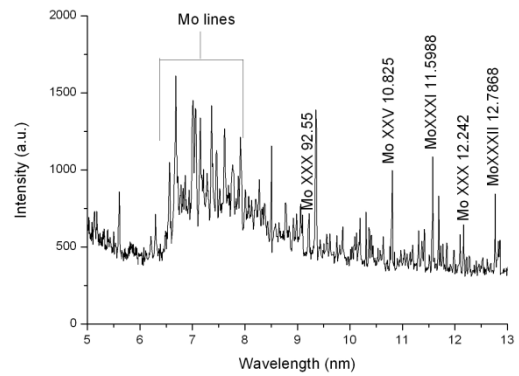
Fig.3 Mo spectrum in 5-13 nm.
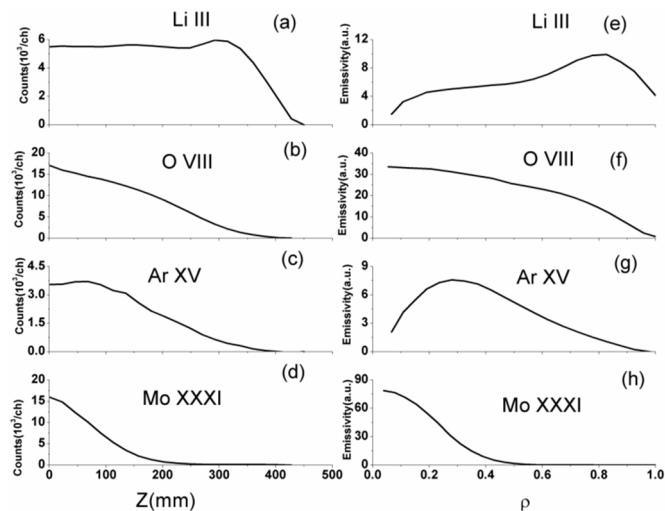
Fig.4 Radial profiles of (a) Li III, (b) O VIII, (c) Ar XV and (d) Mo XXXI and local emissivities of (e) Li III, (f) O VIII, (g) Ar XV and (h) Mo XXXI.
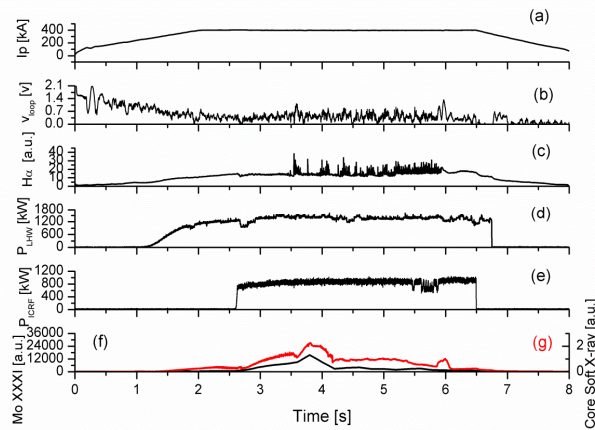
Fig.5 The time evolution of shot 38300 (a) plasma current, (b) loop voltage, (c) H_α intensity, (c) LHCD power, (d), (e) ICRF power, intensity of (f) Mo XXXI (11.59nm) and (g) core soft x-ray.
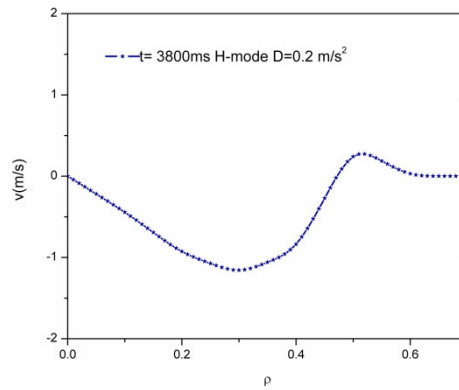
Fig. 6 Radial profiles of convective velocity with diffusion coefficient set at D = 0.2 m/s^2 for the best-fit calculated ion density profiles of Mo XXX, Mo XXXI and Mo XXXII.
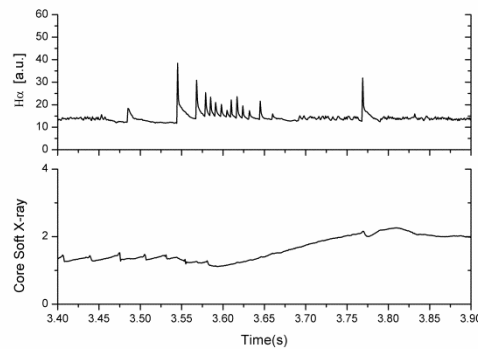
Fig. 6 Time histories of H_α intensity and core soft x-ray intensity at t= 3.4 -3.9 s. Big ELM happens at t =3.55 s and the core soft x-ray intensity begins to increase at t = 3.6 s.

Repetitive "snakes" and their damping effect on core toroidal rotation in EAST plasmas with multiple H-L-H transitions

XU Li-Qing and HU Li-Qun

Institute of Plasma Physics, Chinese Academy of Sciences, Hefei 230031, China

Abstract

Repetitive impurity snake-modes have been observed after H-L mode transitions (high to low confinement modes) in EAST plasmas exhibiting multiple H-L-H transitions. Such snake-modes have been observed to lower the core plasma toroidal rotation. A critical impurity strength factor associated with snake-mode formation has been estimated to be as high as $\alpha_{Z,c} = n_{Z,c} Z^2 / n_e \sim 0.75$. These observations have implications for ITER H-mode sustainability when the heating power is only slightly above the H-mode power threshold.

Key words: repetitive "snakes"; rotation damping 1/1 mode; impurity; L-H transition

Email: lqxu@ipp.cas.cn

1. Introduction

The presence of MHD perturbations from equilibrium conditions often limits the performance of tokamak plasmas and leads to global confinement degradation [1]. Moreover, macroscopic MHD perturbations often dampen plasma rotation. Currently, it remains a challenge to understand the stability of 1/1 helical (or "snake") modes in the core of an otherwise axisymmetric toroidal configuration. The so called snake mode is very interesting. It can be used as a probe for the existence of a q=1 surface or for toroidal plasma rotation inside q=1 and as an indicator of high-Z impurity accumulation [2]. These snake-modes have been closely associated with sawtooth oscillations, and understanding their behavior is important for ITER in which the q = 1 radius could be as large as half of the minor radius. The spontaneous occurrence of snake-modes arising from impurity accumulation - especially high-Z impurity accumulation - in ASDEX, suggest that such modes will probably occur in ITER as well [3]. Long-lasting macroscopic snakes could also occur in ITER when the heating power is close to the H-mode power threshold.

The H-mode is the projected baseline operational scenario for ITER. Reducing the H-mode power threshold will be a critical issue during the initial phase of ITER operations because the available heating power is limited [4]. In this early phase of operation, high-Z impurity accumulation will likely be intolerable; thus understanding plasma impurity transport is extremely important for the success of ITER.

This paper reports observations concerning repetitive impurity-laden snake-modes in the EAST tokamak and their interaction with repetitive H-modes. These snake-modes have been seen to slow the plasma rotation. Further, dampening of core toroidal rotation amplitude appeared to depend

on the perturbation displacement of the 1/1 snake-mode.

The remainder of this paper is organized as follows: section 2 describes the experimental setup, Section 3 presents an overview of the experimental observations and section 4 is a summary of the work.

2. Experimental set-up

EAST, with major radius R_0=1.8 m and minor radius a=0.45 m, is the first fully superconducting tokamak with both single and double-null divertor configurations [5]. The experiments described in this work were performed in deuterium H-mode plasmas driven and heated by lower hybrid wave (LHW) and ion-cyclotron resonance frequency (ICRF) as well as by LHW only. 1/1 Helical snake-mode oscillations were observed reproducibly after repetitive H-L transitions in these discharges. Typical plasmas parameters were as follows: I_p > 400 kA, B_T = 1.8 T, q_{95} = 3.5–4.1, line-averaged electron density n_e = (3.5–4.5) ×10^{19} m^{-3} (at R = 1.820 m), and electron temperature T_e about 1 keV. The plasma configurations employed in this work were either lower single null (LSN) or double null (DN). Core plasma rotation was determined from Doppler shifts of line emission from trace amounts of highly ionized argon as measured by a high-resolution imaging tangential X-ray crystal spectrometer system (TXCS) [6]. Molybdenum (Mo) emission was obtained from two flat-field grating spectrometers using a varied line spacing grating to image 1–13 and 5–50 nm spectrums [7]. Observed 1/1 snake-mode behavior was analyzed using a soft X-ray (SXR) imaging system [8]. In addition, the plasma-stored energy and plasma radiation were measured by edge diamagnetic coils and an absolute extreme ultraviolet (AXUV) photodiode system, respectively.

3. Experimental Observations
3.1. Repetitive bursting of snake mode

Fig. 1 exhibits repetitive bursting of helical snake-modes in an EAST discharge. The oscillating 1/1 helical nature of these snake-modes is illustrated by the sinusoidal core SXR signal. Located inside the q=1 region, the onset of the impurity-laden snake-modes appears to limit the growth rate of plasma stored energy. Examination of the data in Fig 1 demonstrates that the 1/1 snake-mode only occurs when dW/dt >0 during the confinement-improvement stage following the H-L phase of an H-L-H transition as the plasma starts to recover the H-mode. By examining all EAST shots which exhibited repetitive H-L-H transitions, it was observed that repetitive bursting of snake-modes was correlated with repetitive H-mode phases, with the first snake-mode starting after the first H-L transition. Further, snake-modes were observed to start within 20 ms of the associated L-H return transition. The vertical dashed line in Fig. 1 marks the termination of a typical snake-mode and the beginning of a "slow ramp-up" phase toward maximal stored energy – before the beginning of another H-L-H transition and the formation of another snake-mode.
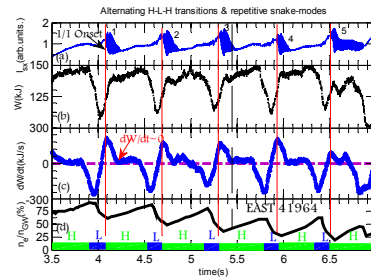
FIG.1. Shown are repetitive snakes in an EAST discharge with multiple H-L-H transitions: (a) the core soft X-ray signal I_{sx}; (b) the plasma stored energy W; (c) the plasma stored energy growth rate dW/dt; (d) $\overline{n_{e0}} / n_{GW}$, where $n_{GW}(10^{20} m^{-3}) = I_p(MA) / \pi a(m)^2$ is the "Greenwald limit" density. The vertical dashed line designates the end of a snake-mode and the beginning of a slow "ramp-up" to maximal stored energy. L and H letters in the bottom indicate the

low-confinement and high-confinement, respectively.

As illustrated in Fig 1(d), repetitive H-L-H transitions were only observed in discharges with a high initial density ($n_{e0}/n_{GW} \sim 75\%$). This may be due to the fact that the heating power employed in these discharges was only slightly above the H-mode power threshold.

Similarly, because of possible insufficient heating power in the initial phase of ITER, the accumulation of high-Z impurities should be avoided in order to help in ensuring H-mode sustainability. However, due to the high-Z impurity (lower radiation loss) transport or absorption by the 1/1 snake-mode, repetitive snake-mode bursting could be beneficial for entering the H-mode again.

The data discussed in this work were taken during the 2012 run campaign. Just before that campaign the first wall of EAST was changed from graphite to Mo. Fig. 2 (a-c) shows good correlation between the SXR signal and Mo emission observed during this work. It is clear that the formation of snake-modes is associated with the accumulation of impurity ions (Mo and other high-Z ions) in the plasma core. This has also been observed and reported in CMOD [9].
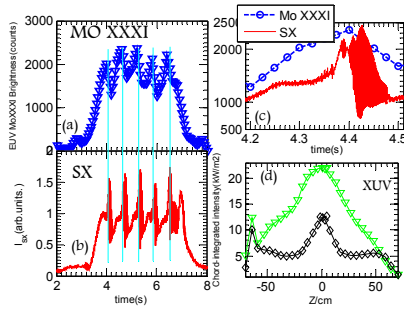
FIG.2. In this figure (a) & (b) show good correlation between SXR radiation and Mo emission. The Mo^{30+} emission was measured with the EUV system [7]. Panel (c) shows expanded core SXR and Mo^{30+} emission signals from (a) and (b). In (d) the background plasma radiation (in black) is compared to the enhanced radiation just before snake formation (in green). In both cases the data was taken from the AXUV system. The horizontal axis in (d) is the vertical position of XUV line-integrated chord (the minor radius of EAST is 45cm). Data from EAST shot 41964.

The increase in plasma confinement during L-H transitions and the erosion of the plasma facing components caused by both higher edge temperature and increased heat load from large edge localized modes (ELMs) account for the Mo impurity influx during H-mode plasmas. During rapid H-L transitions, Mo impurities accumulate in the EAST core because of the absence of both sawteeth and ELMs. This paradigm explains why it appears that the first snake-mode always commences after the first H-L transition and snake-modes always occur in EAST discharges that are free of large sawteeth (Fig. 3(a) and (b)). Moreover, the enhanced plasma radiation prior to the formation of snake-modes is also evidence of the high-Z impurity (Mo) accumulation, as shown in Fig. 2(d).
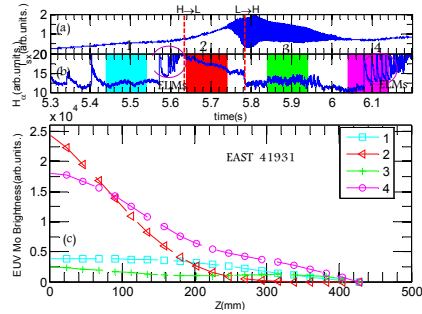
FIG.3. A detailed Mo profile of the snake in an H-L-H transition: (a) Core SXR signal; (b) H_α signal; (c) time history of brightness profiles of the Mo^{30+} line. The time span (time resolution: 100 ms) of profiles (1 4) correspond to the colored regions in (a) and (b), respectively. Formation of central impurity peaking profiles near the q=1 surface just before snake formation is demonstrated in this figure.

3.2. Impurity density threshold for recurrent snake formation

Impurity-ion fluctuations in the plasma

core region lead to core electron density oscillations. Hence, in this work core electron density fluctuations induced by snake-modes were studied with the EAST hydrogen cyanide (HCN) laser interferometer. Measured snake-mode density fluctuations were typically $\delta n_{e0} \sim 0.2 \times 10^{19} m^{-3}$ while the background electron density was $n_{e0} \sim 4 \times 10^{19} m^{-3}$. As shown in Fig. 4, the $\delta n_{e0} / n_{e0}$ ratio could reach values as high as 9%. Although detailed measurements of high-Z impurity ion (Mo, Ar, Fe, Cr, Ti, Cu…) densities were not available for the EAST discharges discussed in this work, reasonable inferences can be drawn from the data. Assuming, for example, a mean charge state of Z~30and an average electron fluctuation of $\delta n_{e0} \sim 0.2 \times 10^{19} m^{-3}$ (Fig.4), the associated impurity density would be $\delta n_Z \sim \delta n_e / Z \sim 6.6 \times 10^{16} m^{-3}$, $\delta n_Z / n_e \sim 0.16\%$ ($n_{mo} / n_e \sim 0.01\%$ from spectrometer measurements). Further assuming $Z_{eff,0} \sim 2$, the measured charge perturbations could have reached as high as $\delta Z_{eff,0} / Z_{eff,0} \sim 75\%$, which is consistent with the visible bremsstrahlung system measurement (see fig.8 in Ref. 8). The repetitive bursting of snake-modes suggests that there is a threshold core impurity concentration leading to their formation. An impurity strength factor [10] defined as $\alpha_{Z,c} = n_{Z,c} Z^2 / n_e$ was used to quantify and characterize the core impurity concentration. As demonstrated by the statistical results shown in Fig. 4, the minimum core electron density fluctuations resulting from

snake-mode formation was $\delta n_{e0} / n_{e0} \sim 2.5\%$. Therefore, the associated critical impurity strength factor for snake destabilization observed in this survey of EAST data was $\alpha_{Z,c} = Z \delta n_e / n_e \sim 0.75$. To sustainment of long-live saturated pressure-kink mode, a critical core impurity density perturbation [11] due to the neoclassical inward pinch of the heavy impurities is needed. The damping and depleting of snake originated from the disappearance of the impurity pinch. The impurity pinch in L phase of H-L-H also deteriorated the coupling of LHCD, thus unfavorable to H mode maintain. The H-L and L-H transitions near H mode power threshold related to the LHCD coupling efficiency, impurity radiation, impurity pinch, plasma radiation, turbulence activity and so on, were beyond of the scope of this paper.
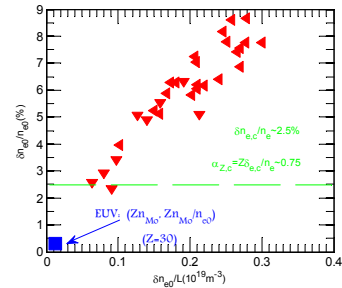
FIG.4. Shown are statistical results taken from different shots of the normalized core electron density perturbation $\delta n_{e,0}$ caused by the impurity-laden snake-mode plotted against the line-average density fluctuation. Normalized density fluctuations $\delta n_e / n_{e0}$ clearly reached as high as 9%. The background density was determined from an HCN laser interferometer channel located at R = 1.82 m. The blue point $(Zn_{Mo}, Zn_{Mo} / n_{e0})$ from the EUV system is shown as a reference. A clear impurity threshold strength factor of 0.75 may be seen in the data and is indicated by the green horizontal line.

$\delta n_e \big/ L$ means the line-average density fluctuation, L is the length of HCN chord.

3.3. **Influence of snake-modes on the core plasma rotation**

The evolution of a mode frequency measured in the LAB frame comes from two contributions: (1) from the fluid motion of the background plasma (as measured by Doppler frequency) and (2) from mode propagation in the plasma frame of reference. Within measurement error the mode frequency of snake-modes was nearly zero, as shown in Fig. 5. The plasma frequency is measured by TXCS in Fig.5. Note that the rotation data measurement by TXCS system includes not only the rotation frequency of the bulk plasma but also the ion diamagnetic drift frequency. Thus, the evolution of the snake-mode frequency in the LAB frame should just follows the rate of rotation of the bulk plasma.
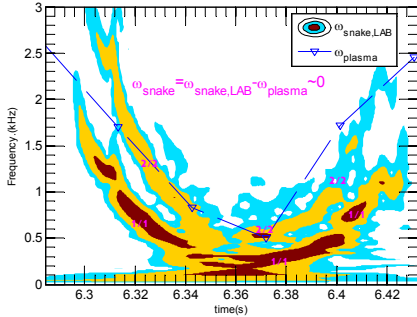
FIG.5. Displayed is a comparison of the LAB-frame mode frequency and the local bulk plasma toroidal rotation, $\omega_{snake} \sim 0$. The color map is time-frequency spectrum of snake, and the superposed dot line with triangle is plasma rotation frequency near q=1 radius. The harmonic mode shown in the time-frequency spectrum is the geometric effect of the 1/1 mode, the frequency of m=2 harmonic mode is double of m=1 mode: $f_{2/2} = 2f_{1/1}$. Data from EAST shot 38512.

$\omega_{plasma} = v_{TXCS} / 2\pi R_1$, v_{TXCS} from TXCS in EAST, R_1 is the major radius in q=1 surface.

The strong toroidal rotation damping due to the 1/1 snake-mode has been observed and is shown in Fig. 6(c). Macroscopic instabilities can reduce the plasma rotation thereby deteriorating plasma confinement. In these experiments, it has been observed that the reduced plasma rotation is related to the displacement of the 1/1 snake-mode, as shown in Fig. 6(b) and (c). This displacement of snake mode was measured by the SXR system

[13, 14], $\xi = \dfrac{1}{\sqrt{2}} \sqrt{\kappa_0 (R - R_0)^2 + \dfrac{(Z - Z_0)^2}{\kappa_0^2}}$,

where (R,Z) is the position of maximum emissivity within the hot core, (R_0 Z_0) refers to the time point before the snake develops and κ_0 is the elongation at the plasma centre.

In our calculation we take κ_0 =1, and (R, Z), (R_0 Z_0) from the 2D soft x-ray tomography [8]. The rotation of the m=1 mode [13] depends on the growth of the displacement of 1/1 snake (Fig.7). As shown in the Fig.7 the snake-mode frequency decrease correlates with the increase of the snake displacement ξ reasonably closely. It can be seen that the evolution of the snake-mode frequency estimated by $f = f_0 \xi_{m=1,0} / \xi_{m=1}$ [15] is generally consistent with the experimental frequency. Here, f_0 means take the frequency of m=1 mode at t=4.082s, $\xi_{m=1,0}$ means take the displacement of m=1 mode at t=4.082s. Since the plasma rotation in q=1 surface is roughly equal to the rotation of m=1 snake mode (see Fig. 5), thus form Fig.7 it is reasonable to infer that the bulk plasma rotation decrease correlates with the increase of the snake displacement ξ reasonably

closely. These observations are in reasonable agreement with reference [16,17] in which plasma rotation damping was understood in terms of the neoclassical toroidal viscosity torque arising from toroidal symmetry breaking due to the presence of the 1/1 snake-mode.
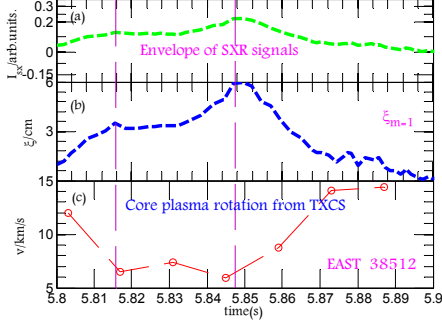
FIG.6. Shown is an example of core plasma toroidal rotation dampening by a snake-mode. (a) Displays the envelope of the core SXR sinusoidal signal. (b) Shows the displacement $\xi_{m=1}$ [13]. (c) Displays the core plasma toroidal rotation Δv_ϕ.

Envelope of SXR signal in (a) means take the mean of peaks and valleys of core SXR sinusoidal signal. The core plasma rotation (r/a~0.2) shown in (c) is measured by TXCS system in EAST.
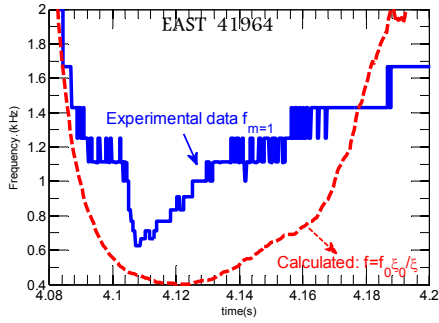
FIG.7. Shown is a comparison of the experimentally measured frequency and estimated frequency of the snake-mode - where ξ is the perturbation displacement of the 1/1 mode. The blue curve in figure is the time evolution of m=1 mode frequency from core SXR signal. The red dot curve shown in figure is calculated time evolution frequency for m=1 mode by means of the formula: $f = f_0 \xi_{m=1,0} / \xi_{m=1}$. $\xi_{m=1}$ estimated by the same

way with Fig.6. f_0 and $\xi_{m=1,0}$ are the initial frequency (t=4.082s) and initial perturbation displacement of m=1 mode, respectively.

4. Summary

Repetitive bursting snake-modes have been observed to be synchronous with L-H transitions associated with repetitive H-L-H transitions in EAST. Snake-mode formation was seen to be correlated with alternating H-mode phases, with the first snake beginning after the first H-L transition. Snake-modes reproducibly limited the maximum energy stored in the plasma and strongly dampened the plasma toroidal rotation.

The discharges investigated in this work were taken during the 2012 EAST run campaign after most plasma-facing surfaces were changed from graphite to Mo. Generally, high-Z metal walls (like Mo and tungsten) appear to help reduce the H-mode power threshold. It is clear, however, that accumulation of high-Z impurities in the plasma column is undesirable. These observations of deleterious snake-mode behavior in EAST suggest that high-Z impurity accumulation should be avoided during the beginning phase of ITER, when the heating power could be only slightly above H-mode power threshold.

Control of snake-modes is essential for sustainability of H-mode operations near threshold and will be investigated in future EAST experiments.

Acknowledgments

References

[1] Snipes J A, Campbell D J, Hender T C , Hellermann M V and Weisen H, 1990 Nucl. Fusion 30 205

[2] Weller A , Cheetham A D, Edwards A W, Gill R D, Gondhalekar A , Granetz R S, J. Snipes J A and Wesson J A , 1987 Phys. Rev. Lett. 59 2303

[3] Naujoks D, Asmussen K, Bessenrodt-Weberpals M, Deschka S, Dux R, Engelhardt W, Field A R, Fussmann R, Fuchs J C, Garcia-Rosales C, Hirsch S, Ignacz P, Lieder R, Mast K F, Neu R, Radtke R, Roth J and Wenzel U, 1996 Nucl. Fusion 36, 671

[4] Xu G S, Wan B N, Li G J, Gong X Z, Hu J S, Shan J F, Li H, Mansfield D K, Humphreys D A, Naulin V , 2011 Nucl. Fusion 51 072001

[9] Delgado-Aparicio L, Sugiyama L, Granetz R, Gates D A, Rice J E, Reinke M L, Bitter M, Fredrickson E, Gao C, Greenwald M, Hill K, Hubbard A, Hughes J W, Marmar E, Pablant N, Podpaly Y, Scott S, Wilson R, Wolfe S, and Wukitch S 2013 Phys. Rev. Lett. 110 065006.

[10] Suggested by L. Delgado-Aparicio (PPPL) 2014.

[11] Wesson Plasma J 1995 Phys. Control. Fusion 37 A337

[12] Delgado-Aparicio L, Sugiyama L, Granetz R, Gates D A, Rice J E, Reinke M L, Bitter M, Fredrickson E, Gao C, Greenwald M, Hill K, Hubbard A, Hughes J W, Marmar E, Pablant N, Podpaly Y, Scott S, Wilson R, Wolfe S, and Wukitch S 2013 Nucl. Fusion 53 043019

[13] Furno I , Angioni C, Porcelli F, Weisen H, Behn R, Goodman T P 2001 Nucl. Fusion 41 403

[14] Sun Y, Liang Y, Shaing K C, Liu Y Q 2012 Nucl. Fusion 52 083007

[15] Nave M F F, Coelho R, Lazzaro E and Serra F 2000Eur Phys. J. D 8, 287

[5] Wan B N, Li J G, Guo H Y, Liang Y F, Xu G S and Gong X Z 2013 Nucl. Fusion 53 104006.

[6] Shi Y, Wang F, Wan B, Bitter M, Lee S, Bak J , Hill K, Fu J, Li Y, Zhang W, Ti A, and Ling B, 2010 Plasma Phys. Controlled Fusion52   085014

[7] Shen Y, Du X, Zhang W, Wang Q, Li Y, Fu J, Wang F, Xu J, Lu B, Shi Y, and Wan B, Nucl. 2013 Instrum. Methods Phys. Res., Sect. A 700   86

[8] Xu L, Hu L, Chen K, Li E, Wang F, Xu M, Duan Y, Shi T, Zhang J, Zhou R, and Chen Y, Phys. Plasmas 19, 122504 (2012).

[16] Seol J, Lee S G, Park B H, Lee H H, Terzolo L, Shaing K C, You K I, Yun G S, Kim K C, Lee K D, Ko K H, Kwak J G, Kim K C, Oh Y K, Kim J K, Kim K K, and Ida K, 2012 Phys. Rev. Lett. 109 195003

[17] Hua M D, Chapman I T, Field A R, Hastie R J, Pinches S D and the MAST Team 2010 Plasma Phys. Control. Fusion 52 035009

Upgrade activities of long pulse operation in KSTAR ECH/CD system

J. H. Jeong[a], Y. S. Bae[a], M. Joung[a], J. W. Han[a], J. G. Kwak[a], Y. K. Oh[a], H. Park[a], W. Namkung[b],
M. H. Cho[b], K. Sakamoto[c], K. Kajiwara[c], Y. Oda[c], J. Hosea[d] and R. Ellis[d]

[a] National Fusion Research Institute, Daejeon, Korea
[b] Department of Physics, POSTECH, Pohang, Korea
[c] Japan Atomic Energy Agency, Naka, Japan
[d] Princeton Plasma Physics Laboratory, Princeton, USA

Email: jhjeong@nfri.re.kr

The purpose of the initial KSTAR ECH system using second-harmonic EC wave was to use it for reliable start-up with a low loop voltage to save the volt-seconds during the breakdown and current ramp-up phases. Since the successful operation of KSTAR plasma using the second-harmonic ECH-assisted start-up, the localized and controllable EC heating and current drive has been an attractive tool for interesting tokamak physics studies, such as the investigation of the MHD physics issues and core impurity control for long pulse discharge in KSTAR. Especially, to contribute to high performance long pulse experiments in KSTAR, the 1MW for 20 sec with an ITER pre-prototype of gyrotron achieved in high power operation before 2014 campaign. The critical issues for the long pulse operation was decay in beam current of the gyrotron which comes from the cathode cooling by continuous electron emission. As a countermeasure for this issue, active adjustments for the heater voltage and anode voltage during the pulse have tried to extend the duration of a RF oscillation for the gyrotron. As a result, 1MW for 50 s have been achieved up to now. To enhance the power capability of launcher system up to 300s, the original passively cooled mirrors are replaced with active water-cooling mirrors and 1MW for 41sec EC beam successfully injected to KSTAR. The increase of mirror temperature was 2.6 degrees in C for 41 sec operation. In this paper, the issues and present status of 170GHz ECH systems are described from a point of requirements for obtaining long pulse ECH system.

1. Introduction

A high-power electron cyclotron range of frequency (ECRF) heating system was introduced into KSTAR to realize high performance plasmas by controlling profiles of electron temperature, plasma current, plasma pressure and so on via its plasma heating and current drive. Since the successful operation of KSTAR plasma using the second-harmonic ECH-assisted start-up [1, 2], the localized and controllable EC heating and current drive has been an attractive tool for interesting tokamak physics studies, such as the investigation of the MHD physics issues of sawteeth, toroidal rotation, pedestal and ELM characteristics, TM/NTM control, and core impurity control for long pulse discharge [3]. In order to carry out various experiments, technologies relevant to power modulation, increasing power, and especially extension of the pulse duration have been developed. Especially, the most important technology issue before 2014 campaign was to extend the pulse duration of ECH system because the main mission of KSTAR in 2014 was the demonstration of long-pulse discharge operation with high-β. But the pulse duration of gyrotron was limited at 20sec by the mode shift effect caused by the decrease of beam current during pulse due to the cathode cooling of well-known phenomenon. The power capability of launcher mirror was also just 15 sec by the passively cooled mirrors. As result, maximum duration delivered EC beam to KSTAR in 2013 campaign was 0.8MW/10sec and the longer pulse required to support long

pulse operation of KSTAR in 2014 campaign.

The first step on the extension of pulse duration for gyrotron was anode voltage control as well as heater boosting to avoid RF termination by the decrease of beam current. Because the pitch factor of the electron beam strongly affects the oscillation condition, anode voltage actively controlled to avoid mode suppression by taking a full advantage of the triode electron gun [4]. And the passively-cooled launcher mirrors are replaced with water-cooled mirrors to enhance the power capability of mirrors upto 1MW steady-state operation. Therefore, the maximum pulse duration of 0.8MW/41sec EC beam at the launcher delivered to KSTAR to support the long pulse of KSTAR operation with high performance. In this paper, the system layout of 170GHz in KSTAR will be introduced briefly in section 2 and the extension of pulse duration of gyrotron by active control of anode voltage and heater voltage will be focused in section 3. Development of steady-state mirrors with experimental results is described in section 4.

2. High power operation of an 170 GHz gyrotron

2.1. 170GHz, 1MW ECH&CD system

Schematic diagram of the 170 GHz, 1 MW gyrotron and the configuration of the power supply system is shown in Fig.1. The present gyrotron is an ITER pre-prototype model which is loaned from JAEA. The model is newly developed, with an operation mode of $TE_{31,12}$ at the cavity and a triode-type magnetron injection gun and depressed collector improving efficiency by a factor of 1.5. The nominal operation beam voltage of the gyrotron is 72 kV with the depressed collector voltage at 23 kV and the beam current at ~50 A. The anode voltage between the cathode and anode is optimized according to the magnetic field in the cavity region. The overall efficiency of the gyrotron was about 40 % with the RF power of 1 MW [2]. In order to acquire a stable oscillation, the cathode voltage is regulated within ±1% of stability using the feedback control [5]. The electron beam pitch factor (α), as it is defined as the ratio of the perpendicular velocity to the parallel velocity of the electron beam at the cathode, is also independently controlled by changing the anode voltage with respect to the cathode by keeping the beam voltage of the cathode-body voltage.
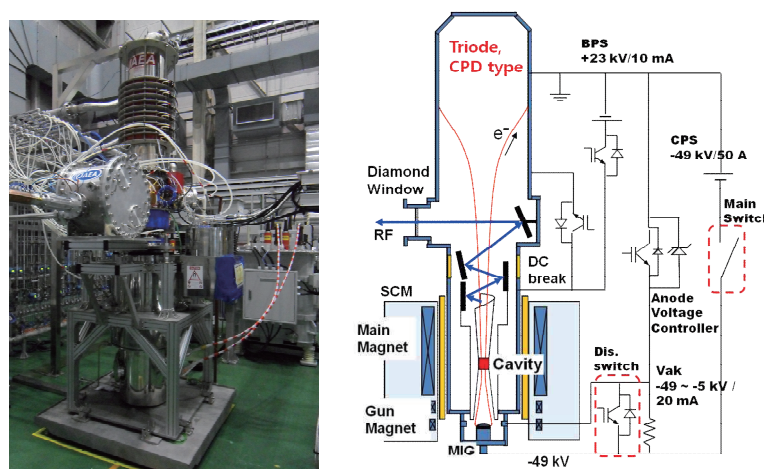
Fig. 1. 170 GHz, 1 MW gyrotron (left) and the configuration of gyrotron with the power supply system (right)

2.2. 1MW output achievement of gyrotron

One of the merits of the triode MIG is that the pitch factor can be controlled independently with other parameters by changing the anode voltage V_{ak} ($=V_{cathode}-V_{anode}$). Consequently, electron beam parameters, such as the electron cyclotron angular frequency in the resonator ω_{ce} and α were optimized by the active control of B_c (cavity field) and V_{ak} during the oscillation to acieve 1MW output from the gyrotron. Figure 2 shows the test results of the cavity-field dependence of the gyrotron output power and its efficiency. Here, the beam voltage ($V_{beam} = V_{body}-V_{cathode}$) is fixed at 72 kV and the average beam current was approximately 50 A. Through active control of V_{ak} and B_c, the beam parameters (ω_{ce}, α) at the cavity are optimized, consequently, high efficiency is obtained, e.g. $\sim$ 38% at V_{body} = 23 kV, V_{ak} = 43 kV and the cavity field of 6.641 Tesla (magnet current of 109.2 A).
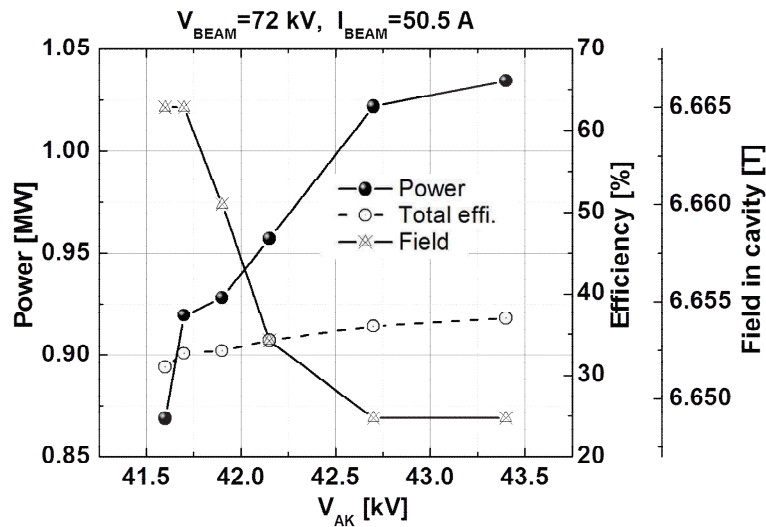
Fig. 2. Cavity field dependence of the output power. The output power is optimized by the control of V_{ak} and B_c. The beam voltage is fixed at 72 kV and the output power is maximized at V_{body} = 23 kV, V_{ak} = 43 kV and the cavity field of 6.641 Tesla (magnet current of 109.2 A).

3. Gyrotron operation for a long pulse

Figure 3 shows the waveform of a 20 sec operation at 1 MW in 2012-2013 campaign. This figure shows the applied voltages, beam current ($\sim$50 A) and RF signal using the diode detector from power monitoring miterbend. The beam current decreased as pulse duration expanded from 52 A to 47 A at a fixed beam voltage of 72 kV. Consequently, the power decreased from 1 MW (at the start phase of pulse) to 0.8 MW as the current decreased. Decrease of beam current is mainly caused by cathode cooling due to electron emission and it can be a reason of oscillation mode change from $TE_{31,12}$ to $TE_{31,10}$, so called mode jump. Therefore, the control of oscillation condition by changing of pitch factor (α) at the cavity is important to suppress of mode jump. In addition, it was found that power decrease was also caused by decrease in pitch factor for long pulse operation, which is caused by reduction of the space charge of the electron beam due to the ion trapping [6]. For this reason, output power for long pulse duration decreased in comparison with the power in short pulse.
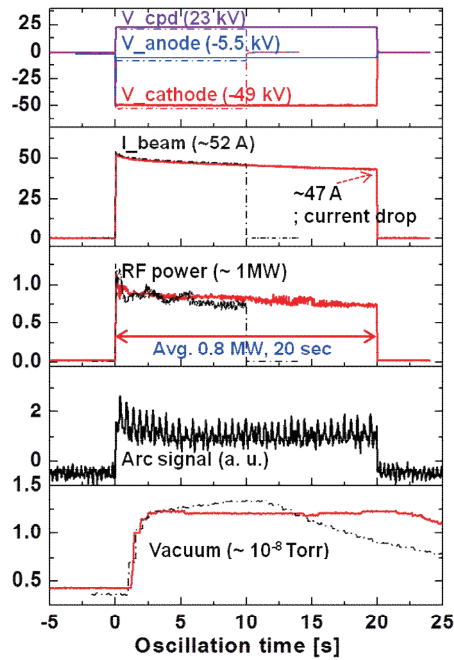
Fig. 3. Time evolution of 20 sec operation of the 170 GHz gyrotron at 1.0 MW. The efficiency is 40 % with depressed collector.

The most important issue for KSTAR ECH system in 2014 was long pulse capabilities of not only the gyrotron but also the entire system to support long pulse discharge operation with high-β operation of KSTAR. So, new operation technique with active control of anode voltage has been developed to extend pulse duration of gyrotron by changing the pitch factor of electron beam. Because the pitch factor of electron beam strongly affects the oscillation condition [4]. Figure 4 shows a configuration of new anode system which has the power capability of 50 kV/1A and connected series in the cathode voltage.
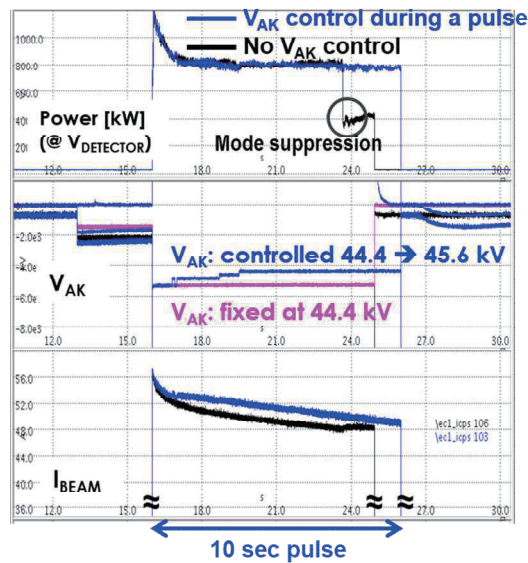
Fig. 4. Oscillation duration has been extended by anode voltage control, modifying the electron pitch angle and keeping the oscillation condition against the beam current decay.

Figure 4 shows the demonstration of extension of pulse duration by active control of anode voltage during the decrease of beam current. In the nominal operation without anode voltage control, mode shift appeared around 7.5 sec and the gyrotron oscillation was terminated around 9 sec. So, new technique with active control of anode voltage according to decrease of beam current is realized to anode power supply system to overcome this problem. As result, adjusting the anode voltage on the way during the pulse, the mode shift disappeared and pulse duration extended successfully. The change of anode voltage was 1.6 kV during 10 sec pulse and the voltage gain optimized considering the limitation of anode power supply. However, pulse duration limited by 30sec due to the limitation of increase of anode voltage and thus, required additional heater control to compensate the decrease of beam current. Before the application of heater boosting for long pulse operation, the effect of heater control observed by the pre-heating of heater before beam extraction. The heater voltage increased from 28V to 30V during 30sec before 1 minutes of pulse. The beam current increased about 1A by overheat and successfully mode shift disappeared as shown in Fig. 5.
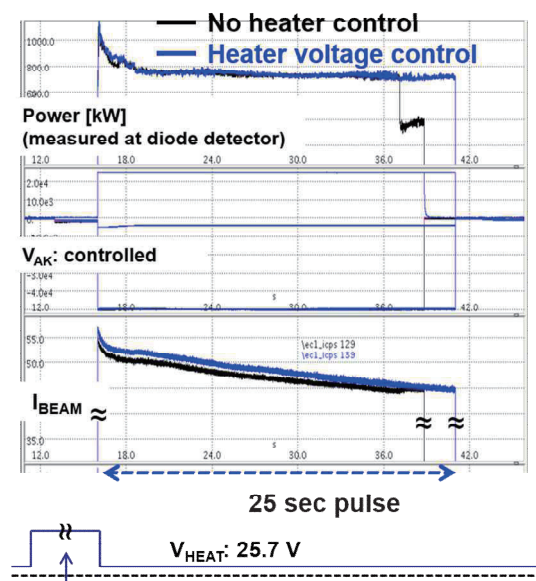
Fig. 5. Oscillation duration has been extended with cathode temperature control by eater current, compensating the beam current decay.

4. Development of steady-state mirrors for 170GHz ECH launcher

Another main technology issues in steady-state operation of ECH system was upgrade of launcher mirrors because the power capability of both mirrors are only 1MW, 15 sec by passively cooled, meaning that they cool during long intervals between pulses by radiating heat. The fixed mirror is made of solid Glidcop and the steerable mirror is made of a 0.5-mm-thick CuCrZr alloy with inlaid stainless steel blocks on the back side to maximize heat removal by radiation cooling and to reduce eddy currents by the high resistance of stainless steel. The large temperature excursions inherent in this type of design result in significant thermal fatigue stresses, and these mirrors are thus "finite life" [7]. Therefore, the original 170 GHz ECH launcher mirror should be upgraded to be capable of steady-state operation and it was a very challengeable issue in 2014 KSTAR campaign.

4.1 Design of launcher mirrors

The major heat load on the mirror surface is Ohmic loss of RF power and heat flux from the plasma. Therefore, the steady-state mirrors by active cooling were designed to have adequate convection and conduction between the coolant and the reflecting surface, and adequate coolant flow to provide a steady-state power balance with low required pressure as possible. Conduction between the fluid boundary and the reflecting surface is proportional to the thermal conductivity and inversely proportional to the distance between the two. The circular coolant path for fixed mirror milled in CuCrZr body and the blanks are brazed to make a series water coolant path by fill up the hole as shown in Fig. 6. In case of steerable mirror, the rectangular grooves for the cooling tubes milled in the body not a circular to increase thermal conductivity via larger fluid boundary and coolant tubes brazed in, and the series connections for fixed mirror. Also, the stainless steel cover used for steerable mirror as water-coolant path cover to reduce the eddy current due to the plasma disruption by increasing the resistance as shown in Fig. 7. Electromagnetic forces, due to eddy currents during a plasma disruption, are typically proportional to the mirror thickness and conductivity. So, the thickness of 2 mm layer between the fluid and reflecting surface decided to maximize heat transfer and minimizes electromagnetic forces, but is acceptable from catastrophic failure.
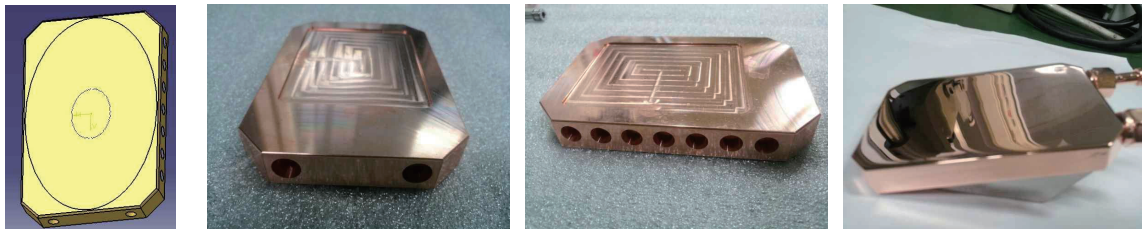
Fig. 6. Conceptual design (left) and pictures for fixed mirror. The water coolant path milled in the CuCrZr body and the blank made a series of water coolant path.
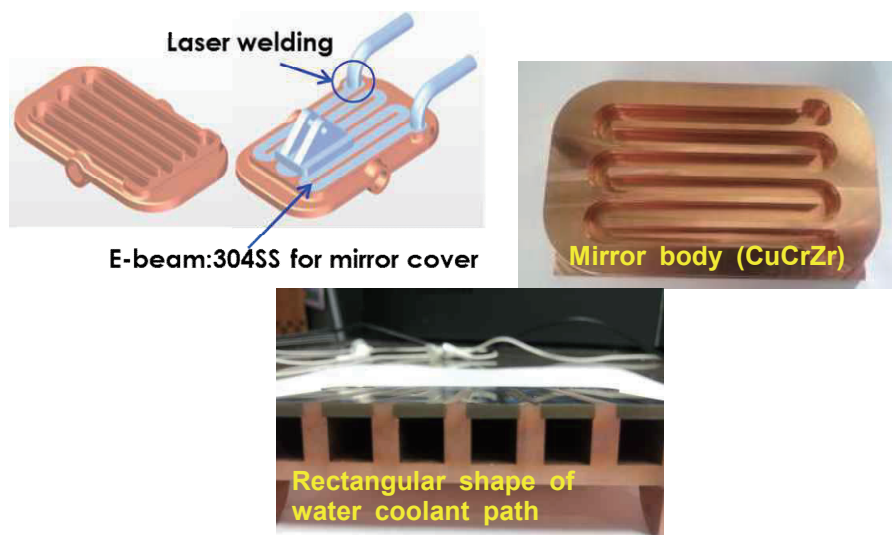
Fig. 7. Conceptual design and pictures for steerable mirror. The rectangular shape of water coolant path milled in the CuCrZr body and the stainless steel cover used to reduce the eddy current caused by plasma disruption.

Finite element thermal analysis of the mirror were performed in ANSYS code and a film coefficient of 1.2W/cm2·K is assumed for analysis which obtained by experiment. For the

design value, marginable power of 1.2MW considered with Bessel squared heat flux distribution and 30W/cm2 heat flux from the plasma is assumed for steerable mirror. The maximum temperature of mirror increased to 91ºC for steerable mirror and 71ºC for foxed mirror, respectively.

4.2 Successful injection of EC beam to KSTAR with 0.8 MW/41sec

Figure 8 shows the waveforms of longest pulse of ECH using water-cooled mirrors in 2014 campaign. 1 MW EC beam at the gyrotron window delivered to KSTAR successfully during 41sec without problems. Differential temperatures for both of mirrors are saturated within 2.6°C and it means that the input power to mirror by the heat flux balanced with heat removal by coolant flow. Therefore, longer-pulse performance is possible in 1 MW condition. The RF power losses at the mirror surface obtained by calorimetric are 1.4 kW for steerable mirror and 1.28kW for fixed mirror. Delivered power of 0.8 MW at the mirror surface obtained assuming the fraction of absorption of 0.18%.
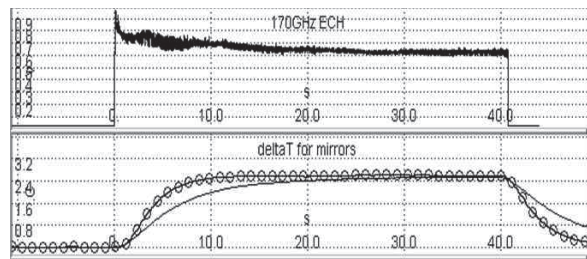
Fig. 8. Successful injection of 1MW for 41sec EC beam to KSTAR using water-cooled steady-state mirrors

5. Summary

The development of high power and long pulse operation of ECH system has been performed in KSTAR. Remarkable progress was long pulse operation of gyrotron by developing a new operation technique that results in achievement of an oscillation of 1MW for 50 sec with an efficiency of 40 %. And also, development of water-cooled mirrors for steady-state operation was essential to achievement of 0.8 MW for 41 sec EC beam injection to KSTAR. These progresses significantly contributed to long pulse operation of KSTAR with high performance and will be contribute to enhancing the long pulse capability of the ECH system toward KSTAR.

References

[1] Y. S. Bae *et al.*, Nuclear Fusion Letter, **49**, 022001 (2009)

[2] J. H. Jeong *et al.*, 17th Joint Workshop on Electron Cyclotron Emission and Electron Cyclotron Resonance Heating, **32** 02019 (2012).

[3] Y. S. Bae *et al.*, Fusion Sci. and Technol. **65**, 88 (2014)

[4] D.R. Whaley *et al.*, Phys. Lev. Lett. **75** 1304 (1995)

[5] J. H. Jeong *et al.*, Fusion engineering and Design, **88**, 380 (2013)

[6] T. Kobayashi *et al.*, Nuclear Fusion, **51**, 103037 (2011)

[7] R. Ellis *et al.*, Fusion Engineering (SOFE), 2013 IEEE 25th Symposium on. Date of Conference 13846149 (2013)

The Characteristics of RF Heating in KSTAR

S. J. Wang, H.J. Kim, S.H.Kim*, Jeehyun Kim, G. Taylor[#], J. Hosea[#],
S.H. Seo, B.H. Park, and J.G. Kwak
National Fusion Research Institute, Daejeon, Korea
*Korea Atomic Energy Research Institute (KAERI), Korea
[#]Princeton Plasma Physics Laboratory (PPPL), USA
Email : sjwang@nfri.re.kr

For the KSTAR plasmas, ICRF power coupling dependencies on plasma-antenna distance is analyzed. Antenna loading resistance which is a measure of coupling and efficiency is found to be exponentially decaying along with plasma-antenna distance. The decaying power of 1.7 is deduced in H-mode plasma when the symmetric antenna phase is used. In L-mode plasma, the loading resistance increased by up to 2 times at the same plasma-antenna distance compared to extrapolated loading resistance of H-mode. The dependency on the static magnetic field is as expected from the fast wave cutoff density. However, the dependency on the parallel wave number is unclear. It might be there was uncontrolled loss channel when the antenna phase is not symmetric. In H-mode plasma with 2 T of magnetic field and 0.6 MA of plasma current, the delivered RF power is almost same to the absorbed RF power. It means that there was no stray loss channel such as sheath heating or collisional SOL heating. While it is expected that the minority concentration may be near 16% from spectroscopic measurement, measured electron power absorption profile agrees well with simulated one with minority concentration of 5%. The increase of ion temperature is far below than the increased electron temperature while the most of power, 86%, is expected to be absorbed by ions. It may be understood that the fast ions generated by RF or RF heated NB fast ions remain un-thermalized.

1. Introduction

The maximum deliverable power to plasma is proportional to plasma loading resistance and square of maximum RF voltage in the transmission line. Therefore, in a given system, with limitation of stand-off voltage, loading resistance is a key parameter for increasing delivered power. Also, because of finite conductivity of antenna system, loading resistance which can be modeled as a series connection with antenna resistance is a measure of power efficiency. With simplified plasma model, loading resistance can be written as a exponential decaying function along with plasma-antenna distance [1]. Therefore, higher loading resistance can be achieved by reduced gap distance. However, narrow gap distance can degrade plasma confinement and elevate engineering difficulties. Therefore, compromise is required to balance high power delivery and high confinement.

In this paper, the dependency of loading resistance on the gap distance, parallel wave number and static magnetic field is analyzed with measured loading resistance in KSTAR plasmas. In addition, delivered power and absorbed power is compared to check the power partition in a given plasma conditions.

2. KSTAR ICRF System

Figure 1. shows KSTAR ICRF circuit made of single 2 MW transmitter, transmission line system and four-strap antenna system. Due to the decoupler and hybrid junction, arbitrary antenna phase and transmitter protection are possible. Frequency range is 25~60 MHz.
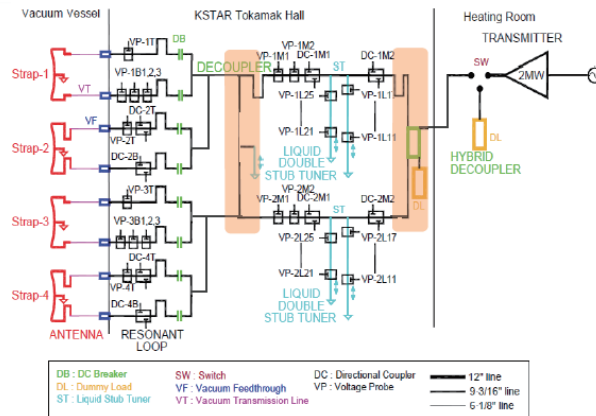
Figure 1. KSTAR ICRF circuit.
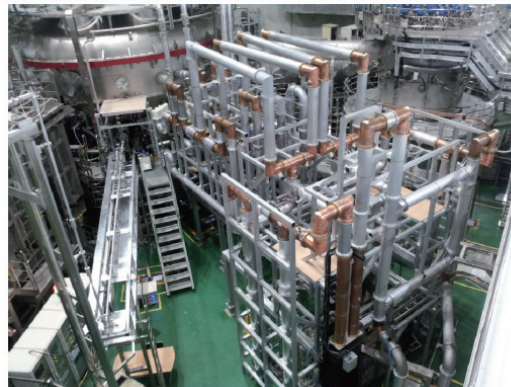
Figure 2. Bird view of ICRF transmission line.

3. Loading Resistance

The distance between plasma and antenna is varied to measure the dependency of loading resistance on that distance as in Figure 3. In this shot, plasma is moved outward from 3 s to 4 with fixed inboard last closed flux surface, and moved inward from 4 s to 9 s. The result is about 6 cm excursion of outboard last closed flux surface. Static magnetic field at magnetic axis is 2 T and plasma current is 0.6 MA. Figure 4 shows the relation of loading resistance with gapout which is defined by the distance between the last closed flux surface and poloidal outboard limiter. Fitting the loading resistance with exponentially decaying function reveals that the decaying power is ~1.7 when symmetric antenna phase for this shot is used. Usually, decaying power varies between 1~2 depending on the plasmas and machines. It can be also seen that the loading resistance in L-mode plasma is maximum 2 times higher than H-mode case because of higher electron density and lower gradient of electron density in front of antenna in L-mode plasma. In L-mode plasmas, NBI heated plasma seems to have higher loading resistance.
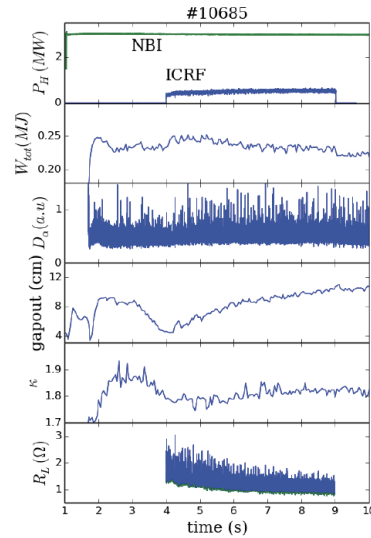
Figure 3. Shot overview. plasma-antenna distance is increased from 4.
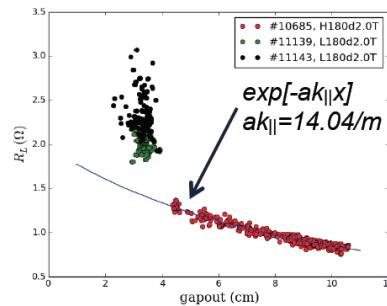
Figure 4. Loading resistance in H-mode plasma (red dots) and L-mode plasmas as a function of gapout.

4. Power Balance

Figure 5 is a typical heating result of H-mode plasma. The axial magnetic field is 2 T and plasma current is 0.6 MA. About 0.6 MW of ICRF power is injected from 6 s to 11 s. Before the ICRF heating, there are back and forth mode transitions possibly due to the marginal H-mode power. During the ICRF heating, plasma is fixed to H-mode and increases of plasma stored energy and 3He count are observed. The analysis of plasma stored energy at the end of ICRF power reveals that total absorbed power by each species in plasma is ~400kW. Since antenna Ohmic loss for the same maximum RF voltage in transmission line with this shot is ~200 KW, delivered power to plasma is same to absorbed power. It means there is no significant stray loss in the system.

Figure 6 shows electron power absorption profile measured by ECE and reflectometer and calculated profiles with different minority concentration. Minority concentration affect electron power absorption due to the mode conversion to ion Bernstein wave. From figure 6, it can be seen that electron absorption at outer region of plasma becomes large when the concentration is larger than 0.09. The absorption comparison shows that measured profile and calculated one agrees well with the concentration of 0.05 which is quite lower than expected value through the spectroscopic measurement. It seems that measured high concentration is localized at the outer region of plasma where neutrals are populated.

In spite of good agreement of electron power absorption, analyzing ion power absorption is not easy. Measured ion temperature increment is far lower that electron temperature increment even the calculation shows that the ion absorption is dominant for this shot. It can be understood that the significant portion of fast ions generated by RF heating of thermal ions and NB ions remains un-thermalized.
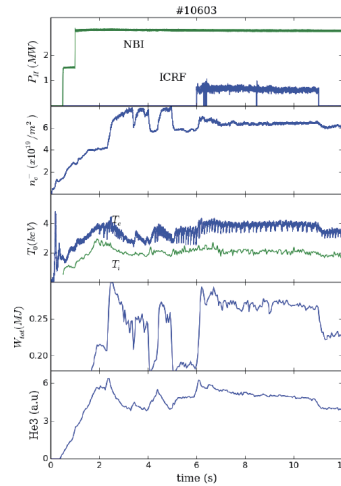
Figure 5. Overview of shot number 10603. ICRF power is injected from 6 s to 11 s in H-mode plasma.
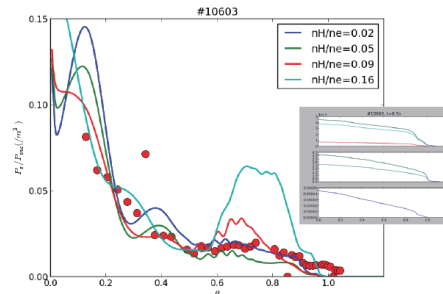
Figure 6. Comparison of measured electron absorption power with calculated absorption profiles with differenct minority concentraion.

5. Summary

It is shown that the behavior of loading resistance qualitatively agrees with expected plasma coupling relations formulated by simple model. It is also found that in KSTAR H-mode plasmas, delivered power exactly matches with total absorbed power and electron absorption profile agrees well with calculated one when minority concentration is adjusted. The diagnostics for the measurement of minority concentration in the core plasma is necessary.

Acknowledgement

References
[1] R. Bilato *et al.*, Nucl. Fusion **45,** L5 (2005)

Reliable high power RF injection through the upgrade of ICRF transmission line system

Haejin Kim, Sonjong Wang, Byoung Ho Park, Suk-Ho Hong,
Sun-Ho Kim*, and Jong-Gu Kwak
National Fusion Research Institute, Daejeon, Korea
*Korea Atomic Energy Research Institute (KAERI), Korea
Email: haejin@nfri.re.kr

We have upgraded the ICRF transmission line system installing newly a decoupler and a 3 dB hybrid coupler for load-resilient operation in KSTAR plasma experiments since 2012. Load resilient operation has been successfully performed in 2012 plasma experiments. In L/H-mode plasmas, the ratio between two powers measured at the isolated port of the hybrid coupler and reflected from two resonant loops becomes approximately 1. However, the maximum injected RF power to the plasma was limited to 500 kW with pulse length of 3 s by breakdowns frequently occurred in the vacuum feedthrough in the 2013 campaign. So we have to focus on the reliable high power RF injection to the plasmas through the upgrade of ICRF transmission line components such as 6-inch vacuum feedthrough and 6-to-9 inch U-link coaxial in order to increase the voltage standoff during the 2014 campaign. With several activities such as modification of outer conductor's shape in the VFTs and low surface roughness of inner conductor of VFT and high voltage RF test on VFTs, we could increase the voltage standoff up to 28kV. Finally we could successfully inject 1MW, 3s pulse into L-mode plasma and 700kW, 5s pulse into H-mode plasmas without any arcs during the 2014 plasmas experiments.

1. Introduction

The KSTAR Ion Cyclotron Range of Frequency (ICRF) system has been developed for high-power, long-pulse plasma heating at frequencies from 25 to 60 MHz. Heating and current drive using fast wave have been proposed as one of the main features for the steady-state operation of KSTAR [1]. KSTAR achieved the first high-performance H-mode plasma in the 2010 experimental campaign [2]. This makes the machine capable of long pulse operation to study the plasma physics of future steady-state fusion plants. In general, fusion plasma is not quiescent and exhibits many transient phenomena, such as L-H mode transitions or ELM bursts. Since the time scale of the transition is often too short for mechanical tuners, an effective-load resilient-mean is mandatory for reliable and efficient ICRF power transmission. When the loading resistance changes during L-H transitions, the transmitted power becomes reflected from the resonant loops. It became essential requirements for predictable H-mode operation to inject reliable high rf power into the plasma. We upgraded the KSTAR ICRF TL system by installing a hybrid splitter and a decoupler circuit for load-resilient high-power, long-pulse operation for the 2012 KSTAR campaign. With a coaxial hybrid coupler, the reflected power will go to the dummy load and will not be seen by the generator. This allows the RF transmitter to maintain full output power regardless of the plasma loading variation. Due to such an issue, a 3-dB hybrid coupler was installed and tested on DIII-D [3], ASDEX Upgrade [4], and JET [5]. We also installed a load-resilient TL consisting of a hybrid splitter, 9-3/16 inches coaxial TL, and a high power dummy load. The total length of the coaxial TL from the hybrid splitter to a 2 MW dummy load is approximately 65 meters. We designed the hybrid splitter with the operating

frequency of 30.8 MHz and two-section hybrid coupler for wideband frequency application using a three-dimensional simulation code, HFSS [6, 7]. The single-section hybrid splitter was fabricated, tested, and installed successfully for load-resilient operation in 2012. The decoupler circuit was also installed to compensate for power imbalances between resonant loops A and B. The decoupler circuit worked well and the reactive mutual admittance of resonant loops was canceled by varying the shorted plate of the decoupler [8]. Figure 1 shows a schematic diagram and a photograph of the 2014 KSTAR ICRF system for long-pulse, high-power RF operation.

(a)   (b)
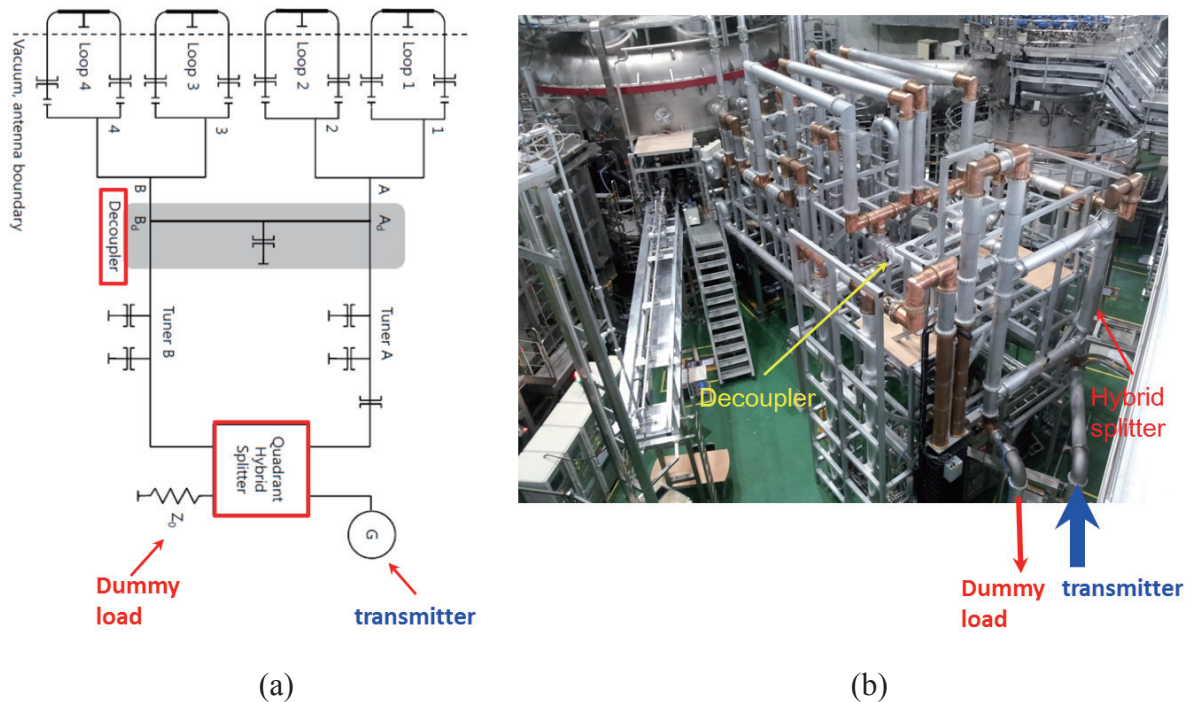
Figure 1. (a) Schematic diagram and (b) photograph of 2014 KSTAR ICRF system upgraded for load-resilient operation.

2. Issues on ICRF VFT for high power operation

In the ICRF system, the vacuum feedthrough was fabricated and utilized for vacuum sealing between the pressurized TL and the evacuated [9]. It has to withstand high RF voltage or large RF current while keeping the antenna in high vacuum. However, breakdowns frequently occurred at the 6-inch coaxial vacuum feedthroughs (VFT) connected to the ICRF antenna for KSTAR tokamak when high RF power around 500 kW was injected during 2013 KSTAR campaign as depicted in Fig. 2. After the campaign we have slightly modified and cut out the high electric field area of outer conductor and also cleaned the surface of inner conductor with super polishing process in order to increase a voltage standoff at the VFTs as shown in Figs. 3 and 4. Figures 5 and 6 show that the schematic diagram of high voltage RF test of VFT and VFT conditioning with the vacuum chamber in the high power RF operation using a 2 MW transmitter. In 2014, we repaired the damaged surfaces of inner/outer conductors and also fabricated the fast interlock circuit to prevent VTF damage caused by breakdowns. The fast interlock can be turned off the rf transmitter within 400 ns. In order to increase the voltage standoff of VFTs, we modified the geometrical shape of the outer conductor and tested the feedthroughs with hot-pulse, high voltage applied until breakdown

in the vacuum chamber. Normally, the vacuum pressure on the evacuated side of a VFT is approximately 1~5*10-5 mbar. As shown in Table 1, RF voltages of the 8 VFTs were measured and increased around 50 kV0p through RF high voltage conditioning
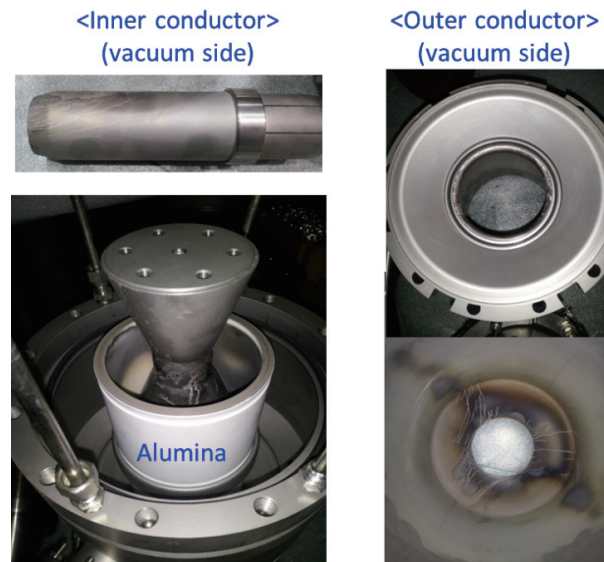
Figure 2. Photographs of damaged inner and outer conductors by arcs during the 2013 KSTAR campaign.
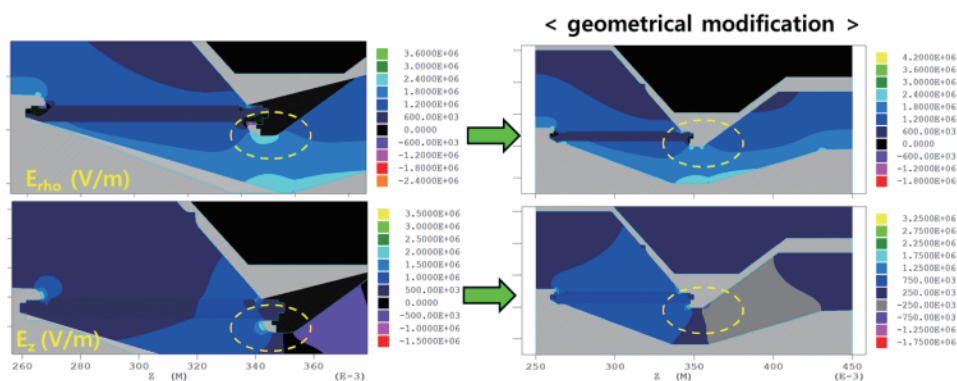
Figure 3. Geometrical modification to reduce radial and axial electric field at the VFT using MAGIC2D simulations.

(a)   (b)
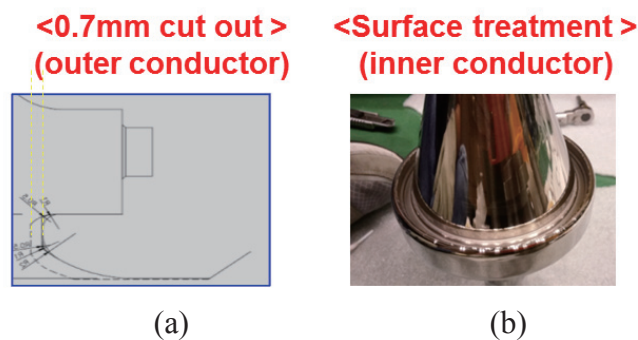
Figure 4. (a) cut-out of outer conductor and (b) surface of inner conductor after surface

treatment to increase the voltage standoff in the VFTs.

(a)   (b)
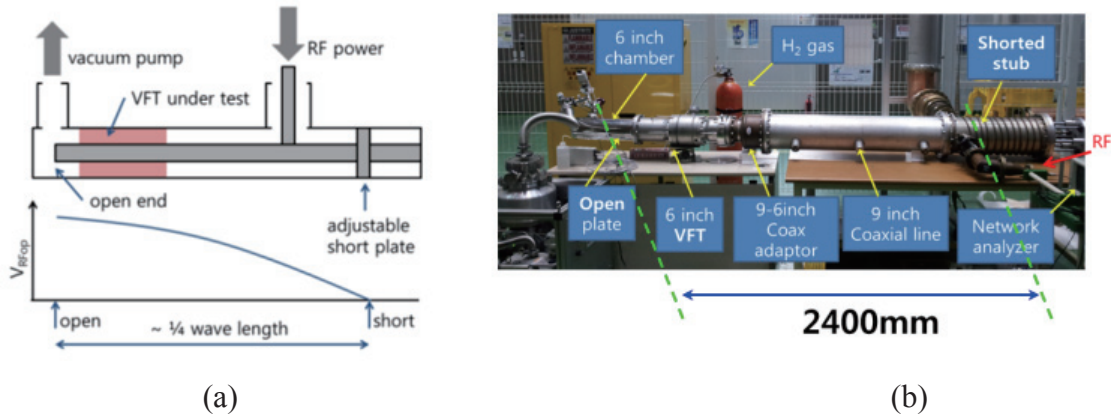
Figure 5. (a) Schematic diagram of high voltage RF test for VFT and (b) VFT Hi-pot test-stand with vacuum chamber.

Table 1. Measured RF voltage of the 8 VFTs with Hi-pot test .

VFT	V_{0p} (kV)	Pulse length (s)
1T	55.8	0.7
1B	55.8	1.0
2T	56.6	1.0
2B	49.5	0.5
3T	55.4	1.0
3B	55.8	2.0
4T	55.8	0.7
4B	54.2	2.0

3. High power RF injection to L/H-mode plasmas in the 2014 KSTAR campaign

In the 2014 KSTAR campaign we have to focus on the reliable high power RF injection to the plasmas through the upgrade of ICRF transmission line components such as 6-inch vacuum feedthrough and 6-to-9 inch U-link coaxial in order to increase the voltage standoff during the 2014 campaign. With several activities such as modification of outer conductor's shape in the VFTs and low surface roughness of inner conductor of VFT and high voltage RF test on VFTs, we could increase the voltage standoff up to 28kV. Figure 6 shows the RF injected into the L-mode plasma in shot # 9979 achieved about 900 kW with 0.5 s pulse in the 2014 KSTAR experiments. Through the upgrade of transmission line components such as a 3 dB hybrid splitter, a decoupler, and VFTs, RF injected power could be increased almost twice than the injection power of the 2013 shot (#9258). High power of 700 kW with 10 s and 700 kW and 5 s pulse, respectively, have been injected into the L and H-mode plasmas successfully as shown in Figs. 7 and 8. We could successfully inject 1MW, 3s pulse into L-mode plasma and 700kW, 5s pulse into H-mode plasmas without any arcs during the 2014 plasmas experiments. Plasma heating by ICRF was observed clearly during the 2014 KSTAR campaign.
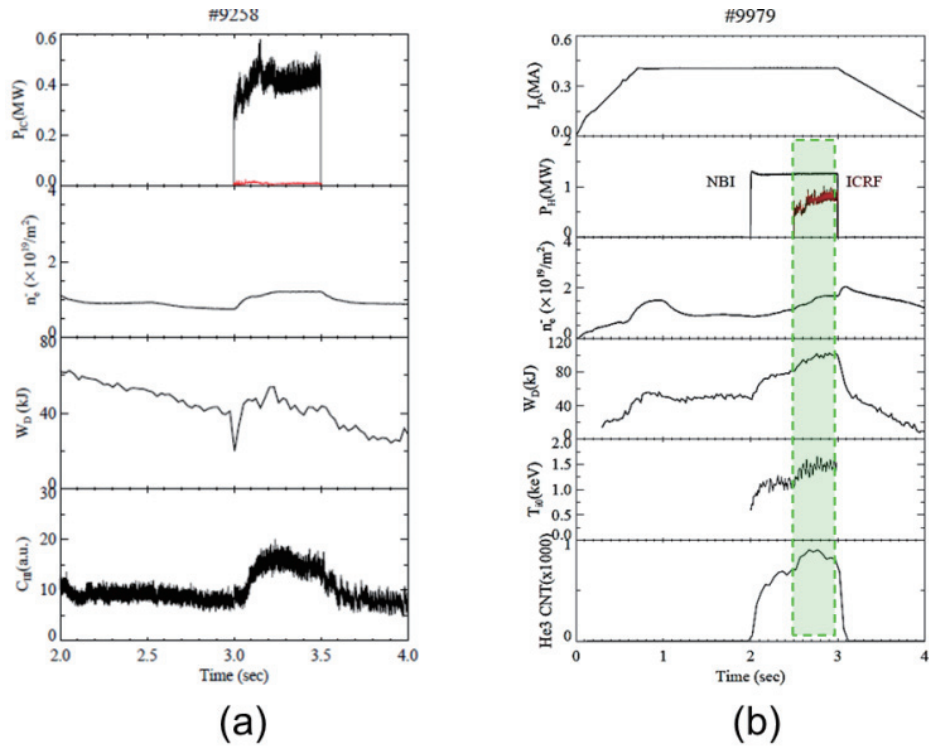
Figure 6. Comparison of ICRF injection powers into L-mode plasmas
between (a) 2013 and (b) 2014 KSTAR
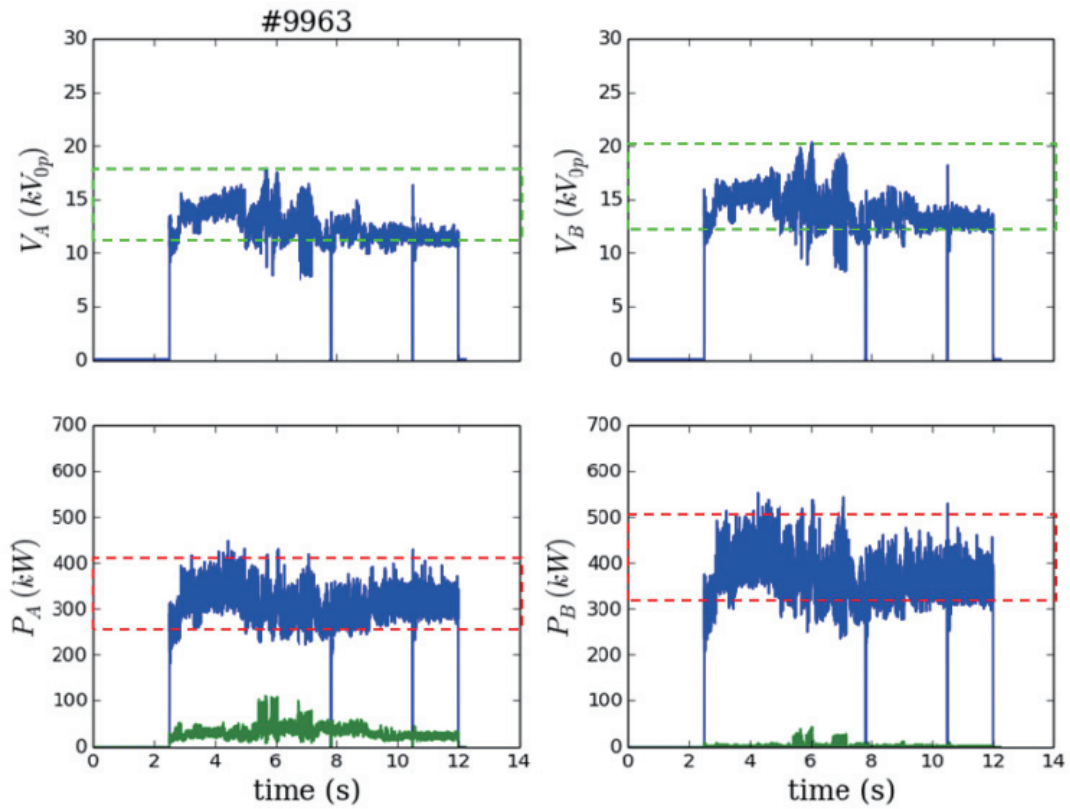
Figure 7. Measured voltage standoff and transmitted/reflected powers at resonant loop A
and B during # 9963 (L-mode plasma)
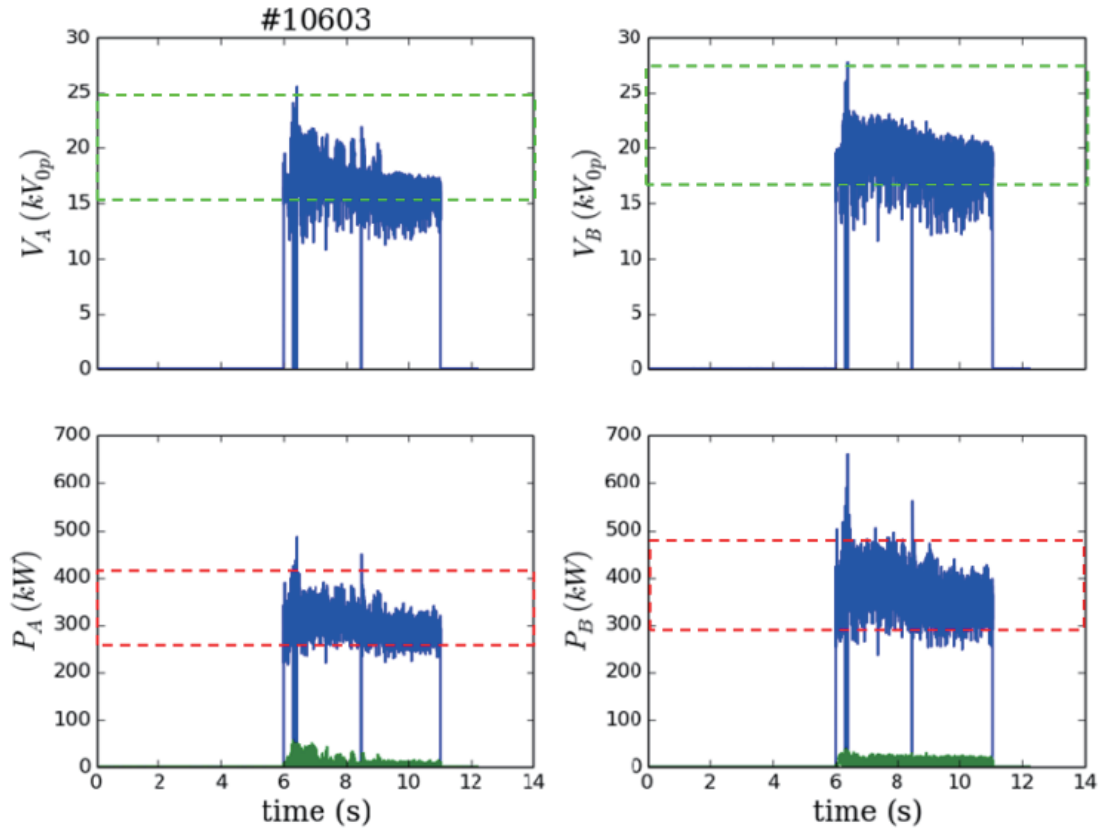
Figure 8. Measured voltage standoff and transmitted/reflected powers at resonant loop A and B during # 10603 (H-mode plasma)

4. Summary

During the 2014 campaign we have focused on the reliable high power RF injection to the plasmas through the upgrade of ICRF transmission line components such as 6-inch vacuum feedthrough and 6-to-9 inch U-link coaxial in order to increase the voltage standoff. With several activities such as modification of outer conductor's shape in the VFTs and low surface roughness of inner conductor of VFT and high voltage RF test on VFTs, we could increase the voltage standoff up to 28kV. Finally we could successfully inject 1MW, 3s pulse into L-mode plasma and 700kW, 5s pulse into H-mode plasmas without any arcs during the 2014 plasmas experiments. For 2015 KSTAR ICRF heating power will be upgraded up to 1.5 MW using the anode power supply (24 kV), tungsten coated VFTs, and SF6 pressurized transmission line.

Acknowledgement

References
[1] J.-G. Kwak, S. J. Wang, J. S. Yoon et al., Fusion Eng. Des. 84, 1140-1143 (2009).
[2] S. W. Yoon, et al., Nucl. Fusion Eng. Des. 51, 113009 (2011).
[3] C. C. Petty, F. W. Baity, J. S. Grassie, et al., Nucl. Fusion 39, 1421 (1999).
[4] J. –M. Noterdaeme, V. V. Bobkov, S. Bremond, A. Parisot, I. Monakhov et al., Fusion

Eng. Des. 74, 191-198 (2005).

[5] A. Messiaen, M. Vervier, P. Dumortier, D. Grine, P. U. Lamalle, F. Durodie et al., Nucl. Fusion 49, 055004 (2009).

[6] High Frequency Structure Simulator, Version 12.0, Ansoft Co. Ltd., Pittsburgh, PA, 2010.

[7] H. J. Kim, Y. S. Bae, H. L. Yang et al., Appl. Phys. Letters 100, 263506, (2012).

[8] S. J. Wang, S. H. Kim, S. K. Kim, H. J. Kim, Fusion Eng. Des., 88, 129-135 (2013).

[9] Y. D. Bae, J. G. Kwak, J. S. Yoon, S. U. Jeong and B. G. Hong, J. Korean Phys. Soc. 44, 1189-1194 (2004).

Current status of ICRF system on EAST

C.M. Qin[1], Y.P. Zhao[1], X.J. Zhang[1], B.N. Wan[1], X.Z. Gong[1], Y.Z. Mao[1], S. Yuan[1], G. Chen[1], Y. Chen[1] L. Zhang[1], J.F. Chang[1], F.D. Wang[1], Y.M. Duan[1]

[1]Institute of Plasma Physics, Chinese Academy of Sciences, Hefei 230031, China

Email contact of main author: chmq@ipp.ac.cn

Abstract
The ICRF heating system on EAST upgraded by active cooling aims for long pulse operation. In this paper, the main technical features of the ICRF system are described. One of a major challenges for long pulse operation is RF-edge interactions induced impurity production and heat loading. In EAST, ICRF antenna protections and Faraday screen bars damaged due to LH electron beam are found. Preliminary results for the analysis of the interaction between LHCD and ICRF antenna are discussed. Increase of metal impurities in the plasma during RF pulse and in a larger core radiation are also shown. These RF-edge interactions at EAST and some preliminary results for the optimizing RF performance will be presented.
Keywords: long pulse, ICRF, heat-load
PACS: 52.50.Qt. 52.55.Hc, 52.35.Bj

INTRODUCTION

One of the research objectives of Experimental Advanced Superconducting Tokomak (EAST) is to perform a steady-state operation in a high performance regime [1]. Heating and current drive using fast wave in the Ion Cyclotron Range of Frequency (ICRF) have been proposed as one of the main tools for the advanced tokamak operation of EAST. The ICRF system on EAST has been developed for several years, which is upgraded by active cooling aims for long pulse operation with a frequency range of 25-70MHz. The ICRF system will deliver 12 MW($1.5MW \times 8$ transmitter) of RF power to the plasma using two different ICRF antennas mounted in a mid-plane port[2]. The 2×2 loop antenna at B-port is fed at end and grounded at the other end. The 1×4 folded antenna at I-port is a fed at center and grounded at the other end. Both the current straps and Faraday shield of the two antennas are made of stainless steel and coated by B4C for mitigation high Z impurities.

EXPERIMENTAL RESULTS

In EAST, all the transmission lines including liquid stub tuners are upgraded as active water cooling for long pulse operation. In order to remove the dissipated RF power and incoming plasma heat loads ,the straps, Faraday shield and RF limiters also should be water cooled. The high voltage distribution region on the transmission line between antenna and liquid stub tuner is pressurized with 3 kg/cm^2 N$_2$ to minimize the arcing(Fig.1).

To guarantee that all the elements inside the EAST chamber are leak tight, they have to comply with an independent qualification tests before their installation on the tokamak. Especially, high pressure and high vacuum tests of water cooling circuits for the faraday screen were carried out. These tests are conducted on a vacuum test bed, capable of baking the two faradays to 200° C. The helium leak test at room temperature is made with the water cooling channel pressurized up to 60 bars, and to 40 bars at 200° C. The maximum allowed leak rate at 40 bars and T~200° C is 1×10^{-8} Pam^3 s^{-1}, while at 60 bars and T<60° C it is reduced to 1×10^{-10} Pam^{3}s^{-1}. This procedure ensures that there is no water leak on components before their connection to the machine vacuum.

As the straps for the EAST ICRF antenna are closely packed, the phased current distribution at straps causes a power imbalance at each strap owing to the large mutual couplings between straps[3]. The RF matching are quite difficult due to the cross-talking between the current straps and power flows from one strap to the other, and often a high VSWR on the transmission line causes arcing. In order to mitigate the effect on the matching circuit, a resonant loop circuit decouples system is included. A schematic of the decouples system is illustrated in Fig. 2. A decouples circuit connected to each arm of the strap with an asymmetric feeding point accomplishes the out-of-phase condition at the strap feeding points. The total length of the top and bottom arms of the loop is a multiple wavelength, and the length difference is a half wavelength plus a multiple wavelength. The resonant loop feed points will be choice at

voltage maximum (purely real input impedance) to be independent of the resistive component of the antenna load. Fig.3 shows the decouplers distribution for I-port antenna and B-port antenna. in the case of I-port antenna, Five resonance loop circuits for I-port antenna and four resonance loop circuits for the 2×2 straps B-port antenna were constructed by using available standard coaxial components. Therefore, in the ICRF program of 2014 EAST campaign, priority was given to the system reliability with the decouples. After installation of these nine resonant loop circuits, the admittance matrix was measured. By fine tuning at a frequency of 35 MHz, the decoupled forward scattering drops from -14dB to -50 dB at the frequency. Fig.4 shows the ICRF system reliable operation are achieved with injected RF power of 2.8MW. Fig.3b indicates that the 2×2 straps B-port antenna and 4-straps I-port antenna work well by the adopting of nine decouples.
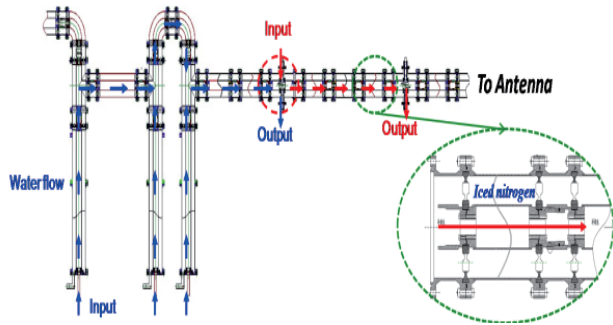
Figure1. Water cooling for matching system and transmission line with 3 kg/cm^2 N$_2$ for long pulse operation.
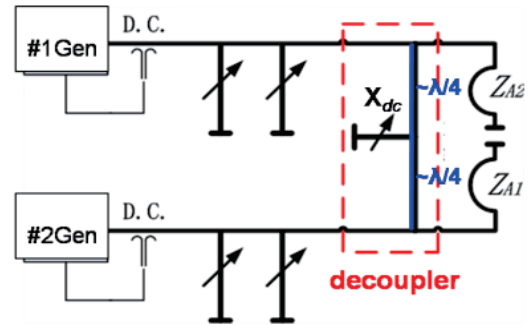
Figure2. A schematic of the decouples is included for two straps. The adopting of decouples cancels reactive mutual admittance by adjusting Xdc.
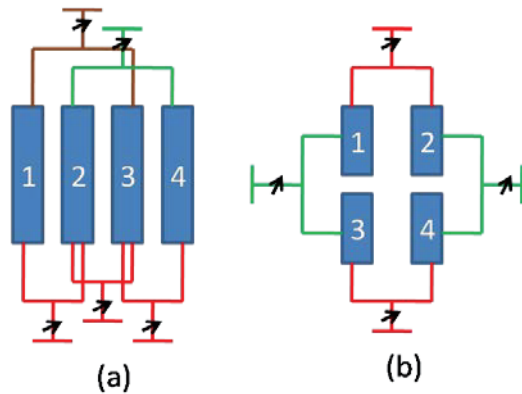
Figure3 Decouplers distribution for I-port antenna (a)and for B-port antenna(b).
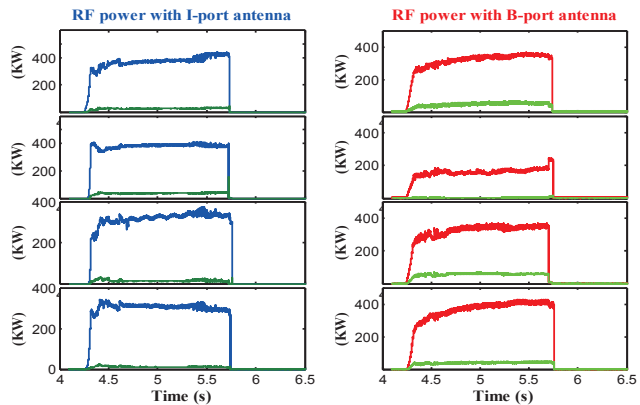
Figure 4. After installation of the decouplers, two antennas on EAST are reliable operation at 2.8MW power lever with nine resonance loop cuircuits.

In the case of ICRF system stable operation, both ions and electrons heating were observed in the H-minority heating scheme in a deuterium majority plasma. An typical shot of ICRF heated discharge at Bt=2.5T, Ip=500kA and H/(H+D)~7% is shown in Fig.5. The increase in the central ions and electrons temperature measured by X-ray crystal spectrometer were above 0.5keV during ICRF pulse. The stored energy has an increase of 15kJ and electron density drops by about 20%. Heating by ICRF waves may affect the underlying transport of particles in tokamak plasmas. Enhanced transport of particles may thus lead to reduced electron density.

One challenge to ICRF utilization for long pulse operation is its interaction with the edge plasma. A damage on the faraday screen bars of B-port antenna are observed. The most likely causes of the energetic electrons accelerated by launched LH waves, which follow magnetic field lines and thus intercept with ICRF antenna magnetic connection to LH grill waveguides. This phenomenon was observed previously on JET[4] and Tore Supra[5]. Fig.6a. shows a sketch of the field mapping between the LH Antenna and the LH launcher, both N-port LH and E-port LH antennas have some magnetic connections with B-port ICRF antenna. However, according to the direction of plasma, the electron side of the E-port LH antennas is consistent with the side of the melt FS(Fig.6b). As the RF limiters are located at the largest ripple of magnetic field and there is likely radial extension of the electron beam, so the FS is not protected by the RF limiter.
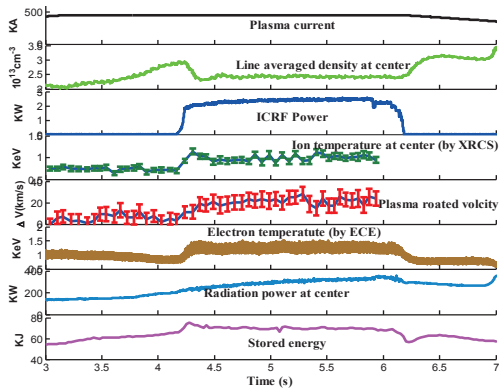
Figure 5. An example of typical ICRF Heating plasma discharge in EAST with 2.2MW of ICRF power injected show effective electron and ions heating.
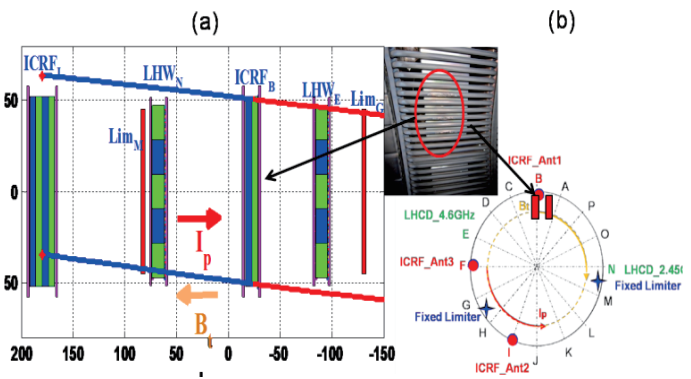
Figure 6. (a) A sketch of the magnetically connection between the LH Antenna and the LH launcher. (b) ICRF,LHCD and plasma limiter distribution on the top view of EAST. A damaged on the B-port Faraday screen bars E-port LH.

To monitor heat flux to the ICRF antenna, the antenna is instrumented with 5 thermocouples in the antenna each side protection tiles. Results from a statistical B-port and I-port side protection tiles measured by thermocouples, Fig.6 shows that the B-port antenna magnetic connection with LH powered receives significantly more heat flux. It suspects that fast electron beam production from E-port antenna and lead to more heat loads on the B-port antenna protect tiles. It is also found that warming up is very sensitive to LH pulse, the temperature increase greatly with long LH pulse. Without LH powered, B-port and I-port protection tiles have the similar temperature. #1 and #3 thermocouples responding to upper and middle region have much higher temperature than bottom protection tiles.
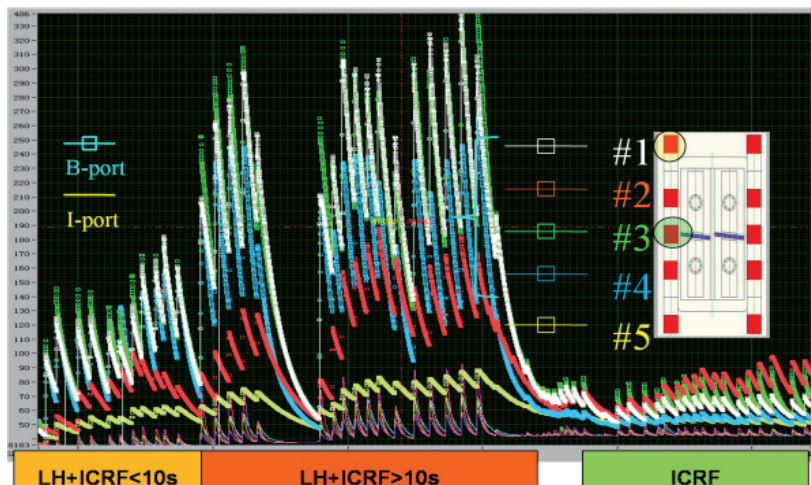
Figure 7. Temperature increase of protection limiter on the B-port and I-port. solid line with square maker is B-port temperature and solid line is I-port antenna. The square line is B-port ICRF antenna left limiter temperature measured by thermocouples, and solid line is I-port antenna left limiter temperature.

Release of metal impurities during ICRF pulse is often observed in many devices, especially in high Z metal Plasma Facing Components (PFCs) machine[AUG, JET, C-Mod]. EAST PFCs has been upgraded with tungsten upper divertor, molybdenum (Mo) first wall and C lower divertor since 2014 campaign. Signals from both, the bolometer and the UV spectrometer, Carbon and Mo, Fe and Cu impurities increase when the applying of ICRF power(see Fig8). However the intensity of Mo, Fe and Cu are more weaker than the intensity of CVI and N light impurities(Fig.9), and W line emission spectroscopy did not found during RF pulse. The intensity of CVI significantly enhancement is likely related to RF-sheaths due to lower divertor magnetic connection with active

ICRF antennas.

Figure 8. Mo, Fe ,Cu and CVI line intensity (mid-plane VUV spectroscopy) increase during ICRF pulse.

Figure 9. Impurities line emission spectroscopy at t=5s, during ICRF pulse, the same shot as Fig.8.

SUMMARY

In summary, the ICRF system on EAST has been upgraded aiming at long pulse and high power operation recently. All the antenna components and match system were equipped with water cooling system. Initial operation focus on the system checkup of reliability, since the large mutual couplings between four straps for each antenna will cause a power imbalance at each strap and leads to matching problem. A decoupler was installed between straps for each antenna, the decoupled forward scattering decrease by factor of double at frequency of 35MHz. ICRF antennas stable operation are achieved with injected RF power of 2.8MW in 2014 campaign. Results from statics measured by thermocouples found a much higher effect on the ICRF antenna limiter located on the electron side of the LH launchers. Suggestions of moving ICRF antenna behind of LH launcher or adding limiter between them will decrease these effect. Although no serious metal impurity during RF pulse was observed. However, the associated heat loads could be limiting for EAST high power and long pulse operation in the future.

ACKNOWLEDGMENTS

REFERENCES

[1] B. Wan. et al.,Nucl. Fusion**49** 104011 (2009).

[2] Y.P. Zhao, X.J. Zhang, Y.Z. Mao, S. Yuan, D.Y. Xue, X. Deng, L. Wang et al.,Fus. Eng. Design **89**, 2642 (2014).

[3] R.I. Pinsker, C.C. Petty, W.P. Cary, F.W. Baity, R.H. Goulding, 1994 Proc. 15th IEEE/NPSS Symp. Fusion Eng. (Hyannis 1993), Piscataway, NJ: IEEE, 1994, p. 1077.

[4] K.K. Kirov, J. Mailloux, A. Ekedah, AIP Conference Proceedings 787, 315 (2005)

[5] Ekedahl, A; Basiuk, V; Bucalossi, J; Colas, L; Corre, Y; Dumont, R; Eriksson, L G et al., 2007,17th RF Top Conf, Clearwater, 8/5-07.

First Quasi-snwoflake Divertor Experiment on EAST

B.J. Xiao[1,2], G. Calabrò[3], Y. Guo[1], Z.P. Luo[1], R. Albanese[4], R. Ambrosino[4], L. Barbato[4], F. Crisanti[3], G. De Tommasi[4], E. Giovannozzi[3], S. Mastrostefano[4], A. Pironti[4], V. Pericoli Ridolfini[4], G. Ramogida[3], A.A. Tuccillo[3], F. Villone[4], B. Viola[3], R. Zagórski[5]

[1]*Institute of Plasma Physics, Chinese Academy of Sciences, Hefei, 230031, China*

[2]*School of Nuclear Science and Technology, University of Science and Technology of China, Hefei, 230026, China*

[3]*ENEA Unità Tecnica Fusione, C.R. Frascati, Via E. Fermi 45, 00044 Frascati, Roma, Italy*

[4]*CREATE, Università di Napoli Federico II, Università di Cassino and Università di Napoli Parthenope, Via Claudio 19, 80125 Napoli, Italy*

[5]*Institute of Plasma Physics and Laser Microfusion, Warsaw, Poland*

Abstract: Heat and particle loads on the plasma-facing components are among the most challenging points to be solved for ITER and a reactor design. Alternative magnetic configuration, such as the X-divertor, Super X-divertor and Snowflake divertor may enable tokamak operation at lower peak heat load than a standard Single Null divertor. This paper reports on the modelling of the variations of the second null point present in the advanced magnetic divertor, here so-called quasi-Snowflake configuration, and first experiments performed on the EAST tokamak in 2014.

1. Introduction

Handling fusion power and particle exhaust, reducing heat loads below a limit on plasma-facing components, especially on divertor plates, are one of the critical issues for the long-pulse or steady-state operation ITER and future fusion reactor. Plasma detachment from a divertor target is one of the most attractive methods for handling the exhaust power and fusion ash, sparing the divertor targets from unacceptable localized power loads [1]. Another approach to handling the heat exhaust power is to use alternative magnetic configurations, such as the snowflake divertor (SF) [2] and the single-legged X-divertor [3]. The single-legged X divertor places the second X-point near the plate, casuing flared field lines there, which spreads the heat over a larger area and increases the line connection length. The SF configuration is characterized by a second-order null (X-point) in the poloidal magnetic field (B_p),

where both B_p itself and its spatial derivatives vanish ($B_p = 0$, $\nabla B_p = 0$). This splits the separatrix near the null into six segments: two of them enclose the confined plasma and four lead to the machine wall (the divertor legs) [4]. The poloidal cross-section of the obtained magnetic flux surfaces with a hexagonal null-point has the appearance of a snowflake. Theoretical studies indicate that the SF magnetic geometry may led to both higher power losses during scrape-off layer (SOL) transport and an increased plasma wetted area of the wall [5,6]. The former results from an increase in the connection length and the divertor volume, the latter from an increase in flux expansion and SOL width. The SF was estabilished on TCV[7], NSTX [8] and DIIID [9].

Exact SF configuration has several problems (for instance are intrinsically

unstable) and for this reason the first experiments performed on the Experimental Advanced Superconducting Tokamak (EAST) and discussed in this paper, are mainly devoted to the study of the role of the reciprocal position of the two x-points characterizing the so-called quasi-SF (QSF) configuration. Each of them in its vicinity behaves as a first-order null, with the magnetic field growing linearly with the distance from the null, but the coefficient in this linear dependence 'knows' of the presence of the second null. This coefficient depends linearly on the distance between the nulls, as discussed in SF's theory [10] and, in a close vicinity of each null, does not depend on the direction.

As shown in Fig. 1, EAST is constructed to be up-down symmetric, with the following main parameters [11]: major radius R = 1.8 m, minor radius a = 0.45 m, toroidal field B_T up to 3.5 T, and plasma current I_p up to 1 MA for highly elongated plasma with elongation κ = 1.9. It can be operated in quite flexible plasma shapes with an elongation factor κ = 1.5-2.0 and triangularity δ = 0.3-0.6 for double null (DN) or SN divertor configurations. EAST is equipped with 14 superconducting poloidal field coils (PFCs) for ohmic heating, ohmic current drive, shaping and position control [12]. It should be noted that PFCs 7 and 9 are connected in series as are PFCs 8 and 10. Thus, there are in total 12 independent PF power supplies (maximum current I_{PF} = 14.5kA). EAST also has in-vessel active feedback coils (IC coils) for fast control of the plasma vertical instability; they consist of two 2-turn coils symmetrically located in the upper and lower part of the vessel and connected in anti-series in order to provide an horizontal field. Unlike DIII-D and NSTX, EAST does not have dedicated divertor coils which could be used to shape the local flux distribution within the divertor region. It should be noted that in EAST, due to the location of PF coils and target plates, as will be discussed in the next section, the secondary x-point could be moved around from the primary one to form a magnetic configuration that features the SF+/- (characterized by a contracting geometry near the plate) or an X divertor (X-d) configuration (characterized by a flaring geometry near the plate). In the rest of the paper, we shall refer to the configurations and related experiments with a two-null divertor geometry as quasi-SF (QSF) scenarios, indicating for each configuration the features of contracting or flaring geometry.
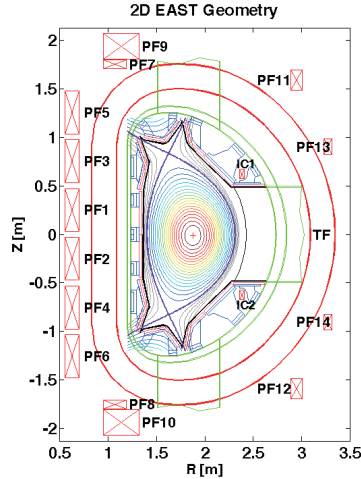
Figure 1. Tow-dimensional EAST geometry schematic view.

2. EAST QSF equilibria modeling and optimization

QSF equilibria have been designed and optimized by means of CREATE-NL code [13], in combination with EFIT [14] and FIXFRESS [15] codes. The tokamak simulation code (TSC) [16], a numerical model of the axisymmetric tokamak plasma and the associated control systems, has been then used to model the EAST QSF full plasma time evolution scenario. The procedure proposed for the design and optimization of QSF equilibrium using the CREATE-NL code exploits the linearized relation between the plasma-wall gaps and the PF currents, as discussed in reference [17]. It is composed of two steps:

1) the first step allows to have a first cut of the QSF equilibrium starting from a standard single null plasma configuration: a new equilibrium with a second null point within a limited distance from SN x-point is obtained, forcing the plasma boundary to be almost unchanged, apart from the region in the vicinity of the null point;

2) the second step refines the plasma shape and possibly reduces the PF coil currents while fulfilling the machine technological constraints.

Here, QSF equilibria are identified as modifications of experimental reference EAST SN discharge #43362 ($I_P \sim 400kA$, $B_T = 1.8T$, internal plasma inductance $l_i \sim 1.4$, poloidal beta $\beta_p \sim 0.1$) with the following constraints to be verified:

a) PF coil currents I_k far enough from their limits: $I_{min} + \Delta I \leq I_k \leq I_{max} - \Delta I$, with $\Delta I = 0.1 \max\{|I_{min}|, |I_{max}|\}$;

b) vertical instability growth rate not much larger than reference SN configuration;

c) strike points on vertical targets;

d) at least 40 mm clearance (gap) between plasma boundary and first wall.

The objectives of the QSF design and optimization procedure consists in the definition of a set of QSF equilibria, at low (0.1) and high β_p (0.45) with the secondary x-point close or far from the vessel structures maximizing the plasma

current. The optimized QSF configurations obtained with CREATE-NL and then verified by EFIT and FIXFREE code are summarized in Table I. The simulated QSF and experimental reference SN equilibria at low β_p are shown in Figure 2.
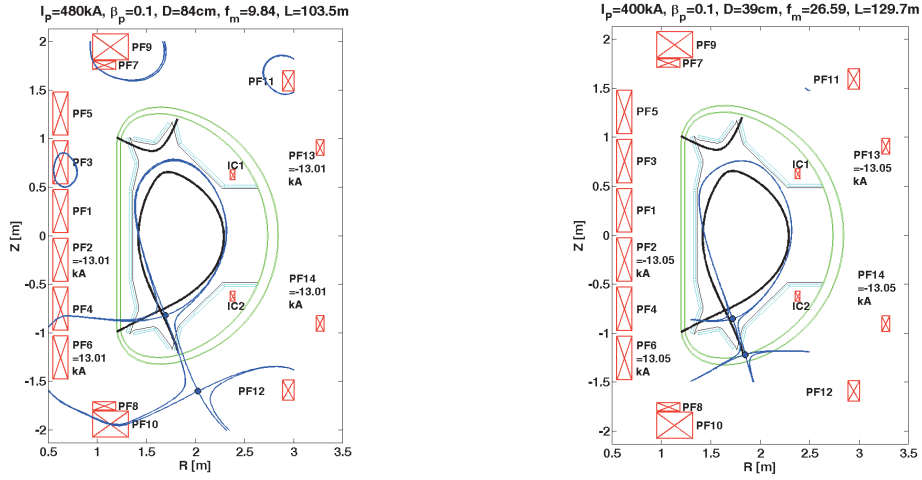
Figure 2. Plasma boundary of optimized QSF (blue solid line) and reference SN equilibria (black solid line), at low β_p, calculated by CREATE-NL code. Also the x-point separation D, the connection length L, the polodal magnetic flux expansion f_m in outer SP region and maximum obtained PF currents are reported for QSF equilibria. For the SN configuration: L=95m, f_m=2.1.

For the QSF configurations with I_P=400 kA the secondary x-point is located on the vessel (on the inner shell at low beta, on the outer shell location for a high beta plasma, not shown here), see figure 2.

However, the secondary x-point point may be brought inside the vessel at the price of a slightly lower plasma current or a higher plasma elongation and/or a futher optmization of the coil corrents. Finally, the "close nulls" QSF equilibria present higher flux expansion on the divertor plates. The high β_p configurations (not shown here) are slightly more demanding in terms of PF currents.

Table I. EAST optimized QSF configurations by CREATE-NL code

	QSF low β_p 400kA "close nulls"	QSF high β_p 400kA "close nulls"	QSF low β_p 480kA "far nulls"	QSF high β_p 480kA "far nulls"	Reference SN 43362
I_P [kA]	400	400	480	480	388
β_p	0.1	0.45	0.1	0.45	0.1
l_i	1.4	1.4	1.4	1.4	1.26
IPF1 [A]	2560	3789	3366	6897	-196
IPF2 [A]	-13050	-13051	-13016	-13027	-203
IPF3 [A]	9407	9513	6635	4319	222
IPF4 [A]	2707	2028	2050	306	-1432
IPF5 [A]	-9398	-12706	-7363	-10229	2158
IPF6 [A]	13050	13051	13016	13027	3956
IPF7_9 [A]	1198	2649	2222	4020	5233
IPF8_10 [A]	-970	-742	218	566	5282
IPF11 [A]	5322	4368	4033	2769	-6055
IPF12 [A]	7145	6779	5557	5255	-5981

IPF13 [A]	-13050	-13051	-13016	-13027	-192
IPF14 [A]	-13050	-13051	-13016	-13027	-622
max(abs(currents)) [A]	13050	13051	13016	13027	6055
x-points separation D (only for QSF cases)	39	45	84	92	-
κ	1.73	1.72	1.71	1.71	1.65
Volume [m^3]	12.21	12.59	12.28	12.76	11.02
Flux Expansion f_m	26.59	22.29	9.84	11.09	2.09
Connection length L (m)	129.74	126.23	103.50	101.47	94.93
Growth rate lower bound [s^{-1}]	186	161	148	120	88
Growth rate upper bound [s^{-1}]	474	339	341	241	195
Growth rate with 3D model [s^{-1}]	454	312	258	198	120
Stability margin with 2D model	0.46	0.52	0.55	0.66	0.86

3 Experimental results

First QSF experiments have been performed on EAST in 2014, after nearly 20-month-long upgrading break. In these experiments the simplest form of plasma current and position (i.e. plasma centroid) control has been used, the so-called RZIP control [18]. The control parameters are regulated by adjusting the current in PF coils. The requested PF coil current is composed of the sum of feed-forward (FF) and feedback (FB) components. The PFC currents discussed in Section 2 have been used as FF component target in RZIP control for QSF experiments (here only "far nulls" case). Magnetic and plasma characteristics of QSF have been studied in discharges with I_P = 0.25MA and B_T = 1.8T, κ ~ 1.9, q_{95} ~ 8, ohmic and with 0.4MW of NBI heating. It should be noted that the plasma current in this first QSF experiments has been purposely kept low for safety reasons. Figure 3 shows the experimental magnetic equilibria at different time, reconstructed with EFIT using standard magnetic constraints for ohmic discharge #47660. In EAST, as previously discussed, the secondary x-point could be moved around and configurations could vary from a SF to X-d divertor configuration.
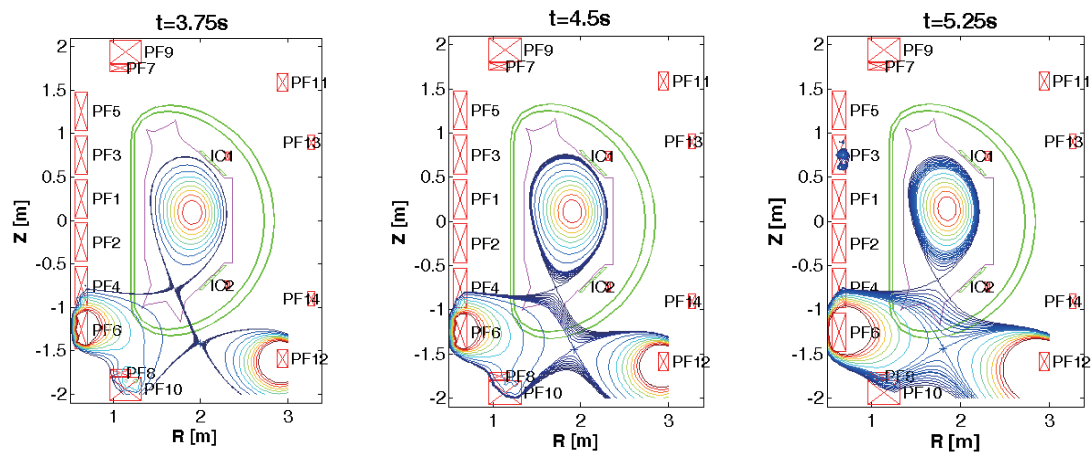
Figure 3. Sequence of EFIT equilibria for ohmic QSF discharge #47660 at 3.75, 4.5 and 5.25s.

A simple comparison between QSF and lower single null (LSN) are carried on in

experiment. Shot 48971 is QSF experiment with NBI injected at 4.00, while shot 47038 is LSN configuration with LHW injection. The plasma quantities are similar after 4.5 sec, shown as figure 4. Diverter probes give the spatial-temporal profile of ion saturation current density jsat for these two shots, shown as figure 5. jsat is stable for LSN discharge. For QSF discharge, jsat at the outer target significantly decreases after 4.5 sec when the QSF configuration is formed. It indicates QSF could reduce the heat flux on the divertor. In figure 6. the EFIT reconstructed equilibria for QSF #48971 (at t=4.5s, with β_p = 0.76 and l_i = 1.28) and SN #47038 (at t=4.5s, with β_p = 0.58 and l_i = 1.56) discharges are shown. Experimental magnetic geometry properties for both configurations are compared in Table II.
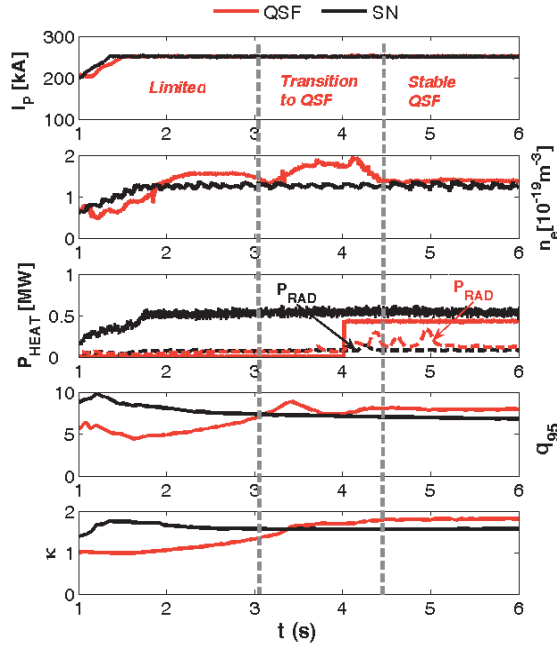
Figure 4. Time evolution of main plasma quantities for LSN (#47038, black line) and QSF (#48971, red line)
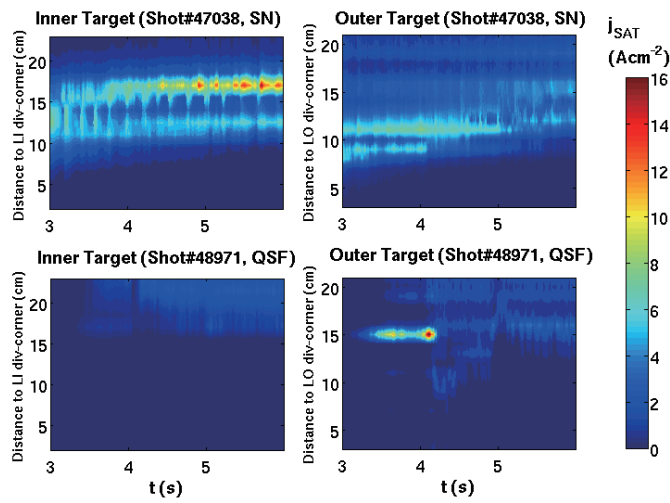
Figure 5. Spatio-temporal profiles of ion saturation current density j_{SAT} for SN (#47038) and QSF discharge (#48971). Once QSF configuration becomes stable, the peak of j_{SAT} is observed to drastically drop indicating a possible heat flux reduction.
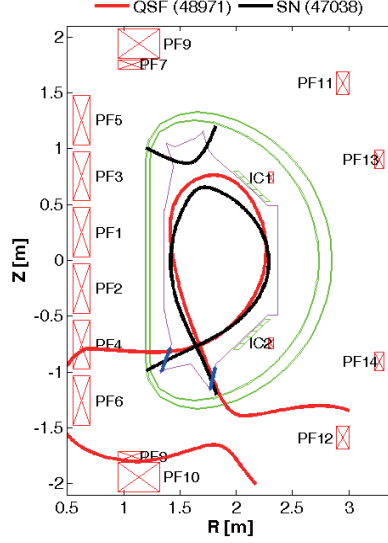
Figure 6. Schematic 2D view of EAST with SN #47039 at t=4.5s (black solid line) and QSF (red solid line) at t=4.5s plasma boundaries. The x-point separation D is = 79cm for the QSF discharge.

Table II: Main magnetic geometry for SN and QSF configurations, assuming SOL width at midplane of 2mm

	QSF, #48971 at t=4.5s	SN, #47038 at t=4.5s
SOL Volume [m^3]	0.389	0.260
Connection Length [m]	189.91	144.38
Magnetic flux expansion at outer SP $f_{m,out}$	8.22	2.01
Magnetic field angle at outer SP α_{out} [deg]	0.33	1.22
Magnetic flux expansion at inner SP $f_{m,in}$	4.71	2.34
Magnetic field angle at inner SP α_{in} [deg]	0.90	1.29

These results confirm the predictions discussed in the previous sections: the presence of a secondary null-point in QSF reduces B_p/B_{tot} in the divertor separatrix region, where B_{tot} is total magnetic field, and this increases the connection length by ~30% and the flux expansion in the outer SP region by a factor ~4. This obtained QSF configuration shows a value PF6 = 8.3kA as the maximum current during the discharge evolution, well below the limit. The experimental connection length is higher than the predictive one, discussed in section 2, of a factor ~1.5 for both QSF and SN, as expected due to the fact that the experimental I_P is ~45% lower than the simulated one.

4 Conclusions

It has been experimentally demonstrated that the possibility of creating and controlling the two-null divertor QSF configuration on EAST. In the present preliminary experiments, the presence of a secondary X-point increases the connection length by ~30% and the flux expansion in the outer SP region by a factor

~4, confirming the predictions of the optimization study set up by CREATE-NL tools in combination with EFIT and FIXFREE codes. It has been observed that in L-mode discharge the peak of ion saturation current density drops once the QSF configuration becomes stable compared to SN case, which could indicate a heat flux reduction. These first experiments also indicate that the plasma current could be increased by a further optimization of the configuration and that it is possible to play around with the reciprocal distance of the two X-points in order to change the topological features of the configuration. In the coming EAST experiments the already upgrade of ISOFLUX control system will allow to control the exact position of secondary X-point. This will permit to the increase the additional heating power and to easily vary some of the features of the topological configuration.

References

[1] A. R. Raffray, et al., *Fusion Eng. Des.,* 39-41, 323-348, 1998.
[2] D. D. Ryutov, et al., *Phys. Plasmas*, 14, 064502, 2007
[3] M. Kotschenreuther, et al., *Phys. Plasmas*, 20, 102507, 2013
[4] W. A. Vijvers, et al., *Nucl. Fusion*, 54, 023009, 2014
[5] D. D. Ryutov, et al., *Phys. Plasma*, 15, 092501, 2008
[6] D. D. Ryutov, et al., *Phys. Scr.*, 89, 88002, 2014
[7] F. Piras, et al., *Plasma Phys. Control. Fusion*, 51, 055009, 2009
[8] V. A. Soukhanovskii, et al., *J. Nucl. Mater.*, 415, S365-8, 2011
[9] S. Allen, et al., *Proc. 24th Int. Conf. on Fusion Energy (San Diego, CA, 8-13 October 2012)*, 2012
[10] D. D. Ryutov, et al., *Plasma Phys. Control. Fusion*, 52, 105001, 2010
[11] Y. X. WAN, et al., *Overview progress and future plan of EAST Project Proc. 21th Int. Conf. on Fusion Energy 2006 (Chengdu, China 2006) (Vienna: IAEA)* CD-ROM file OV/1-1 and www-naweb.iaea.org/napc/physics/fec/ fec2006/html/index.htm

[12] B.J. XIAO, et al., *Fusion Eng. Des.*, **83,** 181, 2008

[13] M. Mattei, et al., CREATE-NL+: a robust control-oriented free boundary dynamic plasma equilibrium solver *28th Symp. on Fusion Technology (San Sebastian, Spain 2014)* P1.036
[14] L. L. Lao, et al., *Nucl. Fusion*, 25, 1611, 1985
[15] F. Alladio, and F. Crisanti, *Nucl. Fusion*, 26, 1143, 1986
[16] Y. Guo, et al., *Plasma Phys. Control. Fusion*, 54, 085022, 2012
[17] R. Albanese, et al., *Plasma Phys. Control. Fusion*, 56, 035008, 2014
[18] B. J. Xiao, et al., *Fusion Eng. Des.*, 87, 1887, 2012

Validation of comprehensive magnetohydrodynamic hybrid simulations for Alfvén eigenmode induced energetic particle transport in DIII-D plasmas

Y. Todo[1,2], M. A. Van Zeeland[3], A. Bierwage[4], W. W. Heidbrink[5], and M. E. Austin[6]

[1]National Institute for Fusion Science, Toki,Gifu 509-5292, Japan

[2]Department of Fusion Science, SOKENDAI (The Graduate University for Advanced Studies), Toki, Gifu 509-5292, Japan

[3]General Atomics, San Diego, CA 92186-5608, USA

[4]Japan Atomic Energy Agency, Rokkasho, Aomori 039-3212, Japan

[5]Department of Physics and Astronomy, University of California, Irvine, CA 92697, USA

[6]Institute for Fusion Studies, University of Texas at Austin, Austin, TX 78712 USA

E-mail: `todo@nifs.ac.jp`

Abstract. A multi-phase simulation, which is a combination of classical simulation and hybrid simulation for energetic particles interacting with a magnetohydrodynamic (MHD) fluid including neutral beam injection, slowing-down, and pitch angle scattering, is applied to DIII-D discharge #142111 where the fast ion spatial profile is significantly flattened due to multiple Alfvén eigenmodes (AEs). The large fast ion pressure profile flattening observed experimentally is successfully reproduced by these first of a kind comprehensive simulations. Temperature fluctuations due to three of the dominant toroidal Alfvén eigenmodes in the simulation results are compared in detail with electron cyclotron emission measurements in the experiment. It is demonstrated that the temperature fluctuation profile and the phase profile are in very good agreement with the measurement, and the amplitude is also in agreement within a factor of two. This level of agreement validates the multi-phase hybrid simulation for the prediction of AE activity and alpha particle transport in burning plasmas.

1. Introduction

Alfvén eigenmodes (AEs) are one of the major concerns of burning plasmas because they can transport energetic alpha particles and reduce the alpha heating efficiency leading to deterioration of the plasma performance [1, 2]. In DIII-D experiments, significant flattening of the fast ion profile was observed during Alfvén eigenmode (AE) activity[3]. In the experiments, a rich spectrum of toroidal Alfvén eigenmodes (TAEs) and reversed shear Alfvén eigenmodes (RSAEs) driven by ∼80keV neutral beam injection is observed during the current ramp-up phase with reversed magnetic shear. Many theoretical studies have been devoted to the DIII-D experiments, and they can be categorized

into three groups, 1) studies of properties of AEs [4, 5, 6, 7, 8], 2) studies of fast ion transport and losses [9, 10, 11], and 3) nonlinear simulations [12, 13, 14]. For example, excellent agreement was found between ideal magnetohydrodymanic (MHD) NOVA predictions and electron cyclotron emission (ECE) measurements of the electron temperature fluctuation amplitude profile due to a TAE mode [4]. Fast ion induced shearing of 2-dimensional AE mode profile was measured by ECE imaging and well described by the gyrofluid-MHD hybrid code TAEFL [5]. It was demonstrated with the ORBIT simulation that multiple low-amplitude AE modes with $\delta B/B \sim O(10^{-4})$ can account for significant modification of fast ion distributions [9, 10]. The scintillator detector measurements of fast ion losses due to AE modes were reproduced with the ORBIT code [11].

Since the fast ion distribution in the DIII-D experiments is significantly affected by AEs, a comprehensive simulation, which deals with both the AEs and the fast ion transport as self-consistently and realistically as possible, yet attainable on a tractable timescale, is needed. We have developed a multi-phase simulation, which is a combination of classical simulation and hybrid simulation for energetic particles interacting with an MHD fluid, in order to investigate a fast ion distribution formation process with beam injection, collisions, losses, and transport due to the AEs [15]. We run alternately the classical simulation and the hybrid simulation in the multi-phase simulation. In the classical phase of the simulation, the fast ion distribution is built up with the beam injection and collisions. In the subsequent hybrid phase, the built-up fast ion distribution destabilizes AEs leading to the relaxation of the distribution. It was demonstrated with the multi-phase simulation that the fast ion spatial profile is significantly flattened due to the interaction with the multiple AEs with amplitude $\delta B/B \sim O(10^{-4})$, which is consistent with Refs. [9, 10] where resonance overlap of multiple AEs [16] was found to be the key mechanism for fast ion transport. The nonlinear MHD effects [17, 18, 19, 20, 21] that prevent the AE amplitude from growing up to large amplitude observed in a reduced simulation [22] are included in the hybrid simulation.

For the prediction of AE activity and energetic particle transport in burning plasmas, validation of simulations on the present experiments are important and indispensable. In this paper, we present the first comprehensive simulation that predicts both the nonlinear saturated amplitude of AEs and fast ion spatial profile consistent with measured values in experiment.

2. Simulation results and comparison with experiment

We have run a multi-phase simulation and a classical simulation for the DIII-D discharge #142111 at t=525ms. We use experimental values for collision frequencies, the beam deposition power 6.25MW (for the full, half, and third energy components). 8 million computational particles are injected at a constant rate over a 150ms time interval, although both the multi-phase and classical simulations are terminated before t=150ms.
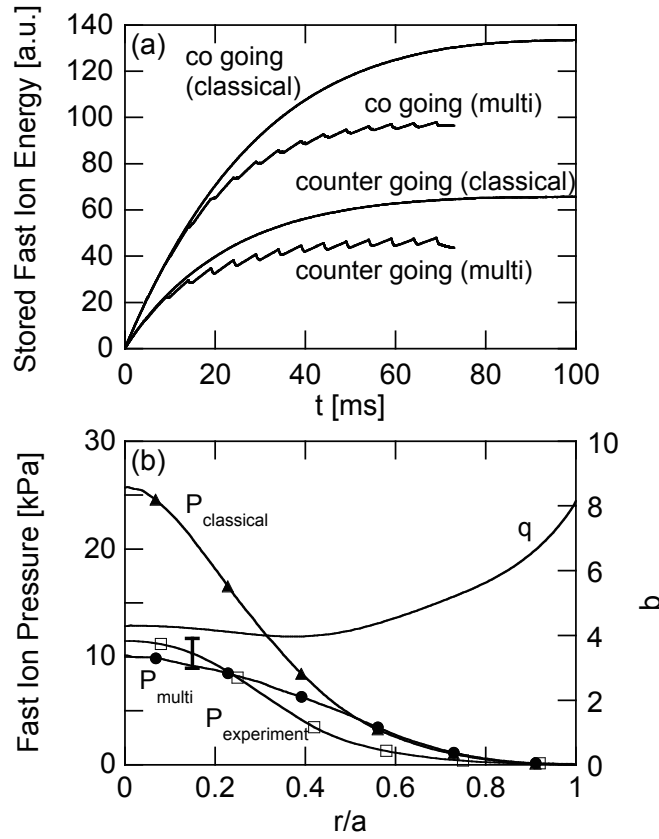
Figure 1. Time evolution of stored fast ion energy in multi-phase and classical simulations; (a), and comparison of fast ion pressure profile among multi-phase simulation (circle), classical simulation (triangle), and experiment (square) with an error bar shown in the figure; (b). The random error in the experimental fast-ion pressure associated with subtraction of the thermal pressure is represented by the error bar; the uncertainty in determination of the total pressure from equilibrium reconstructions contributes a comparable systematic error.

We restrict the toroidal mode number of energetic particle drive in the simulation to $n = 1 - 5$ in order to reduce the numerical noise. This is supported by the experimental observation that the toroidal mode number of the AE modes is $n = 1 - 5$ at $t \sim 525$ms [7]. Figure 1(a) shows the time evolution of stored fast ion energy. The multi-phase simulation was run with alternating classical phase for 4ms and hybrid phase for 1ms. This combination was repeated until stored fast ion energy is saturated at $t = 70$ms, after which, the hybrid simulation was continuously run until $t = 72$ms. Figure 1(b) compares the fast ion pressure profiles among the multi-phase simulation at $t = 72$ms and the classical simulation at $t = 100$ms, and the experiment. The fast ion pressure profile in the experiment is inferred from the Motional Stark Effect (MSE) constrained equilibrium reconstruction and the subtraction of the thermal pressure. We see in Fig. 1(b) that significant flattening of fast ion pressure profile takes place in the multi-phase simulation. The root-mean-square of the deviations from the experimental profile in $0 \leq r/a \leq 1$ is 1.36kPa, which is 12% of the experimental central value and the
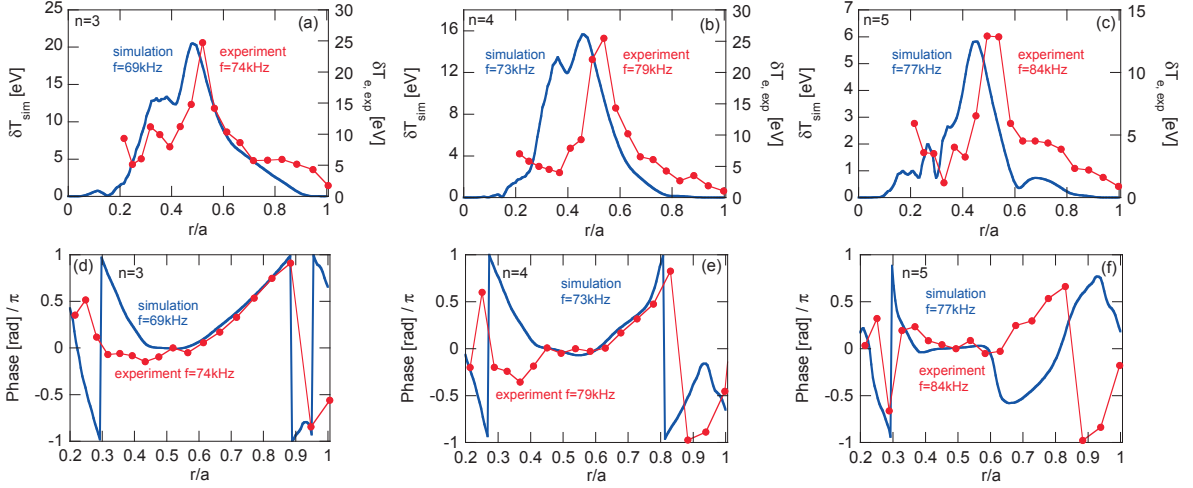
Figure 2. Comparison of electron temperature fluctuation profile for (a) $n = 3$, (b) $n = 4$, (c) $n = 5$, and the phase profile for (d) $n = 3$, (e) $n = 4$, (f) $n = 5$ between simulation and experiment. Left vertical axis is for simulation, while right for experiment in panels (a), (b), and (c).

Table 1. Quantification of electron temperature fluctuation profile comparison for (a) $n = 3$, (b) $n = 4$, (c) $n = 5$. R_A is normalized by the peak fluctuation level for each mode in the experiment. R_ϕ is measured for the 8 channels at $0.4 < r/a < 0.8$.

	A	α/a	R_A	R_ϕ/π
(a)	0.50	0.03	0.13	0.06
(b)	0.62	0.08	0.15	0.06
(c)	1.14	0.08	0.16	0.36

same as the error bar shown in the figure. The multi-phase simulation gives the fast ion pressure profile closer to that in the experiment than our previous simulation [15]. This is attributed to the beam deposition power (6.25MW) with the full, half, and third energy components employed in the present simulation is higher than that in the previous simulation (4.95MW) where only the full energy component was considered.

Next, we compare the simulation results with the ECE measurements in the experiment assuming equal temperature for electron and ion in the simulation. The spatial profiles of the temperature fluctuation and the phase are analysed for the dominant frequency of toroidal mode numbers $n = 3, 4$ and 5. Figure 2 compares the electron temperature fluctuations for the $n = 3 - 5$ mode with those observed with the ECE measurements in the experiment. In Fig. 2 (d)-(f), we see the phase ϕ in the experiment rises from the fluctuation peak locations at $r/a \sim 0.5$ towards the plasma edge, which indicate the shearing profiles. For quantitative comparison, we measure the following root-mean-square of deviations for amplitude (R_A) and phase (R_ϕ) over ECE measurement channels represented by i,

$$R_A = \left\{ \frac{1}{N} \sum_{i=1}^{N} [A \delta T_{e,\text{sim}}(r_i - \alpha) - \delta T_{e,\text{exp}}(r_i)]^2 \right\}^{1/2}, \tag{1}$$

Validation of comprehensive magnetohydrodynamic hybrid simulations

$$R_\phi = \left\{ \frac{1}{N_\phi} \sum_{i=i0}^{i0+N_\phi-1} [\phi_{\text{sim}}(r_i) - \phi_0 - \phi_{\text{exp}}(r_i)]^2 \right\}^{1/2}. \tag{2}$$

For the comparison of amplitude, we find the optimum values of A and α that minimize R_A for the 18 channels shown in Fig. 2. The results are summarized in Table I. For the $n = 3$ mode, the optimum value $A = 0.50$ means that the absolute amplitude of the simulation is in agreement with the experiment by a factor of 2. The deviation of the spatial profile is represented by R_A, which corresponds to 13% of the peak amplitude of the experiment. The optimum value of $\alpha = 0.03a$ indicates very good agreement in radial location. For $n = 4$ and 5, we see also good agreement for amplitude profile (R_A) and absolute amplitude (A). We see $\alpha = 0.08a$ for $n = 4$ and 5 for radial location. Since the magnetic shear is weak around $r/a = 0.5$, another equilibrium reconstruction with safety factor profile modified slightly within the experimental measurement error might lead to better agreement in radial location. For the comparison of phase, we find the optimum value of ϕ_0 that minimizes R_ϕ for the 8 channels at $0.4 < r/a < 0.8$. We do not include channels at $r/a < 0.4$ to neglect effect of the interaction with continuum. Channels at $r/a > 0.8$ are also neglected because the fixed boundary condition employed in the simulation may affect the phase. For the $n = 3$ and 4 modes, we have a remarkable agreement in phase with $R_\phi/\pi = 0.06$. Also for the $n = 5$ mode with $R_\phi = 0.36$, we see good agreement for $0.3 < r/a < 0.6$ in Fig. 2(f).

3. Summary

In this paper, we presented new results of multi-phase simulation of DIII-D discharge #142111, where we use an extended MHD model with the thermal ion diamagnetic drift and the equilibrium toroidal flow, and we take account of the full, half, and third energy components of the injected beam. We have demonstrated that the fast ion spatial profile is significantly flattened due to the interaction with the multiple AEs and the fast ion pressure profile is in agreement with that of the experiment with the root-mean-square of the deviations same as the error bar. We quantitatively compared the predicted temperature fluctuation profiles of $n = 3, 4$, and 5 modes with ECE measurements, and it was found that the fluctuation profiles as well as phase profiles are in very good agreement with the measurements. Additionally, the saturated amplitudes are within a factor of 2 of those measured. We would like to emphasize that this validation exercise highlights the utility of our multi-phase simulation approach as a useful tool for the reliable prediction of AE activity and energetic particle transport in burning plasmas.

References

[1] FASOLI, A., GORMENZANO, C., BERK, H., et al., Nuclear Fusion **47** (2007) S264.

[2] HEIDBRINK, W. W., Phys. Plasmas **15** (2008) 055501.

[3] HEIDBRINK, W. W., GORELENKOV, N. N., LUO, Y., et al., Phys. Rev. Lett. **99** (2007) 245002.

[4] VAN ZEELAND, M. A., HEIDBRINK, W., NAZIKIAN, R., et al., Nuclear Fusion **49** (2009) 065003.

[5] TOBIAS, B. J., CLASSEN, I. G. J., DOMIER, C. W., et al., Phys. Rev. Lett. **106** (2011) 075003.

[6] SPONG, D. A., BASS, E. M., DENG, W., et al., Physics of Plasmas (1994-present) **19** (2012) .

[7] VAN ZEELAND, M. A., GORELENKOV, N., HEIDBRINK, W., et al., Nuclear Fusion **52** (2012) 094023.

[8] WANG, Z., LIN, Z., HOLOD, I., et al., Phys. Rev. Lett. **111** (2013) 145003.

[9] WHITE, R. B., GORELENKOV, N., HEIDBRINK, W. W., and VAN ZEELAND, M. A., Plasma Physics and Controlled Fusion **52** (2010) 045012.

[10] WHITE, R. B., GORELENKOV, N., HEIDBRINK, W. W., and VAN ZEELAND, M. A., Physics of Plasmas (1994-present) **17** (2010) .

[11] VAN ZEELAND, M. A., HEIDBRINK, W. W., FISHER, R. K., et al., Physics of Plasmas (1994-present) **18** (2011) .

[12] VLAD, G., BRIGUGLIO, S., FOGACCIA, G., et al., Nuclear Fusion **49** (2009) 075024.

[13] CHEN, Y., MUNSAT, T., PARKER, S. E., et al., Physics of Plasmas (1994-present) **20** (2013) .

[14] SPONG, D. A., Plasma Fusion Res. **9** (2014) 3403077.

[15] TODO, Y., VAN ZEELAND, M. A., BIERWAGE, A., and HEIDBRINK, W., Nuclear Fusion **54** (2014) 104012.

[16] BERK, H., BREIZMAN, B., and PEKKER, M., Nuclear Fusion **35** (1995) 1713.

[17] SPONG, D. A., CARRERAS, B. A., and HEDRICK, C. L., Physics of Plasmas (1994-present) **1** (1994) 1503.

[18] ZONCA, F., ROMANELLI, F., VLAD, G., and KAR, C., Phys. Rev. Lett. **74** (1995) 698.

[19] TODO, Y., BERK, H., and BREIZMAN, B., Nuclear Fusion **50** (2010) 084016.

[20] TODO, Y., BERK, H., and BREIZMAN, B., Nuclear Fusion **52** (2012) 033003.

[21] TODO, Y., BERK, H., and BREIZMAN, B., Nuclear Fusion **52** (2012) 094018.

[22] TODO, Y., BERK, H. L., and BREIZMAN, B. N., Physics of Plasmas (1994-present) **10** (2003) 2888.

Simulations of energetic particles driven modes on EAST tokamak

by Youbin Pei[1], Nong Xiang[1], Youjun Hu[1], Y. Todo[2], L. Q. Xu[1]

1. Institute of Plasma Physics, Chinese Academy of Sciences, Hefei, Anhui 230031, China
2. National Institute for Fusion Science, Toki, Japan

Abstract

Kinetic-MHD hybrid simulations using MEGA code are carried out to investigate the fast ions driven fishbone instabilities on EAST tokamak. The simulations use anisotropic slowing down distributions to model the distribution of the fast ions from the neutral beam injection. The simulation results indicate when the pressure of the fast ions is larger than a threshold, the fast ions excite the fishbone modes with the mode frequency close to the toroidal procession frequency of the fast ions. The frequency and mode structures in the simulations are in agreement with the EAST experimental observations. By changing the central pitch angle θ_0 of the fast ions in the simulations, we find the threshold for the excitation of the fishbone modes decreases with the increasing of $\sin^2\theta_0$. Furthermore it is found that the frequency and the growth rate of the modes increase with the increasing of $\sin^2\theta_0$. In the nonlinear stage, the pressure profile of the fast ions is flattened and the location of the steepest pressure gradient moves out radially, with the mode location also moving out.

1 Introduction

Fishbone instability was first observed in the experiments with near perpendicular neutral beam injection (NBI) in the Poloidal Divertor eXperiments (PDX)[3]. The fishbone modes are internal kink modes destabilized by energetic particles[4, 7]. Fishbone modes can cause loss of NBI-produced energetic particles, thus reducing the efficiency of plasma heating and possibly damaging the first wall. The fishbone instabilities have been observed in EAST discharge #48605.

In this work, kinetic-MHD hybrid simulations using MEGA code are carried out to investigate the fishbone instabilities on EAST. The MEGA code has been extensively used to study Alfven eigenmodes (AEs) and energetic particle modes (EPMs)[5, 6]. In the simulation, anisotropic slowing down distributions are used to model the distribution of the fast ions from the neutral beam injection.

The simulation results indicate that when the pressure of fast ions are small, the fast ions have stabilizing effects on internal kink modes.[4] For larger beta value, the fast ions have destabilizing effects on the internal kink modes. When the pressure of the fast ions is larger than a threshold, the fast ions excite the fishbone modes with the mode frequency close to the toroidal procession frequency of the fast ions. The frequency and mode structures in the simulations are in agreement with the EAST experimental observations. By changing the central pitch angle θ_0 of the fast ions in the simulations, we find the threshold for the excitation of the fishbone modes decreases with the increasing of $\sin^2\theta_0$. Furthermore it is found that the frequency and the growth rate of the modes increase with the increasing of $\sin^2\theta_0$. In the nonlinear stage, the pressure profile of the fast ions is flattened and the location of the steepest pressure gradient moves out radially, with the mode location also moving out.

2 Simulation model

MEGA is a numerical code that calculates the interaction of thermal plasmas and energetic particles (EPs)[6]. In MEGA, the thermal plasmas are described by the full MHD equations while the EPs are described by the gyro-kinetic or drift-kinetic equation. MEGA code uses the cylindrical coordinates to discretize the MHD equations and follow the orbits of the energetic particles. Magnetic flux coordinates (ψ, θ, ϕ) are used when analyzing the MEGA simulation results, where ψ is a flux surface label, ϕ is the usual toroidal angle, θ is chosen to make magnetic field lines straight on (θ, ϕ) plane.

The simulation region on the poloidal is a rectangle with $R_{\min} < R < R_{\max}$ and $Z_{\min} < Z < Z_{\max}$, where $R_{\min}$, $R_{\max}$, $Z_{\min}$, and $Z_{\max}$ are the extreme points on the flux surface that encloses 99% poloidal magnetic flux. The equilibrium used in the simulation is constructed by EFIT code with the data from EAST discharge #48605@4.6s. The flux surfaces shape and the profile of the safety factor q are shown in Fig. 1. The electron density profile and pressure profile of bulk plasma are shown in Fig. 2.
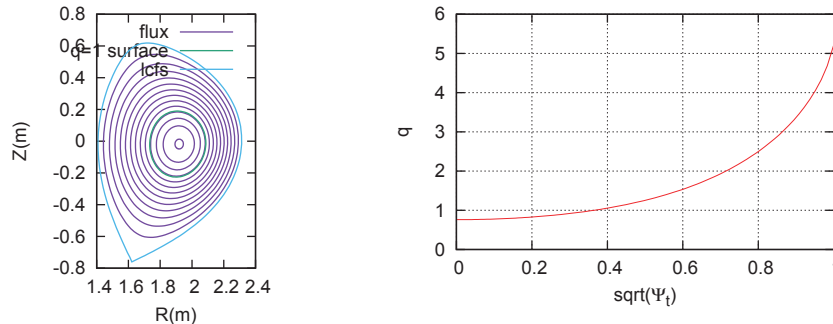
Figure 1. The flux surface(left) and safety factor profile(right) of EAST discharge #48605 at 4.6s used in the simulation. The magnetic field strength at the magnetic axis ($R = 1.91m$) $B_0 = 1.73T$, the plasma current $I_p = 400kA$, the value of the safety factor at the magnetic axis $q_0 = 0.75$.
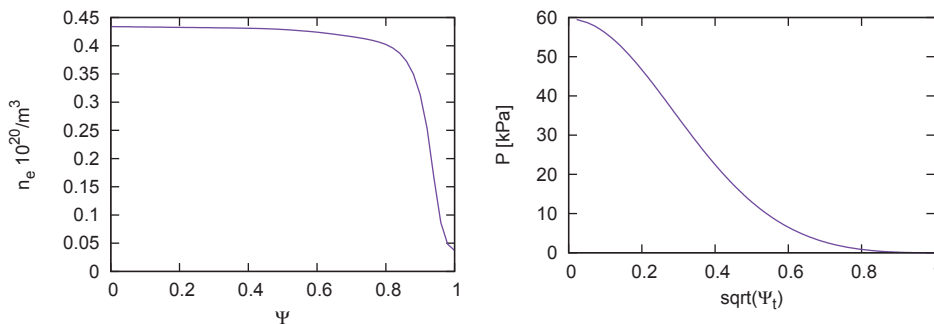
Figure 2. Electron density profile(left) and bulk plasma pressure profile(right) of EAST discharge #48605 at 4.686s. The pressure and the beta of the bulk plasma at magnetic axis are $P_{b0} = 6 \times 10^4$Pa and $\beta_{b0} = 5.0\%$, respectively.

The number of particle markers used in the simulation is 5.2×10^5. The viscosity and diffusive for MHD density and pressure are set to be $\nu_0 = \nu_{n0} = \chi_0 = 10^{-5}V_{A0}R_0 = 75.4m^2/s$ and the resistivity η_0 is set to zero in the simulation, where $V_{A0} = 4.05 \times 10^6 m/s$ is the Alfven velocity at magnetic axis. The numbers of grid points used in the simulation are $(128 \times 16 \times 128)$ for cylindrical coordinates (R, ϕ, Z).

To model the fast ions generated from NBI, we use an anisotropic slowing down distribution given by

$$f = C \exp\left(-\frac{\psi}{\psi_{\text{scale}}}\right)\frac{1}{v^3 + v_{\text{crit}}^3}\frac{1}{2}\text{erfc}\left(\frac{v - v_{\text{birth}}}{\Delta_v}\right)\exp\left(-\frac{(\Lambda - \Lambda_0)^2}{\Delta\Lambda^2}\right), \tag{1}$$

where ψ is the normalized poloidal flux, $\psi_{\text{scale}} = 0.3$, v_{crit} is the critical velocity, v_{birth} is the fast ions injection velocity (in this work, $v_{\text{birth}} = 0.59V_{A0}$, corresponding to the particle energy $E = 60$keV), $\Delta v = 0.1V_{A0}$, $\Lambda = \mu B_0/E$, μ and E are the magnetic moment and energy of fast ions, $\Lambda_0 = 0.88$, $\Delta\Lambda = 0.1$. The constant C is set in MEGA code to obtain desired value of parallel pressure of EPs at the magnetic axis.

3 Simulation results

3.1 Mode structure

In analyzing the data, the positive direction of ϕ is chosen in the direction of toroidal magnetic field (for the equilibrium we used, the direction of the plasma current is in the opposite direction of the toroidal magnetic field). The positive direction of θ is chosen in the counter-clock direction when viewed in the positive direction of ϕ.

In the simulation, we keep only the $n = -1, 0, 1$ toroidal harmonics. The dominant modes in the simulations is $m/n = 1/(-1)$.

Figure 3a gives the radial mode structure of fishbone modes, which shows that the mode has a two-step structure within the $q = 1$ surface, which is consistent with the previous study[8]. For comparison, we also carry out a simulation with very low beta value of fast ions ($\beta_{h0} = 1 \times 10^{-8}$). In this case, we find the typical mode structure of the internal kink mode, as is shown in Fig. 3b.
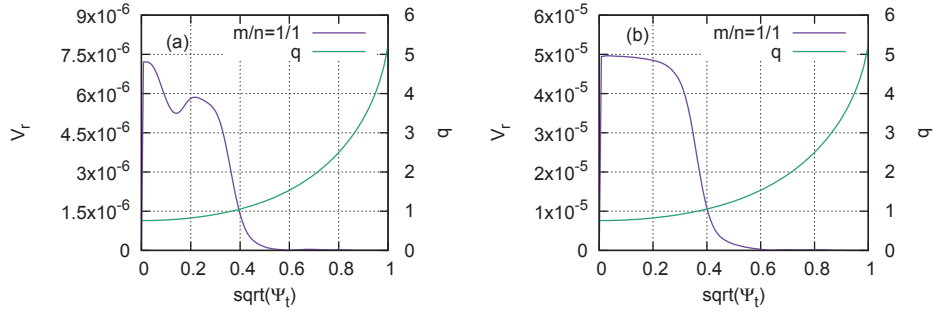
Figure 3. Comparison of the radial velocity of the fishbone mode (a) with the internal kink mode (b). In the former case $\beta_{h0} = 1.1\%$ while in the latter $\beta_{h0} = 1 \times 10^{-8}$.

Figure 4a plots the two-dimensional structure of the fishbone mode on the poloidal plane, which shows that the mode has a twist structure. The mode twist is due to the radial phase variation induced by the kinetic effects of the fast ions[7]. For comparison, we also carry out a simulation with very low beta value of fast ions ($\beta_{h0} = 1 \times 10^{-8}$). The two-dimensional structure for this case is given in Fig. 4b, which does not show obvious mode twist on the poloidal plane.
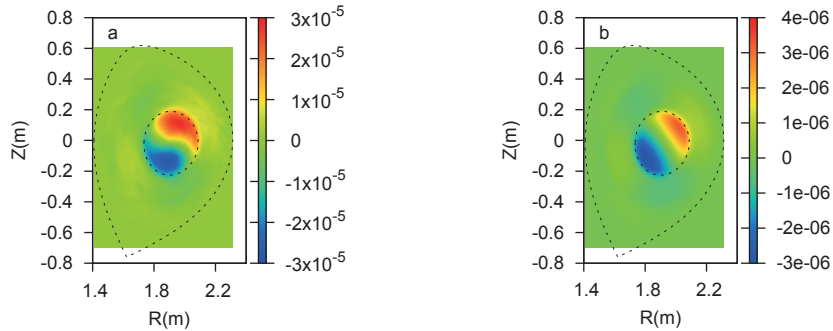
Figure 4. Comparison of toroidal electric field E_ϕ of the fishbone (a) and internal kink mode (b) on the poloidal plane. In the former case $\beta_{h0} = 1.1\%$ while in the latter $\beta_{h0} = 1 \times 10^{-8}$.

Figure 5 gives the contour plots of the toroidal electric field E_ϕ at different time from linear to nonlinear phase. During the time evolution, the radial location of the mode moves out radially, which is due to that the location of the steepest pressure gradient of fast ions moves out radially, i.e, the fast ions drive moves out radially.
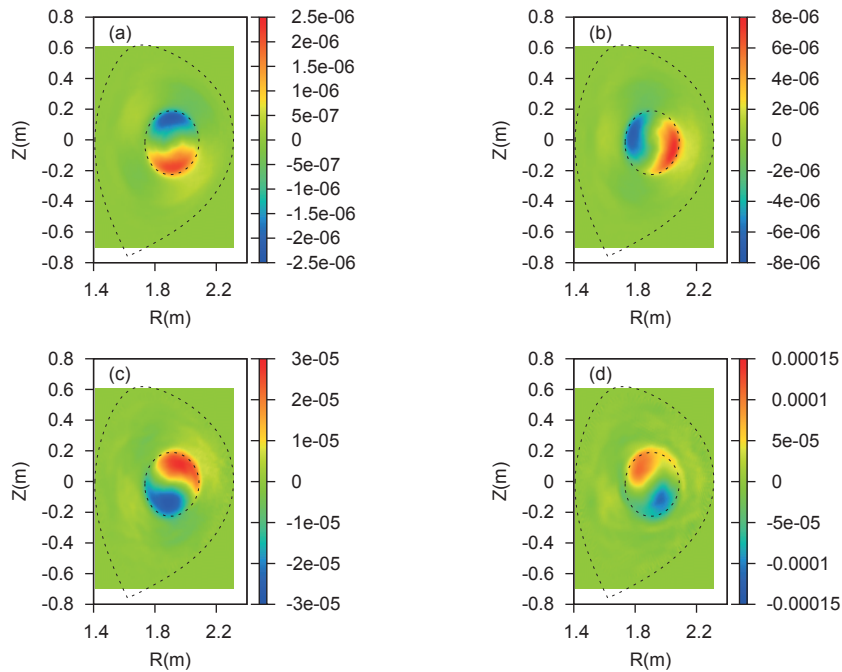
Figure 5. Contour of the toroidal electric field E_ϕ at $0.72ms$ (a), $0.78ms$ (b), $0.84ms$ (c), and $0.9ms$ (d). The duration of the time evolution given in the figure is less than one mode period ($f \approx 3\text{kHz}$). The figure shows that the mode rotate in the counter clockwise direction, which is identical to the direction of the ion diamagnetic drift.

3.2 Mode frequency

The fishbone mode frequency in the simulations is about $3\sim4\text{kHz}$ in the linear phase, as is shown in Fig.6b, which is consistent with the Soft X-ray observation on EAST discharge $\#48605$ at $4.686s$. The precessional frequency of the energetic particles with energy 35keV and normalized magnetic momentum $\Lambda_0 = 0.88$ at $q = 1$ surface is about 4kHz, which is close to the mode frequency in our simulation and the experiment observation[1].
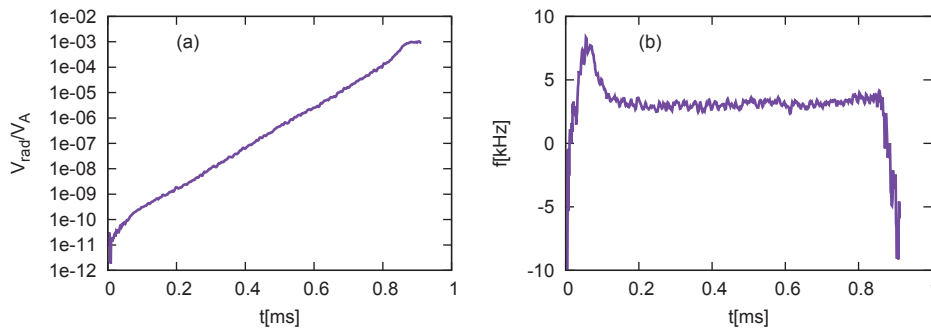
Figure 6. (a) Amplitude of $m/n = 1/-1$ harmonic of the radial velocity. (b) Frequency evolution of the $m/n = 1/-1$ harmonic of the radial velocity.

3.3 Dependence of mode frequency and growth rate on beta value and pitch angle of fast ions

Figure 7 shows that when the fast ions beta β_{h0} is small, the growth rate decreases with the increasing of β_{h0}, i.e., the fast ion can improve the stability of the MHD. For larger β_{h0} the growth rate increases with the increasing of β_{h0}. The real frequency of the mode increases with the increasing of β_{h0}.
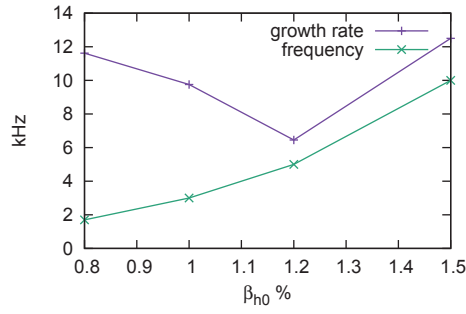
Figure 7. The fishbone mode frequency and growth rate vs energetic particle beta value.

Figure 8 shows that the growth rate and real frequency increase with the increasing of the central pitch angle parameter Λ_0.
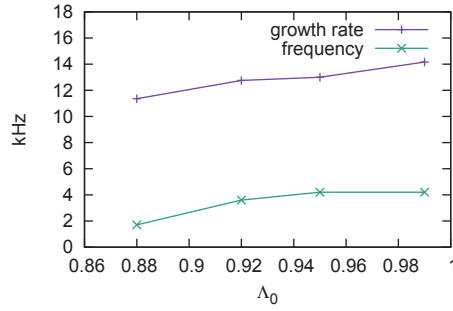
Figure 8. The dependence of the fishbone mode frequency and growth rate on the central pitch angle parameter Λ_0.

3.4 Threshold of fast ions beta for exciting fishbones

The characteristic of fishbone modes is that they have a nonzero frequency close to the characteristic frequency of the fast ions. We use this characteristic to distinguish between the fishbone modes and internal kink modes. The threshold of fast ions beta for exciting fishbones is defined as the beta value for which the modes have an obvious nonzero frequency. Figure 9 gives the dependence of the threshold on the central pitch angle of the fast ions, which show that the threshold decreases with the increasing of the central pitch angle parameter Λ_0.
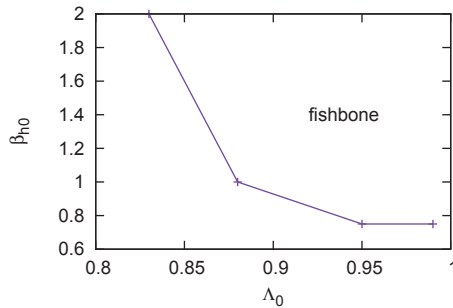
Figure 9. Threshold of the fast ions beta for exciting fishbone modes decreases with the increasing of the pitch angle parameter Λ_0.

3.5 Flattening of the pressure profile of fast ions

Figure 10 gives the time evolution of the parallel and perpendicular pressure profiles of the fast ions ($m/n = 0/0$). The results indicate that in the linear phase the pressure profile keeps constant, i.e., the fishbone mode in the early stage has little effects on the transport of the fast ions. In the later phase, the pressure profile is flattened, mainly in the core region. Furthermore the shoulder of the flattening region moves out radially, which is consistent with the previous theory[2].
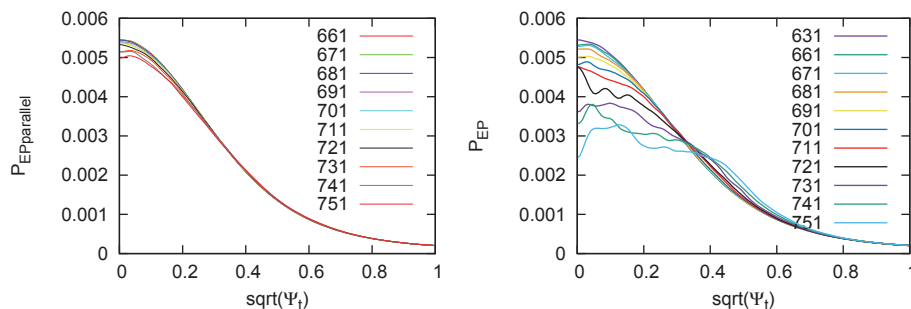
Figure 10. Time evolution of the parallel pressure (left) and perpendicular pressure (right) of the fast ions ($m/n = 0/0$). The labels on the figure indicate different time in unit of the Alfven time R_0/V_{A0}.

4 Summary

Kinetic-MHD hybrid simulations using MEGA code are carried out to investigate the fast ions driven fishbone instabilities on EAST tokamak. The simulation results indicate when the pressure of the fast ions is larger than a threshold, the fast ions excite the fishbone modes with the mode frequency close to the toroidal procession frequency of the fast ions. The frequency and mode structures in the simulations are in agreement with the EAST experimental observations. By changing the central pitch angle θ_0 of the fast ions in the simulations, we find the threshold for the excitation of the fishbone modes decreases with the increasing of $\sin^2\theta_0$. Furthermore it is found that the frequency and the growth rate of the modes increase with the increasing of $\sin^2\theta_0$. In the nonlinear stage, the pressure profile of the fast ions is flattened and the location of the steepest pressure gradient moves out radially, with the mode location also moving out.

Bibliography

[1] Liu Chen, R. B. White and M. N. Rosenbluth. Excitation of internal kink modes by trapped energetic beam ions. *Phys. Rev. Lett.*, 52:1122–1125, Mar 1984.

[2] G. Y. Fu, W. Park, H. R. Strauss, J. Breslau, J. Chen, S. Jardin and L. E. Sugiyama. Global hybrid simulations of energetic particle effects on the n=1 mode in tokamaks: internal kink and fishbone instability. *Physics of Plasmas (1994-present)*, 13(5):0, 2006.

[3] K. McGuire, R. Goldston, M. Bell, M. Bitter, K. Bol, K. Brau, D. Buchenauer, T. Crowley, S. Davis, F. Dylla, H. Eubank, H. Fishman, R. Fonck, B. Grek, R. Grimm, R. Hawryluk, H. Hsuan, R. Hulse, R. Izzo, R. Kaita, S. Kaye, H. Kugel, D. Johnson, J. Manickam, D. Manos, D. Mansfield, E. Mazzucato, R. McCann, D. McCune, D. Monticello, R. Motley, D. Mueller, K. Oasa, M. Okabayashi, K. Owens, W. Park, M. Reusch, N. Sauthoff, G. Schmidt, S. Sesnic, J. Strachan, C. Surko, R. Slusher, H. Takahashi, F. Tenney, P. Thomas, H. Towner, J. Valley and R. White. Study of high-beta magnetohydrodynamic modes and fast-ion losses in pdx. *Phys. Rev. Lett.*, 50:891–895, Mar 1983.

[4] F Porcelli. Fast particle stabilisation. *Plasma Physics and Controlled Fusion*, 33(13):1601, 1991.

[5] Y. Todo. Properties of energetic-particle continuum modes destabilized by energetic ions with beam-like velocity distributions. *Physics of Plasmas*, 13(8):0, 2006.

[6] Y. Todo and T. Sato. Linear and nonlinear particle-magnetohydrodynamic simulations of the toroidal alfvāľn eigenmode. *Physics of Plasmas*, 5(5):1321–1327, 1998.

[7] Feng Wang, G. Y. Fu, J. A. Breslau and J. Y. Liu. Linear stability and nonlinear dynamics of the fishbone mode in spherical tokamaks. *Physics of Plasmas (1994-present)*, 20(10):0, 2013.

[8] A. ÃŬdblom, B. N. Breizman, S. E. Sharapov, T. C. Hender and V. P. Pastukhov. Nonlinear magnetohydrodynamical effects in precessional fishbone oscillations. *Physics of Plasmas (1994-present)*, 9(1):155–166, 2002.

Development of the fusion-neutron diagnostics for the

HL-2A tokamak

Y. Liu [1], W.L. Zhong [1], Z. B. Shi [1], Y.H.Xu [1], M. Isobe[2], Y. P. Zhang[1], W. Deng[1], X.Q. Ji[1]
1) *Southwestern Institute of Physics, P.O. Box 432, Chengdu 610041, China*
2) National Institute for Fusion Science (NIFS), Toki, Gifu, Japan

[1] *Southwestern Institute of Physics, P.O. Box 432, Chengdu 610041, China*
[2] *National Institute for Fusion Science, 322-6 Oroshi-cho, Toki 509-5259, Japan*

a) Corresponding author: YLiu, E-mial: yiliu@swip.ac.cn, Tel: +86-28-82850312

Abstract: A new scintillator-based lost fast-ion probe (SLIP) has been developed and operated in the HL-2A tokamak to measure the lossess of neutral beam ions. The design of the probe is based on the concept of the α-particle detectors on Tokamak Fusion Test Reactor (TFTR) using scintillator plates. The probe is capable of traveling across an equatorial plane port and sweeping the aperture angle rotationally with respect to the axis of the probe shaft by two step motors, in order to optimize the radial position and the collimator angle. The energy and the pitch angle of the lost fast ions can be simultaneously measured if the two-dimensional image of scintillation light intensity due to the impact of the lost fast ions is detected. Measurements of the fast-ion losses using the probe have been performed during HL-2A neutral beam injection (NBI) discharges. The clear experimental evidence of enhanced losses of beam ions during disruptions has been obtained by means of the SLIP system. A detailed description of the probe system and the first experimental results are reported.

I. INTRODUCTION

Since the good confinement property of fast ions is an essential requirement for realization of an ignited fusion reactor, the behavior of fast ions in magnetically confined fusion plasmas is one of the important research subjects in fusion studies.[1-3] Self-maintained fusion plasmas are expected to be heated mainly by D-T born α-particles. If α-particles are substantially lost from the plasma due to various reasons, the self-maintained state is inevitably terminated.[4] In addition, fast ions generated by plasma auxiliary heating systems such as neutral beam injection (NBI) and ion

cyclotron resonance heating (ICRH) will support the plasma operation by additional heating and current drive. For efficient plasma heating, good confinement of the fast ions is required. In contrast, significant losses of fast ions will reduce the heating efficiency and NBI current drive.[5] Furthermore, the localized heat load on the plasma facing components (PFCs) due to the impact of the significant escaping fast ions may damage drastically the PFCs or pollute the plasma.[6] For all above reasons, understanding the physics of fast ions is crucial to achieve the safe operation for a fusion reactor.

The confinement, diffusion, convection and losses of the neutral beam-injected fast ions are a fundamental topic of plasma theory and experiment. Measurements for the losses of the fast ions related to their confinement and plasma performance are thus crucial. Therefore, it is desirable to measure the losses of fast ions from the plasma, and furthermore to understand the mechanisms in an eventual hope to mitigate or eliminate those losses. Measurements of the fast-ion losses can be performed by a number of diagnostics, such as Faraday cups, surface barrier diode detectors, track detector, exposure samples, infrared imaging, calorimeter probes, and scintillator probes.Among them, scintillator probes have the advantage to detect the energy and pitch angle of the lost ions as a function of time during a discharge. For a given magnetic field configuration, the orbits of the lost ions can be reconstructed, which may improve our understanding on associated physical processes. For this purpose a scintillator-based lost-fast-ion probe (SLIP) has been developed in the HL-2A tokamak.

The purpose of this paper is to give a detailed description of the newly developed SLIP system in the HL-2A tokamak together with the first experimental results. Sec. II is dedicated to describe the setup of the HL-2A SLIP system. The first experimental results obtained from the SLIP system are presented in Sec. III. Finally, a summary is given in Sec. IV.

II. DIAGNOSTIC SETUP

The design of the HL-2A SLIP originates from the concept of the α-particle probe which has been developed by Zweben and used in TFTR for the first time.The probe system mainly consists of a detector head, a long optical shaft system and a detection system. A schematic overview of the SLIP setup in the HL-2A tokamak is shown in Fig. 1. The detector head shown in Fig. 1 is mounted at the end of an adjustable long shaft. The entire head is capable of inserting into and withdrawing from the HL-2A vacuum chamber, and sweeping the aperture angle rotationally with respect to the axis of the long shaft in the vacuum chamber.

The detector head is composed of a scintillator screen, a 3D ion collimator, a light-tight stainless steel box and a graphite armored box to prevent the heat load, as shown in Fig.2. The design starts with the shaping of the detector head. The proper geometry of detector head is key to measure the lost ions without blocking particles trajectories with a certain range of energy and pitch angle in the HL-2A device. The size of the scintillator screen must be close to the fast ion gyroradius. The energy of the deuterium neutral beam ions is typically about 40 keV in HL-2A, the gyroradius of the beam ions at the plasma boundary in the outer midplane is about 25 mm. Thus, the size of the scintillator screen is 25×25 mm^2.
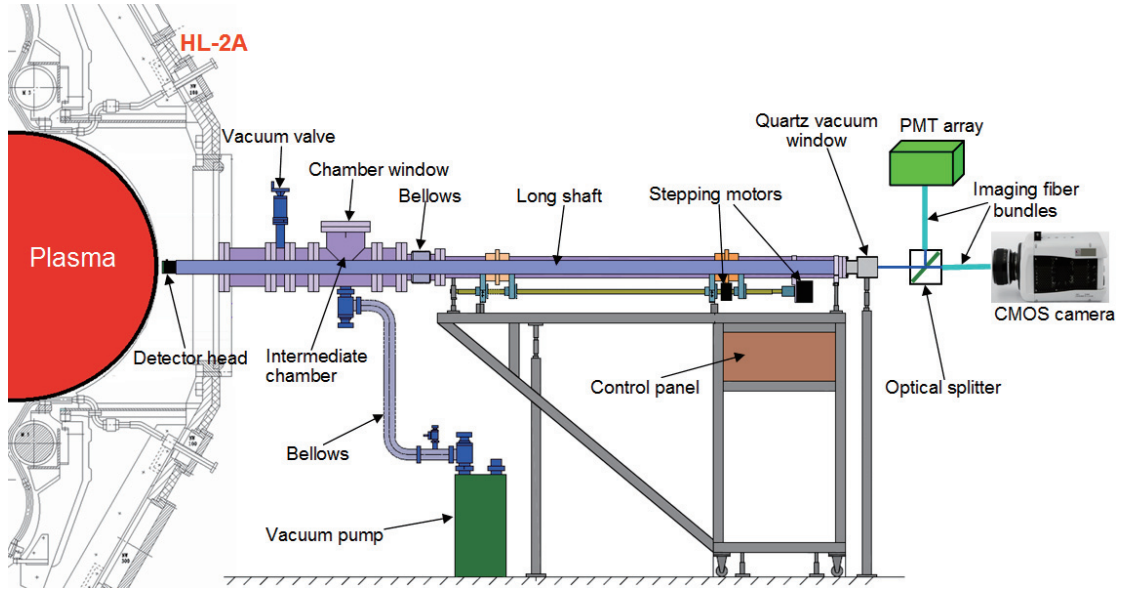
FIG. 1. A schematic overview of the fast-ion-loss diagnostic located at one cross section of the HL-2A tokamak. The probe system mainly consists of a detector head, a long optical shaft and a detection system.

Once the size of the scintillator screen is determined, the design of the 3D collimator is the next important step for the design of the detector head. The three dimension is considered in order that the lost fast ions can enter the slit opening without being stopped by the edge of the collimator. The Lorentz orbit code was used for the development of the 3D collimator. Fast ions have been traced backward in time starting randomly distributed along the front aperture within the appropriate gyrophase cone and with energies and pitch angles in the required range. The resolution with the current collimator geometry has been calculated and the results are shown in Fig.2. Figure 2(a) shows the calculated gyroradius distributions for 10, 15, and 20 mm at a pitch angle of 60°. The full widths at half maximum (FWHM) for this set of gyroradii are 2.0, 3.2 and 4.4 mm, respectively. It can be seen that the energy resolution becomes worst with increasing energy, which imply that the collimating effect of the 3D collimator becomes weaker for the ions with higher energy. Figure 2(b) shows the calculated pitch angle distributions for 80, 70 and 60 at a gyroradius of 20 mm. The results indicate that the pitch angle resolution is better than the energy resolution and the probe has the same FWHM ≈ 5° for all pitch angles. Furthermore, other collimators with different sizes can be made to get the desired pitch angle and energy resolution.
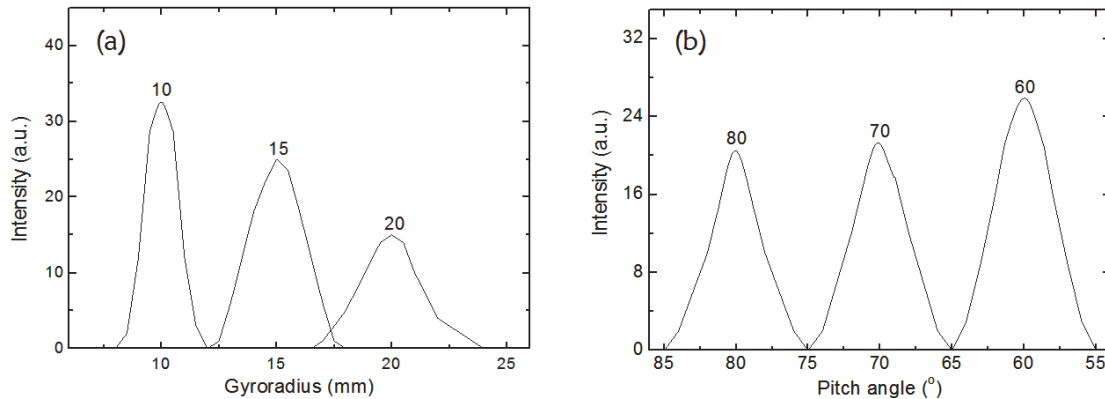
FIG. 2. (a) The calculated gyroradius centroid distributions for 10, 15 and 20 mm at a pitch angle of 60°; (b) The calculated pitch angle distributions for 80°, 70° and 60° at a gyroradius of 20 mm.

The ultimate time resolution of the SLIP system is decided by the decay time of the scintillation process of the scintillator material. The property of the material can significantly affect the SLIP performance. The scintillator material used for SLIP in fusion devices need to meet following requirements: (i) high sensitivity to fast ions such as NBI beam ions and α-particles; (ii) low sensitivity to the non-required particles such as electrons and neutrons, as well as the x-ray; (iii) fast response, particularly short decay time, because the MHD induced fast-ion losses are very fast processes; (iv) high saturation levels. Considering the manufacturability and the above-mentioned requirements of the scintillator screen, ZnS:Ag (P11 in EIA designation) has been selected as the scintillator material for the HL-2A SLIP. The emission peak and the decay time of ZnS:Ag scintillator are 450 nm and 70 ns, respectively ZnS:Ag scintillator phosphor was deposited onto a 25×25 mm^2 Aluminum substrate. The average thickness of the scintillator layer is 9 ± 1 μm. The scintillator plate is installed on the bottom of the light-tight stainless steel box with a graphite armor.

Since the plasma discharge conditions, such as plasma configurations and the NBI power, are variable, the detector head need to be positioned in order to optimize the radial position and the incident angle of the collimator. To achieve the required capabilities of radial movement and angle rotation in the vacuum vessel, the magnetic coupling drive system was adopted outside of the vacuum system. The long shaft is driven by two stepping motors shown in Fig. 1 via magnetic coupling, one motor is for the radial movement and the other is for the angle rotation. Figure 5 shows the photograph of the SLIP inside the HL-2A vacuum chamber. These motors can be precisely operated via a control panel. The step-size and step-angle are 1 mm and 1°, respectively. The long shaft is guided in the vacuum vessel by the rail to avoid the excessive vibration and deflection. The shaft system can provide a long traveling distance (2.7 m), which is very important in the actual operation because the available space in the vicinity of tokamak is limited.

The detector head was removed from the HL-2A vacuum chamber after the 2013 experimental campaign. The detector head was intact and the total SLIP system was well protected. The only minor problem is that the graphite armored box was slightly eroded by the impact of plasma flows.

III. INITIAL EXPERIMENTAL RESULTS

The HL-2A device is a medium-size tokamak with closed divertor chambers. The main parameters of HL-2A are major radius $R=1.65$ m, minor radius $a=0.4$ m, and plasma current (I_p) up to 0.5 MA. Sixteen toroidal field coils can create and maintain a toroidal magnetic field (B_t) up to 2.8 T. The magnetic field is directed to be clockwise (top view), whereas the plasma current is counter-clockwise in the standard operation. The divertor of HL-2A is designed with two closed chamber. At present, it is operated with a lower single null configuration. An NBI is installed on the HL-2A tokamak with four-positive-ion sources. Each ion source consists of a multi-pole plasma generator and an accel-decel extraction system. The beam injection energy is typically 40 keV and the total beam power can reach 2.0 MW. The neutral beam is tangentially co-injected with a radius of 1.4 m. The fast-ion-loss probe was put into application in the 2013 experiment campaign. However, the PMT array is still under development. Therefore, only experimental results obtained by the camera are presented in this paper.

The SLIP system has been operated during the first phase of deuterium discharges heated by NBI pulses. The scintillation signals were collected by a low-speed camera with compact volume,

which is for the convenience of the test and validation of the SLIP system. During this phase, the response of the detector was checked at different radial positions, collimator angles, and plasma conditions.

The light emitted from the scintillator plate during NBI has been observed in various cases. Figure 3 shows the prompt loss pattern produced by NBI on the scintillator screen. The plasma current was about 180 kA and the toroidal magnetic field was 1.3 T. The neutral deuterium beam with a power of 0.7 MW was injected into the plasma during the plasma current flat-top phase and lasted for about 400 ms. The camera has a frame rate of 3 fps, and hence, two pictures with available fast-ion losses can be obtained in one discharge, as shown in Fig. 3(a)-(b). The localized scintillation spot appears on the screen immediately after NBI turn-on. In the subsequent frame, the light spot becomes much brighter during the NBI phase, which is due to longer exposure time of the camera. After NBI turn-off, the scintillation light disappears as expected. Therefore, it is reasonably concluded that the measured scintillation light spot is caused by the impact of escaping beam ions. In addition, the orbits of the lost beam ions are calculated backward in time from the energy and pitch-angle, detected by the SLIP, as shown in Fig. 3(d). The wide bean shaped red curve is the envelope of the orbit of a beam ion. The impact area of the lost beam ions on the scintillator screen have been computed under the same plasma condition (B_t=1.3 T, I_p=180 kA), as depicted in Fig. 3(e). It can be found that the measurements are well consistent with the calculations.
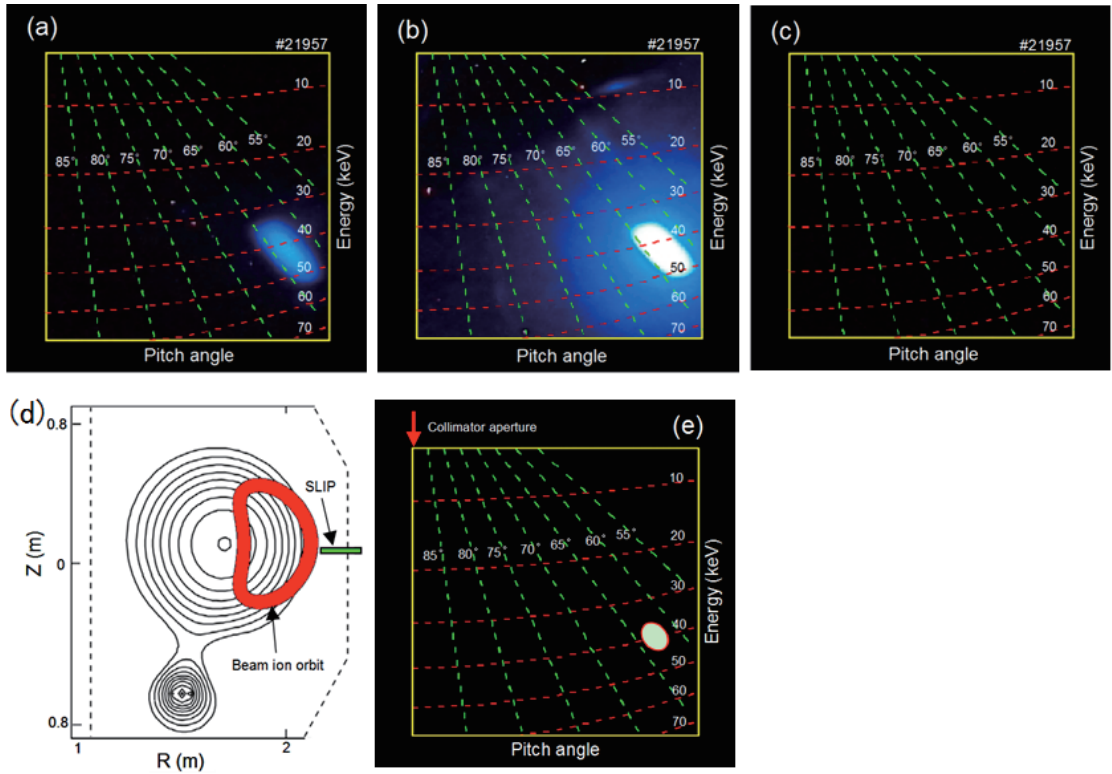
FIG. 3. (Color online) (a)-(c) Images emitted from the scintillator screen obtained by a low-speed camera with compact volume in a discharge with NBI. (a) right after NBI turn-on, (b) during NBI, (c) after NBI turn-off. (d) Calculated the envelope of the banana orbit of the beam ions in HL-2A. (e) Calculated impact area of the lost beam ions on the scintillator screen in HL-2A (B_t=1.3 T, I_p=180 kA).

IV. SUMMARY

A new fast-ion-loss probe system has been developed and operated in the HL-2A tokamak to measure the lost NBI ions. The design of the probe originates from the concept of the α-particle detectors on TFTR. The detector head is capable of inserting into and withdrawing from the HL-2A vacuum chamber, and sweeping the aperture angle rotationally by the magnetic coupling drive system. The 2D images of the scintillation light have been detected by means of an 8×8 PMT array and a fast CMOS camera.

The SLIP system has been implemented in the 2013 experiment campaign in the HL-2A tokamak. Measurements of the fast-ion losses using the SLIP system have been performed during NBI discharges. The 2D images of the scintillation light produced by the fast ions were detected and their energy-pitch angle information was obtained as well. The clear experimental evidence of enhanced loss of beam ions during a disruption has been achieved for the first time by the SLIP system. The transport of beam ions from the plasma core to the edge would be changed dramatically during disruptions due to the strong magnetic perturbations and the change of the plasma current profile. Moreover, the boundary of the scintillator screen is also identified during the disruption, which provides a direct verification for the calibration result. In the next campaign in HL-2A, a PMT array (8×8) with a bandwidth of 1 MHz will be applied and the effect of fast-ion driven MHD instabilities on fast-ion transport and/or loss will be investigated.

References

[1] W. W. Heidbrink, J. Kim, and R. J. Groebner, Nucl. Fusion **28**, 1897 (1988).

[2] W. W. Heidbrink, Phys. Fluids B **2**, 4 (1990).

[3] M. Isobe, K. Tobita, T. Nishitani, Y. Kusama, and M. Sasao, Nucl. Fusion **37**, 437 (1997).

[4] M. García-Muñoz, H.-U. Fahrbach, S. Günter, V. Igochine, M. J. Mantsinen, M. Maraschek, P. Martin, P. Piovesan, K. Sassenberg, and H. Zohm, Phys. Rev. Lett. **100**, 055005 (2008).

[5] C. B. Forest, J. R. Ferron, T. Gianakon, R. W. Harvey, W. W. Heidbrink, A. W. Hyatt, R. J. La Haye, M. Murakami, P. A. Politzer, and H. E. St. John, Phys. Rev. Lett. **79**, **427** (1997).

[6] D. S. Darrow, R. Majeski, N. J. Fisch, R. F. Heeter, H. W. Herrmann, M. C. Herrmann, M. C. Zarnstorff, and S. J. Zweben, Nucl. Fusion **36**, 509 (1996).

Study of the ICRF minority heating performance by neutron signal on EAST

Guoqiang Zhong，Liqun Hu，Ruijie Zhou, Shiyao Lin, Xinjun Zhang, Haiqing Liu

Institute of plasma physics, Chinese academy of sciences, Hefei 230031, China

E-mail: gqzhong@ipp.ac.cn

Ion cyclotron range of frequencies (ICRF) heating has been considered as an effective means for upraise ion temperature in magnetic confinement fusion plasma. We were employment the time resolved neutron fluence and energy spectrum diagnostics to study the ICRF heating on EAST tokamak. The phenomenon of neutron yield rapid rise has been observed during the power of wave effect launch into deuterium plasma. However, that obvious increase was difficult occur in Lower Hybrid Wave (LHW) heating alone. The ICRF dominant heat minority hydrogen ions were supported by below 5% of n_H/n_D and depression high-energy tail in neutron spectrum that measurement by liquid scintillator. In this case, adopt neutron fluence and plasma density signals to inverse calculation the central ion temperature by classical fusion equation. Calculation results indicate that central ion temperature growth approximate 30% in L-mode plasma, and excess 50% in H-mode plasma during ICRF heating. Compare with other diagnostics, such as x-ray crystal spectrometer (XCS), those results were accordant. Furthermore, the relationship of neutron yield associate with plasma current and ICRF inject power has been statistic in this article.

Keywords: Neutron diagnostic, ICRF heating, Fusion

Introduction

Campaign of 2012 year, the plasma auxiliary heating experiment of EAST depends on LHW and ICRF; theirs source power were 2MW and 6MW respectively. The LHW of 2.45 GHz frequency drive high temperature deuterium plasma with quasi-steady-state operation excess four hundreds successfully and the central electron temperature nearly 2 keV. However, it toward the efficiency of fuel ion temperature promoting was weakly [1]. The ions heating mostly rely with high power ICRF. On EAST tokamak, four sets of 1.5MW transmitter were operated in this campaign that the ICRF total source power up to 6.0MW and the frequency can be changed from 25MHz to 70MHz. Unfortunately, mismatch plasma shape, antenna design and the gap between antenna and plasma that could induce wave coupling become badly and reflect worse. Generally, half of source power could be launch to plasma at the present of ICRF heating experiment. The transmissible fast wave interaction with deuterium plasma has a complex process, thus some shots of ICRF heating effect was indistinct. The DD yield provide a most intuitionistic way to estimation the ion heating effect by ICRF, case of the DD reaction rate with ion temperature in relationship of $<\sigma v> \approx \kappa T_i^{\gamma}$, Ti near 1keV then $\gamma \approx 5$ [2].

Furthermore, other electron and ion temperature measurement diagnostics can be provide lots of effective heating evidence such as poloidal XCS. That could be combination with neutron diagnostics result to research ICRF heating.

Diagnostic setup

The neutron diagnostic arrangement on EAST tokamak comprised time resolved emission monitor and DD neutron spectrometer. Neutron emission monitor systems have five channels of independent measurement that basis on four ^{3}He counters and one ^{235}U fission chamber. Those include two kinds of ^{3}He proportion counters which sensitivity were 133 cps/nv and 15 cps/nv respectively [3]. High sensitivity counters suitable for lower neutron produce plasma experiment of Ohmic and LHW. The fission chamber was coated with 1.4 gram uranium-235 which efficiency of thermal neutron reached 1.16 cps/nv. All neutron flux monitor counters were operated on counts mode. Besides these counters, liquid scintillator has been used to measurement neutron spectrum and profile emission rate. There is employment 2 inch diameter and thickness scintillator manufacture by Saint-Gobain which type is BC-501A [4]. One scintillator implemented to DD neutron spectrum measurement and another six were disposed in a superior radiation shield assembly with fan array collimation for neutron rate profile monitor. These detect system were used pulse shape discrimination technology to distinguish neutron and gamma signals that basis on traditional electronic circuit. The profile emission rate monitor system was first engineering test in the campaign of 2012 year. In addition, a BGO detector has been position with BC-501A sintillator in the same shield to monitor γ-ray strength and energy that signals will be used to judgment n/γ discrimination reliability in neutron spectrometer. Arrangement of neutron diagnostics around on EAST tokamak is shown in figure 1, which sub graph display the neutron counter configuration.
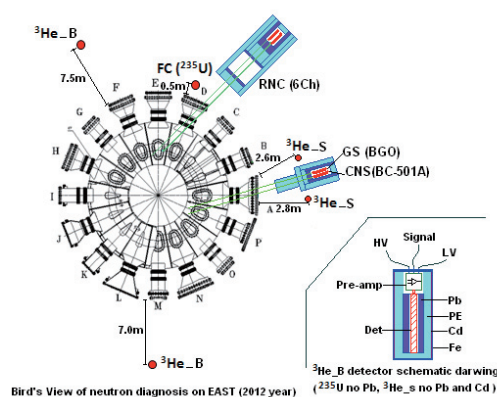
Figure 1. Diagram of the neutron diagnostics arranged on EAST tokamak (2012 year). ^{3}He_B, ^{3}He_S and FC denote high, lower sensitive ^{3}He counter and ^{235}U fission chamber respectively. CNS and GS express BC-501A neutron and BGO gamma spectrometer. RNC was 6 channel of neutron profile monitor array testing on this campaign.

A part of detectors has been calibration with neutron source that was generated by ion accelerator in the Nuclear Physics and Technology lab of Peking University. The detection efficiency of two sensitive ^{3}He and ^{235}U was absolute calibration by 2.5MeV neutrons that results were 7%, 6.9% and 0.14% respectively. Liquid sintillator for spectrum measurement has been make six points monoenergetic

neutron calibration at the accelerator, and done three points gamma energy calibration by isotopic radioactive source at ours lab. The energy of neutron calibration is 1.61MeV, 2.02MeV, 2.45MeV, 3.00MeV, 3.60MeV and 4.27MeV, and the gamma calibration adopt [22]Na and ^{137}Cs source which energy are 0.511MeV, 1.275MeV and 0.661MeV respectively [5]. Presently tokamak device transport coefficient with DD neutron has not obtained by [252]Cf source in situ calibration. Thus we were adopted a three dimension model, construct by 1/8 of EAST device, to do simulation with Monte Carlo code (MCNP) [6]. The coefficient computing results indicate in figure 2. Consider the factors of detector efficiency, distance, capture area and time resolution for [235]U fission chamber signal, the absolute conversion coefficient is $4.1 \times 10^9 ns^{-1}$/count.
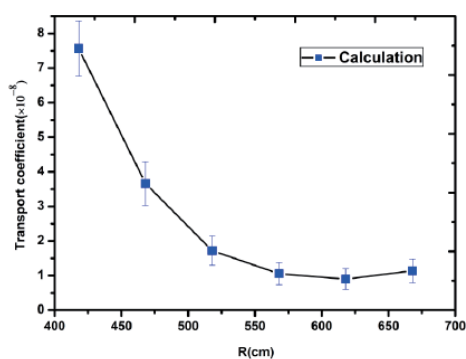
Figure 2. Neutron transport coefficient of EAST tokamak simulation by monte carlo method.

Experiment and result

Generally the ICRF heating experiment do not expect the background parameter of plasma too lower, because of lower current, density and temperature are disadvantage for RF wave energy absorbed. Therefore, during ICRF experiment on EAST, plasma current (I_p) exceed 400kA and the central electron density (n_e) high than $1.5 \times 10^{19} m^{-3}$ ordinarily. Beside this there is often cooperation heating with LHCD in order to increase background temperature. A typical shot (#40441) of ICRF heating deuterium plasma experiment data waveforms are shown in Figure 3. In this shot, the phase of plasma current plateau, I_p was constant with 500kA and n_e raise from $2.1 \times 10^{19} m^{-3}$ to $2.5 \times 10^{19} m^{-3}$ during ICRF launch. Premeditation injecting power of LHCD was 1.5MW and their reflect rate less than 10% in plateau. The 30MHz frequency of ICRF feed in to plasma through four antennas that total power was 1.4MW. Unfortunately, one set of transmitter reflecting protection lead to injected power lost about 30% after 5.5 second. The plasma store energy was calculated by diamagnetic signals, central electron and ion temperature were calculated by soft X-ray energy spectrum and X-ray Crystal Spectrometer (XCS) that measure Ar atom excitation spectra. The neutron yields deriver from the product of [235]U fission chamber pulse counts and DD neutron transport coefficient. In addition, the time resolved of core ion temperature was estimated by neutron yield display on last row with XCS calculation result in this figure. As for inverse calculation ion temperature by neutron signal will detail in follow text. The preferable ion heating performance was appeared on ICRF inject that bring the neutron yield sharp increase five times

and the central ion and electron temperature upraise more than 0.3keV. Besides, the plasma store energy gains 35kJ and energy confinement time $\tau_e \approx 54ms$. In this shot, high field side at 1.358m and the removable limiter of low field side at 2.335m on toroidal major radius, the antenna position of LHCD and ICRF were 2.345m and 2.335m respectively. So the ICRF antenna positing closely plasma edge was an important factor for valid heating than conjecture support by next experiment practical.
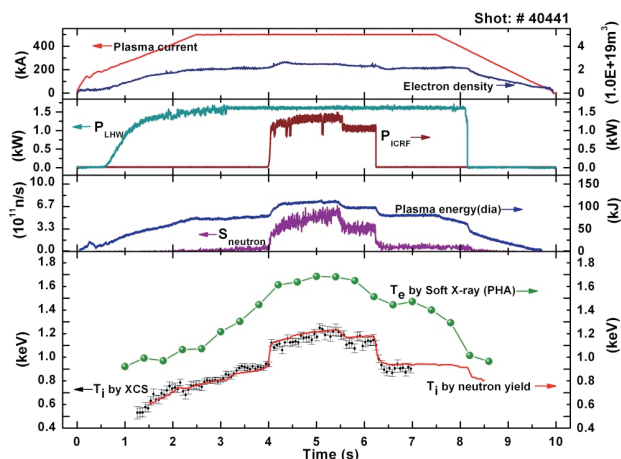
Figure 3. EAST experiment data waveform of ICRF coupled heating on L-mode plasma (#40441). Te and Ti indicate the central temperature of electron ant ion respectively.

The spectrums of recoil proton measurement by BC-501A scintillator are shown in figure 4. Another shot (#40349) of result adopt to compare with the coupling heating (#40441), that have similarly plasma current and density except without ICRF injection. The compare result indicated that high energy tail of recoil protons are nothing serious during ICRF heating, in despite of there is high event counts of relatively. Furthermore, than reflect the contribution of second harmonic ICRF heating was weakly on this type of experiment condition [7][8]. Impurity spectrum of hydrogen give a judgment of n_H/n_D was lower than 5% in #40441 shot, and synthetically analysis with the resonance layer position of hydrogen that minority heating was occupied domination. So the injection RF energy mostly absorbed by hydrogen ions which through kinetics collision to transport energy heating bulk plasma. There are plentiful event counts in low energy region of the recoil proton spectrums that due to heaviest scattered neutrons. We had attempt two methods to unfold the recoil proton spectrum with the detector response function [9]. Unfold obtain the DD fusion neutron spectra is show on figure 5. The 2.45MeV fusion neutron peak demonstrates a similar Maxwell distribution that the full width at half maximum (FWHM) is approximately 90keV. Estimate the average temperature of central deuterium ion about 1keV by formula of $FWHM(keV)=82.6(Ti)^{1/2}$, that result agrees with XCS despite recently it none time resolution and lower precision. In order to obtain better time resolve temperature information by neutron signals, there could be inverse calculation with DD neutron yield [10]. However this method was always adopting in Ohmic plasma. During ICRF minority heating process in EAST recently experiment, the neutron yield measured by ^{235}U detector is generally

unnecessary to consider the contribution of photo reaction and fast ion that improved by DD neutron spectra. So, we were attempt calculation central ion temperature $T_i(0)$ with neutron yield that results compare with SXC are show on figure 6. There are fifteen shots of ICRF minority heating employment and each shot take two or three points. Classical neutron yield formulas basis on the thermal reactive given by Bosch and Hale were express with computer code to inverse calculation $T_i(0)$ [11]. The temperature and density distribution on plasma were adopted a invariable type of value for EAST. Central deuterium ion density had been take HCN laser interferometer measurement the central electron density multiplies 0.8 to substitute. There inverse calculation results agree with SCX in despite input many parameters with assuming that because of DD neutron yield strong correlation with fuel ion temperature.
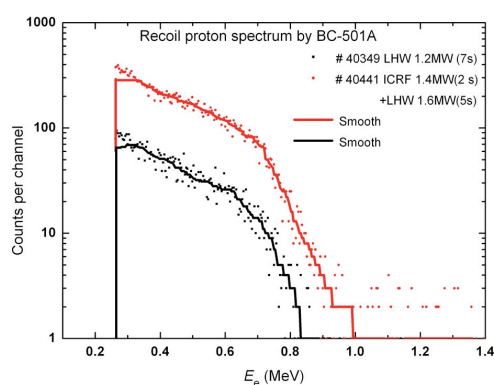
Figure 4. Liquid scintillator measured the DD neutron recoil proton spectrum in RF heating plasma.
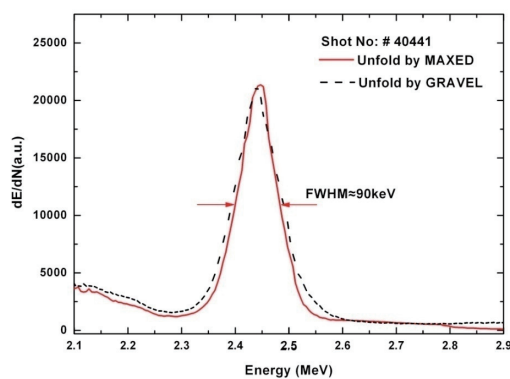
Figure 5. BC-501A scintillator obtain the DD neutron energy spectrum unfold by two method.
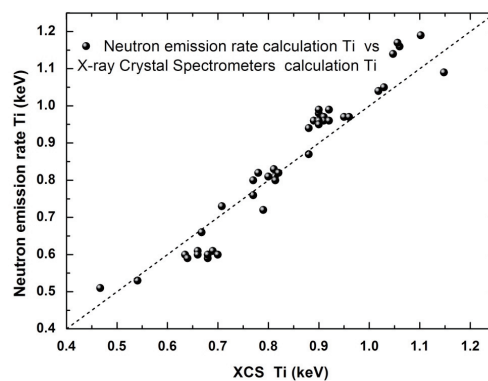
At present experiment of EAST, there was high confinement of H-mode plasma regular obtainment on the condition of total heating power excess a threshold. LHW and ICRF were achieved H-mode plasma respectively, but this always to thought decrease plasma parameter and power threshold. Thus the RF coupled heating were easily access H-mode on ordinary discharge status [12]. Figure 7 displays a shot of ELMs H-mode plasma on coupled heating. The injection power of LHW has maintained on 1.5MW except small reflecting fluctuate. However, the ICRF injected power was slow raise from 1.0MW to 1.4MW. When total power excess threshold, there was access H-mode status that could be indicate by Dα and MHD signals. The neutron yield, plasma story energy and central ion temperature have twice obvious upraise at the time of ICRF launch and H-mode transform. In the phase of ICRF injected, ion temperature increase from 0.7keV to 1.15keV (up 64％) that heating effect had a decided advantage over the L-mode operation. The electron temperature fall in the H-mode transition that cause was plasma density and electron collision rate raise along with particle confinement improve.
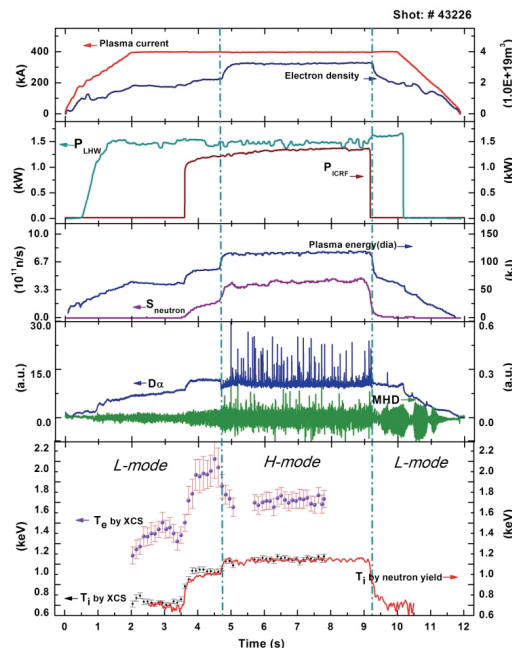
Figure 7. H-mode plasma operation on ICRF and LHW coupled heating condition.

Data statistics

The neutron yield direct relative with fuel ion temperature but plasma current and ICRF absorb power are important indirect influence factors. More than 80 shots statistic of neutron yield verses ICRF heating power in L-mode plasma are show on figure 8. They were having same toroidal field (Bt), RF frequency, antenna distance and single heating operation condition. The plasma density was little different in these shots but it influence neutron yield are not serious (less than 35%) for this verses. There are obvious trend on statistical result indications of the neutron yield increase with current and RF power raise. In order to get distinct scaling relation with current and RF power, we were fitting these experiment results and obtained a

scale law of $Y(n)=5.3\times10^{11} \cdot P_{ICRF}^{1.59} \cdot I_P^{2.51}(s^{-1})$. This scale law calculated neutron yield compare with diagnostic measurement results are show in figure 9. That can be satisfaction the recently experiment status on EAST.
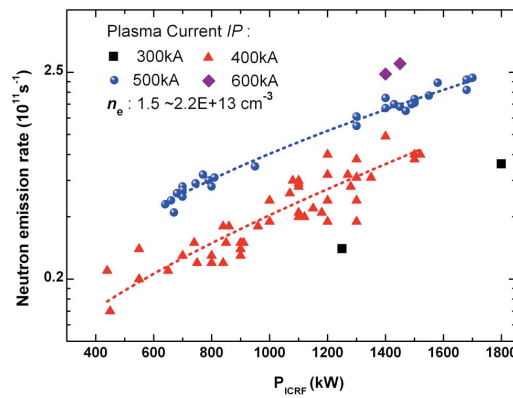
Figure 8. DD neutron yield verses inject ICRF power on different current plateau of L-mode plasma.
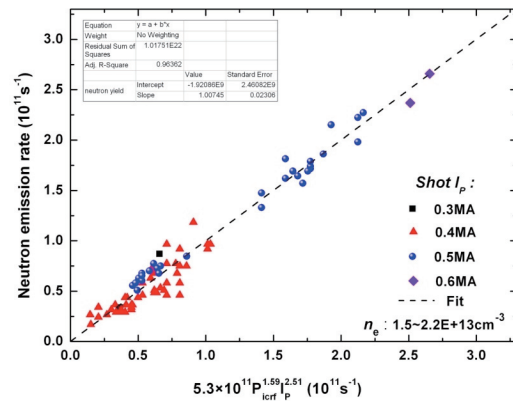
Figure 9. Statistic gets the DD neutron yield scale law with injection ICRF power and plasma current in thermal plasma.

Conclusion

The ICRF minority heating plasma effective was directly observation by neutron diagnostic, and achievement attempt calculation central ion temperature by DD neutron yield. Those results are agreed with other ion temperature diagnostic such as XCS. The H-mode plasma heating by ICRF has better effective than ordinary L-mode, and the ion temperature increase more than 50% by neutron yield calculation. Statistic 85 shots of ICRF heating, we are obtain a neutron yield scaling law with plasma current and RF injected power that suitable for recently experiment on EAST.

Acknowledgements

References

[1] Xiaoling Li, Baonian Wan, Guoqiang Zhong, et al. 2010, Plasma phys. Control. Fusion 52:105006

[2] B.Wolle. 1999, Physics Reort **312**: 1

[3] Guoqiang Zhong, Liqun Hu, Xiaoling Li, et al. 2011, Plasma Sci. Tech. **13**: 162

[4] Xing Zhang, Xi Yuan, Xufei Xie, et al. 2013, Rev. Sci. Instrum **84**:033506

[5] Xi Yuan, Xing Zhang, Xufei Xie, et al. J. Instrum. In Revision

[6] Xiaoling Li, Baonian Wan, Guoqiang Zhong, et al. 2013, Plasma Sci. Tech. **15**: 411

[7] C.Hellesen, M.Gatu Johnson, E.Anderson Sundén, et al. 2010, Nucl. Fusion 50:022001

[8] Xiaoling Li, Baonian Wan, Guoqiang Zhong, et al. 2011, CHIN.PHYS.LETT **28**:105202

[9] Xufei Xie, Xi Yuan, Xing Zhang, et al. 2012, Plasma Sci. Tech. **14**: 553

[10] O.N.Jarvis. 1994, Plasma phys. Control. Fusion, 36:209

[11] H. S. Bosch, G.M. Hale. 1992, Nucl. Fusion **32**: 611

[12] P.U.Lamalle, M.j.Mantsinen, J.-M.Noterdaeme, et al. 2006, Nucl. Fusion **46**:391

Effects of surface conditions on the plasma-driven permeation behavior through a ferritic steel alloy observed in VEHICLE-1 and QUEST*

H. Zhou[a], Y. Hirooka[b], H. Zushi[c], A. Kuzmin[c], N. Ashikawa[b], T. Muroga[b], A. Sagara[b] and the QUEST group[c]

[a] Institute of Plasma Physics, Chinese Academy of Sciences, P.O. Box 1126, Hefei, China
[b] National Institute for Fusion Science,322-6 Oroshi-cho, Toki 509-5292, Japan
[c] RIAM, Kyushu University, Kasuga, Fukuoka, 816-8580, Japan

Abstract

Effects of surface conditions on the plasma-driven permeation of hydrogen through a ferritic steel alloy F82H have been studied in a laboratory-scale plasma device: VEHICLE-1 and the medium-sized spherical tokamak: QUEST. Both of the surface contamination and area effects have been examined and discussed. Thick surface impurity film has been found to act as a second layer for diffusion and affect the permeation behavior in laboratory-scale and tokamak experiments. Hydrogen diffusion coefficient in the impurity layer has been estimated using the multi-layer diffusion model. A decrease in steady state permeation flux has been measured when increasing the plasma-facing surface area, which is in good agreement with theoretical prediction.

1. Introduction

In magnetic fusion power reactors, hydrogenic particles will escape from the confinement region and then migrate through the first wall by plasma-driven permeation (PDP) [1-10]. Hydrogen isotopes (deuterium and tritium) flowing into the blanket by PDP will hinder the recovery of tritium and will probably necessitate isotope separation [2]. Tritium permeation through the first wall may raise reactor safety issues as well.

Under reactor operational conditions, the plasma-facing side of the first wall would not be as smooth and clean as polished samples used in laboratories. The wall will be either covered by contaminations, or eroded by plasma bombardment, depending upon the local plasma conditions [11]. Although it is known that plasma-driven permeation is affected by the surface conditions of membranes [3-10], more detailed study on this issue is still needed, especially concerning the surface area effects.

In our previous studies, some surface condition effects on PDP through a ferritic steel alloy F82H have been observed [8]. The present work is a further investigation of these effects, in which two aspects are separately examined: one is the influence of surface contamination; and the other is the surface area effects. The experimental results presented in this paper cover the PDP data from the laboratory-scale steady state plasma device: VEHICLE-1 [12] as well as from the medium-sized spherical tokamak QUEST [13].

2. Models on surface modification effects on PDP

Some possible mechanisms related to the surface condition effects on plasma-driven permeation are briefly reviewed in this section, including both contamination and area effects. The validity of these theoretical models is shown in section 4.

2.1. Surface contamination effects on PDP

In the steady state plasma-driven permeation model, three regimes are considered [1]: the diffusion-diffusion (DD) limited regime, the recombination-diffusion (RD) limited regime and the recombination-recombination (RR) limited regime. Our previous experiments indicated that hydrogen PDP through F82H under current experimental conditions takes place in the RD limited regime, i.e., recombination-limited at the front surface and diffusion-limited inside the bulk, as shown in Fig. 1(a). Steady state permeation can be expressed by the following equations:
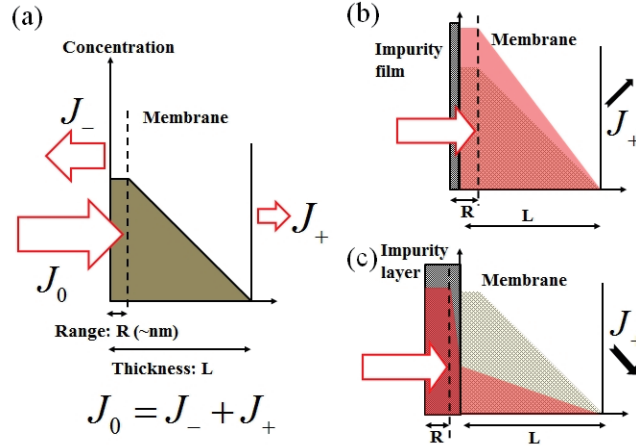
Fig.1. Plasma-driven permeation takes place in the RD-limited regime for (a) a clean surface, (b) a contaminated surface with thin film and (c) a contaminated surface with thick impurity layer.

$$J_0 = J_- + J_+ \qquad\qquad (1),$$

$$J_- = K_r \cdot C_s^2 \qquad\qquad (2) \text{ and}$$

$$J_+ = D \cdot C_s / L \approx D / L \cdot \sqrt{J_0 / K_r} \qquad\qquad (3),$$

where J_0 is the net implantation flux, J_- is the recombination release (i.e. reemission) flux from the upstream surface, J_+ is the permeation flux, C_s is the front surface hydrogen concentration and K_r is the recombination coefficient of the plasma-facing surface.

Some literature data suggest that the hydrogen PDP flux J_+ is enhanced when the plasma-facing surface is contaminated [4-7]. That is because recombination release J_- is suppressed by the presence of impurity film, as shown in Fig. 1(b). However, it is also true that if the contaminated layer is thick enough to act as a second layer for diffusion, hydrogen PDP will be suppressed (Fig. 1(c)) [8,9]. The latter case is of interest from the fusion engineering point of view as it suggests a potential measure to reduce hydrogen PDP through the first wall in a reactor.

2.2. Surface area effects on PDP

The surface of plasma-facing walls can be modified significantly by plasma bombardment. Surface morphologies such as bubbles [14], coral-like structures and cones [11] may be formed, depending on the plasma conditions, material property, temperature and impurity seeding, etc. Those micron scale structures will change the plasma exposure area and result in higher hydrogen release at the front surface. Considering particle conservation and surface reflection, the net implantation fluxes can be expressed as $J_1 = J_p \cdot (1-R_1)$ for a polished surface and $J_2 = J_p \cdot A_1/A_2 \cdot (1-R_2)$ for a modified surface, where J_p is the ion incident flux, A_1 and A_2 are the surface areas for a polished surface and a modified surface, respectively, and R_1 and R_2 are the corresponding particle reflection coefficients. Using Eq. (3), the steady state permeation flux ratio J_{2+}/J_{1+} of the two cases can be given:

$$J_{2+} / J_{1+} \propto \sqrt{A_1 / A_2} \qquad\qquad (4),$$

i.e., the permeation flux is reversely proportional to the square root of surface area.

3. Experimental

Details of the PDP experimental setup in VEHICLE-1 and QUEST have already been presented elsewhere [2,3,13]. In this section, some of the important features of the PDP experiments will be described.

For the PDP experiments in VEHICLE-1, the hydrogen permeation flux is measured by a quadrupole mass spectrometer (QMS) at the downstream side. The plasma density is of the order of 10^9-10^{10} cm^{-3} and the electron temperature is ~3.5 eV. The particle bombarding energy is controlled by a negative bias voltage applied on the membrane flange. A bias of -50 V or -100 V is used in the present experiments. A resistive heater is set beneath the membrane to control the temperature, which is measured by a thermocouple mechanically attached to the sample.

By taking into account particle reflection [15] and the ion species mix [3,12], the net implantation fluxes in the PDP experiments can be estimated from the electron and density data measured by a Langmuir probe in VEHICLE-1. The particle reflection coefficients are calculated from the Monte Carlo programs, such as SRIM [15]. Although the Binary Collision Approximation (BCA) models such as SRIM may be not necessarily accurate at low implantation energy of several eV, the particle reflection coefficients given by Monte Carlo programs are relatively consistent (~0.5) in the energy range of 50-100 eV [2]. The ion species mix of the hydrogen plasmas is estimated using a zero-dimensional model. This model includes not only the rate balance equations for H^+, H_2^+, H_3^+ and H atoms, as Hollmann did in his work [16], but also the rate balance equation for H^-, whose concentration should not be ignored for plasmas with an electron temperature lower than 3 eV [17]. Hydrogen molecules are regarded as the particle source in this model, which is more relevant to the electron cyclone resonance (ECR) discharge conditions in VEHICLE-1. The modelling results indicate that H_3^+ is the dominant ion species at the electron temperature and neutral hydrogen gas pressure (~10^{-3} Torr) in our experiments. The concentration of H^+ increases as the increase of electron temperature and becomes the dominant species when the electron temperature is higher than ~4 eV.

Surface oxidization effects on PDP have been studied in VEHICLE-1 because oxide would be one of the possible contaminations for the first wall of fusion reactors. The plasma-facing side of the F82H membrane is oxidized at ~ 450 ℃ at an oxygen gas pressure of 10^{-4} Torr. For the area effects experiments, the surface morphology of the samples is modified by plasma bombardment or machining.

QUEST [18] is a medium size spherical tokamak with a full metal chamber made of stainless steel. A permeation probe made from F82H has been installed near the mid-plane in QUEST and the permeation membrane is 35 mm away from the outboard wall in the radial direction. During plasma discharges, the membrane temperature is kept in a range of 200-300 ℃, which is also measured by a thermocouple.

Samples made of F82H are prepared in the same dimensions as those commercially available conflat flanges, except that the circular area inside the knife-edge is machined down to thicknesses between 0.14 mm and 5 mm. The "standard" (i.e., not intentionally modified) F82H membranes are mechanically polished and then cleaned in an ultrasonic bath. The membrane diameters are 35 mm for the VEHECLE-1 samples and 16 mm for the QUEST ones, respectively.

Post-mortem analysis such as scanning electron microscopy (SEM), optical microscopy and X-ray photoelectron spectroscopy (XPS) are utilized to evaluate the surface conditions before and after experiments.

4. Results and discussion

4.1. Surface contamination effects observed in VEHICLE-1 and QUEST

The hydrogen PDP behavior with/without surface oxidation is shown in Fig.2. After oxidization, it takes a longer time for the permeation flux to reach steady state, suggesting a lower effective diffusion coefficient for the oxidized samples.
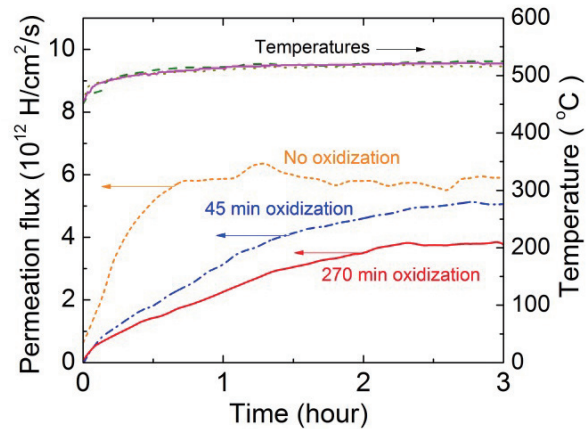
Fig.2. Hydrogen PDP through clean and oxidized F82H membranes at a temperature around 520 ℃.

Figure 3 shows the XPS analysis results for (a) a polished surface before PDP, (b) a surface after 0.75 h oxidization and (c) a surface after 0.75 h oxidization and 3 h plasma exposure. Notice that the implantation range of hydrogen particles in iron is less than several nm at an implantation energy of <50 eV, as calculated by SRIM [15], while the thickness of the oxide layer is tens of nm, which should be thick enough to act as a second layer for diffusion, as illustrated in Fig.1(c). Plasma exposure can reduce the impurity layer thickness by chemical sputtering, which has been observed by measuring the water partial pressure in the plasma side during the PDP experiments (Fig.3(d)). However, the XPS results indicate that the surface oxides would never be depleted completely under current experimental conditions (as shown in Fig.3(c)), and as a result, the steady state PDP through these oxidized membranes is lower than a polished one.
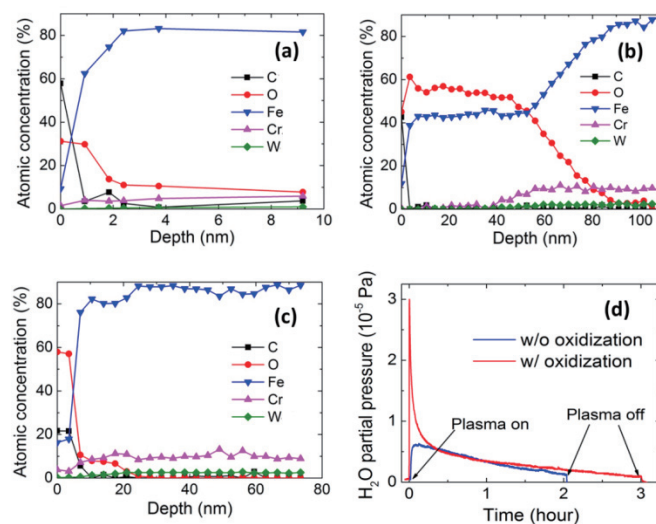
Fig.3. XPS results for (a) a polished surface, (b) a surface oxidized at ~450 °C by oxygen gas at 1×10^{-4} Torr for 0.75 h, (c) a surface after 0.75 h oxidization and 3 h plasma exposure and (d) water partial pressure measurements at the plasma side in the PDP experiments for oxidized and clean samples, respectively.

Surface contamination effects on permeation through F82H have been observed in tokamak PDP experiments as well. It has been found that the diffusion coefficients estimated from the QUEST data are lower by a factor of 3 to 4 than those taken in VEHICLE-1, although the sample membranes are essentially the same [13,19]. A ~12 nm thick impurity layer containing carbon, tungsten and oxygen has been detected on the membrane surface by XPS. A membrane composed of two sheets of thicknesses L_1, L_2 and diffusion coefficients D_1, D_2 has an effective diffusion coefficient D_{eff}, given by [20]:

$$L_1 / D_1 + L_2 / D_2 = L / D_{eff} \qquad (5),$$

where L is the total thickness of the membrane. Using the diffusion coefficient data for F82H from previous experiments [19]:

$$D = 7.5 \times 10^{-4} \exp(\frac{-0.14 \, [eV]}{kT}) . \qquad (6),$$

the hydrogen diffusion coefficient in the impurity layer has been estimated to be ~2×10^{-10} cm^{2}s^{-1}, which is close to the hydrogen diffusion coefficient for tungsten measured in the same temperature range [21].

4.2. Surface area effects on PDP

To verify the area effects model proposed in Section 2.2, PDP experiments have been performed using samples with well controlled surface morphology. The sample membranes are heated up to a steady state temperature of ~500 ℃ by resistive heater radiation and plasma bombardment.
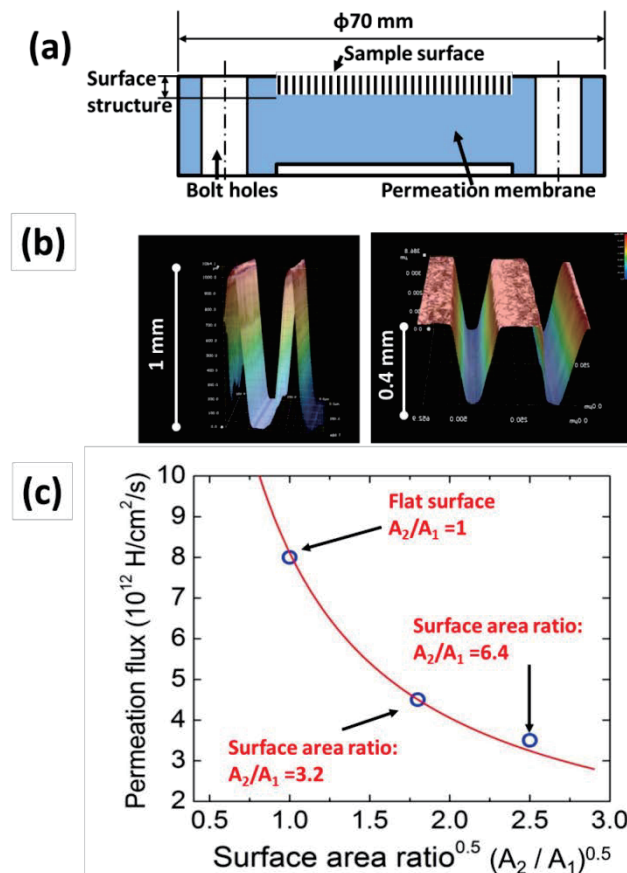
Fig.4. (a) A schematic diagram of the modified permeation sample membrane; (b) 3D figures observed by an optical microscope and (c) measured PDP fluxes as a function of the square root surface area.

Figure 4(a) shows a schematic diagram of the surface-modified permeation membrane. The first 1 mm or 0.4 mm of the 5 mm thick F82H membrane is machined into V-shape grooves to increase the surface area. From the dimension measurements by a microscope (as shown in Fig. 4(b)), the areas of the modified surfaces are measured to be larger by a factor of ~6.4 and ~3.2 than a flat one, respectively. The effective thickness of the modified sample membrane is between 4 to 5 mm. Equation (4) suggests that when plasma-driven permeation is in the RD limited regime, the steady state permeation flux is inversely proportional to the square root of surface area.

Shown in Fig.4(c) are the PDP flux data as a function of the square root of surface area ratio. The measured steady state permeation flux has been found to be inversely proportional to the square root of surface area, which is in excellent agreement with the model prediction.

4.3. Compound surface condition effects on PDP

Notice that the two surface effects are independent on each other, which means these two effects can be multiplied. The surface area modified sample (1 mm deep groove) shown in Fig. 4(a) has been oxidized at ~500 ^{o}C for 4.5 h and then exposed to hydrogen plasma again.

Figure 5 shows that a further reduction of hydrogen permeation has been observed. The steady state permeation flux has been found to be lower than that of the sample before oxidization by a factor of 1.4, which is in good agreement with the separate surface contamination effect data shown in Fig. 2. Compared with the clean and polished surface, the overall permeation flux has been found to be reduced by a factor of ~3.2.
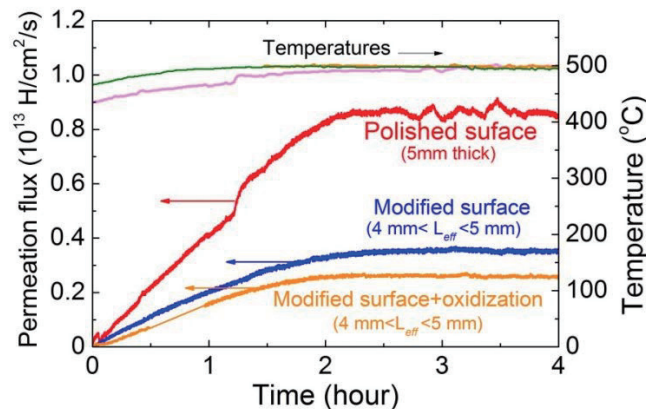
Fig.5. The compound surface condition effects on PDP.

5. Conclusion

Hydrogen plasma-driven permeation behavior has been found to be affected both by surface contamination and area. The steady state hydrogen PDP flux can be reduced by a factor of 2 or 3 by surface treatment. However, such amount of reduction in hydrogen isotopes permeation is still not acceptable for a reactor operation and tens of g/day of tritium may still penetrate through the first wall by PDP [6,19]. The compound effects of surface contamination and area may be a possible solution, which warrants further investigation.

Reference

[1] B.L. Doyle, J. Nucl. Mater. 111&112 (1982) 628.
[2] Y. Hirooka et al., Fusion Sci. Technol. 64 (2013) 345.
[3] H. Zhou et al., Fusion Sci. Technol. 63 (2013) T361.
[4] R. A. Causey et al., J. Nucl. Mater. 122&123 (1984) 1547.
[5] A. I. Livshits et al., J. Appl. Phys. 84 (1998) 2558.
[6] O. V. Ogorodnikova, et al., Fusion Eng. Des. 49-50 (2000) 921.
[7] M. Takizawa et al., J. Nucl. Mater. 248 (1997) 15.
[8] Y. Hirooka and H. Zhou, Fusion Sci. Technol. 66 (2014) 63.
[9] Y. Hatano et al, Vac. Sci. Technol. A 16 (1998) 2078.
[10] H. Zhou et al., Plasma Fusion Res. 8 (2013) 2402065.
[11] Y. Hirooka et al., Nucl. Instr. and Meth. B23 (1987) 458.
[12] Y. Hirooka et al., J. Nucl. Mater. 337-339 (2005) 585-589.
[13] H. Zhou et al., Plasma Fusion Res. 9 (2014) 3405041.
[14] R. A. Causey et al., J. Nucl. Mater. 300 (2002) 91.
[15] J. F. Ziegler et al., Nucl. Instr. Meth. B12 (2010) 1818.
[16] E. M. Hollmann et al., Phys. Plasmas 9 (2002) 4330.
[17] A. Tonegawa et al., J. Nucl. Mater. 313- 316 (2003) 1046.
[18] K. Hanada et al., Plasma Fusion Res. 5 (2010) S1007.
[19] H. Zhou et al., J. Nucl. Mater. 455 (2014) 470.
[20] J. Crank, The Mathematics of Diffusion, 2nd ed., Clarendon Press, Oxford, London, 1975.
[21] T. Otsuka, T. Hoshihira, T. Tanabe, Phys. Scripta T138 (2010) 014052.

Exploration of extremely low q_{edge} regime in KSTAR

Jayhyun Kim, Y. In, B.H. Park, A. Aydemir, and the KSTAR team

National Fusion Research Institute, Daejeon, Korea

Email: jayhyunkim@nfri.re.kr

The q_{edge} <2 regime had long been regarded as an experimentally forbidden regime due to magneto-hydrodynamic instabilities. However, RFX-MOD experiment demonstrated that the control of error field could enable the entrance and sustainment of the discharge even in the forbidden regime. We explored q_{edge} <2 regime in Korea superconducting tokamak advanced research (KSTAR) without any feedback or feedforward control of error field since the intrinsic level of error field in KSTAR is inherently comparable to the controlled level of other device. The discharge sustained at q_{95} ~1.9 for 800 ms that is at least one order of magnitude longer than the resistive wall time of the device. Furthermore, *simulated* error field applied by field error correction coils prevented the passage of q_{edge}=3 integer rational surface before reaching q_{edge}=2. The detailed analysis is on-going for revealing the role of error field in the excitation of limiting instability.

1. Introduction

Confinement in toroidal magnetic fusion devices has a tendency to increase linearly with the plasma current. On the other hand, magneto-hydrodynamic (MHD) stability requirement limits the allowed plasma current for a given toroidal magnetic field generated by external coils. For this reason, the safety factor q, which is proportional to the ratio of the toroidal field to the poloidal field (*i.e.*, the plasma current), is used as a metric of MHD stability in toroidal magnetic devices.
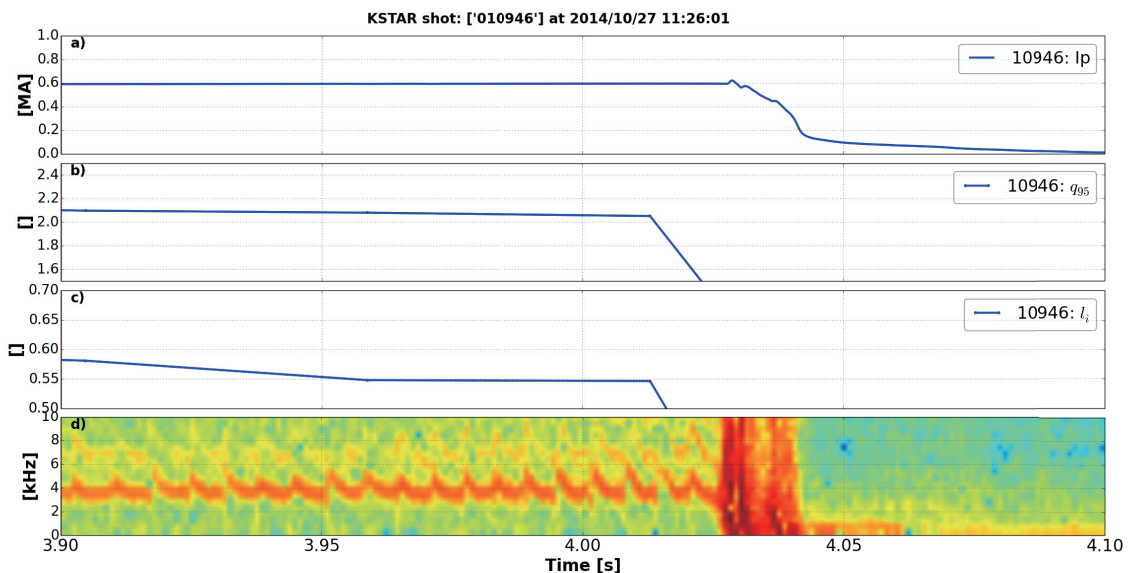
Figure 1. a) plasma current, b) edge safety factor q_{95}, c) internal inductance l_i, and d) spectrogram of Mirnov coil.

As calculated by MHD theory, the discharge becomes unstable when the edge safety factor, q_{edge} passes certain rational surfaces such as q=4, 3, and 2. The instability near the

integer rational surfaces could cause a plasma disruption, and the q_{edge} <2 regime had been generally regarded as an experimentally forbidden regime. Moreover, even the passage of q_{edge}=4 or 3 is also difficult depending on the plasma parameters such as the current distribution profile or edge current density.

External kink mode driven by plasma current is regarded as a typical MHD instability in determining the allowed level of q_{edge}. It is known that the stabilities of external kink mode and resistive wall mode are affected by non-axisymmetric field components in intrinsically axisymmetric toroidal magnetic device. Thus RFX-MOD and DIII-D recently achieved the operation of q_{edge} (q_{95}) <2 regime through the dynamic error field correction and feedback suppression of resistive wall mode (*i.e.* the control of non-axisymmetric field components) [1][2].

In the 2013 campaign, level of intrinsic non-axisymmetric field (*i.e.* intrinsic error field) in KSTAR was found to be at least one order of magnitude lower than the seen in other major devices [3]. The intrinsic level of non-axisymmetric field in KSTAR, $\delta B/B_T \leq 10^{-5}$ is inherently comparable to the controlled level of other major devices. From the above result, we attempted the exploration of q_{edge} <2 regime without any feedforward correction or feedback control of the non-axisymmetric field.
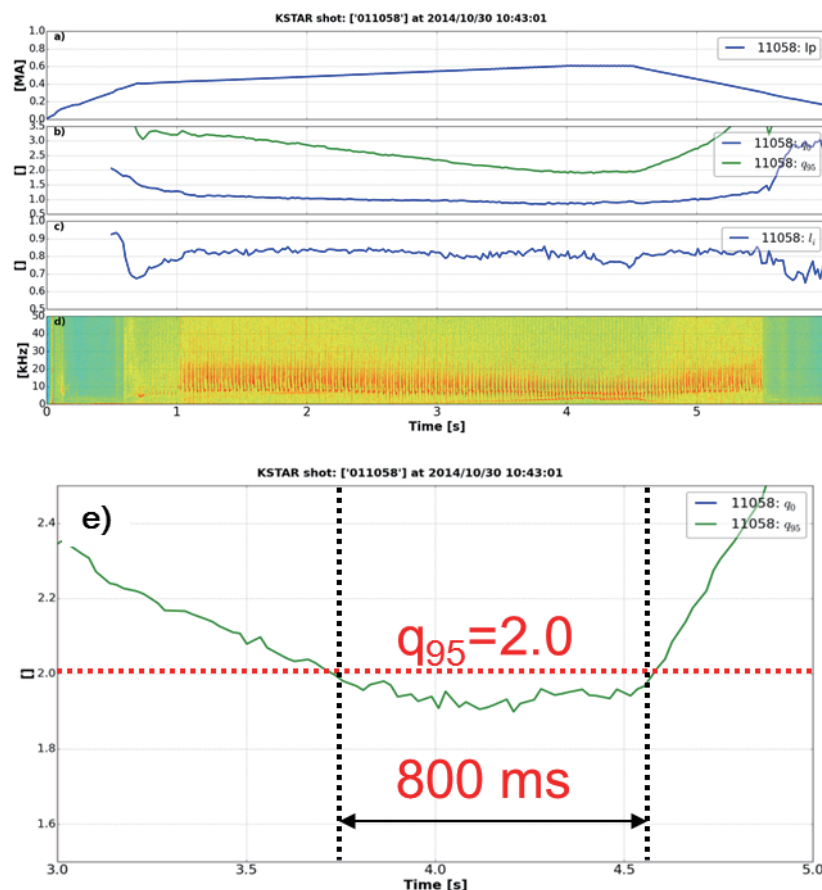
Figure 2. a) plasma current, b) safety factors, q_0 and q_{95}, c) internal inductance l_i, d) spectrogram of Mirnov coil, and e) enlargement of figure 2b) during q_{95} <2 regime.

2. Attempt of extremely low q_{edge} regime

At the initial attempts, we approached the q_{edge} <2 regime in pure Ohmic discharges without any auxiliary heating in order to exclude unintended stabilization effect from plasma rotation or fast ions. However, the discharges included a tearing-like MHD mode from an early phase due to the nearly circular plasma shape. We adopted a small circumference for discharges to lower q_{edge} in moderate levels of plasma current. Consequently, the pre-existing mode prevented the passage of q_{edge}=2 since it locked and caused a disruption when q_{edge} reached 2 as shown in figure 1d).

Therefore, neutral beam was injected in order to avoid the locking of the pre-existing mode and the discharge sustained in q_{95}~1.9 for 800 ms. Furthermore, it stably came back to q_{edge} >2 regime as shown in figure 2. The 800 ms duration is at least one order of magnitude longer than the resistive wall time of KSTAR. The usage of neutral beam could be justified if the kink mode driven by plasma current is the ultimate obstacle to passing through q_{edge}=2 since plasma rotation or fast ions cannot stabilize the current driven kink mode [4].
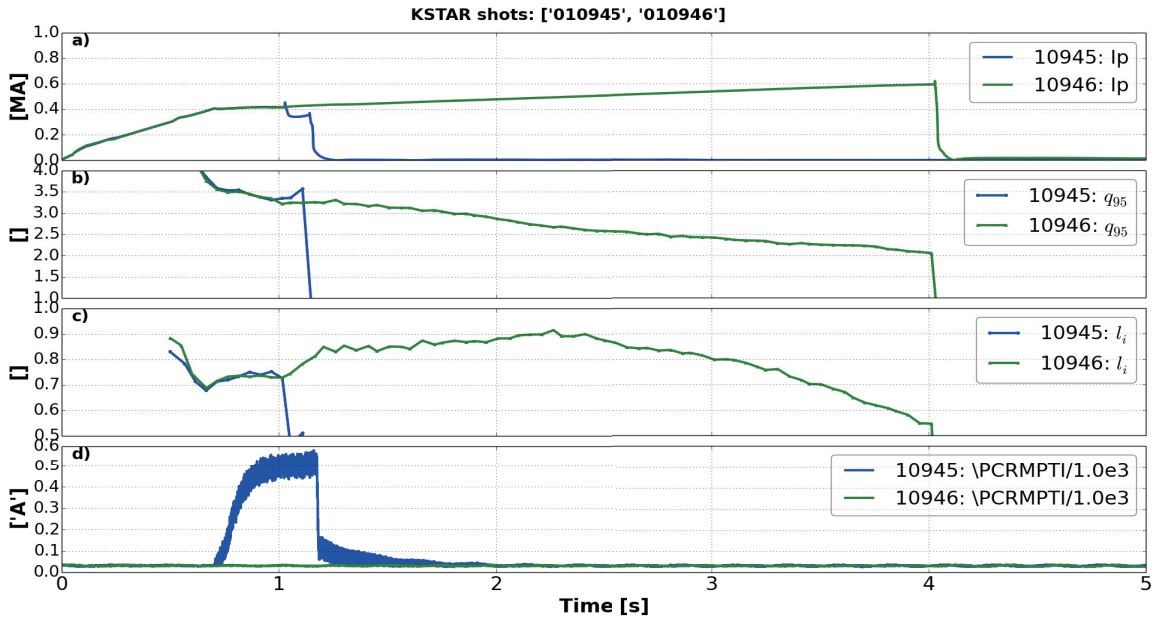
Figure 3. a) plasma current, b) edge safety factor q_{95}, c) internal inductance l_i, and d) current of field error correction coil.

As previously mentioned, we conjectured that extremely low level of intrinsic error field in KSTAR enabled the achievement of q_{edge} <2 regime without any error field suppression while other devices almost unconditionally need dynamic error field correction or feedback suppression of resistive wall mode. In order to verify the hypothesis, *simulated* error field was intentionally applied by field error correction coils and the passage of integer rational surfaces was attempted in exactly same way. The level of *simulated* error field, $\delta B/B_T$~10^{-4} was comparable to the typical level of intrinsic error field in other major devices.

As depicted in figure 3, the *simulated* error field caused a disruption even near q_{edge}~3 before reaching q_{edge}=2. From this result, we concluded that the control of error field is a crucial in enlarging the operational boundary of toroidal magnetic devices and the intrinsic level of error field in KSTAR is really low when compared with other major devices [3].

3. Summary and discussion

In this research, we demonstrated that q_{edge} <2 regime is not an absolute operational

boundary of toroidal magnetic devices and non-axisymmetric fields such as the intrinsic error field could play a crucial role in passing through critical integer rational surfaces. The result suggests detailed study in uncovering the relationship among the non-axisymmetric fields, external kink mode, and resistive wall mode [5]. For the purpose, we will extend our exploration of the forbidden regime with including the active control of non-axisymmetric fields in the 2015 campaign.

In addition, as q_{edge} becomes low, the importance of $q=1$ surface also increases since the inversion radius and the area affected by the $q=1$ instability (*i.e.* sawtooth crash) increases in low q_{edge} operation. Thus we should take into account the whole q or current profile in order to control both the internal and external MHD instabilities. In this sense, internal inductance l_i could act as a useful metric.

So far, we solely focused on the limiting MHD instability for entering $q_{edge} <2$ regime. Based on this experience, we plan to conduct a systematic exploration of new operational regimes where both enhanced confinement and MHD stability are satisfied. For this purpose, the follow-up experiments in the 2015 campaign need to be conducted in diverted instead of limited plasmas for reducing the interaction with plasma facing wall.

References

[1] P. Martin *et al.*, Fusion Energy Conference (2014).
[2] P. Piovesan *et al.*, Phys. Rev. Lett. **113**, 045003 (2014).
[3] Y. In *et al.*, Nucl. Fusion accepted.
[4] Z.R. Wang *et al.*, Phys. Plasmas **19**, 072518 (2012).
[5] Y. In *et al.*, Nucl. Fusion **50**, 042001 (2010).

LHD Neutron Diagnostics

M. Isobe[1,2], K. Ogawa[1], T. Kobuchi[1], H. Miyake[1], H. Hayashi[1], H. Tomita[3], K. Watanabe[3], J.H. Kaneko[4], S. Murakami[5], E. Takada[6], A. Uritani[3], and Y. Takeiri[1,2]

[1]*National Institute for Fusion Science, Toki, Japan*

[2]*SOKENDAI (The Graduate University for Advanced Studies), Toki, Japan*

[3]*Nagoya University, Nagoya, Japan*

[4]*Hokkaido University, Sapporo, Japan*

[5]*Kyoto University, Kyoto, Japan*

[6]*National Institute of Technology, Toyama College, Toyama, Japan*

1. Introduction

The Large Helical Device (LHD) project will step into a next stage, i.e. experiment by using deuterium gases after two years of preparation. A comprehensive set of neutron and γ-ray diagnostics is going to be installed on the LHD towards extension of energetic-particle (EP) physics research in heliotron plasmas [1]. Conceptual design of fusion products diagnostics for the LHD was made in late 1990s [2]. After conclusion of agreements for the LHD deuterium experiment with local government bodies, development of FPs diagnostics has begun lately. Because there are a lot of tasks to do, all Japan fusion neutron and γ-ray diagnostics team has been organized in the collaboration framework of National Institute for Fusion Science. FPs diagnostics system on the LHD will consist of 1) wide dynamic range neutron flux monitor (NFM) [3], 2) neutron activation system (NAS), 3) vertical neutron camera (VNC) [4]. In addition to these, we are developing a directional scintillating fiber detector, an artificial diamond detector [5] and a γ-ray scintillation detector for confinement study of MeV ions. A neutron energy spectrometer prototype is also being developed and tested in KSTAR [6, 7]. In this paper, roles of NFM, NAS and VNC and current status of implementation onto the LHD are briefly described.

2. Neutron flux monitor

In a deuterium discharge of LHD, a maximum neutron emission rate is expected to be over 10^{16} (n/s) when full power heating by five neutral beam injectors (NBIs). Also, the neutron rate can change largely according to injection pattern of NBIs and also changes rapidly within a time scale of beam ion's slowing down time after the beam turn-off. Therefore, a neutron flux monitor (NFM) having fast time response and wide dynamic range capability is required for the LHD. Note that because an annual neutron budget will be set for a reason of radiation safety, management of neutron yield is quite important in the operation of the LHD. The LHD will be equipped with three NFMs as shown in Fig. 1. Note that antecedent to full-scale

design of the NFM, characterizations of neutron field in the vicinity of the LHD were performed by using the MCNP code [8-11]. Each NFM will consist of a ^{235}U fission chamber (FC) for a middle-high neutron yield shot and a ^3He or ^{10}B detector for a low yield shot. The FC system plays an essential role for management of neutron yield. To realize wide dynamic range capability for the FC system, pulse counting and Campbelling (or MSV) modes are employed jointly [12, 13]. The wide dynamic range FC system had been used in large tokamaks in 1980s~1990s [14]. However, those electronics are based on traditional analogue technologies and

Fig. 1 Neutron flux monitor for the LHD.

are no longer commercially available at this moment. Therefore, we have developed a digital signal-processing unit (DSPU) by using leading-edge technologies. Details of the DSPU are described in Ref. 3.
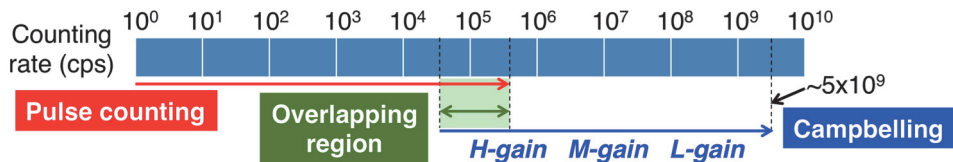
Fig. 2 Coverage of pulse and Campbelling modes in pulse counting rate for the FC system.

Our DSPU can provides the maximum pulse counting rate up to $\sim 5\times 10^9$ (cps). A processing time of DSPU is variable and is typically set to be 0.5 ms. Coverage of each mode in a range of pulse counting rate is shown in Fig. 2. Note that the technology developed for the LHD is universal and is applicable to the NFM for ITER, and other fusion machines. Installation of the NFM system is ongoing and will be completed in March, 2015, except three ^{235}U fission chambers.

In the LHD, *in-situ* absolute calibration of the NFM will be performed by using a ^{252}Cf neutron source of 800 MBq. This is an indispensable work to evaluate total neutron emission rate from the pulse counting rate measured with the NFM. The method consists of laying circular railroad track at the major radius of 3.74 m inside the vacuum vessel of the LHD. The track designed for the LHD is depicted in Fig. 3. To approximate the ring-shaped neutron source, we let the ^{252}Cf source mounted on the train run on the track inside the LHD vacuum vessel.
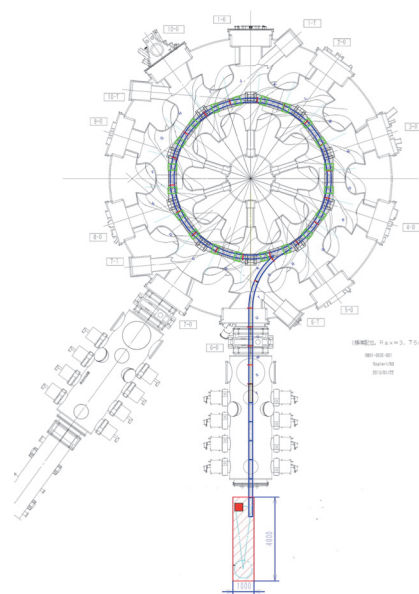
Fig. 3 Track line designed for *in-situ* calibration of the LHD-NFM.

154

3. Neutron activation system

A neutron activation system (NAS) will be employed to secure reliability of neutron emission rate evaluated by the NFM. It also can work as a tool of confinement study of MeV tritons. Because the NAS is essentially insensitive to γ-rays, it can provide reliable, absolute neutron flux at an irradiation point. We are preparing two irradiation ends at the 2.5-L and the 8-O ports on the LHD. An activation foil is placed in a capsule (18.5 mmϕ x 40 mm) made of polyethylene called "rabbit" at the measurement room (1) in the material research laboratory area. The system receives a voltage pulse from the LHD control before a shot and then the capsule is launched towards the irradiation end by using compressed air. After the discharge, the capsule goes back to the original place and then the activated foil is analyzed through γ-ray spectroscopy by using high-pure germanium (HPGe) detector (CANBERRA Industries Inc./ GX3018-7935-7-RDC-4-2002C). Note that the NAS can provide shot-integrated neutron flux. Figure 4 shows overall perspective of the NAS system. The pneumatic tube length between the rabbit control unit at the measurement room (1) and the irradiation end at the LHD torus is about 93 m for the 8-O line and 80 m for the 2.5-L line. The implementation of the NAS system will be finished in March, 2015.
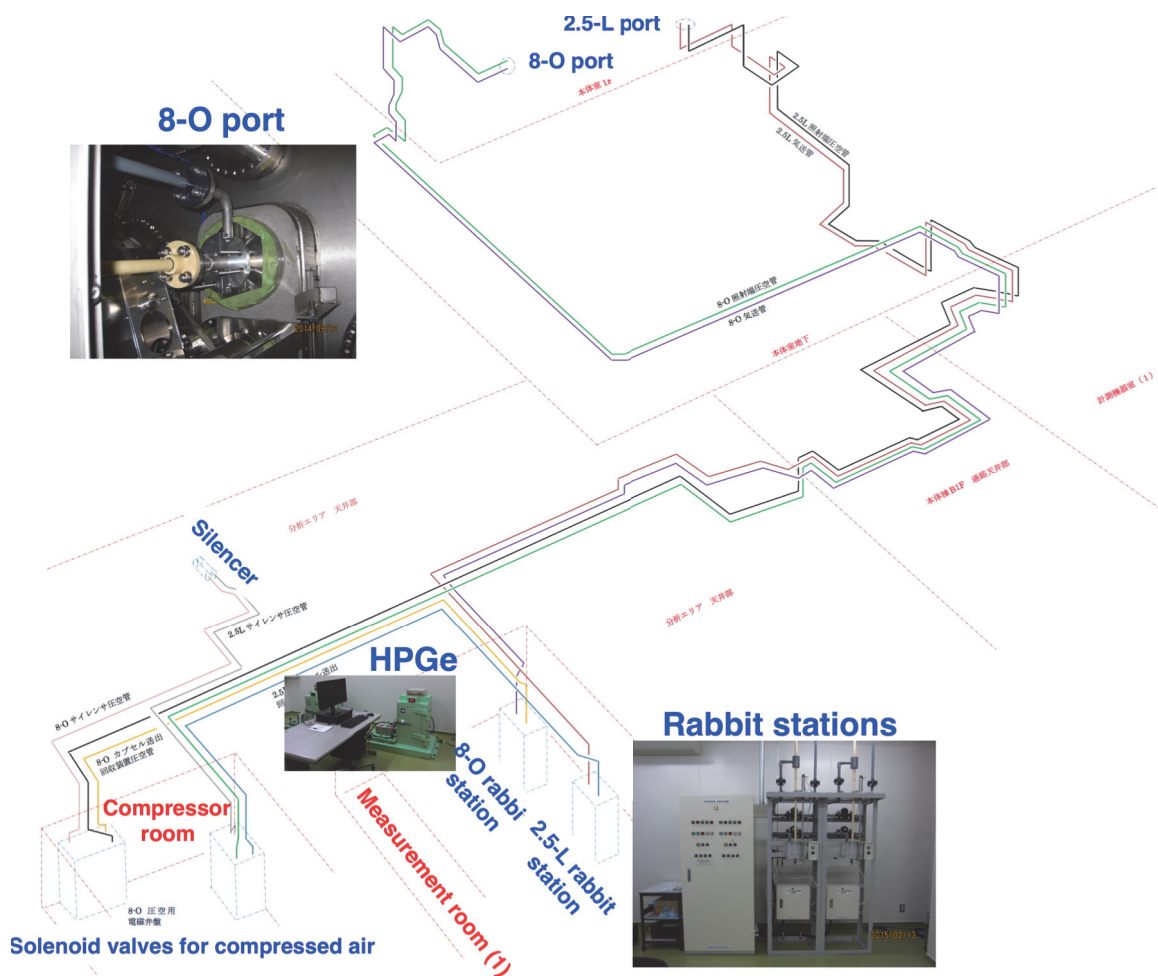
Fig. 4 Overview of neutron activation system for the LHD.

4. Vertical neutron camera

Because radial EP transport, in particular, while toroidicity-induced Alfvén eigenmodes destabilized by EPs is of our great concern, we have been developing a vertical neutron camera (VNC) consisting of fast-neutron scintillation detectors maximized in the counting rate capability and cylindrical collimators of 11 channels made of heavy concrete [4]. Schematic drawing of the LHD-VNC is shown in Fig. 5. As for the fast-neutron detector section, our targets in development are 1) stable operation at counting rate up to 10^6 cps, and 2) online n-γ discrimination. So far, we have tested four different fast-neutron scintillators, i.e. stilbene crystal, BC-501A liquid scintillator, EJ-299-33 plastic scintillator capable of pulse shape discrimination, and BC-720 consisting of ZnS(Ag) phosphor embedded in a clear hydrogenous plastic at accelerator based fusion neutron source and research fission reactor. At the same time, we also tested a couple of fast analog-to-digital convertor (ADC) modules having a function of pulse shape discrimination (PSD) by using field programmable gate array (FPGA) technology suitable for our purpose. In addition, we have searched for optimized n-γ discrimination methods [15]. As a result of the intensive tests above mentioned, we chose stilbene as a fast-neutron detector for the LHD-VNC. The stilbene scintillator (20 mmϕ x 10 mm) is connected to a photomultiplier tube (PMT) (Hamamatsu Photonics K.K. /H11934-100-10MOD) equipped with a so-called active divider. Pulses from the PMT are fed into a fast digitizer module having an automatic online PSD function (Techno AP Co./APV8104-14). Our fast-neutron detector system offers no significant gain shift of PMT up to 10^6 cps and good n-γ discrimination as seen in Ref. 4. An opening of the 2 m concrete floor of the LHD torus is utilized for a neutron collimator. Actually, we install the VNC at the 2.5-L port of the LHD. Therefore, a multichannel cylindrical collimator
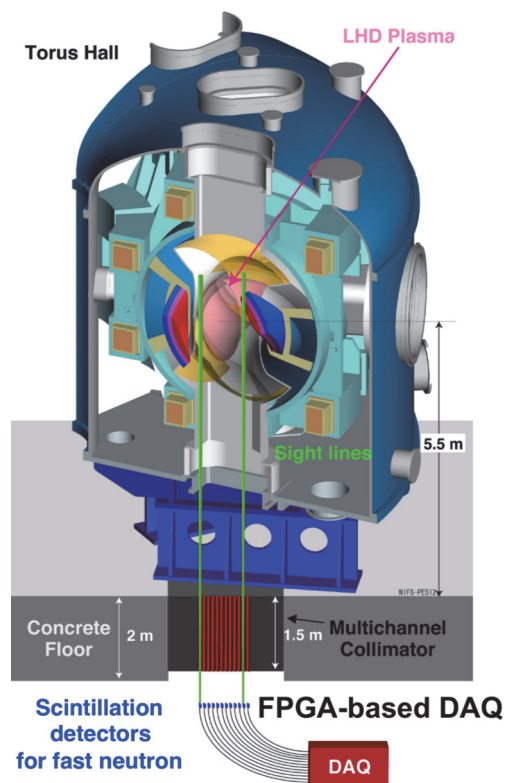
Fig. 5 Schematic drawing of the LHD-VNC system.

Fig. 6 Installation of the neutron collimator made of heavy concrete.

(l=1.5 m) made of heavy concrete (3.5 g/cm^3) is placed in the floor opening right under the 2.5-L port. The diameter of each collimator is variable, i.e. 10, 20, and 30 mm ϕ and the distance between the two neighboring holes is 90 mm. Figure 6 shows a picture when the collimator stack is placed into the floor opening. Installation of the neutron collimator will be completed in March, 2015. After this work, implementation of the measurement section will be initiated.

5. Summary

The LHD deuterium project will start after two years of preparation. A comprehensive set of neutron and γ-ray diagnostics will be employed in the LHD to extend energetic-particle physics research in a helical plasma. In particular, the NFM based on the FC plays an essential role in operating the LHD in terms of management of neutron yield because the annual neutron budget will be set in the deuterium experiment regime. We have developed the NFM having fast time response and wide dynamic range capability by using leading-edge digital signal processing technologies. The NAS is also used to ensure accuracy of neutron mission rate evaluated by the NFM. The VNC is a physics-oriented diagnostics. It will reveal radial transport of EPs while EP-driven MHD instabilities occur and will provide a great opportunity to explore scenarios for suppression of MHD amplitude and transport of EPs. Preparation of the NFM, NAS, and VNC is steadily ongoing towards the LHD deuterium operation.

Acknowledgements

References

[1] M. Isobe *et al*., Rev. Sci. Instrum., **81** (2010) 10D310.

[2] M. Sasao *et al*., Fus. Eng. Des, **34-35** (1997) 595.

[3] M. Isobe *et al*., Rev. Sci. Instrum., **85** (2014) 11E114.

[4] K. Ogawa *et al*., Rev. Sci. Instrum., **85** (2014) 11E110.

[5] J.H. Kaneko *et al*., Diamond and Related Materials, **26** (2012) 45.

[6] H. Tomita *et al*., Rev. Sci. Instrum., **81** (2010) 10E309.

[7] H. Tomita *et al*., Rev. Sci. Instrum., **85** (2014) 11E120.

[8] N. Nishio *et al*., Rev. Sci. Instrum., **81** (2010) 10D306.

[9] N. Nishio *et al*., Plasma Fus. Res., **6** (2010) 2405115.

[10] Y. Nakano *et al*., Rev. Sci. Instrum., **85** (2014) 11E116.

[11] Y. Nakano *et al*., Plasma Fus. Res., **9** (2014) 3405141.

[12] M. Oda *et al*., IEEE Trans. Nucl. Sci., **NS-23** (1976) 304.

[13] Y. Endo et al., IEEE Trans. Nucl. Sci., **NS-29** (1982) 714.

[14] A. England *et al*., Rev. Sci. Instrum., **57** (1986) 1754.

[15] Y. Uchida *et al*., Rev. Sci. Instrum. **85** (2014) 11E118.

Electron temperature measurement using backward and forward Thomson scatterings in the LHD Thomson scattering system

Ichihiro YAMADA

National Institute for Fusion Science, 322-6 Oroshi, Toki, Gifu 509-5292, Japan

INTRODUCTION

The large helical device (LHD) Thomson scattering system measures electron temperature and density profiles of LHD plasmas along the LHD major radius. In the original design, an oblique backward scattering configuration with a typical scattering angle of 167-degree was adopted, and the laser pulses are simply absorbed by a beam dump after traveling through LHD plasma. [1-3] Recently we removed the beam dump and installed a beam-returning mirror, a relay lens and an optical delay path of 30 m to observe forward Thomson scatting signals as shown in Fig.1. In the forward scattering configuration, typical scattering angle is 13‾degree. By combining the backward and forward scattering measurements, some applications will be possible. In this paper, extension of measurable temperature range and search of temperature anistoropy are discussed.
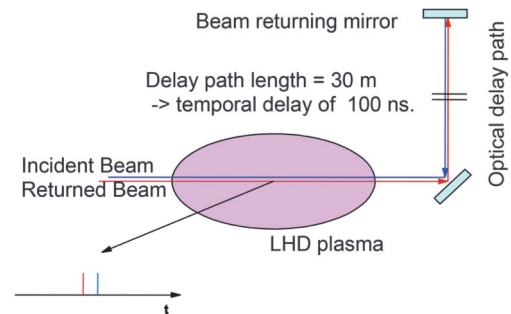
Fig. 1. Schematic diagram of the backward and forward scattering configurations.

EXTENSION OF MEAUREBALE TEMPERATURE RANGE

In the original design of the LHD Thomson scattering system, the optimized electron temperature (T_e) range was set to be T_e = 50 eV – 10 keV. In recent LHD experiments, high-T_e plasmas with the $T_e \geq 20$ keV were generated. So, extending measurable T_e range is one of
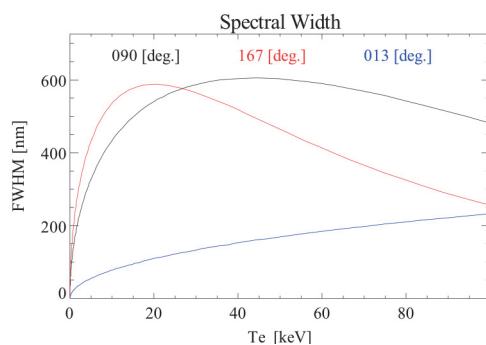
Fig. 2 a) Thomson scattering width as a function of electron temperature for the scattering angles of 90-, 167- and 13-degree.
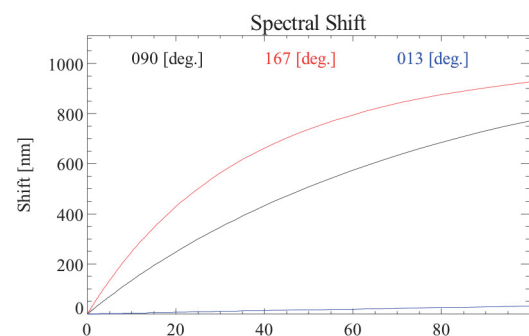
Fig. 2 b) Wavelength shift at which the Thomson scattering spectrum reaches maximum for the scattering angles of 90-, 167- and 13-degree.

Email: yamadai@nifs.ac.jp

the important issues in the LHD Thomson scattering system. Figures 2 a) and b) show the spectral width and the relativistic peak position shift as a function of electron temperature respectively for 90-, 167- and 13-degree scattering configurations. The two Thomson scattering spectrum are quite different. By using the differences of the Thomson scattering spectrum of the backward and forward scatterings, measurable T_e range will be extended without any modification of light collection optics and polychromators because. The experimental T_e error estimated by using mock data is shown in Fig. 3. In the backward scattering configuration, the T_e error is less than 10 % at $T_e \leq 10$ keV. However, it rapidly increases above 3 keV and exceeds 10 % at $T_e \geq 10$ keV. On contrast, the T_e error in forward scattering measurement is larger then 10 % at $T_e \leq 1$ keV, and becomes smaller above 1 keV. So, the electron temperature range where the T_e error is less than 10% will be extended as T_e = 1 eV – more than 50 keV by using the two scattering configurations complementarily.
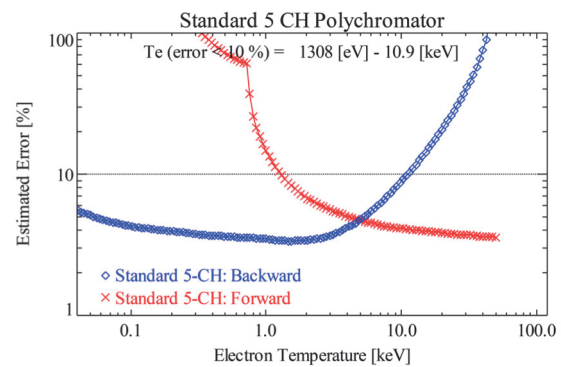
Fig.3. Estimated experimental error in T_e for the backward and forward scattering configurations.

SEARCH OF ELECTRON TEMPERATURE ANISTOROPY

In general, the electron velocity along the vector difference of the incident laser direction and observation direction is observed in Thomson scattering measurements. Following the principle, the temperature component is nearly parallel to the incident laser beam direction in the backward scattering measurement and that is almost perpendicular to the incident laser beam in the backward scattering measurement as shown in Fig. 4. By using the feature, we can search electron temperature anisotropy in high-temperature fusion plasmas. [4-5]

Fig. 4. Temperature component directions obtained from the backward and forward scattering configurations.
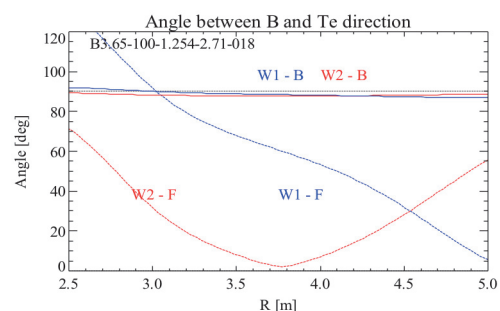
Fig. 5. Angle between the magnetic field line and observed temperature direction as a function of the LHD major radius.

The LHD Thomson scattering system has two observation windows, W1 and W2, on the LHD. Then, total four electron temperature components can be measured. Figure 5 shows the angle between the magnetic field line and observed temperature direction as a function of the measurement point along the LHD major radius. In the backward scattering measurement, the angles between the magnetic field line and measured temperature direction are about 90-degree for both W1 and W2, in the whole observation region. On the other hand, the angles are about 0-degree at R = 4.6 m and 5 m for the forward scattering measurements using the W1 and W2, respectively. Forward scattering measurements using the W1 and W2 are suitable for the observation of the component parallel to the magnetic field line near the plasma edge and center regions, respectively.

FIRST RESULTS OF FORWARD SCATTERING MEASUREMENTS IN LHD

In the 2012 LHD experiment campaign, the forward scattering signals were been clearly observed as well as the backward scattering signals as shown in Fig. 6. The preceding and trailing pulses are backward and forward Thomson scattering signals respectively. The rectangle pulse shows an ADC gate pulse. The temporal difference between the backward and forward scatterings is ~100 nsec, which is caused by the optical delay path of ~30 m as shown in Fig. 1.
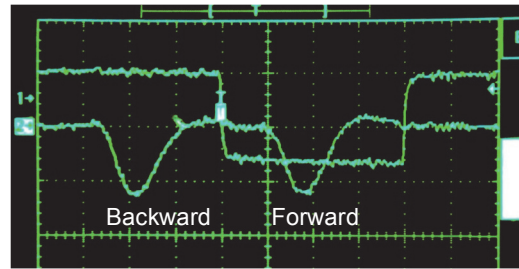
Fig. 6. Thomson scattering signals and ADC gate pulse. The preceding and trailing pulses are the backward and forward scattering signals respectively.

A comparison of electron temperatures obtained from the backward and forward scattering measurements in a plasma discharge is shown in Fig. 7 a). In this case, they show good agreements from the beginning of the discharge to the end. Figure 7 b) shows a
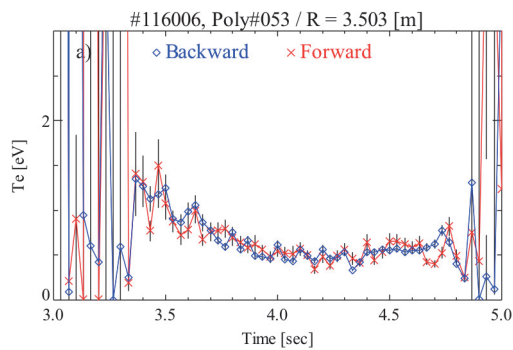
Fig. 7 a) Comparison of T_es obtained from the backward and forward scattering measurements in a plasma discharge.
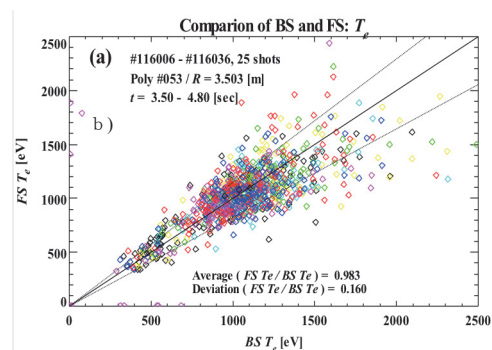
Fig. 7 b) Summary of comparisons of T_es obtained from the backward and forward scattering measurements.

summary of comparisons of electron temperatures for 30 plasma discharges. The data show good agreements within the standard deviation of 16 %.

SUMMARY

The LHD Thomson scattering system has been upgraded as a multipass Thomson scattering system with the aims of extension of measurable temperature range and study of electron temperature isotropy in fusion plasmas. The first results were successfully obtained in the 2012 LHD experiment campaign. Further improvements, such as development of 10 wavelength polychromator, are now in progress.

References
[1] K. Narihara et al., Fusion Eng. Design, **34-35**, 67 (1997).
[2] K. Narihara et al., Rev. Sci. Instrum., **72**, 1122 (2001).
[3] I. Yamada et al., Fusion Sci. Tech., **58**, 345 (2010).
[4] I. Yamada *et al.*, 40th EPS conference, Espoo, Finland (2013).
[5] I. Yamada *et al.*, 41th EPS conference, Berlin, Germany (2014)

Heat pulse propagation experiments with the MHD event for the estimation of the magnetic field topology

Satoshi OHDACHI

National Institute for Fusion Science, Toki 509-5292, Gifu, Japan

1. Purpose of study

Importance of the measurement of the magnetic field with RMP is now recognized widely. Though ELM mitigation or suppression is observed in limited experimental conditions, the condition for the mitigation / suppression, e.g. toroidal mode number and edge safety factor q95, is not the consistent in different device. That means understanding of this phenomena is not enough so far. RMP field is shielded and/or amplified at the rational surfaces. The way how the plasma responses to the RMP are fairy complicated and is not fully understood. Therefore measuring method to detect the magnetic field structure is quite important to discuss the physical process.

Transport of the plasma is significantly affected by the RMP application. The heat flux is much larger in the direction parallel to the magnetic field than that perpendicular to the flux surfaces. When the RMP is applied, the magnetic islands and the magnetic stochastic region are formed (see, fig. 1). The heat flux is thereby becomes two dimensionally and overpass of the magnetic island at the X-point (1) and enhancement of the heat flux at the magnetic stochastic region is expected. In fact, such modification of the heat flux is observed in the Large Helical Device [1]. From the change of the transport, change of the magnetic field topology can be derived. In this experiment of the Ref [1], propagation profile of the heat pulses produced by the modulated electron cyclotron heating (MECH) are used. Here, we propose the usage of the heat exhausts produced by the MHD activities, e.g. sawtooth activities. Analysis of the sinusoidal-like shape of the heat pulses (MECH) can be done using the Fourier transform. However, the heat pulses by the sawtooth crashes are quite different from the sinusoidal wave. They contain higher harmonics and the direct Fourier analysis is not applicable. In section 2, the delay time and amplitude profile are shown to be useful to resolve the local transport coefficient. In section 3, initial experiment done in the KSTAR Tokamak using this technique is introduced.
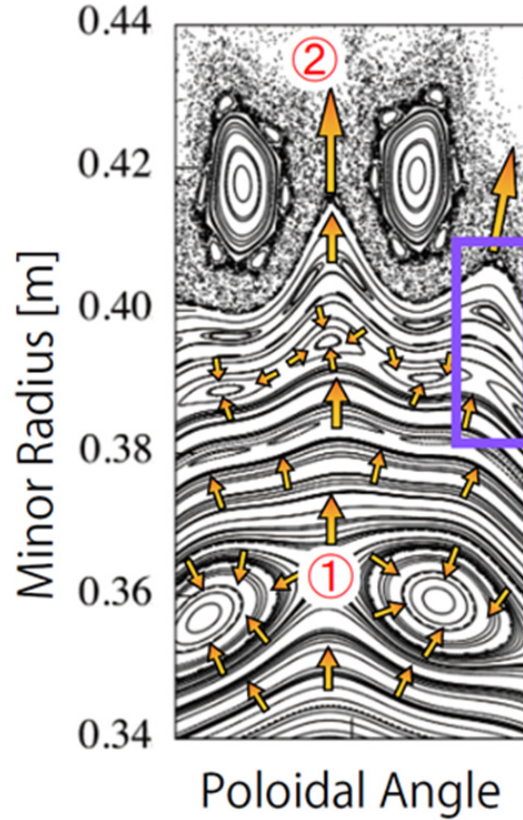
Fig. 1 Schematic diagram of the heat pulse propagation with RMP field.

2. Simple 1D simulation of heat pulse

Simple 1D simulation shown by the following equations for the heat pulse propagation is performed in the cylindrical coordinate. A constant scholar heat conductivity χ_e is assumed.

$$\frac{3}{2}n_e\frac{\partial \tilde{T}_e}{\partial t} = -\nabla \cdot \tilde{q}$$

$$\frac{3}{2}a^2 n_e\frac{\partial \tilde{T}_e}{\partial t} = \frac{1}{\rho}\frac{\partial}{\partial \rho}\left(\rho n_e \chi_e \frac{\partial \tilde{T}_e}{\partial \rho}\right) \quad (1)$$

The solution of this kind of the system in the slab geometry is evaluated as,

$$\sim e^{-\rho/\lambda}e^{i(\omega t-\xi)}$$

$$\lambda = \sqrt{2\chi_e/\omega}, \xi = \rho\sqrt{\omega/2\chi_e} \quad (2)$$

From eq. (2), it is clear that the delay time and the amplitude profile are strongly related with the heat conductivity χ_e. The heat pulses in the cylindrical coordinate are simulated in the Fig. 2. The delay of the pulse and amplitude are obtained and shown as the radial profile simultaneously...

164
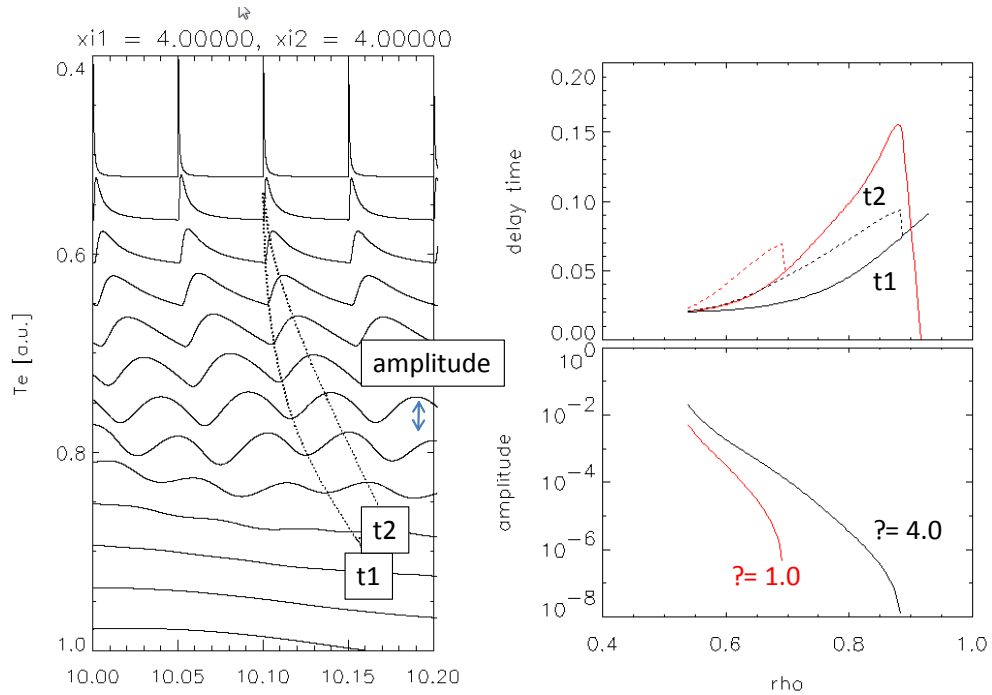
Fig. 2 Heat pulse propagation simulation (left) and the delay time profile (right upper) and the amplitude profile (right lower) assuming two heat conductivities $\chi = 4.0$(red) and $\chi = 1.0$(Black).

This figure shows that if we can measure the delay time and amplitude, change of the heat conductivity can be estimated. Therefore, this method can be useful to detect the change of the magnetic field topology due the RMP field application.

3. Initial experiments in the KSTAR Tokamak

In the KSTAR, ELMs are successfully suppressed / mitigated by the n =1 RMP application. By analyzing the heat pulse propagation profile of the mitigated experiments, the penetration depth of the RMP field is estimated. Fig. 3 shows the time evolution of the plasma parameters of the discharge which was analyzed. When the n=1 RMP field is applied, clear suppression of the ELM can be seen. From the ECE measurements, sawtooth activities, whose heat pulses can be used for analysis, are destabilized continuously in this shot. Fig. 4 shows the propagation profile of the heat pulses. Heat pulses propagate to the high-field side in this case. The heat pulse propagation profile, especially the amplitude profile is quite different with and with RMP. Note that the estimation of the time delay is more difficult when the heat pulse becomes prolonged. However the height of the heat pulse can be determined accurately even in this case. It is found that the heat pulses propagate faster and reaches farer region with RMP. It is consistent with the idea, that the heat transport is enhanced by the stochastisation of the magnetic field due to the RMP. In these experiment, the RMP field penetrate almost close to the q=1 surface. It is surprising that the transport is so much affected. Further compilation of the data is required to confirm this observation.

165
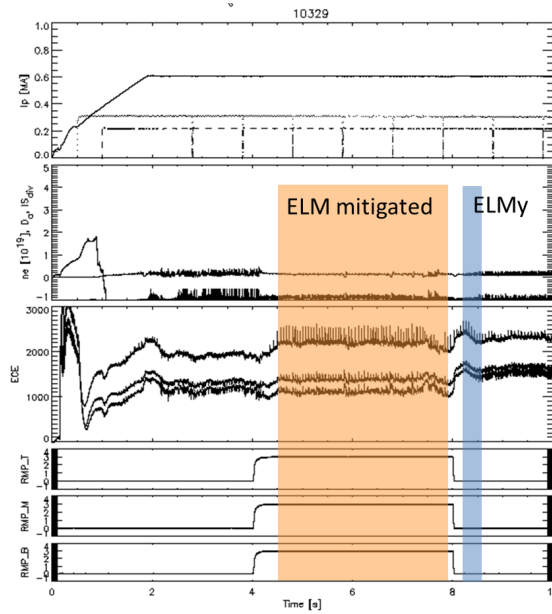
Fig. 3 Time evolution of the plasma parameters.
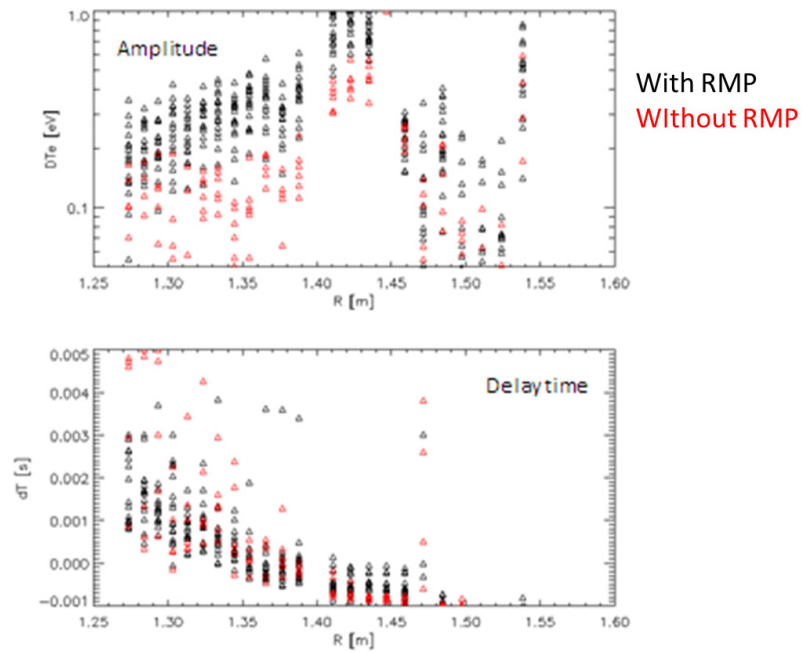
Fig. 4 Amplitude and delay time profile of the heat pulses

Acknowledgements

[1] K. Ida, et. al, New J. Phys. 15(2013), 013061

The Residual Zonal dynamics in a Toroidally Rotating Tokamak

Deng Zhou

Institute of Plasma Physics, Chinese Academy of Sciences, Hefei 230031, P. R. China

Centre for Magnetic Fusion Theory, Chinese Academy of Sciences, Hefei 230031, P. R. China

Abstract

Zonal flows, initially driven by ion-temperature-gradient turbulence, may evolve due to the neoclassic polarization in a collisionless tokamak plasma. In this presentation, the form of the residual zonal flow is presented for tokamak plasmas rotating toroidally at arbitrary velocity. The gyro-kinetic equation is analytically solved to give the expression of residual zonal flows with arbitrary rotating velocity. The zonal flow level decreases as the rotating velocity increases. The numerical evaluation is in good agreement with the previous simulation result for high aspect ratio tokamaks.

I. INTRODUCTION

Zonal flows (ZFs) in magnetic confinement devices are symmetric low frequency electrostatic perturbations with long radial wave length. They are on the one hand excited by the nonlinear interaction of drift wave turbulence, and on the other hand regulate the turbulence level through the radially sheared plasma flow and meanwhile as a turbulence energy sink[1,2]. A recent numerical fluid simulation confirmed that ZFs play a dominant role in the saturation of turbulence in the core of tokamak plasmas where the safety factor is low3. Recent gyro-kinetic simulations of ion temperature gradient (ITG) modes indicated that the plasma heat flux grows

to a high level without saturation when the plasma pressure ratio exceeds a threshold. The mechanism behind this phenomenon is the decrease of zonal flow level caused by the magnetic flutter in plasmas with high thermal/magnetic pressure ratio[4,5]. The reduction of turbulence transport levels was also observed in recent stellarator experiments as ZFs presented[6]. Because of the significant role played by ZFs in plasma turbulence evolution, the investigation of their driving, damping and time evolution is thus of critical importance in determination of turbulence levels for a tokamak discharge. Hence, in the past two decades, ZFs remain to be one of active research areas in fusion plasmas.

The long time (much longer than the ion transit/bounce time) evolution of the flow is determined by the neoclassic polarization, and is expressed as

$$\phi(t) = \left(1 + 1.6q^2/\sqrt{\varepsilon}\right)^{-1}\phi(0) \quad (1)$$

in a large aspect ratio circular cross section approximation, where q is the safety factor and ε is the inverse aspect ratio. This result is called the residual zonal flow in later publications[8-10]. Rosenbluth and Hinton further suggested that this result be adopted in gyro-fluid codes to improve turbulence simulations.

Recent experiments have revealed that plasma rotation, or in other words the plasma mean mass flow, seems ubiquitous in tokamak plasmas, even without momentum injection[11,12]. Hence, it is necessary to extend the study for static plasmas to that for plasmas with rotations. The eigen-value problem of geodesic acoustic modes in such toroidally rotating plasmas was investigated by some authors using fluid models. The mean flow effect on zonal flow generation in slab geometry was considered by Lashkin[15]. Recent kinetic numerical simulations for rotating plasmas indicated that the residual zonal flow level decreases with increasing rotation[16].

In this work, we present a general expression for residual ZFs in a collisionless tokamak

plasma rotating toroidally at arbitrary velocity. The gyro-kinetic equation for the rotating plasma is firstly solved as an initial value problem for high and low Mach numbers. Then a general form of residual ZFs in the intermediate velocity region is introduced through interpolation. The result in the present work is in good agreement with the kinetic numerical simulation for high aspect ratio tokamaks.

II. STARTING EQUATIONS

The linearized gyro-kinetic equation developed by Artun and Tang[18] for toroidally rotating plasmas is solved in response to an initial axisymmetric source potential driven by ITG turbulence. The velocity of equilibrium toroidal flow is $\mathbf{V} = \omega_R(\psi) R^2 \nabla \zeta$, with ζ the toroidal angle variable, R the major radius, ψ the label of magnetic surfaces and $\omega_R(\psi)$ the angular velocity. We introduce a new velocity variable $\mathbf{c} = \mathbf{v} - \mathbf{V}$ and define the guiding center position $\mathbf{X} = \mathbf{x} - \boldsymbol{\rho}$, where $\mathbf{x}$ is the particle position, $\boldsymbol{\rho} = \mathbf{b} \times \mathbf{c} / \Omega$ is the gyro-radius with $\mathbf{b}$ the unit vector along equilibrium magnetic field and $\Omega = eB/m$ is the gyro-frequency. The total particle distribution function is $f = F_0 + \delta f$, with F_0 the equilibrium distribution. The perturbation distribution δf is the summation of two parts, $\delta f = (e\phi) \partial F_0 / \partial E + \delta h$, where ϕ is the perturbation of electrostatic potential and E is the energy variable to be defined in Eq. (4). The equation for the non-adiabatic part δh, in the electrostatic case, is[17]

$$\left[\frac{\partial}{\partial t} + \left(c_\parallel \mathbf{b} + \mathbf{V} + \mathbf{C_D} \right) \cdot \frac{\partial}{\partial \mathbf{X}} \right] \delta h = -e \frac{\partial F_0}{\partial E} \left(\frac{\partial}{\partial t} + \mathbf{V} \cdot \frac{\partial}{\partial \mathbf{X}} \right) [J_0 \phi(\mathbf{X})] - J_0 \frac{e}{\Omega} \mathbf{b} \times \frac{\partial \phi}{\partial \mathbf{X}} \cdot \frac{\partial F_0}{\partial \mathbf{X}}$$

$$+ J_0 \frac{e}{\Omega} \mathbf{b} \times \frac{\partial \phi}{\partial \mathbf{X}} \cdot \left[\left(c_\parallel \mathbf{b} + \mathbf{V} \right) \cdot \nabla \mathbf{V} + \nabla \mathbf{V} \cdot \left(c_\parallel \mathbf{b} + \mathbf{V} \right) \right] \frac{\partial F_0}{\partial E} + S_{nl} \qquad (2)$$

with the drift velocity and energy variable

$$\mathbf{C_D} = \frac{\mathbf{b}}{\Omega} \times \left[\frac{e}{m} \nabla \Phi_0 + \frac{c_\perp^2}{2} \nabla \ln B + \left(c_\parallel \mathbf{b} + \mathbf{V} \right) \cdot \left(\nabla \mathbf{V} + c_\parallel \nabla \mathbf{b} \right) \right] \qquad (3)$$

$$E = \frac{m}{2}c_{\parallel}^{2} + \frac{m}{2}c_{\perp}^{2} - \frac{m}{2}\mathbf{V}^{2} + e\Phi_{0} \qquad (4)$$

where $J_{0} = J_{0}(k_{\perp}\rho)$ is the usual Bessel function, S_{nl} is the initial source contributed from the nonlinear interaction of ITG turbulence, Φ_{0} is the equilibrium electrostatic potential. We have written potential perturbation in an eikonal form, i. e. $\phi(\mathbf{x}) = \phi_{k}\exp[iS(\mathbf{x}_{\perp})]$, and defined $\mathbf{k}_{\perp} = \nabla S$. The equilibrium distribution is a function of two adiabatic invariables, the energy variable given by Eq. (4) and the magnetic moment variable defined as $\mu = (1/2B)mc_{\perp}^{2}$. The usual form of the equilibrium distribution is

$$F_{0} = \frac{N_{0}(\psi)}{\mathbf{v}_{T}^{2}\pi^{3/2}}\exp(-E/T) \qquad (5)$$

where $T = T(\psi)$ is temperature and $\mathbf{v}_{T} = (2T/m)^{1/2}$.

Thus far, particle species are not distinguished. For a simple plasma consisting of electrons and one species of ions with unit charge, the equilibrium quasi-neutrality condition requires the equilibrium potential to take the form[18-20]

$$\Phi_{0} = \frac{m_{i}V^{2}}{2e(1+\tau^{-1})} \qquad (6)$$

where $\tau = T_{e}/T_{i}$. For plasmas with multiple ions the potential can only be obtained by a numerical procedure. In the present work, for simplicity, we adopt the form of Eq. (6) and the energy variable is thus written as

$$E = \frac{m}{2}c_{\parallel}^{2} + \frac{m}{2}c_{\perp}^{2} - \frac{m}{2(1+\tau)}\mathbf{V}^{2} \qquad (7)$$

The perturbation distribution is also written in an eikonal form, i. e. $\delta h = \delta h_{k}\exp[iS(\mathbf{X}_{\perp})]$. The perturbative potential is axisymmetric with toroidal mode number $n = 0$ and dominant poloidal mode number $m = 0$, so that the eikonal is only the function of ψ. It is obvious that terms involving $\mathbf{V}\cdot\frac{\partial}{\partial\mathbf{X}}$ and the second term on the right hand side of Eq. (2) are both equal

to 0. Making use of the explicit form $\nabla \mathbf{V} = \omega_R R(\nabla R \nabla \zeta - \nabla \zeta \nabla R) + R^2 \nabla \omega_R \nabla \zeta$, it is ready to obtain

$$\mathbf{C}_D \cdot \nabla \psi = \frac{mI}{e} c_\parallel \mathbf{b} \cdot \nabla \left(\frac{c_\parallel}{B} \right) + \frac{m}{e} c_\parallel \mathbf{b} \cdot \nabla \left(\omega_R^2 \right) \qquad (8)$$

where we have taken the equilibrium magnetic field to be $\mathbf{B} = \nabla \zeta \times \nabla \psi + I \nabla \zeta$.

Eq. (2) is then reduced to

$$\left\{ \frac{\partial}{\partial t} + \left[c_\parallel \mathbf{b} \cdot \nabla + c_\parallel \mathbf{b} \cdot \nabla (iQ) \right] \right\} \delta h_k = J_0 e \frac{F_0}{T} \frac{\partial \phi_k}{\partial t} + iJ_0 \frac{mF_0}{T} S' \omega_R \phi_k c_\parallel \mathbf{b} \cdot \nabla R^2 + S_k F_0 \qquad (9)$$

where

$$Q = \frac{mS'}{e} \left(I \frac{c_\parallel}{B} + \omega_R R^2 \right) \qquad (10)$$

Noticing that $S' = k_\perp / |\nabla \psi| = k_\perp / RB_p$, we get $Q \sim k_\perp \delta_b$, where δ_b is the ion orbit width. Q is used as a small parameter for the series expansions in the following section. The potential is derived using the quasi-neutrality condition

$$-\frac{e}{T_i} n_0 \phi_k + \int d^3 \mathbf{v} J_0 \delta h_{ik} = \frac{e}{T_e} n_0 \phi_k + \int d^3 \mathbf{v} \delta h_{ek} \qquad (11)$$

where the nonperturbative particle density is no longer a surface function, instead it is

$$n_0 = \int d^3 \mathbf{v} F_0 = N_0 (\psi) e^{\frac{mV^2}{2(T_i + T_e)}} \qquad (12)$$

Eqs. (9) and (11) form a closure to obtain the potential evolution. We have solved the long time evolution of potential for sonic flow cases in Ref. 17, and the form of residual ZFs is exactly the same as the R-H form to the order of $O(Q^2)$.

III. RESIDUAL ZONAL FLOWS AT LOW ROTATION VELOCITY

In this section, we consider a plasma rotating at very low speed, i. e. $\omega_R \sim \partial / \partial t \sim 0$ and the evolution time is much longer than the ion bounce/transit time. The leading order equation

for ions, from Eq. (9), is then

$$\left[c_\| \mathbf{b} \cdot \nabla + c_\| \mathbf{b} \cdot \nabla (iQ) \right] \delta h_{k0} = 0 \qquad (13)$$

We have made an expansion of the distribution by the ordering of ω / ω_b. Writing the solution

in the form $\delta h_{k0} = g \exp(-iQ)$, one obtains

$$\mathbf{b} \cdot \nabla g = 0 \qquad (14)$$

The next ordering components of Eq. (9) for ions yield

$$\frac{\partial}{\partial t} \left(g e^{-iQ} \right) + \left[c_\| \mathbf{b} \cdot \nabla + c_\| \mathbf{b} \cdot \nabla (iQ) \right] \delta h_{k1} = J_0 e \frac{F_{i0}}{T_i} \frac{\partial \phi_k}{\partial t} + i J_0 \frac{m_i F_{i0}}{T_i} S' \omega_R \phi_k c_\| \mathbf{b} \cdot \nabla R^2 + S_{ik} F_{i0} \quad (15)$$

Multiplying by e^{iQ} on both sides and taking the orbit average, one reaches

$$\frac{\partial}{\partial t} g = \overline{J_0 e^{iQ}} \frac{e F_{i0}}{T_i} \frac{\partial \phi_k}{\partial t} + i \frac{m_i F_{i0}}{T_i} S' \omega_R \phi_k \overline{J_0 e^{iQ} c_\| \mathbf{b} \cdot \nabla R^2} + \overline{e^{iQ} S_{ik}} F_{i0} \qquad (16)$$

where the orbit average is defined as

$$\overline{A} = \frac{\oint A dl / |c_\||}{\oint dl / |c_\||} \qquad (17)$$

the integration is carried out along the trajectory of particles while its poloidal projection forms

a closed line.

The electron distribution is readily obtained from Eq. (9) to be

$$\delta h_{ek} = -(e F_{e0} / T_e) \phi_k \qquad (18)$$

For ions, we need to specify the source term. For ITG turbulence, we take $S_{ek} = 0$ and

$S_{ik} = [\delta n(0) / n_0] \delta(t)$. The potential perturbation is accompanied by an initial density

perturbation in a few gyro-periods due to the classical polarization and quasi-neutrality

condition. Thus, we have[7] $\delta n(0) = (k_\perp \rho_t)^2 (e / T_i) \phi_k(0)$, where

$\rho_t = (T_i / m_i)^{-1/2} / \Omega_i$

Taking the Laplace transformation of Eq. (16), noting the time scale separation between the

particle transition/bounce and the potential evolution, one obtains

$$G(p) = \frac{eF_{i0}}{T_i} J_0 e^{iQ} \Phi_k(p) + \frac{1}{p}\left[\frac{eF_{i0}}{T_i}(k_\perp \rho_t)^2 \overline{e^{iQ}} \phi_k(0) + i\frac{m_i F_{i0}}{T_i} S' \omega_R \overline{J_0 e^{iQ} c_\parallel \mathbf{b}\cdot \nabla R^2}\Phi_k(p) \right]$$

(19)

where $G(p) = \int_0^{+\infty} g(t)e^{-pt}dt$ and the same operation to get $\Phi_k(p)$.

Making Laplace transformation and the surface average on Eq. (11), inserting Eqs. (18) and (19), one finally obtains

$$\Phi_k(p) = \frac{\Phi_k(0)(k_\perp \rho_t)^2 \oint \dfrac{dl}{B} n_0}{p\left[\oint \dfrac{dl}{B} n_0 - \oint \dfrac{dl}{B}\int d^3\mathbf{v} J_0 e^{-iQ}\overline{J_0 e^{iQ}}F_{i0}\right] - i\oint\dfrac{dl}{B}\int d^3\mathbf{v}\dfrac{m_i F_{i0}}{e} S'\omega_R \overline{J_0 e^{iQ}c_\parallel \mathbf{b}\cdot\nabla R^2}}$$

(20)

It is obvious that the second term in the denominator is zero since the term under integration is an odd function of velocity. The denominator can be further simplified. Using

$$d^3\mathbf{v} = d^3\mathbf{c} = \sum_{\sigma_v = \pm 1} \frac{2\pi B}{m^2 |c_\parallel|} d\mu dE , \text{ we notice that}$$

$$\oint\frac{dl}{B}\int d^3\mathbf{v}\overline{A} = \oint\frac{dl}{B}\int d^3\mathbf{v}A \quad (21)$$

Making the power expansion

$$J_0 e^{iQ} \cong 1 - iQ - Q^2/2 - (k_\perp \rho)^2/4 \quad (22)$$

and keeping up to $O(Q^2)$ in the denominator of (20), one reaches

$$\Phi_k(p) = \frac{(k_\perp \rho_t)^2 \langle n_0\rangle \phi_k(0)}{p\left[(k_\perp \rho_t)^2 \langle n_0\rangle + \oint\dfrac{dl}{B}\int d^3\mathbf{v}\left(\overline{Q^2} - \overline{Q}^2\right)F_{i0}\right]} \quad (23)$$

where $\langle n_0\rangle = \oint\dfrac{n_0 dl}{B}$.

Eq. (23) has exactly the same form as that of R-H except for the definitions of Q and the orbit average.

We consider a large aspect ratio tokamak with circular cross section and set $I = B_0 R_0$ in Eq. (10). Inserting (10) in (23), using (21) and making an inverse Laplace transformation, one

173

can write the residual ZFs in the form of Eq. (1)

$$\phi(t) = \left(1 + q^2 F(M)/\sqrt{\varepsilon}\right)^{-1} \phi(0) \quad (24)$$

with $q = rB_0/R_0 B_p$ the usual safety factor, $\varepsilon = r/R_0$ the inverse aspect ratio and

$$F(M) = F_1(M) + F_2(M) \quad (25a)$$

$$F_1(M) = \frac{1}{\langle n_0 \rangle v_t^2 \varepsilon^{3/2}} \oint \frac{dl}{B} \int d^3 v \left[\left(c_{\parallel} B_0/B\right)^2 - \overline{\left(c_{\parallel} B_0/B\right)^2}\right] F_{i0} \quad (25b)$$

$$F_2(M) = \frac{2(1+\tau)M^2}{\langle n_0 \rangle \varepsilon^{3/2}} \oint \frac{dl}{B} \int d^3 v \left[\left(R/R_0\right)^4 - \overline{\left(R/R_0\right)^2}^2\right] F_{i0} \quad (25c)$$

where we define the Mach number $M = \omega_R R_0 /[2(T_e + T_i)/m_i]^{1/2}$ and $v_t = (T_i/m_i)^{1/2}$.

Eqs. (24) (25) are derived under the assumption of slow rotation, $i.\ e.$ $M \ll 1$. Obviously,

the R-H result is recovered for $M = 0$.

In the previous work, we have derived residual ZFs for $M \sim 1$ in the form of Eq. (24) with

$F_2(M) = 0$. It is difficult to solve the problem for arbitrary flow velocity since the ordering

expansion of Eq. (9) is not applicable except for $M \sim 0$ and $M \sim 1$. We can obtain the form

of residual ZFs for arbitrary Mach numbers through an interpolation. One such a

generalization is

$$F_2(M) = \frac{2(1+\tau)M^2}{\langle n_0 \rangle \varepsilon^{3/2}} e^{-\xi M^2} \oint \frac{dl}{B} \int d^3 v \left[\left(R/R_0\right)^4 - \overline{\left(R/R_0\right)^2}^2\right] F_{i0} \quad (26)$$

with ξ a large number to ensure that $F_2(M) \sim 0$ for $M \sim 1$. In the next section, we show

that $F_2(M)$ is negligible in the whole range of M.

IV NUMERICAL RESULTS OF RESIDUAL ZFS AND COMPARISON WITH
SIMULATION

In this section, we give some numerical results of residual ZFs for a large aspect ratio circular

tokamak. The major radius $R = R_0 + r\cos\theta$, the equilibrium magnetic field

$B = B_0 /(1 + \varepsilon \cos \theta)$. Then in the power expansion of ε we have

$$\langle n_0 \rangle = 2\pi q R_0 N_0 e^{M^2} [1 + (1.5 + M^2) M^2 \varepsilon^2 + \cdots] / B_0 \qquad (27)$$

for convenience we introduce $\sigma = 1 + (1.5 + M^2) M^2 \varepsilon^2 + \cdots$.

It is straightforward to carry out the integration for the first parts in the square brackets of (25b) and (26) for any Mach number. Also in the power series of ε, one obtains

$$F_1(M) = \frac{1}{\sigma \varepsilon^{3/2}} \left\{ \left[1 + \left(1.5 + 3.5 M^2 + M^4 \right) \varepsilon^2 + \cdots \right] - \frac{B_0}{2\pi q R_0 N_0 e^{M^2}} \oint \frac{dl}{B} \int d^3 v \overline{(c_\parallel B_0 / B)}^2 F_{i0} \right\} \qquad (28)$$

and

$$F_2(M) = \frac{2(1+\tau) M^2}{\sigma \varepsilon^{3/2}} e^{-\xi M^2} \left\{ \left[1 + \left(5 + 5.5 M^2 + M^4 \right) \varepsilon^2 + \cdots \right] - \frac{B_0}{2\pi q R_0} \oint \frac{dl}{B} \int d^3 v \overline{(R / R_0)}^2 F_{i0} \right\} \qquad (29)$$

To perform integrations in (28) (29), we introduce two variables: $\hat{E} = E + A_M$ and $\lambda = \dfrac{\mu B_0}{\hat{E}}$, where $A_{M/m} = \dfrac{m \omega_R^2 R_{M/m}^2}{2(1+\tau)}$ and $R_{M/m} = R_0 (1 \pm \varepsilon)$ is the maximum/minimum values of R. Then, from Eq. (7), we obtain the parallel velocity

$$|c_\parallel| = \left(\frac{2\hat{E}}{m} \right)^{1/2} \left[1 - \frac{m \omega_R^2}{2\hat{E}(1+\tau)} \left(R_M^2 - R^2 \right) - \frac{\lambda B}{B_0} \right]^{1/2} \qquad (30)$$

The regions of passing and trapped particles can be figured out in $(\mu, \hat{E})$ as shown in Fig. 1 of Ref. 17. It is obvious that only passing particles contribute to the integral in (28) while all particles contribute in (29). The integration over passing particles is

$$\iint (\cdots) d\mu dE = \int_{\Delta A}^{+\infty} d\hat{E} \int_{\varepsilon + (1-\varepsilon)\Delta A / \hat{E}}^{1} (\cdots)(\hat{E} / B_0) d\eta \qquad (31)$$

where $\eta = 1 - \lambda$ and $\Delta A = A_M - A_m$.

For small ε, we can use the expansion technique to carry out the integration in (28), the process is tedious but straightforward[8,10]. The final result involves the incomplete Gamma function $\int_{4M^2}^{+\infty} x^{3/2-k} e^{-x} dx$. Further analytical expression is impossible for arbitrary M values. For $M \sim 1$, we have made an adiabatic expansion of the incomplete Gamma function and given an approximate expression[17]

$$F_1(M) \cong 4.4M^3 + 0.32M + 0.66M^{-1} + 0.015M^{-3} + (0.5 + 2.5M^2 - 2M^4)\varepsilon^{1/2} + \cdots \quad (32)$$

For $M \sim 0$, we can make a Taylor series expansion in evaluating the incomplete Gamma function and get an approximate expression

$$F_1(M) \cong 1.6 + 3.34M^2 - 1.6M^4 + (0.5 - 2M^4)\varepsilon^{1/2} + (0.375 - 2.4M^2 + 3.9M^4)\varepsilon + \cdots \quad (33)$$

It is difficult to find such approximate expressions for $F_2(M)$ since it is much involved to have an integration over trapped particles in (29). We have also calculated $F_1(M)$ and $F_2(M)$ by numerically carrying out the integration in (28) and (29).

Plotted in Fig. 1 are the curves of $F_1(M)$ and $F_2(M)$, with parameters $q = 2.5$, $\varepsilon = 0.3$ and $\xi = 10$. The horizontal axis is labeled by M^2 instead of M since it is M^2 that appears in most formulas. Numerical and approximate expansion results of $F_1(M)$ are in good agreement. It is obvious that $F_2(M)$ is negligible since it accounts for less than 5% of $F(M)$ for the whole range of M. In Fig. 2 we plot the level of residual ZFs changing with the square Mach number, as well as the R-H result given by $F(M) \cong 1.6 + 0.5\varepsilon^{1/2} + 0.375\varepsilon + \cdots$. The level of ZFs decreases with increasing Mach number which is in qualitative agreement with a recent numerical gyro-kinetic simulation[16]. The physical explanation is that in a rotating plasma the fraction of trapped particles increases because of the inertial forces and as a result the neoclassic polarization effect increases to lower the residual ZFs. To have a quantitative comparison with the numerical simulation, we calculate residual ZFs using the same parameters as those in Ref. 16. Results are shown in Fig. 3 with the horizontal axis labeled by M. Making a careful comparison between Fig. 3 and the Fig. 12 of Ref. 16, we notice that good agreement is achieved for low ε values while higher discrepancies appear for higher ε values. It is understandable because we have made Taylor series expansions in ε to derive (28) and (29), higher ε may bring about larger errors in expansions.

V. SUMMARY AND DISCUSSION

In this work a general form of residual ZFs in a tokamak plasma toroidally rotating at arbitrary velocity is presented. We first solve the gyro-kinetic equation by ordering expansion for low rotation velocity and then apply the quasi-neutrality condition to derive the long time potential evolution. The form of residual ZFs at low Mach numbers is given by Eq. (24) together with Eqs. (25a-c). The generalized form is given by Eq. (24) together with Eqs. (25a,b) and (26). Numerical evaluation indicates that in Eq. (25a) F_2 is much lower than F_1 for the whole range of Mach numbers. If the F_2 term is neglected, the form of residual ZFs given by Eq. (24) is exactly the same as the R-H form except for the definition of orbit average. This is not a mere coincidency. The neoclassic polarization arises from the difference of guiding center orbits between ions and electrons. If we transform to the rotating framework, process of the neoclassic polarization would be the same except for that the drift of single particles is changed by inertial forces, which is embodied in the definition of orbit average. Although expressions are the same, the numerical result is different due to the different definition of orbit average, the different fraction of trapped particles and the non-uniformity of density on magnetic surfaces.

Numerical evaluation indicates that the level of residual ZFs decreases with increasing Mach numbers which is qualitative agreement with previous gyro-kinetic simulations. Quantitative agreement is satisfactory in high aspect ratio limit. The discrepancy in lower aspect ratio is due to the power series expansion in inverse aspect ratio in our calculation. So the general expression given by Eq. (24) is valid for arbitrary rotation velocity and can be adopted in plasma simulations.

REFERENCES

[1] P. H. Diamond, S.-I. Itoh, K. Itoh, and T. S. Hahm, Plasma Phys. Controlled Fusion 47, R35 (2005).

[2] K. Itoh, S.-I. Itoh, P. H. Diamond, T. S. Hahm, A. Fujisawa, G. R. Tynan, M. Yagi, and Y. Nagashima, Phys. Plasmas 13, 055502 (2006).

[3] R. E. Waltz and C. Holland, Phys. Plasmas 15, 122503 (2008).

[4] M. J. Pueschel, P. W. Terry, F. Jenko, D. R. Hatch, T. Gorler, W. M. Nevins, and D. Told, Phys. Rev. Lett. 110, 155005 (2013).

[5] P. W. Terry, M. J. Pueschel, D. Carmody, and W. M. Nevins, Phys. Plasmas 20, 112502 (2013).

[6] G. Birkenmeier, M. Ramisch, B. Schmid, and U. Stroth, Phys. Rev. Lett. 110, 145004 (2013).

[7] M. N. Rosenbluth and F. L. Hinton, Phys. Rev. Lett. 80, 724 (1998).

[8] Y. Xiao and P. J. Catto, Phys. Plasmas 13, 082307 (2006).

[9] Y. Xiao, P. J. Catto, and W. Dorland, Phys. Plasmas 14, 055910 (2007).

[10] D. Zhou and W. Yu, Phys. Plasmas 18, 052505 (2011).

[11] M. Yoshida, Y. Kamada, H. Takenaga, Y. Sakamoto, H. Urano, N. Oyama, G. Matsunaga, and the JT-60 Team, Phys. Rev. Lett. 100, 105002 (2008).

[12] W. M. Solomon, K. H. Burrell, A. M. Garofalo, S. M. Kaye, R. E. Bell, A. J. Cole, J. S. deGrassie, P. H. Diamond, T. S. Hahm, G. L. Jackson, M. J. Lanctot, C. C. Petty, H. Reimerdes, S. A. Sabbagh, E. J. Strait, T. Tala and R. E. Waltz, Phys. Plasmas 17, 056108 (2010).

[13] S. Wang, Phys. Rev. Lett. 97, 085002 (2006).

[14] C. Wahlberg, Phys. Rev. Lett. 101, 115003 (2008).

[15] V. M. Lashkin, Phys. Plasmas 15, 124502 (2008).

[16] F. J. Casson, A. G. Peeters, C. Angioni, Y. Camenen, W. A. Hornsby, A. P. Snodin, and G. Szepesi, Phys. Plasmas 17, 102305 (2010).

[17] D. Zhou, Nucl. Fusion 54, 042002 (2014).

[18] M. Artun and W. M. Tang, Phys. Plasmas 1, 2682 (1994).

[19] L.-J. Zheng and M. Tessarotto, Phys. Plasmas 5, 1403 (1998).

[20] A. G. Peeters, D. Strintzi, Y. Camenen, C. Angioni, F. J. Casson, W. A. Hornsby, and A. P. Snodin, Phys. Plasmas 16, 042310 (2009).

[21] E. Kim and P. H. Diamond, Phys. Plasmas 10, 1698 (2003).

[22] J. Anderson and Y. Kishimoto, Phys. Plasmas 13, 102304 (2006).

[23] Deng Zhou, The residual zonal flow in tokamak plasmas toroidally rotating at arbitrary velocity, Phys. Plasmas, Vol. 21, 082508, 2014.
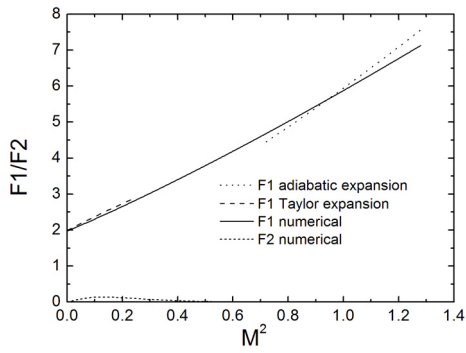
Fig. 1 Values of F_1 and F_2, with parameters $q = 2.5$, $\varepsilon = 0.3$ and $\xi = 10$.
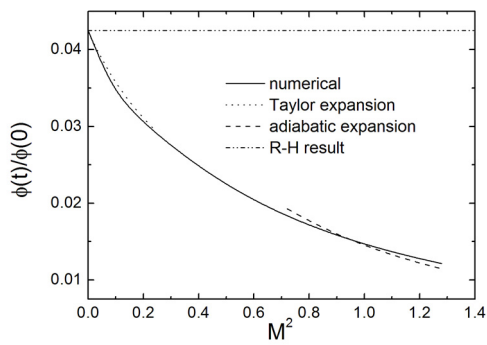
Fig. 2 The residual zonal flow level changes with squared Mach numbers with parameters $q = 2.5$, $\varepsilon = 0.3$ and $\xi = 10$. Solid line is the result by numerically carrying out the integration in (25b) and (26). Dot line is the result given by (24) and (33) with F_2 neglected. Dash line is given by (24) and (32).
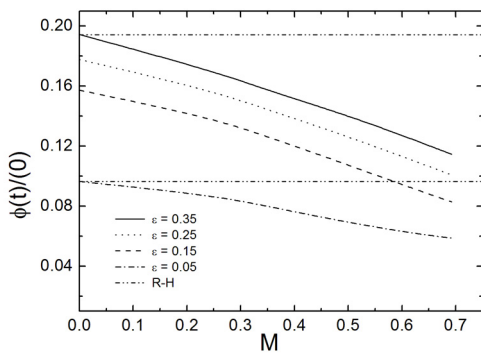
Fig. 3 The residual zonal flow level changes with Mach numbers with parameters $q = 1.1$ and $\xi = 10$ for different ε values.

Design of geometric phase measurement on EAST Tokamak

T. Lan[12], H. Q. Liu[2], J. Liu[1], Y. X. Jie[2], X. Gao[2], H. Qin[1]

1. Department of Modern Physics, University of Science and Technology of China, Hefei, Anhui 230026, China

2. Institute of Plasma Physics, Chinese Academy of Sciences, Hefei, Anhui 230031, China

Abstract:

The optimum scheme for geometric phase measurement in plasma is proposed. The theoretical values of geometric phase for the probe beams of EAST Polarimeter/Interferometer (POINT) system are calculated by path integration in parameter space and the influences of some controllable parameters on geometric phase are evaluated. The feasibility and problems of distinguishing geometric effect in the POINT signal are assessed.

Keywords: Geometric phase measurement; Faraday rotation angle; Ray tracing equations;

1. Introduction:

Geometric phase is firstly discovered in quantum mechanics, afterwards proved to exist in classical mechanics. Lately J. Liu and H. Qin prove that the variation of the propagation direction of circularly polarized waves results in geometric phase, which also contributes to the Faraday rotation, in addition to the standard dynamical phase. This research can amend the diagnostic accuracy of POINT system in tokamak, the diagnostic principle of which is to obtain the current density profile by reversal of the Faraday rotation angle. The present data processing method for POINT system only takes the dynamical phase which depends on the plasma dispersion relation into account in the Faraday rotation angle while ignoring the geometric phase which depends on the wave propagation path. As a result the geometric effect is an error source in the tokamak current diagnosis and the influence would be higher in the future ITER and other fusion reactors with higher parameters. Verification and assessment of the geometric quotient in Faraday rotation experimentally is of physical significance and feasible in hardware with the POINT system.

Theories about geometric phase are abundant while relevant experiments are comparatively rare. One typical experiment designed for verifying the existence of geometric phase is performed by comparing the Faraday rotation angle of a linearly polarized laser before and after transmitting through helical fibers of different deformation modes, which inspires that the light propagation path should be explicit to calculate the theoretical value of geometric phase in plasma.

In this paper, the beam path in plasma is simulated by ray-tracing equations with the fourth-order Runge-Kutta method employed, afterwards the geometric phase is computed by integrating along wave vector in parameter space with Polynomial fitting.

Given that various parameters have different levels of impact on geometric effect and appropriate combination gives the optimum experimental conditions for geometric phase measurement in plasma, the simulation results can be divided into three parts: Firstly, the refraction and frequency of incident wave effect on geometric phase are demonstrated; Secondly, the density distribution and safety factor q effect on geometric phase are estimated; Thirdly, the toroidal installation error effect and the retro reflector effect on geometric phase are investigated. The feasibility of distinguishing geometric effect in the POINT signal is assessed, and the optimum scheme for geometric phase measurement in plasma is proposed.

2. Significance and hardware conditions for geometric phase measurement on EAST Tokamak

As an important diagnosis in tokamak, three waves polarimeter-interferometer (PI) technique utilizes two collinearly circular polarized lasers of counter-rotating to acquire current density profile by reversal of the Faraday rotation angle and one linearly polarized laser as reference light to obtain electron density profile by reversal of phase shift. Considering that the geometric phases for left and right circularly polarized lights in the same path are equal and opposite, the geometric amendment would exist in the Faraday rotation angle and counteract in the phase shift for the linearly polarized probe beam, which can be decomposed into left and right circularly polarized lights. Therefore in inhomogeneous plasma the rotation angle of polarization direction for linearly polarized probe beam contains two parts: the dynamic phase which depends on the plasma dispersion relation, and the geometric phase which depends on the wave propagation path. Considering that geometric effect is greater with higher plasma parameters, verification and assessment of the geometric quotient in Faraday rotation would be more and more necessary in the future discharge of fusion device.

The present far-infrared double-pass, radially-viewing, multichannel EAST POINT system gives reasonable current density profiles with Faraday rotation angle resolution of about 0.1 degree, which lays a solid foundation for the hardware design of geometric measurement.

3. Theoretical calculations for geometric phase in plasma

In collisionless cold plasma the dispersion relations for right and left circularly polarized waves paralleled to the magnetic field are:

$$N^2 = 1 - \sum_\alpha \frac{\omega_{p\alpha}^2}{\omega(\omega \pm \omega_{c\alpha})} \cdots \cdots \quad (1)$$

Where $\omega_{p\alpha}$ and $\omega_{c\alpha}$ are the plasma frequency and gyrofrequency for particles of species α, respectively. And the right and left here are defined with respect to the background field. When the characteristic variation length scale and variation time scale of the plasma are much longer than the wave-length and the period of incident wave, the Ray tracing equations can be used:

$$\vec{k} = \frac{\partial D}{\partial \vec{r}} \Big/ \frac{\partial D}{\partial \omega} = F_a$$
$$\vec{r} = -\frac{\partial D}{\partial \vec{k}} \Big/ \frac{\partial D}{\partial \omega} = F_b \Bigg\} \cdots \cdots \quad (2)$$

Here $D = k^2 - \dfrac{\omega^2}{c^2} N^2$ characterizes the plasma properties. With equation (1) substituted, we can get:

$$\frac{\partial D}{\partial \vec{r}} = \frac{1}{c^2} \sum_\alpha \left[\frac{\omega \omega_{p\alpha}^2}{(\omega \mp \omega_{c\alpha}) n_\alpha} \cdot \frac{\partial n_\alpha}{\partial \vec{r}} \pm \frac{\omega \omega_{p\alpha}^2 q_\alpha}{(\omega \mp \omega_{c\alpha})^2 m_\alpha} \cdot \frac{\partial B}{\partial \vec{r}} \right]$$
$$\frac{\partial D}{\partial \omega} = \frac{1}{c^2} \left[-2\omega \mp \sum_\alpha \frac{\omega_{p\alpha}^2 \omega_{c\alpha}}{(\omega \mp \omega_{c\alpha})^2} \right] \Bigg\} \cdots \quad (3)$$
$$\frac{\partial D}{\partial \vec{k}} = 2\vec{k}$$

With cylindrical approximation, the magnetic field can be expressed as:

$$\vec{B} \approx \frac{B_0 R_0}{R} \vec{e}_z + \frac{r B_t}{qR} \vec{e}_\varphi \cdots \cdots \quad (4)$$

The density profile and safety factor profile are assumed as:

$$q = c_1 [(x - R_0)^2 + y^2]^{N_q/2} + c_2 \cdots \cdots \quad (5)$$
$$n_\alpha = c_4 [(x - R_0)^2 + y^2]^{N_n/2} + c_3 \cdots \cdots \quad (6)$$

With Fourth-order Runge-Kutta method employed, the ray tracing equations can be expressed as follows:

$$\vec{k}(n+1) = \vec{k}(n) + \Delta t F_a[\vec{r}(n)]$$
$$\vec{r}(n+1) = \vec{r}(n) + \frac{\Delta t}{6} \left\{ F_{b1}[\vec{r}(n), \vec{k}(n)] + 2 F_{b2}[\vec{r}(n), \vec{k}(n)] \right.$$
$$\left. + 2 F_{b3}[\vec{r}(n), \vec{k}(n)] + F_{b4}[\vec{r}(n), \vec{k}(n)] \right\}$$
$$F_{b1}[\vec{r}(n), \vec{k}(n)] = F_b[\vec{r}(n), \vec{k}(n)]$$
$$F_{b2}[\vec{r}(n), \vec{k}(n)] = F_b[\vec{r}(n) + \frac{\Delta t}{2} F_{b1}[\vec{r}(n), \vec{k}(n)], \vec{k}(n) + \frac{\Delta t}{2} F_a[\vec{r}(n)]]$$
$$F_{b3}[\vec{r}(n), \vec{k}(n)] = F_b[\vec{r}(n) + \frac{\Delta t}{2} F_{b2}[\vec{r}(n), \vec{k}(n)], \vec{k}(n) + \frac{\Delta t}{2} F_a[\vec{r}(n)]]$$
$$F_{b4}[\vec{r}(n), \vec{k}(n)] = F_b[\vec{r}(n) + \Delta t F_{b3}[\vec{r}(n), \vec{k}(n)], \vec{k}(n) + \Delta t F_a[\vec{r}(n)]]$$
$$(7)$$

With equations (2)~(7), the trajectory of probe beam in plasma can be decided.

Considering the wave vector changing slowly because of adiabatic approximation, the expression of type I geometric phase can be calculated by polynomial fitting shown as equation (8).

$$\theta_{gl} = m\int_{incident\ point}^{emergent\ point} \frac{k_z(K_x dK_y - K_y dK_x)}{K(K_x^2 + K_y^2)}\ldots\ldots \quad (8)$$

4. Conclusions

In summary, the refraction effect in inhomogeneous plasma results in different levels of path deflection for left and right circularly polarized waves, and hence leads to observable geometric effects of different quotient in the Faraday rotation measurement. The incident frequency, incidence position, density profile, safety factor profile, toroidal and poloidal installation angles can influence the geometric effect in varying degrees. Controlling the incident frequency or density profile in the right position can increase the geometric phase to 0.01°, while the present Faraday rotation angle resolution is 0.1°, not big enough to distinguish the geometric effect. Increasing the toroidal installation angle can add the geometric angle up to 0.1°; nevertheless the cotton mutton effect would increase as well. Given these, the geometric phase is difficult to distinguish in the present POINT system. Next step three improvement approaches can be adopt to realize the geometric measurement experiment. Firstly, the system resolution can be improved to 0.05° by collinear adjustment; secondly, an optical path can be desired for Geometric measurement, for example, increasing the path length in plasma or increasing the density and density gradient; Thirdly, deliberately controlling the included angle between detected beam and toroidal magnetic field would work if the cotton mutton effect and geometric effect can be told apart. At the same time, the geometric phase generated by discrete optical systems can be calculated by the theory of M. Kitano, given that most mirrors can be considered as ideal conductor for far infrared light.

5. Reference

[1] Akira Tomita Observation of Berry's Topological Phase by Use of an Optical Fiber

[2] jianliu Geometric phases of the Faraday rotation of electromagnetic waves in magnetized plasmas

[3] H Q Liu Design of far-infrared polarimeter_interferometer system for EAST tokamak

[4] M. V. Berry, Quantal phase factors accompanying adiabatic changes

[5] M. Kitano Comment on Observation of Berry's Topological Phase by Use of an Optical Fiber

[6] Barry Simon Holonomy, the Quantum Adiabatic Theorem, and Berry's Phase

[7] T. Lan Study of the propagation properties of 432 lm laser reflected by retro reflector array

[8] G. Dodel and W. Kunz, A far-infrared 'polari-interferometer' for simultaneous electron density and magnetic field measurement in plasmas.

Numerical simulation on nonlinear effects in extraordinary to Bernstein mode conversion

Jianyuan Xiao,[1,2] Jian Liu,[1,2,*] Hong Qin,[1,3] Zhi Yu,[4] and Nong Xiang[4]

[1] *Department of Modern Physics and School of Nuclear Science and Technology, University of Science and Technology of China, Hefei, Anhui 230026, China*

[2] *Key Laboratory of Geospace Environment, CAS, Hefei, Anhui 230026, China*

[3] *Plasma Physics Laboratory, Princeton University, Princeton, New Jersey 08543, USA*

[4] *Theory and Simulation Division, Institute of Plasma Physics, Chinese Academy of Sciences, Hefei, Anhui 230031, China*

I. INTRODUCTION

Electron Bernstein waves (EBWs) have shown the potential for providing heating and current drive in overdense plasmas [1–4], where the usual electron cyclotron heating and current driving (ECH and ECCD) are unusable. Two different approaches are commonly used for coupling rf power to EBWs, The first one O-X-B is a double mode conversion process. In this scheme an O mode is launched obliquely relative to the magnetic field into the plasma and is then coupled to the slow X mode, which is in turn mode converted into an EBW [4, 5]. The second technique X-B involves tunneling of a perpendicularly launched fast X mode through a cutoff region at the plasma edge to the slow X mode, which in turn converts to an EBW. The X-B scheme requires steeper plasma density profile, which is available in some sperical tokamaks (STs) [6–9]. In this paper, we report the first variational symplectic PIC simulation study of nonlinear mode conversion of extraordinary waves in nonuniform magnetized plasmas [10]. For nonlinear mode conversions, where the timescale of the mode conversion is much larger than the periods of the rf waves, long-term simulations are inevitably required. Suffering no accumulation of the global errors, the variational symplectic PIC method shows its unparalleled advantage in the long-term simulations and provides accurate nonlinear results. Simulation results show that nonlinear effects significantly modify the physics of the radio-frequency (rf) injection in magnetized plasmas. The evolutions of the rf wave reectivity and the energy deposition are observed, as well as the self-interaction of the Bernstein waves and mode excitations.

II. RESULTS OF X-B MODE CONVERSION

The simulation parameters are $n_0 = 2 \times 10^{19} \mathrm{m}^{-3}, B_z = 0.55\mathrm{T}, T_e = 57.6\mathrm{eV}, \Delta l = 2.77 \times 10^{-5}\mathrm{m}, \Delta t = \Delta l/\mathrm{c}, E_1 = 1\mathrm{MV/m}, \omega = 1.62\omega_{ce}$, and

$$n_e(x) = n_0 \exp\left(-\frac{\left(\frac{x}{\Delta l} - (n_r + 320)\right)^2}{(2(n_r/3.5)^2)}\right) \tag{1}$$

where ω is the frequency of the incident wave. Δl is the grid length. Absorbing boundary conditions are used at $x = 0$ and $x = 1792\Delta l$. First phenomenon is the new mode generation. The spectra are investigated and plotted in Fig. 1. It is shown that the mode with frequency 2ω and $\omega' = 0.77\omega$ are generated during the mode conversion.

(a) $[580/\omega, 754/\omega]$ (b) $[812/\omega, 986/\omega]$
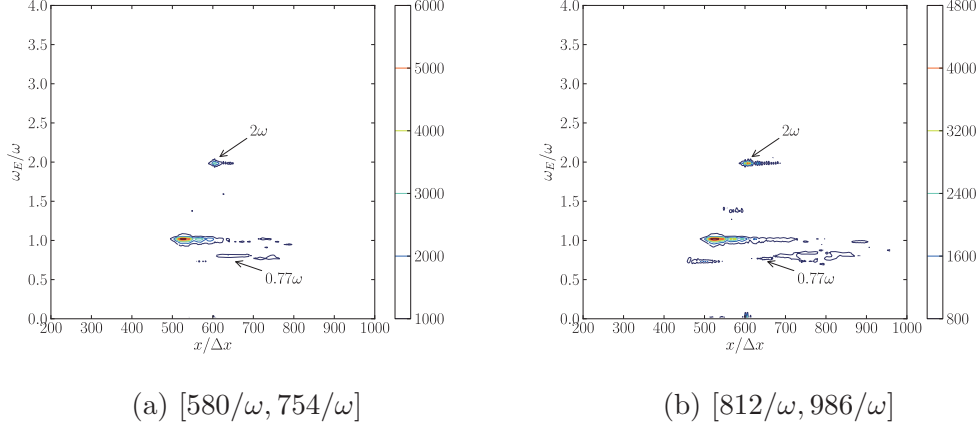
FIG. 1: The evolution of frequency spectra of $E_x(x,t)$ during the nonlinear X-B mode conversion.
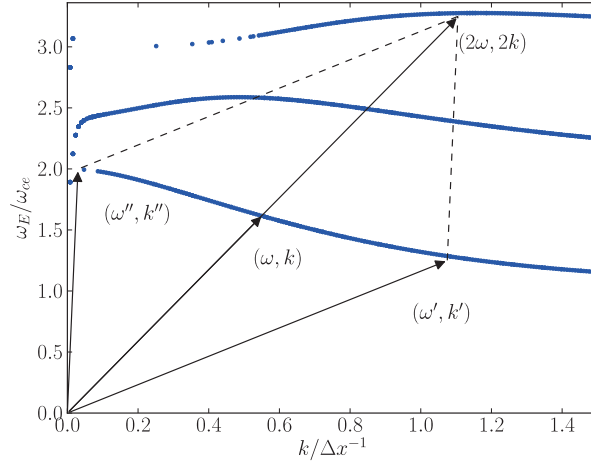
FIG. 2: The dispersion relation of electromagnetic EBWs (blue dots) and wave vectors of the coupled modes (solid arrows). These modes satisfy the relation $k'' + k' = 2k$ and $\omega'' + \omega' = 2\omega$.

This result can be interpreted as a three-wave interation during the X-B mode conversion.

For the wave heating and current driving, one key indicator is the reflectivity of the wave. The relation of reflectivity and density gradient is also investigated, and the results are plotted in Fig. 3. We can see that the reflectivity is increasing during the wave injection,

186
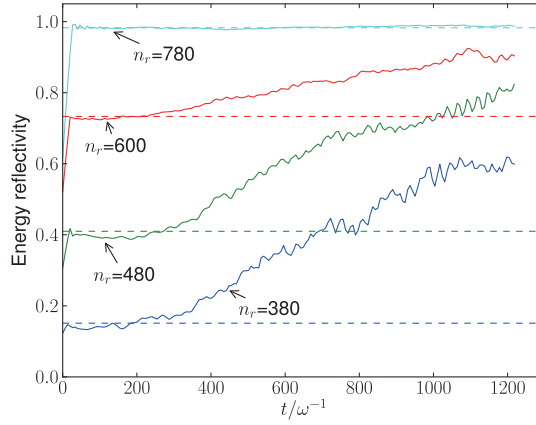
FIG. 3: Comparison of reflectivity with different density gradients. Dashed lines are the reflectivity obtained from linear theory.

and the relation of reflectivity and density gradient is very sensitive.

---

[1] K. Ushigusa, T. Imai, Y. Ikeda, O. Naito, K. Uehara, H. Yoshida, H. Kubo, *et al.*, Nucl. Fusion **29**, 1052 (1989).

[2] Z. Lianmin, S. Jiafang, L. Fukun, J. Hua, W. Mao, L. Liang, W. Xiaojie, and X. Handong, Plasma Sci. Technol. **12**, 118 (2010).

[3] D. Start, J. Jacquinot, V. Bergeaud, V. Bhatnagar, G. Cottrell, S. Clement, L. Eriksson, A. Fasoli, A. Gondhalekar, C. Gormezano, *et al.*, Phys. Rev. Lett. **80**, 4681 (1998).

[4] H. Laqua, V. Erckmann, H. Hartfuß, H. Laqua, *et al.*, Phys. Rev. Lett. **78**, 3467 (1997).

[5] R. Cairns and C. Lashmore-Davies, Phys. Plasmas **7**, 4126 (2000).

[6] H. Kuehl, Phys. Rev. **154**, 124 (1967).

[7] A. Ram and S. D. Schultz, Phys. Plasmas **7**, 4084 (2000).

[8] B. Jones, P. Efthimion, G. Taylor, T. Munsat, J. Wilson, J. Hosea, R. Kaita, R. Majeski, R. Maingi, S. Shiraiwa, *et al.*, Phys. Rev. Lett. **90**, 165001 (2003).

[9] S. Shiraiwa, K. Hanada, M. Hasegawa, H. Idei, H. Kasahara, O. Mitarai, K. Nakamura, N. Nishino, H. Nozato, M. Sakamoto, *et al.*, Phys. Rev. Lett. **96**, 185003 (2006).

[10] J. Xiao, J. Liu, H. Qin, and Z. Yu, Phys. Plasmas **20**, 102517 (2013).

Simulation of Long-term Dynamic Behavior of Runaway Electrons

Yulei Wang, Jian Liu, Ruili Zhang, Yang He

Abstract

The secular dynamics of runaway electrons in Tokamak electromagnetic field is studied. The radiation effect is added into a relativistic volume-preserving algorithm to gain long-term stability of calcucation. The results shows that the method we used is able to reveal the behavior of a runaway electron in configuration space.

Runaway electrons play an important role in the safe operation of Tokamak. Through experimental observations, it has been proved that large mounts of runaway electrons are generated during fast plasma shut down[1] and the disruption[2] in large Tokamaks. Accelerated continuously by electic field[3], a runaway electron may carry considerably high energy up to tens of MeVs, which becomes a serious threat to the life of all the plasma-facing components(PFCs). Besides experimenters, extensive theorists have been devoted to the study of runaway electrons. Because the physical process of runaway electrons has multi-scale in both time and space, theorical and simulation studies are mostly based on guiding-center model. Through averaging out the fast gyromotion and reducing the timespace scale by two or three magnitude orders, gyrocenter approximation saves lots of computation resources and some macroscope dynamical behavior of runaway electrons can be effectively predicted analytically[4-6] and numerically[7, 8].

In our resent work, a probe particle model is established for simulating the secular dynamical behavior of runaway electrons in Tokamaks. Radiation effect is added into the relativistic motion equation while collision resistance is ignored because of the high speed of runaway electrons[3, 9]. In order to gain long-term stability, we have combined radiation terms with a relativisctic volume-preserving algorithm(VPA) [10]. VPAs are a series of advanced geometric algorithm that can preserve the phase-space volume of dynamical system no matter how many steps the calcucation needs. Although the combination of radiation and VPA weakens the geometric property of algorithm, the stability of secular computation remains. During our long-term simulation typically requiring tens of billion steps, some macroscope behaviors of a runaway electron, including circle orbit of passing particles and neo-classical drift of runaway orbit, match well with the results of guiding center theory[7, 11, 12].

The motion of a runaway electron is governed by the relativistic Lorenz force formula[13]. Within our consideration, the collision resistance is ignorable because the speed of simulated runaway electrons is considerably high[3, 9]. And all the energy dissipation comes from the radiaton emitted through the interaction between the electron and background field. In our model, a radiation drag force providing all the radiation energy loss is constructed, which leads to the motion equation with radiation,

$$\frac{d\mathbf{x}}{dt} = \mathbf{v},\qquad(1)$$

$$\frac{d\mathbf{p}}{dt} = q_e(\mathbf{E} + \mathbf{v} \times \mathbf{B}) + \mathbf{F}_R \, ,$$

$$\mathbf{p} = \gamma \mathrm{m}_0 \mathbf{v} \, ,$$

where $\mathbf{x,}$ $\mathbf{v}$ and $\mathbf{p}$ are, respectively, the positon, velocity and mechanical momentum of a runaway electron, q_e denotes the charge of an electron, m_0 is the rest mass of an electron, $\mathbf{E}$ and $\mathbf{B}$ are the electric and magnetic field, and the Lorentz factor γ is defined as

$$\gamma = \sqrt{1 + \frac{p^2}{\mathrm{m}_0^2 c^2}} = \frac{1}{\sqrt{1 - (v/c)^2}} \, . \tag{2}$$

Finally, $\mathbf{F}_R$ denotes the radiation drag force, namely,

$$\mathbf{F}_R = -P_R \frac{\mathbf{v}}{v^2} \, . \tag{3}$$

The radiation power for relativistic charged particle, the Larmor formula[13], is

$$P_R = \frac{q_e^2}{6\pi\epsilon_0 c} \gamma^6 \left[\left(\frac{\mathbf{a}}{c}\right)^2 - \left(\frac{\mathbf{v}}{c} \times \frac{\mathbf{a}}{c}\right)^2 \right] , \tag{4}$$

where ϵ_0 is the permittivity in vacuum, c is the speed of light in vacuum, $\mathbf{a} = d\mathbf{v}/dt$ denotes the acceleration of the particle. According to Eqs. (2)-(4), radiation drag force is a function of velocity and acceleration, namely, $\mathbf{F}_R = \mathbf{F}_R(\mathbf{v}, \mathbf{a})$.

Since the dynamics of a runaway electron has multi-scale in time and space, it is necessary to compute tens of billion steps for a complete simulation. In order to guarantee secular stability, we discretize the motion Eq. (1) based on a relativistic volume-preserving algorithm, namely,

$$\mathbf{a}^k = \frac{\mathbf{v}^k - \mathbf{v}^{k-1}}{\Delta t} \, ,$$

$$\mathbf{F}_R^k = \mathbf{F}_R^k(\mathbf{v}^k, \mathbf{a}^k) \, ,$$

$$\mathbf{x}^{k+1/2} = \mathbf{x}^k + \frac{\Delta t}{2} \frac{\mathbf{p}^k}{\sqrt{\mathrm{m}_0^2 + (p^k/c)^2}} \, ,$$

$$\mathbf{p}^- = \mathbf{p}^k + \frac{\Delta t}{2} \left(q_e \mathbf{E}^{k+1/2} + \mathbf{F}_R^k\right) , \tag{5}$$

$$\mathbf{p}^+ = \mathbf{p}^- + q_e \Delta t \left(\frac{\mathbf{p}^- + \mathbf{p}^+}{2\sqrt{\mathrm{m}_0^2 + (p^-/c)^2}} \times \mathbf{B}^{k+1/2}\right) ,$$

$$\mathbf{p}^{k+1} = \mathbf{p}^+ + \frac{\Delta t}{2} \left(q_e \mathbf{E}^{k+1/2} + \mathbf{F}_R^k\right) ,$$

$$\mathbf{x}^{k+1} = \mathbf{x}^{k+1/2} + \frac{\Delta t}{2} \frac{\mathbf{p}^{k+1}}{\sqrt{\mathrm{m}_0^2 + (p^{k+1}/c)^2}} \, .$$

Without radiation terms, the discreted equation is exactly a time-symmetry volume-preserving algorithm(VPA) [10]. Known as excellent property of conservation, volume-preserving algorithms belong to a branch of advanced geometric algorithms that have been widely used in plasma physics[7, 8, 14-18]. Although the added radiation terms in Eq. (5) weakens the geometric property of VPA, the long-term stability of the algorithm remains, which can be prove by the simulation results.

The motion of a runaway electron is calculated in a background electromagnetic field in the form of

$$\mathbf{B} = \frac{B_0 R_0}{R} \mathbf{e}_\xi - \frac{B_0 \sqrt{(R - R_0)^2 + z^2}}{qR} \mathbf{e}_\theta,$$

$$\mathbf{E} = E_l \frac{R_0}{R} \mathbf{e}_\xi,$$

(6)

where $R = \sqrt{x^2 + y^2}$, ξ and z denote, respectively, the radial distance, the azimuth and the height of cylindrical coordinate system, $\mathbf{e}_\xi$ and $\mathbf{e}_\theta$ are the toriodal and poloidal direction of the torus, and q is the safty factor. We choose the parameters based on EAST Tokamak[19]. The center magnetic field intensity is chosen to be $B_0 = 3$T, while the center loop voltage is $E_l = 3$V/m. The major radius is set as $R_0 = 1.7$m. And the safty factor is $q = 2$. The motion of a typical runaway electron, with initial momentum $p_{\parallel 0} = 5 m_0 c$, $p_{\perp 0} = 1 m_0 c$ and initial position $r = 0.1$m, $\theta = \xi = 0$, is computed. Snapshots of the runaway drifting orbit on the poloidal plane at $t = 0 {\sim} 0.045 s$ are depicted in Fig. 1. The drift of circle orbit tells about the macroscope dynamics of a runaway electron. The drift velocity, about 2m/s, matches well with the result of guiding center theory[7] while the radiation effect is weak enough for the first 0.1s. The result serves as an evidence for the secular stability of the discrete format given by Eq. (5).
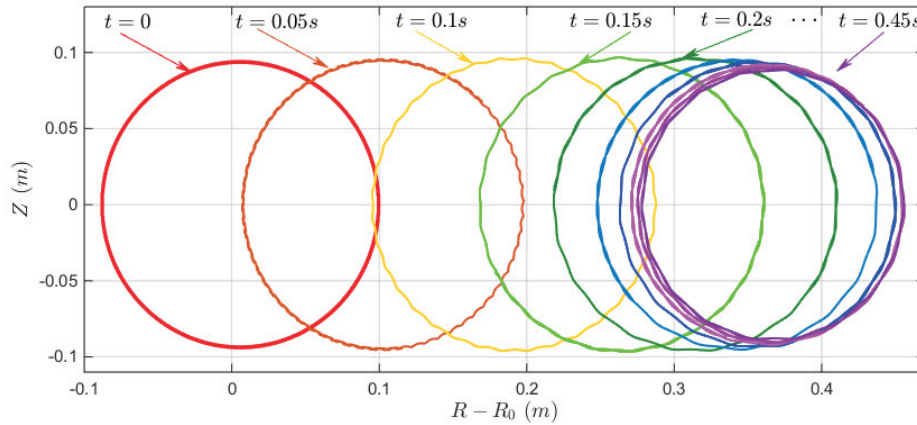
Fig. 1 Snapshots of the runaway drifting orbit projected on the poloidal plane from $t = 0$ to $t = 0.045$s.

References

1. Yoshino, R., et al., *Fast plasma shutdown by killer pellet injection in JT-60U with reduced heat flux on the divertor plate and avoiding runaway electron generation.* Plasma phys. control. fusion, 1997. **39**(2): p. 313.

2. Jaspers, R., et al., *Disruption generated runaway electrons in TEXTOR and ITER.* Nuclear fusion, 1996. **36**(3): p. 367.

3. Dreicer, H., *Electron and ion runaway in a fully ionized gas. I.* Physical Review, 1959. **115**(2): p. 238.

4. Martın-Solıs, J., et al., *Momentum–space structure of relativistic runaway electrons.* Physics of Plasmas (1994-present), 1998. **5**(6): p. 2370-2377.

5. Martin-Solis, J., et al., *Energy limits on runaway electrons in tokamak plasmas.* Phys. Plasmas, 1999. **6**(1): p. 238-252.

6.   Bakhtiari, M., G.J. Kramer, and D.G. Whyte, *Momentum-space study of the effect of bremsstrahlung radiation on the energy of runaway electrons in tokamaks.* Phys. Plasmas, 2005. **12**(10): p. 102503.

7.   Guan, X., H. Qin, and N.J. Fisch, *Phase-space dynamics of runaway electrons in tokamaks.* Phys. Plasmas, 2010. **17**(9): p. 092502.

8.   Liu, J., et al., *What is the fate of runaway positrons in tokamaks?* Phys. Plasmas, 2014. **21**(6): p. 064503.

9.   Connor, J. and R. Hastie, *Relativistic limitations on runaway electrons.* Nuclear Fusion, 1975. **15**(3): p. 415.

10.   Zhang, R., et al., *Volume-preserving algorithm for secular relativistic dynamics of charged particles.* Physics of Plasmas (1994-present), 2015. **22**(4): p. 044501.

11.   Wesson, J., *Tokamaks*. Vol. 149. 2011: Oxford University Press.

12.   Knoepfel, H. and D.A. Spong, *RUNAWAY ELECTRONS IN TOROIDAL DISCHARGES.* Nuclear Fusion, 1979. **19**(6): p. 785-829.

13.   Jackson, J.D. and J.D. Jackson, *Classical electrodynamics*. Vol. 3. 1962: Wiley New York etc.

14.   He, Y., et al., *Volume-preserving algorithms for charged particle dynamics.* Journal of Computational Physics, 2015. **281**: p. 135-147.

15.   Qin, H. and X. Guan, *Variational symplectic integrator for long-time simulations of the guiding-center motion of charged particles in general magnetic fields.* Physical review letters, 2008. **100**(3): p. 035006.

16.   Qin, H., et al., *Why is Boris algorithm so good?* Physics of Plasmas (1994-present), 2013. **20**(8): p. 084503.

17.   Xiao, J., et al., *A variational multi-symplectic particle-in-cell algorithm with smoothing functions for the Vlasov-Maxwell system.* Physics of Plasmas (1994-present), 2013. **20**(10): p. 102517.

18.   Zhang, R., et al., *Canonicalization and symplectic simulation of the gyrocenter dynamics in time-independent magnetic fields.* Physics of Plasmas (1994-present), 2014. **21**(3): p. 032504.

19.   Wu, S., *An overview of the EAST project.* Fusion Engineering and Design, 2007. **82**(5): p. 463-471.

Stochastic Simulation of Backward Runaway Electrons

Wentao Wu[1], Hong Qin[1, 2], Nathanial Fisch[2, 3], Jian Liu[1], and RuiLi Zhang[1]

1) Department of Modern Physics, University of Science and Technology, Hefei, China
2) Princeton Plasma Physics Laboratory, Princeton University, Princeton, NJ, USA
3) Department of Astrophysical Sciences, Princeton University, Princeton, NJ, USA

Abstract

In this paper a stochastic approach to solve the probability of backward runaway. A stochastic differential equation for electrons in fully ionized plasma is derived using Cadjan-Ivanov method. An energy-preserving algorithm is presented. Using this method, the backward runaway probability is calculated statically.

Introduction

In fully ionized plasma, when an electron is moving along external electric field, it suffers from a competition between electric field and the velocity drag $-\boldsymbol{v}/v^3$ due to collisions. If the velocity is small enough that the velocity drag dominant, the electron will be stopped by collisions. But if the velocity is high and the electric field is larger, it will be accelerated to extreme high velocity until is hit the boundary. This phenomenon is called the forward runaway. The Dreicer velocity[1] indicates which electrons have high enough velocity to run away.

However, if the initial velocity of an electrons is in the opposite direction of the external electric field, it is not certain to run away or be stopped. If an electrons gains a high perpendicular velocity large enough before its parallel velocity reduces to zero, it could transformed into a forward runaway electron, otherwise, it will be stopped. Since the collision effect is a random factor, an electrons has a certain probability to run away[2].

This paper is organized as following, In Section. II, the stochastic differential equation is derived for electrons in fully ionized plasma. In Section. III, an energy-preserving algorithm is present to numerically solve the SDEs. And the simulation results are presented in Section IV.

Stochastic Differential Equation for Lorentz Plasma

The distribution function of runaway electrons obeys Boltzmann equation with collisional operator

$$\frac{\partial f}{\partial t} + v \cdot \frac{\partial f}{\partial x} + \frac{q}{m}(E + v \times B) \cdot \frac{\partial f}{\partial v} = \left(\frac{\partial f}{\partial t}\right)_c \tag{1}$$

For electron-ion collision with Z_i being the charge carried by ion, Lorentz collision term is included

$$\left(\frac{\partial f}{\partial t}\right)_{e-i} = \frac{Z_i \Gamma}{2} \frac{\partial}{\partial v} \cdot \left(\frac{v^2 I - vv}{v^3} \cdot \frac{\partial f}{\partial v}\right)$$

For electron-electron collision, it should be noted that a velocity drag damping is introduced

$$\left(\frac{\partial f}{\partial t}\right)_{e-e} = \Gamma \frac{\vec{v}}{v^3} \cdot \frac{\partial f}{\partial \vec{v}} + \frac{\Gamma}{2} \frac{\partial}{\partial \vec{v}} \cdot \left(\frac{v^2 I - vv}{v^3} \cdot \frac{\partial f}{\partial \vec{v}}\right)$$

To sum up, the final Boltzmann equation reads[1, 2]

$$\frac{\partial f}{\partial t} + \left(\frac{qE}{m} - \Gamma \frac{v}{v^3}\right) \cdot \frac{\partial f}{\partial v} = \frac{\Gamma(1 + Z_i)}{2} \frac{\partial}{\partial v} \cdot \left(\frac{v^2 I - vv}{v^3} \cdot \frac{\partial f}{\partial v}\right) \tag{2}$$

Boltzmann equation for spatial homogeneous Lorentz plasma can be rewritten in form

$$\frac{\partial f}{\partial t} + v \cdot \frac{\partial f}{\partial x} + \frac{e}{m}(E + v \times B) \cdot \frac{\partial f}{\partial v} = \left(\frac{\partial f}{\partial t}\right)_c, \text{ where}$$

$$\left(\frac{\partial f}{\partial t}\right)_c = \frac{\partial}{\partial v_i}\left(-\left\{-Z_i \Gamma \frac{v_i}{v^3}\right\}f + \frac{1}{2}\frac{\partial}{\partial v_k}\left\{Z_i \Gamma \frac{v^2 \delta_{ik} - v_i v_k}{v^3}\right\}f\right).$$

And Γ is a constant defined $\Gamma = \frac{ne^4 \ln \Lambda}{4\pi \epsilon_0^2 m_e^2}$.

Tt can also be solved by statistics over solutions of a Stratonovich stochastic equation[3, 4],

$$dv = \frac{e}{m}(E + v \times B) + \sqrt{\frac{Z_i \Gamma}{v^5}} v \times v \times {}^\circ d\vec{W} \tag{3}$$

One can easily verify the square root by multiplication.

The final Boltzmann equation with collisions of electrons and ions included is

$$\frac{\partial f}{\partial t} + \left(\frac{qE}{m} - \Gamma \frac{v}{v^3}\right) \cdot \frac{\partial f}{\partial v} = \frac{\Gamma(1 + Z_i)}{2} \frac{\partial}{\partial \vec{v}} \cdot \left(\frac{v^2 I - vv}{v^3} \cdot \frac{\partial f}{\partial v}\right)$$

The corresponding stochastic differential equation is

$$d\vec{v} = \left(\frac{qE}{m} - \Gamma \frac{v}{v^3}\right)dt - \sqrt{\frac{(1 + Z_i)\Gamma}{v^5}} v \times v \times {}^\circ dW,$$

Which is renormalized parameters by $\tilde{v} = v/v_{Dreicer}$, $\tilde{t} = t/\tau_{Dreicer}$, where $\tau_{Dreicer} = v_{Dreicer}^3/\Gamma$, $\tilde{W} = W(\tau_{Drecier}\tilde{t})/\sqrt{\tau_{Drecier}}$, $\tilde{E} = \frac{qE}{m}/F_0$, where $F_0 = m\Gamma/v_{Dreicer}$

The dimensionless equation is

$$d\tilde{v} = \left(\tilde{E} - \frac{\tilde{v}}{\tilde{v}^3}\right)dt - \sqrt{1 + Z_i}\tilde{v}^{-\frac{5}{2}}\tilde{v} \times \tilde{v} \times {}^\circ d\tilde{W} \tag{4}$$

Energy-Preserving Algorithms

For $dX(t) = \mu(X,t)dt + \sigma(X,t)^\circ dW_t$ in Stratonovich sense.
The midpoint implicit method[5, 6] is

$$X_0^n = X_0$$

$$X_i^n - X_{i-1}^n = \mu\left(\frac{1}{2}(X_i^n + X_{i-1}^n), \frac{1}{2}(t_i + t_{i-1})\right)\Delta_i +$$

$$\sigma\left(\frac{1}{2}(X_i^n + X_{i-1}^n), \frac{1}{2}(t_i + t_{i-1})\right)\Delta_i \widetilde{W} \qquad (5)$$

Where

$$\Delta_i \widetilde{W} = \begin{cases} -A_h, & \Delta_i W < A_h \\ \Delta_i W, & |\Delta_i W| \leq A_h \\ A_h, & \Delta_i W > A_h \end{cases}$$

$A_h = \sqrt{2k|\ln h|}$, $h = \min(\Delta_i)$ and $k \geq 1$. And $\widetilde{W}$ is the standard Winer process. It can easily to proof that this algorithm preserves that energy of an electron.

Simulation Results

A sample solution path of a test electron without velocity drag is plotted in Fig. 1. Because of the energy is conserved, it looks like a random walk on energy spherical surface. The energy of using energy-preserving method is compared with commonly used Euler-Maruyama[7] method in Fig. 2. It can be seen that the energy is numerically conserved.
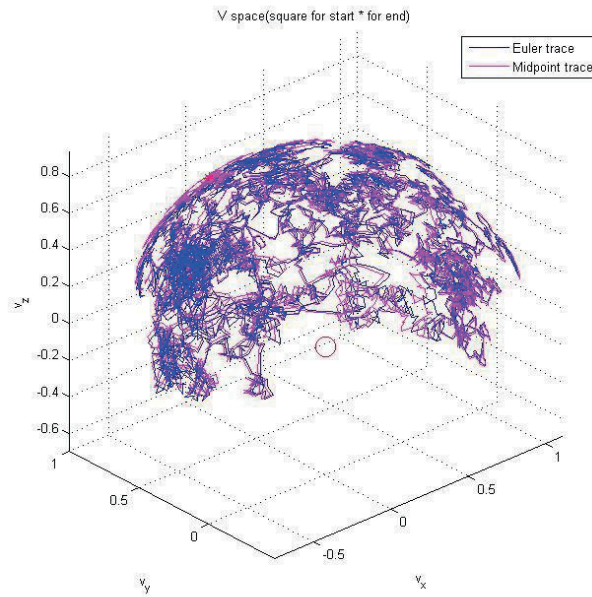
Fig. 1 A sample solution process of electron

194
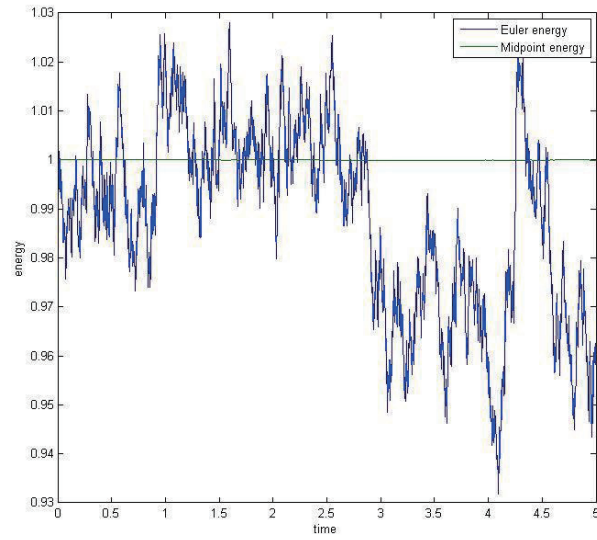
Fig. 2 Energy-time of the sample process. Midpoint method preserves the energy exactly.

In Fig. 3, the left side shows the typical backward runaway and the stopped trajectories. Sample electrons are all initialized at velocity $v_0 = (-5,0,0)v_D$, external electric field is set to $qE = (1,0,0)F_D$, time step for simulation is $\Delta\tau = \tau_D/500$ and simulation ends at $t_{end} = 10\tau_D$. Charge carried by ion is $Z_i = 1$. When the magnitude of velocity is less than $0.1v_D$, the particle is assigned to be stopped.
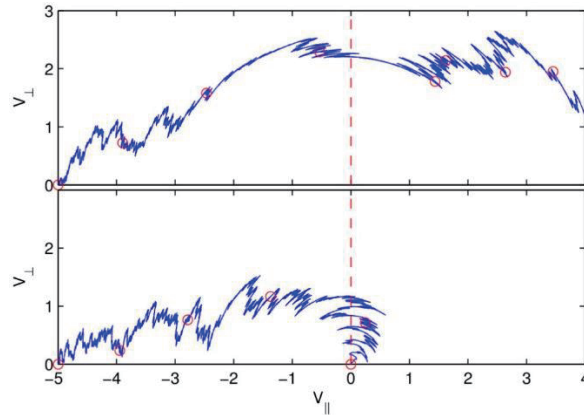
Fig. 3. Typical backward runaway and stopped particle trajectories.

Runaway probability defined by unstopped/total number of particles at time $t = 10\tau_D$ on $v_\parallel$-$v_\perp$ space. It is coincident with [1, 2] obtained by adjoint method. The contour is plotted in Fig. 4. In addition, the contour of averaged perpendicular velocity when partial passing through runaway surface defined to be $v_\parallel = 3$. Still it is coincident with previous work. It is shown in Fig. 5.
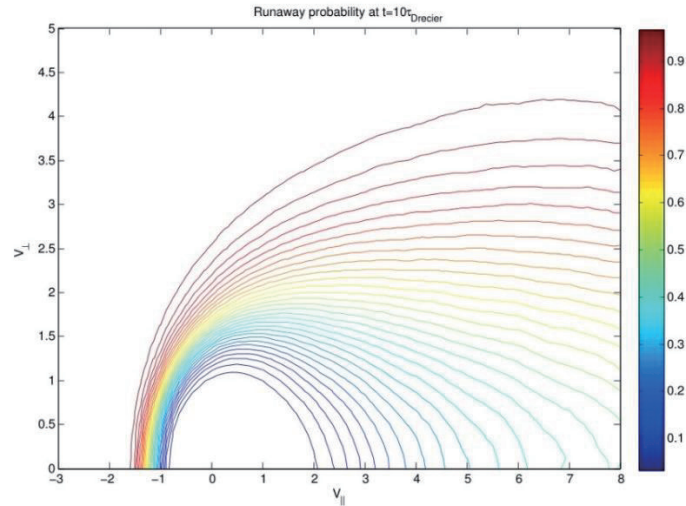
Fig. 4 Contour of runaway probability
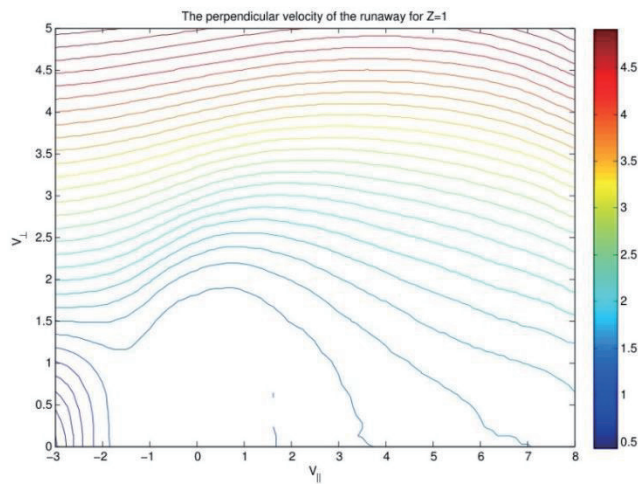
Fig. 5 Contour of averaged perpendicular velocity when partial passing through runaway surface

Summary

There is a connection between partial differential equation and stochastic differential equation. Collision effects can be described by a stochastic differential equation. Energy-preserving algorithm is applied to the stochastic differential equation.

In the following works, we are going to investigate the runaway electrons in Tokamak geometry. And figure out the characteristics of backward runaway electrons in order to find out the way to reduce the backward runaway electrons in real tokamak.

1.   Fisch, N.J., *Theory of Current Drive in Plasmas.* Reviews of Modern Physics, 1987. **59**(1): p. 175-234.
2.   Karney, C.F.F. and N.J. Fisch, *Current in Wave-Driven Plasmas.* Physics of Fluids, 1986. **29**(1): p.

180-192.

3.   Cadjan, M.G. and M.F. Ivanov, *Langevin approach to plasma kinetics with Coulomb collisions.* Journal of Plasma Physics, 1999. **61**: p. 89-106.

4.   Cadjan, M.G. and M.F. Ivanov, *Stochastic approach to laser plasma kinetics with Coulomb collisions.* Physics Letters A, 1997. **236**(3): p. 227-231.

5.   Milstein, G.N., Y.M. Repin, and M.V. Tretyakov, *Numerical methods for stochastic systems preserving symplectic structure.* Siam Journal on Numerical Analysis, 2002. **40**(4): p. 1583-1604.

6.   Milstein, G.N. and M.V. Tretyakov, *Stochastic numerics for mathematical physics*. 2004: Springer.

7.   Øksendal, B., *Stochastic differential equations*. 2003: Springer.

Evaluation of poloidal distribution from edge impurity emissions measured at different toroidal positions in Large Helical Device

H. M. Zhang[1], S. Morita[1, 2], T. Ohishi[1, 2], M. Kobayashi[1, 2], M. Goto[1, 2] and X. L. Huang[1]

[1]Graduate University for Advanced Studies, Toki 509-5292, Gifu, Japan

[2]National Institute for Fusion Science, Toki 509-5292, Gifu, Japan

Abstract

Two-dimensional (2-D) distribution of edge impurity line emissions has been measured for CIV, CVI, FeXV and FeXVIII using a space-resolved extreme ultraviolet (EUV) spectrometer in Large Helical Device (LHD). A strong emission trajectory along the plasma boundary is observed at the top and the bottom edges in the 2-D distribution. The poloidal distribution of impurity emissivity has been evaluated by analyzing the 2-D distribution against magnetic surfaces calculated with a 3-D equilibrium code, VMEC. Inner and outer boundaries of the edge impurity location are estimated by analyzing each vertical emission profile measured at different toroidal positions. The observation chord length passing through an emission contour is calculated based on the radial thickness of the impurity emission location. The poloidal distribution of CIV, CVI, FeXV and FeXVIII with different ionization energies is thus reconstructed from the 2-D distribution. A non-uniform poloidal distribution is clearly observed for all these impurity species located different plasma radii. It is experimentally confirmed that the poloidal distribution becomes gradually uniform as the radial location of impurity ions moves from the ergodic layer to the plasma core. The non-uniform poloidal distribution of CIV emissivity is also confirmed by the simulation with a 3-D edge transport code, EMC3-EIRENE.

1. Introduction

In LHD, the core plasma is surrounded by the ergodic layer, in which magnetic fields with a three-dimensional (3-D) structure are formed by higher order components in magnetic fields created with a pair of helical coils and by overlapping of edge small islands [1-3]. A 2-D space-resolved EUV spectrometer system has been developed to measure the 2-D distribution of impurity line emissions in the ergodic layer [4]. The 2-D distribution of edge impurity emissions has been measured for various impurity species, e.g. CIV, HeII and FeXVI [4,5]. An entirely non-uniform 2-D distribution has been observed for such edge impurity emissions. These impurity emissions are enhanced at the top and bottom plasma boundaries and in the vicinity of X-points. The 2-D distribution measured here may reflect a non-uniform poloidal distribution in the edge impurity emission. Therefore, it is important to evaluate the poloidal distribution of edge impurity emissions for gaining a deeper understanding of the impurity behavior in the plasma edge, in particular, in the ergodic layer. Since the LHD plasma shape poloidally rotates five times during one toroidal turn, the poloidal distribution of edge impurity emissions can be estimated from 2-D distributions. In practice, the poloidal distribution of impurity emissivity is obtained by analyzing each vertical profile measured at different toroidal positions. In this paper, the poloidal impurity distribution is presented for CIV, CVI, FeXV and FeXVIII with different ionization energies. The result is compared with simulation with the EMC3-EIRENE code.

2. EUV spectrometer and 2-D distribution measurement

A 2-D space-resolved EUV spectrometer has been developed to measure the 2-D distribution of impurity emissions in the wavelength range of 60–400 Å by horizontally scanning optical axis of the spectrometer [4]. The horizontal view of LHD plasmas with ergodic layer is shown in Fig. 1. The LHD port is denoted with diamond a solid line. The observation range of 2-D distribution measurement is then limited by 120cm and 90cm in vertical and horizontal directions, respectively. Inboard and outboard X-point trajectories are denoted with dotted and dashed lines, respectively.

The 2-D distribution of impurity emissions is shown in Fig. 2 for CIV (384.174 Å, E_i = 64.0 eV), CVI (2 × 33.73 Å, 490.0 eV), FeXV (284.164 Å, 456.2 eV) and FeXVIII (93.92 Å, 1357.8 eV) in low-density ($n_e \sim 1 \times 10^{13} cm^{-3}$) ICRF discharges with magnetic axis position of R_{ax} = 3.60 m. The intensity of impurity line emissions is absolutely calibrated using radial profiles of bremsstrahlung continuum in EUV and visible ranges [6]. In the 2-D distribution emissions near the top and the bottom plasma boundaries are enhanced due to a long chord length passing through the edge plasma. The inboard X-point trajectory (see Fig. 1) is also enhanced for CIV and CVI indicating a non-uniform poloidal distribution to line emissions in the ergodic layer.
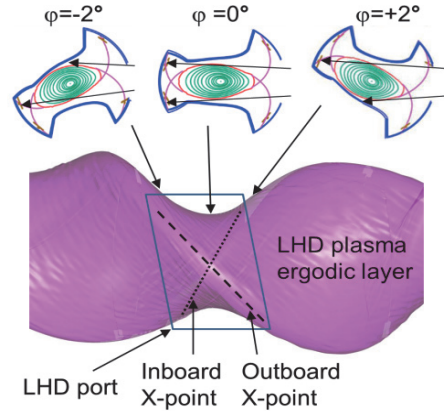
Fig. 1 Horizontal view of LHD ergodic layer and poloidal plasma cross sections at three different toroidal angles of φ = − 2°, 0° and + 2°.

3. Analysis of poloidal distribution

The elliptical cross section of LHD plasmas within the observation range is shown in Fig. 1 at three different toroidal positions of φ=-2°, 0° and +2°. The observation chord passing through the top and the bottom plasma boundaries are also indicated with two solid arrows in each poloidal cross section. In the figure it is clear that the emission intensity in the top and the bottom edges measured at different toroidal positions can express information on the poloidal distribution of impurity emissions. Then, an evaluation of the poloidal distribution of edge impurity emissions is attempted by analyzing the impurity emission at the top and the bottom edges in the 2-D distribution. In the analysis data from X-points with extremely non-uniform emissions are not used.

As the first step, the magnetic flux surface of LHD is calculated with a 3-D equilibrium code, VMEC, as a function of pressure profile. Although no magnetic surface exists in the ergodic layer, virtual magnetic surfaces are assumed at ρ > 1, which are calculated by extrapolating the magnetic flux surface at last closed flux surface (LCFS). This assumption is usually used in LHD when an edge plasma in the ergodic layer is analyzed.

An example of the vertical profile of impurity emissions at the top edge is shown in Fig. 3 for CIV measured at Y = 0, which means φ=0° (see Fig. 2). A sharp peak is observed near the plasma edge boundary. Here, inner and outer boundaries of the impurity vertical profile are defined by intensities at the peak and the half maximum, respectively. In the figure, then, the inner and outer boundaries of CIV radial profiles are estimated to be ρ = 1.02 and ρ = 1.06, respectively.

After analyzing the inner and outer boundaries of impurity emissions, the chord-integrated intensity is estimated by integrating the emission between inner and outer boundaries. The chord-integrated intensity of CIV emissions at the top plasma edge is calculated as a function of horizontal position. It is shown in Fig. 4 (a). The observation chord length calculated at each toroidal position is shown in Fig.4 (b). The local emissivity of CIV is then obtained in dividing the chord-integrated intensity by the chord length. The result is plotted in Fig. 4 (c).
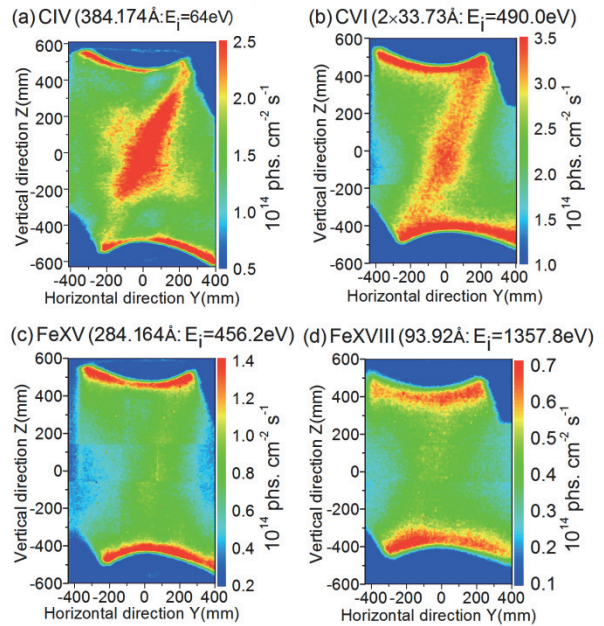
Fig. 2 2-D distributions of (a) CIV, (b) CVI, (c) FeXV and (d) FeXVIII at R_{ax} = 3.60 m.

The poloidal angle at the top plasma edge is calculated for each horizontal position from the assumed magnetic flux surface in the ergodic layer, as shown in Fig. 4 (d). Thus, the poloidal distribution of CIV emissivity near the top edge can be reconstructed from the 2-D CIV distribution with vertical and horizontal coordinates. The poloidal distribution of CIV emissivity near the bottom edge can be also analyzed in the same manner.

Fig. 3 CIV vertical profile at Y = 0 as a function of vertical position (also see Fig. 2).

4. Results

The poloidal emissivity distribution evaluated from the 2-D distribution in Figs. 2 (a)-(d) is shown in Figs. 5 (a)-(d) as a function of poloidal angles θ_{Top} and θ_{Bottom} at the top and bottom edges, respectively. Here, the poloidal angle is defined by an angle toward counter-clock-wise direction as a reference point of long axis of elliptical plasma shape at outboard side. The poloidal distribution measured at the top and bottom edges is plotted with dashed and solid lines, respectively. Due to a limited observation range of the EUV spectrometer system, the distribution is obtained in ranges of $55° \leq \theta_{Top} \leq 110°$ and $255° \leq \theta_{Bottom} \leq 320°$. The poloidal distribution of these impurity species is also plotted against horizontally elongated plasma cross section. The result shown in Fig. 6 indicates the radial location of impurity ions moves inwardly as the ionization energy increases. Seeing Figs. 5 and 6 it is clear that the poloidal distribution is non-uniform for impurity ions existing in the ergodic layer and in the vicinity of LCFS and the non-uniformity becomes stronger with reduction of the ionization energy of impurity ions. This means impurity ions located in outer region of the ergodic layer exhibit larger non-uniformity in the poloidal distribution. In addition, the emissivity is stronger as the impurity location is close to the X-point, while it is weak at both the top and the bottom O-points defined by poloidal positions of the elliptical plasma boundary adjacent to helical coils.

The emissivity distribution is normalized by emissivity at the bottom O-point, $\theta_{Bottom} = 270°$, to compare the non-uniformity among four impurity species in details. The result is shown in Fig. 7. The normalized poloidal distribution becomes gradually uniform as the radial location of impurity ions moves inside. The
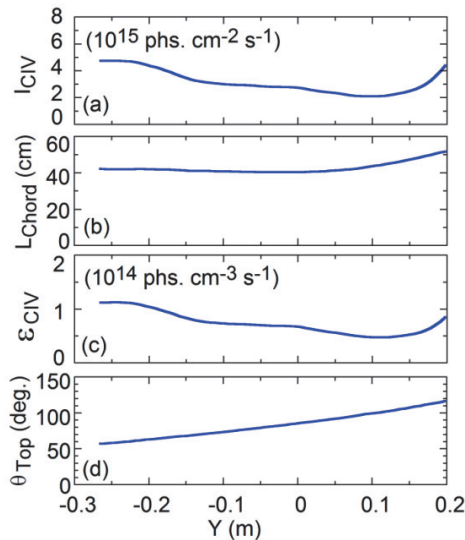
Fig. 4 (a) Chord-integrated intensity of CIV, (b) observation chord length, (c) CIV emissivity and (d) poloidal angle at the top plasma edge as a function of horizontal position, Y.
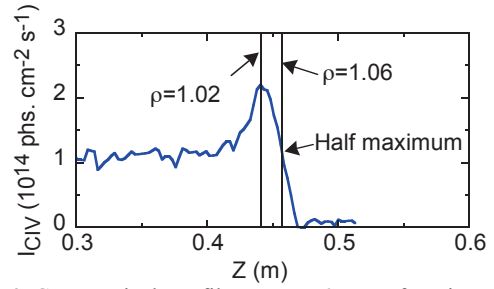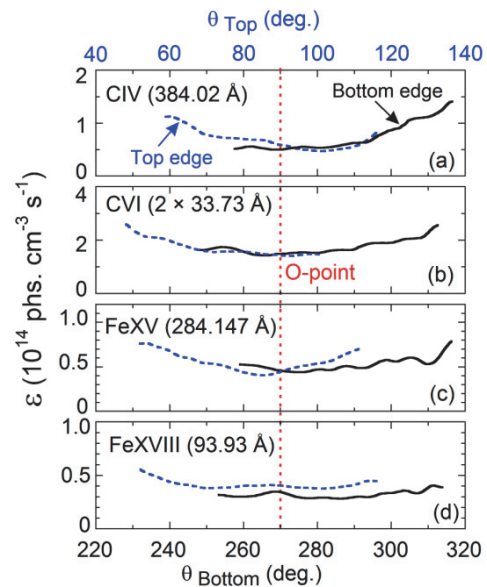
Fig. 5 Poloidal distributions of (a) CIV, (b) CVI, (c) FeXV and (d) FeXVIII as a function of poloidal angles of θ_{Top} and θ_{Bottom}.

poloidal profile of CIV shows an extremely non-uniform distribution. Since the C^{3+} ions with low ionization energy ($E_i = 64$ eV) is located near the edge boundary in the ergodic layer, the C^{3+} ion is strongly affected by a specific edge impurity transport, which is dominant in the ergodic layer with 3-D magnetic field structure. On the contrary, the poloidal profile of FeXVIII located at $0.78 \leq \rho \leq 0.90$ indicates a relatively flat distribution. This means the FeXVIII emissivity is a function of magnetic surface.

The carbon distribution in the ergodic layer has been also analyzed with a 3-D edge plasma transport code, EMC3-EIRINE [7]. The emissivity distribution of CIV (312.4 Å) simulated with the code is plotted in Fig. 8. This indicates that the CIV emission located in the ergodic layer is stronger when the radial location moves outside. The simulated result well supports our present result, while the estimation of the poloidal distribution is obtained from the 2-D distribution. Therefore, the present analysis can provide a reliable method to evaluate the impurity poloidal distribution.

5. Summary

The poloidal impurity emissivity distribution of CIV, CVI, FeXV and FeXVIII is reconstructed from the 2-D distribution measured with space-resolved EUV spectrometer system in LHD. A non-uniform poloidal distribution is clearly observed for CIV, while the FeXVIII distribution is basically a function of magnetic surface. The present result for CIV is well supported by the 3-D simulation.

References

[1]. N. Ohyabu, *et al*., Nucl. Fusion **34**, 387 (1994).
[2]. T. Morisaki, *et al*., J. Nucl. Mater. **31**, 3548 (2003).
[3]. S. Morita, *et al*., Nucl. Fusion **53**, 093017 (2013).
[4]. E. H. Wang, *et al*., Rev. Sci. Instrum. **83**, 043503 (2012).
[5]. S. Morita, *et al*., Plasma Phys. Control. Fusion **56**, 094007 (2014).
[6]. C. F. Dong, *et al*., Rev. Sci. Instrum. **83**, 10D509 (2012).
[7]. M. Kobayashi, *et al.*, Nucl. Fusion **53**, 033011 (2013).
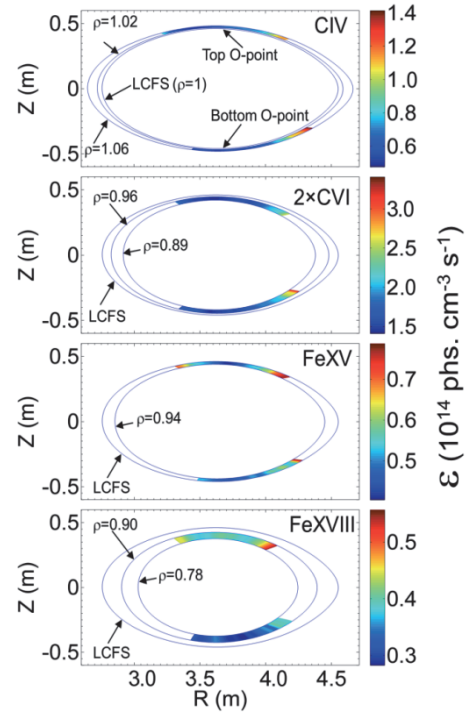
Fig. 6 Poloidal distributions of (a) CIV, (b) CVI, (c) FeXV and (d) FeXVIII at horizontally elongated plasma cross section. The emissivity is expressed in different colors.
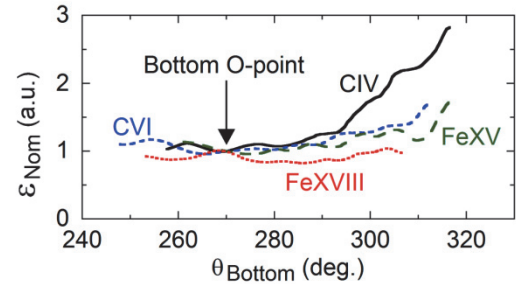
Fig. 7 Emissivity profiles of CIV, CVI, FeXV and FeXVIII normalized at $\theta_{Bottom} = 270°$.
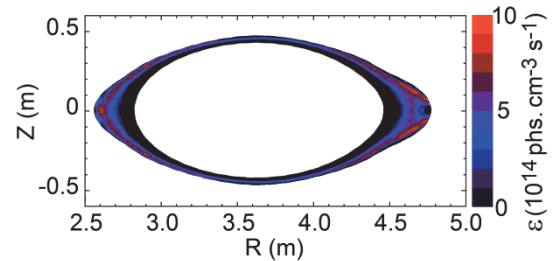
Fig.8 Simulation of emissivity distribution of CIV (312.4Å) using EMC3-EIRINE.

Analysis of Z_{eff} profiles based on space-resolved measurement of extreme ultraviolet bremsstrahlung in the Large Helical Device

X. L. HUANG[1], S. Morita[1,2], T. Oishi[1,2], M. Goto[1,2] and H. M. Zhang[1]

[1] *Department of Fusion Science, Graduate University for Advanced Studies, Toki 509-5292, Gifu, Japan*

[2] *National Institute for Fusion Science, Toki 509-5292, Gifu, Japan*

Abstract

Z_{eff} profile analysis has been carried out in a low-density and high-T_i discharge with carbon pellet injection. The evolution of the Z_{eff} profile shows a centrally peaked profile just after the pellet injection which then gradually returns to a flat profile. Comparison between the evolution of Z_{eff} and T_i profiles strongly suggests there is a positive relation between Z_{eff} and T_i.

I. Introduction

Study on impurities in fusion devices has been a major subject in fusion research because of the important role of impurities in plasma performance. The impurity content is commonly characterized by the effective ion charge $Z_{eff} = \sum_i n_i Z_i^2 / \sum_i n_i Z_i = \sum_i n_i Z_i^2 / n_e$. The value of Z_{eff} is known as a key parameter in increasing the ion temperature T_i of plasmas with neutral beam injection (NBI) in the Large Helical Device (LHD) [1,2]. Improvement of plasma performance including increase in T_i has been observed with carbon pellet injection [3]. Extremely hollow profiles of carbon impurity, denoted as "impurity hole", occur after the carbon pellet injection [4]. In order to understand the role in the process of plasma performance improvement, it is necessary to measure the radial distribution of Z_{eff} in the high T_i discharges.

Z_{eff} can be derived from the emissivity of bremsstrahlung, which is expressed by the following equation;

$$\varepsilon_{brem} = \frac{1.89 \times 10^{-28} n_e^2 g_{ff} Z_{eff}}{T_e^{1/2} \lambda^2} \exp(\frac{-12400}{T_e \lambda}), \quad (1)$$

where ε_{brem} (W·cm^{-3}·Å), n_e (cm^{-3}), g_{ff}, T_e (eV) and λ(Å) stand for the emissivity, the electron density, the free-free gaunt factor, the electron temperature and the wavelength, respectively.

A Czerny–Turner spectrometer has been installed on the LHD to measure the radial bremsstrahlung profile in the visible range [5]. However, the visible bremsstrahlung profile is strongly affected and distorted by bremsstrahlung emission from the edge boundary of the LHD ergodic layer in low-density discharges [6]. As the electron density in high T_i discharges is usually below 2×10^{13} cm^{-3}, it becomes difficult to obtain Z_{eff} profiles using the visible spectrometer. On the contrary, the bremsstrahlung in the extreme ultraviolet (EUV) range is free of the non-uniform edge bremsstrahlung emission because of the higher photon energy in the EUV range compared with that in the visible range. In addition, the bremsstrahlung is much stronger in the EUV range. Therefore, Z_{eff} profiles in high-T_i discharges can be evaluated from the space-resolved measurement of EUV bremsstrahlung.

II. Experimental setup

Two space-resolved EUV spectrometers have been installed on LHD [7,8]. Both spectrometers include an entrance slit, a spatial-resolution slit, a varied-line-spacing holographic grating and a charge-coupled device (CCD) detector with 1024×255 pixels. Time resolution of the two systems was 200ms in 2012 and has been improved to 50ms after the installation of a new CCD for each system in 2013. The vertical spatial resolution of the systems is roughly 3cm. One of the space-resolved spectrometer called "EUV-Short2" works in the wavelength range of 10-130Å, and can measure only upper half of the elliptical plasma, as shown in Fig. 1. The other spectrometer called "EUV-Long2" works in the wavelength range of 30-650Å, which can measure either upper or lower half profile. A 0.5μm-thick filter made of polyethylene terephthalate (PET) is installed in each system to reduce spike noises caused by high-energy NBI particles. The filter can effectively eliminate the spike noise. A spectrum measured by EUV-Long2 in a low density discharge is shown in Fig. 2. The continuum can be observed at the base line of the spectrum.
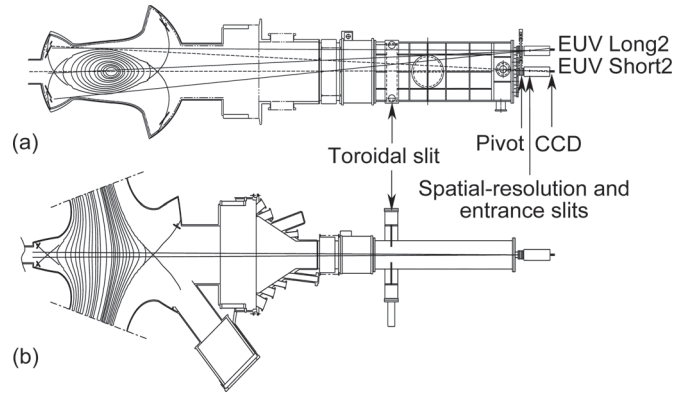
Fig. 1 (a) Side view and (b) top view of EUV systems on the LHD.
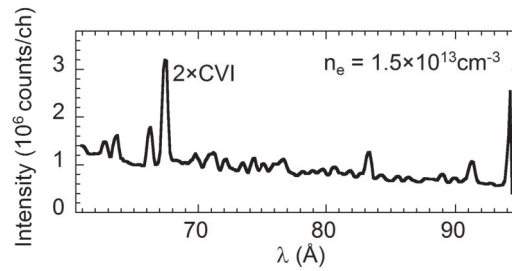
Fig. 2 EUV spectrum measured in a low-density discharge.

In order to obtain a better signal-to-noise ratio, the aperture size of the slits in the EUV systems are changed to 200 μm (width of entrance slit) × 2 mm (height of space-resolved slit), which is four and two times as large as the sizes of the usually used slits for EUV-Short2 and EUV-Long2, respectively. Consequently, new intensity calibration is necessary to obtain the absolute intensity. The EUV systems are calibrated by means of comparison between visible and EUV bremsstrahlung profiles. The visible bremsstrahlung profile has been measured by the above-mentioned Czerny–Turner spectrometer. Figure 3 shows the calibration results. Fitting with previous calibration curves are also plotted with solid lines. The calibration factor shows that the system brightness is enhanced by a factor of 4.0 and 2.2 for EUV-Short2 and EUV-Long2, respectively. This means the system brightness is approximately proportional to the size of the slit aperture.
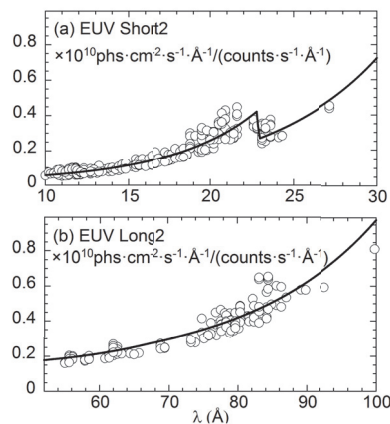
Fig. 3 Intensity calibration factors as a function of wavelength for (a) EUV Short2 and (b) EUV Long2. Solid lines denote fitting curves using previous calibration results.

203

III. Analysis of Z_{eff} Profile

A typical example of Z_{eff} profile analysis at $\lambda = 77.4$ Å -80.0 Å is shown in Fig. 4. The vertical profile of the line-integrated signal is plotted in Fig. 4(a) and radial profiles of n_e, T_e, ε and Z_{eff} are shown in Figs. 4(b)-(e), respectively. The emissivity profile, ε, is derived from the line-integrated profile based on Abel inversion. The magnetic surface used in the inversion is calculated with VMEC code [9]. The emissivity near the last closed flux surface (LCFS) is much larger than that in the plasma core ($\rho < 0.75$) as seen in Fig. 4(d). It seems that the large amount of continuum radiation is attributed to recombination radiation instead of bremsstrahlung because the intensity of bremsstrahlung is limited by Z_{eff}, which should be less than 6 if the impurity density is determined by only carbon. Since the photon energy is around 158 eV, the recombination radiation mainly originates in C^{4+} and C^{5+}. This is verified by comparison of the edge continuum emissivity profile and the carbon line emissions, C VI 33.73Å and C V 40.27Å+40.73Å, as shown in Fig. 4(d). The line emission profiles reflect the distributions of corresponding ions. The edge emissivity profile seems to be a superposition of the shapes of the two line emission profiles. Despite the large amount of recombination radiation in the edge, the emissivity profile is basically free of recombination radiation in the plasma core ($\rho < 0.75$) because of the following reasons. First, the enhancement of continuum emissivity due to recombination radiation dramatically decreases with increasing electron temperature [10]. For instance, the enhancement factor of recombination radiation caused by C^{5+} is around 12 at $T_e = 0.2$ keV while the factor decreases to 1.2 at $T_e = 2$ keV. Second, the impurity ions contributing to the observed recombination radiation, namely, C^{4+} and C^{5+}, are mainly located in the edge. Therefore, the emission from the plasma core certainly consists of only the bremsstrahlung.
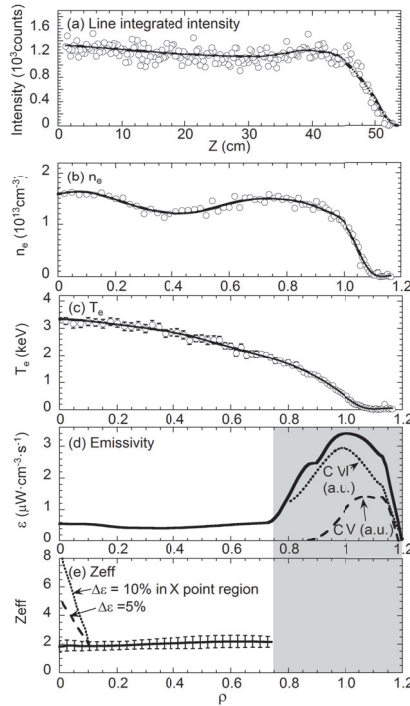
Fig. 4   (a) Vertical profile of line-integrated signal and radial profiles of (b) electron density, (c) electron temperature, (d) continuum emissivity at 77.4 Å-80.0 Å and (e) effective ion charge. Solid lines in (a)-(c) indicate curve fitting, and shaded area in (d) and (e) denotes the region affected by recombination radiation. Dashed and dotted lines in (d) denote shapes of C V and C VI emissions. Dashed and dotted lines in (e) indicate Z_{eff} deviation assuming strong emissions from the X point region.

In order to complete the Abel inversion, the magnetic surface obtained with the VMEC code is extrapolated to the region of $1 < \rho \leq 1.3$. If the bremsstrahlung continuum or impurity emissivity outside the LCFS is nonuniform in the poloidal direction, the measured line-integrated profile will be distorted. However, it is not the case in the EUV bremsstrahlung measurement because the energy is relatively high. The C^{4+} and

C^{5+} ions distribute around the LCFS where the connection length L_c is still quite long, e.g. $L_c > 10^3$ m. Therefore, the ion density can be considered to be uniform in the poloidal direction and then the resultant recombination radiation with such ions will be also uniform. This is verified by an impurity simulation in the ergodic layer [11]. A possible uncertainty caused by the recombination radiation from X points of the ergodic layer should be also taken into account. Assuming that the integrated emissivity outside the LCFS along a viewing chord of the spectrometer is enhanced by emissions from the X point region by a percentage of 5% or 10%, the Z_{eff} near plasma center increases abruptly, as shown in Fig. 4(e). This effect is sometime observed in the measurement. Fortunately, the X point region with relatively strong emissions is usually narrow in the vertical direction, usually within $Z = \pm 5$cm. Therefore, only the viewing chord passing through this narrow vertical region is affected by unnecessary emissions. It corresponds to the radial region of $\rho < 0.1$. In other words, the Z_{eff} profile can be always measured successfully in most radial ranges in the plasma core.

The error bars plotted in Fig. 4(e) is calculated from the data scattering involved in the line-integrated intensity, the electron density and the electron temperature. The total uncertainty is estimated to be 20% - 30%.

IV. Evolution of Z_{eff} Profile in High-T_i Discharges

Time evolution of the NBI port-through power P_{NBI}, n_e, T_e, T_i, the plasma stored energy W_p and the radiation power P_{rad} are shown in Fig. 5. The Z_{eff} profile analysis is performed in six time frames, designated as F1- F6 as denoted in Fig. 5. A carbon pellet is injected at t = 4.5s. The line-integrated density n_e increases from 1.0×10^{13} cm^{-3} to 2.2×10^{13} cm^{-3} after the pellet injection and then gradually decays to 1.4×10^{13} cm^{-3}. The electron temperature T_e is not significantly affected by the pellet. The ion temperature T_i increases from 3.1 keV to 4.2 keV and becomes higher than T_e after the injection (F2). The value of T_i is maintained at around 4.0 keV for 200 ms (F3). The decrease in T_i starts from t = 5.0s and becomes lower than T_e after t = 5.25s.
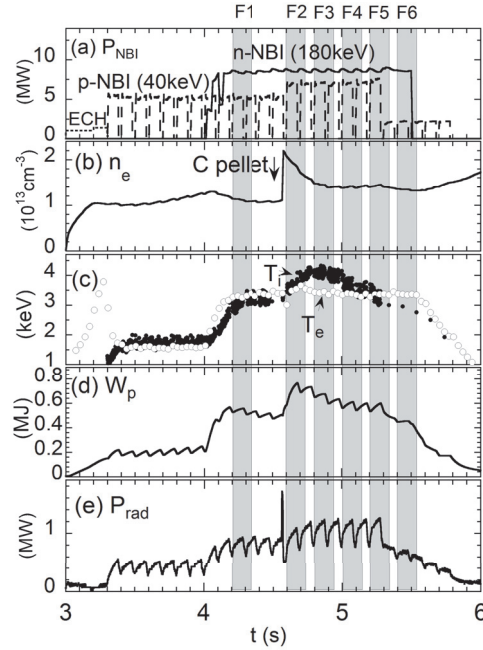
Fig. 5 Time evolution of (a) NBI port-through power, (b) electron density, (c) electron temperature and ion temperature, (d) plasma stored energy and (e) radiation power. Dashed areas indicate six time frames of F1-F6 used for the analysis.

The profiles of Z_{eff}, T_i and T_e in the above-mentioned time frames F1-F6 are shown in Fig. 6. The Z_{eff} profile is basically flat before the pellet injection. In the frame just after the injection (F2), the line-averaged Z_{eff} value increases by approximately 0.8 and a centrally peaked Z_{eff} profile occurs. At the same time, the T_i profile is increased as a whole and becomes higher than T_e in the central region ($\rho < 0.6$). All three profiles are maintained in the next time frame when the central T_i stays at 4.0 keV (F3). When the T_i starts to decrease at t = 5.0s, the Z_{eff} profile gradually returns to the original shape before the injection. The T_i profile tends to exhibit a similar behavior to Z_{eff} profile. The T_e profile remains basically unchanged in all

the time frames.

Comparison between the Z_{eff} and T_i profiles strongly indicates that there is a positive relation between Z_{eff} and T_i. Possible explanations are an enhancement of the absorption efficiency of NBI power and ion heating power per ion with increasing Z_{eff}. It has been also identified that the plasma confinement is improved in such high T_i discharges with carbon pellet injection. A recent study shows there is a strong relation between the density of the carbon impurity and the thermal diffusivity [12]. The time behavior of the Z_{eff} and T_i profiles also suggests that Z_{eff} plays an important role in the confinement improvement.
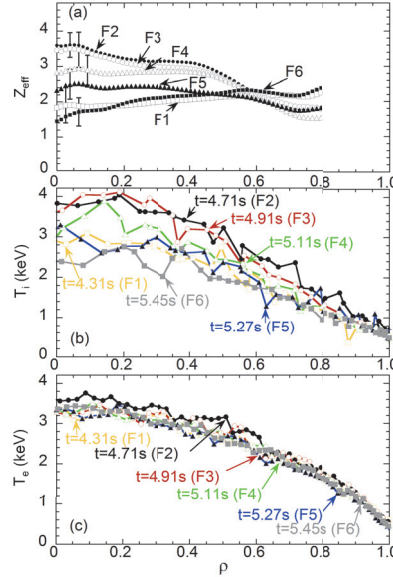
Fig. 6 Profiles of (a) Z_{eff}, (b) T_i and (c) T_e in the six time frames of F1-F6.

V. Summary

The Z_{eff} profile has been successfully obtained in the plasma core ($\rho < 0.75$) from space-resolved profiles of bremsstrahlung in the EUV range. The recombination radiation can give a significant effect on the bremsstrahlung profile, in particular, in the edge region ($\rho > 0.75$) and also in a small region ($\rho < 0.1$) near the plasma center. The time behavior of Z_{eff} profiles suggests a strong relation between Z_{eff} and T_i.

References

[1] H. Takahashi *et al.*, Nucl. Fusion **53**, 073034 (2013).
[2] Y. Takeiri *et al.*, Nucl. Fusion **45**, 565 (2005).
[3] S. Morita *et al.*, Plasma Sci. Technol. **13**, 290 (2011).
[4] M. Yoshinuma *et al.*, Nucl. Fusion **49**, 062002 (2009).
[5] H. Y. Zhou *et al.*, Rev. Sci. Instrum. **79**, 10F536 (2008).
[6] H. Y. Zhou *et al.*, Rev. Sci. Instrum. **81**, 10D706 (2010).
[7] C. F. Dong *et al.*, Rev. Sci. Instrum. **81**, 033107 (2010).
[8] X. L. Huang *et al.*, Rev. Sci. Instrum. **85**, 043511 (2014).
[9] K. Yamazaki, J. Plasma Fusion Res. **79**, 739 (2003).
[10] E. H. Silver, *et al.*, Rev. Sci. Instrum. **53**, 1198 (1982).
[11] E. H. Wang, *Development of two-dimensional EUV spectroscopy for study of impurity behavior in ergodic layer of LHD* (The Graduate University for Advanced Studies, 2013) p.111-p.115.
[12] M. Osakabe *et al.*, Plasma Phys. Control. Fusion **56,** 095011 (2014).

Filterscope diagnostic System on EAST tokamak

Z.Xu[1,2] , Z.W.Wu[1], W.Gao[1,*], L.Zhang[1], J.Huang[1],Y.J.Chen[1], C.R.Wu[1,2], P.F.Zhang[1,2]

[1]Institute of Plasma Physics, Chinese Academy of Science, Hefei 230031, China

[2]Science Island Branch of Graduate School, University of Science & Technology of China, Hefei 230031, China

Email: gw118@ipp.ac.cn

Filterscope diagnostic system, which is designed for monitoring the line emission in fusion plasma has been widely used on fusion devices such as DIII-D, NSTX, CDX-U, KSTAR etc.On EAST (Experimental Advanced Superconducting Tokamak), a filterscope diagnostic system has been mounted to observe the line emission and visible bremsstrahlung emission in plasma from discharge campaign of 2014. It plays a crucial role in studying Edge Localized Modes (ELM) and H-mode [1], thanks to its high temporal resolution (0.005ms) and good spatial resolution (~2cm). Furthermore, multi-channel signals at up to 200kHz sampling rates can be digitized simultaneously. The wavelength covers He II (468.5nm), Li I (670.8nm), Li II (548.3nm), C III (465.0nm), O II (441.5nm), Mo I (386.4nm), W I (400.9nm) and visible bremsstrahlung radiation at 538nm besides $D\alpha$ (656.1nm) and $D\gamma$ (433.9nm)with the corresponding wavelength filters. The new developed filterscope system was operating during the EAST 2014 fall experimental campaign and several types ELMs has been observed.

I.   INTRODUCTION

Line emission intensity measurement with particular filtered photomultipliers (PMTs) named the "Filterscope" first applied on the D-III and NSTX tokamaks, which can provide line emission measurements from plasma with high sensitivity and high temporal resolution, till now, has been also successfully employed on the fusion devices such as DIII-D, NSTX, CDX-U, KSTAR etc., and served for the 2012 campaign of EAST. A modified filterscope system was fixed on EAST after being absolutely calibrated by an integrating sphere [2], the filterscope can be used for daily diagnostic tool during the discharge experiment.

The EAST tokamak has been finished the third phase upgrade, aimed to achieve long pulse operation over 1000 seconds and high parameters ($I_p\sim$ 1MA, T_e>10keV, and $n_e\sim n_{GW}$). As shown in FIG.1, the graphite tiles is replaced with all molybdenum tiles in the first wall and all tungsten tiles in the upper divertor. The resonant magnetic perturbation (RMPs) coils are applied for ELMs mitigation and the neutral beam injection (NBI) system is invested for heating the plasma. Therefore, the diagnostic system must be upgraded or rebuilt to accommodate the new experimental conditions. No doubt, the fitterscope as a regular diagnostic system must have promotions so as to supply more information for the EAST.

The modified filterscope on EAST has been employed to study edge and divertor physics, including H-mode characteristic, L-H transition and ELM behavior etc., as well as benchmark for plasma edge modeling codes, such as BOUT++ for ELM stimulation [3] and DIVIMP for particle transport stimulation [4], etc. Also, filterscope was endowed with a new function, for monitoring the visible bremsstrahlung radiation, which is used to estimate the level of impurities and calculate the effective charge number Z_{eff} [5]. The filterscope system is updated or rebuilt both in hardware and software, such as electric shutters, optical fibers, filters, photomultiplier tubes (PMTs), circuits, and upper-PC software for controller and calibration, etc. details are discussed in later sections.

The reminder of the paper is structured as follows: section II describes the specific of the filterscope

system on the EAST, section III provides some results and examples, which illustrate the attained performance that expected, section IV contains a summary and some ideals for further work.
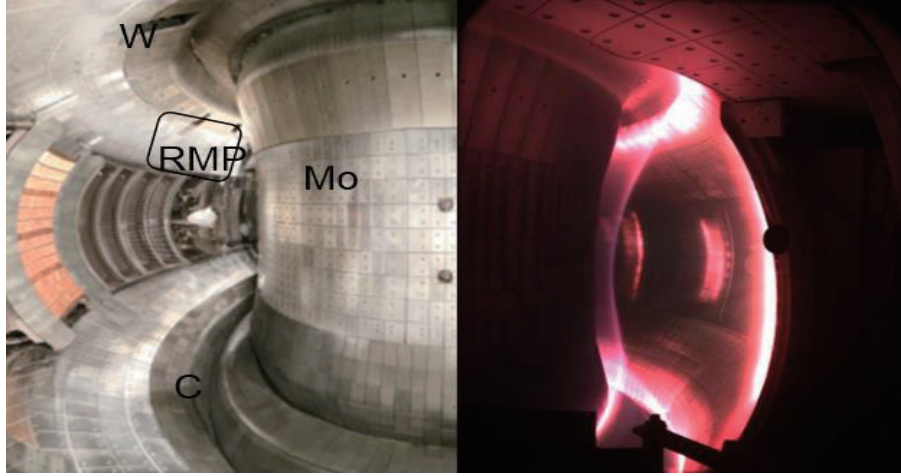
FIG. 1. EAST internal view at 2014 campaign. Left: The main chamber is covered with molybdenum PFCs, upper and lower divertors is equipped with tungsten and graphite tiles respectively. Right: An image of the shot48475 which shows an H-mode discharge by NBI heating.

II.   Design of FILTERSCOPE ON EAST

A.   Arrangement of view chords

EAST is a fully superconducting divertor tokamak with a D-shaped poloidal cross-section. The major parameters are: major radius R=1.85m, minor radius a=0.45m, toroidal magnetic field B_T =2-3.5T, and elongation k=1.2~2. EAST can be running in both single null (SN) and double null (DN) divertor configuration. The major working gas is Deuterium (D_2). The filterscope has three arrays, the sight chords viewing tangentially and poloidally is shown in FIG.2 (Right).   In G port, three cylinders containing the optical structures of filterscope are fixed, as shown in FIG.2 (Left). The cylinders probe into the vessel to maximize the optical sight range. At the end of the cylinders, three observation windows made of sapphires are mounted, which have tolerance of high temperature (350℃). Three electric shutter assemblies which driven by the remote controlled stepping-motors for protecting the sapphires during each wall-condition period are adopted, each window has 13 viewing chords, distributed in tangential mid-plane, upper and lower divertor regions, respectively. The spatial resolution (diameter of the blue dot on the first wall shown in FIG.2) is about 2cm.

Light from the plasma imaged onto the fiber bundle with the lenses which focal length are about 165cm, then the light transfer into the optical fibers run a distance of 40 meters from the machine chamber to the isolated laboratory in basement, finally, light from each fiber is split into seven branches through beam splitting fibers.
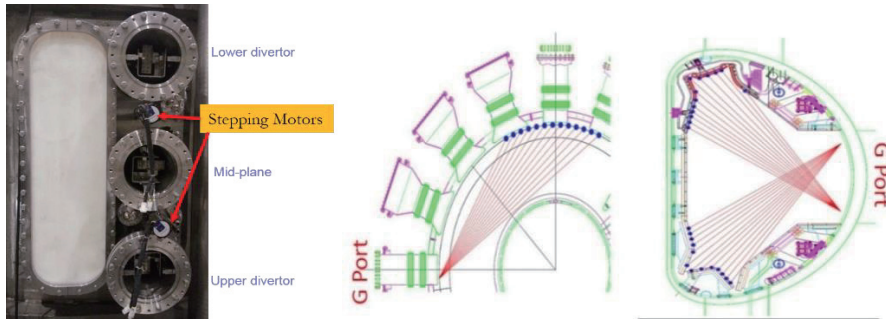
FIG. 2. Left: the photograph of G port; Middle (vertical view): 13 viewing chords ended on the low filed side (LFS) in the tangential at the mid-plane; Right (poloidal cross section): Two arrays, each one has 13 viewing chords pointed to the upper divertor tiles (W- materials) and lower divertor tiles, respectively.
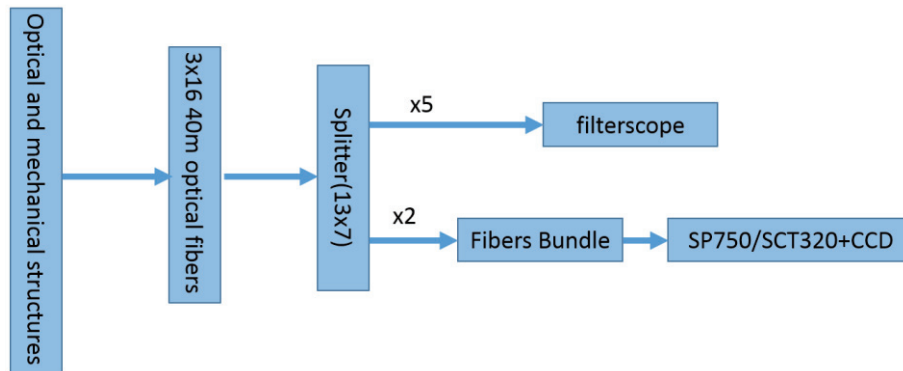
FIG.3. Arrangement of EAST filterscope optical path. Light from the plasma imaged onto the fiber bundle transfer to the optical fibers about 40m away from the machine chamber, then is split into seven ways in the isolated laboratory and transferred to filterscope.

After splitting, different kinds of filter are fixed just between the fibers and the PMTs. The central wavelength of the filters are given in TABLE I. There are 39 channels for toroidal and poloidal Balmer Dα and CIII monitoring, located at the tangential middle plane and upper/lower divertor of EAST, respectively. 13 channels of W I (at 400.9nm) situate upper divertor, and 13 visible bremsstrahlung radiation (VB) at 538nm viewing channels to the tangential middle plane are set. Besides, Impurities emission such as He I (448.1nm), Li I (670.8nm)/Li II (548nm), O II (441.5nm), Mo I (386.4nm) are also included in the filterscope system. The band pass filter for each wavelength has bandwidth of 5nm and at least 70% transparency. Totally, 121 photo multitubes are employed on the EAST filterscope in 2014 fall experimental campaign.

TABLE.I. The numbers of viewing chords with different special lines.

Lines(nm) / View position	Dα/Hα (656.1)	C III (465.0)	W I (400.9)	Dγ/Hγ (433.9)	Li I (670.8)	Li II (548.3)	MoI (386.4)	He II (468.5)	O II (441.5)	VB (538.0)
Middle plane	13	13		1	1	1	1	1	2	13
Upperdivertor	13	13	13	1	1	1	1	1	1	
Lowerdivertor	13	13		3	1	1	1	1	1	

B. Arrangement of Circuits
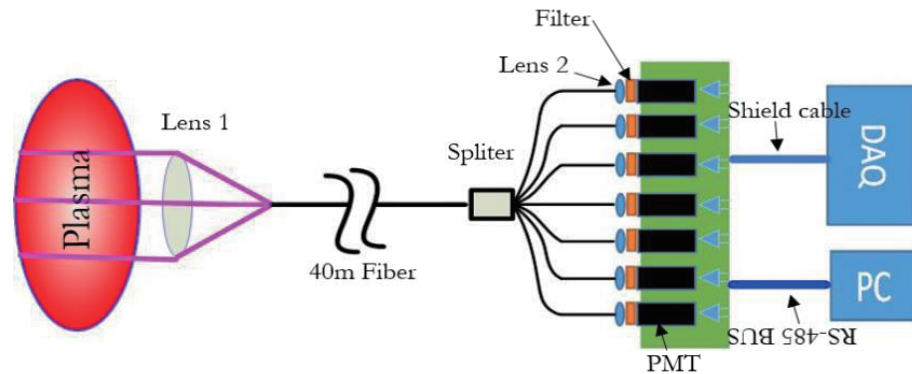
FIG.4. Schematic of the filterscope.

The emission information in the burning plasma is conveyed by a series of fibers to the PMT modules. Before entering the PMTs, the optical signals are collimated by a lens and filtered, as shown in FiG.4. After transformed in electric signals and amplified in the PMT modules, the electric signals in voltage are sent the public DAQ systems and digitized. The type of PMTs are Hamamatsu H7827 series, the H7827-002 and H7827-012 are applied to cater the different needs for wavelength response. The PMT module has a current-to-voltage conversion factor 0.1V/μA, a frequency bandwidth of DC to 200 kHz, and the control voltage adjustment range (for controlling the high voltage in the modules) is from +0.5V to +1.1V. In addition, these two types of PMTs with different spectral response characteristics are provided for measurement in the visible range or visible to near IR range，the more details refer to TABLE II. The public DAQ system has a maximum sampling rate of 250kHz, however, 10kHz and100kHz sampling rate are just switched for filterscope signals during the discharge campaign.

TABLE II. Feature of H7827 series PMTs.

Type No.	Spectral Response	Current-to-Voltage Conversion Factor	Frequency Bandwidth	Adjust Range
H7827-002	300nm-650nm	0.1v/μA	DC ~200kHz	+0.5~+1.1
H7827-012	300nm-850nm			

All the filters and PMTs are integrated in the bins, as shown in FIG.5. On the front panel of the bins, there are fiber connectors and cable adapters for every PMTs. Every bin includes six modules, every module has seven PMTs implanted on printed circuit board (PCB) give the output signal to cables by the RS-485 BUS, the PCB is connected with upper computer, which can adjust the controlling voltage of PMTs through software.
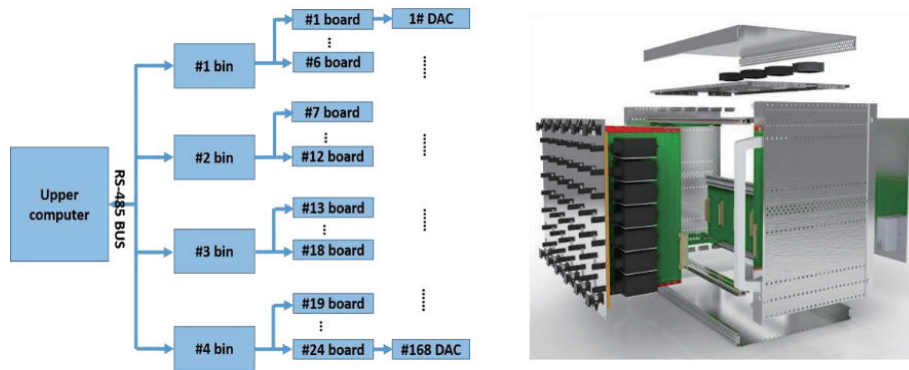
FIG. 5. Left: the layout of the PMT modules; right: view of one filterscope bin.
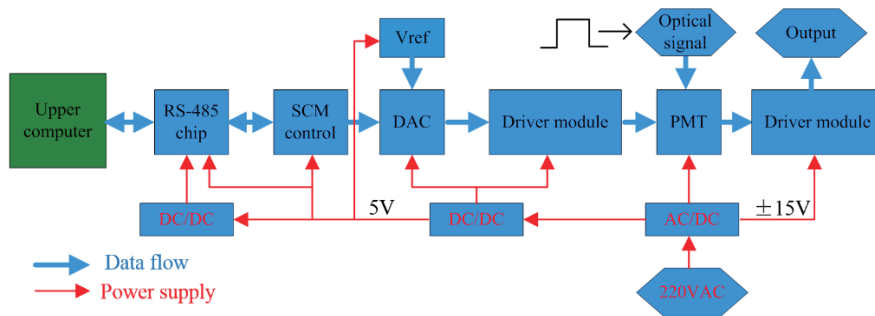
FIG .6. Block diagram of filterscope circuits for a module. The blue arrows indicate data flow; the red arrows indicate the power supplied to the circuits.

In the PCBs, feedback regime is designed to shun saturation of the output signals. As shown in FIG.6, a voltage (Vref) is set to compare with the output signal and the feedback factor is given to the computer as a reference to change the PMT control voltage for maintaining the output signals at a level that neither saturated by ELMs nor dominated by digitizer noise.

C. The software design

Based on above, the program for control and management of the filterscope has been developed. This program is written in Chinese surface by C language, as shown in FIG.7. The data communication between the computer and the each PMT can be accurate transferred by using Jumper addresses encoded in manual switch arrays on PCBs. And, this program can change the PMTs control voltage automatically or manually depending on the switches that marked by the red frame in the FIG.7. Also, a subprogram for multiple PMT-modules (usually 7 PMTs as a set) calibration has been applied in the debug stage which can give the average value of the output signal. For manual case, the all of data has been uploaded to the computer in order to get absolute value that PMT measured.
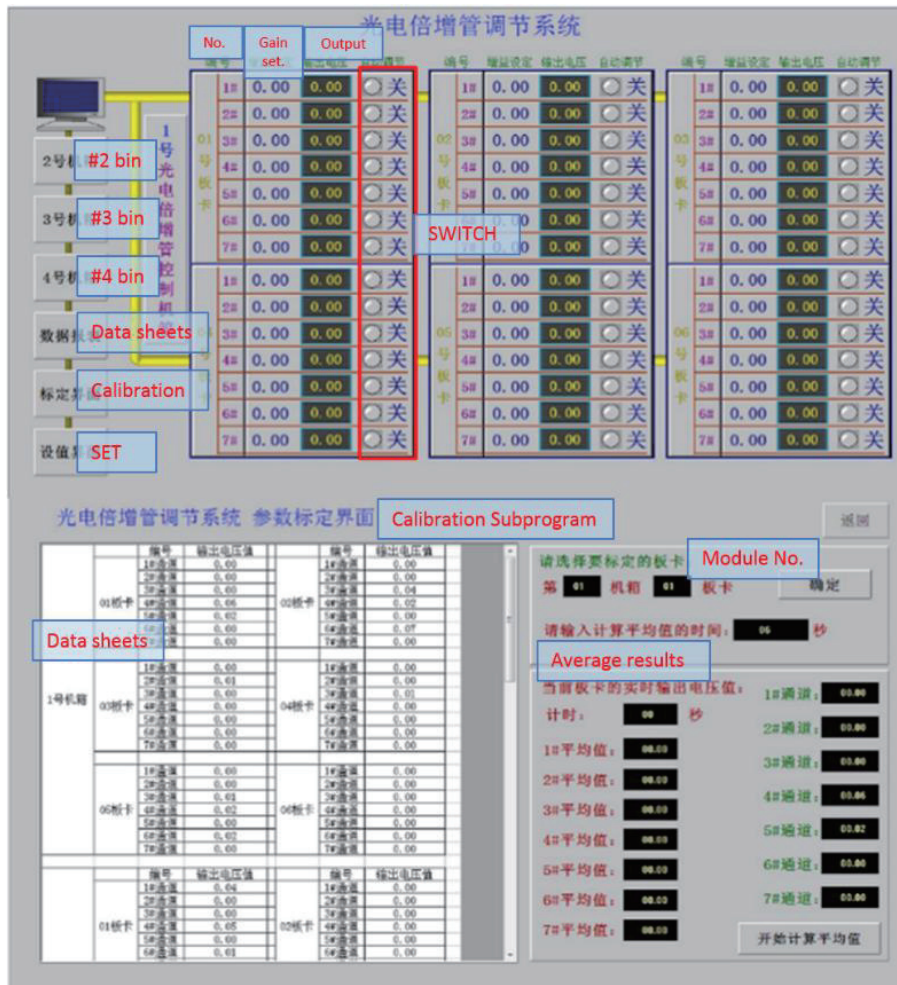
FIG.7. View of the filterscope controlling software in Chinese interface, for controlling voltage adjustment and PMTs calibration.

D. Characteristics of the filterscope modules

The characteristics of the filterscope modules were tested using the LED light source modulated by the square-wave in the laboratory, including frequency response, signal-to-noise ratio (SNR), and the relationship between output and control voltage, etc. For Dα module as an example, it was tested by a modulated LED at frequency range from 0.5kHz to 150kHz, and the frequency response was indicated by calculating the wave shape factor which could be gotten from the ratio of full width of half maximum (FWHM) and full width of 1/10 maximum (FWTM), as shown in FIG.8. All the data was acquired under control voltage at 0.8V, and the modulation voltage of LED is kept constant. The FIG. 8 shows that the wave shape factor changed from 1 to 0.65 when the LED twinkles from 0.5kHz to 150kHz. The figure (a) and (b) in FIG.8 give the wave shape of output signals at 10kHz and 100kHz respectively, which reflect the capacity of describing some burst signals such as ELM events.

In FIG.9, the output gain at different control voltage fitting with cubic splines is shown, the fit results as a function was recorded, which can provide as a reference for setting the control voltage and calibration. The SNR in Fig. 9 is the average signal to noise ratio in 1 second time window at 10MHz sampling rate. It is found that SNR is decreased when the controlling voltage of PMT increases. This result suggests that the PMT should work at a low controlling voltage if the light input allows.
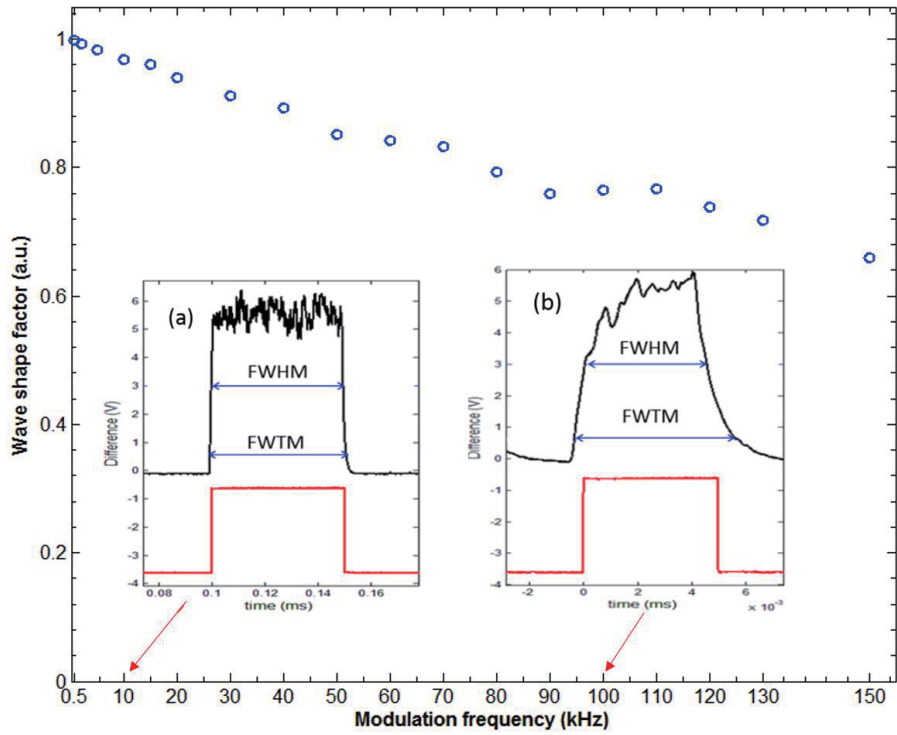
FIG.8. Wave shape factor (the ratio between FWHM and FWTM, as blue dots shows) verse modulation frequency from 0.5kHz to 150kHz. The black line indicate the output signal from the PMT modules, the red line indicate the input signals onto the modulated LED. In figure (a) and (b), the LED are modulated at 10kHz and 100kHz respectively.
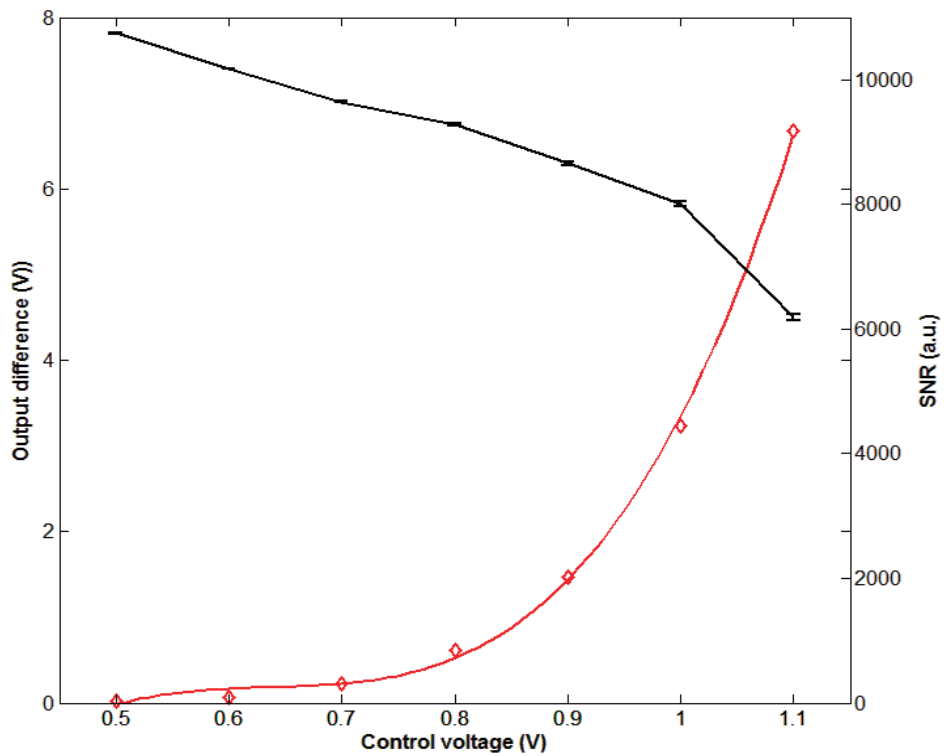
III.   EXPERIMENT RESULTS OF FILTERSCOPE

The filterscope is designed to obtain the absolute intensity of line emission and the characteristic of H-mode. The absolute intensity of signals is obtained by scaling the raw data with the calibration factor that was done in absolute calibration using an integrating sphere. To judge the H-mode characteristics [6] (such as L-H transition, ELMs), the important step is set the $D\alpha$ data at a higher digitized sampling rate. Examples are shown below to illustrate some of the application.

In shot#52346, there is an obvious effect of increasing metal impurity influx caused by neutral beam injection (NBI) and ion cyclotron range of frequency (ICRF) heating, as shown in Fig.10. And the ion effective charge number (Z_{eff}) was calculated by the visible bremsstrahlung (VB) from filterscope data to reveal the total impurity level during the discharge as shown in Fig.10 (D) [1]. Fig.10.(B) is comprised of edge oscillations, individual cycles of which are expanded in (a) and (b) [red box portion of trace (B)].(a) shows an example of "predator-prey" edge plasma oscillations about 1.2kHz, and Fig.10.(B) shows an example of "high frequency relaxation oscillation" about 1.5kHz after NBI off. 5-80Hz type-I ELM, 50-700Hz type-III ELM and 1-2kHz edge oscillation have been manifested by the statistic during the later experiment discharge phase. These data show a good capacity of filterscope in showing the H-mode and ELM characters.
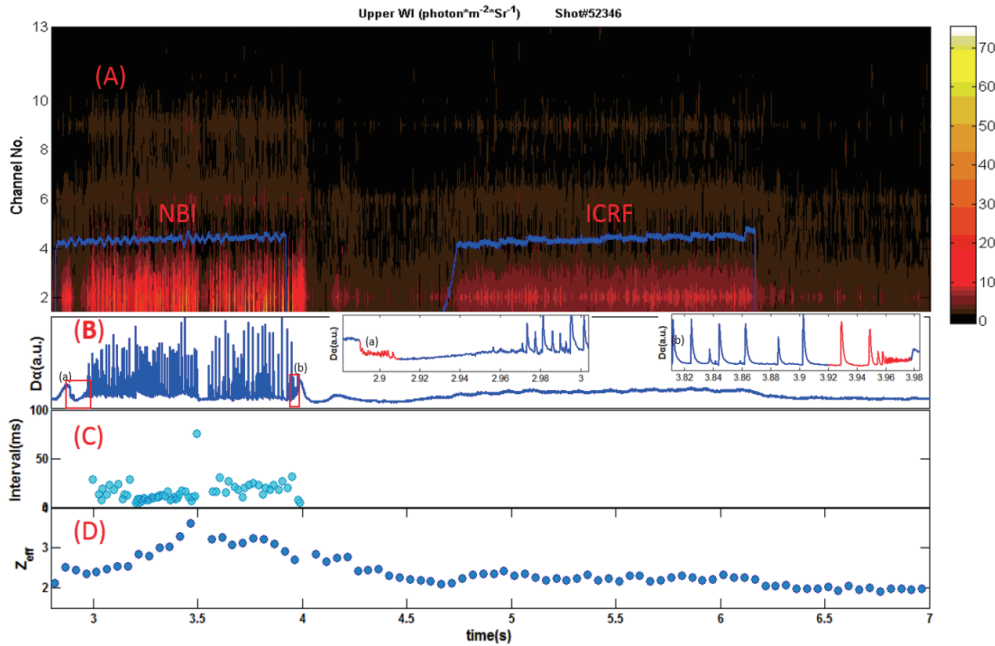
FIG.10.Shot#52346, (A) Contour plot of WI light intensity from the upper dovertor filterscope during the NBI and ICRF heating; (B) $D\alpha$ intensity from the upper divertor filterscope (viewing chord DAU3, digitized at a 100kHz sampling rate), (a) $D\alpha$ signal at 2.89s-3.12s, (b) $D\alpha$ signal at 3.8s-4s; (C) statistic of the interval between two ELM burst events; (D) the ion effective charge number (Z_{eff}) calculated from filterscope data.

IV.   SUMMARY

The absolute calibrated filterscope data has been used for analysis the edge particle transport by using some simulation codes and the Z_{eff} has also been used for evaluating the impurity level under high-Z plasma-facing components discharges in EAST. The frequency response of the PMT modules to the high frequency provide the confidence to study the burst process of ELMs and high frequency oscillation (HFO). Several types of ELMs and several kHz edge oscillation have been observed during the later of 2014 experiment discharge, and these high quality data will be in use to study the H-mode and edge physics.

ACKNOWLEDGMENTS

Reference

[1] N.H.Brooks, et al., Rev. Sci. Instrum. 79, 10F330 (2008)

[2] Zhang Ling, et al., Journal of Atomic and Molecular Physics. 30(2004)1000-0364

[3] F.Q.Wang et al, Nuclear Fusion. 54(2014)093002

[4]X.Q. Xu et al., Phys. Rev. Lett., 105, 175005 (2010) 468231

[5] Yingjie Chen, et al., Fusion Engineer and Design 88 (2013) 2825-2829

[6] E.M.Hollmann, et al., Contrib. Plasma Phys. 44(2004)301-306

Transmission Simulation and Shielding Design of Microwave for EAST Bolometer diagnostic system

Yanmin Duan [*], Zhengkun Hao, Liqun Hu, Songtao Mao

Institute of Plasma Physics, Chinese Academy of Sciences, Hefei, Anhui , China

Abstract: The metal foil resistive bolometer signals are found to be interfered by low hybrid wave
in EAST experiment. The performance of microwave transmission and shielding are studied using the simulation software HFSS (High Frequency Structure Simulator). It is possible for microwave stray in the vacuum vessel to reach the sensors through the front collimating aperture which is bared without any shielding at present. Shielding properties of Circle holes with different diameter are compared for low hybrid wave at 2.45GHz and 4.6GHz. The result shows that a hole with diameter less than $\lambda/30$ can shield the microwave well to ensure the coupled E field bellow 4V/m near the sensor which is evaluated as the equivalent power of sensor background noise. The parameter of shielding metal mesh is chosen for EAST bolometer according the simulation results.

Key words: Metal foil resistive bolometer, microwave shielding, HFSS simulation

1. Introduction

The Experimental Advanced Superconducting Tokamak (EAST) is a fully superconducting tokamak with ITER-like divertor geometry. It can achieve both single null (SN) and double null (DN) diverter configurations [1-2]. The plasma facing components (PFC) have been improved to molybdenum (Mo) tiles for main chamber wall with upper tungsten divertor and lower graphite divertor [3]. The RF auxiliary heating system include three subsystems: LHW system at 2.45GHz and 4.6 GHz, ICRF system at 27MHz and ECRH system at 140GHz. The unabsorbed RF wave can be reflected multiply by the in-vessel components and then affected some

diagnostic systems. The bolometer diagnostic is broad -band sensitive and easily experiences RF interference during LHW or ECRH heating [4-6].The microwave transition property is simulated and the shielding design are studied for EAST bolometer system in the article.

2. Bolometer diagnostics on EAST

Bolometer diagnostic is the basic diagnostic for nuclear fusion experiment, which has been used to determine the total radiated power and the radiation emission profile in magnetically confined plasma. The metal foil resistive bolometer system on EAST consists of 3 cameras with a total of 48 channels [7]. The middle camera with 32 channels views main plasma with a spatial resolution of ~4 cm and the two edge cameras, each with 8 channels, view the upper and lower divertor region separately with a spatial resolution of ~3cm, as shown in figure 1. The metal foil resistive bolometer choose Pt material as the absorbing foil and resistors. It has a wide spectral response from infrared to soft X-ray with the advantage of independence on photon energy. Additionally, it is also sensitive to neutral particles, as well as microwave. The bolometer sensors are fixed in an enclosed shielding box with three bared collimating aperture of 3×10 mm, which is installed in the adjacent diagnostic port of LHW antenna, as shows in figure 2. So it is important to shield the microwave interference for the bolometer measurement system.
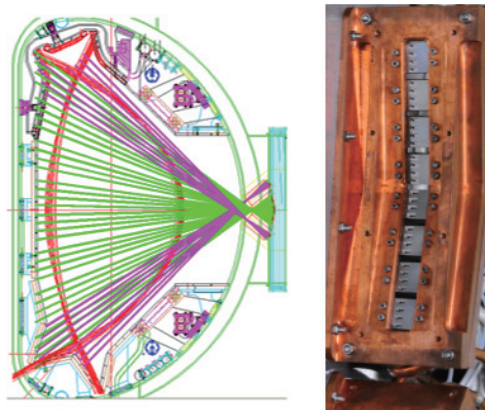
Fig.1 viewing chords geometry of resistive bolometer on EAST
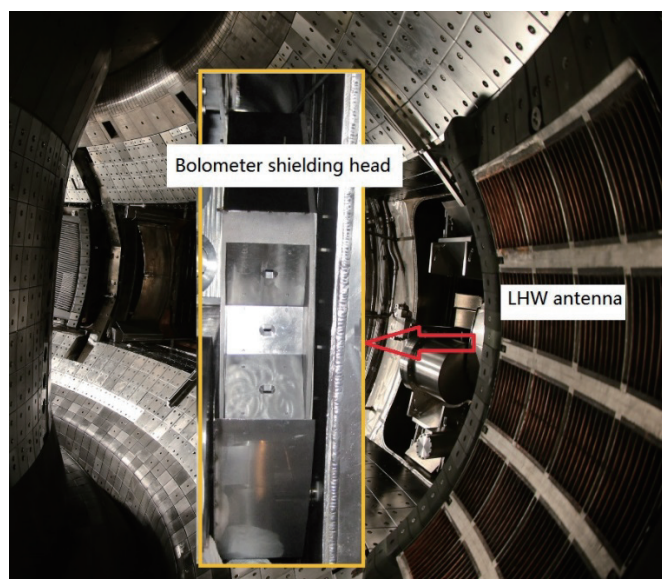
Fig. 2 Enclosed bolometer shielding box with bared collimating apertures

The metal foil bolometer signals are found to be interfered by low hybrid wave at 2.45GHz and 4.6GHz in 2014 EAST experiment. The interfered signals of bolometer have the same trend as LHW reflected waveform sometimes or have a very high voltage. It is confirmed by testing that microwave stray in the vacuum vessel can reach the bolometer detector through the front apertures, and then are absorbed by metal foil bolometer detector.

3. Transmission simulation and shielding design

The dynamic range of bolometer output voltage ranges from 0.01V to 10V. Here, the background noise of the system is 0.01V at the normal gain 1000. The equivalent power of background noise absorbed by detector is evaluated and then the coupled microwave E field through aperture can be deduced on the assumption that the signals completely come from the interfered wave. The lower limit of coupled E fielding through aperture is about 4V/m. So, the shielding design to ensure the E fielding below 4V/m is necessary and effective.

The simplified model of bolometer sensors shielding box in the vacuum vessel is built in the software platform HFSS (high frequency structural simulator). The real size of bolometer shielding head are reconstructed and a larger square chamber is built as the vacuum, as shown in figure 3. The microwave with 100kW power are

injected from a front port. The vacuum is large enough to reflect the injected wave multiply in order to achieve isotropic polarization. The properties of microwave transmission and shielding through apertures with different size are simulated. The result show that the coupled E filed near the bolometer sensors increase with the aperture size whether the aperture position is in front side or in the reverse side. Instead of the shielding size of λ/4, the result shows that a hole with λ/30 can shield the stray microwave effectively with a low E field bellow 4V/m inside the sensor shielding box. The simulation result is given in figure 4. It is verified that the present bared aperture of 3×10mm cannot shield the microwave at 2.45GHz and the metal mesh in front of the aperture is necessary.
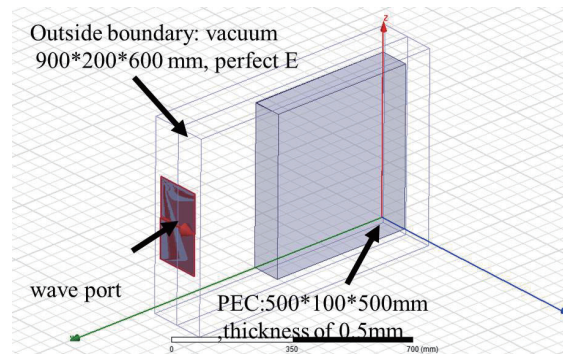
Fig.3 The simplified model of bolometer sensors shielding box
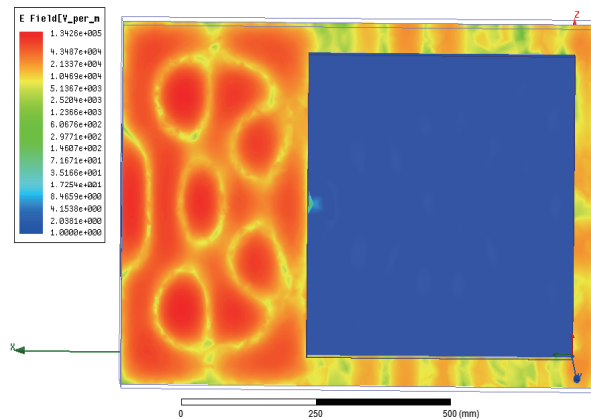
Fig. 4 The coupled E filed distribution in the vacuum and bolometer shielding box with hole

of λ/30

Research found that metal shielding meshes can shield the microwave efficiently with well-designed parameters [6]. The spacing g and the wire diameter d

of mesh grid are two critical parameters. According the long wave transmission theory formulas in reference [6], microwave transmissions fraction as function of mesh grid parameters g/λ and g/d are showed in figure 5. It shows that the microwave transition fraction increases with g/d and g/λ. However, the balance between the screening efficiency and the photon transmission is also important. The best parameter $g/d\sim 3$ perform good shielding and moderate photon transmission with maximum ratio of photon transmission fraction to microwave transmission fraction. The simulation result shows that the E field near bolometer sensors through mesh grid with $g/\lambda\sim 3 /80$ and $g/d\sim 3$ is about 0.5V/m, as shown in figure 6.
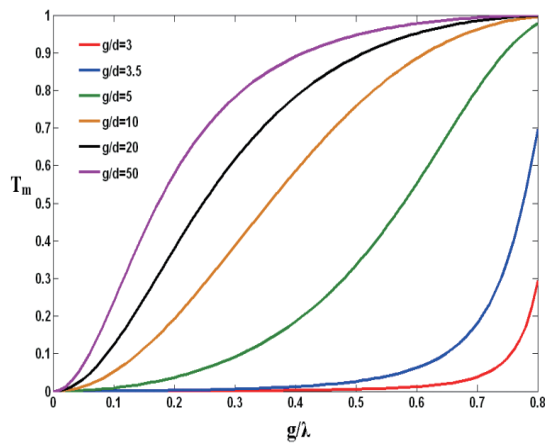
Fig. 5 Microwave transmissions at 2.45GHz as function of mesh grid parameter
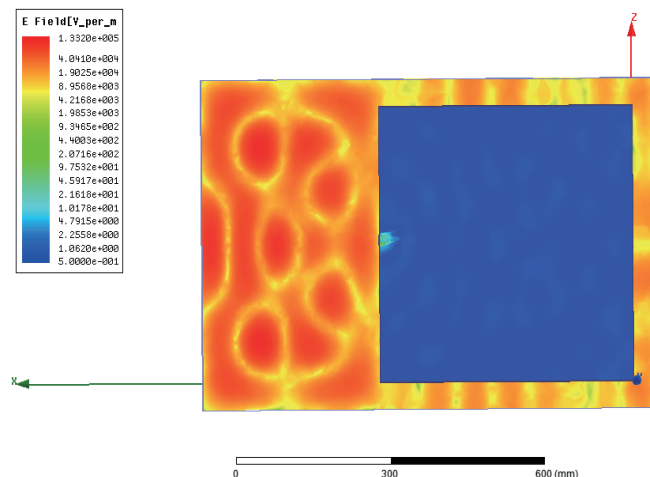
Fig. 6 The coupled E filed distribution in the vacuum and bolometer shielding box with mesh grid parameter $g/\lambda\sim 3 /80$ and $g/d\sim 3$

4 Summary

The properties of microwave transmission and shielding through bolometer front

apertures with different size are simulated based on the HFSS software platform. The mesh grid in front of aperture for microwave shielding are analyzed. The spacing g and the wire diameter d of mesh grid are two critical parameter. Good shielding performance can be achieved in the condition of $g/\lambda \sim 3/80$ and $g/d \sim 3$ for EAST low hybrid wave at 2.45GHz. In consider of the 140GHz and 4.6GHz LHCD in the next round of EAST experiment, the metal mesh with spacing $g \sim 0.635$mm and wire diameter $d \sim 0.15$ are installed in front of the collimating aperture. The optical transmission fraction is 60%.

Acknowledgments

References

[1]Y. Wan, et al, Nucl. Fusion, 40(2000)1057.

[2] B.Wan, et al., Nucl. Fusion **53** (2013) 104006.

[3] Y. T. Song, et al., IEEE Transactions on Plasma Science, 42(2014) 415.

[4] A. Huber, et al., Fusion Engineering and Design 82 (2007) 1327.

[5] D. Hathiramani,et al., Fusion Engineering and Design 88 (2013) 1232.

[6] D.Zhang,et al, 38th EPS Conference on Plasma Physics (2011) P5.056.

[7] Y.M.Duan, et al., Rev. Sci. Instrum. **83** (2012) 093501.

Numerical Modeling of 3D Magnetic Field Topology under RMPs and the comparison with experimental observations on EAST

Manni Jia[1,2], Y. W. Sun[2], F. C. Zhong[1] , L. Wang, K. Gan, & EAST teams[2]

[1]*College of Science, Donghua University, Shanghai 201620, People's Republic of China*
[2]*Institute of Plasma Physics, Chinese Academy of Sciences,, Hefei 230031, China*

Email: jiamanni@mail.dhu.edu.cn

ABSTRACT

A numerical code using field line tracing for modeling the three-dimensional magnetic field topology under resonant magnetic perturbations (RMPs) has been developed and applied in Experimental Advanced Superconducting Tokamak (EAST) 2014 campaign. Currently, the model is simplified by using vacuum paradigm and neglecting the toroidal field ripple.

The modeling result predicts that the possible strike point splitting on plasma facing component and the lobes like structure on the boundary are observable in various diagnostics at different locations.It is shown that the strike point splitting strongly depends on the edge stochasticity, which is a combined effect of both perturbation spectrum and equilibrium properties.

In a lower single null configuration, it is found that RMP may also change the magnetic structure near the upper x-point and form a similar strike point splitting on the upper divertor. It depends on the distance between the two separatrix, whichthreshold value depends on both the RMP strength and the equilibrium properties.

To examine the RMP system on EAST and its effect on plasmas, some experiments with RMPs were hold in the 2014 campaign. The static and rotational perturbation were both tested and results confirm the RMP efficiency.Particle flux profiles on divertor targets measured by divertor probes had verified the existing strike point splitting induced by RMPs.The results are consistent with the numerical modelingwithin measurement uncertaintiesand confirm the edge stochasticity induced by RMPs.

Background

H-mode is a favored experimental regime on varies tokamak devices and a promising operation mode of ITER and other future reactors. The accompanied repetitive instabilities, known as edge localized modes (ELMs), help to release impurities out of plasma region but on the contrary, especially the so-called Type-I ELMs, release large amounts of particles and energy flux directly to the first wall and divertor target plates, which will become a threat to the lifetime of divertors and other plasma facing components. Furthermore, impurities being sputtered from the wall may enter the core then cause energy losses and even disruptions. According to the estimation by Hawryluk[1], there will be about 0.2-20MJ energy loss per ELM eruption on ITER similar shape and collisionality, about 20 times of the suffering limit of current material candidates (carbon fiber or tungsten). So ELM-control has become a hot topic in fusion research. The goal of ELM control is to eliminate ELMs or increase the ELM frequency and reduce the extent. At the same time, fine confinement properties should be kept as far as possible. Resonant magnetic perturbations, lower hybrid waves and pellet injection etc. are all reported with ELM control ability.

As one of the effective way to control ELMs, resonant magnetic perturbations (RMPs) have been put into use in various tokamak devices. One highlight is the experiments with n=3 RMPs on DIII-D which have achieved reproducible elimination of Type-I ELMs during H-mode[2][3][4]. Similar experiments on JET, MAST, ASDEX-Upgrade, NSTX, KSTAR were also carried out but he ELM-control effects vary a lot among different devices and different experiment parameters. So the physical mechanism of ELM-control is still unclear. More experimental and theoretical researches should be made.

The understanding of the 3D magnetic field topology formed due to the RMPs is significant for the study of ELM-control mechanism. The separatrix and strike point splitting have been observed during RMP experiments[5][6][7]. The 3D topology as well as theoretical edge stochastic degree induced by RMPs can be modeled and calculated with numerical methods. The modeling results on MAST, JET, DIII-D etc. have played important roles in ELM-control analysis and successfully predict the topology changes induced by magnetic perturbations.

EAST is an ITER-like tokamak and it can provide important experimental experiences for ITER. And in steady long pulse operation on EAST, it is necessary to demonstrate the capability of handling the large transient heat load induced by type-I ELMs on divertor and PFCs.

RMP coils on EAST

One RMP coil system designed for ELM control, error field studies and resistive wall mode (RWM) control has been installed on EAST in 2014[8][9]. There are two in-vessel up-down symmetric arrays. Each array has 8 coils uniformly distributed along the toroidal direction, and each coil has four turns. Their location can be seen in Figure 1. With enough power supplies, the RMP-coil system is flexible in generating perturbation spectrum. The maximum coil current is designed to be 2.5 kA per turn. Besides, the perturbation spectrum can be switched during one shot as Figure 2 shows.
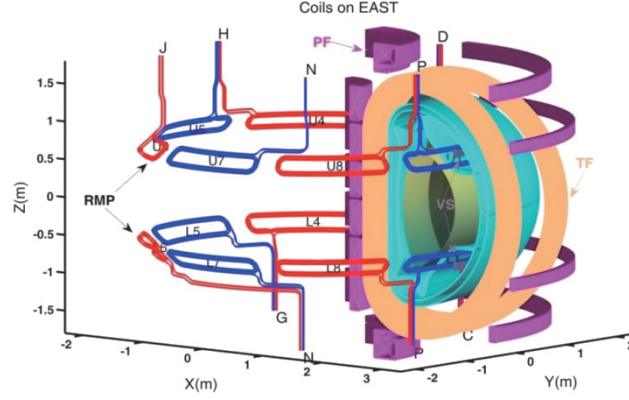
Figure 1. RMP coils on EAST
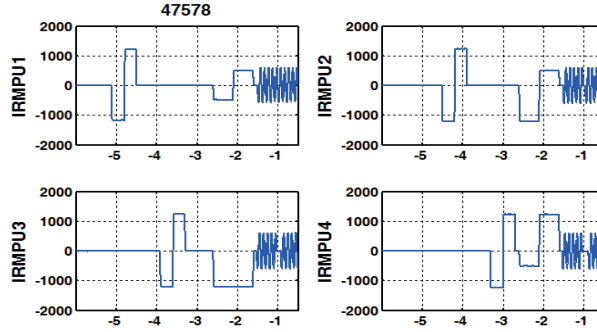
Figure 2. An example of the flexible perturbation spectrum switching of RMP coils on EAST.

Numerical Modeling of 3D magnetic topology

The basic method to model the magnetic field topology is field line tracing. We have developed MAPS code for RMP perturbation spectrum analysis [8] and there is one module named TOP2D, which is developed for modeling 3D magnetic topology both inside and outside separatrix[10]. The field line is traced by integrating two dimensional field line equations in laboratory coordinante with fixed step size $d\phi$,

$$\begin{cases} \dfrac{dR}{dl_\phi} = \dfrac{\partial}{\partial Z}\left(\dfrac{\psi_p}{g}\right) \\[2mm] \dfrac{dZ}{dl_\phi} = -\dfrac{\partial}{\partial R}\left(\dfrac{\psi_p}{g}\right) \end{cases} \tag{1}$$

where $dl_\phi = Rd\phi$ and g is a fuction of ψ_P. Here ψ_P is the combination of equilibrium part ψ_{p0} and the perturbation $\overline{\psi}_p$. As RMP coils are separated along turus, the actual perturbation spectrum contain components with a set of mode number n. To save time, the perturbation of every (R, Z) grids can be written with subscript of mode number n as,

$$\overline{\psi}_p = \sum_n \overline{\psi}_{pn}(R,Z)e^{in(\phi+\phi_0)}. \tag{2}$$

Here ϕ_0 is the tracing initial toroidal location and n=1,2,… can be chosen and combined freely according to the calculation demand.

Field line tracing can start at points on poloidal planes, divertor plates, or any other points of interest. The tracing of one field line will be terminated when it crosses PFCs or the tracing turn has reached the initially set maximum turns. The topology

structure can be presented with Poincaré plot and magnetic footprint patterns. Figure 3 shows the Poincaré plot of even n=2 RMPs. Figure 4 shows the footprint of even n=1,3 and 4 RMP fields.
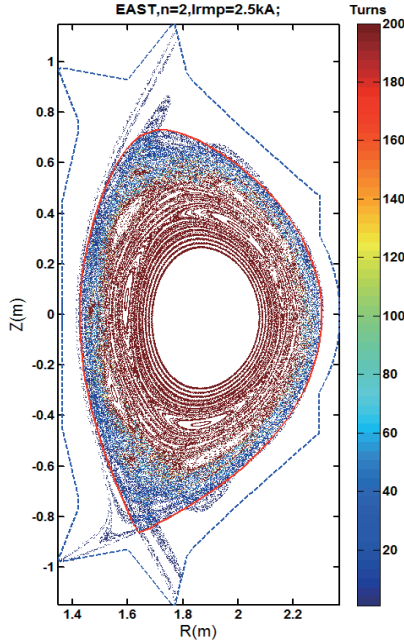
Figure 3. Poincaré plot of even n=2 RMPs on $\phi = 0°$.
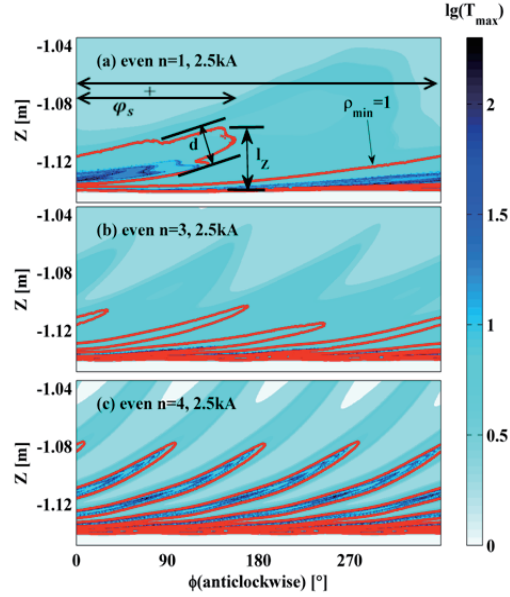
Figure 4. Footprint patterns of even n=1,3,4 RMPs. In (a) the three parameters to estimate the splitting degree is labeled.

Three parameters are used to characterize footprint's splitting degree. They are labeled on Figure 3(a) as we choose strike points with $\rho_{min} = 1$ as the new fromed 3D separatrix. The first parameter is the width of each stripe d. The second is the splitting width in vertical direction from the peak to the bottom of the stripe represented by l_z. And the third is the total toroidal angle that each stripe covers ϕ_s.

We study the dependence of strike points splitting on edge stochasticity by TOP2D code. Edge stochasticity is measured by stochastic layer width $W_{sto} = 1 - \rho_{\sigma=1}$, where $\rho_{\sigma=1}$ represents the innermost normalized flux with Chirikov parameter $\sigma_{chir} \geq 1$. The modeling results shows that with same coil configuration, the ramp-up coil current will make wider stochastic region in the plasma boundary and make the splitting larger. The splitting degree at lower outer divertor on $\phi = 100°$ of ramp-up coil current is shown in Figure 5. The edge stochasticity and the splitting degree parameters can be seen in Figure 6. We use three plasma equilibriums of different q profiles (q95=3.0, 4.5 and 6.0 respectively.) They are obtaioned from equilibrium modeling based on the EAST experimental discharge of shot 38300 at 3.9s[11]. With q95 increasing in this case, the resonant components become stronger and the stochastic layer in the edge becomes wider, so strike point splitting is become stronger. It can be referred by the much larger connection length and wider peaks region in Figure 7.
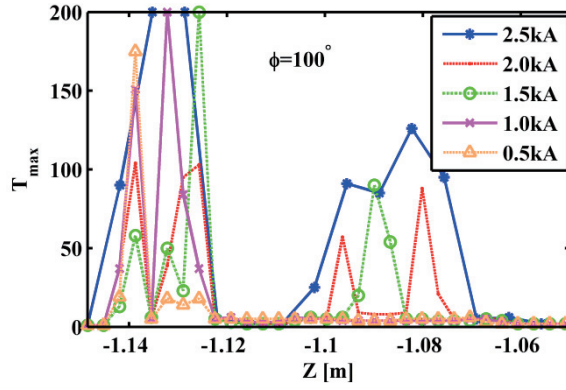
Figure 5. The profile of connect length of strike points distributed on $\phi = 100°$.
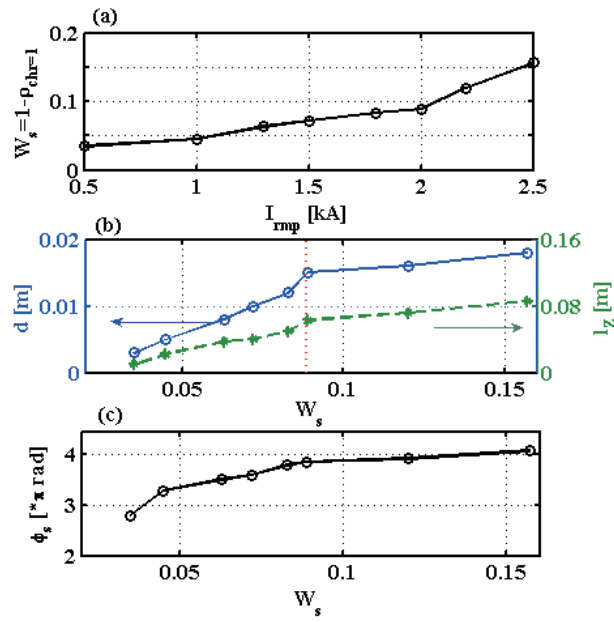
Figure 6. Footprints' characteristics for I_{RMP} scanned from 0.5 kA to 2.5 kA. The dependence of stochastic width on coil current is shown in (a). The dependence of the stripe width d and peak-bottom distances l_z on Ws are shown in (b). (c) shows the dependence of the covered toroidal angle of each stripe on W_{sto}.

Stronger resonance on the edge
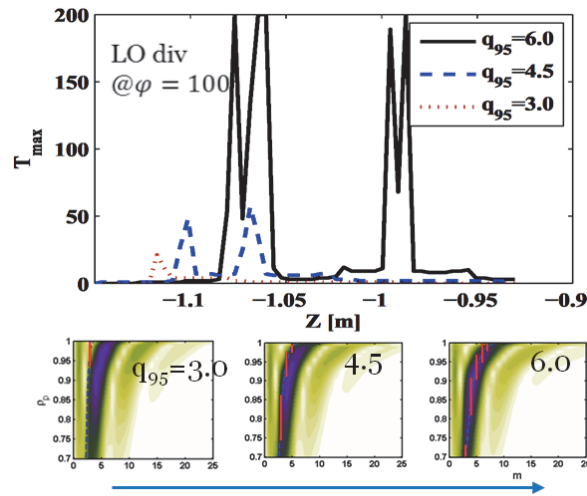
Figure 7. The connection length profiles when q95=3.0, 4.5 and 6.0. As the edge magnetic surface move into the stronger resonant part of the spectrum, larger splitting was caused.

We also discussed the upper strike point in near-DN configurations. dR_{sep} is defined as the physical radial separation of the X-points' flux surfaces. A similar strike point splitting appears on the upper divertor induced by RMP in a near-DN on EAST. It depends on the distance between the two separatrix. To avoid the upper strike points near the upper x-point, it is necessary to keep the distance between the two separatrix larger than a threshold value that depends on the RMP strength and the equilibrium properties.
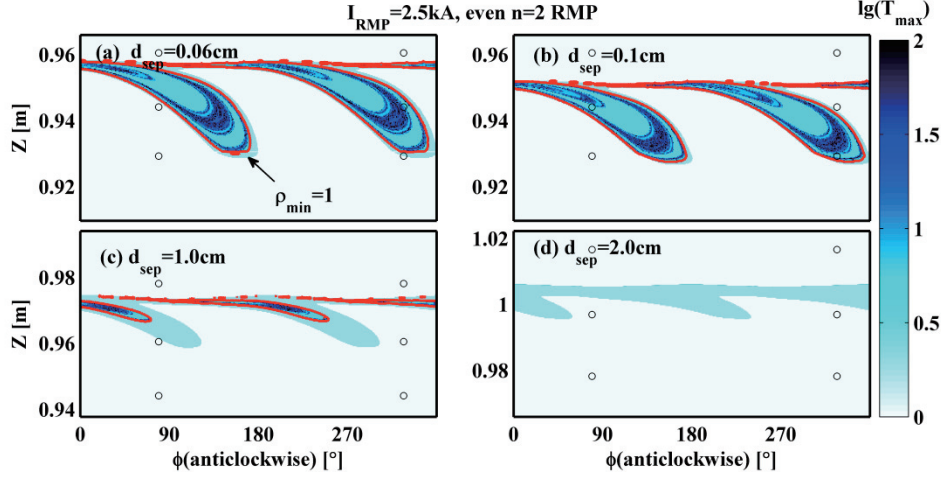
Figure 8. The footprints on UOdiv of $\left|dR_{sep}\right|$ = 0.06cm (a), 0.1 cm (b), 1.0 cm (c) and 2.0 cm (d). Points are superimposed with colors represent $\lg(T_{max})$. The red line overlaid on each subgraph is the contour line of strike points with ρ_{min} =1.0. Note that the vertical axis of four subgraphs is in different Z range because the strike region is changing. But the scales are kept unchanged.

Recent experimental observations in EAST RMP experiments

RMP experiments have been primarily operated in the EAST 2014 campaign. The experimental observations are compared with the numerical modeling. Highspeed visible CCD camera, infrared CCD camera and divertor probes all observed strike point splitting during RMP experiments.

The visible and infrared high-speed CCD cameras which observe the poloidal section of vacuum vessel and part of the divertors are possible to be used for observing the lobes on the boundary and strike point splitting. The spacial resolutions are about 3mm (visible) and 4mm (infrared). One example of the observed heat load patterns on lower-outer divertor is presented in Figure 9.
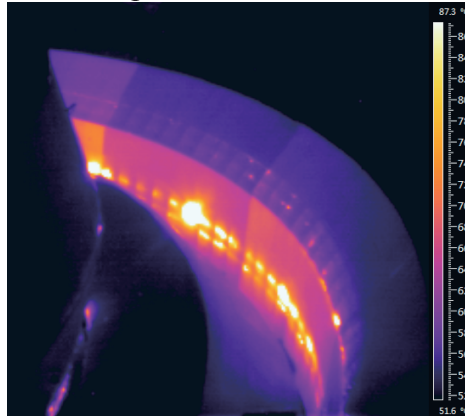
Figure 9. Heat load patterns observed by infrared CCD camera in shot 47004, which related to strike point splitting resulted by RMP fields.

The divertor probe arrays measure particle fluxes on divertor targets. The spacial resolutions of divertor probes on EAST are about 12-18mm (upper) and 10-15mm (lower). The probes on upper divertor are located at D port and O port while those on lower divertor are located from D port to O port.

In shot 52340, static even n=1 RMPs are applied from 3.2s to 3.5s. The coil current is 10kAt. The plasma during this time is with B0=2.3T, Ip=400kA and q_{95}=5. The signals of divertor probes are shown in Figure 10. The subfigure (a), (b) and (c) represent the time evolution of upper-outer probes in D port, O port and lower-outter probes from D to G port respectively. We compared these signals with numerical modeling result and plotted in Figure 11. We use simulated T_{max} profiles along the corresponding probe location to make comparison with saturated ion flux (js in A/cm^2) measured by divertor probes. The js profiles without and with RMP is plotted by red circles and blue dashed lines respectively. The simulated T_{max} profiles are plotted by green lines. The new formed peaks are obvious and marked by the dotted red line. It should be noted that to meet the experimental observation the simulated results is shifted accordingly as the green arrows in each subfigure. The considerable mismatch may come from errors of EFIT calculation, tracing assumptions and measuring error. It will be checked carefully in future experiments.
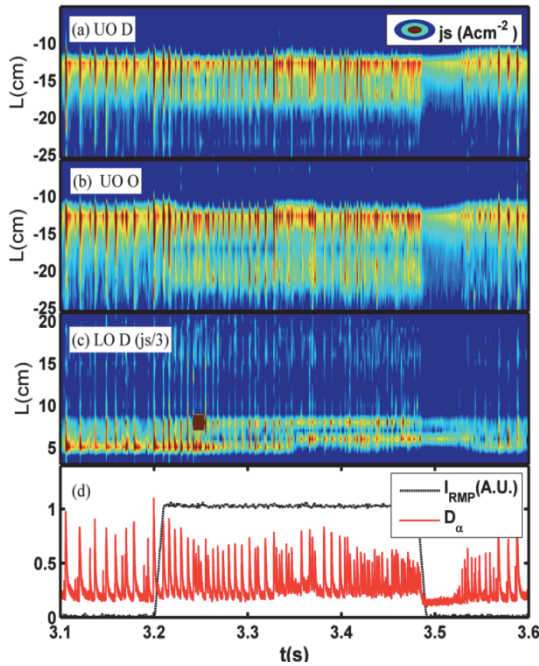
Figure 10. Profiles of saturated ion fluxes measured by divertor probes in upper-outer D port (a) and O port (b) and lower-outer D-G port (c).
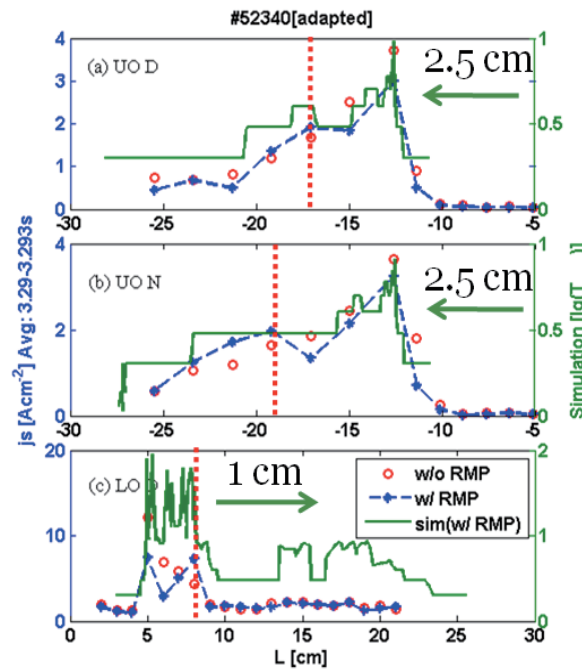
Figure 11. The experiment signals are compared with the simulated results.

In shot 52342, we tested rotate RMP fields from 3.2 to 3.5 s, as shown in Figure 12 (d). The coil current is 10kAt. The plasma parameters is almost the same with that of shot 52340. The RMP fields is even n=1. The js signals are shown in Figure 12 (a) to (c). The overlapped red contours are the simulated ρ_{min} contours without any shift. The observed structure is almost coincide with the vacuum simulated results, except a little inconformity in L direction. The structure observed by divertor signals again proved the effect of the RMP field, which will generate 3D magnetic topology.
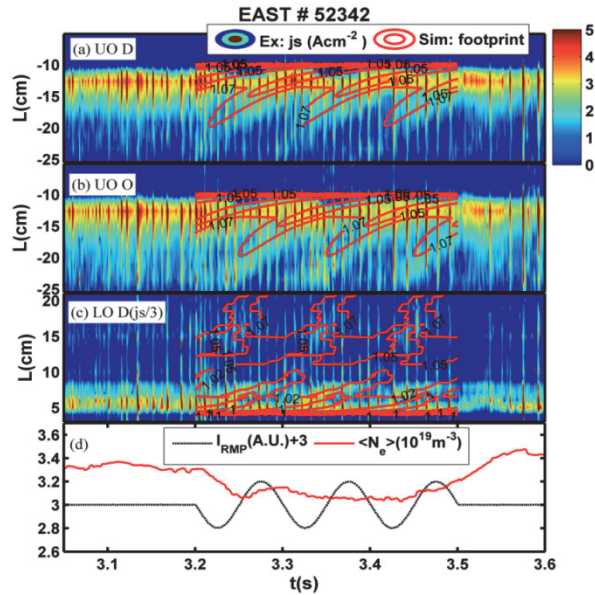
Figure 12. In shot 52342, even n=1 rotate RMP fields are applied in three periods from 3.2 s to 3.5s. Saturated ion fluxes profiles of upper-outer divertor probes and lower-outer divertor probes are presented and overlapped with simulated results. In general, the 3D structure presented by probe signals and the simulated results are almost consistent.

Summary

3D Magnetic topology under RMPs with lobes on the plasma boundary and strike point splitting on the divertor board is modeled by TOP2D code. The splitting degree has close relation with the edge stochasticity, which is determined both by RMP spectrum and equilibrium parameters, according to the numerical modeling.

The RMP experiments on EAST have shown the efficiency of RMPs on ELM mitigation. The divertor probes detected the splitting of particle fluxes on divertor board, and the results are almost consistent with numerical modeling results.

Plasma response and toroidal ripple will be considered in the modeling and more experiments will be done in the future. The process of stochastic transport will then be studied.

References

[1] R. J. Hawryluk *et al.,* 2009 Nucl. Fusion **49**, 065012

[2] T. Evans *et al. ,* 2005 Nucl. Fusion **45**, 595

[3] T. Evans *et al. ,* 2004, Phys. Rev. Lett. **92**, 235003

[4] M. E. Fenstermacher *et al.*, 2007, J. Nucl. Mater 363-365, 476

[5] M. W. Shafer *et al.*, 2012 Nucl. Fusion **52**, 122001

[6] D. M. Harting *et al.*, 2012 Nucl. Fusion **52**, 054009

[7] A. Kirk *et al.*, 2012 Phys. Rev. Lett. **108**, 255003

[8] Y. Sun *et al.*, 2014 'Modelling of non-axisymmetric magnetic perturbations in tokamaks', Submitted to Plasma Phys.Control. Fusion

[9] Y. Song *et al.*, 2014 IEEE Trans. Plasma Sci. **42**, 415

[10] M. Jia *et al.*, 2014, submitted to PPCF

[11] G. Li *et al*., 2013 Plasma Phys. Control. Fusion **55**,125008

The response of short-scale density fluctuations to the activity of beta-induced Alfvén eigenmodes during strong tearing modes on EAST tokamak

G. M. Cao[1], Y. D. Li[1], Q. Li[2], P. J. Sun[1], G. J. Wu[1], L. Q. Hu[1] and the EAST Team

1 *Institute of Plasma Physics, Chinese Academy of Sciences, PO Box 1126, Hefei, Anhui 230031,China*

2 *School of Physics and Optoelectronic Engineering, Guangdong University of Technology, Guangzhou 510006,China*

Beta-induced Alfvén eigenmodes (BAEs) during strong tearing modes (TMs) have been frequently observed in fast-electron plasmas of EAST tokamak. The dynamics of the short-scale ($k_{\perp}\rho_s \sim 1.5-4.3$) density fluctuations during the activity of BAEs with strong TMs has been preliminarily investigated by a tangential CO_2 laser collective scattering system. The results suggest the active, but different, response of short-scale density fluctuations to the TMs and BAEs. In the low-frequency (0-10 kHz) part of density fluctuations, there are harmonic oscillations totally corresponding to those of TMs. In the medium-high frequency (10-250 kHz) part of density fluctuations, with the appearance of the BAEs, the medium-high frequency density fluctuations begin to be dominated by several quasi-coherent (QC) modes, and the frequencies of the QC modes are closely related to the changes of BAEs. These results would shed some light on the understanding of the multi-scale interaction physics.

I. INTRODUCTION

In magnetically confined plasmas, short-scale turbulent fluctuations, e.g., ion temperature gradient (ITG) turbulence, trapped electron mode (TEM) turbulence, and electron temperature gradient (ETG) turbulence, are well believed to be a major candidate in producing anomalous transport and and thereby degrading the confinement [1-4]. Substantial theoretical and experimental investigations [5-11] suggest that, the large-scale instabilities, e.g., magnetohydrodynamic (MHD) activity and Alfvén eigenmodes (AEs), could interact with short-scale turbulent fluctuations and concomitantly affect the plasma confinement. Thereinto, a better understanding about MHD and short-scale turbulence has been achieved by lots of experimental studies, for example, the tearing modes (TMs) can locally modify both density and temperature profiles, and therefore modulate the short-scale turbulence and the associated transport [12, 13]. However, the experimental studies on the interaction between AEs and short-scale turbulence are still scarce, probably due to the limitation of diagnostic tools and experimental condition.

The AEs are fundamental low-frequency electromagnetic oscillations in magnetized plasmas, and are always found to be excited by energetic particles in fusion plasmas [14, 15]. Beta-induced Alfvén eigenmodes (BAE) , one kind of the most common AEs, can be used to transfer the energy of fusion-born-alpha-particle to the thermonuclear plasma, and could be important for the future fusion devices [16, 17, 21]. The BAEs are situated in the low-frequency gap of the Alfvén continuum with the parallel wave-number $k_{\parallel} \approx 0$, and are formed due to the finite compressibility of plasma pressure [11]. The BAE activities have been widely observed in tokamak fusion devices, such as DIII-D, TFTR, Tore-Supra, ASDEX Upgrade, HL-2A, etc [16-21].

On EAST tokamak, the BAEs during strong TMs have been frequently observed during the lower hybrid wave (LHW) plasmas or the runaway discharge of Ohmic plasmas [22]. A tangential CO_2 laser collective scattering system [23] was first employed to investigate the response of short-scale ($k_{\perp}\rho_s \sim 1.5-4.3$) density fluctuations to the activity of BAEs during strong TMs. It is observed that, the low-frequency (0-10 kHz) density fluctuations always have harmonic oscillations fully corresponding to those of TMs, and this response appears to result from the direct modulation of TMs; however, with the appearance of the BAEs, the medium-high frequency (10-250 kHz) density fluctuations begins to be dominated by several quasi-coherent (QC) modes, and the frequencies of the QC modes are closely related to the changes of BAEs. These results indicate the active, but different, roles of TMs and BAEs in the modulation of the background density fluctuations.

II. EXPERIMENTAL SETUP

EAST is a superconducting tokamak with major radius $\mathbf{R} = 1.88\,\text{m}$ and minor radius $\mathbf{a} = 0.45\,\text{m}$. The experiments are performed in deuterium plasmas with plasma current $I_P < 1\,\text{MA}$, toroidal magnetic field $B_t < 3\,\text{T}$ and inverse aspect ratio $\varepsilon = 0.24$. The magnetic fluctuations are measured simultaneously by the low-frequency (0-50 kHz) Mirnov probes and high-frequency (0-250 kHz) Mirnov probes, and the chord-averaged electron density is measured by a far-infrared (FIR) hydrogen cyanide (HCN) laser interferometer.

A CO_2 laser collective scattering system [23] was first employed on EAST to provide the measurement of short-

scale density fluctuations. It was designed according to the scheme—the oblique propagation of the probe beam with respect to the magnetic field [24]. Due to the strong anisotropy of the short-scale turbulence in tokamak plasmas [1, 25], the scattering geometry of this scheme can take advantage of the curvature of magnetic field lines, and the enhanced spatial localization along the probe beam direction can be achieved. Four detecting channels were deployed to provide the simultaneous measurement of the core density fluctuations with the wave-vector of k_1 and k_2, and the outer density fluctuations with the wave-vector of k_3 and k_4. The wave-numbers of the measured density fluctuations is $k_1=k_3=10 \mathrm{cm}^{-1}$ and $k_2=k_4=18 \mathrm{cm}^{-1}$, and correspondingly $k_\perp \rho_s \sim 1.5-4.3$, where $k_\perp$ is the wave-number perpendicular to magnetic surface and ρ_s is the ion gyro-radius with electron temperature. Base on the ray tracing calculation and the equilibrium reconstruction by the EFIT code [26], the radial localization of core and outer density fluctuations can be calculated as $r/a \approx 0.4-0.5$ and $r/a \approx 0.7-1$, respectively. The wave-number resolution Δk is about $2 \mathrm{cm}^{-1}$ and the sampling rate is $2 \mathrm{MHz}$. It should be noted that, in the EAST scattering system, both the probe beam and the four detecting beams pass through the plasmas, and almost have the same optical path due to the small scattering angles, and therefore the scattering system can remove the spurious information caused by the interference effects in the measurement [23].

III. RESULTS AND DISCUSSIONS

On the EAST tokamak, the BAEs during strong TMs have been frequently observed in the runaway discharges of Ohmic plasmas [22]. As shown in the spectrogram of Mirnov signals in figure 1(g), the low-frequency part ($0<f<10 \mathrm{kHz}$) demonstrates $m/n=2/1$ TMs and the corresponding harmonic oscillations, which propagate in the electron diamagnetic drift direction. And the BAEs are characterized by a pair of high-frequency modes (f_{H1} and f_{H2}), which propagate toroidally and poloidally in opposite directions. It has been identified that the frequencies of the BAEs are closely associated with the magnetic island width, and the frequency difference between the pair modes is exactly twice the fundamental frequency f_{tm} of TMs, i.e., $f_{H2}-f_{H1}=2f_{tm}$ [21, 22]. The mode numbers of the two BAE modes f_{H2} and f_{H1} are $m/n=2/1$ (co-rotation with the magnetic island), and $m/n=-2/-1$ (counter-rotation with the magnetic island), respectively.

Figure 1 demonstrates a runaway discharge of Ohmic plasma with plasma current $I_P=250\mathrm{kA}$ and toroidal magnetic field $B_t=1.8 \mathrm{T}$. As shown in figure 1(b), the central-chord-averaged electron density has a large decrease at 2.162 s due to a slight disruption, and the TMs are excited greatly with the fundamental frequency f_{tm} about 1.4 kHz. After the slight disruption, the fundamental
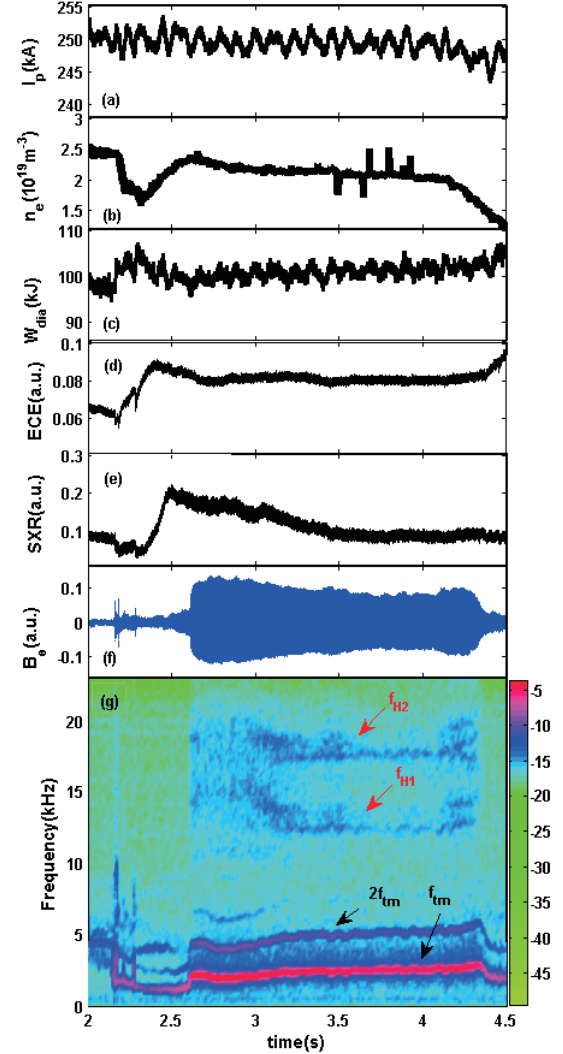
FIG. 1. Spectrograms of Mirnov signals for EAST shot 40111. From top to bottom: (a) plasma current I_P, (b) the central-chord-averaged electron density n_e, (c) plasma stored energy W_{dia}, (d) ECE signal, (e) SXR signal, (f) Mirnov signal, and (g) the spectrogram of Mirnov signal.

frequency of the TMs increases to about 2.5 kHz, and the amplitude was also enhanced. Meanwhile, the amplitude of the Mirnov signal increases significantly and the BAEs are excited. It can be observed that, the intensity of the TMs is much larger than that of the BAEs. The frequencies of the BAE modes show a characteristic of down-sweeping from 2.609 s to 3.317 s, and afterwards are stable at about 12.5 kHz and 17.68 kHz, respectively. It is worth noting that, there appears to be spectral broadening of BAEs during about 3.354-3.521 s and within 0.124 s before the final disappearance of BAEs, which could be closely related to the nonlinear coupling between the BAEs and TMs [11]. Given in Fig. 2 is the spatiotemporal evolution of the extreme ultraviolet (XUV) radiation during this discharge. During the slight disruption, the XUV intensity in the core

231
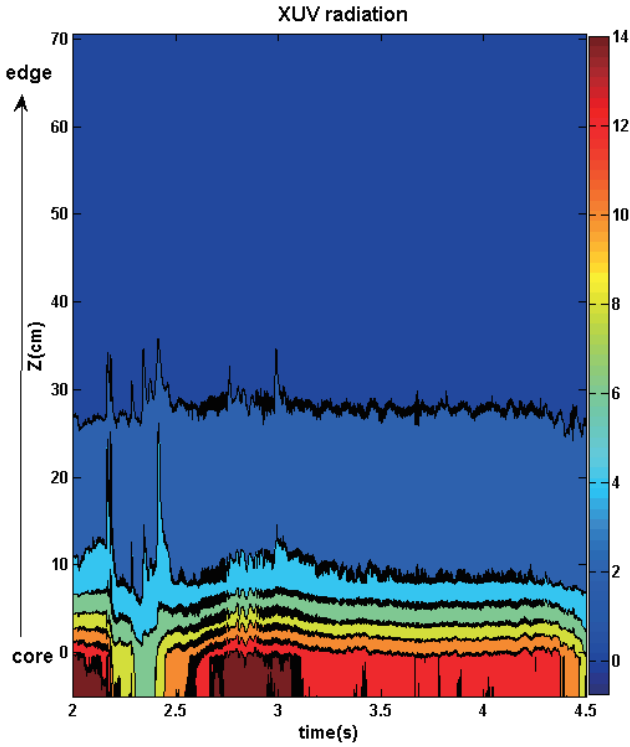
FIG. 2. Time evolution of XUV radiation profile at vertical direction for the discharge in figure 1.

FIG. 3. (a) the spectrogram of low-frequency signal of density fluctuations k_1, and (b) the cross-correlation spectrum between the microturbulence signal and the Mirnov signal. In cross-correlation analysis, the noise level is 0.1024.

has a great decrease, which could result from the appearance of abundant runaway electrons.

Figure 3(a) displays the spectrogram of the low-frequency (0-10 kHz) signal of density fluctuations k_1. Considering the noise level of the scattering system, the fluctuation signal lower than 1.5 kHz is filtered out. It can be observed that, the spectrogram of the low-frequency density fluctuations show significant harmonic modes, and their frequencies are corresponding to those of the TMs. The cross-correlation spectrum analysis between the low frequency density fluctuation signal and the Mirnov signal is given in figure 3(b). The cross-correlation level between density fluctuations and magnetic fluctuations is much higher than the noise level in the frequency range of these harmonic modes, which suggests that the short-scale density fluctuations could be modulated directly by the strong TMs. This response of density fluctuations to TMs had been always observed in experiments [7-9], and a plausible underlying mechanism could be that, due to the MHD equilibrium condition $\nabla P = \mathbf{j} \times \mathbf{B}$ [27], the low-frequency magnetic fluctuations would induce the perturbation of the pressure gradient of the same frequency, and further lead to the oscillations of the short-scale density fluctuations.

Figure 4(b) shows the spectrogram of the medium-high frequency (10-250 kHz) signal of density fluctuations k_1. In order to facilitate the comparison, the contour plot of spectral density of magnetic fluctuations is given in figure 4(a). The period of the BAE activity is divided into four phases, i.e., phase I, II, III and IV. During the slight

disruption from 2.162 s to 2.609 s before phase I, various kinds of modes with obvious frequency chirping are greatly destabilized probably due to the abundant runaway electrons, and these modes can not be observed in the magnetic fluctuations, suggesting the characteristics of electrostatic modes. The strongest one of these modes is a low-frequency quasi-coherent (QC) mode, mainly concentrating on about 13.2-21.5 kHz. When the BAEs are excited in phase I, additional medium-high frequency QC modes are excited, and the previous low-frequency QC mode becomes weak slightly. That is to say, with the appearance of the BAEs, the medium-high frequency density fluctuations begins to be dominated by these QC modes. It is worth noting that, during phase II and phase IV, the BAEs appear to have spectral broadening, and correspondingly the frequencies of the QC modes have up- and down-jump behaviors. After phase IV, the BAEs disappear, and afterwards the QC modes also vanish gradually.

The corresponding power spectrum of magnetic fluctuations and density fluctuations k_1 during phase I and III are displayed in figure 5. Thereinto, the low-frequency (0-10 kHz) part, reflecting the direct modulation of the TMs on density fluctuations, has the same phenomenon as figure 3. For the the medium-high frequency (10-250 kHz)

232
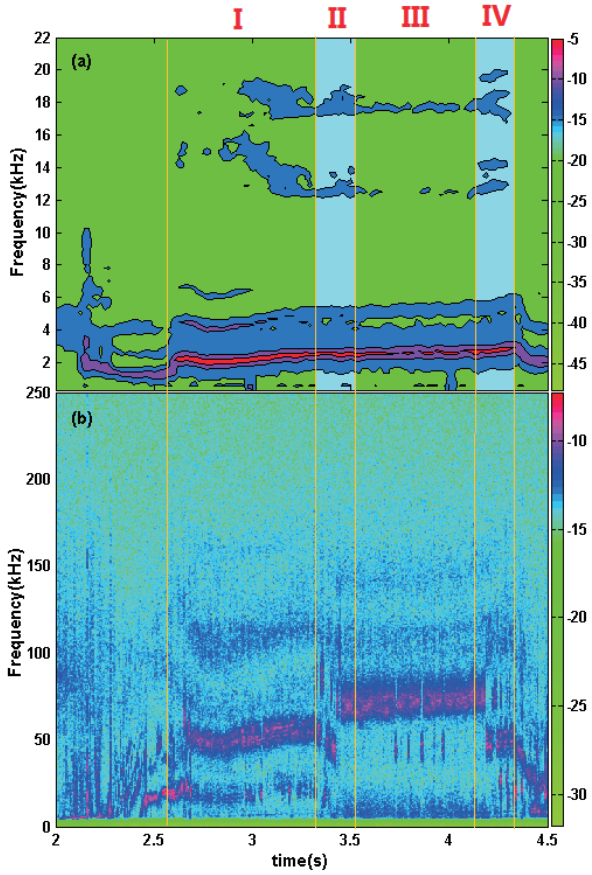
FIG. 4. (a) The contour plot of the spectrogram of Mirnov signal, and (b) the spectrogram of the medium-high-frequency signal of density fluctuations k_1. The spectra power is in units of dB.

FIG. 5. (a) The corresponding power spectrum of the magnetic fluctuations (green) and density fluctuations k_1 (purple) in phase I, and (b) the power spectrum of the magnetic fluctuations (green) and density fluctuations k_1 (purple) in phase III. The spectra power is in units of dB

part, with the appearance of the BAEs during phase I, the density fluctuations begins to be dominated by four QC modes, as shown in figure 5(a). The frequency bands of these QC modes in phase I are $f_{QC1} \sim 13.6 - 21.3\,\text{kHz}$, $f_{QC2} \sim 40.7 - 65.4\,\text{kHz}$, $f_{QC3} \sim 94.5 - 125.2\,\text{kHz}$ and $f_{QC4} \sim 150.3 - 167.2\,\text{kHz}$, respectively. It is obvious that these QC modes are not multiple harmonics, and the QC mode f_{QC2} has the maximum amplitude. In phase III, the frequency bands of the QC modes become $f_{QC1} \sim 35.2 - 51.7\,\text{kHz}$, $f_{QC2} \sim 60.8 - 88.4\,\text{kHz}$, $f_{QC3} \sim 94.9 - 124.3\,\text{kHz}$ and $f_{QC4} \sim 131.1 - 149.7\,\text{kHz}$, respectively, as shown in figure 5(b). It is obvious that, after the jump behaviors of phase II, the frequencies of the QC mode f_{QC1} and f_{QC2} have an sudden increase of about 20 kHz, and that of the QC mode f_{QC3} basically remains unchanged, however, that of the QC mode f_{QC4} has a significant decrease of about 19 kHz. The results suggest that, these QC modes are closely related to the appearance and changes of the BAEs.

In order to achieve a comprehensive observation of the response of density fluctuations with different scales and/or regions to the BAEs, the spectrograms of medium-

high frequency part of the density fluctuations k_1, k_2, k_3 and k_4 are all displayed in figure 6. In general, the response of the density fluctuations detected by the four channels have the similar dynamic features across this discharge. It should also be noted that, the energy distribution of these QC modes in core density fluctuations (k_1 and k_2) appear to be slightly different from that of the outer density fluctuations (k_3 and k_4). The cross-correlation spectrum analysis between the medium-high frequency density fluctuation signal and the Mirnov signal, similar to the analysis in figure 3(b), has been also taken. And it is found that, there is no obvious cross-correlation between the medium-high frequency density fluctuations and magnetic fluctuations, including in the frequency bands of the QC modes. Therefore, it can be deduced that, the effect of the BAEs on the short-scale density fluctuations could be greatly different from the direct modulation of the TMs on the density fluctuations. One plausible mechanism is that, the BAEs is electromagnetic and their electrostatic components could affect the short-scale density fluctuations, or, there could be nonlinear coupling between the BAEs and short-scale density fluctuations. The underlying mechanism is still under investigation, and needs the validation of more experiments in future.

IV. SUMMARY
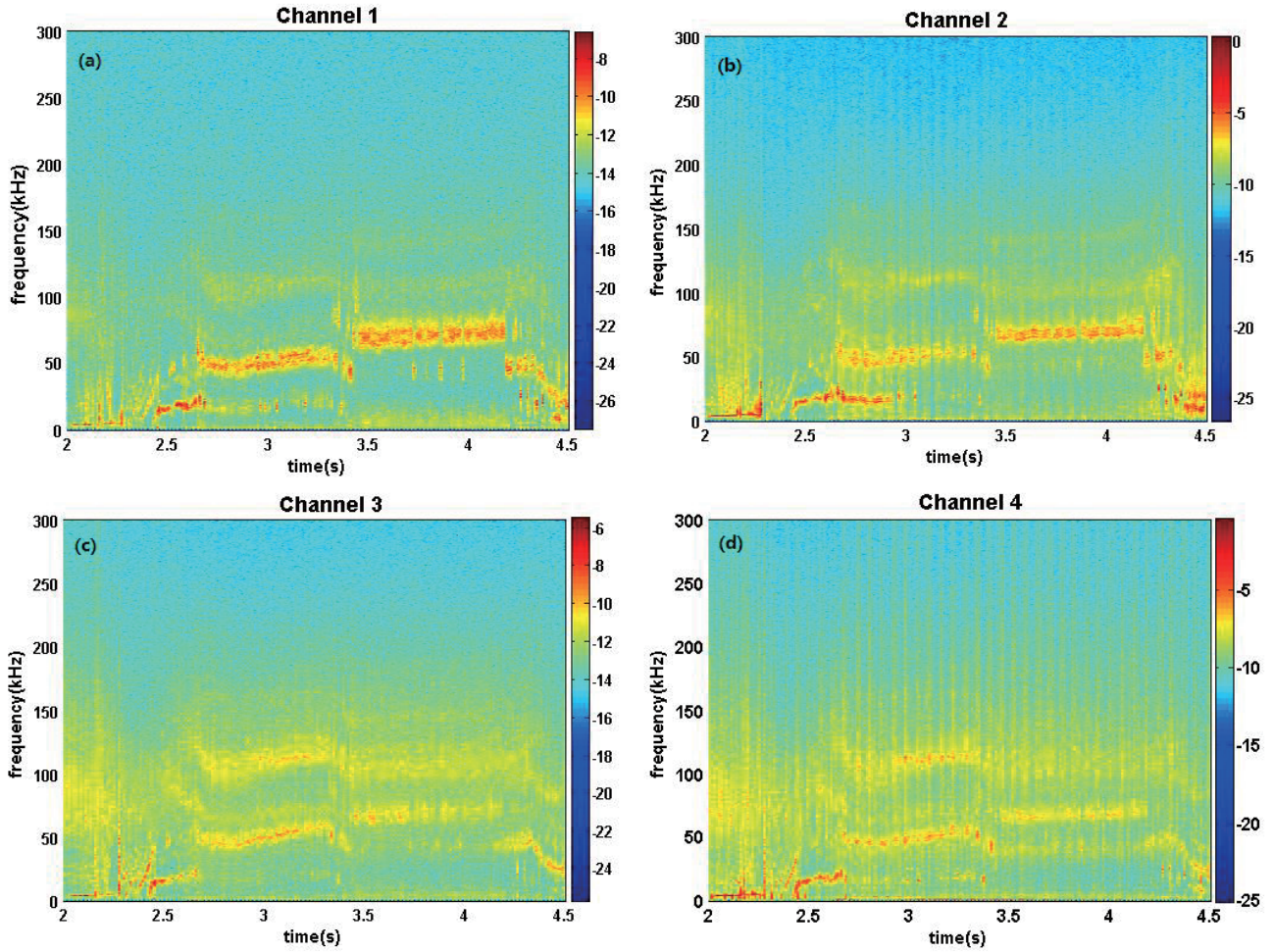
FIG. 6. The spectrograms of the the medium-high-frequency signal of density fluctuations k_1 (a), k_2 (b), k_3 (c), and k_4 (d). The measured region of the density fluctuations k_1 and k_2 is the core region $r/a \approx 0.4$-0.5, and that of the density fluctuations k_3 and k_4 is the outer region $r/a \approx 0.7$-1. The wave-numbers are $k_1 = k_3 = 10\,cm^{-1}$, and $k_2 = k_4 = 18\,cm^{-1}$.

BAEs during strong TM activity have been frequently observed in fast-electron plasmas of EAST tokamak. A tangential CO_2 laser collective scattering system was employed to preliminarily investigate the dynamics of the short-scale ($k_\perp \rho_s \sim 1.5 - 4.3$) density fluctuations during the activity of BAEs with strong TMs. It is found that, the response of short-scale density fluctuations to the TMs and BAEs are active, but different. In the low-frequency (0-10 kHz) part of density fluctuations, there are harmonic oscillations which are totally corresponding to those of TMs in frequency. In the medium-high frequency (10-250 kHz) part of density fluctuations, with the appearance of the BAEs, the medium-high frequency density fluctuations begin to be dominated by several quasi-coherent (QC) modes, and the frequencies of the QC modes are closely related to the changes of BAEs. In can be deduced that, the TMs could modulate directly the short-scale density fluctuations, and the effect of the BAEs on the short-scale density fluctuations could be greatly different from the direct modulation of the TMs on the density fluctuations. These results suggest the active, but different, roles of TMs and BAEs in the modulation of the background short-scale

density fluctuations. Besides, the underlying mechanism by which the BAEs affect the background short-scale density fluctuations is still under investigation, and many more detailed studies in this direction would advance the understanding of multi-scale interaction physics in tokamak plasmas.

ACKNOWLEDGMENTS

REFERENCES

[1] Horton W 1999 Rev. Mod. Phys. 71 735
[2] Terry P W 2000 Rev. Mod. Phys. 72 109
[3] Doyle E J et al 2007 Nucl. Fusion. 47 S18
[4] G.R. Tynan et al 2009 Plasma Physics and Controlled Fusion 51 113001
[5] A. Muhm et al, 1992 Phys. Fluids B 4 336
[6] P. W. Terry et al 1992 Plasma Phys. Control. Fusion 2 313

[7] S. Takeji et al 2002 Nucl. Fusion 42 634

[8] K. Tanaka et al 2006 Nucl. Fusion 46 110

[9] G. Z. dos Santos Lima et al 2009 Phys. Plasma 16 042508

[10] F. Zonca et al 1999 Phys. Plasmas 6 1917

[11] W. Chen et al 2013 Nucl. Fusion 53 113010

[12] P. J. Sun et al 2012 Phys. Scr. 85 055504

[13] R. Jaenicke, W VII-A Team 1988 Nucl. Fusion 28 1737

[14] L. Chen and F. Zonca 1995 Phys. Scr. T60 81-90

[15] P. K. Shukla and L. Stenflo 1995 Phys. Scr. T60 32-35

[16] M. S. Chu et al, 1992 Phys. Fluids B 4 3713

[17] W. W. Heidbrink et al, 1993 Phys. Rev. Lett. 71 855

[18] R. Nazikian et al, 1996 Phys. Plasmas 3 593

[19] R. Sabot et al, 2009 Nucl. Fusion 49 085033

[20] M. Garcia-Munoz et al, 2009 Phys. Rev. Lett. 100 055005

[21] W. Chen et al, 2011 Nucl. Fusion 51 063010

[22] M. Xu et al, 2013 Plasma Phys. Control. Fusion 55 065002

[23] G. M. Cao et al, 2014 Fusion Eng. Des. 89 3016

[24] E. Mazzucato, 2006 Plasma Physics and Controlled Fusion 48 1749

[25] J. W. Connor and H. R. Wilson, 1994 Plasma Phys. Control. Fusion 36 719

[26] D. R. Smith et al, 2008 Rev. Sci. Instrum. 79 123501

[27] S. P. Hirshman and J. C. Whitson, 1983 Phys. Fluids 26 3553

Bifurcation of radial electric field in tokamak edge plasmas due to ion orbit loss

G. J. Wu, X. D. Zhang

Institute of Plasma Physics, Chinese Academy of Sciences, Hefei 230031, China

Abstract: The ion orbit loss and the formation of radial electric field Er in tokamak edge region are calculated. The ion orbit loss generates a negative Er, which in turn affects the ion loss. As a result, Er can saturates at either a low or a high value, depending on the plasma parameters. When the ion temperature in the plasma edge is higher than a threshold a self-sustaining growth in both the ion loss and Er is found, leading to a high saturation value of Er in the milliseconds time. This mechanism provides a possible explanation for the formation of the edge radial electric field during the L to H-mode transition observed in tokamak experiments.

1. Introduction

The formation of the radial electric field and related spontaneous plasma rotation in fusion devices are of great interest in plasma physics. The underlying mechanism is not well understood despite extensive experimental and theoretical efforts devoting to it. It is well known that intrinsic plasma rotation exists even in Ohmic tokamak discharges without momentum input. Experimental measurements have revealed that the L to H-mode transitionis triggered by a sudden increase of a negative radial electric field Er in the edge region, and the resulting Er shear suppresses the local plasma turbulence and anomalous transport, leading to the so-called pedestal region inside the last closed flux surface (LCFS) of H-mode plasmas [1-4]. In L-mode plasmas, a weaker radial electric field has also been observed in the edge region. It has been a long standing challenge to find out a proper nonambipolar transport mechanism which can lead to such a strong Er inside the LCFS during L-H transition. Experimental evidences show that a heating power threshold exists for this transition. Usually a low ion collisionality in the edge correlates with the occurrence of an H mode, while at high collisionality the plasma remained in the L mode for the same amount of heating power [5]. Lower ion collisionality can lead more collisionless ions to loss through the X point region to the divertor target plates in a divertor configuration. Hamiltonian guiding center simulations show that a strong Er can be generated in a thin layer just inside the separatrix because of ion orbit loss [6,7]. By considering the orbit loss, Er in the tokamak plasma edge has been simulated by using neoclassical Monte Carlo particle following code, and the Er shear is found to reach a high value. However, a spontaneous bifurcation in Er has not be revealed yet [8,9].

In the tokamak edge region, the radial electron transport is affected by the microscopic instabilities. Studies indicate that these instabilities can cause enhanced radial electron transport [10,11]. According to the non-ambipolarity ion loss and electron loss, Itoh and Itoh have proposed a L-H transition model, in which the bifurcation phenomena and critical condition are deduced [10]. However, a more positive value of Er was found to correlates to improved plasma confinement.

As the bifurcation in the edge radial electric field is one of the most important characteristics in L-H transition, in this paper a new model based on the ion orbit loss together with electron turbulence transport is considered. The calculation results show that, if the ion temperature in plasma edge region is higher than a threshold, a self-sustaining growth in the ion loss and Er will be triggered, and Er saturates at a high value in milliseconds. In the opposite case, Er only reaches a lower saturation value. Such a bifurcation in Er provides a possible explanation for the L-H mode transition.

2. Model and Results

An equilibrium magnetic field for a single null divertor configuration, obtained from EFIT code, is utilized with the following parameters: plasma major radius R_0=1.75m, minor radius a=0.46m, elongation k=1.7, tri-angularity δ=0.56, plasma current I_p=1MA, and toroidal field B_0=2T. Using guiding center approximation and assuming the conservation of ion energy, magnetic moment, and toroidal angular momentum [12], the ion motion orbit is calculated.

Fig. 1 shows the change of ion loss region in velocity space for different values of negative Er, where δ is the angle between the direction of ion motion and that of the magnetic field line, and E is the ion energy. Initially ions are assumed to have a Maxwellian distribution and be located at a launch point L, which is 1 cm inside the LCFS in the horizontal midplane on the low field side. The lost ion are found from calculations if they drift outside the LCFS and hit the divertor plate. For a given magnetic configuration and launch point, a minimum ion energy E_{min} is required for the ion orbit loss. With the increase of negative Er, the nose region [12] (the long and narrow part on the left part of the loss region) is prolonged to smaller δ values and narrowed, since the ion drift orbit is affected by the electric drift in addition to the magnetic field gradient/curvature drift. When $Er=Er_0$, the nose region becomes longest. When $Er=Er_m$, it disappears. The fraction of ions in the nose region is affected by the ion temperature. For deuterium plasmas with an ion temperature T_i=200eV at the L point, almost all the loss ions come from the nose region where the ion energy is not too high.

Corresponding to Fig. 1, E_{min} is shown in Fig. 2 as a function of the radial location of the launch point in the horizontal midplane on the low field side. E_{min} increases exponentially with increasing the distance from the LCFS. The choice of the launch point to be 1cm away from the LCFS for Fig. 1 is based on the existing results that the plasma turbulence is important just inside the LCFS, which could lead to locally enhanced radial electron (and ion) flux being comparable to that due to ion orbit loss. The radial correlation length of plasma edge turbulence, Lr, is measured to be about 1cm on ASDEX [13]. Therefore, we assume that the radial electron and ion flux are comparable inside the Lr region as marked in Fig. 2, but it is much smaller in the inner part extending from the left edge of the Lr region towards the magnetic axis. The regions labeled as "ion loss region" and "ion loss region and electron loss region" in Figure 2 shows the assumption mentioned above.

The fraction of deuterium ions in the loss region, $\eta=d\Gamma_{iloss}/\Gamma_i$, is shown in Fig. 3 as a function of the negative Er, where $d\Gamma_{iloss}$ and Γ_i are the number of ions in the loss region and in the whole velocity space respectively. It is clearly that the ions in the loss region gradually become more and more with the increase of the negative Er till to a critical value Er_c that is just a little bit bigger than the Er_0 shown in figure 1. For $Er>Er_c$, the lost ion fraction decreases sharply.

In Figs. 1-3 the ion loss is only considered at the L-point as mentioned above. With the magnetic configuration utilized here, the loss fraction changes with the polodal location of the launch point along the magnetic surface. However, because of the fast ion motion along the magnetic field line, the ion loss averaged on the magnetic surface is close to that at the L-point. The averaged ion orbit loss over polodal angles on the same magnetic surface is found to be about 1/8 of at the L-point.
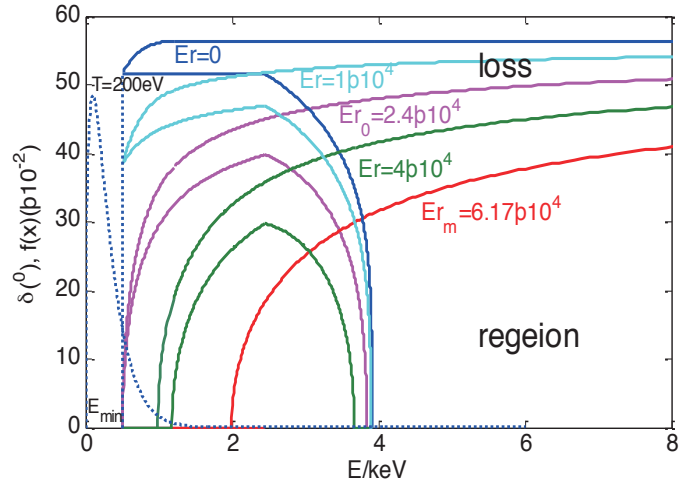
Fig. 1 The changes of deuterium ion loss region in velocity space for different negative Er (Unit of Er: -V/m) and the Maxwellian distribution of deuterium ion with T_i=200eV (dotted line).
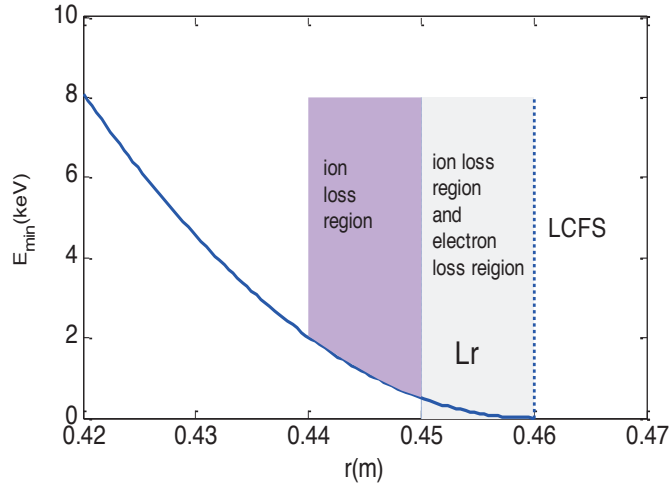
Fig. 2 Minimum ion energy E_{min} required for ion loss versus the location of the ion launch point on the low field side in the horizontal midplane (solid curve).
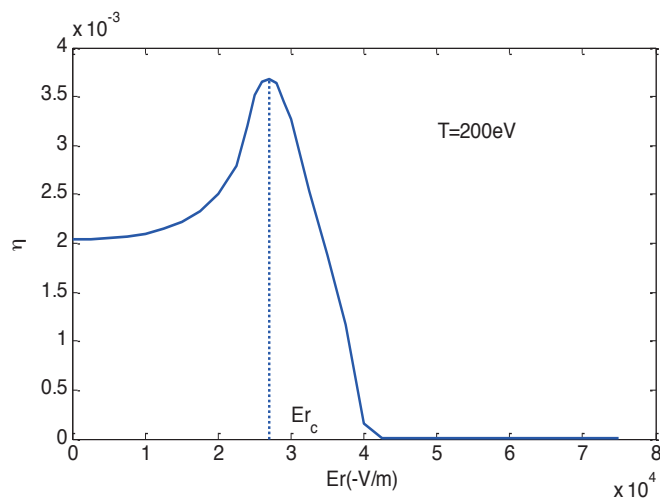
Fig. 3 The fraction of deuterium ions in the loss region *versus* negative Er.

The ion orbit loss will lead to the formation of a negative Er. Because Er and the ion loss region affect each other as seen from Figs 1 and 3, the generated radial electric field by ion orbit loss are quite

different for different plasma parameters. Fig. 3 indicates that the increase of the ion loss fraction for Er<Er_c can lead to a self-sustaining growth of Er for a sufficiently high ion temperature. To simplify the calculation of self-sustaining growth process, the following assumptions are made which don't affect the general characteristics of our results: (1) plasma is electrically neutral in the initial time; (2) the electron losses is only important within the Lr region as shown in Fig.2, and the radial electrical field is assumed to be zero at the LCFS and to linearly increase towards the launch point due to the combined role of ion and electron radial flux , (3) The ion temperature and density linearly decreases from inner region towards the LCFS, and (4) the negative Er at the L point due to ion orbit loss is a linearly proportional to the ion loss fraction in the L point neighborhood (the actual Er is of course a nonlinear increasing function of the ion orbit loss fraction in the L point neighborhood, but our calculations have shown that the above assumption has no significant effect on the self-sustaining growth process of Er).

Under above assumptions, the obtained ion orbit loss fraction η is shown as a function of time in Fig. 4 for the ion density $n_i=1\times10^{19}$. When the ion temperature is lower than the threshold, the loss fraction decreases in time as shown by Curve 1. Only when the ion temperature is higher than a threshold, the self-sustaining growth process in ion loss fraction is seen (curve 2). After a peak loss fraction with $\eta=0.018\%$, the ion loss fraction decreases due to the formation of a strong radial electric field.

The change of radial electric field as a function of time, corresponding to the self-sustaining growth of η shown by curve 2 in Fig. 4 , is shown in Fig. 7. Er saturates at a high value in the milliseconds. While for a lower ion temperature, Ti=50ev, only a low value of Er is formed. The time period of the self-sustaining growth in Er is usually found to be in the order of milliseconds, and the time scale decreases with increasing ion temperature and density.
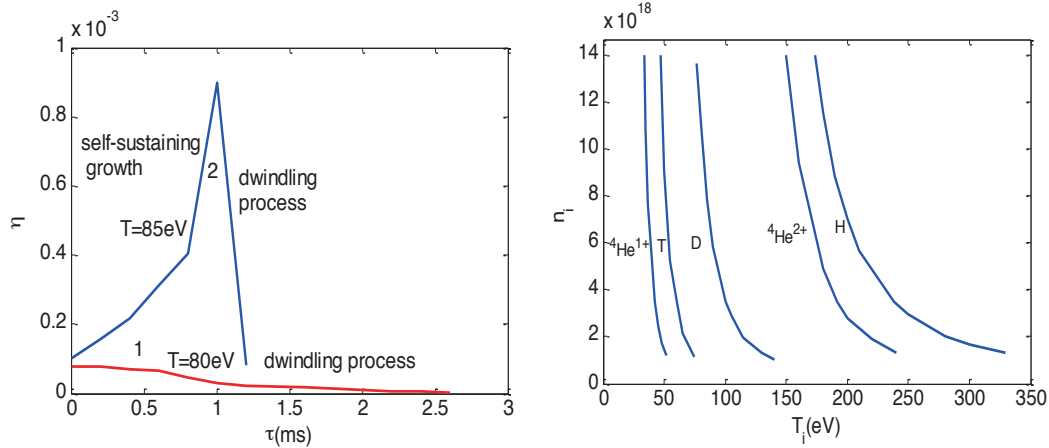
Fig. 4 The bifurcation in ion orbit loss fraction.   Fig 5 Threshold of T_i and n_e for self-sustaining growth of Er in the L point neighborhood

The threshold for the self-sustaining growth of Er is shown as a function of T_i and n_e for different type of ions in Fig 5. Only when the edge plasma parameters T_i and n_e exceed the threshold, a self-sustaining growth in Er is found. The threshold is lower for the ions with the higher mass number or smaller electric charge number.

The effect the toroidal field B_t on the threshold is shown in Fig. 6, where threshold for the self-sustaining growth of Er is shown as a function of T_i and n_e for $B_t = 1$ and 2T, respectively. The threshold is higher with increasing B_t.
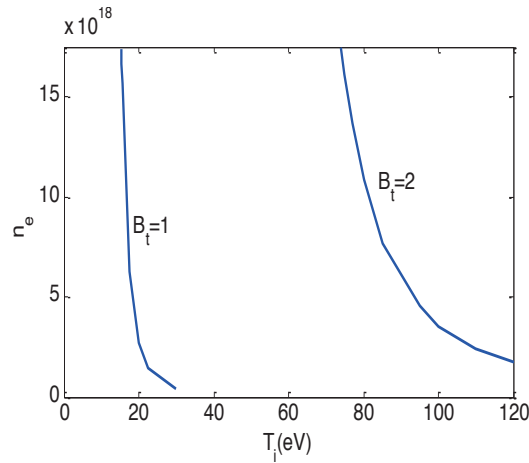
Fig. 6 The effect of B_t on the threshold.
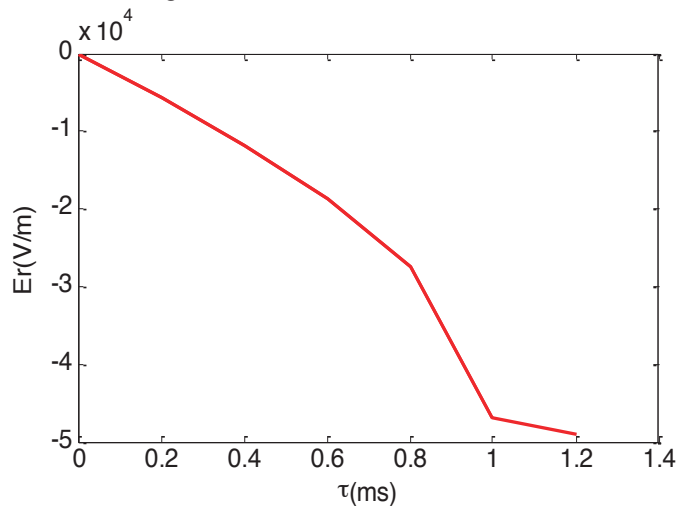
Fig. 7 Corresponding to figure 3, Er versus time

Assuming that the ion temperature and density at 1 cm inside the L point are 1.2 times of those at L point, the calculated Er profiles for different ion temperature are shown in Fig. 8. Here the Er profiles within the Lr region are simply assumed to be a linear function of the minor radius, and the value of Er at the LCFS is assumed to be zero, as mentioned above. It is seen that only a low value of Er is obtained for low ion temperature at L point, T_L=70eV and 80eV. However, a much larger Er is found for a slightly higher ion temperature, T_L=85eV, indicating a bifurcation in Er with increasing ion temperature. The values of Er decrease sharply with decreasing the minor radius, indicating that a strong Er can be formed only in a few cm inside the LCFS due to ion orbit loss, in agreement with H-mode experimental results [16].
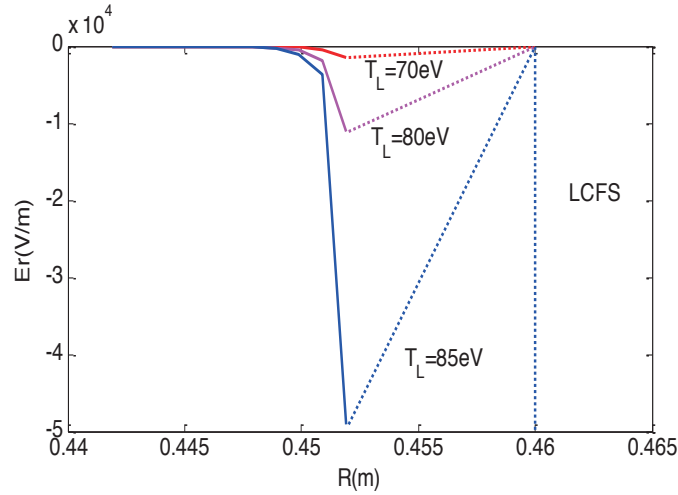
Fig. 8 The *Er* profiles for the different ion temperature and density inside the LCFS.

L-H mode transition as a bifurcation phenomenon has been manifested in all experiments if a heating power threshold is exceeded, and a strong negative *Er*, in the order 10^4-10^5V/m, is observed inside the LCFS in milliseconds after L-H transition, indicating a self-sustaining growth of the *Er* during the transition. The heating power threshold for L-H transition corresponds to a threshold in the edge ion temperature for the same ion density or a threshold in the ion density for the same temperature. Our results show that, if the edge ion temperature and density are sufficiently high, there is a self-sustaining growth in the radial electric field due to the interaction between the ion orbit loss and the radial electric field, and the ion loss fraction can reach the order 1/1000 in edge region, leading to a strong negative *Er* in milliseconds, as seen in the experiments. The results shown in Fig.5 and Fig.6 are consistent with ASDEX Upgrade experimental results[15], which demonstrate a similar dependence of the L-H transition threshold on the ion temperature and density. Regarding the isotope effect for L-H transition, a larger ion mass is found to correspond to a lower threshold for the self-sustaining growth in Er as seen from Fig. 5, being in agreement with experiment observation [17,18]. In ^{4}He discharges, usually there is also a considerable fraction of ^{4}He^{1+} ions in the plasma edge [19], so the power threshold changes from a lower value to a higher one with increasing ^{4}He^{1+} fraction. Our results predict that, if the ions are all ^{4}He^{1+} in the edge, the threshold is less than that of D plasmas; while for pure ^{4}He^{2+} ions, the threshold will be higher, being in agreement with JET experimental results [18]. These can give a reasonable explanation about the variability of the L-H transition power threshold in a helium-4 discharge in Ref. [20]. If the plasma temperature *T* is proportional to the heating power and the toroidal field B_t, the effect of the toroidal field on the threshold as shown in Fig. 6 is in line with experimental results. Our results extend the early understanding about the bifurcation of *Er* [9,14].

By scanning over the plasma density in experiments, it is found that there is a minimum in the power threshold for L-H transition in the low plasma density regime. Our results is more relevant for the low plasma density regime, since ion collisions have not been taken into account in our model, and which could be important for plasmas with high edge density. The collisional effect will be further considered in our future work.

In summary, a self-sustaining growth in radial electric field due to its interaction with the ion orbit loss is found for a sufficiently high edge ion temperature and density. The ion loss fraction reaches the order 0.1% in edge region, leading to a strong local negative *Er* as seen in H-mode experiments. The obtained results can explain some important features of experimental findings, such

as the threshold power for L-H transition, the L-H transition time, isotope effect, and the radial width of *Er*.

REFERENCES

[1] S. I. Itoh, K. Itoh, J Phys Soc Japan, **59**, 3815 (1990).

[2] F. L. Hinton. Phys Flui ds B, **3**, 696 (1991).

[3] K. C. Shaing. Physics of Fluids B: Plasma Physics, **31**, 2249 (1988).

[4] H. Biglari, P. H. Diamond, and P.W. Terry, Phys. Fluids B2, 1 (1990).

[5] K. H. Burrell, et al., Plasma. Phys. Control. Fusion, **34**, 1859 (1992).

[6] C. S. Chang, S. Kue, and H. Weitzner, Phys. Plasmas **9**, 3884 (2002).

[7] C. S. Chang, S. Ku, and H. Weitzner, Phys. Plasmas **11**, 2649 (2004).

[8] J. A. Heikkinen, J. A. Heikkinen, and A. G. Peeters, Phys Rev Lett. 84, 487(2000).

[9] T. P. Kiviniemi, et al., Plasma. Phys. Plasmas **10**, 2604 (2003)

[10] S. I. Itoh, K. Itoh, Phys Rev Lett. **60**, 2276 (1988).

[11] J. W. Connor, and H. R. Wilson, plasma. Phys. Control. Fusion, **36**, 719 (1994).

[12] A. V. Chankin, G. M. Mccracken, Nucl. Fusion **33**, 1459 (1993).

[13] Schirmer J, Conway G, D, Holzhauer E, et al, 33th EPS Conference on Plasma Physics(Roma, Italy, 2006).

[14] K. C. Shaing, E. C. Crume, Phys Rev Lett. **63**, 2369 (1989).

[15] W Suttropy, et al, Plasma Phys. Control. Fusion **39**, 2051 (1997).

[16] P. Gohil, K.H. Burrell, et al., Nucl. Fusion **34**, 1057 (1993).

[17] ASDEX Team, Nucl. Fusion, **29**, 1959 (1989).

[18] E. Righi, D.V. Bartlett, J. P. Christiansen, et al., Nucl. Fusion. **39**, 309 (1999).

[19] Gurchenko A D, Gusakov E Z, Lashkul S I, et al, 38th EPS Conference on Plasma Physics (Strasbourg, France, 2011).

[20] G. Calabrò, D. C. McDonald, M. Beurskens, I. Day, et al., 37th EPS Conference on Plasma Physics(Dublin, Ireland, 2010).

Development of plasma fueling on EAST

X.J. Yao[a], X.W. Zheng[a], C.Z. Li[a], Y. Chen[a]

a Institute of Plasma Physics, P.O. Box 1126, Hefei 230031, China

Abstract: To achieve better plasma density control, experimental advanced superconducting tokamak (EAST) has already equipped with gas puffing (GP), supersonic molecular beam injection (SMBI) and pellet injection (PI). During the past few years, lots of experiments and ameliorations have been done. The performance of the SMBI and gas puffing (GP) feedback systems were used and compared. And the preliminary result of pellet injection was also presented here. The results shows the PI and SMBI were more compatible to the long pulse high density discharge on EAST.

1. Introduction

Plasma fueling has been a popular research field for a long time in the fusion society. To sustain the plasma reaction, the fueling is essential for the tokamak device with a long pulse and high performance. Density control and even ELM control can be done with the fueling system. All the big devices like JET, DIII-D, ASDEX-U and EAST have been engaged on such research.

To achieve better plasma fuelling and density control, several techniques have been tested on EAST, such as gas puffing [1], SMBI [1], and pellet injection [2]. In 2012, SMBI and pellet injection system were successfully developed and firstly used on EAST for plasma fuelling and ELM mitigation. Intensive efforts have been made to find out the possibility of ELM mitigation on EAST using SMBI and pellet injection. It will not only contribute for the database and techniques of ELM mitigation for EAST and future devices, such as ITER but also for the high confinement plasma discharge.

2. Plasma fueling system on EAST

GP, SMBI and PI are mainly for plasma fueling on EAST, however some density control experiments were also carried out. The GP is a basic fueling technique, it provides working medium for plasma establishment, XCS, LHCD, and divertor experiment. Figure 1 show the layout of the GP system during the 2014 campaign. There some modifications in the GP system compared to the 2012 campaign to adapt to the new requirement of EAST experiments.

Figure 1. schematic of the gas puffing system on EAST

The detailed structure of the SMBI device is shown in figure 2. The components of this system are a high-pressure gas source (1–2MPa), a solenoid valve, the Laval nozzle and the magnetic shielding etc. The Laval nozzle is installed in front of the solenoid valve which is ∼2m away from the plasma. The molecular beam source is a small chamber in which the working gas can be kept at a definite pressure and temperature. The principle of SMBI is that a supersonic beam will be formed when subsonic gas injects to vacuum zone through a Laval nozzle. The key characteristic is that the beam is ejected freely to the vacuum chamber without any guiding pipe. Compared to GP, the molecular supersonic beam has a higher speed and a lower divergence [3]. The system has been calibrated on EAST and it has a favorable linear relationship between gas input and pulse length of the valve signal This system has been integrated into the plasma density feedback control system to achieve better control of plasma density during the 2012 EAST experimental campaign.

Figure 2. Schematic diagram of SMBI device: 1, magnetic shielding; 2, cold trap; 3, solenoid valve; 4,

nozzle; 5, LN2 pipeline; 6, high-pressure gas source.

A schematic of EAST pellet injection system is shown in Figure 3. It was installed on the EAST horizontal port and pellets can be injected either through the horizontal port (LFS) or the inner wall (HFS).The pellet injector was designed by PELIN, LLC on the base of early developed injectors for plasma fuelling of LHD, TORE-SUPRA and JET. It consists of a vacuum chamber, an extruder, a cutter and fast valve, etc. Figure 4 shows the schematic drawing of EAST pellet injector. It is capable of producing hydrogen/deuterium ice rod continuously for 1000 s or more at speed from 10 to 30 mm/s. The length and diameter of the cylinder shaped pellet are both 2 mm. The nominal atoms for each pellet are 3.78×1020. The injector can achieve steady state mode with pellet velocity adjustable from 150to 300 m/s and maximum injection frequency up to 10 Hz.
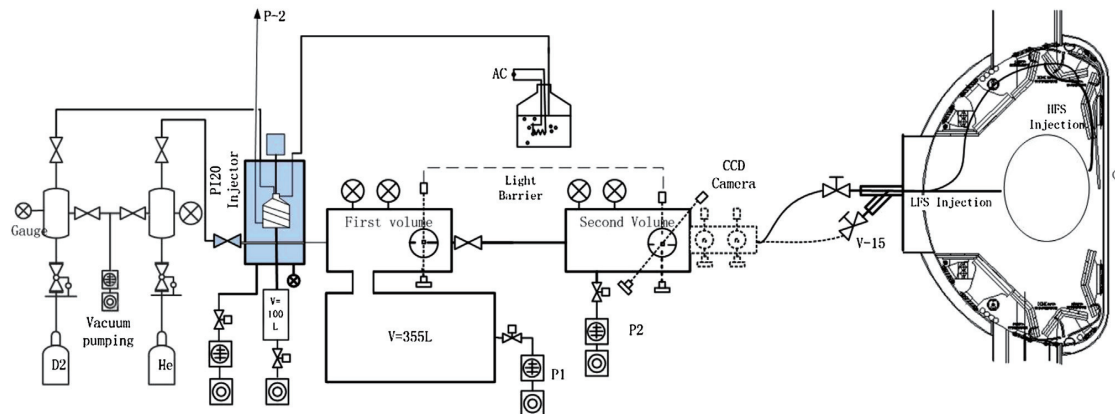
Figure 3. Schematic diagram of the pellet injection system installed on EAST tokamak.
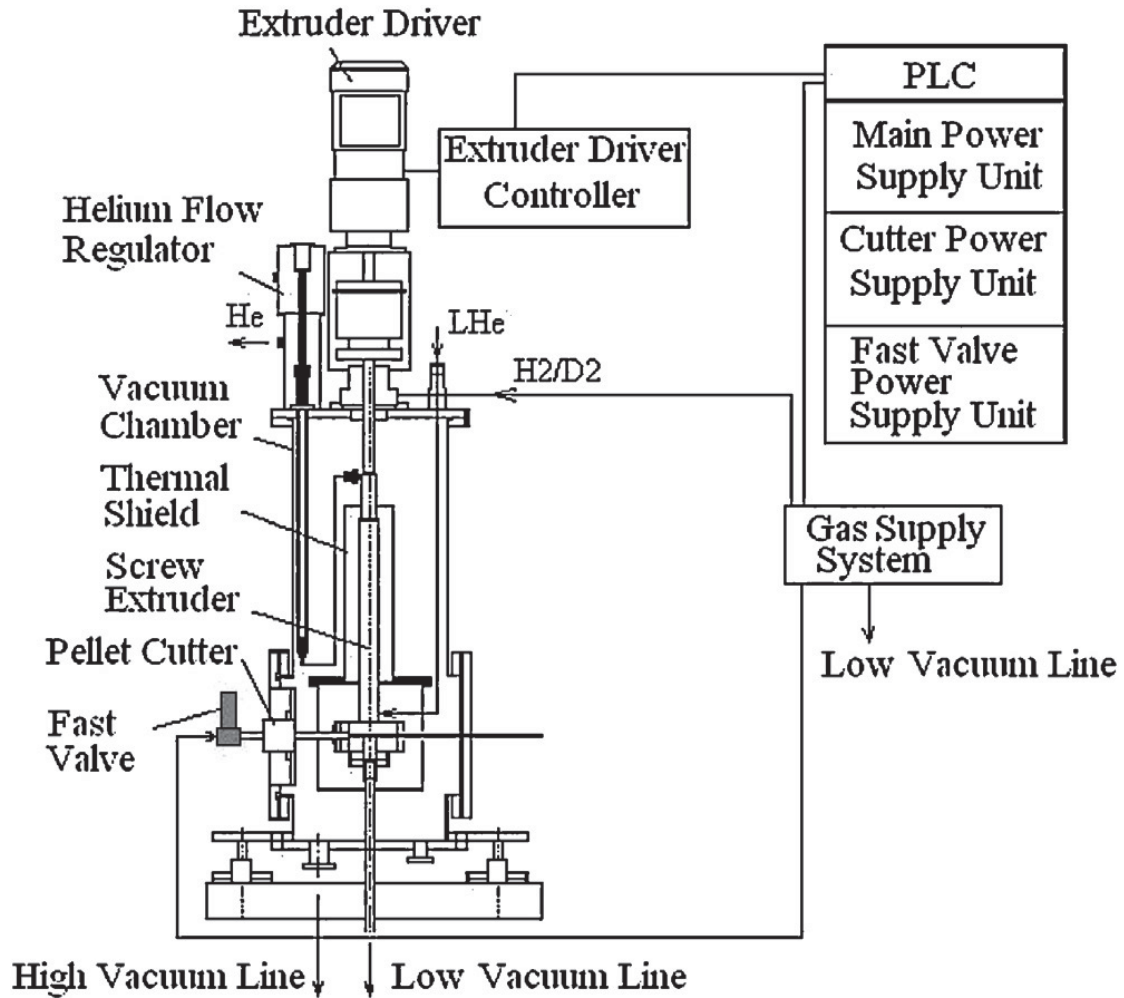
Figure 4. Schematic drawing of EAST pellet injector.

3. Results and discussion

3.1. GP density feedback control experiment

Figure 5 shows the two typical shots ($n_e = 2.0 \times 10^{19}$ m^{-3}, $I_p = 400$ kA, the same condition of the pumping system) with voltage modulation mode (#40432) and pulse width modulation mode (#40423). These two shots were the 43rd and 52nd discharge of one day's experiment, respectively. According to the argument obtained later in this paper, the wall conditions of both shots are assumed to be similar. So the most important factor that influences the plasma density behavior should be the fueling method. The plasma density of shot 40432 was kept almost steady in the flat top phase, with a slight oscillation around the reference density. This oscillation was mainly caused by the response time of the GPS. Therefore, in the voltage modulation mode the valve signal must be preset according to experiences, just as the overall trend of the valve signal shown in figure 5(a). Figure 5(b) shows the results from shot 40423 by using pulse width modulation, which is obviously better than that from shot 40432. The density was constant during the whole flat top phase, and the error between real density and the

reference one was only ~5%. In shot 40432 the valve was opened during the discharge, which made it hard to control the gas flow rate. The enhanced performance of pulse width modulation mode is mainly because that the gas flow in every single pulse is small, which makes it more accurate to control the density.
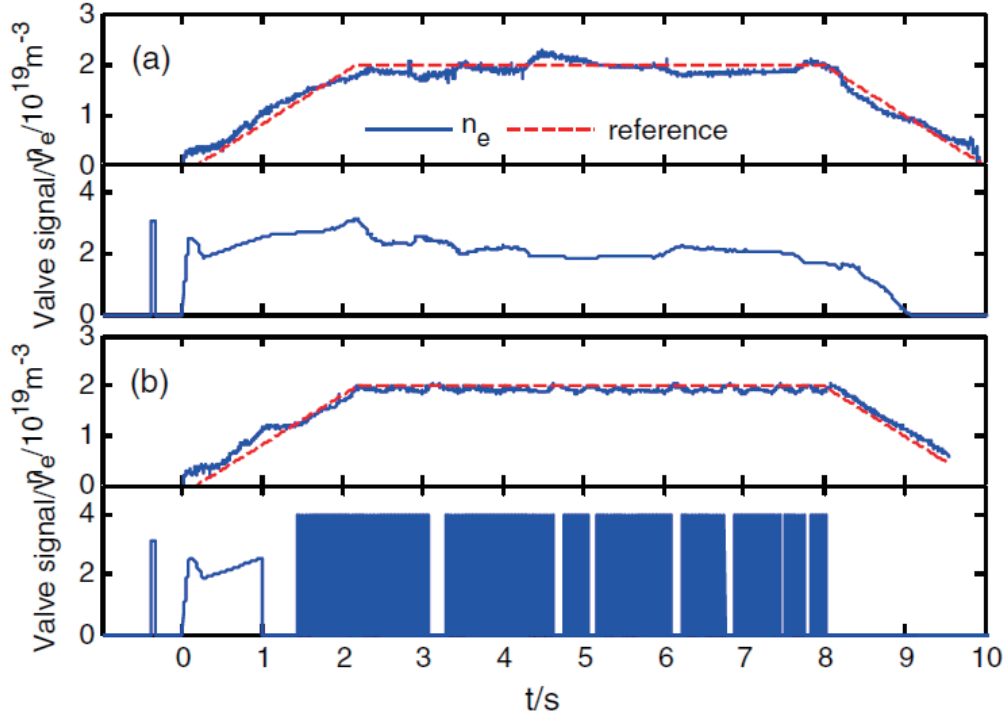
Figure 5. The density feedback experiments by using (*a*) voltagemodulation mode (#40432); (*b*) pulse width modulation mode (#40423).

To achieve better plasma performance, ion cyclotron resonance frequency (ICRF) cleaning and lithium coating were carried out every day after the experiments [4, 5]. These methods offered a high pumping ability and made plasma density control feasible. Figure 6 shows the gas inputs of 71 shots with similar plasma parameters in a whole day, performed in OH conditions and consecutively without any wall conditioning in between. Considered the vacuum pressure and other experimental changes, the inter-shot time is about 8–20 min. At the beginning of the experiment stage, the gas input was as high as 10^{22} (D_2) order of magnitude, which was about 100 times greater than plasma inventory. It is due to the high pumping effect of the clean wall and the fresh lithium film. In the first 20 discharges, the plasma density was accurately controlled and the injected particles inventory of every single shot decreased approximately exponentially. The wall pumping capacity decreased shot by shot due to retention. Then disruptions started to appear due to poor control of the plasma position. After about 30 shots, the gas input of a discharge stay stable around $3 \times 10^{21} D_2$. It suggests that the pumping ability of the wall is also maintained at a stable level. The coated lithium film's pumping ability changes dramatically in the first 30 shots and then maintains at a relatively stable level in the following discharges. The disruptions that occurred after ~60 shots were mainly due to that the density exceeded the Greenwald limit. It was because of the impurity radiation and the uncontrollable desorption of particles retained in the wall, which indicates that the wall tended to be saturated. The disruptions made a large amount of particles desorbed from the wall. Therefore, the wall recovered a certain amount of pumping ability and following discharges can be performed normally.

247
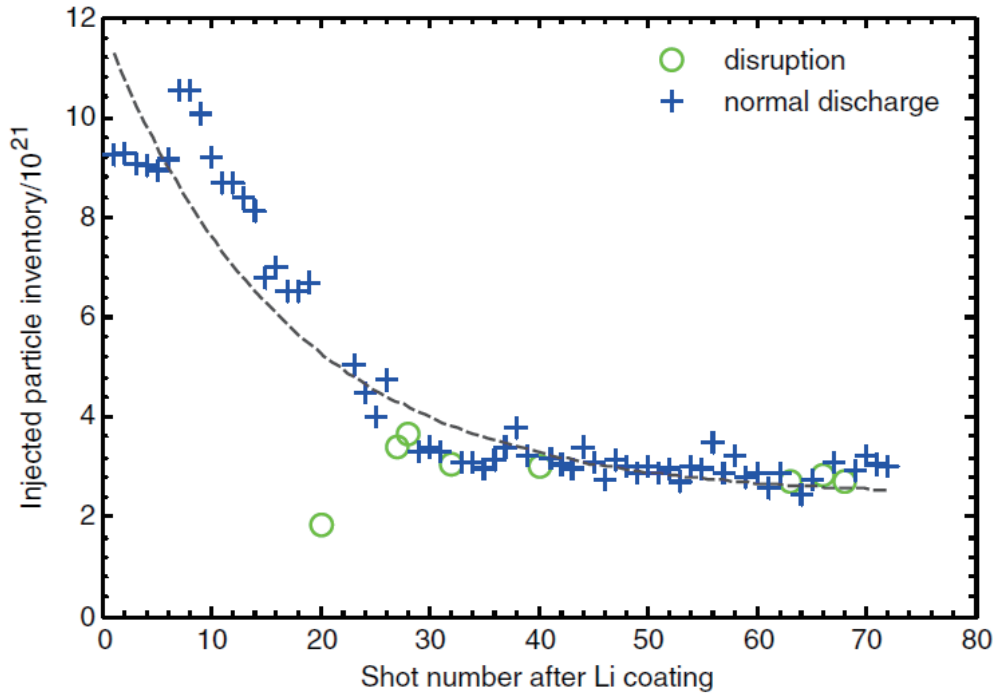
Figure 6. Injected particle inventory of a single shot as a function of shot number.

For further understanding the fuel retention in one-day experiment, particle balance analysis was carried out on these 71 shots. Figure 7 shows the overall evolution of the wall inventory, injected inventory and exhaust inventory, which were integrated shot by shot. The out gassing between the discharges, which is short-term retention, was not considered. The long-term retention was obtained through integrating the exhaust inventory of every shot until 4 min after the discharge. Figure 8 shows the particle retention ratio as a function of shot number. The result is consistent with analysis of the change of gas inputs. It is showed in the figure that the evaluation of the wall retention can be divided into two phase. In the first phase, namely the first ~20 shots, the wall retention increased very fast and the retention ratio was as high as 0.8–0.9. During this period, because of the powerful pumping ability offered by the clean wall and fresh lithium film, the main mechanism of the retention is absorption and implantation [6]. But there may be a small amount of co-deposition which is correlated with the erosion of the carbon wall. However, the global wall retention maintained its level and only increased slightly in the second phase when particle retention ratio is in a range of 0.5–0.7. But the injected particle inventory of every shot was small, as can be seen from figure 6. Therefore, the fuel retention of a single shot is not as high as in the first phase. The out gassing between the discharges ensured that the wall recovered a part of pumping ability. The results from particle balance cannot distinguish between retention because of implantation and retention because of co-deposition. This needs the sample analysis which will be discussed in future work.
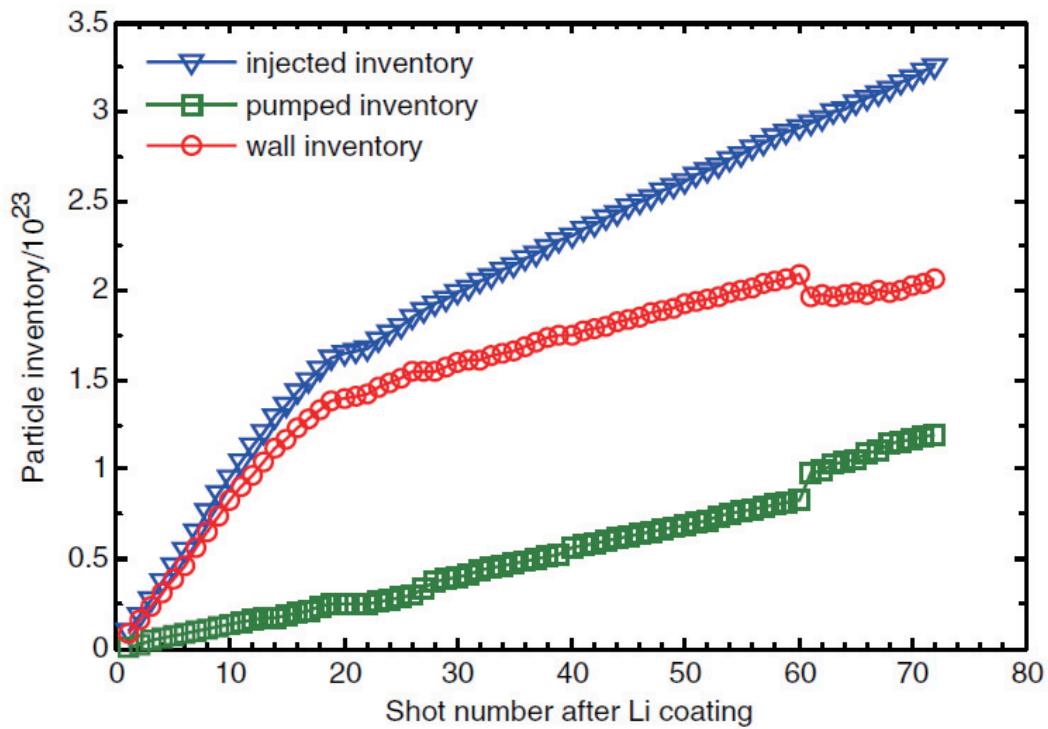
Figure 7. Particle balance for one-day experiment as a function of shot number.
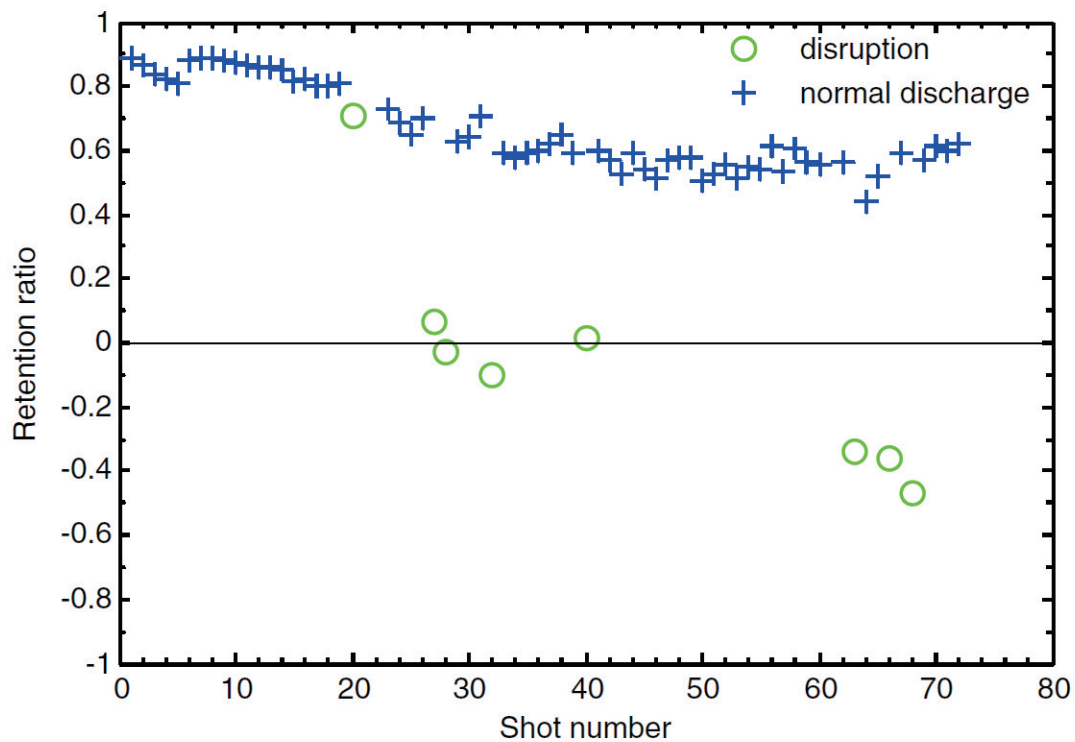
Figure 8. Particle retention ratio as a function of shot number.

It also can be seen from figure 8 that the disruptions enable the wall to reduce its inventory effectively. In those disruption discharges, the retention ratio was close to zero or negative. It is because the generated high energy particles from the disruption bombard the wall, and then large amount of particles were desorbed. But the cleaning efficiencies of these disruptions are not

consistently at a high level. In the disruptions whose retention ratio was close to zero, their power that loaded on the wall did not notably influence the global wall condition. So the net wall retention was not changed a lot and the gas inputs of the discharges following these disruptions not obviously increased.

3.2. SMBI density feedback experiment

SMBI has a different influence on the plasma performance compared to conventional GP. Figure 9 shows the results from shot 40326 where a 50ms GP pulse and two SMB (10,15 ms) were injected. The 50 ms GP pulse and the 10 ms SMBI have similar particle numbers of $\sim 9 \times 10^{19}$ D_2. But the plasma density rise caused by SMBI ($\_n_e = 0.5 \times 10^{19}$ m^{-3}) is higher than that caused by GP ($\_n_e = 0.35 \times 10^{19}$ m^{-3}). The fueling efficiency (defined as the increase in plasma particle content divided by the number of injected particles) is 15% and 25%, respectively. The delay time (defined as the interval between when the injection signal is sent and when the density start to grow) is $\sim$50 ms for GP pulse but only $\sim$5ms for SMBI, and thus the feedback control of plasma density by SMBI is more prompt. The fueling efficiency of SMBI is calculated in many OH discharges and it is in the range of 15–30%, as shown in figure 10, which is higher than that of GP. But it is lower than data obtained from Tore Supra and HL-2A which are in the range of 30–50%. In our system, the long distance ($\sim$2m) between the plasma and the Laval nozzle and the relatively low backpressure (1.5MPa) of the gas tank may lead to a slower velocity and a higher divergence. This could be the reason for the difference of fueling efficiency between EAST and Tore Supra.
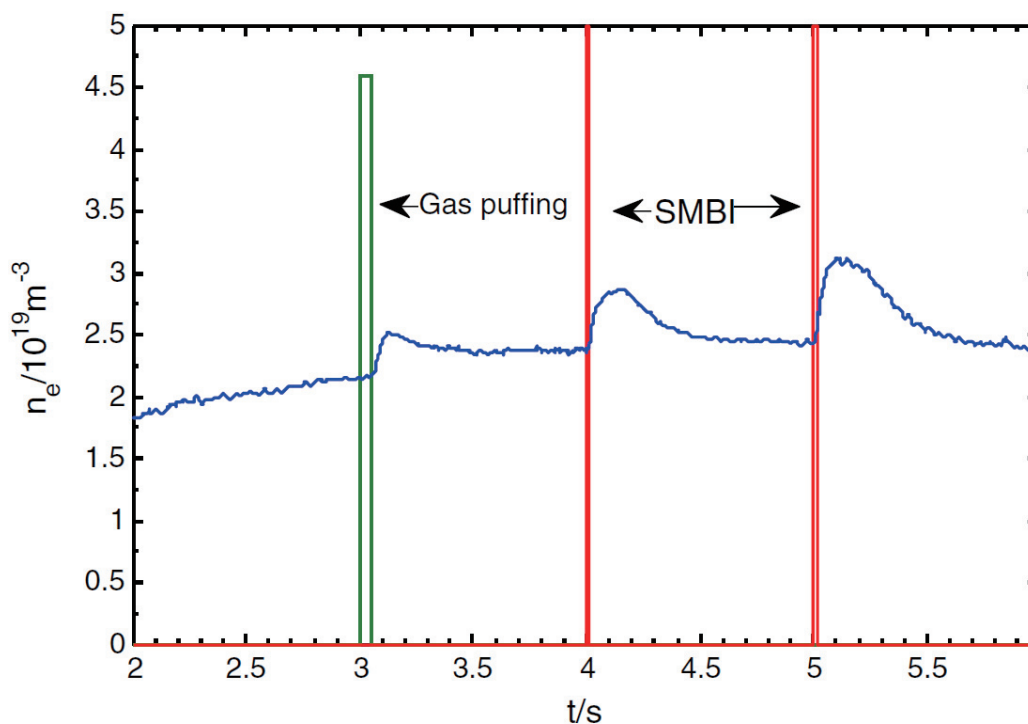
Figure 9. Comparison of the plasma density response caused by GP pulse and SMBI.
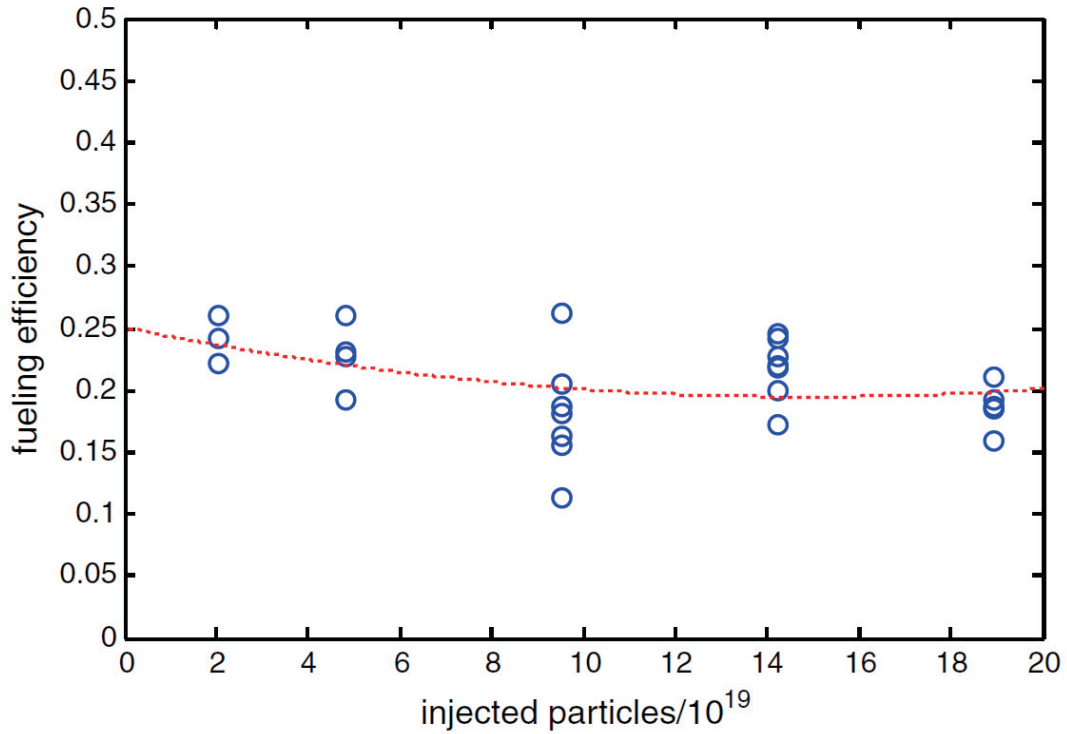
Figure 10. The fueling efficiency of SMBI as the function of injected particles.

To have a better control of plasma density, the SMBI system has been integrated into the plasma density feedback control system by the same control method gas puff used (pulse width modulation). Because of the faster response time of SMBI, the density can be controlled more accurately. Figure 11 shows a discharge feedback controlled by SMBI. The pre-filling by GP lasted at 1.2 s and then it was switched to SMBI. The density increases linearly from 1.8×10^{19} to 3.8×10^{19} m^{-3}, and the error between the real density and the reference one was only ~3%. It shows the controllability of SMBI. During 2012 EAST experimental campaign, plasma density up to 0.7 Greenwald limit has been easily reached by using SMBI density feedback control system which suggests that SMBI can control the density accurately even under the high plasma density operation condition where GP showed unfavorable manner due to very high pumping with Li coated wall.
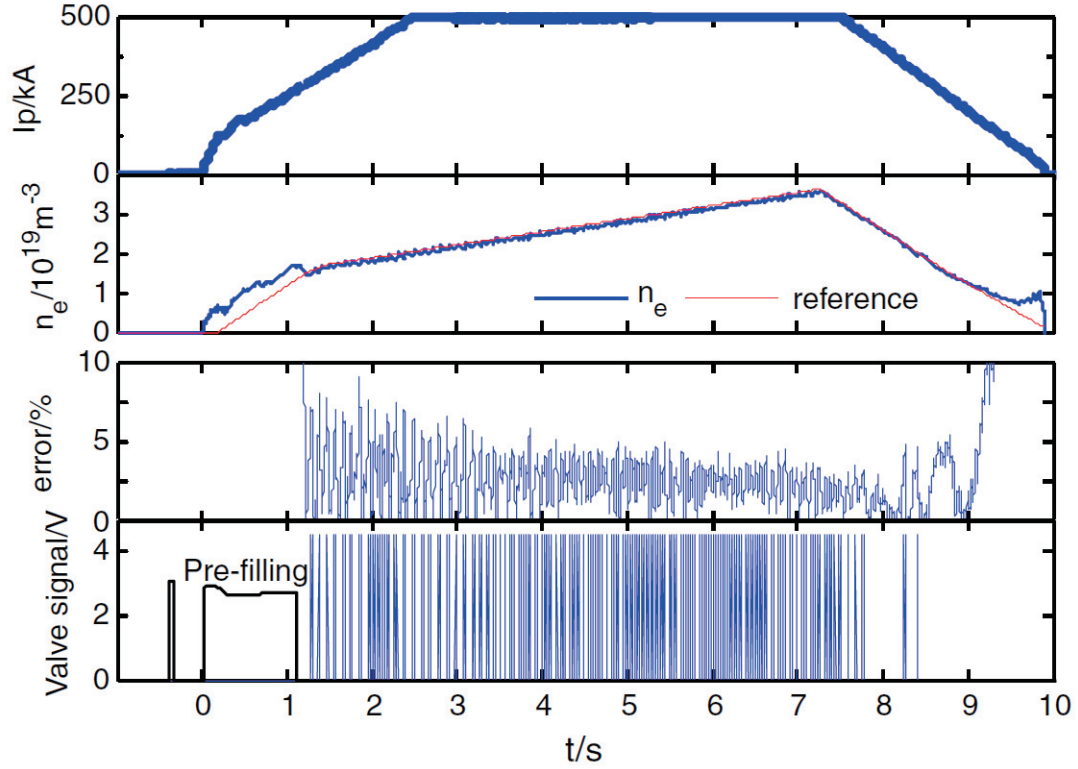
Figure 11. SMBI density feedback experiment (#42211).

The different influence of the two fueling methods on the wall retention has been investigated. Figure 12 shows two similar discharges ($n_e = 2.5 \times 10^{19}\,\mathrm{m}^{-3}$, $I_p = 400$ kA, the same condition of pumping system) feedback controlled by GP (#40312) and SMBI(#40306), respectively. These two shots was the 41st and 47th discharge of one day's experiment, respectively. So the wall conditions of both shots are assumed to be similar. The reference density of the two discharges is the same. Compared with shot 40312, the gas input needed to maintain the density in shot 40306 is reduced by 30%, and the exhaust inventory is only reduced by about 14%. So the resulting wall retention is reduced by 43%, which should be due to a higher fueling efficiency of SMBI and different plasma edge properties caused by SMBI. And this result is consistent with that obtained from Tore Supra. This could be an advantage the long pulse plasma discharges, where wall retention may affect the plasma performance strongly in later stage of plasma discharge.
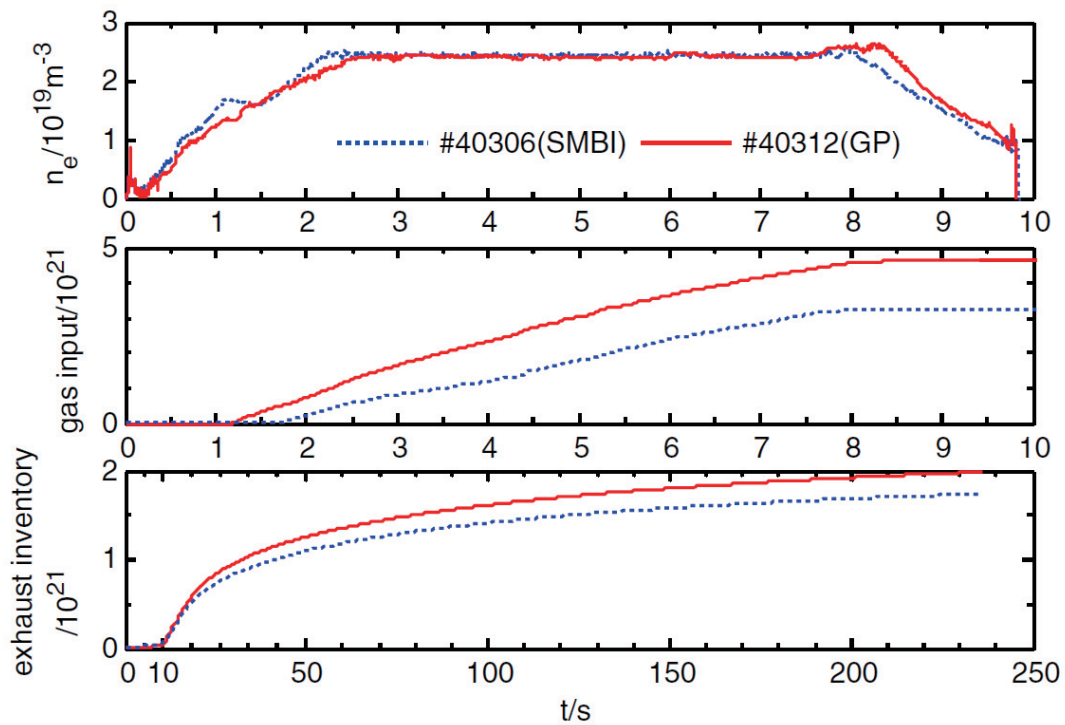
Figure 12. Comparison of two similar discharges feedback with SMBI and GP, respectively.

3.3. Pellet injection experiments

3.3.1. Engineering commissioning results

Bench tests had been carried out before the injection system was connected to the EAST vacuum vessel. Tests showed that the sys-tem can inject H2 or D2pellets in steady mode with different launch speeds and injection frequencies. Figure 13 shows high quality deuterium ice rod and Figure 14 shows D2 pellets in flight captured by CCD camera. In this test, the pellet launch speed is 340 m/s and injection frequency is 10 Hz, and pellets were fired in 100 s continuously.
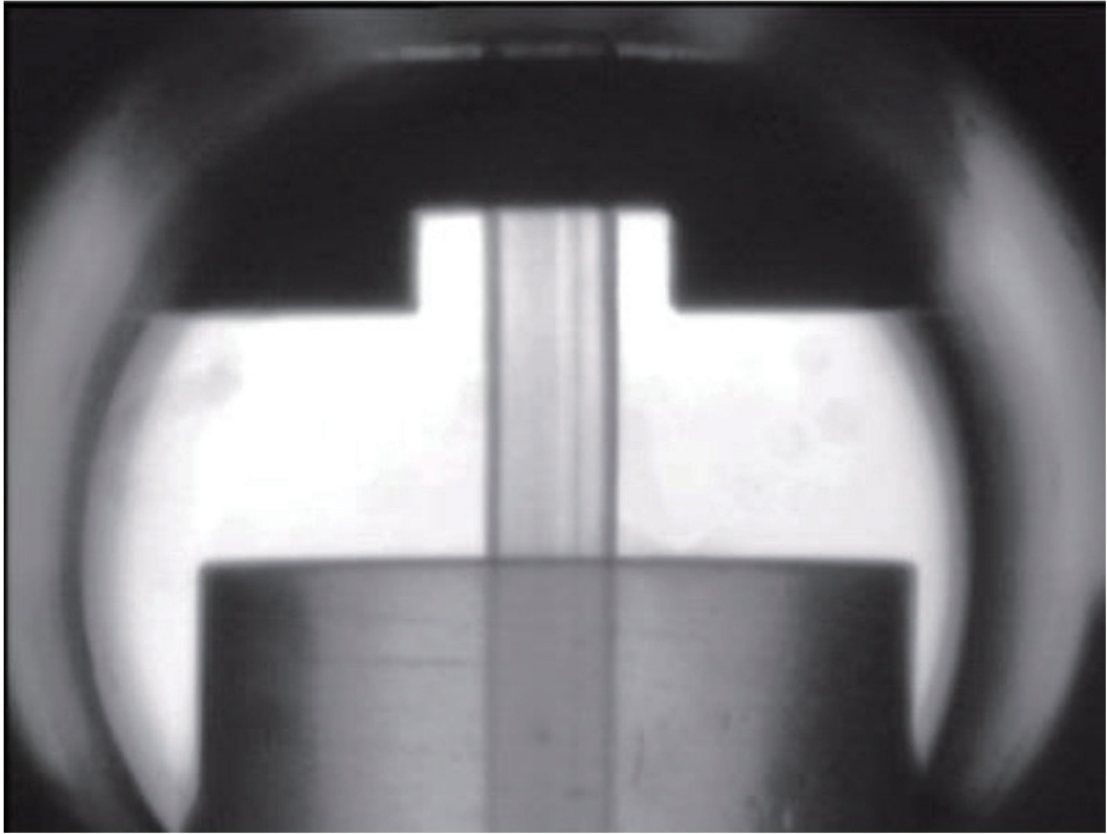
Figure 13. Rectangular D2 ice rod pushed away from the screw extruder.

Figure 14. D2 pellets in flight after acceleration (from left to right).

Tests have also been done to confirm whether pellet can get into the EAST vacuum vessel after flying in curved guide tubes with such a long distance. A small vacuum chamber made of

aluminum-foil paper was installed at the terminal of convey tube inside the machine, and aluminum-foil paper was a target to receive high speed pellet. Results presented in Figure 15 show that pellets both from LFS and HFS guide tubes can successfully enter into vacuum vessel.

<center>(a)   (b)   (c)</center>
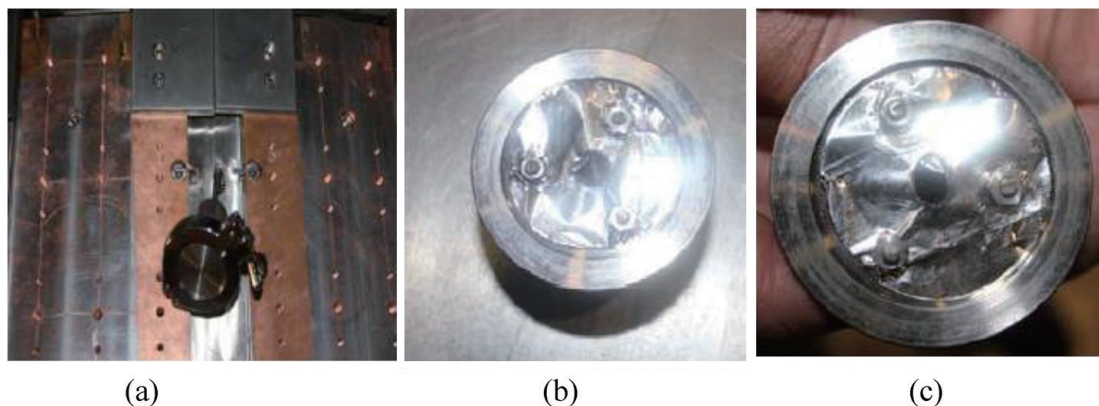
Figure 15. (a) A small vacuum chamber made of aluminum-foil installed at high field side, (b) LFS aluminum-foil destroyed by a pellet and (c) HFS aluminum-foil destroyed byanother pellet.
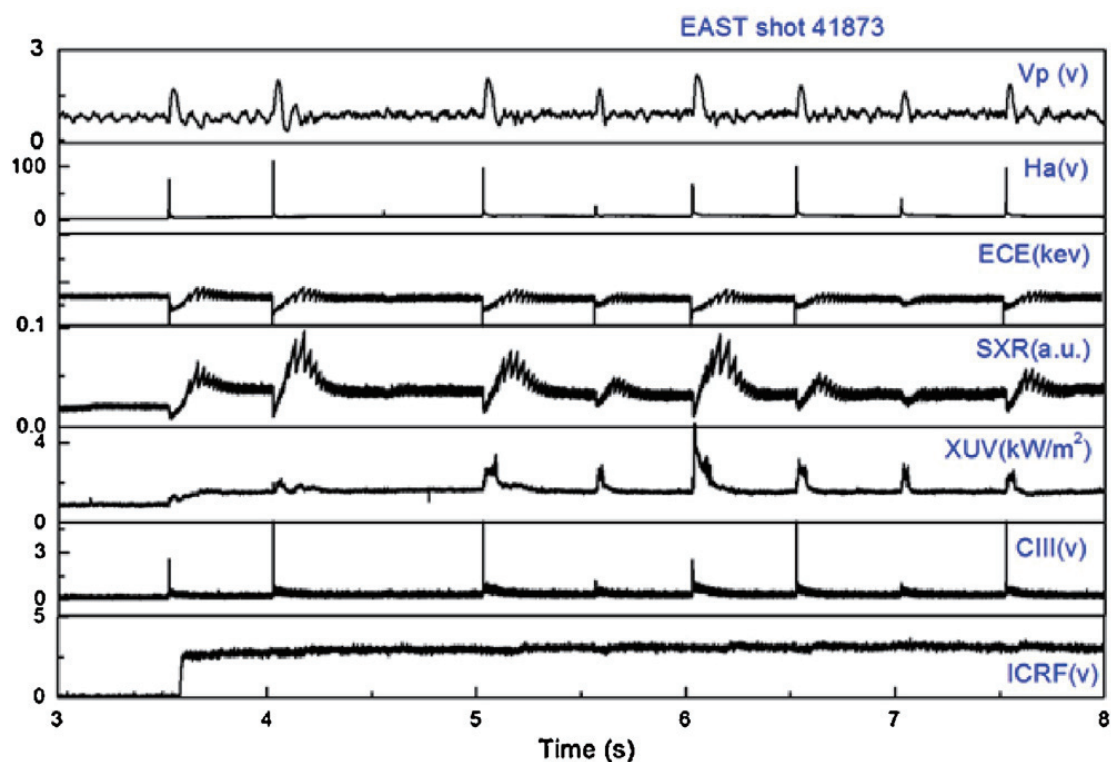
Figure 16. Waveform of LFS pellets injected discharge.

3.3.2. Injection experiments

In the EAST 2012 campaign, single and multi-pellet injection experiments were performed. Pellets were injected into ohmically and LHCD/ICRF heated plasmas. Figure 16 shows nine pellets fired into ICRF heating plasmas in EAST shot 41873. In this shot, the plasma current (IP) ~400 kA, plasma electron density (ne)~2.0×10^{19}m^{-3}, pellet launch velocity (V_p) ~257 m/s. Pellets fired at 3.5 s from low field side and the interval time between each pellet was 500 ms. Except for the third pellet (the pellet might broke during delivery process), other pellets were successfully delivered.

<center>255</center>

A comparison has been made between line-averaged central electron density (R = 1.73 m, the major radius of EAST Ro= 1.75 m) increment from LFS injection and HFS injection. In these two ohmic discharges, IP~400 kA, Bt~2 T, and pellet velocity was ~250 m/s. Results are shown in Figure 17. The density increment from LFS injection is about half of that from HFS injection (0.65 × 10^{19}m^{-3}for LFS while 1.3×10^{19}m^{-3}for HFS). In some cases, however, the density increment caused by single pellet from HFS injection is only a little higher or almost the same as that from LFS injection. The phenomenon indicates that pellets broken and vaporized in the long curved guide tube, thus lead to a lot pellet mass loss. However, it is necessary to install a pellet mass detector such as a micro wave cavity to determine the pellet mass loss in the HFS guide tube later.

Additionally, we found the pellet injection reliability during experiments is lower than bench tests. During bench tests, the liquid helium was supplied for the extruder cooling from a 100 l Dewar vessel. However, during experiments the liquid helium was delivered from the cryogenic valve box (CVB) located far from the injector. The long pipe between the box and the injector some leaded to longer cooling down time and bad quality ice rod sometimes. That would make the pellet more easily to be broken in the convey tube, especially for HFS curved tube. Next, we plan to shorten the pipe length.
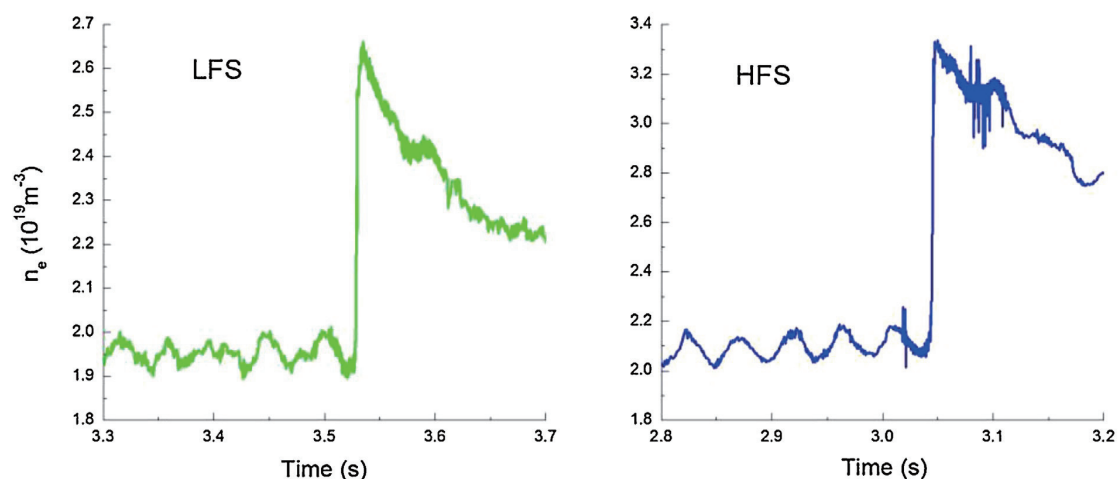
Figure 17. A comparison between density increment caused by single pellet from LFS injection and HFS injection in ohmic discharges.

4. Conclusion

During the 2014 campaign, EAST has a better and more robust gas puffing system to support the experiments. SMBI can strongly reduce the amplitude of ELMs, and enhance the ELM frequency by a factor of 5-10. Both single pulse and multi-pulse can have a long mitigation effect on ELM. Two new SMBI start service for EAST in 2014. We found that SMBI increased the local plasma radiation, and reduce the heat load on the divertor. With the PI-20 injection system, ELM was successfully triggered by D2 pellet injected from LFS with a velocity of approximately 150m/s. The new high pellet injector was assembled in PELIN, and H2 pellets were produced as expected. Together with the two pellet injector, more pellet experiments could be performed in the next campaign.

Acknowledgement

Reference

[1] X.W. Zheng, et al., Plasma Phys. Control. Fusion 55 (2013) 115010
[2] C.Z. Li, et al., Fusion Eng. Des. 89 (2014) 99
[3] Z.B. Shi, et al., Acta Phys. Sin. 56 (2007) 4771
[4] J.S. Hu, et al., Fusion Eng. Des. 84 (2009) 2167
[5] G.Z. Zuo, et al., Plasma Sci. Technol. 12 (2010) 646
[6] B. Cao, et al., Vacuum 86 (2012) 857

Development of flowing liquid lithium limiter on EAST

J. Ren[1], G. Z. Zuo[1], J. S. Hu[1*], Z. Sun[1], Q. X. Yang[1], J. G. Li[1], L. E. Zakharov[2], H. Xie[1], Z. X. Chen[1]

[1] *Institute of Plasma Physics, Chinese Academy of Sciences, 230031 Hefei, China*

[2] *USA Princeton Plasma Physics Laboratory, NJ 08543 Princeton, USA*

ABSTRACT

The application of lithium in fusion reactors has been tested in Tokamak and other magnetic confinement devices for many years. In recent years, the field of fusion has focused on the limiter with a continuously flowing liquid lithium surface called flowing liquid lithium limiter because its ability not only in improving the plasma confinement but in resisting a higher heat flux and particle flux and protecting plasma facing components from plasma by a sacrificial evaporation.

Exploiting the capabilities of the existing material and plasma evaluation system (MAPES) on EAST, a flowing liquid lithium (FLiLi) limiter will be pre-wetted with Li and mechanically translated to the edge of EAST during plasma discharges. In order to drive liquid Li from the collector into the distributor of the limiter, two electrodes have been designed to provide an external voltage at the bottom of the collector. In addition, a simulation of incoming heat flux has shown that the distribution of heat flux on the limiter surface is acceptable for a future test of power extraction on EAST. The reliability and compatibility of a flowing liquid lithium limiter with Tokamak were firstly experimental demonstrated on EAST Tokamak in 2014. During the experiment, it was observed that liquid Li flow was driven electro-magnetically by interaction of the vertical current caused via an external voltage with the toroidal magnetic field of EAST. Besides, it was found that the flowing liquid lithium limiter was effective for absorbing H and resulted in a low ratio of H/(H+D). A significant increase of wall retention rate was also achieved due to the outstanding pumping ability to D particles of flowing liquid lithium limiters. Impurities were decreased by using of limiters as well as using of lithium coating. And it was encouraging to see that effective Z, Dα and XUV radiation reduced the by application of flowing liquid lithium. Most important, it was observed that LiII line radiate along toroidal direction with same horizontal position of limiter during the Li strongly interacting with plasma. In this period of time, the power deposition width on divertor increase and the peak heat load reduced. Moreover, using the flowing liquid lithium limiter, H-mode was achieved with Lower Hybrid Current Drive and neutral beam injection[1].

During this experiment, engineering design of the limiter has been tested. The interaction between lithium and high performance plasmas with long pulse durations has been investigated in this campaign. This test of flowing liquid lithium limiter is an important step forward toward the flowing liquid lithium devertor on EAST.

I. INTRODUCTION

In future fusion devices, traditional solid plasma-facing components (PFCs) are considered only marginally able to endure the high heat flux from a burning plasma and thus able to operate reliably for a sufficient durations.[2]

For example, in the demonstration power plant (DEMO), the steady-state heat-handling capability of the envisioned tungsten divertor design is limited to only about 5–10 MW/m^2.[3] It would be desirable to increase that limit by at least an order of magnitude; however, at present, there is no solid material capable of handling the level of heat flux.

Fortunately, liquid Li, serving as PFC, represents a potential solution to the future problems of power extraction. Li has low ionization energy and can be ionized in the edge of plasma easily. In burning plasmas, bremsstrahlung radiation intensity is related to the Z of impurities. As a low Z impurity, plasma has a higher tolerance for Li. On the other hand, Li could significantly reduce the impurities level in plasma and restrain the recycling in edge due to its high chemical activity and adsorption capacity. And, low edge recycling raises the edge temperature and creates a flattened temperature distribution, which should reduce turbulence driven by temperature gradients in the plasma. Reduced turbulence, which is the main part of anomalous transport, leads to a high particle and energy confinement. Not only has it been demonstrated that liquid Li PFCs can significantly enhance plasma energy confinement; but also it has been proposed they can lead to an innovative Tokamak regime which would significantly reduce the heat flux from plasmas.[4] Further, liquid Li PFCs can resist higher heat and particle fluxes while protecting PFCs from the plasma by sacrificial evaporation.[5]

It had further been reported that reduced impurity levels and edge particle recycling, increased core electron temperature and enhanced energy confinement were achieved by Li coating in TFTR, NSTX, TJ-Ⅱ and EAST.[6-9] Additionally, in CDX-U, FTU and T-11M, by using of different designs of liquid Li limiters, remarkable improvements to plasma performance have been obtained. These improvements include suppression of edge recycling and increased plasma confinement.[10-12] During the process of testing and improving liquid Li limiters in HT-7, not only remarkable physical results were achieved, but some important and practical techniques needed for handling liquid Li were developed.[13, 14]

Encouraged and informed by the previous results with Li, a movable limiter with a continuously flowing liquid Li surface has been designed for EAST. The guiding principle of the limiter concept is based on plasma physics. The limiter design aims at pumping plasma particles using a flowing liquid Li surface at the plasma edge. This pumping will result in a reduction of particle recycling and thus insulation of the plasma edge from the PFCs. This new and radical approach should uniquely address the goals of the EAST program as well as of fusion energy in general.

In particular, successful experiments with FLiLi limiters on HT-7 Tokamak have motivated the design of a more sophisticated FLiLi limiter for use on EAST during the next experimental campaign.[15] The ultimate aim of Li program at ASIPP is to realize a large-area FLiLi divertor on EAST which corresponds to the plasma pumping edge concept. Accordingly, the objectives of the FLiLi limiter are mastering the technologies of continuously flowing Li in a Tokamak while improving the wall conditions for plasma operation.

II. DESIGN OF THE FLiLi LIMITER
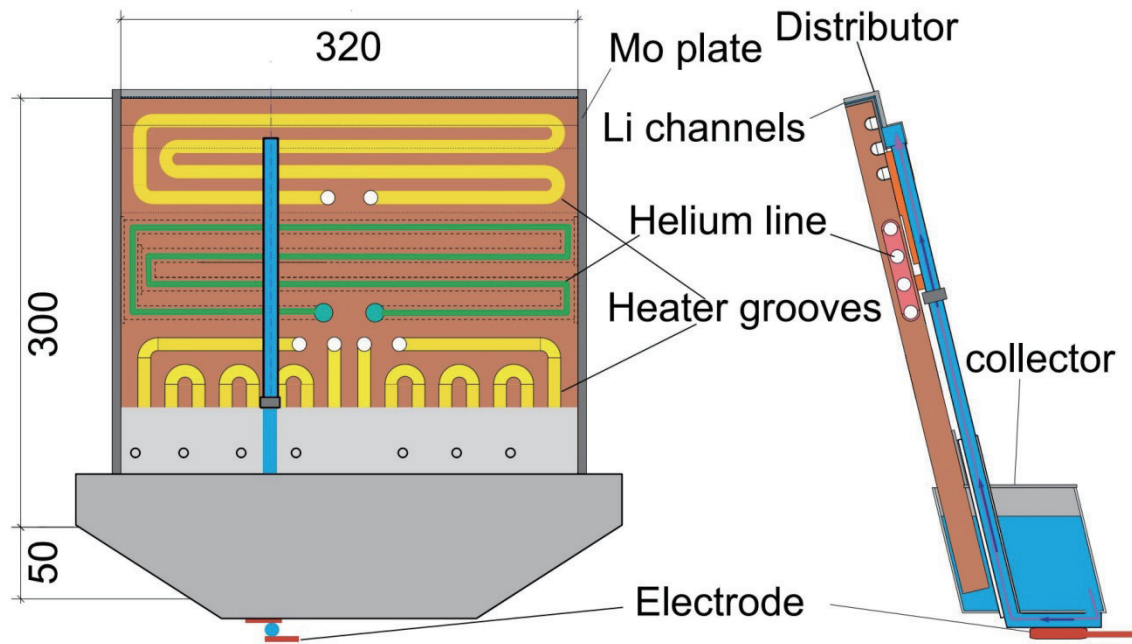
FIG. 1. The FLiLi limiter on EAST. Dimensions are given in mm. The collector is shown as nearly full of liquid Li.

Guided by the experiment objectives, a FLiLi limiter system has been designed and manufactured. The design aimed for simplicity in both structure and manufacturing. For safety reasons the design involves a minimum inventory of Li and uses only low hydrostatic (and electromagnetic) pressure to move that inventory. Further, so as to minimize any effects of corrosion, no mechanical part or joint comes in contact with liquid Li.

As it is shown in Fig. 1, the limiter is composed of two parts: a thick copper plate serving as a thermal heat sink and a Li collector. The copper plate, 350 mm long, 300 mm wide and 19 mm thick, comprises the main body of the limiter. A thick (0.1mm) SS foil brazed to the plasma-facing surface of the copper plate serves as a protective layer between liquid Li and the copper heat sink. In order to provide a uniform supply of Li to the plasma-facing side of limiter, a distributor was developed and positioned at the top of the plate. The distributor employs 200 small (0.8×0.8 mm^2) channels to encourage the gravity-driven viscous flow of liquid Li flow down the plasma-facing surface of the plate. In practice, liquid Li is expected to be guided by gravity and flow slowly (< 10 mm/s) along the plasma-facing guide down to the collector.

Active thermal management of the copper plate - both before and during plasma operation - is critical for the success of the liquid Li limiter concept. Before starting plasma operations with the limiter, it is necessary to wet liquid Li (melting point 182 ℃) onto the thin stainless layer on the plasma-facing side of the copper plate. In order to accomplish the initial wetting, it is desirable to achieve a bulk plate temperature approaching 500 ℃. The heating power required to achieve this elevated temperature is provided by three FeCrAl heating wires each capable of delivering 2.5 kW. These heating units are located in grooves machined into the back surface of the copper plate and insulated by a coating of alumina (Fig. 1). The level of power indicated above should allow for reasonably rapid temperature increases so as to mitigate the oxidation of the stainless steel first surface. As an example, a temperature rise to 350 - 500 ℃ is expected in ~ 5 - 7 minutes.

During plasma operation, the plasma-facing surface of the plate will be limited by the evaporation of liquid Li into the plasma edge. Li evaporation proceeds exponentially with temperature above 400 ℃ and must be kept to level which will be consistent with viable Tokamak operations. Hence to ensure rapid cooling of the copper plate, internal cooling channels have been incorporated into the design as shown in Fig. 1. These channels are part of an active cooling system employing 5 MPa of circulating He gas. In order to monitor the temperature distribution of the plate, 13 thermocouples are attached at various locations on its surface.

The Li collector is a storage vessel for liquid Li which is separated from bottom of the plasma-facing side of the copper plate by a small rectangular gap (Fig. 1). This collector has storage volume of 3.7 liters and is constructed of 1.6 mm welded SS. In case hydrogen produced by lithium-water reaction reaches explosion limit, the lithium stored in collector is limited to less than 2.5 liters. A hole located on the top of collector behind the copper plate is designed to engage with and to accommodate the feed tube at the bottom of the movable Li storage tank in the MAPES exchange box (as described blew). This arrangement allows for the fueling of liquid Li into collector before the limiter is translated to the plasma edge. An additional hole at the bottom of the collector leads directly into a near-vertical distribution tube which is used to supply liquid Li to the distributor at the top of the copper plate against gravity. In order to drive liquid Li from the collector into the distributor, two electric contacts have been designed to provide an external voltage at the bottom of the collector. Two 50 mm long electrode brazed to the upper and lower sides of the horizontal section of the near-vertical distribution tube and provide electric contact with the external low voltage power supply. Upward liquid Li flow will be driven electro-magnetically by interaction of the vertical current caused via the external voltage with the horizontal toroidal magnetic field of EAST by the resulting upward J×B bulk force on the lithium.
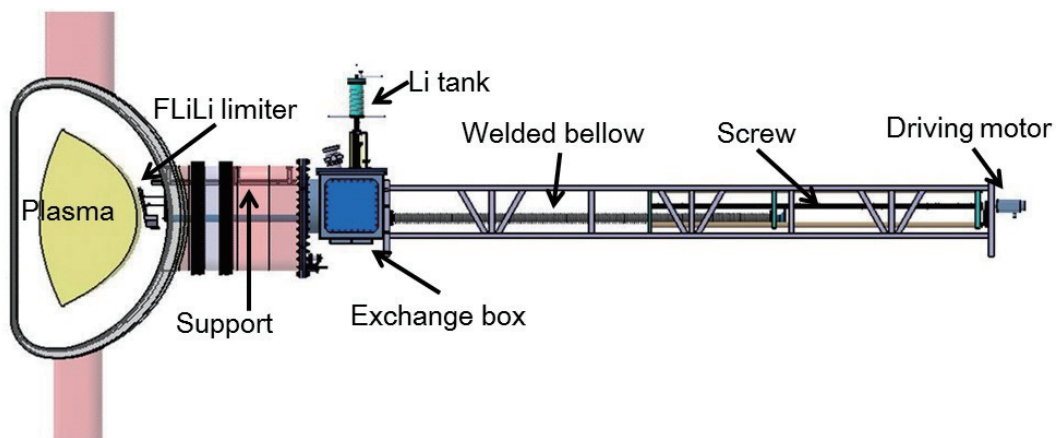
FIG. 2. Overview of the conveyer system based on MAPES.

The FLiLi limiter will take full advantage of the existing MAPES installed at H port on EAST. As shown in Fig. 4, MAPES consists of a 5.8 m long steel scaffold and a step-motor-activated drive screw which can translate objects to the outboard edge of EAST plasmas. In the case of the FLiLi limiter, the necessary copper electric lines, He cooling tubes and thermocouples are connected to the limiter assembly under high vacuum through the long welded bellows (2.6 m stroke) seen in the figure. The collector will be filled with Li from an external overhead tank while being housed in the exchange box (Fig. 3) and the entire limiter unit will then be transported toward the plasma without violating the high vacuum in the plasma chamber. To prevent the vertical displacement of the conveyer rail cause by gravity, a support is installed on the top of the sector H to hang the limiter with a pulley mechanism.

A liquid Li supply system housed on the top of the MAPES exchange box is designed to fill the FLiLi collector and to wet the front surface of limiter prior to positioning inside the EAST vacuum vessel. As it is shown in Fig.3, the supply system consists of a heated movable liquid Li tank terminated by a vertical feed tube. Vertical motion of the entire supply tank is accomplished with a guide screw mechanism and associated bellows. The Li in the vertical feed tube is heated by a thin internal coaxial cartridge heating rod which is able to be translated vertically with respect to the feed tube. Once the Li is melted, the flow of liquid Li through an outlet hole at the bottom of the supply tube is thus initiated by raising the heating rod out of the hole – which is carefully sized to accommodate the rod and prevent the flow of Li. Similarly the flow of Li is terminated by simply lowering the heating rod back into the outlet hole. Once the feed tube engages the collector, the gravitational flow of liquid Li is activated and assisted by pressurized Ar gas applied to the Li tank. A window on an observation port allows for careful monitoring and positioning of the feed tube with respect to the insertion point on the collector.

The procedure used to fill the collector and wet the limiter are as following : 1) deposit solid Li ingots as needed into the external tank and heat to melting, 2) position and insert the feed tube into the hole on the top of collector and inject the liquid Li into the collector to ~ 2/3 full volume, 3) insert the feed tube into the hole in the bottom of the collector (Fig. 1) and fill the distributor box and all associated channels, 4) cause the liquid Li to flow onto the front plate of the limiter using Ar pressure and wet the surface. All of the above steps are accomplished in an Ar atmosphere. After completing preliminary procedures, the FLiLi limiter will be moved to the vacuum chamber for continuous closed-loop operation using electro-magnetic drive (i.e. J×B) drive to cause the Li to circulate between the collector and the front surface of the limiter.
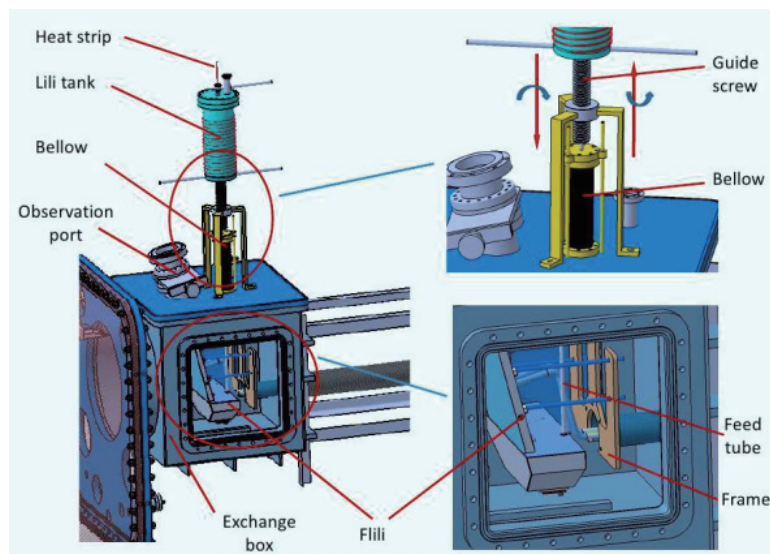
FIG. 3. Overview of the structure of feeding system and illustration of filling and wetting.

Prior to the experiments, the FLiLi system has been installed in the EAST (see Fig. 4) and all critical mechanisms have been tested without Li.

FIG. 4. Two views of the EAST FLiLi limiter assembly. On the left the un-wetted limiter is shown inserted into the EAST vacuum vessel. On the right the limiter is shown in the MAPES exchange box during assembly. The Li supply feed tube is shown inserted into the inlet hole on top of the collector.

III. DESIGN ANALYSIS

A. MHD drop and EM drive

The FLiLi system is designed to generate a thin film of liquid Li distributed uniformly over the large area on the plasma-facing surface of limiter. For this purpose, the design contains a special distributor at the top of the limiter. The distributor is designed to provide a uniform supply of liquid lithium into an array of horizontal channels (0.8x0.8x40 mm^3) between the plasma-facing side and a distributor box filled with liquid lithium on the back side of the copper plate. Liquid Li supplied to the distributor box flows through the channels and spills onto the plasma-facing surface of the limiter. The channels are oriented perpendicular to the toroidal magnetic field. As a result, a magnetohydrodynamic (MHD) drag force is applied to the flow of liquid lithium in the channels. The size and the length of the channels were designed based on the condition that the pressure drop along the channels should be large than the pressure drop between the channels along the distributor box, which is parallel to the toroidal magnetic field. The following formula gives the assessment of the MHD pressure drop along the distributor box and in the channels:

$$\Delta p \cong \sigma^{Li} L \bar{V} B^2 (\frac{\sigma^{SS}}{\sigma^{Li}} d + 2\delta)/(h + \frac{\sigma^{SS}}{\sigma^{Li}} d), \qquad (1)$$

Where L and h are the length and the size of the flow, d is the thickness of SS wall, $\bar{V}$ is the cross-section averaged flow velocity, δ is the Hartmann layer thickness, σ^{Li} and σ^{SS} are the electric conductivity of liquid Li and stainless steel.[16] The MHD pressure drop along the channels $\Delta p_{channels}$ is related to the strong toroidal magnetic field $B_\emptyset$, the total cross-section of 200 channels is 200h^2. The MHD pressure drop Δp_{box} along the distributor box is determined by the poloidal magnetic field $B_\perp$. Invoking the design parameters, the pressure drop along the channels $\Delta p_{channels}$ is much larger than pressure drop along the distributor box Δp_{box}. This guarantees a uniform supply of Li from the channels on distributor.

In addition, the MHD drop in the supply pipe can be assessed by formula (1) or in dimensional form as:

$$\Delta P^{FP} \cong 16000 V_{cm/s}(d/a)B_T^2 L_m. \qquad (2)$$

For the reference design parameters of the EAST FLiLi limiter for EAST, the inner radius of the supply pipe (a) is 5 mm, the wall thickness of the feeding pipe (d) is 0.5 mm, the length of the pipe (L) is 0.5 m, this pressure

can be simplified to $\Delta P^{FP} \cong 800V_{cm/s}B_T^2$. Electric current driven externally across the flow in the vertical direction creates a pressure

$$\Delta P^{j \times B} = 100(I_A/\omega_{cm})B_T, \tag{3}$$

Where I is the current across the flow, and ω is the horizontal width of the flow. This can give an estimate for the current needed to drive the flow, which is written as I= $8\omega_{cm}V_{cm/s}B_T^2$. In the design of FLiLi limiter for EAST, a copper electric line will supply vertical current through the liquid Li, which will be sufficient to drive the Li flow in the magnetic field of EAST. In this design, the horizontal width of the lithium flow is about 1cm, the designed cross-section averaged flow velocity is 1cm/s and toroidal magnetic field is about 2T. So the current across the flow can be estimated as 32A, and the total power required is ~ 20W.

B.   Thermal analysis

Based on experience gained during previous liquid Li experiments on HT-7, successful wetting of the limiter is a critical issue which will determine the results of the future experiment. It has been determined that good temperature control of the guide surface is a requisite for successful wetting. It was reported that higher temperatures of the Li and the guide surface led to a better wetting of the limiter by Li. For Li, the critical wetting temperature of stainless steel is ~ 350℃. Hence it is necessary to keep the temperature of the guide surface above 350℃ to ensure the liquid Li can uniformly wet the limiter surface.

During plasma operation, however, the temperature of the surface must be controlled because the evaporation of Li increases exponentially with temperature about ~ 400℃. The strong heat flux from the plasma also requires thermal monitoring and evaluation to ensure an acceptable limiter temperature.
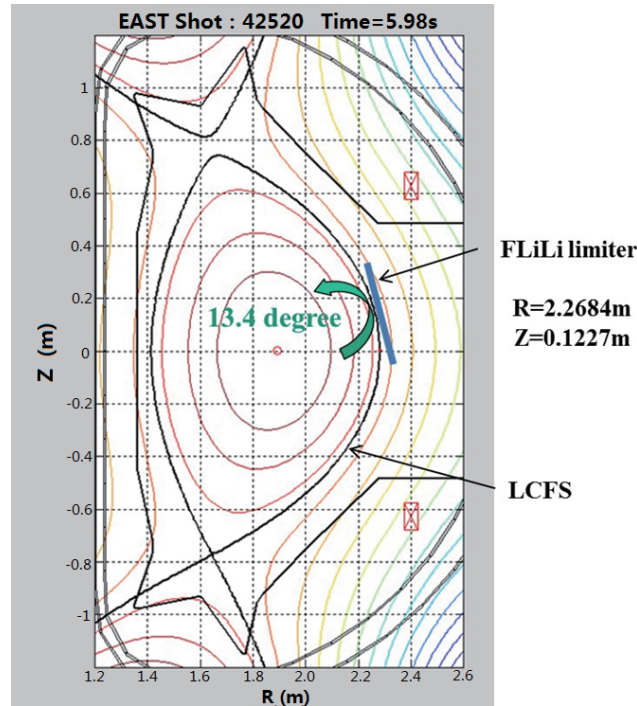
FIG. 5. The postulated location of the FLiLi limiter in shot 42520-a typical EAST divertor discharge. The limiter is positioned close and nearly tangential to the last closed flux surface (LCFS) of the discharge. The limiter plate is oriented at 13.4 degrees with respect to the vertical.

On EAST, the center of the limiter will be located 122.7 mm above the plasma mid-plane. As an initial test, the pre-filled FLiLi limiter will be translated so as to approach the last closed flux surface (LCFS) of the plasma by

using the existing MAPES translation capabilities. In this design, the distance between the deepest position which the limiter / MAPES can achieve and the center of EAST vacuum vessel is ~ 2.26 m. The limiter plane is tilted by 13.4° with respect to the vertical. As an example, shot No.42520 from the most recent EAST experimental run campaign was chosen to evaluate the heat flux on the FLiLi limiter. Shot 42520 was run in double-null configuration with a total injected power of ~ 1.7MW. For this typical divertor discharge, the center of the limiter would have intersected with LCFS at t=5.98s. At this intersection, the LCFS had coordinates of R=2.2684m, Z=0.1227m and tangent to the limiter plane (see Fig. 5). The decrease of plasma parameters along the field lines in the scrape of layer (SOL) with distance to the LCFS is assumed to follow an exponential decay with a characteristic e-folding length λ. Specifically, on the surface of the limiter, the exponential decay of electron density N_e and electron temperature T_e with the distance to the LCFS can be described as:

$$N_e = N_{e0} \exp\left(-\delta/\lambda_{N_e}\right), \tag{4}$$

$$T_e = T_{e0} \exp\left(-\delta/\lambda_{T_e}\right), \tag{5}$$

Where N_{e0} is the electron density at the LCFS, T_{e0} is the electron temperature at LCFS, δ represents the radial distance to the LCFS, λ_{N_e} is the characteristic scale length for radial density decay, and λ_{T_e} is the characteristic scale length for radial electron temperature decay.[17] The incoming heat flux on the limiter surface is related to density and temperature according to the formula:

$$q = q_\parallel \sin\alpha = \gamma N_e C_s T_e \sin\alpha. \tag{6}$$

Where $q_\parallel$ represents the parallel heat flux, C_s is the ion sound speed, T_e is the electron temperature, N_e is the density and α is the angle of magnetic field line tangent to limiter surface.

Using parameters typical for the LCFS and in the SOL (T_{e0}=50eV, N_{e0}=5×10^{18}m^{-3}, $\lambda_{T_e} = \lambda_{N_e}$=15mm), a simulation of incoming heat flux on limiter surface is given in Fig. 6. Because the limiter is flat and therefore not conformal with the toroidal surface of the plasma, the heat flux distribution on the limiter surface is asymmetric and concentrates on the either side of the geometric center as can be seen in Fig 6. Using the parameters given above, the maximum value of the heat flux is approximate 0.8MW/m^2. Based on the heat flux, the temperature distribution on the FLiLi device during a typical discharge can be estimated.[5] The temperature rises on a limiter surface under a heat flux density q (t) can be written as:

$$\Delta T(t) = 1/\sqrt{\pi\rho ck} \int_0^t q(t-t')/\sqrt{t'}\, dt'. \tag{7}$$

To simplify the calculation, it is assumed that the heat flux on the limiter surface is a constant. Hence Eq 7 can be written as:

$$T = T_0 + 2q\sqrt{t/\pi\rho ck}. \tag{8}$$

Where T_0 is the initial temperature of limiter surface, q represents heat flux on the limiter surface, t is the time elapse since initial exposure of the plasma heat flux, c is average specific heat capacity of limiter material, ρ is density of the material and k is thermal conductivity of the material.[18]

For the FLiLi limiter, the initial working temperature of the plate should be from 200℃ to 250℃. Assuming an initial temperature of 230℃, the result from Eq 8 shows the plate surface will rise to 670℃ in 14 seconds. Taking into consider the He cooling system, a simulation of temperature distribution on the FLiLi surface is shown in Fig 7. It can be observed that, with active He cooling system, the temperature increase near the He

cooling tubes (Fig. 1) is significantly reduced. Specifically, the maximum temperature on the limiter surface at t=14 s is only ~ 474°C and the upward trend in temperature obviously slows and tends to rise gently.

The example given above demonstrates that the He cooling system is effective at removing heat and thus at protecting the limiter surface. Hence, in the coming EAST campaign in which the total injected power will be increased to powers over 10 MW, the He cooling system should prove extremely useful. In comparison, the black body thermal radiation power from the limiter can be estimated by $P_r = \sigma S_r T^4$, where σ is Boltzmann constant ($5.669 \times 10^{-8} \text{Wm}^{-2}\text{K}^{-4}$), S_r is the radiating area (~ 0.25m²), T is the thermodynamic temperature. At 400°C, the black body thermal radiation power is ~ 0.012MW/m². Hence comparing with 0.8MW incoming heat flux, the thermally radiated power is a very small quantity. The Li evaporation is related to both temperature and the evaporation surface area according to $G = 3.5 \times 10^{-8} \times e^{(0.015T)} \times T^{-0.5} \times S$, where T is temperature of the evaporation surface and S is evaporation area. At 400°C, the calculated Li evaporation rate is ~ 6.77×10^{-4} g/s, from the 320×300 mm² limiter surface, which is far less than the 2cm³/s flow rate and has a negligible effect on the limiter thermal balance. In the thermal simulations the He cooling was the dominant factor. Further, this thermal simulation demonstrated an acceptable heat removal capability.
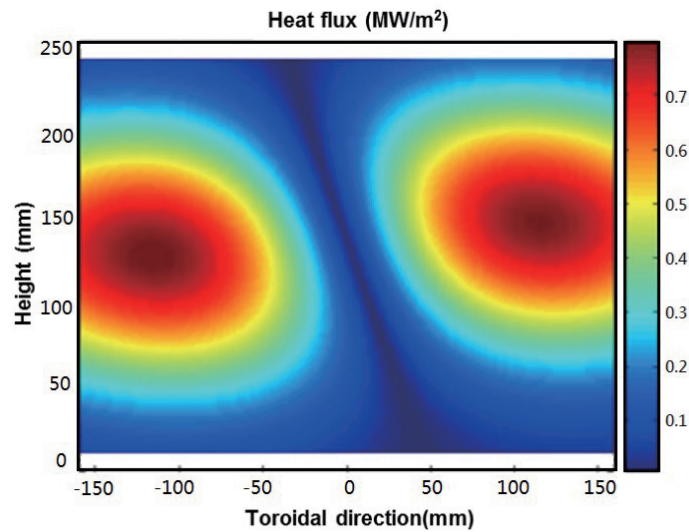
FIG. 6. Incoming heat flux distribution on the FLiLi surface.
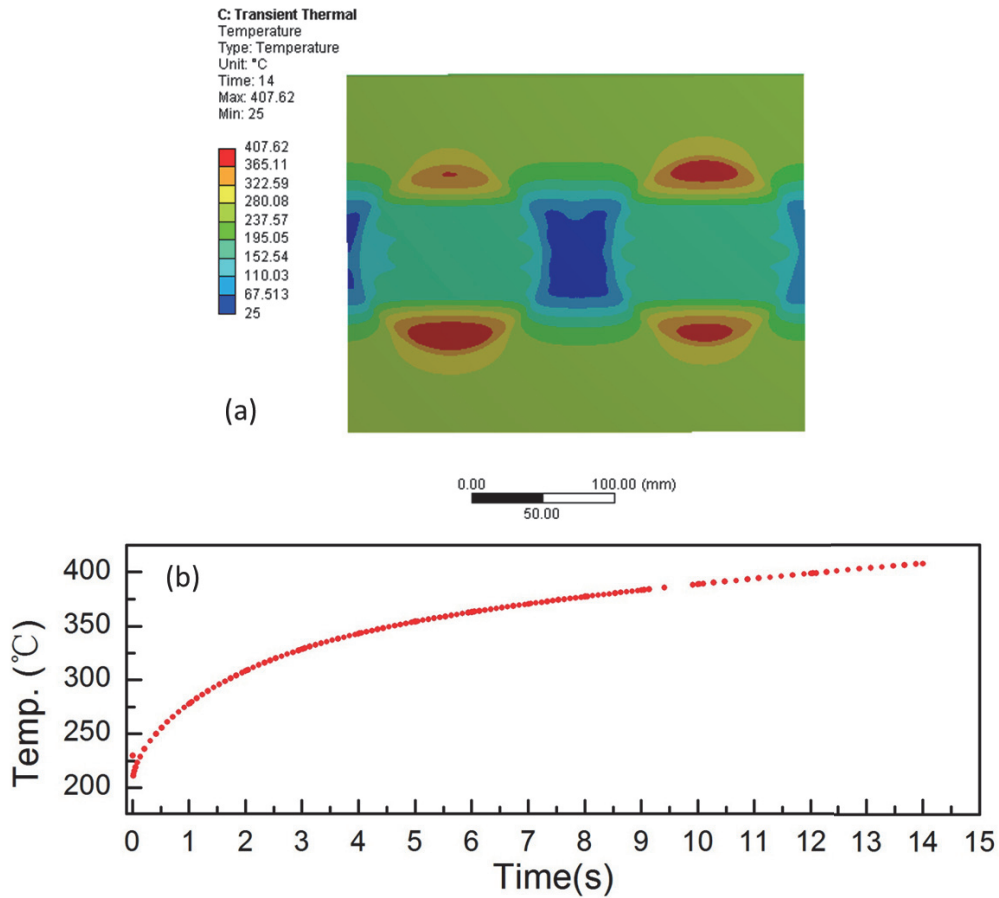
FIG. 7. Temperature distribution on the limiter surface at 14 s (a) and temperature rising curve of the maximum temperature point in 14 s (b).

IV. EXPERIMENTAL RESULTS

The FLiLi limiter experiment has been performed on EAST in October 2014. The feasibility of the design and the compatibility of FLiLi limiter and plasmas had been proved by this experiment. During the experiment, FLiLi limiter was located 65.8mm before to main limiter and almost touched the LCFS. When DC current was applied on the electrodes at the bottom of the collector to drive the liquid Li, it was clearly observed that the LiI and LiII line produced by interaction of plasma and liquid Li at both surface of limiter and edge plasma were very strong. This indicated that the liquid Li had can be driven electro-magnetically to flow on the surface of the limiter after application of DC driving current. Further, it was found the flow rate of the liquid lithium can be controlled by adjusting the DC current. Beside, during the operation of FLiLi limiter, the maximum temperature of the limiter was 435℃. Overall, experimental results showed a good consilience with the designed parameters. On the other hand, decreased impurities level, repressed edge recycling and improved quality of plasma were achieved by using of FLiLi limiter. Also, H-mode was obtained by NBI and LHCD injection while using the FLiLi limiter. Most noticeably of all, it was firstly found that heat load indicated by ion saturation current on divertor significantly reduced and its deposition width increased while using the FLiLi limiter on EAST. It was indicated that Li could provide a shielding from heat flux in edge plasma by evaporation.

V. SUMMARY

Based on experience gained during liquid Li experiments carried out on the HT-7 Tokamak, estimates related to magneto-hydrodynamics liquid lithium flow and heat flux distribution have informed a design of a FLiLi limiter system for the EAST Tokamak. An advanced FLiLi limiter system aimed at achieving a movable plasma-facing limiter surface with continuously flowing liquid Li has been designed and manufactured. The mechanical system (i.e. MAPES) needed for transporting the limiter through the H-port of EAST and for prefilling the limiter with liquid Li were tested in the EAST environment in March 2014 without plasma or lithium. Real lithium operation with plasma discharges has been performed in October 2014 on EAST. During this campaign, interactions between Li and high performance plasmas with long pulse durations have been investigated. The engineering design of the limiter has been tested during this campaign as well. This test of the FLiLi limiter was an important step forward toward the future implementation of a FLiLi divertor on EAST.

ACKNOWLEDGMENTS

REFERENCES

[1] J. Ren, G. Z. Zuo, J. S. Hu, et al., The Review of scientific instruments **86**, 023504**,** (2015).

[2] M. A. Jaworski, T. Abrams, J. P. Allain, et al., Nuclear Fusion **53,** (2013).

[3] M. Ono, M. A. Jaworski, R. Kaita, et al., Nuclear Fusion **53,** (2013).

[4] L. E. Zakharov, N. N. Gorelenkov, R. B. White, S. I. Krasheninnikov and G. V. Pereverzev, Fusion Engineering And Design **72**, 149**,** (2004).

[5] G. Mazzitelli, M. L. Apicella, A. Alexeyev and F. Team, Fusion Engineering and Design **86**, 580**,** (2011).

[6] D. K. Mansfield, K. W. Hill, J. D. Strachan, et al., Phys. Plasmas **3**, 1892**,** (1996).

[7] H. W. Kugel, D. Mansfield, R. Maingi, et al., Journal of Nuclear Materials **390-91**, 1000**,** (2009).

[8] F. L. Tabares, M. A. Ochando, F. Medina, et al., Plasma Phys Contr F **50,** (2008).

[9] G. Z. Zuo, J. S. Hu, J. G. Li, et al., Journal of Nuclear Materials **438**, S90**,** (2013).

[10] R. Majeski, S. Jardin, R. Kaita, et al., Nuclear Fusion **45**, 519**,** (2005).

[11] G. Mazzitelli, M. L. Apicella, D. Frigione, et al., Nuclear Fusion **51,** (2011).

[12] S. V. Mirnov, E. A. Azizov, V. A. Evtikhin, et al., Plasma Phys Contr F **48**, 821**,** (2006).

[13] Z. Sun, J. S. Hu, G. Z. Zuo, et al., Journal of Nuclear Materials **438**, S899**,** (2013).

[14]Q. X. Yang, W. L. Zhao, Y. S. Wang, et al., Fusion Engineering and Design **88**, 1646**,** (2013).

[15]J. Ren, J. S. Hu, G. Z. Zuo, et al., Phys Scripta **T159**, 014033**,** (2014).

[16]C. C. Chang and T. S. Lundgren, Zeitschrift für angewandte Mathematik und Physik **12**, 110**,** (1961).

[17]R. Mitteau, A. Moal, J. Schlosser and D. Guilhem, Journal of Nuclear Materials **266–269**, 798**,** (1999).

[18]J. P. Allain, D. G. Whyte and J. N. Brooks, Nuclear Fusion **44**, 655**,** (2004).

Program of A3 Workshop in Nanning
(6-9 January 2015)

5 January 2015 (Monday)
Registration: 16:00--23:00

Research Category:

Category I: Steady state sustainment of magnetic configurations
   (Current drive and profile control)

Category II: Edge and divertor plasma control
   Category IIa: Transport of edge and divertor plasmas
   Category IIb: Stability of edge plasma

Category III: Confinement of alpha particles
 (Interaction of energetic particle and bulk plasma)

Category IV: Theory and simulation

6 January 2015 (Tuesday)

Session 1 (Opening) Chair: Prof. L.Q. HU	8:30		Welcome speech from ASIPP
	8:45		Meeting announcement
	8:50	Satoru SAKAKIBARA (NIFS)	Recent Progress of LHD Experiments
	9:15	Yeong-Kook OH (NFRI)	Status of the KSTAR operation and upgrade
	9:40	Young-soon BAE (NFRI)	Recent results of long pulse discharge and prospect of steady-state operation in KSTAR
	10:05	Liang WANG (ASIPP)	Recent progress in EAST towards long-pulse high-performance operations
Tea & Coffee Break 10:30-10:50			
Session 3 (Category I) Chair: Prof. Y.K. OH	10:50	Jeehyun KIM (NFRI)	KSTAR LHCD system operation in 2014 campaign
	11:15	Bojiang DING (ASIPP)	Introduction of first LHCD experiments with 4.6GHz system in EAST
	11:40	Jianshen HU (ASIPP)	New steady-state quiescent high confinement plasma in Experimental Advanced Superconducting Tokamak
	12:05	Wenhao WANG (Tsinghua Univ.)	Recent experimental activities in the SUNIST spherical tokamak
Group photo 12:30-12:40 (Entrance A of the Hotel)			
Lunch 12:30-14:00			
Session 4 (Category II) Chair: Prof. M.Y. Ye	14:00	Won-Ha KO (NFRI)	Dynamics of Pedestal Rotation and Ion Temperature Profile Evolution in KSTAR
	14:20	Shigeru MORITA (NIFS)	Tungsten pellet injection in LHD
	14:40	Zhipeng CHEN (HUST)	Investigation of Turbulent Particle and Momentum Transport with Electrode Biasing on J-TEXT Tokamak
	15:00	Tomohiro MORISAKI (NIFS)	Particle transport analyses using transient MHD events and proposal of a new two-dimensional diagnostics
	15:20	Haiqing LIU (ASIPP)	Study of equilibrium current density profile and internal density and magnetic fluctuations with Faraday-effect polarimeter-interferometer system on EAST Tokamak
	15:40	Shoubiao ZHANG (ASIPP)	Experimental study of pedestal turbulence using reflectometry diagnostics on EAST tokamak
Tea & Coffee Break 15:40–16:00			
Session 5 (Category II) Chair: Prof. Y.S. Bae	16:20	Tetsutaro OHISHI (NIFS)	VUV spectroscopy for WVI line spectrum in Large Helical Device
	16:40	Daiji KATO (NIFS)	Near UV-visible line emission from tungsten highly-charged ions in Large Helical Device
	17:00	Ling ZHANG (ASIPP)	A Fast-Response Extreme Ultraviolet Spectrometer for Measurement of Impurity Line Emissions in EAST
	17:20	Chunfeng DONG (SWIP)	Preliminary result and initial analysis onradial profiles of impurity line emissions measured with EUV spectrometer on HL-2A
	17:40	Bo LV (ASIPP)	Impurity behavior and molybdenum transport study on EAST
	18:00	Liqing XU (ASIPP)	Repetitive Snakes in EAST Multiple H-L-H Plasmas
Dinner 18:30-20:00			

7 January 2015 (Wednesday)				
Session 6 (Category I) Chair: Prof. Y. Liu	8:30	Jinhyun JEONG (NFRI)	Upgrade activities of long pulse and steady-state operation in KSTAR ECH/CD system	
	8:50	Sonjong WANG (NFRI)	The characteristics of RF heating in KSTAR	
	9:10	Haejin KIM (NFRI)	Enhancement of RF coupling power by surface treatment on the vacuum feed-through for 2014 KSTAR experiments	
	9:30	Chengming QIN (ASIPP)	Current status of ICRF system on EAST	
	9:50	Bingjia XIAO (ASIPP)	Plasma control for snow-flake configuration	
Tea & Coffee Break 10:10–10:30				
Session 7 (Category III) Chair: Prof. T. MORISAKI	10:30	Yasushi TODO (NIFS)	Validation of Comprehensive Magnetohydrodynamic Hybrid Simulations for Alfvén Eigenmode Induced Energetic Particle Transport in DIII-D Plasmas	
	10:50	Youjun HU (ASIPP)	Simulation of energetic particles driven Alfvén eigenmodes on EAST tokamak	
	11:10	Limin YU (EAST China UST)	Study of the reversed shear Alfvén eigenmodes with down sweeping frequency in the HL-2A experiment at $q_{min} \sim 1$	
	11:30	Tieshuan FAN (Peking Uni.)	Development and Testing of the Time-of-Flight Enhanced Diagnostics (TOFED) Neutron Spectrometer at EAST	
	11:50	Yi LIU (SWIP)	Development of the fusion-neutron diagnostics for the HL-2Atokamak	
	12:10	Guoqiang ZHONG (ASIPP)	Preliminary experiments study the behaviour of fast ions in NBI heating plasma on EAST	
Lunch 12:30-14:00				
Session 8 (Category II) Chair: Prof. Y. TODO	14:00	Suk-Ho HONG (NFRI)	Study on plasma-metal wall interaction in KSTAR	
	14:20	Guangnan LUO (ASIPP)	Development of W/Cu divertor for EAST	
	14:40	Haishan ZHOU (ASIPP)	Effects of surface conditions on hydrogen plasma-driven permeation through a ferritic steel alloy: F82H	
	15:00	Jayhyun KIM (NFRI)	Exploration of low q_edge regime in KSTAR	
	15:20	Hyunyong LEE (KAIST)	Development of impurity particle injection systems for impurity transport study in KSTAR	
Tea & Coffee Break 15:40–16:00				
Session 9 (Category IV) Chair: Prof. Suk-Ho Hong	16:00	Mitsutaka ISOBE (NIFS)	LHD Fusion Product Diagnostics	
	16:20	Ichihiro YAMADA (NIFS)	Electron temperature measurement using backward and forward Thomson scatterings in the LHD Thomson scattering system	
	16:40	Satoshi OHDACHI (NIFS)	Heat pulse propagation experiments with the MHD event for the estimation of the magnetic field topology	
	17:00	Deng ZHOU (ASIPP)	The Residual Zonal Flow in Toroidally Rotating Tokamak Plasmas	
	17:20	Minho KIM (POSTECH)	Commissioning of Hard-X ray System on KSTAR	
	17:40	Bin CHEN (USTC)	Simulation of the divertor heat load for CFETR	
Dinner 18:30-20:00				

8 January 2015 (Thursday)	
Session 10 **Joint** **discussion** (Category I) Chair: Prof. L.Q. Hu	**08:30-10:20 Plenary meeting on future collaboration at category I**
	Plasma heating and current drive, Prof.B.J. Ding Active plasma control, Prof.B.J. Xiao Integrated modelling, Dr.Y.J. Hu MHD instability control, Prof. B. Shen Wall conditioning and effects, Prof.J.S. Hu
	Tea & Coffee Break 10:20–10:40
Session 11 **Joint** **discussion** (Category II) Chair: Prof. Y.K. OH	**10:40-12:30 Plenary meeting on future collaboration at category II**
	Plasma-wall interaction and edge plasma modelling, Prof.G.N. Luo Control of particle and power load, Dr. L. Wang Structure and evolution of pedestal, Dr. S.B. Zhang and Y. Liu Edge plasma diagnostics, Dr.Z.J. Wang The interplay between core, SOL and pedestal, Prof.Y.X. Jie and Dr.L. Zhang
	Lunch 12:30-14:00
Session 12 **Joint** **discussion** (Category III) Chair: Prof. S. MORITA	**14:00-15:30 Plenary meeting on future collaboration at category III**
	Destabilisation of Alfvén waves and Energetic Particle Modes, Prof.Y. Liu Interaction of fast ions with background MHD, Prof. L.Q. Hu Runaways control and simulation, Dr.J. Liu Modification of the PFW by incident particles, Prof.J.L. Chen Identification of the fast particle modes, Prof. Y. Liu
	Tea & Coffee Break 15:30–16:30
Session 13 (Category IV) Chair: Ass. Prof. S.H. Dong	**16:30-18:00 Plenary meeting on future collaboration**
	Education of young scientists and Ph.D students Discussion on coordinator meeting, school, budget and administrative works Discussion on annual report of A3 collaboration, mid-term evaluation Discussions on coming seminar and workshop plans, future study related to A3 collaboration Discussion on personnel exchange, hardware construction and operation of diagnostics and heating devices
Dinner	**18:30-20:00**

9 January 2015 (Friday)			
Session 14 (Category I) Chair: Prof. B.J. Xiao	8:30	Hyun-Seok KIM (SNU)	Multiple control algorithm of plasma profiles and neoclassical tearing mode in a tokamak
	8:45	Ting LAN (ASIPP)	The geometric phase measurement of Faraday rotation angle on EAST tokamak
	9:00	Jianyuan XIAO (USTC)	Numerical simulation on nonlinear effects in extraordinary to Bernstein mode conversion
	9:15	Yulei WANG (USTC)	Simulation of Long-term Dynamic Behavior of Runaway Electrons
	9:30	Wentao WU (USTC)	Stochastic simulation of runaway electrons
	Tea & Coffee Break 09:45–10:05		
Session 15 (Category II) Chair: Prof. Jeehyun Kim	10:05	Joohwan HONG (KAIST)	Effects of non-resonant magnetic perturbation on impurity transport in KSTAR L-mode plasma
	10:20	Juhyeok JANG (KAIST)	Development of multi-energy soft X-ray array diagnostics on KSTAR for MHD mode structure analysis
	10:35	Hongming ZHANG (Sokendai)	Analysis on edge magnetic structure and poloidal distribution of edge impurity emissions in Large Helical Device
	10:50	Xianli HUANG (Sokendai)	Analysis of Z_{eff} Profiles Based on Space-Resolved Measurement of Extreme Ultraviolet Bremsstrahlung in the Large Helical Device
	11:05	ZongXU (ASIPP)	Filterscope diagnostic System on EAST tokamak
	11:20	Hongmin MAO (ASIPP)	First spectroscopic observation on W source at EAST upper divertor
	11:35	Neng PU (ASIPP)	Neutron fluctuation diagnostic on EAST
Lunch	**12:00-14:00**		
Session 16 (Category II) Chair: Prof. S. SAKAKIBARA	14:00	Ayub Muhammad KHAWAR (POSTECH)	ELMs Observation by using KSTAR MIR system
	14:15	Jieun LEE (POSTECH)	Rapid structural changes of the edge localized modes in the KSTAR tokamak
	14:30	Zhengkun HAO (ASIPP)	Transmission Simulation and Shielding Design of Microwave for EAST Bolometer diagnostic system
	14:45	Manni JIA (Donghua Univ.)	Numerical Modeling and Some Experimental Comparison Results of 3D Magnetic Field Topology under Resonant Magnetic Perturbations on EAST
	Tea & Coffee Break 15:00–15:20		
Session 17 (Category III) Chair: Prof. T.S. Fan	15:20	Guangming CAO (ASIPP)	The observation of broadband microturbulence during beta-induced Alfvén eigenmode activity in the EAST superconducting tokamak
	15:35	Guojiang WU (ASIPP)	Bifurcation of negative radial electric field due to ion orbit loss in the tokamak edge plasma during L-H transition
	15:50	Houyin WANG (ASIPP)	Advanced pressure measurement using fast gauge and penning spectrum detector
	16:05	Xingjia YAO (ASIPP)	Development of plasma fueling on EAST
	16:20	Jun REN (ASIPP)	Flowing lithium experiments on EAST
Session 18 (Summary & Closing)	16:35	TBD	A3 collaboration in past 10 years
	17:00	Liqun HU Shigeru MORITA Yeong-Kook OH	Summary reports
	17:10	Yeong-Kook OH (NFRI)	Next meeting
	17:20	Liqun HU (ASIPP)	Meeting closing
Dinner	**18:00-20:00**		

（END）

List of Participants

Name	Affiliation
BAE Young-soon	NFRI
CAO Guangming	ASIPP
CHEN Bin	USTC
CHEN Zhipeng	HUST
DING Bojiang	ASIPP
DONG Chunfeng	SWIP
FAN Tieshuan	Peking Univ.
HAO Zhengkun	ASIPP
HONG Suk-Ho	NFRI
HU Jiansheng	ASIPP
HU Youjun	ASIPP
HUANG Xianli	Sokendai
ISOBE Mitsutaka	NIFS
JANG Juhyeok	KAIST
JEONG Jinhyun	NFRI
JIA Manni	Donghua Univ.
KATO Daiji	NIFS
KHAWAR Ayub Muhammad	POSTECH
KIM Haejin	NFRI
KIM Hyun-Seok	SNU
KIM Jayhyun	NFRI
KIM Jeehyun	NFRI
KIM Minho	POSTECH
KO Won-Ha	NFRI
LAN Ting	ASIPP
LEE Hyunyong	KAIST
LEE Jieun	POSTECH
LIU Haiqing	ASIPP
LIU Yi	SWIP
LUO Guangnan	ASIPP
MAO Hongmin	ASIPP

MORISAKI Tomohiro	NIFS
MORITA Shigeru	NIFS
OH Yeong-Kook	NFRI
OHDACHI Satoshi	NIFS
OHISHI Tetsutaro	NIFS
PU Neng	ASIPP
QIN Chengming	ASIPP
REN Jun	ASIPP
SAKAKIBARA Satoru	NIFS
SHEN Yongcai	Anqing normal Univ.
TODO Yasushi	NIFS
WANG Houyin	ASIPP
WANG Liang	ASIPP
WANG Sonjong	NFRI
WANG Wenhao	Tsinghua Univ.
WANG Yulei	USTC
WU Guojiang	ASIPP
WU Wentao	USTC
XIAO Bingjia	ASIPP
XIAO Jianyuan	USTC
XU Liqing	ASIPP
XU Zong	ASIPP
YAMADA Ichihiro	NIFS
YAO Xingjia	ASIPP
YU Limin	ECUST
ZHANG Hongming	Sokendai
ZHANG Ling	ASIPP
ZHANG Shoubiao	ASIPP
ZHONG Guoqiang	ASIPP
ZHOU Deng	ASIPP
ZHOU Haishan	ASIPP